Harokopio University of Athens, Department of Geography

Long and short term monitoring of ground deformation in Thessaly basin using space-based SAR Interferometry

A dissertation presented to the council
Of Department of Geography
Of Harokopio University of Athens
In partial fulfillment of the requirements for the degree of Doctor of Philosophy

By

Falah Atta Fakhri

Athens June 2013

Harokopio University of Athens, Department of Geography

Long and short term monitoring of ground deformation in Thessaly basin using space-based SAR Interferometry

A dissertation presented to the council
Of Department of Geography
Of Harokopio University of Athens
In partial fulfillment of the requirements for the degree of Doctor of Philosophy

By

Falah Atta Fakhri

Athens June 2013

Harokopio University of Athens, Department of Geography

Long and short term monitoring of ground deformation in Thessaly basin using space-based SAR interferometry

A PhD dissertation

Athens, 2013

PhD Examination committee

Tripartite consultative committee:

Assistant Professor Issaak Parcharidis, Department of Geography, Harokopio University of Athens.

Professor George Mighiros, Lab Mineralogy and Geology, Agricultural University of Athens.

Assistant Professor Efthimis Karymbalis, Department of Geography, Harokopio University of Athens.

Members of the seven-member committee:

Professor Kosmas Pavlopoulos, Department of Geography, Harokopio University of Athens.

Professor George Stamatis, Lab Mineralogy and Geology, Agricultural University of Athens.

Assistant Professor Petros Katsafados, Department of Geography, Harokopio University of Athens.

Assistant Professor Konstantinos Nikolakopoulos, Department of Geology Faculty of Science, University of Patras.

Acknowledgments

First and foremost I owe thanks to my God, Allah most gracious and most merciful, who helps me and gives me patience to accomplish this work.

Many thanks are also due to my family for supporting me.

I am thankful to Dr Issaak Parcharidis, who gave me this opportunity, and to other two supervisors within my tripartite commission, Dr George Mighiros, and Dr Efthimis Karymbalis, for enabling me to realize this work, and my thanks go to the discussion committee for their opinions, which improved this dissertation. Many thanks also go to the State Scholarships Foundation. I would like to express deep gratitude to Dr Psomiadis Emmanouil and Dr Kosmas Pavlopoulos who encouraged me to pursue this work. Many thanks are also owed Dr Urs Wegmuller for giving me his time and opinions during the accomplishment of my dissertation

I would like to acknowledge the European Space Agency (ESA) for providing the ERS_1/2, ENVISAT ASAR data. Also deep thanks go to Decentralized Administration of Thessaly .for providing the groundwater monitoring data.

Many gratitude alos go to Dr. Leonidas Toulios Senior Researcher at the National Agricultural Research Foundation (NAGREF) for providing the soil data.

I would like to express my thanks to Ms Zoi Foulidi, who helped me to carry out all the administrative work relevant to my dissertation during four years.

Last but not least I am thankful to each person who helped me to achieve this work.

Falah A. Fakhri
Athens, 2013

Dedication

To the person of who gives me hope ... my mother.

To my father soul … God’s mercy.

To my daughter Shams and my son Abd-al rahman … flowers of my life.

To the people who open for me the gates of hope and give me the chance to be and to build my thoughts.

To my wounded country… Iraq.

Contents

List of Figures

CHAPTER ONE

CHAPTER TWO

CHAPTER THREE

CHAPTER FOUR

CHAPTER FIVE

CHAPTER SIX

List of Tables

CHAPTER TWO

CHAPTER THREE

CHAPTER FOUR

CHAPTER FIVE

Abstract

This research study is conducted in the eastern part of northern Thessaly, which is located in the middle of Greece and has a total area of 3113.834 km^2. This study area suffers from natural and human hazards which have gradual and rapid impacts and which as a consequence threaten the stability of civil infrastructure and moreover agricultural projects. They are related to huge groundwater withdrawal for agricultural irrigation as well as other uses, type of lithology, active normal faults which cross the study area, earthquakes, and many other minor factors.

According to the historical seismicity, the study area is characterized as having medium to high seismicity due to the fact that the last earthquake of high magnitude (Ms = 6.1) occurred in 1941. However, according to the literature no earthquake with a magnitude greater than Mw = 4 has been observed since 1941.

Given the scientific fact that no earthquake with a magnitude greater than Mw = 4 has been observed since 1941. Furthermore the scientific demands to identify and investigate the causes of low magnitudes earthquakes which have occurred within the study area after 1941 so far. Additionally to investigate the constant and dramatic influences of groundwater withdrawal on the (objects) stabilization which are located within or on the ground; moreover the impact of other participating parameters on ground deformation such as type of lithology and soil. In addition to verifying from the ability of applying Synthetic Aperture Radio detection and ranging Interferometry (SAR Interferometry) techniques to identify ground deformation phenomena resulting from any causes within urban and non-urban areas, this research has been implemented.

Consequently the objectives of this study are to verify the possibility of implementing SAR interferometric techniques to detect short- and long-term deformation as well as to investigate the factors that affect ground deformation within the study area.

Three interferometric SAR techniques have been implemented using GAMMA Software (S/W): the Conventional, Stacking Interferometric, and Persistent Scatterer Interferometric (PSI) techniques. Two datasets from the Earth Resources Satellites (ERS1/2) and the Advanced Synthetic Aperture Radar Environmental Satellite (ASAR ENVISAT) of ascending and descending tracks have been used during the periods 1995–2008 and 1992–2010, respectively.

The results were as follows:

- The results of three techniques within ascending and descending tracks indicate that subsidence and uplift deformations are distributed over the whole of the study area.

- No interferometric deformation patterns have been observed within agricultural fields by implementing the interferometric stacking technique of ascending and descending tracks; however interferometric deformation patterns are confined to urban and mountain areas.

- Interferometric deformation patterns have been observed within urban and agricultural areas through the application of conventional techniques with ascending and descending tracks by applying period of short-term.

- The results of interferometric stacking of the descending track indicate a low distribution of patterns density in comparison with the ascending track; furthermore the number of candidate points within the descending track is smaller than the number of candidate points in the ascending track. An interpretation of this case is occurred in pairs between different seasons typically encounters stronger atmospheric effects (in particular stronger height-dependent atmospheric effects).

- The results showed that the descending track had more difficult phases to unwrap and this may reduce the spatial coverage achieved.

- A direct correlation has been found between the number of inteferograms and the average coherence with ascending and descending tracks within the urban area. However, an inverse correlation has been found between the number of inteferograms and the average coherence within agricultural fields.

- A direct correlation has been found between the long perpendicular baseline and the result for the number of interferograms. In addition a direct correlation has been found between wrapped phases and the long perpendicular baseline.

- A significant correlation has been found between fluctuation of the groundwater level and land deformation within the ascending and descending tracks, despite the short time series data of the ascending track (1995–2006) and the long distance between boreholes and many point candidates of PSI relevant to the descending track. This may be attributable to the short distances between boreholes and many point candidates regarding the ascending track or to the large range of the time series data (1992–2010) of the descending track.

- The results of the conventional technique point to seasonal deformation. This is attributed to the fluctuation of groundwater level, which plays an important role through its impact on ground deformation during short time periods of up to one month.

- Differences in the ground deformation rate of the same settlements resulting from the interferometric stacking technique of two tracks, ascending and descending, may be attributed to the difference between the numbers of interferograms within each interferometric stacking result, since there were 29 items within the ascending track and 70 items within the descending track. Furthermore, there were differences between the time periods of the radar images within each track and between the locations of reference points within each track.

- The persistent scatterer technique, through the application of spatial correlation between the locations of candidate points and fault traces, reveals and/or indicates the possibility of the influence of fault movements on ground deformation.

- The other main reason for deformation is the compaction of materials induced by water pumping and this is related to local deformation. This compression of materials may produce a micro-seismic magnitude (3 to 4).

- SAR interferometry techniques successfully revealed the impact of lithology type on ground deformation through the ascending and descending tracks.

- Many of the parameters participated together furthermore have nested impacts on ground deformation within the study area as well as it is difficult to completely isolate the influence of each single parameter individually in spite of applying statistical correlation.

Περίληψη

Η παρούσα διδακτορική διατριβή πραγματοποιήθηκε στο ανατολικό τμήμα της βόρειας Θεσσαλίας, το οποίο βρίσκεται στην Κεντρική Ελλάδα και έχει συνολική έκταση 3113.834 km^2. Η περιοχή μελέτης χαρακτηρίζεται από πλήθος φυσικών και ανθρωπογενών κινδύνων που έχουν τόσο σταδιακές όσο και ταχείες επιπτώσεις και οι οποίες έχουν ως συνέπεια τη δημιουργία μιας απειλής προς τη σταθερότητα της αστικής υποδομής και των αγροτικών έργων. Έχουν σχέση με την τεράστια υδρομάστευση των υπόγειων υδάτων για γεωργική άρδευση, καθώς και άλλες χρήσεις, με το είδος λιθολογία, τα κανονικά ρήγματα που δραστηριοποιούνται στην περιοχή μελέτης, τους σεισμούς, και πολλούς άλλους μικρότερης σημασίας παράγοντες.

Σύμφωνα με το ιστορικό των σεισμών, η περιοχή μελέτης χαρακτηρίζεται να έχει μία μέση προς υψηλή σεισμικότητα, η οποία οφείλεται στο γεγονός ότι ο τελευταίος μεγάλος σεισμός (Ms = 6.1) εμφανίστηκε το 1941. Ωστόσο, σύμφωνα με τη βιβλιογραφία δεν υπάρχει σεισμός με μέγεθος μεγαλύτερο από Mw = 4 μετά το 1941.

Πρέπει να ληφθεί υπόψη το επιστημονικό γεγονός ότι κανένας σεισμός με μέγεθος μεγαλύτερο από M = 4 δεν έχει παρατηρηθεί από το 1941. Επιπλέον, οι επιστημονικές απαιτήσεις για τον εντοπισμό και τη διερεύνηση των αιτιών του χαμηλού μεγέθους σεισμών που σημειώθηκαν στην περιοχή μελέτης μετά από το 1941 μέχρι σήμερα. Επιπλέον, πρέπει να ερευνηθούν οι συνεχείς και δραματικές επιδράσεις της απόληψης των υπόγειων υδάτων στην (αντικειμενική) σταθεροποίηση του εδάφους και υπεδάφους, καθώς και ο αντίκτυπος των άλλων παραμέτρων που συμμετέχουν στην παραμόρφωση του εδάφους όπως ο τύπος της λιθολογίας και η σύσταση του εδάφους. Η παρούσα έρευνα εφαρμόζεται, για την επαλήθευση της ικανότητας εφαρμογής των τεχνικών συμβολομετρίας Synthetic Aperture Radio (συμβολομετρία SAR) αλλά και την ανίχνευση της εδαφικής παραμόρφωσης που προκύπτει από την επίδρασης οποιαδήποτε αίτιας εντός των αστικών και μη αστικών περιοχών εφαρμοστεί.

Κατά συνέπεια, οι στόχοι της παρούσας μελέτης είναι να εξακριβωθεί η δυνατότητα εφαρμογής των τεχνικών Συμβολομετρίας SAR interferometric στην ανίχνευση βραχυπρόθεσμης και μακροπρόθεσμης παραμόρφωσης, καθώς και η διερεύνηση των παραγόντων που επηρεάζουν την παραμόρφωση του εδάφους στην περιοχή μελέτης.

Τρεις τεχνικές συμβολομετρίας SAR εφαρμόστηκαν με τη χρήση του λογισμικού GAMMA (S / W): Η συμβατική (Conventional), η συμβολομετρίας στοιβάγματος (Stacking Interferometric), και η Persistent Scatterer Interferometric (PSI). Χρησιμοποιήθηκαν, δύο σύνολα δεδομένων από τον δορυφόρο ERS 1/2 και τον περιβαλλοντικό δορυφόρο Advanced Synthetic Aperture Radar

(ASAR ENVISAT), ανερχόμενης και κατερχόμενης τροχιάς κατά τη διάρκεια των περιόδων 1995-2008 και 1992-2010, αντίστοιχα.

Τα αποτελέσματα ήταν τα ακόλουθα:

- Τα αποτελέσματα των τριών τεχνικών στα δεδομένα ανερχόμενης και κατερχόμενης τροχιάς δείχνουν ότι οι παραμορφώσεις καθίζησης και ανύψωσης καττανέμονται σε ολόκληρη την περιοχή μελέτης.

- Κανένα μοτίβο συμβολομετρικής παραμόρφωσης δεν παρατηρήθηκε στις αγροτικές καλλιέργειες την εφαρμογή της συμβολομετρίας στοιβάγματος στις εικόνες ανερχόμενης και κατερχόμενης τροχιάς, Ωστόσο μοτίβα συμβολομετρικής παραμόρφωσης εντοπίστηκαν σε αστικές και ορεινές περιοχές.

- Μοτίβα συμβολομετρικής παραμόρφωσης παρατηρήθηκαν εντός των αστικών και των αγροτικών περιοχών μέσω της εφαρμογής της συμβατικής τεχνικής στις εικόνες ανερχόμενης και κατερχόμενης τροχιάς με την εφαρμογή σε βραχυπρόθεσμη περίοδο.

- Τα αποτελέσματα της συμβολομετρίας στοιβάγματοστων εικόνων κατερχόμενης τροχιάς δείχνουν την μικρή κατανομή των προτύπων πυκνότητας σε σύγκριση με τις εικόνες ανερχόμενης τροχιάς Επιπλέον, ο αριθμός των υποψήφιων σημείων στην κατερχόμενη τροχιά είναι μικρότερος από τον αριθμό των υποψήφιων σημείων στην ανερχόμενη τροχιά. Ερμηνεία αυτή της περίπτωσης λαμβάνει χώρα σε ζεύγη μεταξύ των διαφορετικών εποχών και συνήθως συναντά ισχυρότερες ατμοσφαιρικές επιδράσεις (κυρίως ισχυρότερες ατμοσφαιρικές επιδράσεις ανάλογα με το υψόμετρο).

- Τα αποτελέσματα της συμβολομετρίας στοιβάγματος των εικόνων κατερχόμενης τροχιάς δείχνουν μικρή κατανομή των προτύπων πυκνότητας σε σύγκριση με αυτές της ανερχόμενης τροχιάς.

- Παρατηρήθηκε ,ια άμεση συσχέτιση μεταξύ του αριθμού των συμβολογραμμάτων και της μέσης συνοχής των εικόνων ανερχόμενης και κατερχόμενης τροχιάςκομμάτια εντός της αστικής περιοχής. Ωστόσο, παρατηρήθηκε ένας αντίστροφος συσχετισμός μεταξύ του αριθμού των συμβολογραμμάτων και της μέσης συνοχής στις καλλιεργούμενες περιοχές.

- Παρατηρήθηκε μία άμεση συσχέτιση μεταξύ της μακράς κάθετης γραμμής βάσης και του αποτελέσματος για τον αριθμό των συμβολογραμμάτων. Επιπλέον βρέθηκε μια άμεση συσχέτιση μεταξύ των φάσεων και μακράς κάθετης γραμμή βάσης.

- Βρέθηκε μια σημαντική συσχέτιση μεταξύ της διακύμανσης της στάθμης των υπόγειων υδάτων και της παραμόρφωσης του εδάφους στις εικόνες ανερχόμενης και κατερχόμενης τροχιάς, παρά τις σύντομες χρονοσειρές της ανερχόμενης τροχιά (1995-2006) και τη μεγάλη απόσταση μεταξύ των γεωτρήσεων και των πολλών υποψήφιων σημείων του PSI στις εικόνες κατερχόμενης τροχιάς. Αυτό μπορεί να οφείλεται στις μικρές αποστάσεις μεταξύ των γεωτρήσεων και των πολλών υποψήφιων σημείων που ελήφθησαν για την ανερχόμενη τροχιά ή στο μεγάλο εύρος των δεδομένων των χρονοσειρών (1992-2010) της κατερχόμενης τροχιάς.

- Βρέθηκαν αποτελέσματα από τη συμβατική τεχνική για την εποχιακή παραμόρφωση. Αυτό οφείλεται στη διακύμανση της στάθμης των υπογείων υδάτων, η οποία διαδραματίζει σημαντικό ρόλο μέσω της επίδρασής της στην εδαφική παραμόρφωση σε σύντομα χρονικά διαστήματα έως και ένα μήνα.

- Οι διαφορές στο ποσοστό παραμόρφωσης του εδάφους των ίδιων οικισμών που προκύπτουν από την τεχνική του συμβολομετρικού στοιβάγματος των δύο τροχιών, ανερχόμενης και κατερχόμενης, μπορεί να αποδοθεί στη διαφορά μεταξύ των αριθμών των συμβολογραμμάτων εντός κάθε συμβολομετρικού στοιβάγματος, δεδομένου ότι υπήρχαν 29 εικόνες κατά την ανερχόμενη τροχιά και 70 εικόνες στην κατερχόμενη τροχιά. Επιπλέον, υπήρχαν διαφορές μεταξύ των χρονικών περιόδων των εικόνων radar μέσα σε κάθε τροχιά και μεταξύ των θέσεων των σημείων αναφοράς μέσα σε κάθε τροχιά.

- Η τεχνική PSI, μέσω της εφαρμογής της χωρικής συσχέτισης μεταξύ των θέσεων των υποψήφιων σημείων και τα ίχνη των ρηγμάτων, αποκαλύπτει και/ή υποδεικνύει την πιθανότητα της επιρροής των κινήσεων των ρηγμάτων στην παραμόρφωση του εδάφους.

- Ο άλλος κύριος λόγος για την παραμόρφωση είναι η συμπύκνωση των υλικών που προκαλείται από την υπεράντληση του υπόγειου νερού και αυτό σχετίζεται με την τοπική παραμόρφωση. Αυτή η συμπίεση των υλικών μπορεί να παράγει ένα μικρο-σεισμούς μεγέθους 3 έως 4.

- Οι τεχνικές συμβολομετρίας SAR ανέδειξαν με επιτυχία τις επιπτώσεις του τύπου λιθολογίας στην παραμόρφωση του εδάφους τόσο στις εικόνες ανερχόμενης όσο και στις εικόνες κατερχόμενης τροχιάς.

- Πολλές από τις παραμέτρους επιδρούν ταυτόχρονα και οι επιπτώσεις που επιφέρουν στην παραμόρφωση του εδάφους στην περιοχή μελέτης, είναι δύσκολο να διαχωριστούν και να ξεχωρίσει ποιος παράγοντας επηρεάζει περισσότερο, παρά την εφαρμογή στατιστικής συσχέτισης.

الخلاصة

نفذ بحث الدراسة في الجزء الشمالي الشرقي لمقاطعة ثيساليا الواقعة وسط اليونان حيث تقدر مساحة منطقة الدراسة بحوالي (3113.834) كم^2.

تعاني منطقة الدراسة من آثار الأخطار الطبيعية والبشرية والتي تكون تأثيراتها تدريجيه في بعض الأحيان أو سريعة في أحيان أخرى والتي تهدد بدورها إستقرار البنية التحتيه المدنية بالإضافة الى تهديدها للمشاريع الزراعية.

إن هذه الأخطار تتعلق بكمية المياه الأرضية الهائله من ناحية والتي تسحب للاستخدامات الزراعية فضلا عن الاستخدامات الأخرى، وكذلك بتأثيرات نوع الخصائص الصخرية (الليثولوجي) والتصدعات الطبيعية النشطة التي تخترق منطقة الدراسة من ناحية أخرى، ناهيك عن الزلازل بالاضافة الى العوامل الثانوية الاخرى.

توصف منطقة الدراسة بموجب التسجيلات الزلزالية بأنها ذات قوة زلزالية متوسطة إلى عالية القوة، ويرجع ذلك إلى المصادر الزلزالية لعام 1941، حيث ضرب المنطقة زلزال بقوة 6.1 على مقياس ريختر. ومن الجدير بالملاحظة فإنه لم يضرب المنطقة منذ ذلك الحين زلزال أقوى من 4 درجات على مقياس ريختر.

نظراً لما سبق وبالإضافة إلى الأسباب التالية تم تنفيذ هذا البحث:

١. الحاجة الماسة لاستقصاء وتحديد أسباب إنخفاض درجات قوة الزلازل منذ عام 1941 وحتى الآن.
٢. البحث في سحب المياه الأرضية وتأثيراتها المثيرة والمستمرة على استقرار الأجسام الواقعة على أو داخل الأرض، علاوة على تأثير العوامل الأخرى المساعدة على تشوه الأرض كنوع الخصائص الصخرية ونوع التربة.
٣. البحث في إمكانية تطبيق تقانات التداخل (SAR Interferometry) لفترات قصيرة وطويلة الأمد وذلك باستخدام صور الرادار ذو الفتحة الجانبية لتحديد مظاهر وأسباب تشوه الأرض داخل المنطقة الحضرية وغير الحضرية.

لقد تم تنفيذ تقانات التداخل الثلاث باستخدام برنامج كاما مع الاستعانة بمجموعة من بيانات الأقمار الصناعية المخصصة لدراسة الموارد الأرضية ERS1/2، بالإضافة إلى القمر الصناعي الراداري المخصص لدراسة البيئة ASAR ENVISAT وللفترات 1995- 2008 و 1992 - 2010 للمسارين التصاعدي والتنازلي على التوالي؛ وهذه التقانات هي تقانة التداخل التقليدي Conventional Interferometric، تقانة تداخل التكديس Stacking Interferometric، بالإضافة إلى تقانة التداخل المشتت الثابت Persistent Scatterers interferometry.

كانت النتائج البحث على النحو التالي:

- تشير نتائج التقانات الثلاث لبيانات المسارين التصاعدي والتنازلي إلى تشوه في الارض سواء في الهبوط Subsidence او الرفع uplift وتتوزع في كل انحاء منطقة الدراسة.

- لم تلاحظ أنماط التشوه المتداخل في الحقول الزراعية خلال تنفيذ تقانة التداخل المكدس لكل من المسارين التصاعدي والتنازلي، ولكن انماط التشوه المتداخل قد لوحظت في المناطق الحضرية والجبلية.

- لقد لوحظت أنماط التشوه المتداخل في المناطق الحضرية والزراعية من خلال تطبيق تقانة التداخل التقليدي لكل من المسارين التصاعدي والتنازلي للفترة ذات المدى القصير.

- تشير نتائج تقنية التداخل المكدس للمسار التنازلي إلى وجود انخفاض في كثافة توزيع أنماط التداخل مقارنة بنتائج المسار التصاعدي وعلاوة على ذلك فإن نتائج النقاط المرشحة Candidate points من المسار التنازلي كانت أقل من المسار التصاعدي. ويعزو تفسير هذه الحالة إلى اختلاف المواسم للكثير من أزواج الصور interferograms وبالتالي إلى تأثرها بالغلاف الجوي.

- أظهرت نتائج المسار التنازلي بأن أنماط التداخل كانت أكثر صعوبة في عملية فك اللف للطور phase unwrapping وهذا قد يقلل من التغطية المكانية.

- وجود علاقة مباشرة بين عدد أزواج الصور و متوسط التماسك Coherence لكل من المسارين التصاعدي والتنازلي في المناطق الحضرية. إلا أنه وجدت علاقة عكسية بين عدد الازواج ومتوسط التماسك في االحقول الزراعية.

- وجود علاقة مباشرة بين خط الأساس العمودي Perpendicular baseline وعدد أزواج الصور بالإضافة إلى وجود علاقة مباشرة بين التفاف الأنماط Wrapped phase وخط الأساس العمودي ذو المدى الكبير.

- وجود علاقة ارتباط معنوية بين تذبذب مستوى الماء الأرضي لكل من بيانات المسارين التصاعدي والتنازلي على الرغم من قلة البيانات ضمن المسار التصاعدي للفترة الواقعة بين 1995-2008 والمسافة بين النقاط المرشحة والآبار بالنسبة للمسار التنازلي. وقد يعزى ذلك الى المسافات القصيرة بين الآبار والنقاط المرشحة ضمن المسار التصاعدي أو إلى سعة البيانات للفترة ما بين 1992-2010 ضمن المسار التنازلي.

- تشير نتائج التقانة التقليدية إلى تشوه الأرض الموسمي وهذا يعزى الى تذبذب مستوى الماء الأرضي الذي يلعب دورا مهما من خلال تأثيره على تشوه الأرض خلال مدة قصيرة والتي قد تصل إلى شهر واحد.

- الاختلاف في معدل تشوه الأرض بالنسبة للمستوطنات والناتج عن تطبيق تقانة التداخل المكدس للمسارين التصاعدي والتنازلي و قد يكون السبب في ذلك عدد الأزواج، حيث يبلغ 29 زوجا من أزواج الصور ضمن المسار التصاعدي و 70 زوجا من أزواج الصور ضمن المسار التنازلي إضافة إلى الاختلاف في الفترة الزمنية للصور الرادارية الملتقطة ضمن كل مسار وإلى موقع النقاط المرجعية داخل كل مسار.

- كشفت تقانة التداخل المشتت من خلال تطبيق الترابط المكاني بين موقع النقاط المرشحة بالنسبة إلى التصدعات الأرضية إلى إمكانية تأثير حركات التصدعات على تشوه الأرض.

- يكمن السبب الرئيس الآخر لتشوه الأرض في رص المواد الأرضية Compaction of materials الناجم عن سحب المياه والذي له علاقة بتشوه الأرض الموقعي، إضافة إلى أن ضغط المواد هذا قد يمكن أن يسبب زلازلا ذات قوة صغيرة تقدر ب 3- 4 . على مقياس ريختر.

- كشفت تقانات قياس التداخل SAR وبنجاح تأثير نوع الصخرية (الليثولوجي) على تشوه الأرض ضمن نتائج المسارين التصاعدي و التنازلي.

- هناك الكثير من العوامل التي اشتركت معا بالاضافة الى تاثيراتها المتداخلة على تشوه الارض ضمن منطقة الدراسة اضافة الى ذلك صعوبة عزل تاثير كل عامل بشكل مفرد على الرغم من تطبيق العلاقات الاحصائية.

Chapter One: Introduction

1.1 Introduction

Natural hazards comprise hydro-meteorological hazards, which include floods and flash floods, droughts, wildfires, tropical cyclones and hurricanes, and severe storms; geological hazards, which include tectonic movement, earthquakes, tsunamis, volcanoes and explosive crater lakes, landslides, mudflows, erosion, and siltation; and moreover human-induced hazards, which include wars, groundwater and oil withdrawal, mining, and land degradation. Together, all of these hazards contribute to serious environmental problems which in consequence affect and destroy the economic development of countries and finally, in turn, impact on all walks of life.

The amount of natural and human hazards has to be measured carefully and accurately to determine precisely the environmental and economic damages and furthermore to evaluate the disaster and risk management. The development of new technologies and techniques has dramatically eased and assisted the measurement of hazards and disasters induced by either nature or humans. Furthermore the financial cost of work and manpower has decreased and the speed and accuracy of production of ground deformation maps has increased.

Ground deformation, which is the topic of this research, resulting from either natural or human hazards, is one of the most important hazards which threaten the stability of civil and agricultural construction located on or within the ground, and it causes real disasters. Consequently it is logical and reasonable to expend time and funding on many projects all over the world to find and enhance new, rapid, accurate, and low-cost methods and techniques to determine, manage, and reclaim the damages and furthermore to limit future hazards and disasters if possible.

The new generations of satellites, their newly produced data used for earth monitoring, and furthermore new improvements in software processing can ease the monitoring of ground deformation rapidly, accurately, and economically in comparison with the old geotechnical monitoring methods.

Applications and implementation of the technique of Synthetic Aperture Radio Detection and Ranging (Radar) (SAR) interferometry for monitoring changes in the Earth's surface began in the early 1990s.

The utilization of SAR interferometry for monitoring ground deformation caused a huge revolution in the field of ground deformation and geohazards monitoring and maps production through the facilities of long- and short-term observations in addition to the large spatial coverage of radar images and moreover the high accuracy of deformation measurement, which has reached millimeter-level accuracy.

Since then, the enhancement and increase of radar image resolution and furthermore multi-radio band sensors that can be carried by new-generation satellites as well as the development of data processing software have supported and proved the importance and successfulness of the use of SAR interferometric techniques for monitoring geohazards.

The latest development in this field is the new technique of ground deformation monitoring called Persistent Scatterer Interferometry (PSI), which makes it easier to monitor the deformation of point targets such as columns and buildings.

SAR interferometric techniques have been applied within this research study to monitor and map ground deformation within the study area.

The study area is located in the eastern part of the northern Thessaly prefecture in the middle of Greece, which is depicted in Figure 1. The Thessaly prefecture occupies the eastern side of the Pindus watershed, extending south of Macedonia to the Aegean Sea. The northern tier of Thessaly is defined by a generally southwest–northeast spur of the Pindus Range that includes the Olympus mountain range, close to the Macedonian border. Within that broken spur of mountains are several basins and river valleys. The easternmost extremity of the spur extends southeastward from Mt. Olympus along the Aegean coast, terminating in the Magnesia Peninsula, which envelops the Pagasetic Gulf (also called the Gulf of Volos), and forms an inlet of the Aegean Sea. Thessaly's major river, the Pineios, flows eastward from the central Pindus Range just south of the spur, emptying into the Gulf of Thermaikos (Free Encyclopedia, 2012).

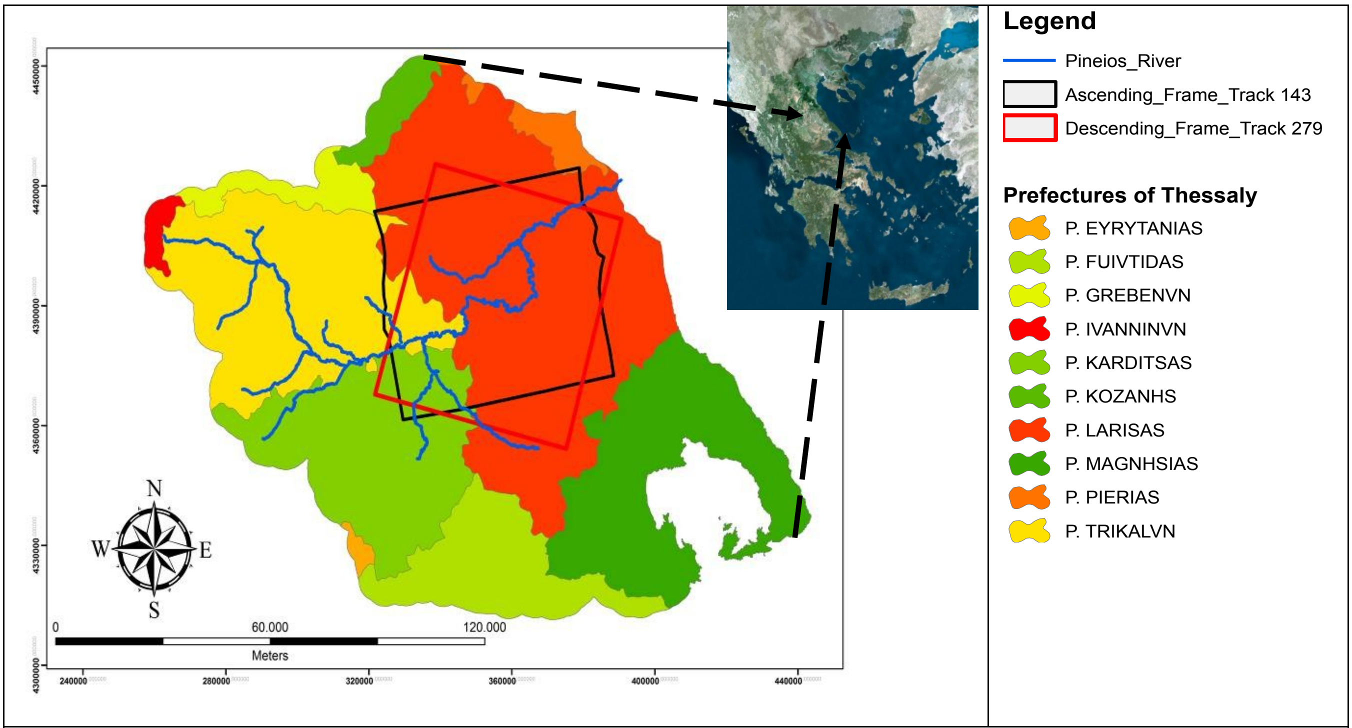

Figure 1. Thessaly prefecture, indicating that the study area exists within the frames of ascending and descending radar image tracks

The study area suffers from a ground deformation phenomenon which affects civil and agricultural construction. Furthermore it is a very complicated area due to the distribution of many natural and human hazards, which include normal faults, groundwater withdrawal, and some other natural characteristics which we consider as cofactors of natural hazards such as the type of lithology.

1.2 Objectives of the Research Study

This research study aims to achieve the following goals:

1- To evaluate the possibility of applying SAR interferometric techniques to monitor and map ground deformation in urban and agricultural lands over the long and short terms.

2- To investigate and identify the causes of ground deformation.

3- To evaluate the possibility of recognizing each individual cause of ground deformation by monitoring the time series behaviour of ground deformation using the statistical results of SAR interferometric techniques.

4- To apply spatial and qualitative correlations between ground deformation and parameters (precipitation, groundwater, fault movement, earthquake, lithology, and soil) to reveal the reality of ground deformation within the study area.

1.3 Methodology of the Research Study

The research plan was done following an extensive review of the literature relevant to the problems of the study area with regard to the causes of ground deformation, its effects, and its time series, the application of SAR interferometry techniques to monitor and map ground deformation, and moreover the search for a means of carrying out qualitative and quantitative correlation between ground deformation and ground parameters. Figure 2 shows a flowchart depicting the methodology of the research study.

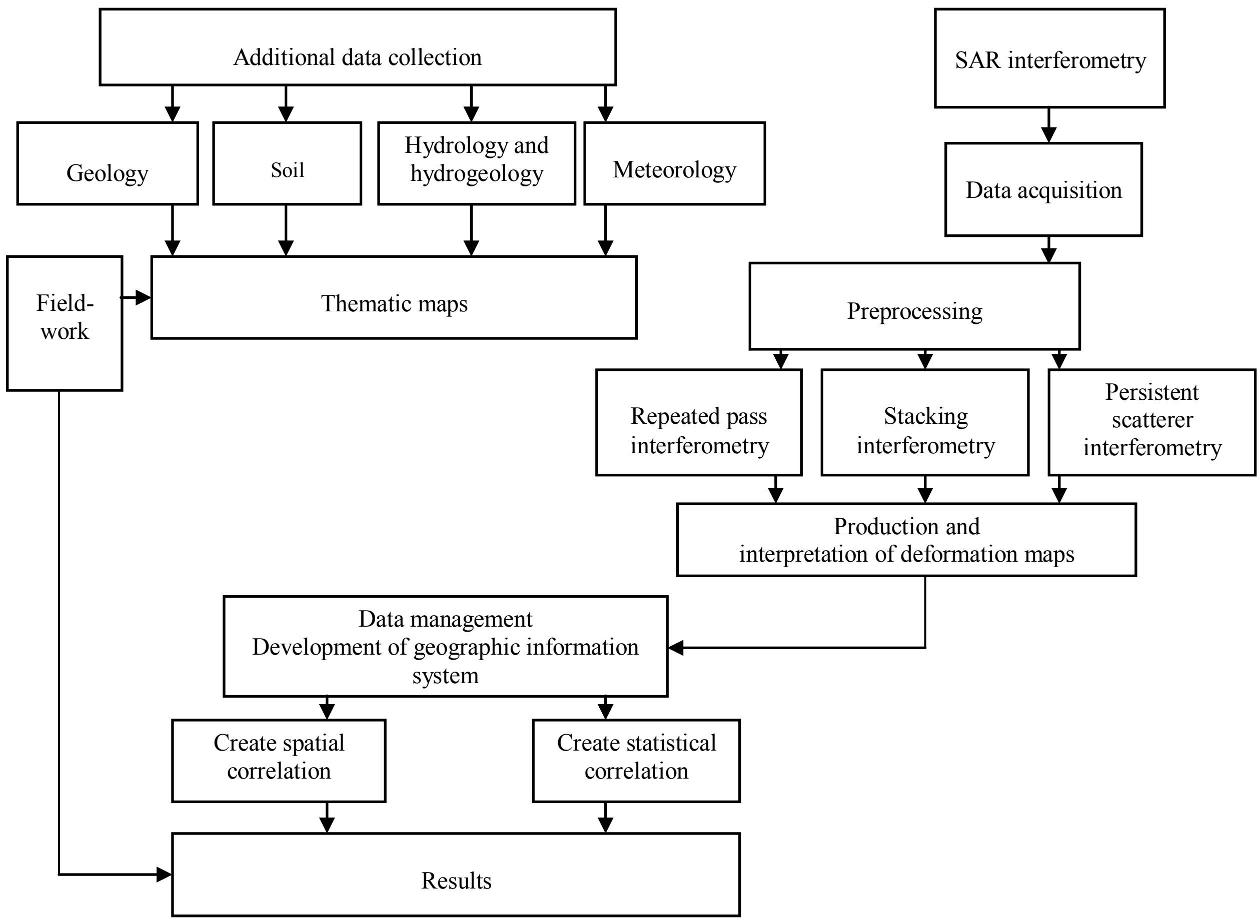

Figure.2.Flowchart of study research methodology

1.4 Organization of Dissertation

This research study is divided into a total of seven chapters including the current one. The chapters are designed to achieve the objectives of this study. The research study is presented in the following chapters:

Chapter Two: Data acquisition and SAR interferometric techniques and processing. This chapter deals with the types and characteristics of SAR data which are used. Furthermore it deals with the types of SAR interferometric techniques which have been implemented and the processing stages of each technique. In addition it deals with how ground deformation can be determined and monitored using those techniques, leading to the final product, which is the ground deformation map.

Chapter Three: Impact of groundwater on ground deformation. This chapter deals with the processes of withdrawal of groundwater and recharging reservoirs and aquifers, and furthermore groundwater impact on ground deformation. Consequently the chapter builds on the ground deformation information resulting from the previous chapter. In addition it deals with the statistical and qualitative correlation between groundwater behaviour and the monthly amount of precipitation, type of lithology, and fault movement and groundwater influences on ground deformation in the short and long terms.

Chapter Four: Impact of fault movement and earthquakes on ground deformation. This chapter deals with the distribution of fault traces and faults type and moreover catalogues the magnitudes of earthquakes and their influences on ground deformation. In addition the chapter deals with the spatial and qualitative correlations between objects which are affected by ground deformation resulting from the second chapter and fault traces.

Chapter Five: Impact of lithology types on ground deformation. This chapter deals with the identification and detection of lithology types and moreover the spatial and qualitative correlations between these types and objects affected by ground deformation resulting from the second chapter. In addition this chapter discuss with how ground deformation can be affected by the type of lithology type.

Chapter Six: Impact of soil on ground deformation. This chapter deals with the soil classes, the varieties of soil deformation, and the behaviour of the soil deformation using statistical analysis; furthermore it deals with the parameters which have a major influence on this deformation.

Chapter Seven: The conclusions derived from this research study and recommendations for future researches.

Chapter Two: Data acquisition and SAR interferometric techniques and processing

2.1 Introduction to Earth Observation Active System and SAR Interferometry Processing

Radio detection and ranging (Radar) refers to a technique as well as an instrument. The radar instrument emits electromagnetic pulses in the radio and microwave regime and detects the reflections of these pulses from objects in its line of sight. The radar technique uses the two-way travel time of the pulse to determine the range of the detected object and it uses backscatter intensity to infer physical quantities, such as size or surface roughness (Hanssen, 2001).

Radar has proved to be valuable because of its day and night capability and ability to penetrate clouds and rain. However, optical instruments have significant advantages in the interpretation of depicted objects. The large wavelength of radar signals limits the achievable resolution in the cross range direction of real aperture radar systems. Thus, imaging cannot be realised using static radar systems (Berens, 2006).

(Fletcher, 2007) stated that the radiation transmitted from the radar has to reach the scatterers on the ground and then return to the radar in order to form the synthetic aperture radar (SAR) image (two-way travel). Scatterers at different distances from the radar (different slant ranges) introduce different delays between the transmission and reception of the radiation. This author also mentioned that owing to the almost purely sinusoidal nature of the transmitted signal, this delay (τ) is equivalent to a phase change (φ) between the transmitted and received signals. Thus, the phase change is proportional to the two-way travel distance (2R) of the radiation divided by the transmitted wavelength (λ). This concept is illustrated in Figure 3.

(Manunta, 2009) declared that the radar self-illuminates an area on the ground by transmitting a series of electromagnetic pulses and following an accurate evaluation of the time delay between the transmitted and the received echoes, is able to determine the distance (called the slant range) between the sensor's position along its flight direction (azimuth) and the illuminated targets on the ground. In addition, this author mentioned that the radar system is characterised well by its attainable spatial resolution, which measures the ability to distinguish two properly separated objects. More precisely, if the objects are sufficiently separated, each will be located in a different resolution cell and thus, will be discernible; otherwise, the radar return will be a complex combination of the reflected energy of the two objects.

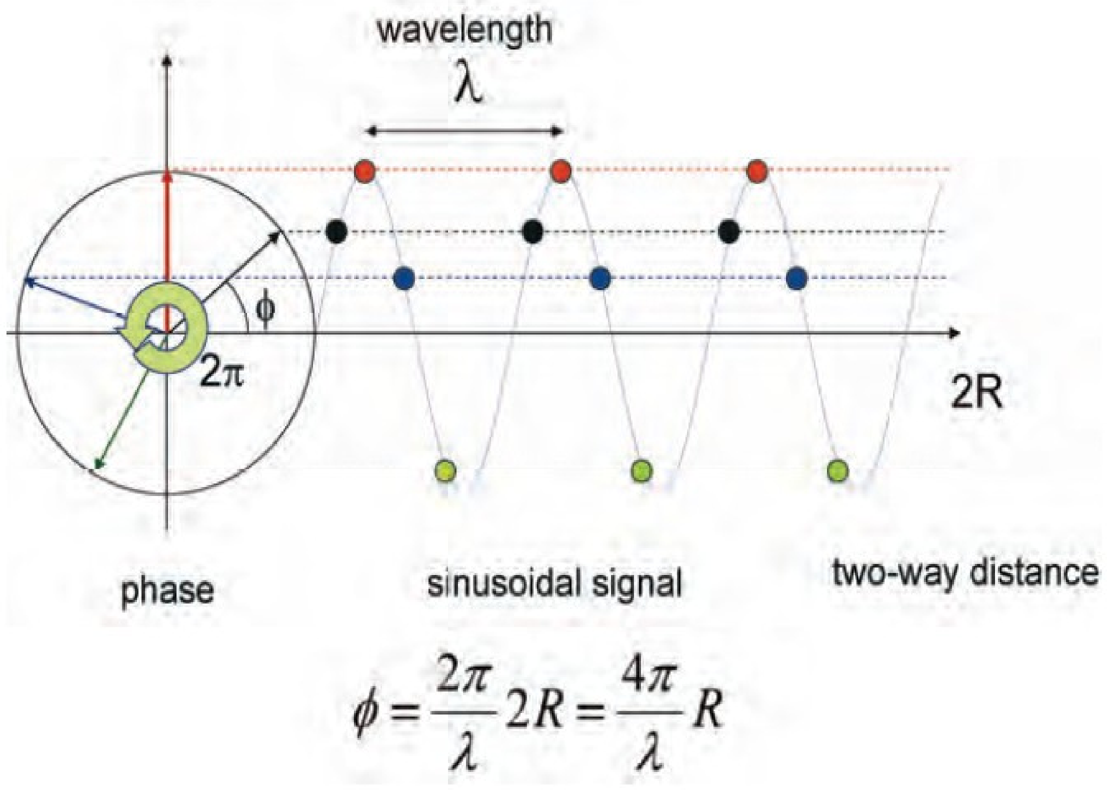

Figure 3. A sinusoidal function sin (φ) is periodic within a (2π) radian period. In the case of a relatively narrow-band SAR (i.e., ERS and ENVISAT), the transmitted signal can be assimilated, as a first approximation, to a pure sinusoid whose angle or phase (φ) has the following linear dependence on the slant range coordinate r:$\varphi = 2\pi\ r / \lambda$ (where λ is the SAR wavelength). Thus, assuming that the phase of the transmitted signal is zero, the received signal that covers the distance 2R from the satellite to the target and back, shows a phase $\varphi = 4\pi R/\lambda$ radians (Fletcher, 2007)

2.2 Synthetic Aperture Radar (SAR)

The principle of synthetic aperture radar was discovered in the early 1950s. Since then, a rapid worldwide development has occurred and there are several of airborne and spaceborne systems operational today. Progress made in technology and digital signal processing has led to very flexible systems useful for military and civilian applications (Berens, 2006).

(Hanssen, 2001) stated that the specific class of radar systems that are imaging radars are those such as side-looking (airborne) radar (SLR or SLAR) and later synthetic aperture radar (SAR). The side-looking geometry of a radar mounted on an aircraft or satellite provided range sensitivity, while avoiding ambiguous reflections. The first

SLARs were incoherent radars i.e., the phase information of the emitted and received waveforms was not retained. The resolution in the direction of flight was obtained by using a physically long antenna; hence, the name real aperture radar (RAR).

SAR is a microwave imaging system, which has cloud-penetrating capabilities because it uses microwaves. It has day and night operational capabilities because it is an active system. Finally, its 'interferometric configuration' (Interferometric SAR or InSAR) allows accurate measurements of the radiation travel path because it is coherent. Measurements of travel path variations as a function of the satellite position and time of acquisition allow the generation of Digital Elevation Models (DEMs) and the measurement of centimetric surface deformations of the terrain (Fletcher, 2007).

(Berens, 2006) mentioned that the idea of SAR is to transmit pulses and store the scene echoes along a synthetic aperture (i.e., the path of the SAR sensor) and to combine the echoes afterwards via the application of an appropriate focussing algorithm.

(Rosen et al., 2000) declared that the SAR interferometry is an imaging technique for measuring the topography of a surface, its changes over time and other changes in the detailed characteristics of the surface.

SAR has a broad range of applications. For remote sensing, several of earth observing satellites, which have imaging sensors working in different spectral areas, are currently in operation. The usability of optical sensors depends not only on daylight but also on the actual weather conditions. Clouds and strong rain are impenetrable for this wavelength. Infrared sensors, which are applicable both day and night, are even more sensitive to weather conditions. Consequently, radar sensors represent a completion of the sensor collection for remote sensing. Beyond the overall availability of SAR images, there are further pros for the utilisation of radar. The coherent nature of SAR enables the user to process images of subsequent over flights for interferometric analyses. Depending on the radar wavelength, the radar signal will be reflected by vegetation or the ground structure. With the choice of a concrete centre frequency of the SAR sensor, the developer decides about the appearance of the resulting radar images. Different combinations of transmit and receive polarisation can also be used, for example, to classify the type of vegetation (Berens, 2006).

This author also mentioned that the propagation and reflection of electromagnetic waves depends strongly on its frequency. SAR systems for wide area surveillance have to operate in frequency areas with minimal attenuation. Beyond the Ka-band, only short-range systems are realisable. Some advantages of systems with a higher frequency are a reduced system size and simplified processing. The X- C- and L-bands are very common for airborne and spaceborne sensors. The wavelength of transmitted signals plays an important role in the reflection characteristics. A rough surface has completely different reflection behaviour compared with a smooth one. However, smoothness is a property that depends on the relation of the surface structure size to the wavelength. Another feature of low frequency waves is that foliage can be penetrated; thus, low frequency systems are useful in some situations.

2.3 Main Radar Systems Used in this Study

2.3.1. ERS-1 & 2

The European remote sensing satellite, ERS-1, was ESA’s first Earth observation satellite. It carried a comprehensive payload including an imaging SAR. Following its launch in July 1991 and the validation of its interferometric capability in September of the same year, an ever-growing set of interferometric data became available to many research groups. ERS-2, which was identical to ERS-1 apart from having an extra instrument, was launched in 1995. Shortly after the launch of ERS-2, ESA decided to link the two spacecraft in the first ever ‘tandem’ mission, which lasted for nine months, from 16 August 1995 until mid-May 1996. During this time, the orbits of the two spacecraft were phased to orbit the Earth only 24 hours apart; thus, providing a 24-hour revisit interval. The huge collection of image pairs from the ERS tandem mission remains uniquely useful even today, because the brief 24-hour revisit time between acquisitions results in much greater interferogram coherence. The increased frequency and level of data available to scientists offered a unique opportunity to generate detailed elevation maps (DEMs) and to observe changes over a very short space of time. Even after the tandem mission ended, the high orbital stability and careful operational control allowed acquisition of further SAR pairs for the remainder of the time that both spacecraft were in orbit, although without the same stringent mission constraints.

The near-polar orbit of ERS, in combination with the Earth's rotation (E-W), enables two acquisitions of the same area to be made from two different look angles on each satellite cycle. If just one acquisition geometry is used, the accuracy of the final DEM in geographic coordinates depends strongly on the local terrain slope and this might not be acceptable for the final user.

Combining the DEMs obtained from the ascending (S-N) and descending (N-S) orbits can mitigate the problems owing to the acquisition geometry and the uneven sampling of the area of interest, especially on areas of hilly terrain. The ERS antenna looks to the right; therefore, for example, a slope that is mainly oriented to the west would be foreshortened on an ascending orbit and thus, a descending orbit should be used instead. In March 2000, the ERS-1 satellite finally ended its operations; however, ERS-2 is expected to continue operating for some time, although with a lower accuracy of attitude control following a gyro failure that occurred in January 2001 (Fletcher, 2007).

2.3.2. ENVISAT ASAR

Launched in 2002, ENVISAT ASAR is the largest Earth observation spacecraft ever built. It carries ten sophisticated optical and radar instruments to provide continuous observation and monitoring of the Earth's land, atmosphere, oceans and ice caps. ENVISAT ASAR data collectively provide a wealth of information on the workings of the Earth system, including insights into factors contributing to climate change.

Furthermore, the data returned by its suite of instruments are also facilitating the development of a number of operational and commercial applications. ENVISAT's largest single instrument is the advanced synthetic aperture radar (ASAR), which operates in the C-band. This ensures continuity of data after ERS-2, despite a small (31 MHz) central frequency shift. It features enhanced capability in terms of coverage, range of incidence angles, polarisation and modes of operation. The improvements allow radar beam elevation steerage and the selection of different swathes, 100 or 400 km wide. ENVISAT ASAR is in a 98.54° sun-synchronous circular orbit at 800 km altitude with a 35-day repeat and the same ground track as ERS-2 (Fletcher, 2007).

2.4. SAR Interferometry

Geophysical applications of radar interferometry to measure changes in the Earth's surface have exploded since the early 1990s. This new geodetic technique calculates the interference pattern caused by the difference in phase between two images acquired by spaceborne SAR at two distinct times. The resulting interferogram is a contour map of the change in distance between the ground and the radar instrument. These maps provide unsurpassed spatial sampling density (100 pixels per Km^2), a competitive precision (1 cm) and a useful observation cadence (1 pass per month). They record movements in the Earth's crust, perturbations in the atmosphere, dielectric modifications in the soil and the relief of the topography. They are also sensitive to technical effects, such as relative variations in the radar's trajectory or variations in its frequency standard (Massonnet and Feigl, 1998).

(Bamler and Hartl, 1998) mentioned that nowadays, it is generally appreciated that SAR interferometry is an extremely powerful tool for mapping the Earth's land, ice and even the sea surface topography. These authors also mentioned that the so-called differential InSAR method (D-InSAR) represents a unique method for detection and mapping of surface displacements over large temporal and spatial scales with centimetre or even millimetre precision. This is of great importance for earthquake and volcanic research, glaciology and monitoring ice sheets, studying tectonic processes and monitoring land subsidence caused by mining and gas, water, and oil extraction. Repeat-pass interferometry allows the detection and mapping of changes of spatial and/or dielectric properties of the land surface by using temporal and spatial coherence characteristics, which can be successfully used for land cover classification, mapping of flooded areas and monitoring of geophysical parameters.

(Hanssen, 2001) said that when compared with conventional geodetic techniques, interferometry provides one capability that has long remained out of reach for radar; the measurement of angles. Similar to a single human eye, which is essentially "blind" in distinguishing the difference in distance between objects, it is impossible for a radar or SAR to distinguish two objects at the same range but at different angles to the instrument. Nature readily provides the simple solution for the problem, i.e., the use of two sensors. The problem is overcome by using two eyes and this idea, together with the use of phase information, cleared the way for interferometry. Using two SAR images, acquired either by two different antennas or by using repeated acquisitions, distance can be obtained in addition to angular measurements. The use of phase measurement multiplicative interferometry enables the observation of relative distances as a fraction of the radar wavelength and the difference in the sensor locations enables the observation of angular differences, necessary for topographic mapping.

(Fletcher, 2007) also mentioned that the satellite SAR could observe the same area from slightly different look angles. This can be done either simultaneously (with two radars mounted on the same platform) or at different times by exploiting repeat orbits of the same satellite. The latter is the case for ERS-1, ERS-2 and ENVISAT. For these satellites, time intervals between observations of 1, 35, or a multiple of 35) days are available. The distance between the two satellites (or orbits) in the plane perpendicular to the orbit is called the interferometer baseline and its projection perpendicular to the slant range is the perpendicular baseline Figure 4.

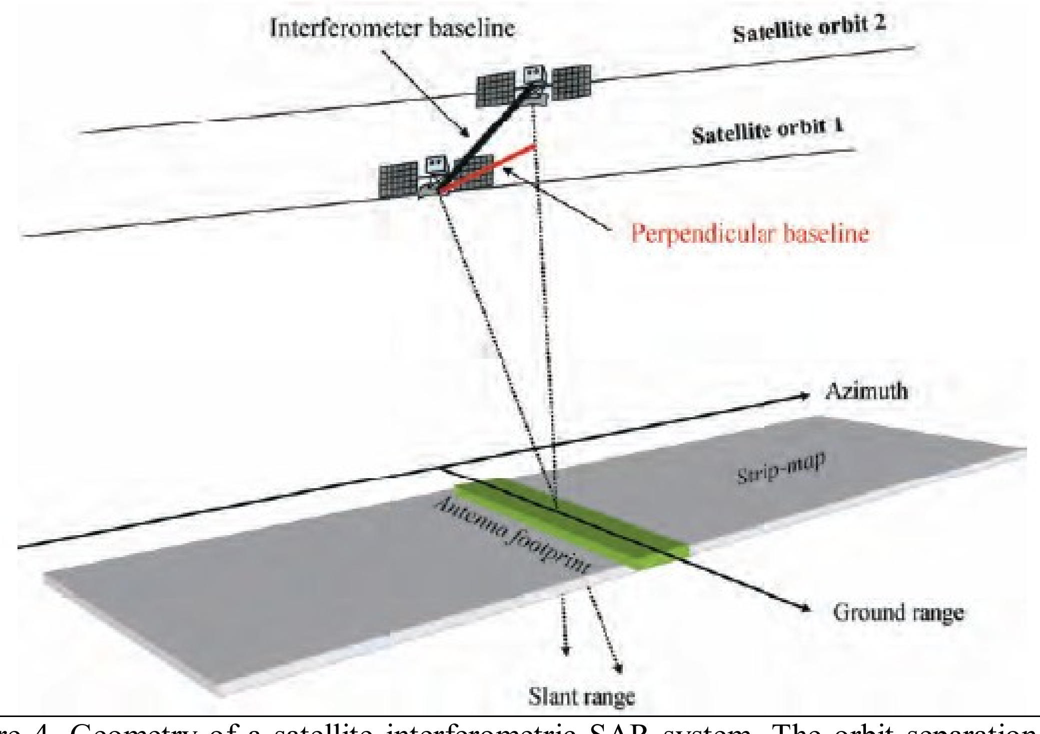

Figure 4. Geometry of a satellite interferometric SAR system. The orbit separation is called the interferometer baseline and its projection perpendicular to the slant range direction is one of the key parameters of SAR interferometry. From (Fletcher, 2007)

(Bamler and Hartl, 1998) stated that interferometric SAR (InSAR) exploits the phase differences of at least two complex-valued SAR images acquired from different orbit positions and/or at different times. The information derived from these interferometric data sets could be used to measure several geophysical quantities, such as topography, deformations (volcanoes, earthquakes and ice fields), glacier flows, ocean currents and vegetation properties.

(Rosen et al., 2000) mentioned that interferometry has transformed radar remote sensing from a largely interpretive science into a quantitative tool with applications in: cartography, geodesy, land cover characterisation and natural hazards.

(Matsuoka and Yamazaki, 2000) declared that SAR interferometric analysis, using phase information of backscattering echoes from objects on the Earth's surface, could be successfully employed to quantify relative ground displacements owing to natural disasters. In addition, the complex coherence derived from interferometric analysis is a suitable and sensitive parameter for the detection of superficial change and the classification of land use.

(Zou et al., 2009) mentioned that InSAR is a new measurement technology exploiting the phase information contained in SAR images. InSAR has been recognised as a potential tool for the generation of DEMs and the measurement of ground surface deformations. However, many critical factors affect the quality of InSAR data and limit its applications.

2.5. SAR Interferometric Techniques

2.5.1. Differential SAR Interferometry (DInSAR)

(Ferretti et al., 1999) stated that differential SAR interferometry (DInSAR) is a unique tool for low-cost, large-coverage monitoring of surface deformations.

(Sheng et al., 2009) mentioned that there are three types of differential SAR interferometry: two-pass differential SAR interferometry, three-pass differential SAR interferometry and four-pass differential SAR interferometry. Two-pass DInSAR uses an interferometric image pair and an external DEM. Of the two single look complex (SLC) images, typically, one is acquired before the surface displacement and the other after the event. The external DEM is converted to a corresponding phase image. Where P is a ground point in the two images, the sensor acquires the first SAR image (which is referred to as the master image) at time t1, measuring the phase Φ_M and then subsequently acquires a second SAR image (the slave image) at time t2, measuring the phase Φ_S. Assuming that the surface displacement occurred during this period, point P is assumed to have moved to P1. After exploiting the phase difference between Φ_M and Φ_S, one obtains the interferometric phase $\Delta\Phi$. Because P moved to P1 between the acquisitions of the two images, the $\Delta\Phi$ includes: Topo Mov Atmos Noise

$$\Delta\Phi = \Phi_{Topo} + \Phi_{Mov} + \Phi_{Atmos} + \Phi_{Noise} \text{ ----------------------------(1)}$$

Where:

Φ_{Topo} is the topographic phase component;

Φ_{Mov} is the terrain change contribution;

Φ_{Atmos} is the atmospheric delay contribution;

Φ_{Noise} is the phase noise.

The two-pass DInSAR uses an external DEM to simulate the topographic phase Φ_{Topo_Simu} and then, the so-called DInSAR phase $\Delta\Phi_{DInSAR}$ can be computed

$$\Delta\Phi\_DInSAR = \Delta\Phi - \Phi\_TOPO\_SIMU \text{ ------------------------------ (2)}$$

$$= \Phi\_Mov + \Phi\_Atmos + \Phi\_Noise + \Phi\_Res\_Top$$

Where, Φ_{Res_Topo} represents the residual component owing to errors in the simulation of Φ_{Topo}. In order to derive information on the terrain change, Φ_{Mov} has to be separated from the other phase components. Figure 5 shows the principle of the two-pass DInSAR.

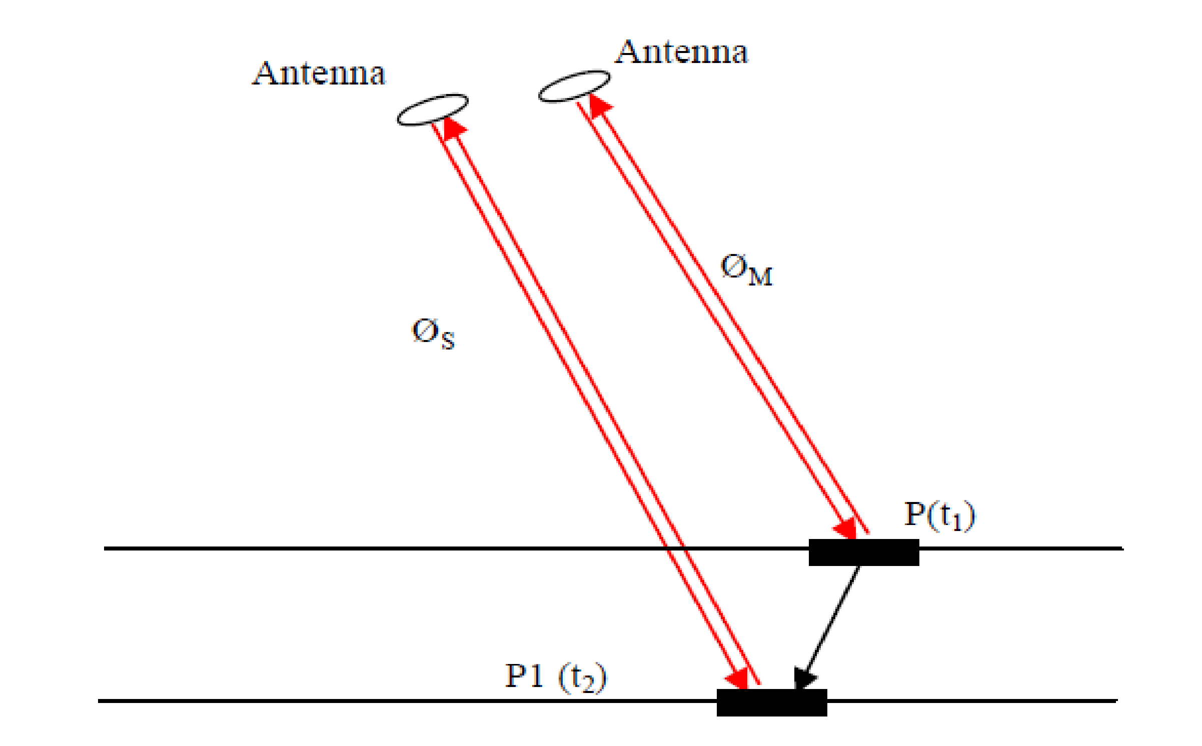

Figure 5 . Principle of two-pass DInSAR from (Sheng et al., 2009)

2.5.2. Repeated pass Interferometry (Conventional InSAR)

(Zhang and Cheng, 2005) indicated that the repeat-pass satellite InSAR could be used to map topography and ground deformations. In addition, these authors mentioned that the interferograms are generated by differencing the phase values of two co-registered radar images acquired at different times over the same area. The DInSAR is a radar technique that detects surface deformations by computing a differential interferogram of the same scene over two repeat-pass acquisitions.

(Wegmóller et al., 2006) reported that in repeat-pass InSAR, two or more SAR images are acquired at different times with the same or a corresponding sensor from almost identical aspect angles. The basic idea of the DInSAR approach is to separate the effects of surface topography and coherent displacement, facilitating the retrieval of displacement maps. This is achieved by subtracting the topography related phase, which can be simulated, based on an available DEM, or estimated from an independent interferogram. The use of a DEM is usually more robust and operationally, is more frequently used.
Additionally, these authors declared that the accuracy of the deformation estimated from individual differential interferograms is mainly limited by the atmospheric path delay term; a well-established method to reduce this error is interferogram stacking.

(Fruneau et al., 2003) found that one major limitation of the DInSAR method is that variations in atmospheric conditions between the acquisitions of the two images could introduce large phase variations in the resulting interferograms, which could be misinterpreted as deformations.

2.5.3. Interferometric Stacking

The basic idea of interferogram stacking is to combine multiple observations into a single result. The main assumption is that the deformation phase is highly correlated and that the error terms (atmosphere, signal noise and baseline) are uncorrelated between the independent pairs. This is not entirely true (e.g., topography related atmospheric error term) but can often been treated as a reasonable assumption. While the signal term of the independent terms add linearly, the error terms increase at a lower rate because they are uncorrelated, which leads to a reduced error in the stacked result. By combining sufficient observation times, it is possible to achieve mm/year accuracies for relatively slow uniform deformations in urban areas. Of course, an important prerequisite is the availability of suitable pairs with adequate time intervals and sufficiently short baselines. Furthermore, it has to be noted that spatial coverage is restricted to the spatial coverage of the individual results (Wegmóller et al., 2006).

(Fletcher, 2007) proposed that each interferogram of a series is initially derived, i.e., the gradients of the phase are computed. The phase gradients are not ambiguous and can be scaled according to the orbital separation in order to reach a normalised topographic sensitivity. After being scaled, the gradients of the series are stacked and averaged. At this stage, any contributor (for instance, the topographic contribution) to the interferometric information could be removed using a priori knowledge. During this operation, one might reasonably hope that atmospheric residuals are affectively attenuated and that their averaged gradient is close to zero. The average interferogram is then reconstructed by integration.

2.5.4. Persistent Scatterers Interferometry (PSI)

(Ferretti et al., 1999) mentioned that the permanent scatterers technique involves interferometric phase comparison of SAR images gathered at different times and has the potential to provide millimetre accuracy. Although temporal de-correlation and atmospheric inhomogeneities strongly affect interferogram quality, reliable deformation measurements can be obtained in a multi-image framework on a small subset of image pixels corresponding to stable areas. These points, hereafter called Permanent Scatterers (PS), could be used as a 'natural GPS network' to monitor terrain motion, by analysing the phase history of each one.

Furthermore, (Ferretti et al., 2000) mentioned that discrete and temporarily stable natural reflectors or permanent scatterers (PSs) could be identified from long temporal series of interferometric SAR images, even with baselines larger than the so-called critical baseline. This subset of image pixels could be exploited successfully for high accuracy differential measurements.

(Ferretti et al., 2001) established a complete procedure for the identification and exploitation of stable natural reflectors or PSs, starting from long temporal series of interferometric SAR images. When, as often happens, the dimension of the PS is smaller than the resolution cell, the coherence is good, even for interferograms with baselines larger than that of the de-correlation. In addition, they mentioned that the starting point is a set of differential interferograms that use the same master acquisition. The DEM used for differential interferogram generation could be either a topographic profile estimated from the Tandem pairs of the ERS data set, or an a priori DEM already available. Its accuracy is not a real constraint, e.g., 20 m is sufficient.

(Werner et al., 2003a) defined a PS technique with another term, which is Interferometric Point Target Analysis (IPTA). This method exploits temporal and spatial characteristics of interferometric signatures, collected from point targets that exhibit long-term coherence, in order to map surface deformations. The use of the interferometric phase from long data time series requires that the correlation remains high over the observation period.

(Werner et al., 2003b) mentioned that the phase model used for IPTA is the same as that used for conventional interferometry. The unwrapped interferometric phase unw φ is expressed as the sum of topographic topo φ, deformation def φ, differential path delay (also called atmospheric phase) phase atm φ and the phase noise φ (or de-correlation) terms.

$$\varphi_{unw} = \varphi_{top} + \varphi_{def} + \varphi_{atm} + \varphi_{nois} \text{ ----------------------------- } (3)$$

Also important in the context of the phase model are the spatial and temporal characteristics of the different terms. For example, atm φ could be considered low-pass in the spatial domain and high-pass (random) in the temporal domain.

(Crosetto et al., 2010) defined a PSI as a radar-based remote-sensing technique to measure and monitor land deformation. It is the most advanced class of DInSAR based on data acquired by spaceborne SAR sensors. Moreover, these authors stated that there are two main differences between the DInSAR and PSI techniques. First, the number of required SAR images (PSI uses a large series of SAR images, typically more than (15–20) and second, the implementation of suitable data modelling and analysis procedures that allow one to obtain the following key PSI products: (i) the time series of the deformation; (ii) the average displacement rates over the observed period; (iii) the atmospheric phase component of each SAR image and (iv) the so-called residual topographic error. From an application viewpoint, the main products of any PSI analysis are given by the map of the average displacement rates and the deformation time series of each measured PS.

2.6. Data and Methodology

2.6.1. SAR Data Selection and Interferometric Processing (Ascending Track 143)

The total dataset consists of 24 Single Look Complex (SLC) SAR C-band images of ERS-1/2, during 1995–2000. Additionally, 15 SLC images of ENVISAT ASAR acquired during 2003–2008 by ESA, which cover the study area, have also been selected along this track, as shown in Tables 1, 2.

Table 1. Datasets of ERS-1/2 SAR images (Ascending Track 143, Frame 785) used in the processing

Id	Missions	Acquisition Date	Orbit
1	ERS1*	19950628	20672
2	**ERS1**	**19951220**	**23177**
3	ERS1	19960228	24179
4	ERS1	19960403	24680
5	ERS1	19960508	25181
6	ERS1	19991020	43217
7	ERS2	19950629	00999
8	ERS2	19951221	03504
9	ERS2	19960229	04506
10	ERS2	19960404	05007
11	ERS2	19960509	05508
12	ERS2	19970320	10017
13	ERS2	19970529	11019
14	ERS2	19970807	12021
15	ERS2	19971225	14025
16	ERS2	19980409	15528
17	ERS2	19980618	16530
18	ERS2	19980827	17532
19	ERS2	19990114	19536
20	ERS2	19990429	21039
21	ERS2	19990603	21540
22	ERS2	19991021	23544
23	**ERS2**	**19991230**	**24546**
24	ERS2	20000518	26550

Table 2. Datasets of ENVISAT ASAR SAR images (Ascending Track 143, Frame 783) used in the processing

Id	Missions	Acquisition Date	Orbit
1	ENVISAT	20030403	05708
2	ENVISAT	20030821	07712
3	ENVISAT	20040108	07712
4	ENVISAT	20040212	10217
5	ENVISAT	20040422	11219
6	ENVISAT	20040527	11720
7	ENVISAT	20040805	12722
8	ENVISAT	20040909	13223
9	ENVISAT	20041014	13724
10	ENVISAT	20050512	16730
11	ENVISAT	20050825	18233
12	ENVISAT	20061228	25247
13	ENVISAT	20070201	25748
14	ENVISAT	20080327	31760
15	ENVISAT	20080605	32762

GAMMA processing software (S/W) has been used for processing and manipulating the SAR images (GAMMA REMOTE SENSING, 2008). The first step in the data processing is the conversion of the SAR images to GAMMA format. Consequently, initial estimations of interferometric baselines were calculated from the available precise orbit state vectors acquired from the Delft Institute (NL) for Earth-Oriented Space Research (Scharoo and Visser, 1998). With regard to the DEM, external DEM data at a spatial resolution of 90 m provided by the Shuttle Radar Topography Mission (SRTM) V3 were used to simulate and remove the topographic phase contribution. These DEM data were also applied for geo-coding the resultant InSAR products from range-Doppler coordinates into map geometry, corresponding to the Universal Transverse Mercator (UTM) coordinate system.

2.6.1.1. Image co-registration

SAR interferometry requires pixel-to-pixel matches between common features in SAR image pairs. Thus, co-registration, the alignment of SAR images from two antennas, is an essential step for the accurate determination of phase difference and noise reduction (Li and Bethel, 2008).

(Zou et al., 2009) stated that co-registration of InSAR Images is the first step and one that influences significantly the accuracy of InSAR products.

(Li and Bethel, 2008) found experimentally that oversampling by a factor of 10 was satisfactory and concluded that a particular 4-parameter transformation was sufficient for subpixel co-registration of ERS/SAR tandem data.

Interferometric processing of complex SAR data combines two SLC images, s1 and s2, into an interferogram. This requires co-registration of the two images at subpixel accuracy; a registration accuracy of better than 0.2 pixels is required in order not to reduce the interferometric correlation by more than 5%. The co-registration of the images is performed by calculation of the local spatial correlation function for up to 1000 small areas throughout the image. The image offsets that maximise the local correlation are determined. These values are used to estimate polynomial coefficients for offsets in both range and azimuth over the whole image. Once the offset functions are known, the two SLC images can be co-registered. As this is done to subpixel resolution, the re-sampling of one of the images is necessary. Appropriate interpolation methods are used to minimise interpolation errors (Wegmuller and Werner, 1997).

The datasets used within this research are derived from two different satellites: ERS and ENVISAT; consequently, an essential step to implement is the image co-registration of the two datasets.

A straightforward idea of image co-registration is to select one image as a master (reference image) and thereafter, transform all the other slave images onto it in order to facilitate obtaining the slave images for the geometrical characteristics of the master image at subpixel accuracy. Two attempts have been performed by choosing a master image from ERS-1/2 and by implementing co-registration of four modes in order to obtain its geometrical characteristics. However, image 19951220 has a problem in the step of creating a multi-look for the co-registered image and consequently, it has been excluded. Another image, 19991230, has problems in the range and azimuth estimation of the offset models using correlation of image intensities; consequently, this image has also been excluded from the dataset. Therefore, the number of images within the ERS-1/2 dataset is just 22.

The ERS-1 image with orbit number 20672 and date 19950628 was selected as the master image and co-registration with four modes was implemented between ERS-1/2. Thereafter, co-registration of ENVISAT/ERS was done by performing many program procedures, which is called the lookup table approach. It is worth mentioning that this approach allows the user to take into account the different range and azimuth sampling, which is not the case when using the traditional cross-correlation algorithm. Therefore, it is possible to check the accuracy of the co-registration through the final model of standard deviation, which must not be more than 0.1 and 0.8 in range and azimuth, respectively. Table 3 shows the final model of standard deviation in range and azimuth. High significant co-registration between the images can be seen through the result of final model of standard deviation.

Table 3. Final model of range and azimuth of images co-registration

Id	Missions	Date	Final model fit std. Dev.	
			range	azimuth
1	ENVISAT	20030403	0.0848	0.7025
2	ENVISAT	20030821	0.0757	0.6589
3	ENVISAT	20040108	0.0596	0.6771
4	ENVISAT	20040212	0.0747	0.7114
5	ENVISAT	20040422	0.0802	0.5191
6	ENVISAT	20040527	0.0781	0.5086
7	ENVISAT	20040805	0.0768	0.4758
8	ENVISAT	20040909	0.0686	0.7318
9	ENVISAT	20041014	0.0527	0.5607
10	ENVISAT	20050512	0.0634	0.5709
11	ENVISAT	20050825	0.0883	0.6436
12	ENVISAT	20061228	0.0946	0.6416
13	ENVISAT	20070201	0.0734	0.5043
14	ENVISAT	20080327	0.0864	0.6710
15	ENVISAT	20080605	0.0980	0.6978

In this study, a subset of approximately 52.835 × 58.915 kilometres was cropped from the original images, which corresponded to the eastern part of northern Thessaly.

Multi-look processing and filtering were implemented after the images were cropped. Multi-looking is performed to reduce the phase noise. Relatively flat areas of intermediate to high coherence are not problematical; however, greater care has to be taken with terrain that is rugged, as well as with areas of low coherence. The next important step is the simulation of the cropped SAR images with a DEM in order to obtain the information of the topographic phase, in addition to cropping the DEM according to the size of the cropped images.

2.6.1.2. Differential Interferogram Creation

The most important step towards DInSAR creation is the perpendicular baseline range selection. Generally, it is preferred to choose a small range baseline; the main reason for this is to avoid geometrical and interferometric signal de-correlation; furthermore, fringes could not be generated with a big perpendicular baseline.

With regard to the study area, as depicted in the multi-look average image in figure 6, the mountains and rugged topography comprise a large area. Consequently, the selection of a long perpendicular baseline would cause geometrical de-correlation. However, one advantage of a long perpendicular baseline selection is the increase of the interferograms item numbers, which eases the monitoring of a wide time series of ground deformation. On the other hand, within the study area, it was not possible to create a mask over the mountainous area or to exclude it by cropping, because this area was very important for choosing the reference point in a stable area.
The perpendicular baseline that was chosen varied in the range 0–200 metres. The reason behind this extended range selection was the low numbers of ERS-1/2 SAR images and ENVISAT ASAR images, which were 37. Consequently, this was a simple solution to increase the interferograms item numbers.

(CANASLAN and USTUN, 2012) implemented a study to verify the relationship between coherence and the impact of the range and temporal perpendicular baseline. They found that the highest coherence in image pairs occurs with the shortest perpendicular baseline. These authors mentioned that, as expected, a longer perpendicular baseline resulted in poorer coherence. This is because the change of the look angle causes different backscattering characteristics over the study area. Coherences values decrease with an increase in the perpendicular and temporal baseline, because of the time span between the acquisitions of the images.
In this research study, many ranges of perpendicular baseline were selected to verify the impact of perpendicular baseline range on the interferograms numbers and their impact on the coherence results. The ranges of perpendicular baselines are depicted in table 4. It is evident that an increase in the perpendicular baseline range increases significantly the total interferogram item numbers. However, no significant differences were observed between the results of coherences averages.

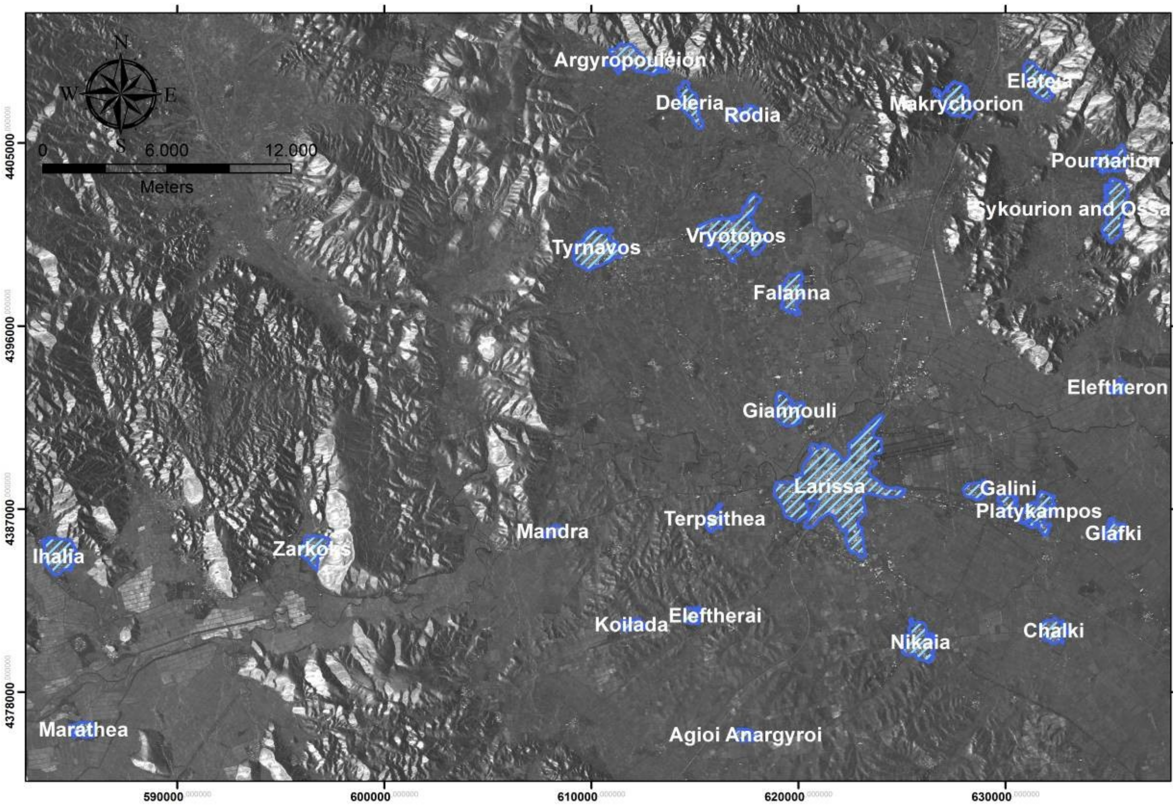

Figure 6. Multi-look average image ascending track highlighting the study area and the mountains around the basin

Table 4. Impact of perpendicular baseline on the interferogram item numbers and coherence

Id	Perpendicular baseline (m.)	Number of interferograms	Statistical data of the coherence map			
			Minimum	Maximum	Mean	Std.dev.
1	0-200	143	0.188	0.878	0.264	0.030
2	0-300	227	0.192	0.875	0.262	0.026
3	0-400	301	0.185	0.907	0.261	0.034

The decision regarding the selection of perpendicular baseline was based on choosing a perpendicular baseline in the range of 0–200 metres, because of the wrapped phase problems of many interferograms with perpendicular baselines in the range 0–300 and 0–400 metres, subsequent to visual checking of each single interferogram. Following the step of perpendicular baseline calculation and selection, the step of creating the interferograms was performed. These interferograms have the properties of the delta time and perpendicular baseline followed by phase adaptation. The next important step following phase adaptation is the phase unwrapping with the initial baseline.

The objective of this step is to look for the correct integer number of phase cycles that needs to be added to each phase measurement in order to obtain the correct slant range distance (Gens, 2006).

(Wegmóller et al., 2006) mentioned that from the complex valued interferograms, interferometric phases are only known modulo (2π). Therefore, the phase unwrapping to estimate unambiguous differential interferometric phases is an important required step.

Within the step of unwrapping, there is sub-process step that is not compulsory to perform, which is the reference point selection. If the reference point is not chosen by the user, the GAMMA software will choose it automatically in the upper left corner of the interferogram. Within this case study, the reference point has been chosen by the software.

2.6.1.3. Reference Point Selection

(Werner et al., 2003a) found that the processing proceeds by performing a least-squares regression on the differential phase to estimate height and deformation rate. The estimates are relative to a reference point in the scene.

The selection of a reference point does not depend on the ground characteristics; consequently, it definitely depends on signal characteristics. One characteristic that assists in choosing the reference point is the coherence, which is one of the many results of the creation of the interferograms.

(Fletcher, 2007) mentioned that local coherence is the cross-correlation coefficient of the SAR image pair, estimated over a small window (a few pixels in range and azimuth), once all the deterministic phase components (mainly owing to the terrain elevation) have been compensated. The coherence map of the scene is then formed by computing the absolute value of γ on a moving window that covers the whole SAR image. The coherence value ranges from 0 (when the interferometric phase is just noise) to 1 (complete absence of phase noise).

Poscolieri et al. (2011) found that the magnitude and the phase of the complex interferograms are generally referred to the degree of coherence (or simply coherence) and the interferometric (InSAR) phase, respectively. The coherence measures the degree of the correlation between two SAR images.

A map of average coherence has been created from the first results of the coherence interferograms. The second result of interferogram coherence is an adaptation and consequently, it might not provide the real value of coherence magnitude.

Figure 7 shows the average coherence map resulting from 143 coherence interferograms. The average coherence magnitude across the scene varies in the range of 0.188–0.878. The yellow colour refers to high coherence, whereas the purple colour refers to a coherence rate that varies in the range of medium–high and the blue colour refers to low coherence**.** It is evidentially observed that low coherence is observed within agricultural fields. This might be attributable to the de-correlation that results from the long time interval of some entire interferograms in addition to the impact of agricultural fields, or in other words, the de-correlation is affected by the influence of vegetation and soil. However, good coherence is observed within urban areas.

(Yanjie and Veronique, 2004) found that the high coherence value could be associated to a ‘good quality’ interferogram.

This observation has been used within this study to evaluate the quality of the reference point. Consequently, larger coherence is associated with a good and stable reference point. The magnitude of the coherence of the reference point that is used later in the step of stacking is 0.865, which additionally has values of range and azimuth of 2296 and 172, respectively.

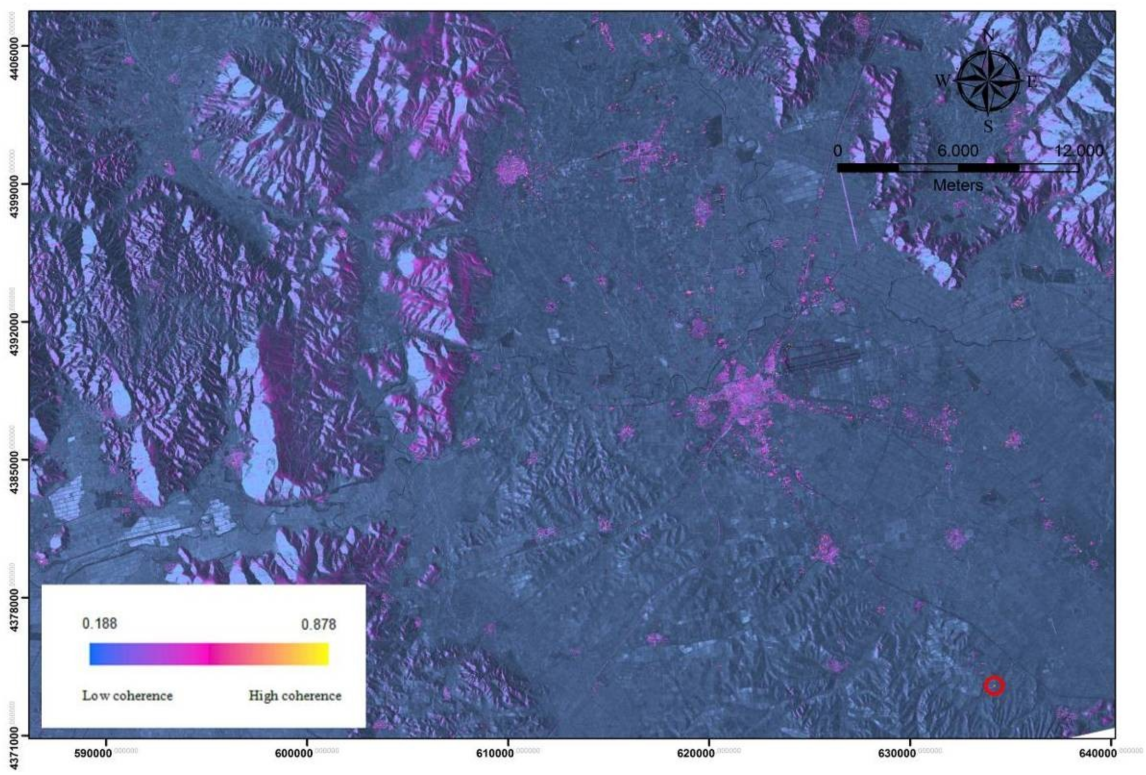

Figure 7. Average coherence for time interval 19950628–20080605 ascending track highlighting the coherence of the reference point inside the red circle

Another requirement in choosing the reference point is that it must be outside of the study area. The reference represents an area comprising many pixels depending on the window size and this entire region will be zero or considered as stable. Before the creation of conventional interferometric and stacking interferograms, the same processing steps as before are applied; however, this time a precise baseline is applied.

Baseline orientation and baseline length are two fundamental parameters in SAR interferometry, which control how topography is mapped into the interferogram phase. In areas of the world with existing DEMs, estimates of the baseline orientation and magnitude are required in order to exploit the DEM data in interferometric processing (Seymour and Cumming, 1996).

First, an estimation of the interferometric baseline was determined from the orbit (track) data or from the average interferogram fringe frequency. This estimation was sufficient for the subtraction of the flat Earth phase trend to facilitate the filtering of the interferogram and the coherence estimation. However, this estimation is not accurate enough to convert the unwrapped interferometric phase into topographic heights. Therefore, a refined baseline estimation is performed using a least squares fit for a number of control points of known height (Wegmuller and Werner, 1997).

2.6.1.4. Repeated pass interferometry processing

The accuracy of deformation estimated from individual differential interferograms is mainly limited by the atmospheric path delay term (Wegmuller et al., 2006).

Additionally, non-continuous stable signals or objects within agricultural fields constitute obstacles to the implementation of this technique.

There are two procedures to implement this technique or to obtain the results of individual differential interferograms. The first procedure is to choose two SAR images: one before the event as the master image and the second after the event as a slave image. Identical steps of processing, as mentioned previously, are applied with this technique.

The second procedure to obtain more than one individual differential interferogram (if there are many SAR images and no precise event has occurred) is implemented through two approaches. The first is to use one master image and to use the other images as slaves and the second is to use multiple master and slave images. However, within the second procedure, the user does not have the freedom of choice time over the interval of images pairs to create the individual interferograms.

With regard to the DEM, either an external DEM is used, or it is created by using tandem SAR images. Within this case study, the second procedure of using multiple master and slave images has been implemented. External DEM data with spatial resolution of 90 m, provided by the Shuttle Radar Topography Mission (SRTM) V3 was used to simulate and remove the topographic phase contribution. These DEM data are also applied for geo-coding the resultant InSAR products from range-Doppler coordinates into map geometry corresponding to the UTM coordinate system and for the co-registration of the ERS and ENVISAT SLC scenes.

From many individual interferograms, one has been selected and the characteristics of this interferogram are depicted in Table 5. The perpendicular baseline is small to avoid residual topographic effects and geometric de-correlation. Furthermore, the short time period increases the quality of the interferogram by decreasing atmospheric effects. The coherence map of this period is depicted in Figure 8. Coherence magnitude varies in range 0.12–0.99 and good coherence covers approximately the entire scene. A high magnitude of coherence is attributed to a low temporal interval, which is 35 days and short perpendicular baseline. The individual differential interferogram is depicted in Figure 9.

Table 5 Parameters of ERS1 SAR images of the individual differential interferogram

Master image	Slave image	$B^{\perp}$ (m)	Interval Days
19960228	19960403	- 66.80	35

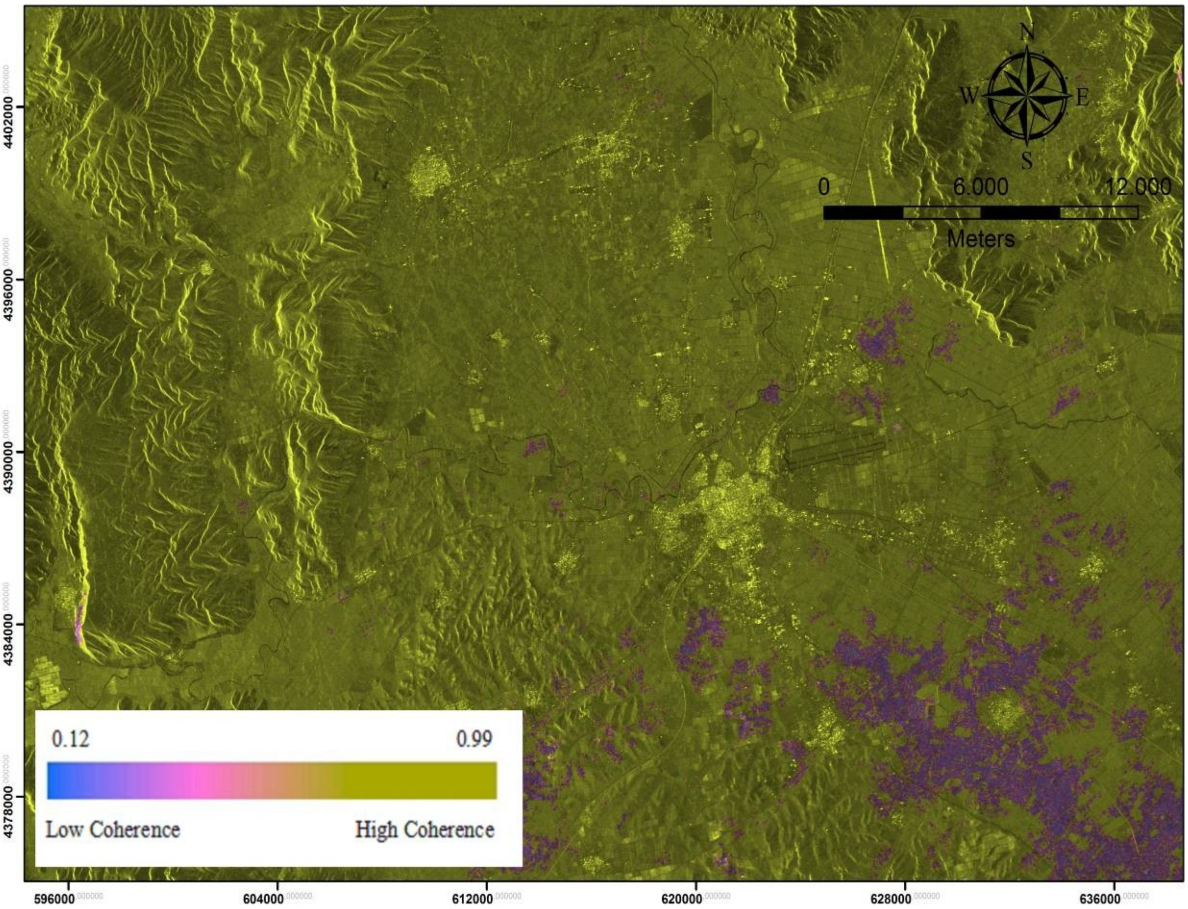

Figure.8 Coherence map for time interval 19960228_19960403 ascending track

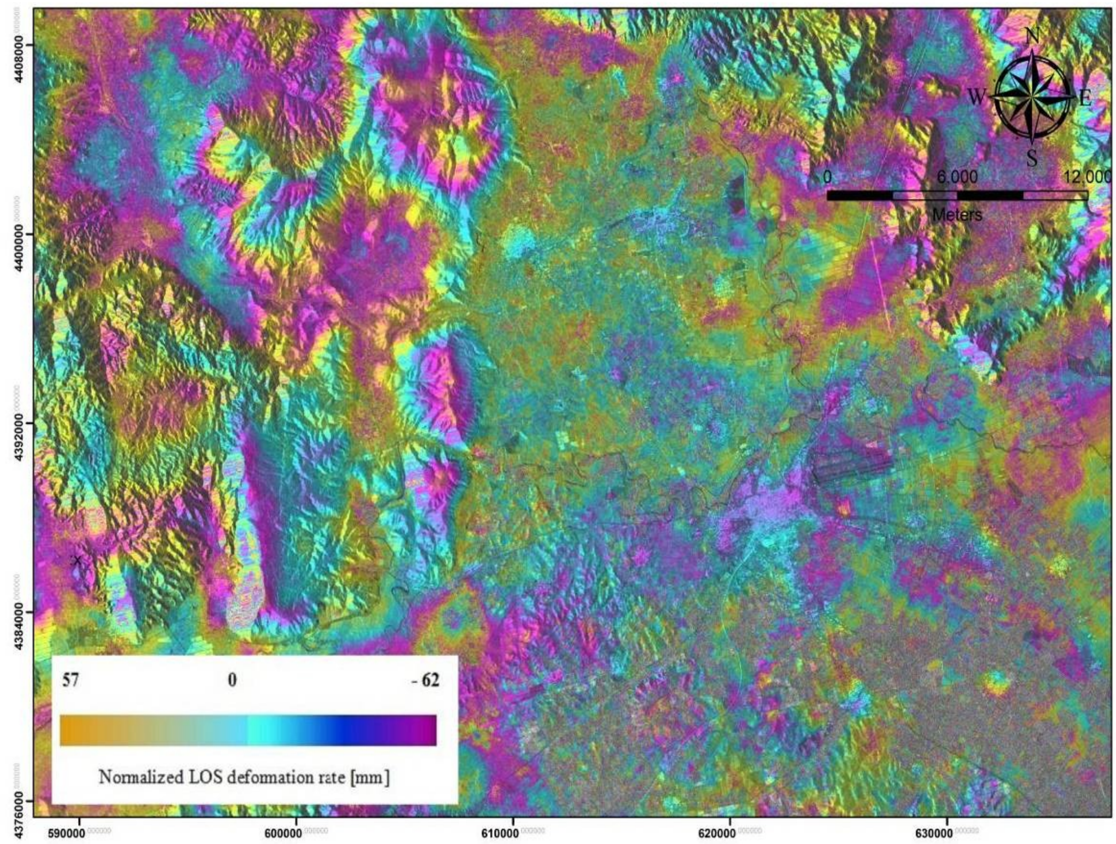

Figure.9 Differential interferogram for time interval 19960228–19960403 ascending track

2.6.1.5. Interferometric stacking processing

Interferometric stacking is a well-established method to estimate the deformation rate for the long-term avoidance of the atmospheric path delay term and to overcome the limitation of the accuracy of deformation estimated from individual differential interferograms.

The basic idea of this technique is to combine multiple interferogram pairs within a single result (Wegmóller et al., 2006).

Thus, the stacking technique (average of phase) calculates the phase of multiple unwrapped interferograms. Moreover, it is used to estimate the linear rate of differential phase using a set of unwrapped differential interferograms. The perpendicular baseline in this study varies in the range of 0–200 metres. The first result was 140 interferogram pairs. From these 140 interferograms, just 29 interferogram pairs were chosen to accomplish the stacking.

The other 131 interferograms were excluded based on the residual phase after the implementation of the unwrapping step by applying a precise perpendicular baseline. It should be noted that the reference point with range and azimuth of 2296 and 172 mentioned previously, was not selected in the unwrapping step. However, it was selected in the stacking step. The average coherence of this point is 0.865. Figure 10 shows the result of the interferometric stacking. Interferometric patterns have been evidentially observed confined to urban and mountains area. However, no interferometric patterns have been observed within agricultural fields within the Larissa basin. As mentioned previously, this is attributed to the time de-correlation as well as to the impact of soil and vegetation on signal loss. It is worth mentioning that these results of interferometric patterns have been correlated with the factors of groundwater, faults, earthquakes and lithology within the next chapters for investigating the causes of ground deformation.

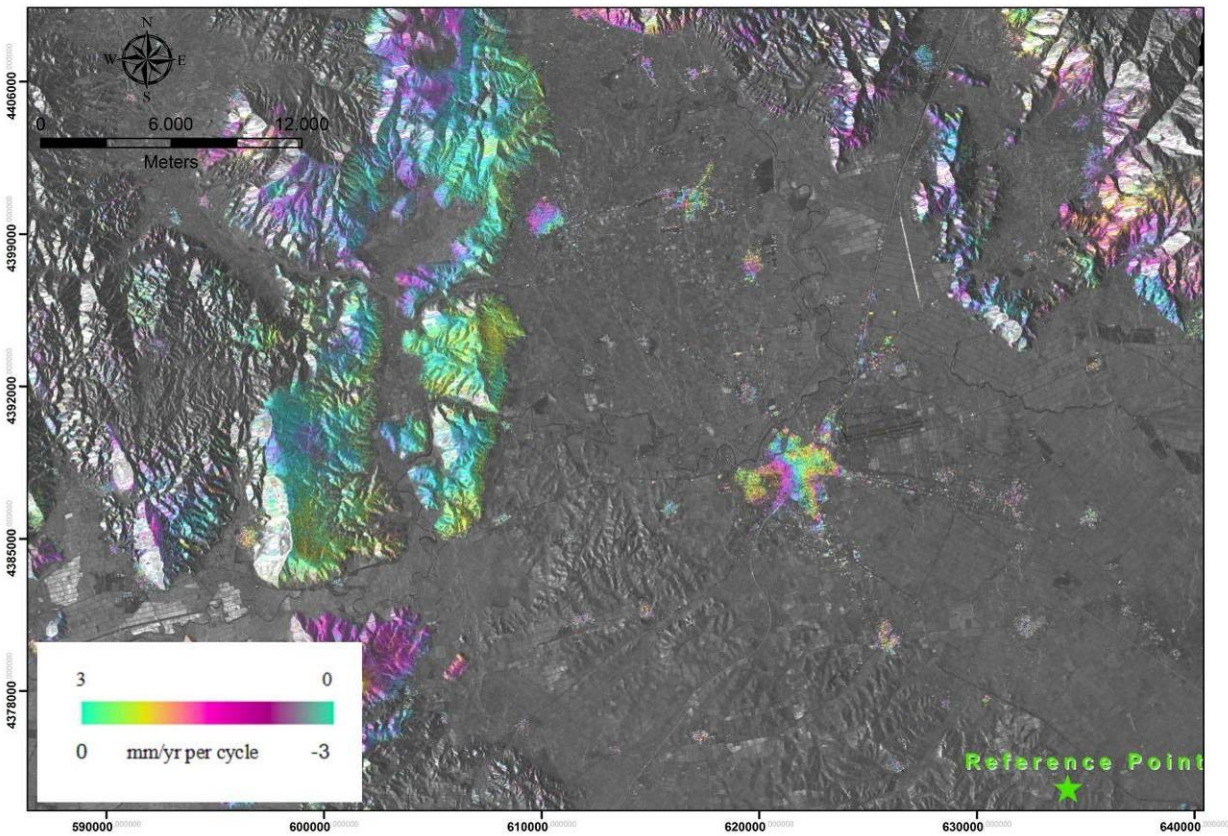

Figure 10. Ground deformation rates along LOS direction deduced by interferometric stacking, for the considered time intervals (1995–2008) Ascending track and different acquisition. Background is an average of multi-look SAR intensities. The selected reference point is marked with a green star

2.6.1.6. Persistent (Permanent) Scatterers Interferometric (PSI)

The processing steps of implementing this technique as well as the results are definitely different from the processing steps and the results of the other techniques that have been applied previously within this research. Consequently, applying the PSI technique (or IPTA algorithm) has many special steps in order to reach the final determination result of the time series deformation of each single candidate point.

It is worth mentioning that in applying this technique there are no stable step sequences and furthermore, no stable parameters to follow. However, it depends on the conditions of the study area in addition to the characteristics of the SAR images.

The PSI processing is initiated by proceeding from the initial step of SAR image co-registration, irrespective of whether the production is from a single or from multiple satellites.

The essential step following the image co-registration is the selection of the master image (reference image). It should be noted that the master image selection has some specific requirements, which are summarised within the following points.

1- It must have a small perpendicular baseline average.

2- It must be near the temporal average of available SAR images.

3- No atmospheric distortion.

4- It must have the smallest temporal and geometrical de-correlation.

The first step towards master image selection is the calculation of perpendicular baseline. There are two methods for calculating the average perpendicular baseline to assist in choosing the best master image. The first one is to assume each single SAR image as a master image and the others as slaves and to iterate this operation until reaching the smallest baseline, in addition to applying all the others conditions previously mentioned as relevant in the selection of a master image. The second method is to correlate a perpendicular baseline series with time and consequently choose the average temporal and smallest perpendicular baseline. The first method has been applied here to select the most appropriate perpendicular magnitude. Thus, image 20040909, which is acquired with an average perpendicular magnitude of 383.813 metres, was chosen as the master image. The perpendicular baseline components relative to the selected reference orbit are depicted in Figure 11. Despite the master image not being in the middle, it was selected as the master image based on its smallest perpendicular baseline. Furthermore, as a result of the individual differential interferogram checking, no atmospheric distortion was observed within this image. The dataset of ERS-1/2 and ENVISAT ASAR are depicted in Table 6.

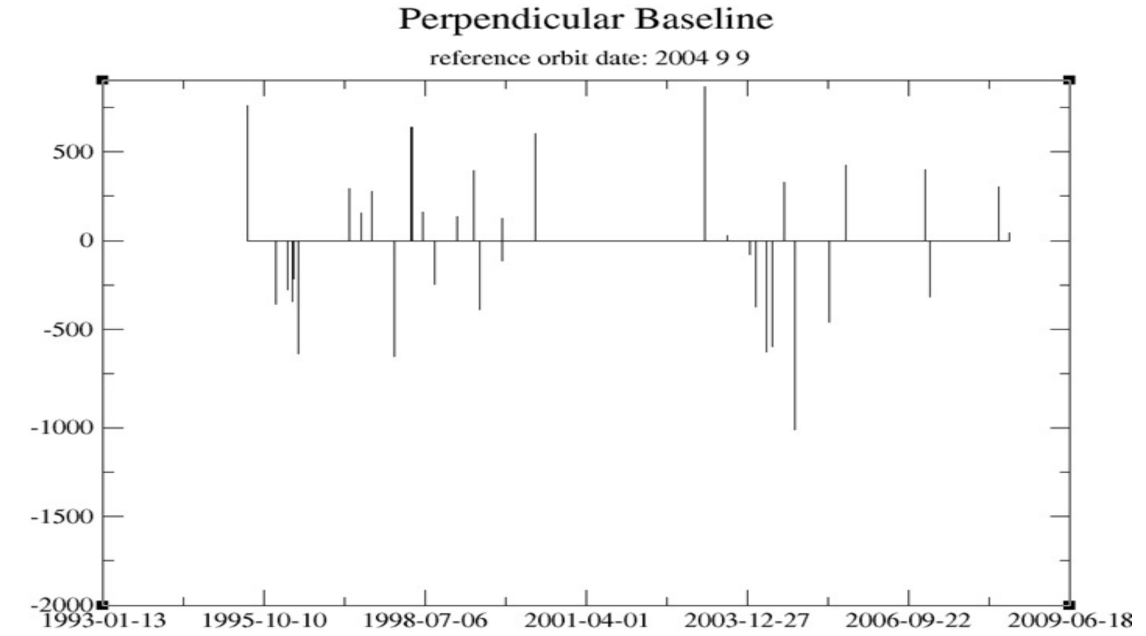

Figure .11 Perpendicular baseline components relative to the selected reference orbit 09 Sept. 2004

Table 6 Dataset of ERS-1/2 ascending track 143, Frame 785 and ENVISAT ASAR track143, frame 783

Id	Date	Orbit	Mission	Bp (m)	Delta time (days)
1	19950628	20672	ERS1	615.44	-3361
2	19950629	999	ERS2	760.036	-3360
3	19951221	3504	ERS2	-355.38	-3185
4	19960228	24179	ERS1	-273.99	-3116
5	19960229	4506	ERS2	-720.395	-3115
6	19960403	24680	ERS1	-340.82	-3081
7	19960404	5007	ERS2	-215.33	-3080
8	19960508	25181	ERS1	-633.79	-3046
9	19960509	5508	ERS2	-517.27	-3045
10	19970320	10017	ERS2	292.54	-2730
11	19971225	14025	ERS2	-649.843	-2450
12	19970807	12021	ERS2	276.35	-2590
13	19970529	11019	ERS2	156.3.97	-2660
14	19990114	19536	ERS2	137.424	-2065
15	19980827	17532	ERS2	-242.85	-2205
16	19980618	16530	ERS2	159.16	-2275
17	19980409	15528	ERS2	637.29	-2345
18	19990603	21540	ERS2	-389.10	-1925
19	19990429	21039	ERS2	394.86	-1960
20	20000518	26550	ERS2	601.616	-1575
21	19991021	23544	ERS2	125.55	-1785
22	19991020	43217	ERS1	-114.30	-1786
23	20040422	11219	ENVISAT	-627.5.0	-140

Supplement of Table 6 dataset of ERS-1/2 Track 143, Frame 785 and ENVISAT ASAR Track 143, Frame 783

Id	Date	Orbit	Mission	Bp (m)	Delta time (days)
24	20040212	10217	ENVISAT	-370.97	-210
25	20040108	7712	ENVISAT	-769.243	-245
26	20030821	7712	ENVISAT	281.569	-385
27	20030403	5708	ENVISAT	866.89	-525
28	20041014	13724	ENVISAT	-1012.07	35
29	**20040909**	**13223**	**ENVISAT**	**0.0000**	**0**
30	20040805	12722	ENVISAT	330.509	-35
31	20040527	11720	ENVISAT	-595.195	-105
32	20070201	25748	ENVISAT	-316.94	875
33	20061228	25247	ENVISAT	397.01	840
34	20050825	18233	ENVISAT	426.83	350
35	20050512	16730	ENVISAT	-460.2.3	245
36	20080605	32762	ENVISAT	420.258	1365
37	20080327	31760	ENVISAT	304.81	1295

Image in bold type is the master image

The second step is to identify candidate points using spectral characteristics, by generating sets of spectral (spectral correlation) and mean/sigma ratio (MSR) images and averaging. Thereafter, candidate points are found from the spectral characteristics, or by generating a point list containing coordinates of image points that satisfy the constraints; the threshold of coherence used here was 0.35.

The resulting number of candidate points is 103999 from the total number of 214224. Thereafter, a point list is generated based on the temporal variability of SLC intensity; the number of candidate points from this step is 5914.

Subsequently, the previous two results of candidate points have been merged, which produces a total number of candidate points of 108853. Following that, the format of the candidate points is changed from raster to vector using the DEM followed by the generation of point interferograms from the SLC point's data stack.

The next step implemented is the estimation of the baseline from the orbit state vectors and the generation of the simulated phase based on DEM heights (topographic phase) and orbital phase term (initial baseline estimates from orbit data), in addition to the simulation of the unwrapped interferometric phase. Following that, the point differential interferograms are generated (no deformation and no atmospheric phase is considered). Subsequently, the least squares model regression is used to determine point target quality and point mask, which creates an output of 37 points from 224967.

The next step is the selection of a reference point target. An important step towards reference point selection in the PSI technique is performed through the application of two sub-steps. Firstly, a spectral candidate point must be created by increasing the threshold of the standard deviation to 0.45. The resulting number of candidate points is 6415. The second sub-step is the temporal intensity, which has been implemented once again; however, this time with the threshold of standard deviation increased to 1.7, which generates 433 candidate points. Thereafter, these are merged together and the number of the total candidate points after merging is 6650.

The result of merging the spectral candidate points and temporal intensity has been used for investigating the reference point. In addition, the previous result of interferometric stacking has been used as a means to verify the deformation of the reference point because it must be stable. Table 7 shows the properties of the reference point (control point), which has been selected. Additionally, Figure 12 shows the reference point behaviour during the time series of the dataset. It is worth mentioning that this reference point was selected after extensive tests and trials.

Table 7 Properties of reference point (control point)

Record	Index	Column	Line	Easting coordinate	Northing coordinate
1	142379	1757	9884	615048.06250000	4405997.50000000

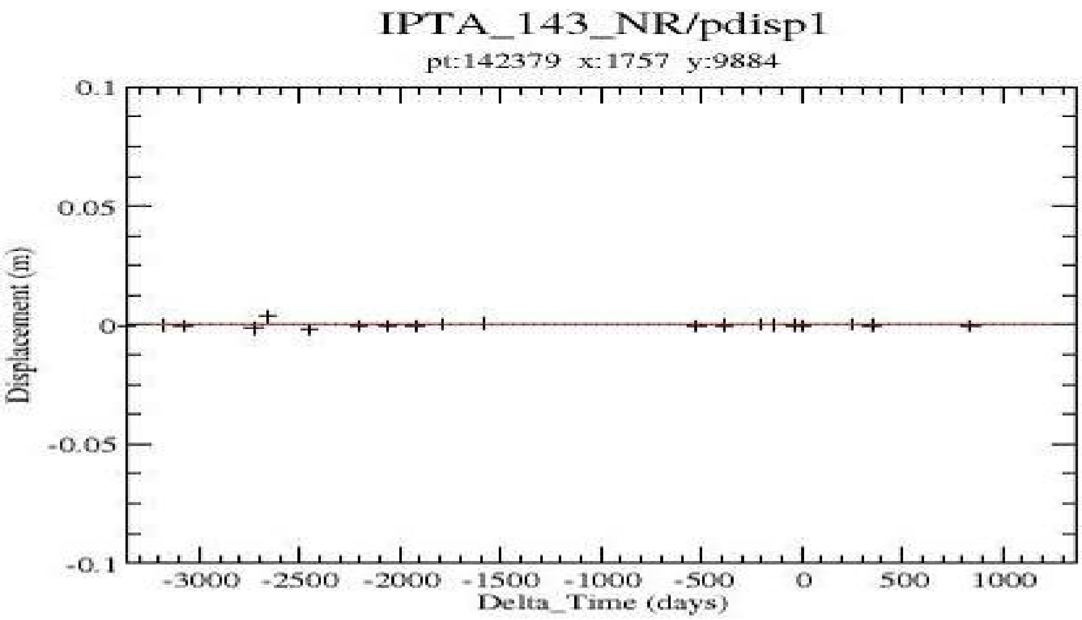

Figure 12. Scatterers Interferometric of reference point mean displacement rates during (1995 – 2006) Ascending Track 143. Movements are in the satellite line of sight direction. No displacement is observed. All values lie along zero value

The next steps are sets of solutions, each of which has many sub-steps for creation of the interferograms, as well as simulating phases by adding, subtracting and repairing. These phases are height, noise, atmospheric and deformation, which ultimately lead to the end step by obtaining temporal and spatial distributions of deformation rate.

2.6.1.6.1. First Solution

The first solution is started with multi-patch estimation of linear deformation. It should be noted that the selection of parameters within each step has strong impact on the implementation program time and on the result that will be achieved. The selected maximum height correction of 60 metres is based on the differences of heights within the study area, which has many mountains around the basin of the settlement of Larissa. Three patch sizes (100, 120, and 200) of range pixels were tested before deciding that 200 worked the best. This can be verified from the matrix results, where number 2 refers to a successful unwrapping, 1 means that there was an attempt to unwrap it and 0 means that the phase remained wrapped.

The selection of 0.01 m/year to represent the maximum deformation rate is based on previous studies. Although higher values might be selected for cases of stronger deformation, this introduces an increased possibility of obtaining results with unwrapping errors. It should be noted that this value does not represent the maximum absolute deformation rate but just the relative rate of deformation between a pair of points; however, higher rates might be detected. The resulting number of valid points is 12491. This step is called the regression analysis and the results of this step are height corrections, linear deformation rate corrections (respectively a first estimate), point quality measurements (phase standard deviation from regression fit), residual phases (deviation from regression fit) for each record and unwrapped interferometric phase and for each record of interferograms stack.

Subsequent steps update heights followed by simulating the unwrapped interferometric phase and subtracting the simulated phase to create the first differential interferograms. Notice that there is no deformation and no atmospheric phases are considered within the initial phase model. Furthermore, initial and not the refined baselines are used. The simulated (unwrapped) phases are subtracted from the complex values point interferograms to obtain point differential interferograms; this results in 37 initial differential interferograms.

Thereafter, spatial filters are applied followed by unwrapping spatially, in order to update the baselines using the unwrapped phase (spatial filter for point data stack). Phase unwrapping for point data stack is performed by using the phase unwrapping algorithm based on Minimum Cost Flow (MCF) optimisation techniques, which is applied to a triangular irregular network.

The subsequent step is adding the unwrapped phase back to the simulated phase, in order to obtain the smooth initial interferogram, followed by the generation of a mask for areas of low deformation rate.

For a better quantitative evaluation between the two unwrapping solutions, the difference between them is calculated, to identify the identical and non-identical values. The resulting number of valid points of this step is 12491.

Following that, the baseline update is performed to calculate the precise baseline (least squares baseline estimation using terrain heights). Thereafter, the precise baseline is used to re-simulate phases and improve the height and deformation. Subsequently, the re-simulated phases are subtracted and the interferograms are created, which is the final step of the first solution.

2.6.1.6.2. Second Solution

The second solution is started by running again the multi-patch estimation of linear deformation; however, here a precise baseline is used. The value of topography was selected as 30 metres, together with the same deformation rate as used in the first solution -0.01 – 0.01 m/year. The patch size in range pixels is 200, which can be verified via the matrix results, as done with the first solution. The resulting number of valid points of this step is 3257. It is worth mentioning that the main results of this step are the residual and unwrapping phases.

The standard deviation phase includes terms related to phase noise, atmospheric path delay related phase, deformation phase and baseline error related phase, as shown in equation (4).

Phase noise is dependent on distance between two points. Consequently, for pairs with short spatial separation, this regression analysis can be done independently of the quality of the atmospheric phase, deformation phase and baseline. The standard deviation of the phase from the regression is used as a quality measurement, which permits the detection and rejection of points that are not suitable for the analysis.

$$\text{Standard deviation} = \varphi_{\_noise} + \varphi_{\_atm} + \varphi_{\_def} + \varphi_{\_bperp} \text{ -------------- } (4)$$

Following verification from the residual phase and by choosing the correct unwrapped layers, 22 of the 37 layers were selected because of good unwrapping. Thereafter, the unwrapped phase has been added back to the simulated phase in order to obtain smooth initial interferograms and additionally, corrections have been added to the height and deformation rate. The next step is to select points with almost no deformation for refinement of the baseline (increasing the threshold of deformation with precise baseline); the threshold selected is between -0.0005 –0.0005. The resulting number of valid points is 87.

Thereafter, the determination of the least squares baseline estimation using terrain heights (baseline with the new threshold of deformation) is performed, followed by the updating of heights and the estimation of linear deformation rates. However, these updates are performed by using the initial and not the refined baselines. Simulated (unwrapped) phases are subtracted from the complex value point of the interferograms in order to obtain the point differential interferograms (complex values). Subsequently, spatial filtering of a triangular weighted average method is applied.

2.6.1.6.3. Third Solution

The first step in the third solution begins with a regression analysis on the updated point's differential interferograms. A patch wise approach is used because the differential interferogram is available only in its wrapped (complex value) form and contains atmospheric phases. The resulting number of valid points numbers is 2854. Subsequently, new point heights and a new deformation for the point mask are updated from the previous step. Both the height and the linear deformation rate corrections are relatively small because the main correction has already been performed. The main benefit of this iteration is to verify the residual phase corrections of the previous layer comparison. The residual phase of this step includes the atmospheric phase.

Thereafter, the combined atmospheric corrections of the interferometric pairs are calculated, followed by the removal of the atmospheric from the differential interferograms.

After that, the least squares method is applied for the spatial filtering of the atmospheric (just to obtain the atmospheric phase).

The verification from the first result of the reference point by checking the regression analysis of pair points is then implemented. Figure 13 shows the regression analysis of pairs of points. A two dimensional phase regression plot is shown for a case with a small relative height correction. In the upper plot, the baseline dependence of the phase difference is shown after compensation for the time dependence and the lower plot shows the time dependence after compensation of the baseline dependence.

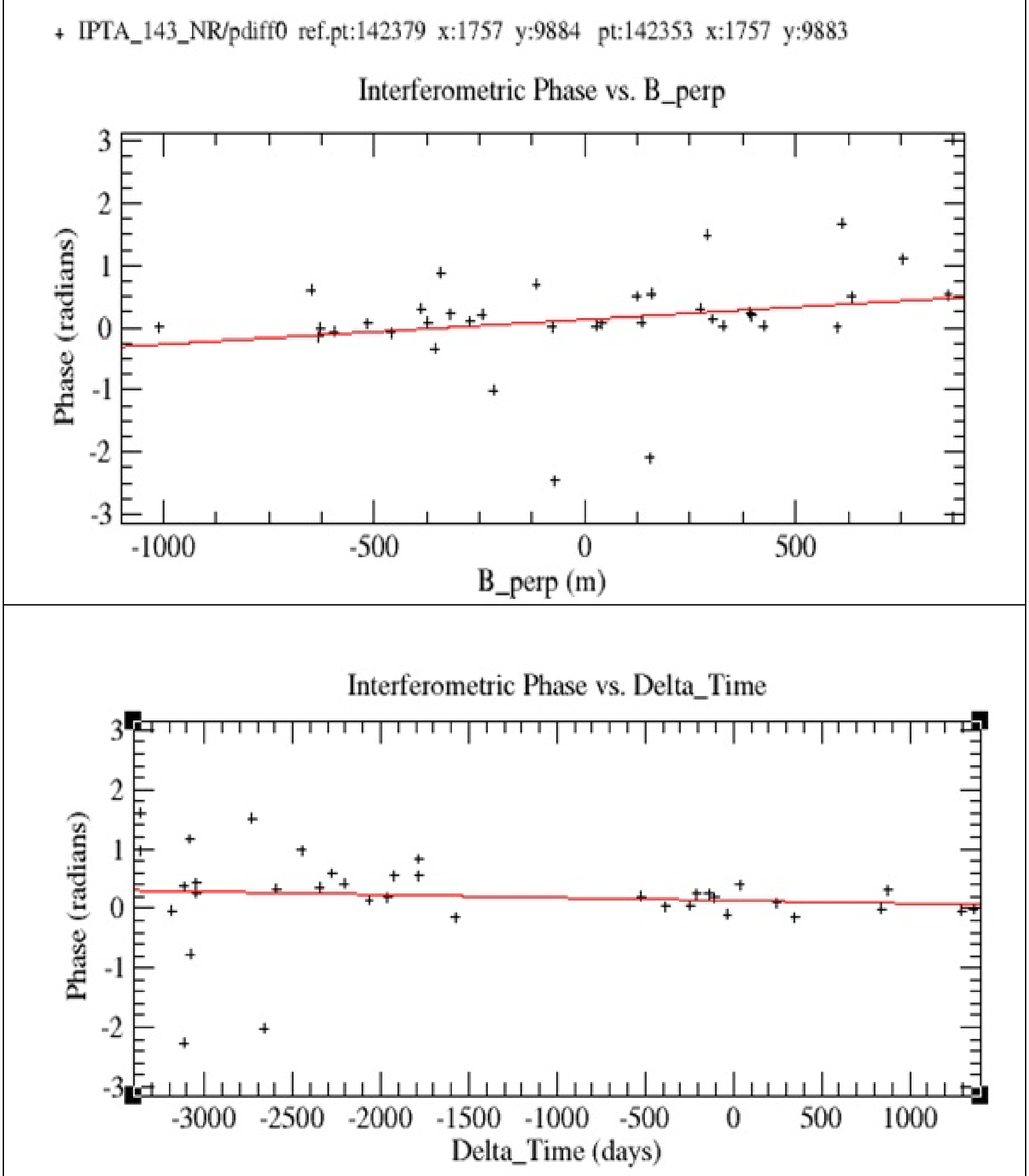

Figure 13. Regression analysis for pair of points

2.6.1.6.4. Fourth Solution

The initial step of the final solution begins by performing a regression analysis on the updated differential interferograms. A patch wise approach is also used here. The differential interferogram is available just in its wrapped (complex value) form and contains atmospheric phases. The resulting number of valid points is 1866. Once again, an update of the point heights and linear deformation rates is performed. The result of the previous step is the final number of valid points.

Thereafter, phase noise is reduced by implementing a spatially filtered signal as a reference. To achieve a reduction of phase noise of the interferometric phases relative to the reference point, filters replace the reference point phases with spatially filtered phases. This is adequate if the area around the reference location can be assumed stable. The next step is filtering; however, this time the temporal filtering uses a long time interval; 180 days is considered as the time filter, which is followed by the simulation of a linear deformation rate. Consequently, a filter step of nonlinear deformation, residual phases and noise phase is implemented from linear deformation rates.

It should be noted that if only a linear deformation rate is important, it is the last result that could be requested and consequently, it could generate just a time series of linear deformation rate. Otherwise, if a time series of linear deformation model is generated and the residual phase is added, this visualises how the values are spread around the linear model and small local nonlinear effects become visible. The atmospheric phase is not included in the last model. Thereafter, the combined phase is converted to the line of sight displacement value. Negative displacement values correspond to subsidence and positive displacement values correspond to uplift.

The results of the candidate points have been transformed from GAMMA (S/W) as database files and an attribute table has been created. Subsequently, these have been superimposed in ArcGIS to identify and investigate spatial and temporal deformation. Figure 14 shows the distribution of candidate points within the study area. The majority of the distribution is within urban areas, specifically in the middle, north-western and south-eastern parts of the Larissa basin. Patterns of subsidence and uplift are spread across the areas in which the candidate points exist. The deformation rate of subsidence and uplift varies in the range of -1 to -38 and 1 to 42 mm/LOS, respectively.

Figure 15 shows the frequency of deformation rate. The minimum frequency varies in the range of 0 – 50 for deformation rate, which varies in the range of -38 to -11 mm/year. The maximum frequency varies in the range of 200 – 300 for deformation rate, which varies in the range 19 – 21 mm/year. It is noticeable that the frequency of subsidence deformation rate is less than the frequency of uplift deformation rate.

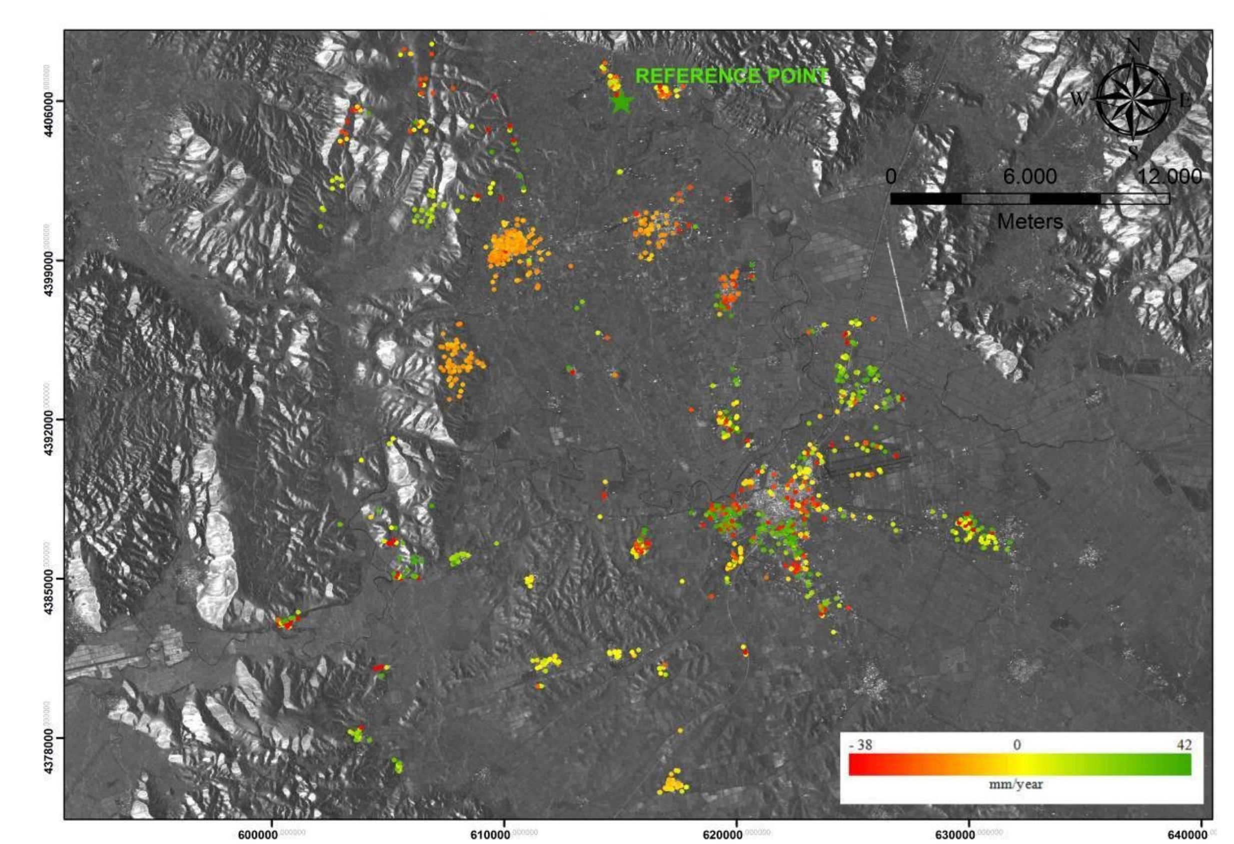

Figure 14 Distribution of geo-coded radar targets (persistent scatterers) in Larissa basin before expansion. The average in line of sight (LOS) velocity (for the period 1995–2006) has been saturated at ± 0.1 m/year for visualisation purposes. Background is a multi-look average SAR image. The reference point is marked with a green star

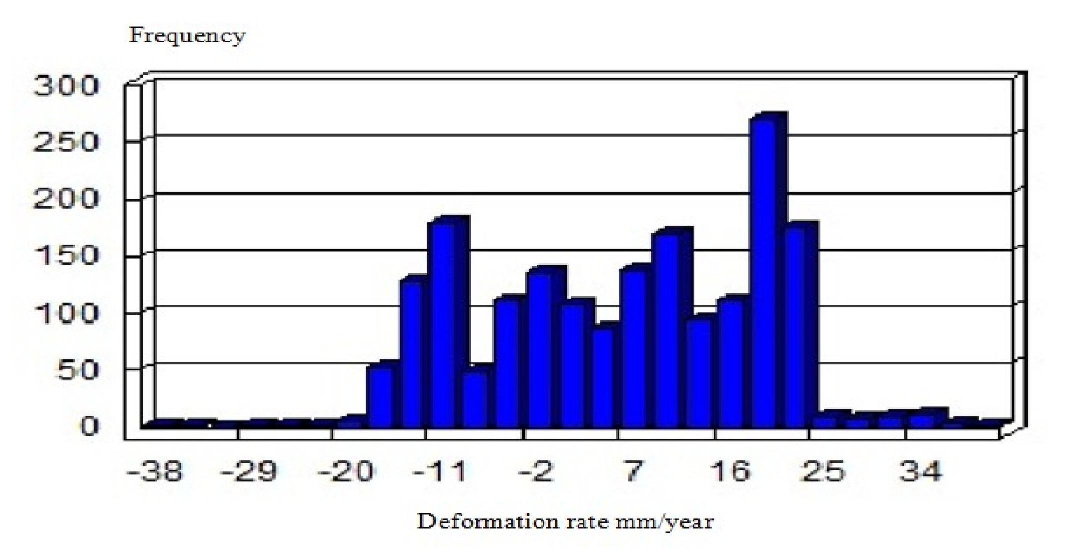

Count: 1886, Minimum: -38, Maximum: 42, Sum: 12172, Mean: 6.523044, Standard Deviation: 12.

Figure 15. Frequency of deformation rate of candidate points first result before expansion

It is worth mentioning that the first result of the point's candidate's has been not used or correlated with other ground data, such as groundwater, fault movements, soil and type of lithology, or other ground features to investigate and identify the causes of ground deformation.

This is because the IPTA processing can build upon an existing solution and check additional points if a solution can be found for them (Wegmóller, 2005).

2.6.1.7. Expansion

Checking the possibility of building upon an existing solution for additional candidate points is called expansion.

(Wegmóller, 2005) mentioned that there are two major advantages of this possibility:

1) The possibility of adding points later makes the decision of reject points much easier.

2) For additional points, an already accepted point is used as a local reference in the integration step. Using a local reference has advantages, such as lower atmospheric and nonlinear deformation phases.

This author also mentioned that the main steps of expansion of an existing result to increase the candidate points are:

1) Expand the existing solution (i.e., the point heights, the linear deformation rate and the atmospheric phases, if nonlinear deformation exists) to further points by interpolation.

2) Calculate the differential interferogram for the combined point list (points with solution and additional points).

3) Conduct regression analyses locally on the differential interferogram phases, using the accepted points as local reference, to determine point height corrections, linear deformation rate corrections and a quality measure for the new points.

4) Update the point list and solution to include additional accepted points.

Expansion processing has many steps that have been implemented to build upon new candidate points.

Expansion begins with the step of expansion of the atmospheric phases followed by an expansion of the linear deformation rate. With regard to the terrain heights, a different approach is performed. An accepted point height correction is used; however, for checking the additional point height corrections, the initial terrain heights of the DEM have been used.

In the next step, the differential interferogram of the combined point list is calculated and the point differential interferograms (considering no deformation and no atmospheric phase) are generated. Thereafter, subtraction of the simulation phases and creation of the first differential interferograms are performed. Subsequently, a regression analysis using the accepted points as local references is performed. These differential interferogram regression analyses are conducted for the additional points using nearby accepted points as local references. Thereafter, the points list is updated to include any additional accepted points. Consequently, the model is updated for the new point list, which includes the additional 'good points'. The resulting number of valid points is increased from 1866 to 62551. A spatial filter is then applied followed by spatial unwrapping to update the baselines using the unwrapped phase (spatial filter for point data stack). Subsequently, a temporal filtering of the residual phases with a filter of 180 days, together with the simulation of linear deformation rate is implemented. Thereafter, if required, filters of the nonlinear deformation, residual phases and noise are added to the linear deformation rates (this step is not compulsory).

Consequently, the result of the deformation rate is converted to LOS displacement. In the final step, the point range Doppler pixel coordinates are converted to map pixel and map projection coordinates and point displacement histories in text format (in map geometry) are generated.

Figure 16 shows the distribution of candidate points within the study area after expansion. A dense distribution of candidate points has been observed throughout the Larissa basin from the southern settlement of Larissa to the extreme north of the basin. However, the distribution of candidate points within urban areas is larger than that in agricultural fields.

Patterns of subsidence and uplift are spread across the areas in which candidate points exist. The deformation rate of subsidence and uplift vary in the range -1 to -38 and 1 to 42 mm/LOS, respectively. No difference was found between the deformation rate before and after the implementation of expansion. This similarity indicates that the deformation rate of the candidate points throughout the Larissa basin is equivalent. Other indicators suggest that the entire Larissa basin has been subject to approximately the same influences deformation. However, it is worth mentioning that the same thresholds of deformation rate have been used before and after the expansion. Differences have been observed between the frequencies of deformation rate before and after expansion. Figure 17 shows the frequency of deformation rate. Minimum frequency varies in the range of 0 – 1.000 for deformation rate, which varies in the range of -38 to -20 mm/year. Maximum frequency varies in the range 4.000 – 5.000 for deformation rate, which varies in the range of -2 to 10 mm/year. It is noticeable that the frequency of maximum subsidence deformation rate is less than the frequency of minimum subsidence deformation rate. In addition, the frequency of uplift deformation rate is higher than the frequency of subsidence deformation rate. It should also be noted that the histogram shows a more normalised deformation rate frequency than the histogram before expansion. It is worth mentioning that the result obtained after expansion has been used within the next chapters for investigating the behaviour of deformation for selective candidate points, in addition to correlating ground deformation with other factors, such as groundwater, faults and earthquakes, type of lithology and soil.

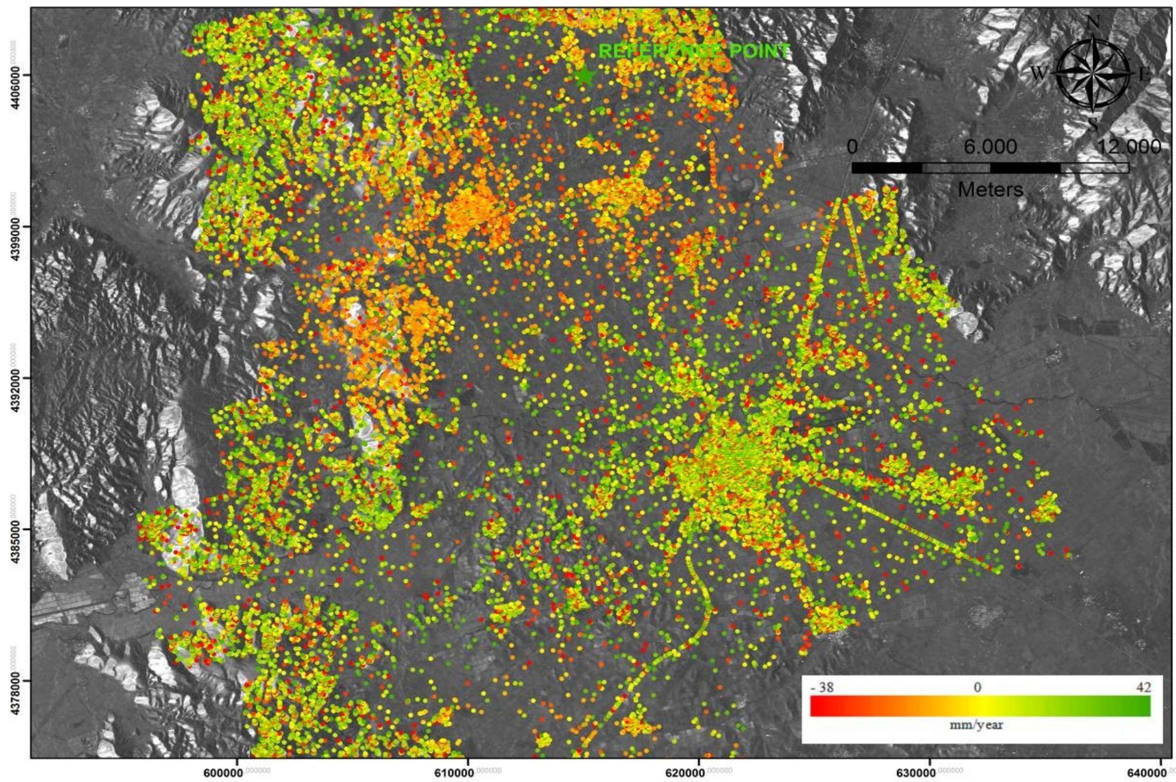

Figure 16. Distribution of geo-coded radar targets (persistent scatterers) in Larissa basin after expansion. The average in line of sight (LOS) velocity (for the period 1995–2006) has been saturated at ± 0.1 m/year for visualisation purposes. Background is a multi-look average SAR image. The reference point is marked with a green star

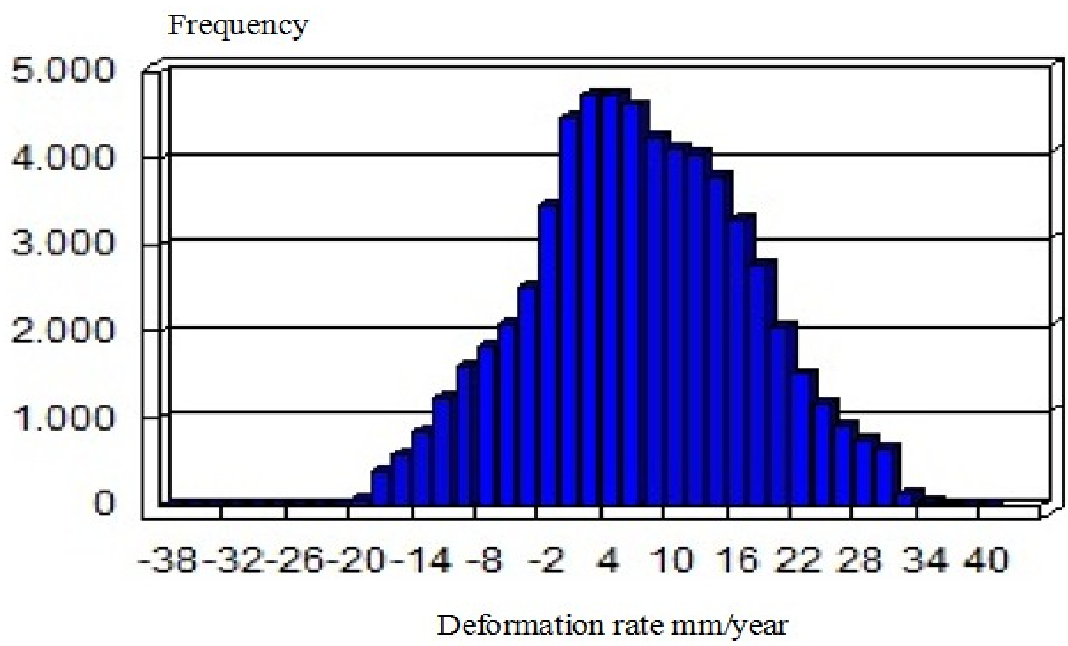

Count: 62551, Minimum: -38, Maximum: 42, Sum: 433327, Mean: 6.927579, Standard Deviation: 10.268733

Figure 17. Frequency of deformation rate of candidate points after expansion

2.6.2. SAR Data Selection and Interferometric Processing (Descending Track 279)

The total dataset consists of 48 SLC SAR C-band images of ERS-1/2 from 1992 – 2000 and additionally, 25 SLC images of ENVISAT ASAR from 2002 – 2010 acquired by ESA,, which cover the study area have been selected along this track, as shown in Tables 8, 9, 10 respectively.

Table 8. Datasets of ERS-1 SAR images descending Track 279, Frame 2812 used in the processing

Id	Missions	Acquisition Date	Orbit
1	ERS1	19921112	6937
2	ERS1	19930610	9943
3	ERS1	19930819	10945
4	ERS1	19931028	11947
5	ERS1	19950325	19305
6	ERS1	19950429	19806
7	ERS1	19950603	20307
8	ERS1	19950708	20808
9	ERS1	19951021	22311
10	ERS1	19951230	23313
11	ERS1	19960309	24315
12	ERS1	19960413	24816
13	ERS1	19960518	25317

Table 9. Datasets of ERS-2 SAR images descending Track 279, Frame 2812 used in the processing

Id	Missions	Acquisition Date	Orbit
1	ERS2	19950813	91521
2	ERS2	19950917	2137
3	ERS2	19951231	3640
4	ERS2	19960414	5143
5	ERS2	19960519	5644
6	ERS2	19960623	6145
7	ERS2	19960901	7147
8	ERS2	19961006	7648
9	ERS2	19961110	8149
10	ERS2	19961215	8650
11	ERS2	19970119	9151
12	ERS2	19970223	9652
13	ERS2	19970504	10654
14	ERS2	19970608	11155
15	ERS2	19970713	11656
16	ERS2	19970817	12157
17	ERS2	19970921	12658
18	ERS2	19971130	13660
19	ERS2	19980104	14161
20	ERS2	19980419	15664
21	ERS2	19980524	16165
22	ERS2	19980628	16666
23	ERS2	19980802	17167
24	ERS2	19980906	17668
25	ERS2	19990228	20173
26	ERS2	19990613	21676
27	ERS2	19990822	22678
28	ERS2	19990926	23179
29	ERS2	19991031	23680
30	ERS2	19991205	24181
31	ERS2	20000109	24682
32	ERS2	20000423	26185
33	ERS2	20000528	26686
34	ERS2	20001119	29191
35	ERS2	20001224	29692

Table10. Datasets of ENVISAT ASAR images descending Track 279, Frame 2807 used in the processing

Id	Missions	Acquisition Date	Orbit
1	ENVISAT	20021020	03339
2*	**ENVISAT**	**20030309**	**05343**
3	ENVISAT	20030622	06846
4	ENVISAT	20031109	08850
5	ENVISAT	20040328	10854
6	ENVISAT	20050206	15363
7	ENVISAT	20050313	15864
8	ENVISAT	20050417	16365
9	ENVISAT	20050522	16866
10	ENVISAT	20050904	18369
11	ENVISAT	20051113	19371
12	ENVISAT	20060226	20874
13	ENVISAT	20060611	22377
14	ENVISAT	20060716	22878
15	ENVISAT	20061029	24381
16	ENVISAT	20070211	25884
17	ENVISAT	20070805	28389
18	ENVISAT	20080406	31896
19	ENVISAT	20080720	33399
20	ENVISAT	20081102	34902
21	ENVISAT	20090111	35904
22	ENVISAT	20090215	36405
23	ENVISAT	20090426	37407
24	ENVISAT	20100620	43419
25	ENVISAT	20101003	44922

Image marked with (*) is the master image

2.6.2.1. Interferometric Processing

Identical steps of pre-processing used with the ascending track have been used in processing the descending track.

2.6.2.2. Image co-registration

As mentioned previously, datasets within this study are derived from two different satellites, ERS and ENVISAT ASAR. Consequently, image co-registration is an initial step in implementing the two datasets.

The image from ENVISAT ASAR with orbit number 33399 and date 20080720 was selected as the master image. Consequently, co-registration of four modes has been performed to facilitate obtaining the slave images for the geometrical characteristics of the master image at sub pixel accuracy. Thereafter, according to (GAMMA REMOTE SENSING, 2008), the co-registration of ERS and ENVISAT has been done by applying many programs of the lookup table approach.

It should be noted that the result of co-registration could be checked through the final mode of standard deviation, which must not be more than 0.1 and 0.8 for the range and azimuth, respectively. However, it is worth mentioning that the final mode of standard deviation was more than the specified thresholds for both range and azimuth. Accordingly, the first solution of this problem is to change the co-registration plan and to choose other master image. Consequently, the ENVISAT ASAR image with orbit number 05343 and date 20030309 was selected as the master image. Another solution to overcome this problem and obtain high quality co-registration is achieved by changing the window within the refining of the co-registration lookup table. A cross-correlation algorithm for two multi-look images has been used with an offset window of 256 × 256 instead of 128 × 128. Tables 11, 12 show final model standard deviation range and azimuth. The results of the final model of range and azimuth indicate high significant co-registration.

Table 11. Final model of range and azimuth of images co-registration of ERS-1

Id	Missions	Date	Final model fit std. Dev.	
			range	azimuth
1	ERS1	19921112	0.0606	0.6328
2	ERS1	19930610	0.0825	0.5697
3	ERS1	19930819	0.0907	0.6988
4	ERS1	19931028	0.0555	0.5140
5	ERS1	19950325	0.0476	0.2555
6	ERS1	19950429	0.0707	0.3518
7	ERS1	19950603	0.0649	0.3413
8	ERS1	19950708	0.0660	0.5484
9	ERS1	19951021	0.0883	0.6396
10	ERS1	19951230	0.0702	0.6485
11	ERS1	19960309	0.0628	0.6610
12	ERS1	19960413	0.0579	0.4099
13	ERS1	19960518	0.0865	0.5612

Table 12. Final model of range and azimuth of images co-registration of ERS-2

Id	Missions	Date	Final model fit std. Dev.	
			range	azimuth
1	ERS2	19950813	0.0763	0.5748
2	ERS2	19950917	0.0744	0.4046
3	ERS2	19951231	0.0649	0.7687
4	ERS2	19960414	0.0601	0.7544
5	ERS2	19960519	0.0763	0.3393
6	ERS2	19960623	0.0733	0.4098
7	ERS2	19960901	0.0839	0.6638
8	ERS2	19961006	0.0655	0.3238
9	ERS2	19961110	0.0617	0.7927
10	ERS2	19961215	0.0633	0.6280
11	ERS2	19970119	0.0725	0.6446
12	ERS2	19970223	0.0712	0.6899
13	ERS2	19970504	0.0701	0.5552
14	ERS2	19970608	0.0675	0.6579
15	ERS2	19970713	0.0821	0.5946
16	ERS2	19970817	0.0776	0.7064
17	ERS2	19970921	0.0617	0.2348
18	ERS2	19971130	0.0616	0.5604
19	ERS2	19980104	0.0622	0.6060
20	ERS2	19980419	0.0714	0.7832
21	ERS2	19980524	0.0641	0.5511
22	ERS2	19980628	0.0721	0.6332
23	ERS2	19980802	0.0884	0.7173
24	ERS2	19980906	0.0834	0.5068
25	ERS2	19990228	0.0586	0.3005
26	ERS2	19990613	0.0883	0.5464
27	ERS2	19990822	0.0725	0.3628
28	ERS2	19990926	0.0676	0.2600
29	ERS2	19991031	0.0636	0.7028
30	ERS2	19991205	0.0623	0.6181
31	ERS2	20000109	0.0600	0.6015
32	ERS2	20000423	0.0711	0.3522
33	ERS2	20000528	0.0694	0.3861
34	ERS2	20001119	0.0852	0.5177
35	ERS2	20001224	0.0794	0.5591

A subset of approximately 68.253 × 59.598 kilometres is cropped from the original images, which relates to the study area of the eastern part of northern Thessaly.

Some processing steps, such as multi-look and filtering have been performed after the image cropping. Multi-looking may be performed to reduce the phase noise. Relatively flat areas of intermediate to high coherence are not problematic; however, greater care must be taken with terrain that is rugged and for areas of low coherence. The next important step is the simulation with the DEM in order to obtain the information of topographic phase for the cropped images, in addition to cropping the DEM according to the size of the cropped images.

The most important step towards the creation of the differential Interferograms (DInSAR) is the range selection of the perpendicular baseline.
Within this track, the perpendicular baseline varies in the range of 0 –150 m. It is noticeable that in the study area, as depicted in the multi-look average image figure 18, the mountains constitute a huge part of the area, as mentioned previously with the ascending track.

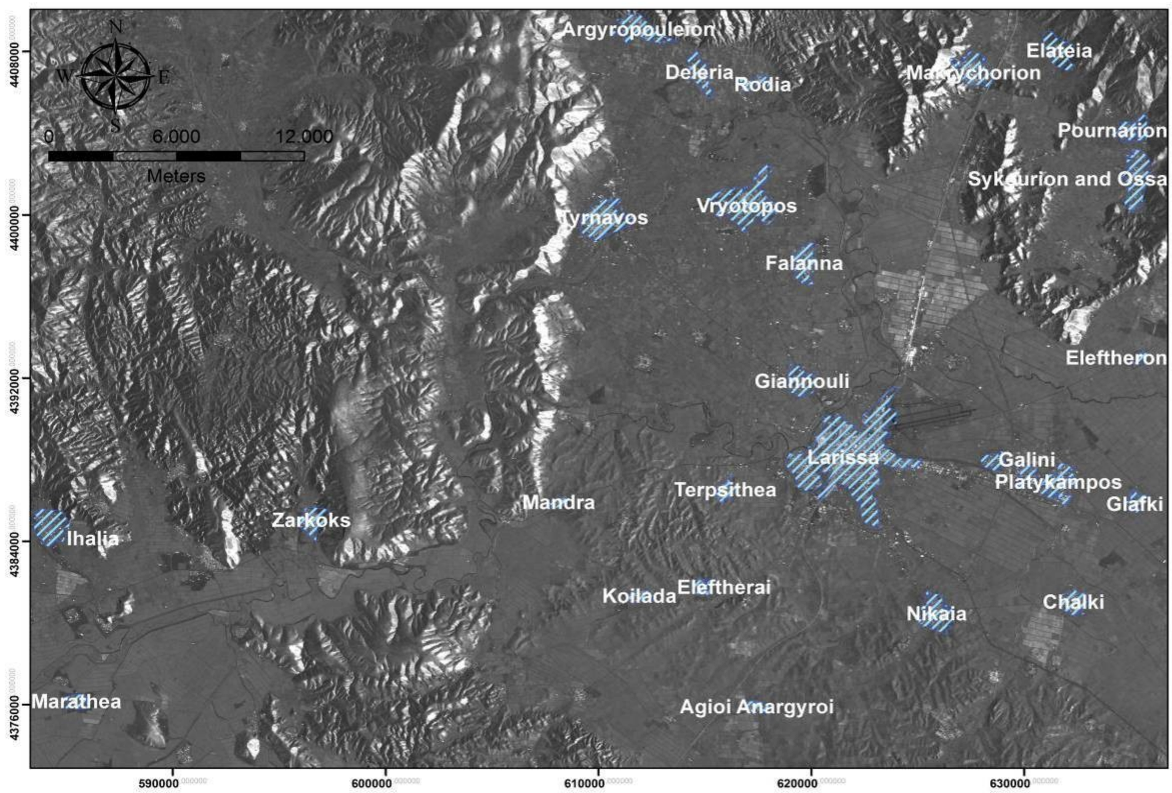

Figure 18. Multi-look average image descending track highlighting the study area and the mountains around the basin

A perpendicular baseline of more than 150 m has not been chosen, even though (Fletcher, 2007) mentioned that will be an upper limit to the perpendicular baseline, beyond which the interferometric signals de-correlate and no fringes can be generated; in the case of ERS, such an optimum baseline is about 300–400 metres. The other reason is that the numbers of SAR images is adequate to create a good number of interferograms. The resulting number of the interferogram pairs was 474. Table 13 shows the characteristics of the interferograms average.

Table 13. Characteristics of interferograms average

Id	Perpendicular baseline (metres)	Number of interferograms	Statistics data of the coherence map			
			Minimum	Maximum	Mean	Std.dev
1	0-150	474	0.195	0.925	0.257	0.035

After interferogram creation, the most important step is phase unwrapping with the initial baseline. Within the step of unwrapping there is the sub-process of reference point selection; however, no reference point has been selected by the researcher and therefore, within this step, the reference point has been selected automatically by the software in the upper left corner of the interferograms. Nevertheless, the reference point has been selected within the step of stacking.

An important aid in choosing reference point within the ascending track, as mentioned previously, is the coherence, which is one of the many results of the creation of the differential interferograms. A map of average coherence has been created from the first results of the differential interferograms. Figure 19 shows the map of average coherence resulting from 474 coherence interferograms. The average magnitude of coherence across the scene varies in the range of 0.195 –0.925. Low coherence is observed within agricultural fields, which might be attributable to the de-correlation resulting from the long time interval, or because of the impact of the agricultural fields, i.e., de-correlation might be affect by the influence of the crops and soil. However, good coherence is observed within the urban areas.

The next important step following the adaptation of phase is the phase unwrapping with the initial baseline. Thereafter, the processing steps before conventional interferometric and interferometric stacking are identical to all previous processing steps; however, a precise baseline is used this time. The magnitude of coherence of the reference point used later in the step of stacking is 0.918 and it has a range and azimuth of 467 and 783, respectively.

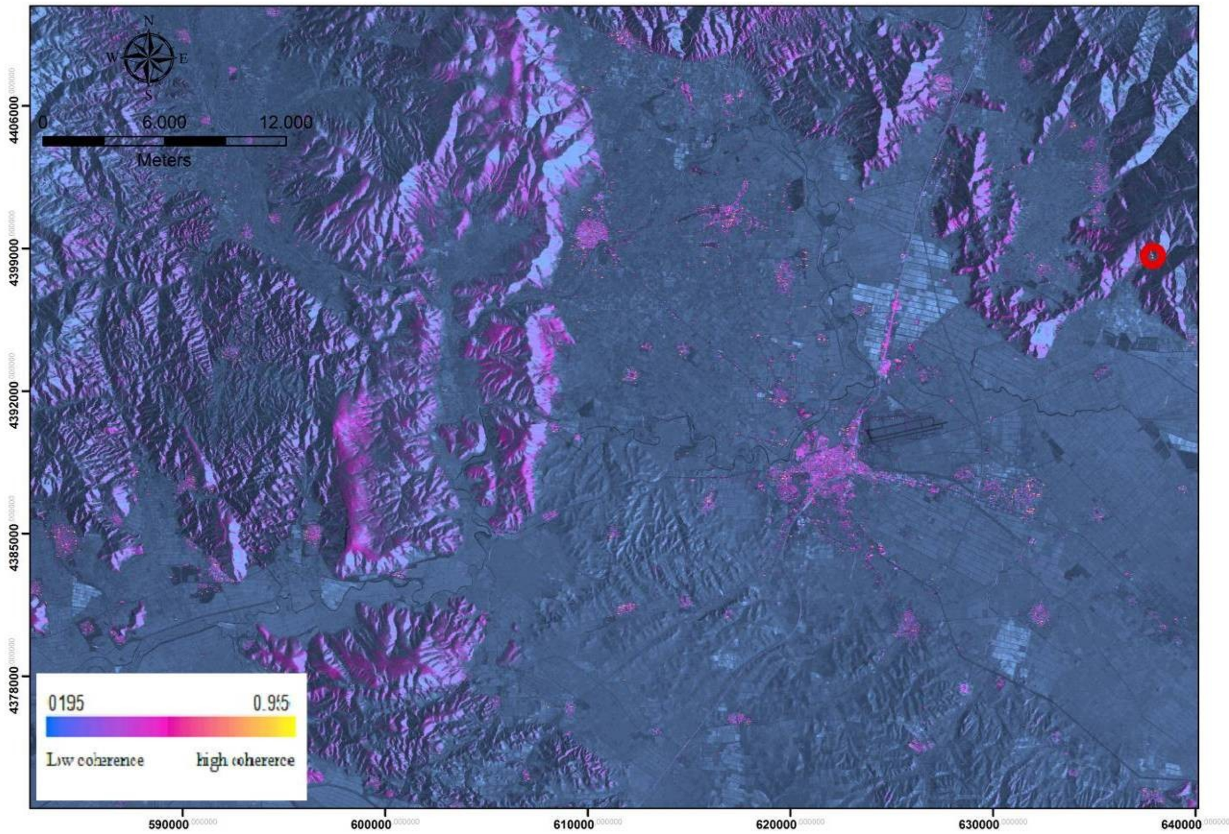

Figure 19. Coherence map for time interval 19921112–20101003 descending track highlighting the coherence of reference point inside the red circle

2.6.2.3. Repeated pass interferometry processing

The procedure using multiple master and slave images has been implemented to obtain the results of conventional SAR interferometrics as individual interferograms. An external DEM, which is provided by SRTM V3, has been used. From many individual interferograms, one has been selected and the characteristics of this interferogram are depicted in Table 14. The perpendicular baseline is small to avoid residual topographic effects and geometric de-correlation. Furthermore, a short time period increases the quality of the interferogram by decreasing the atmospheric impact. Despite the short time interval and small perpendicular baseline, low distribution density of the interferometric phase has been observed. The interferogram is based on summer data and consequently, many causes might participate in reducing the density of the interferometric phase relevant to the phase unwrapping. These causes are relatively strong, small- to medium-scale atmospheric distortions and spatial gaps in the coverage of agricultural fields.

Table14. Parameters of ERS-2 SAR images used within this interferogram

Master image	Slave image	$B_\perp$ (m)	Days
19980802	19980906	- 1.51	35

The coherence map of this period is depicted in Figure 20. The magnitude of coherence varies in the range of 0.10 – 0.99. Good coherence covers approximately the entire scene, except for areas of low coherence within agricultural fields, which are located in the middle north, Middle East and middle southeast and southwest of the scene. Good quality coherence might be attributed to the low time interval, which is 35 days. An individual differential interferogram is depicted in Figure 21.

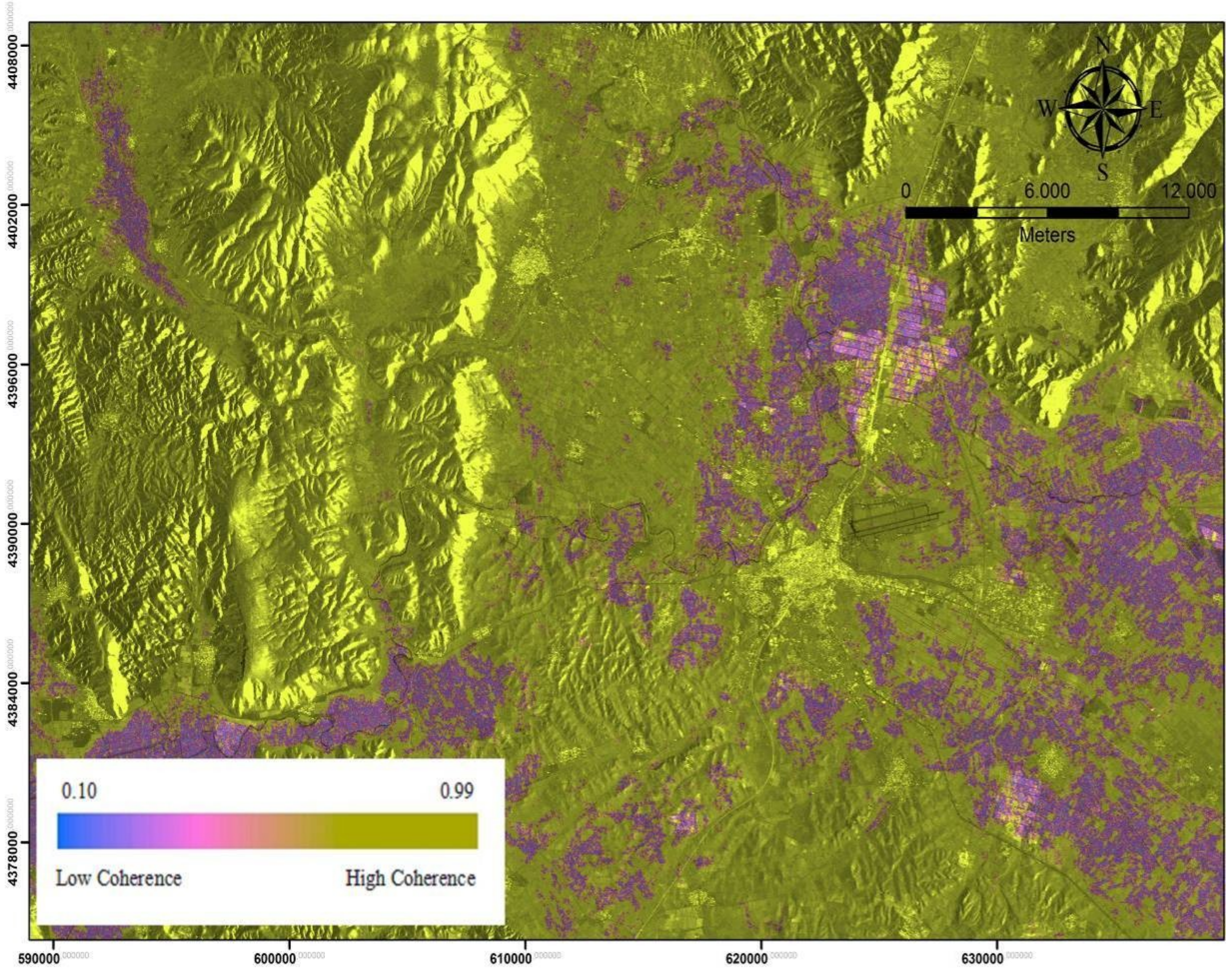

Figure.20 Coherence map for time interval 19980802–19980906 descending track

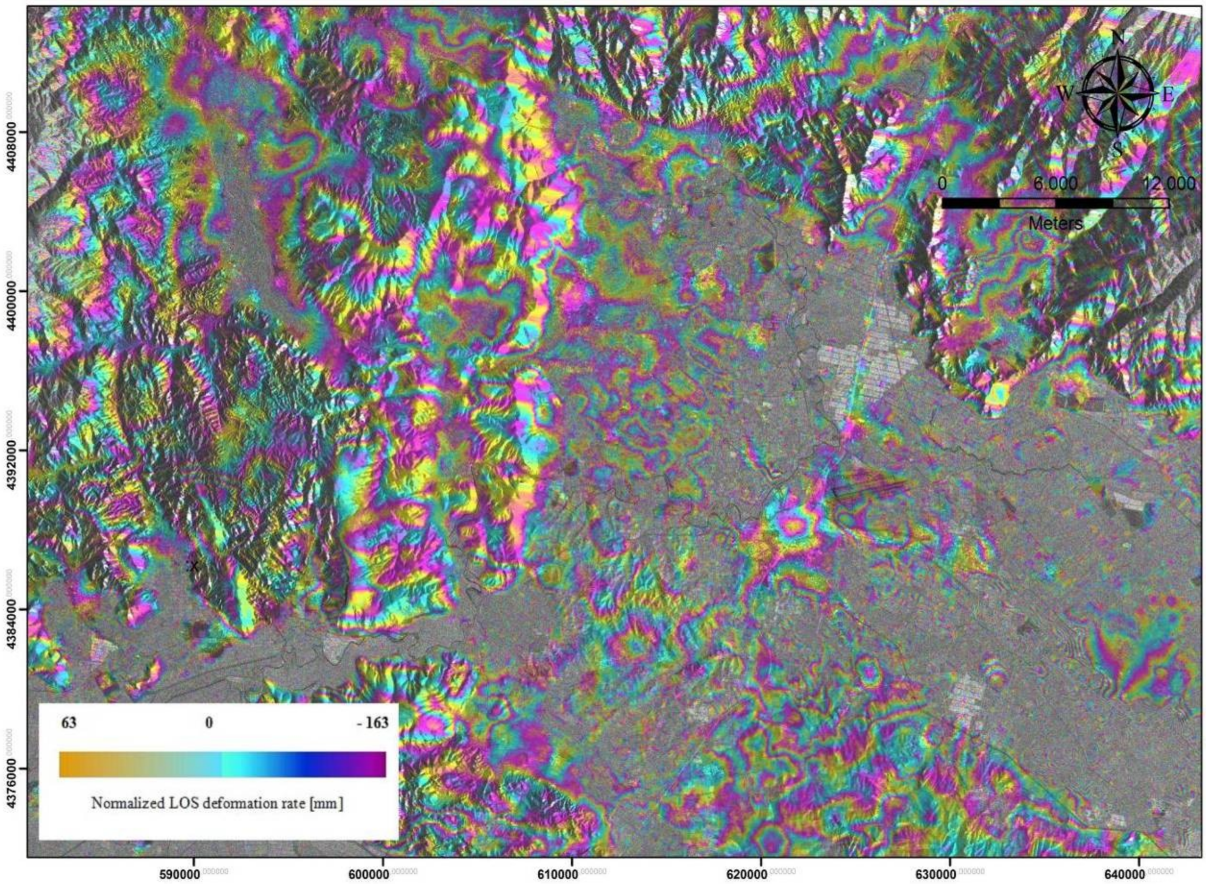

Figure .21 Differential interferogram for time interval 19980802–19980906 descending track

2.6.2.4. Interferometric stacking processing

In order to determine the long-term deformation rate and to avoid the atmospheric path delay term, interferometric stacking has been implemented.

A perpendicular baseline varying in the range of 0 – 150 metres has been selected.

The first result is 474 differential interferograms pairs. Of these 474 interferograms, just 70 interferograms pairs have been chosen in order to achieve the interferometric stacking. The other 404 differential interferograms have been excluded depending on the residual phase following the implementation of the unwrapping step using the precise baseline. The main reasons for this exclusion are the time de-correlation and wrapped phases.

The reference point that has been chosen has a range and azimuth of 467 and 783, respectively. Notice that the reference point has not been selected within the unwrapping step but has been selected within the step of stacking; the average coherence of this point is 0.918.

Figure 22 shows the result of interferometric stacking. It is clear that the interferometric stacking patterns results are confined to urban and mountainous areas. However, no stacking patterns results have been observed within the agricultural fields within the Larissa basin. As mentioned previously, this is attributed to the time de-correlation, which is a result of the impact of crops and soil on signal loss.

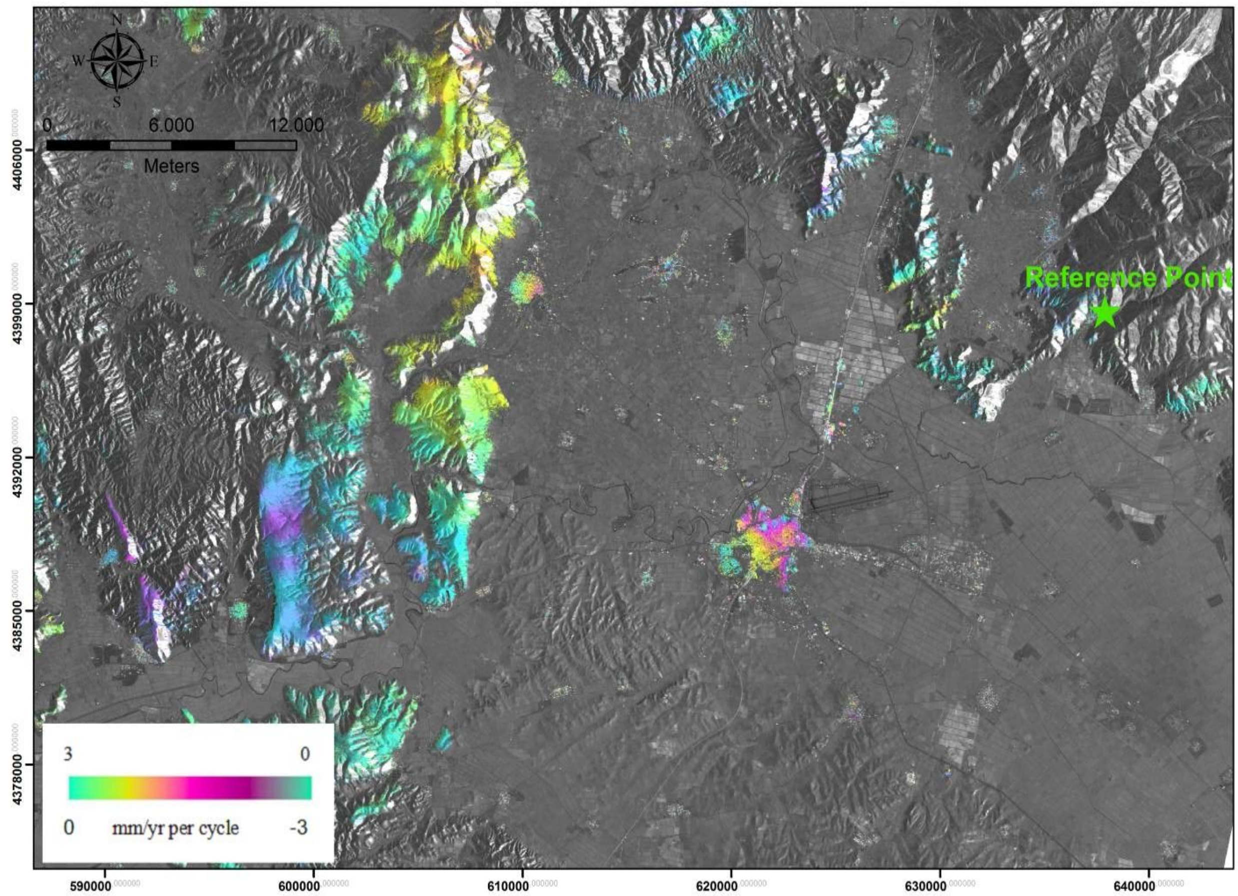

Figure.22 Ground deformation rates along LOS direction deduced by interferometric stacking, for the considered time intervals (1992-2010) Descending track and different acquisition. Background is an average of multi-look SAR intensities. The selected reference point is marked with a green star

2.6.2.5. Persistent (Permanent) Scatterers Interferometry (PSI)

Similar processing steps to those implemented within the PSI technique with the ascending track have been implemented with the descending track.

The first step is the calculation of the perpendicular baseline, which is used as a means by which to choose the master image. The first method has been applied to select the best perpendicular baseline, as mentioned previously within ascending track. Image 20080720 with an average perpendicular magnitude of 373.123 metres was chosen as the master image. This image was selected as the master image based on its smallest perpendicular baseline and because no atmospheric distortion was observed within this image based on the individual differential interferogram investigation. The datasets of ERS-1/2 and ENVISAT ASAR are depicted in Tables 15, 16.

Table15. Datasets of ERS-1/2 SAR images descending track 279, Frame 2812 in the processing

Id	Date	Orbit	Mission	Bp (m)	delta_T (days)
1	19921112	6937	ERS1	719.91	-5729
2	19930610	9943	ERS1	-513.95	-5519
3	19930819	10945	ERS1	-350.55	-5449
4	19931028	11947	ERS1	554.37	-5379
5	19950325	19305	ERS1	-120.21	-4866
6	19950429	19806	ERS1	-549.49	-4831
7	19950603	20307	ERS1	-297.020	-4796
8	19950708	20808	ERS1	-604.40	-4761
9	19951021	22311	ERS1	729.16	-4656
10	19951230	23313	ERS1	413.17	-4586
11	19960309	24315	ERS1	486.84	-4516
12	19960413	24816	ERS1	278.06	-4481
13	19960518	25317	ERS1	124.39	-4446
14	19950813	1636	ERS2	626.791	-4725
15	19950917	2137	ERS2	-384.60	-4690
16	19951231	3640	ERS2	164.08	-4585
17	19960414	5143	ERS2	174.82	-4480
18	19960519	5644	ERS2	476.957	-4445
19	19960623	6145	ERS2	-988.00	-4410
20	19960901	7147	ERS2	-540.43	-4340
21	19961006	7648	ERS2	-408.73	-4305
22	19961110	8149	ERS2	103.82	-4270
23	19961215	8650	ERS2	-340.56	-4235
24	19970119	9151	ERS2	-505.083	-4200
25	19970223	9652	ERS2	-214.12	-4165
26	19970504	10654	ERS2	-391.39	-4095
27	19970608	11155	ERS2	-191.69	-4060
28	19970713	11656	ERS2	-145.11	-4025
29	19970817	12157	ERS2	913.167	-3990
30	19970921	12658	ERS2	-292.54	-3955
31	19971130	13660	ERS2	163.99	-3885
32	19980104	14161	ERS2	844.178	-3850
33	19980419	15664	ERS2	179.44	-3745
34	19980524	16165	ERS2	-160.20	-3710

Supplement Table 15. Datasets of ERS-1/2 SAR images descending track 279, Frame 2812 in the processing

Id	Date	Orbit	Mission	Bp (m)	delta_T (days)
35	19980628	16666	ERS2	-864.13	-3675
36	19980802	17167	ERS2	194.197	-3640
37	19980906	17668	ERS2	178.986	-3605
38	19990228	20173	ERS2	294.68	-3430
39	19990613	21676	ERS2	-568.76	-3325
40	19990822	22678	ERS2	994.93	-3255
41	19990926	23179	ERS2	405.35	-3220
42	19991031	23680	ERS2	332.65	-3185
43	19991205	24181	ERS2	-132.61	-3150
44	20000109	24682	ERS2	-169.35	-3115
45	20000423	26185	ERS2	938.60	-3010
46	20000528	26686	ERS2	798.42	-2975
47	20001119	29191	ERS2	937.79	-2800
48	20001224	29692	ERS2	-503.58	-2765

Table16. Datasets of ENVISAT ASAR images descending track 279, Frame 2807 used in the processing

Id	Date	Orbit	Mission	Bp (m)	delta_T (days)
1	20021020	03339	ENVISAT	-684.50	-2100
2	20030309	05343	ENVISAT	-444.69	-1960
3	20030622	06846	ENVISAT	-264.27	-1855
4	20031109	08850	ENVISAT	-1043.72	-1715
4	20040328	10854	ENVISAT	888.88	-1575
5	20050206	15363	ENVISAT	-518.92	-1260
6	20050313	15864	ENVISAT	304.93	-1225
7	20050417	16365	ENVISAT	113.00	-1190
8	20050522	16866	ENVISAT	-172.90	-1155
9	20050904	18369	ENVISAT	580.66	-1050
10	20051113	19371	ENVISAT	264.08	-980
11	20060226	20874	ENVISAT	-373.02	-875
12	20060611	22377	ENVISAT	-360.50	-770
13	20060716	22878	ENVISAT	753.65	-735
14	20061029	24381	ENVISAT	-531.16	-630
15	20070211	25884	ENVISAT	-339.77	-525
16	20070805	28389	ENVISAT	-210.35	-350
17	20080406	31896	ENVISAT	163.03	-105
18*	**20080720**	33399	**ENVISAT**	**0.0000**	**0**
19	20081102	34902	ENVISAT	-54.03	105
20	20090111	35904	ENVISAT	-98.95	175
21	20090215	36405	ENVISAT	-120.81	210
22	20090426	37407	ENVISAT	-198.48	280
23	20100620	43419	ENVISAT	-52.41	700
24	20101003	44922	ENVISAT	216.18	805

Image marked with (*) is the master image

Consequently, the sub-step processing of the reference point selection has been performed. Identical characteristics of processing have been implemented with the ascending track relevant to reference point selection, as have been performed with the descending track. Table 17 shows the properties of the reference point (control point) and Figure 23 shows the reference point behaviour during the time series of the dataset. It is worth mentioning that this reference point was selected after extensive tests and trials.

Table17. Properties of reference point (control point)

Record	Index	Column	Line	Easting coordinate	Northing coordinate
1	174959	1124	6939	622480.12500000	4389183.50000000

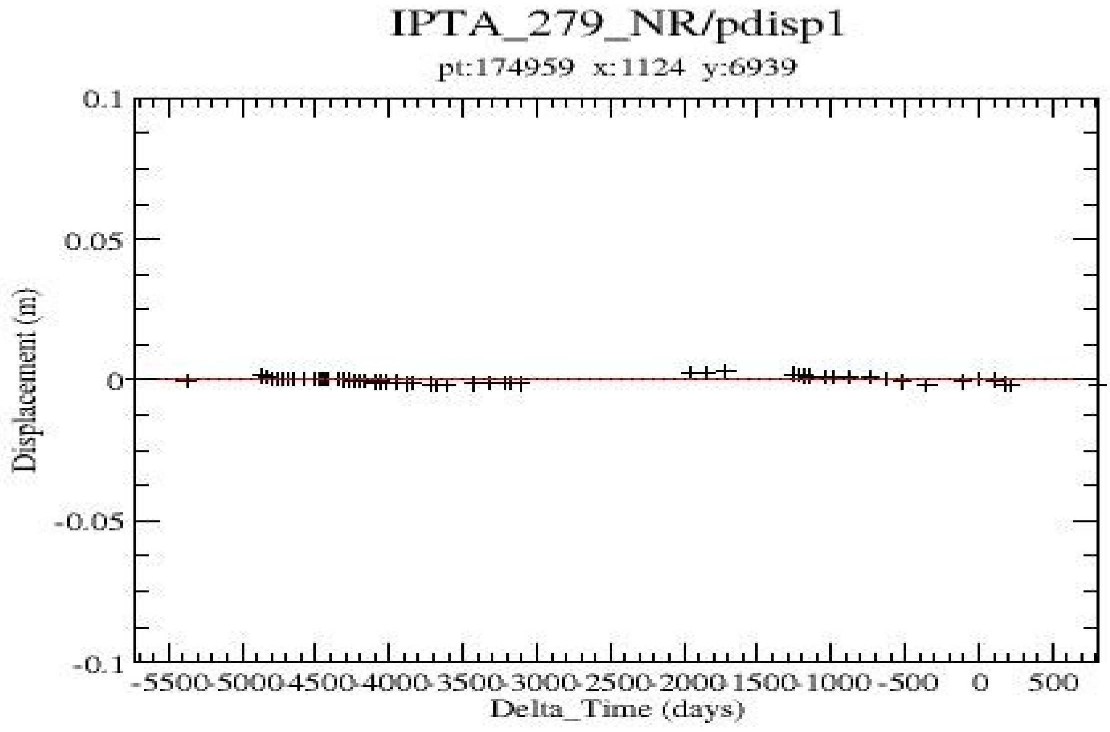

Figure.23 Candidate points of the Point Scatterers Interferometric. Mean displacement rates during (1992 - 2010) Ascending Track 279. Movements are in the satellite line of sight direction. No displacement is observed. All values lie along zero value

Four solution steps of PSI processing have been implemented with the ascending track, as mentioned previously, leading to the end step by obtaining the temporal and spatial distributions of the deformation rate. The result of the previous processing steps is the final number of valid point numbers, which is 1930.

Consequently, the result of the deformation rate has been converted to LOS displacement. The final step is the conversion of point range Doppler pixel coordinates to map pixel and map projection coordinates and additionally, point displacement histories in text format (in map geometry) have been generated.

Thereafter, the results of the candidate points have been transformed from GAMMA (S/W) as database files and an attribute table created. Subsequently, these data have been superimposed in ArcGIS to identify and investigate the spatial and temporal deformation. Figure 24 shows the distribution of the candidate points within the study area.

The majority of the distribution is within urban areas, specifically in the settlement of Larissa. Patterns of subsidence and uplift are spread across the areas in which the candidate points exist. The deformation rate of subsidence and uplift varies in the range of -1 to -6 and 1 to 18 mm/LOS, respectively.

Figure 25 shows the frequency of deformation rate. The minimum frequency varies in the range of 0 – 90 for the deformation rate, which varies in the range of -6 to -0.5 mm/year. The maximum frequency varies in the range of 250 – 500 for the deformation rate, which varies in the range of -0.5 to 2.3 mm/year. It is noticeable that the frequency of uplift deformation rate is larger than the frequency of subsidence deformation rate.

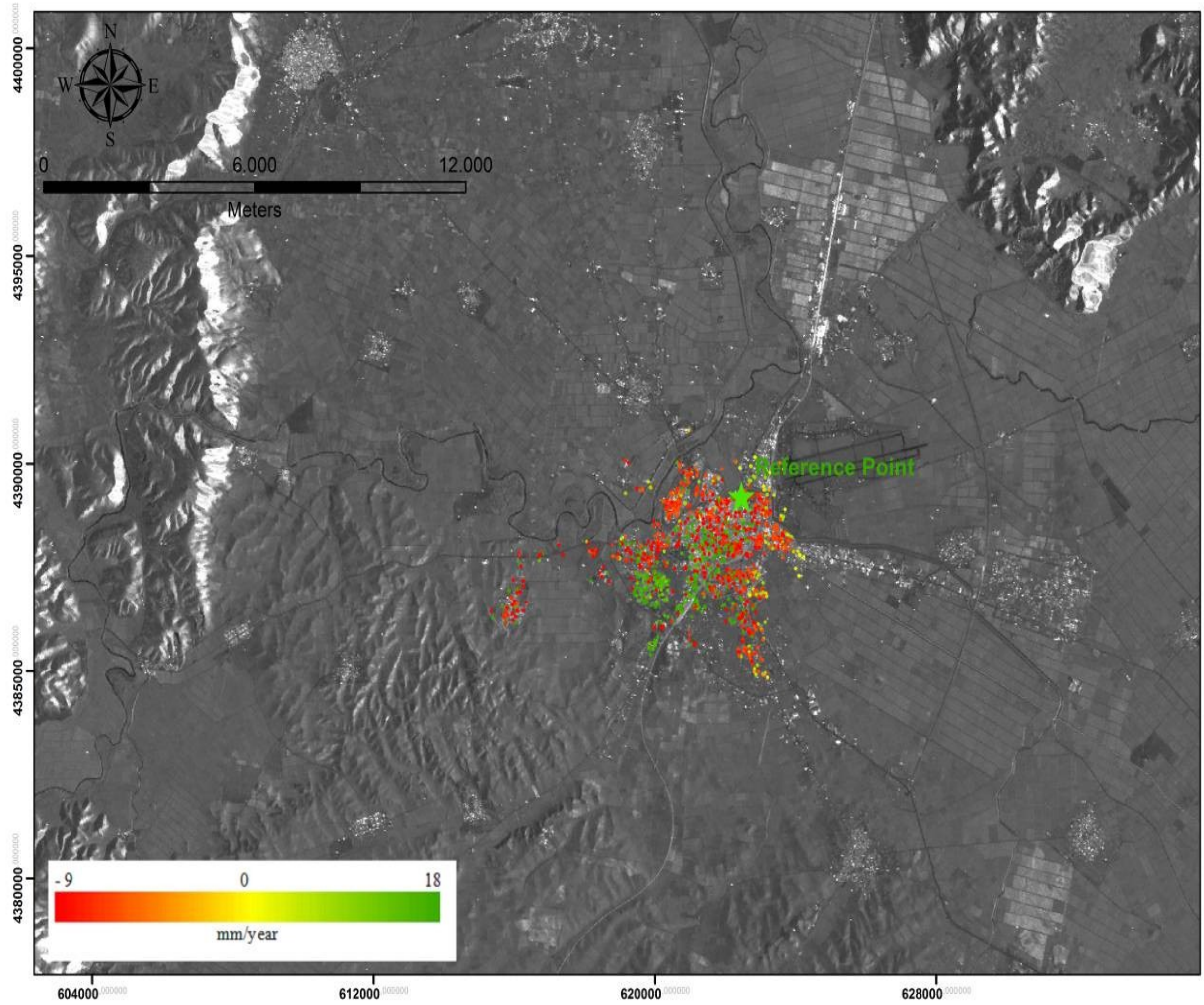

Figure 24. Distribution of geo-coded radar targets (persistent scatterers) in Larissa basin before expansion. The average in line of sight (LOS) velocity (for the period 1992–2010) has been saturated at ± 0.1 m/year for visualisation purposes. Background is a multi-look average SAR image. The reference point is marked with a green star

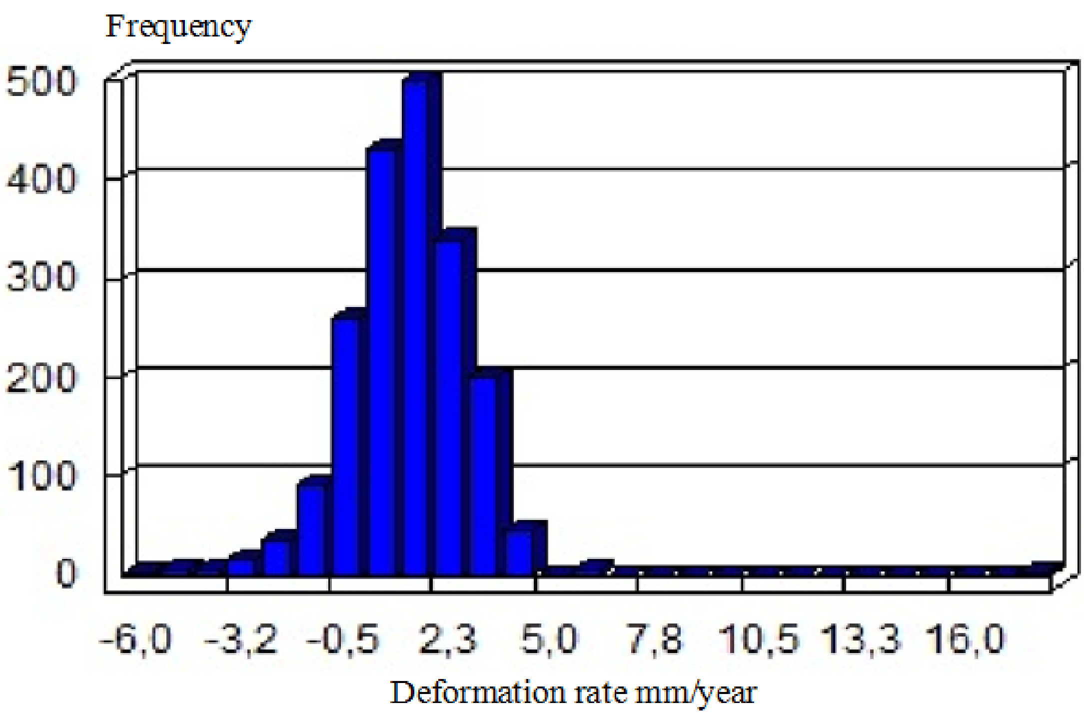

Count: 1930, Minimum: -6, Maximum: 18, Sum: 3264 Mean : 1.691192, Standard Deviation: 1.663686

Figure 25. Frequency of deformation rate of candidate points first result before expansion

It is worth mentioning once again that the first result of the candidate point's distribution has been not used or correlated with other ground data, such as groundwater, fault movements and earthquakes, type of lithology and soil, or other ground features to investigate and identify the causes of ground deformation. For the reason that in the IPTA processing it is possible to build upon an existing solution and check additional points to determine whether a solution can be found for them (Wegmóller, 2005).

2.6.2.6. Expansion

Expansion processing has been implemented by applying many steps to build upon new candidate points, as performed with the ascending track. The resulting number of valid points increased from 1930 to 4801. Figure 26 shows the distribution of candidate points within the study area. A dense distribution of candidate points can be observed in the settlement of Larissa and some other settlements nearby. Patterns of subsidence and uplift are spread across the areas in which the candidate points exist. The deformation rate of subsidence and uplift varies in the range of -1 to -9 and 1 to

18 mm/LOS, respectively. No difference is observed between the deformation rate before and after the implementation of expansion. This similarity indicates that the deformation rate of the candidate points throughout the investigated area is equivalent. Another indicator of this similarity is that the investigated area is affected by the same influencing conditions of deformation. However, it is worth mentioning that the same thresholds of deformation rate have been used before and after expansion.

It should be noted that a difference has been observed between the frequencies of deformation rate before and after expansion. Figure 27 shows the frequency of deformation rate. The minimum frequency varies in the range of 0 – 500 for the deformation rate, which varies in the range of -9 to -0.7 mm/year. The maximum frequency varies in the range of 490–1.000 for the deformation rate, which varies in the range of 2.1 – 4.9 mm/year. It is noticeable that the frequency of maximum subsidence deformation rate is less than the frequency of minimum subsidence deformation rate. In addition, the frequency of uplift deformation rate is higher than the frequency of subsidence deformation rate. It is worth mentioning that this result is similar to the result before expansion. However, the histogram depicts a more normalised distribution of deformation frequency than the histogram of frequency before expansion. The result after expansion has been used for investigating the behaviour of deformation for selective candidate points, in addition to correlating ground deformation with other factors, such as groundwater, fault movements and earthquakes, type of lithology and soil.

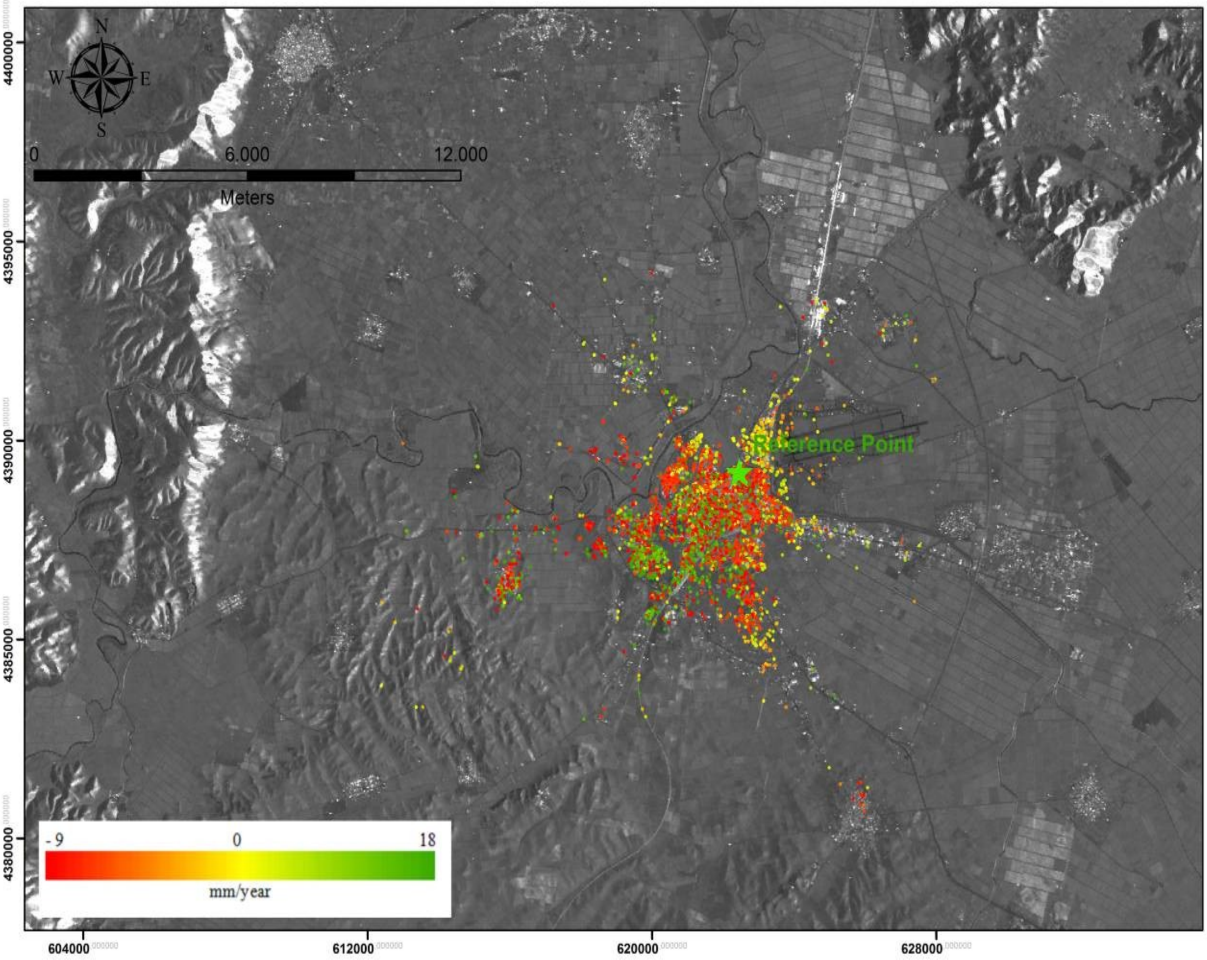

Figure 26. Distribution of geo-coded radar targets (persistent scatterers) in Larissa basin after expansion. The average in line of sight (LOS) velocity (for the period 1992–2010) has been saturated at ± 0.1 m/year for visualisation purposes. Background is a multi-look average SAR image. The reference point is marked with a green star

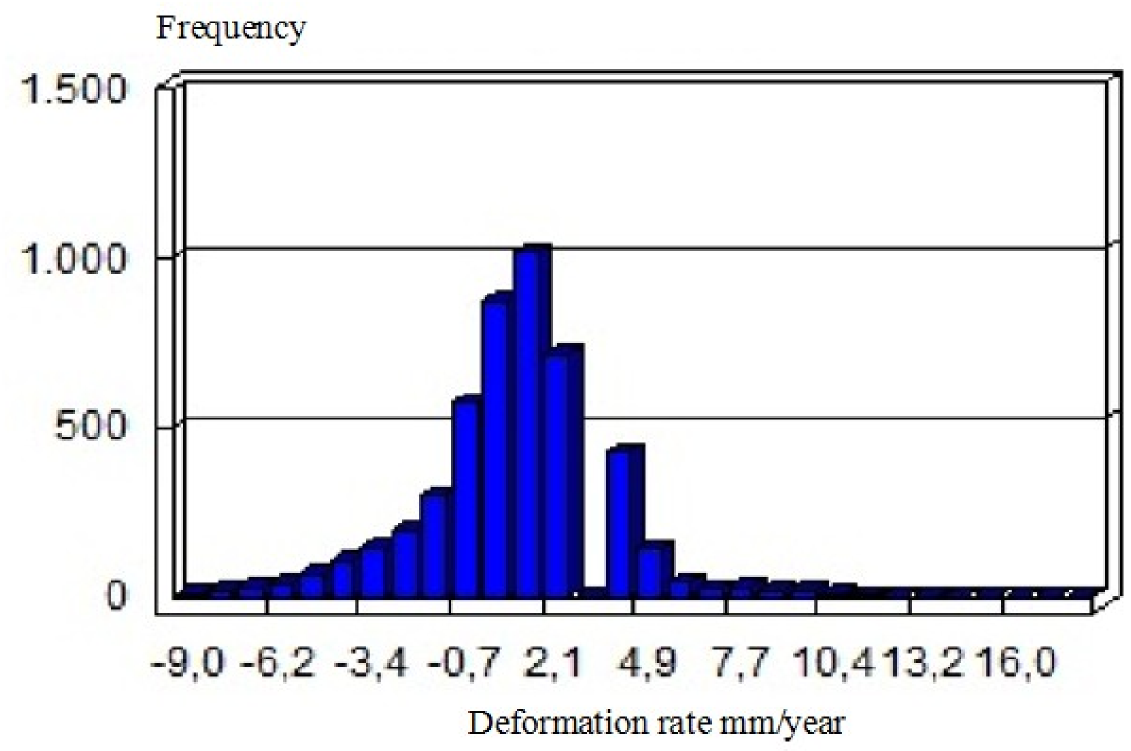

Count: 4801, Minimum: -9, Maximum: 18, Sum: 6142 Mean: 1.279317, Standard Deviation: 2.674544
Figure.27 Frequency of deformation rate of candidate points after expansion

It is noticeable that a comparison after expansion of the candidate point's results, between two ascending and descending tracks, indicates a large difference in the number of candidate points despite the number of SAR images of a descending track being more than the number of SAR images of an ascending track; which are 70 and 37 images, respectively. This could be attributed to the fact that approximately all SAR images of an ascending track are from winter and spring, whereas many SAR images with a descending track are from summer and autumn. Consequently, the relation between the results of the candidate point's number and time of the images is a problem of the wrapped phases for those images acquired in summer and autumn. These problems could be summarised as atmospheric distortions, seasonal deformation effects and agricultural fields around Larissa. Consequently, another attempt at processing has been performed with descending track by excluding all interferograms during the summer and autumn but keeping interferograms from December and May. The number of candidate points increases from 4801, resulting from processing that includes all the interferograms (winter, spring, summer and fall), to 7504 as a result of processing that includes interferograms during December and May. Despite the increase in the number of candidate points after excluding those interferograms during the period mentioned above, the result obtained prior to this exclusion has been used for the integration of the time series of the deformation rate.

Figure 28 shows the distribution of the candidate points within the study area. A dense distribution of candidate points can be observed in the settlement of Larissa and some other settlements nearby. Patterns of subsidence and uplift are spread across all areas in which candidate points exist. The deformation rate of subsidence and uplift varies in the range of -1 to -10 and 1 to 17) mm/year, respectively. Figure 29 shows the frequency of deformation rate. The minimum frequency varies in the range of 0 – 400 for the deformation rate, which varies in the range of -10 to -2.1 mm/year. The maximum frequency varies in the range of 600 – 1100 for the deformation rate, which varies in the range of 3.2 – 0.6 mm/year. In addition, the histogram depicts the normal distribution of deformation rate frequency.

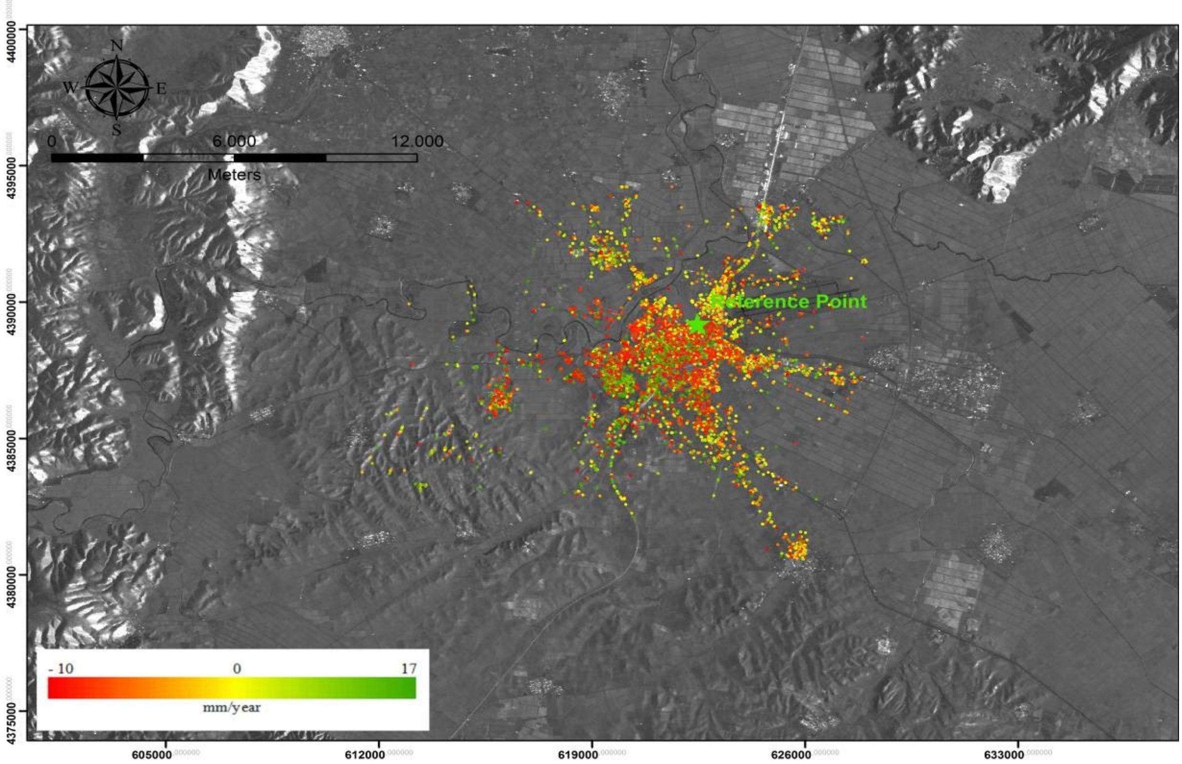

Figure.28 Distribution of geo-coded radar targets (persistent scatterers) in Larissa basin after expansion for SAR images during December and May. The average in line of sight (LOS) velocity (for the period 1992–2010) has been saturated at ± 0.1 m/year for visualisation purposes. Background is a multi-look average SAR image. The reference point is marked with a green star

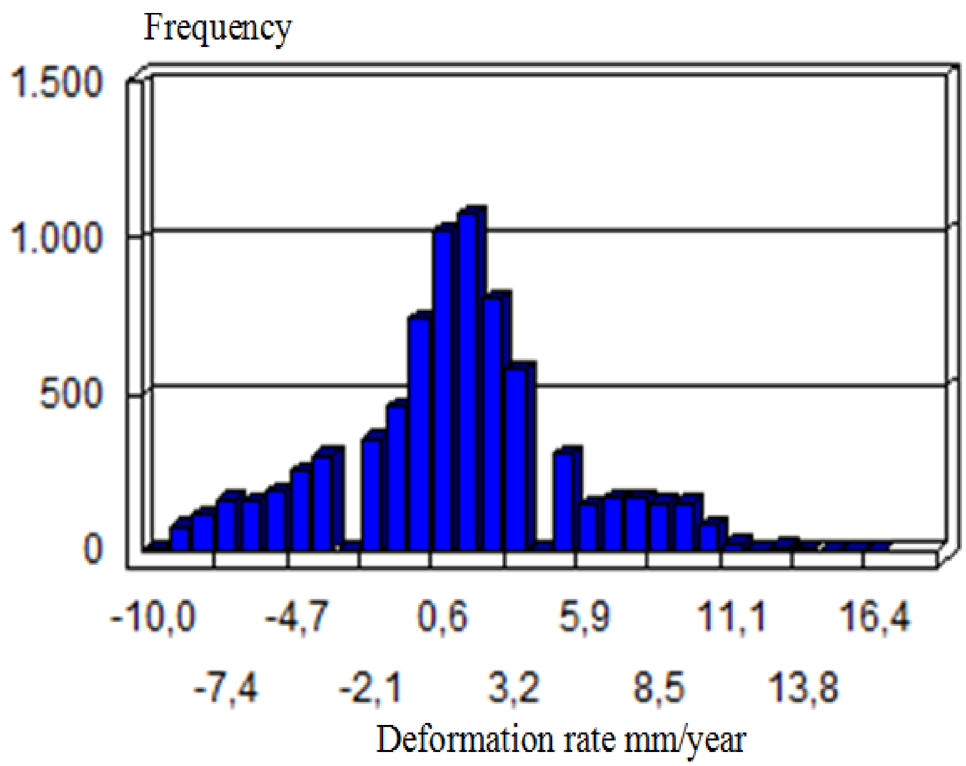

Count: 7504, Minimum: - 10, Maximum: 17, Sum: 9258 Mean: 1.233742, Standard Deviation: 4.092807

Figure.29 Frequency of deformation rate of candidate points after expansion for SAR images during (December – May)

Chapter Three: Impact of groundwater on ground deformation

3.1. Introduction to Groundwater

Groundwater is a huge topic for discussion and is the focus of this chapter. The processes of withdrawal of groundwater and recharging reservoirs and aquifers have a big influence on the upper-layer stability of the soil, affecting the volume and the shape of the ground and creating pores within it. This in turn affects the stability of, and may damage, objects that are located over or within the ground as a result of vertical and horizontal movement. This chapter focuses on three areas: (1) the groundwater level fluctuation sequence along a time series during the periods 1992–2010 and 1995–2008 as corresponding to the data set of RADAR images and its correlation to the monthly precipitation, (2) the impact of groundwater fluctuation on land deformation, which is observed from synthetic aperture radar (SAR) interferometry, and (3) the interference between the water table, precipitation, clay minerals, and land deformation.

3.2. Hydrological background

3.2.1. Description of the groundwater and its demand in the study area

_In order to describe the groundwater in the study area in the eastern part of northern Thessaly, it should be recognised whether of the water is a surface or subsurface water body.

The available quantity of surface water of Thessaly Water District is estimated at 1,220 million m^3, although only about 623 million m^3 is available for use. The annual quantity of groundwater available is estimated at 586 million m^3. The estimation of the annual water balance in Thessaly District is based on the estimation of water resource consumption in relation to the available renewable water resources (Mahleras et al., 2007).

(Mahleras et al., 2007) mentioned that the rest of east Thessaly (Larisa-Karla) is supplied at a slow rate of recharge from the cone of Titarisios. In the Taousani area, the groundwater is supplied by the percolation of rain. These authors also mentioned that in the Thessaly Plain, roughly 500,000 hectares are cultivated, and of these, 252,500 hectares (18.7% of the total irrigated land in Greece) are irrigated. 74,900 hectares are irrigated by surface waters and 177,600 hectares are irrigated by underground water of the Thessaly Plain. At the Prefecture of Larisa, 50% of irrigation water comes from groundwater and 50% from surface water. It is expected that after the construction of planned new dams in the area the percentage of surface water used for irrigation will be increased.

(Loukas et al., 2007) revealed that in the two major basins of the Thessaly region in Greece, namely the Pineios River and the Lake Karla basins, the intensive and extensive cultivation of water-demanding crops, such as cotton and maize, and the absence of reasonable water resources management have led to a remarkable increase in water demand, which is usually fulfilled by the over-exploitation of groundwater resources. This unsustainable practice has deteriorated the already disturbed water balance and accelerated water resources degradation. These authors also mentioned that the Thessaly region in central Greece is the most prominent example of today's water resources problem. The Thessaly Plain is an intensely cultivated region. It is the second largest plain in Greece, after the Macedonian plain, and is traversed by the Pineios River (Figure 30).

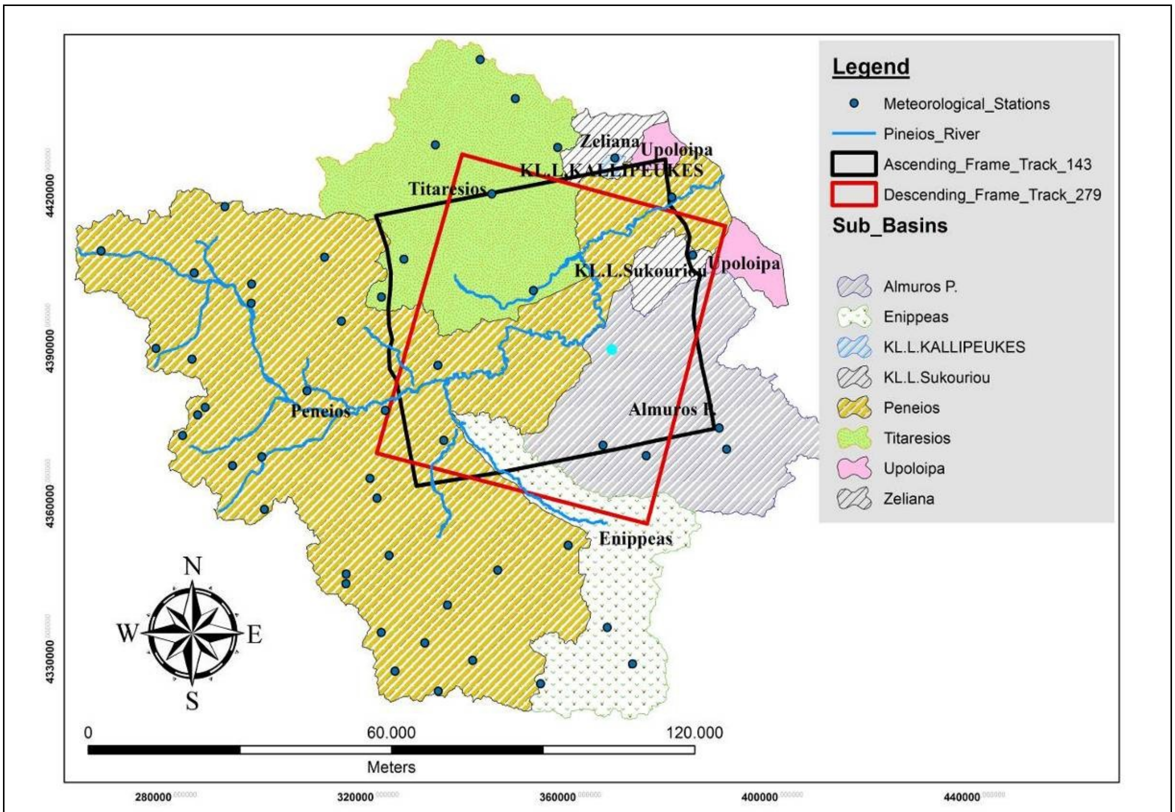

Figure 30. Sub basins and locations of meteorological stations, indicating the ascending and descending frames of RADAR images. The station of Larissa is highlighted.

As an indication of the distribution of water for irrigation (Loukas et al., 2007), the total monthly irrigation water requirement per sub-basin is simply the summation of the monthly irrigation requirements for all crops cultivated in the sub-basin. Figure 31 shows the estimated annual irrigation requirement for each crop and sub-basin of Thessaly for the year 2002. It is clear that the largest irrigation requirements are in the Piniada, Ali Efenti and Larisa sub-basins and the Lake Karla basin. Also, over 70% of the irrigation water volume is used for the irrigation of cotton-cultivated areas.

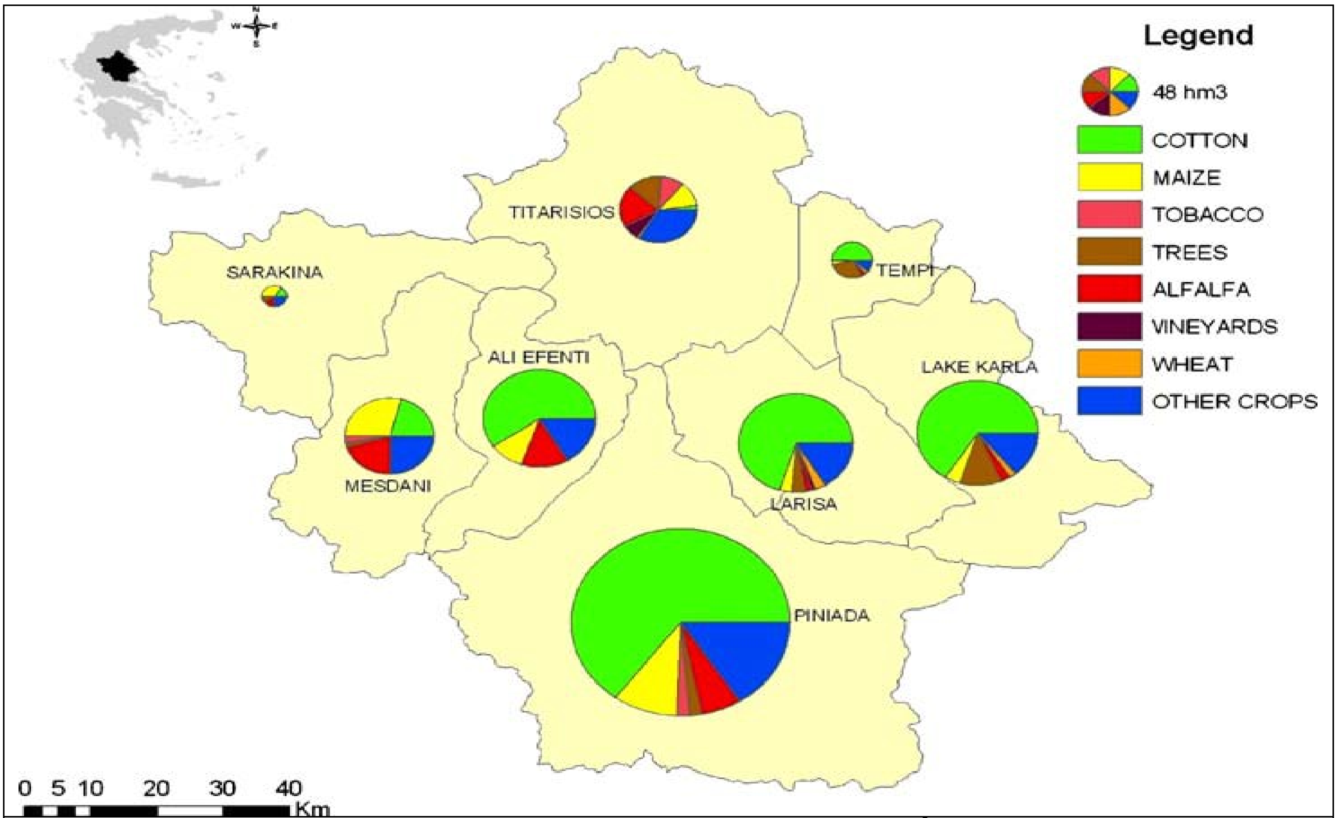

Figure 31. Distribution of mean annual irrigation requirements (in ha^3) per sub-basin and cultivated crops. From (Loukas et al., 2007).

Increased water demand has been associated with severe and persistent droughts during the period from the mid to late 1970s and the period from the late 1980s to mid-1990s, interrupted by the wet period of 1990–1991, which mostly affected the northern part of the Thessaly Basin. These dry conditions resulted in irrigation cutbacks and over-exploitation of groundwater (Loukas and Vasiliades, 2004).

(Petralas et al., 2005) mentioned that a typical example of an area with a serious water shortage due to poor water resources management and increased demand for water is the east basin of Thessaly, which is part of the Pineios river basin.

Additionally, they indicated that aquifer systems are in many cases overexploited. A continuous decline of the water level by as much as 2 m/year has occurred in the last two decades as result of human activities. The major aquifers are contained within the graben and are composed of basin sediments (coarse grained permeable sediments with locally interbedded layers of silt and clay) 300 m thick. Overexploitation of groundwater resources has led to phenomena such as seawater intrusion and land subsidence.

(Rozos et al., 2010) mentioned that the majority of the aquifers in the Thessaly Plain are under a regime of overexploitation, resulting in a systematic drawdown of the groundwater level.

3.2.2. Spatial and temporal description of land deformation corresponding to groundwater (water pumping) as an influence factor

Unfortunately there are no historical data for the amount of groundwater discharge or water withdrawal within the study area. For this reason, groundwater level has been used and has been correlated with the other parameters as an indicator of the impact of groundwater overexploitation on land deformation. Many studies have been implemented to discover and study the influence of groundwater extraction and the huge damage to infrastructure triggered by this operation. However there are not many studies of water extraction and its impact on land deformation within the eastern part of the northern Thessaly basin.

(Cigna et al., 2011) found that groundwater overexploitation is the dominant process driving land subsidence in Morelia, resulting in subsidence-induced shallow faulting which mimics pre-existing faults, possibly with minor contributions from present-day tectonics. In the same study, they also found that the compaction rate is higher for thicker strata of sedimentary material than for thinner strata and also for La Colina and La Paloma faults. Furthermore, they mentioned that the faults in Morelia may also act as barriers for horizontal migration of groundwater between the different basins. The observed weak correlation of Persistent Scatterer Interferometry (PSI) deformation with water extraction rates may be consistent with the hypothesis that compaction of deeper aquifers, communicating with shallow ones, exerts significant influence on land deformation and imparts uniform subsidence throughout the urban area, upon which local influences are superimposed at a few locations (Cigna et al., 2011).

According to the model created by (Mulas et al., 2003), subsidence occurs when water is pumped from the topmost layer of gravels of the deep aquifer. When water is pumped, a vertical gradient is created that causes a downward flow of groundwater from the surface unit (shallow aquifer) towards the deep aquifer, causing a water table.

(Chang et al., 2004) conducted research in southwest Taiwan and found that the subsidence rate is associated with the descending trend of groundwater level. They also found clear interferometric fringes in the dry seasons, especially in the distal parts of the Pingtung Plain. Furthermore, they mentioned that one fringe corresponds to about 2.8 cm of displacement, and the subsidence amount in the distal part of the Pingtung Plain is about 3–6 cm for each dry season in the direction of radar line of sight. In contrast, the interferometric correlation is very poor for the interferograms of the wet season.

(Beibei et al., 2011) carried out research in Beijing municipality, China, and found that seasonal and interannual differences exist in the response model of land subsidence to groundwater funnels with uneven spatial and temporal distribution. Although a consistency was revealed to exist between a groundwater funnel and the spatial distribution characteristics of the corresponding land subsidence funnel, this consistency was not perfect. A comparative analysis of the InSAR deformation response to land subsidence with the evolution of interannual groundwater flow field revealed that the groundwater funnel was mostly consistent with the spatial distribution characteristics of the land subsidence funnel, although the occurrence of land subsidence in Beijing is mainly due to the exploitation of groundwater.

(Doukas et al., 2004) carried out a study in the area of Thessaloniki, a big city in northern Greece, and found that water pumping is one of several serious causes of ground subsidence. The pumping of large volumes of water (e.g. for irrigation and water draining purposes) using ground drillings is very likely to produce ground subsidence, a phenomenon which usually gets worse as water pumping continues. The consequences of such phenomena may be dangerous, especially when the ground subsidence is not smoothly distributed in the problematic area. Furthermore, they defined ground subsidence as the vertical downwards small movements of the ground. Several physical causes (earthquakes, tectonic movements, underground cavities, etc.) as well as human activities can produce ground subsidence.

Regarding the Thessaly province, (Rozos et al., 2010) mentioned that the Thessaly basin is subdivided by a group of hills into two sub basins, the western and the eastern. These sub basins are two main individual hydrogeological units developing high potential aquifers. The overexploitation of these aquifers has led to the manifestation of extended damages due to land subsidence phenomena. Land subsidence in the western part of Thessaly was also found to be triggered by excessive groundwater drawdown and results from the compaction of the drained loose sedimentary formations that have become increasingly manifest over the years.

A SAR interferometry study was carried out in the same study area in the eastern part of northern Thessaly during the period 1992–2006 by (Lagios, 2007), and it was found that systematic subsidence is the predominant feature, reaching maximum amplitude of about 350 mm (Gianouli area) for a time period of about 14 years. However, the Larissa city centre appears to be rather stable compared to its northern and eastern suburbs, which are closer to cultivated regions.

Another SAR interferometry study was carried out by (Parcharidis et al., 2011) in the southern part of the Thessaly Plain, and seasonal deformation signals were recognised at the south-western part of the basin, reaching several centimetres during the summer period. Larger subsidence should be expected when considering the entire summer season, when most of the irrigation and over-exploitation of groundwater takes place. An accurate estimation of the deformation using conventional DInSAR techniques is not easily achieved for larger time spans, due to the extent of decorrelation phenomena in the region. (Parcharidis et al., 2011) also show that deformation patterns corresponding to ground subsidence are evident in interferograms covering the period between May and October for the deformed area (about 180 km^2) in the south-eastern part of the plain. The area of maximum deformation is located to the North of Kileler village, reaching -17.5 cm along the line of site in the summer of 1998 (from August to September), whereas for the same period in 2004, a lower but also significant magnitude of -12.7 cm is observed. During winter seasons, deformation is considerably reduced to -0.5 cm and -0.1 cm for 3.5 months (December 1995–April 1996) and 1.2 months (January–February 2009), respectively. Rebound phenomena with significantly lower values were observed during high precipitation periods, mainly in the north east of the basin.

(Kontogianni et al., 2007) mention that three types of ground deformation have been reported in the Thessaly Plain since 1986: ground fissures, sinkholes and land subsidence. Numerous fissures opened up across the Thessaly Plain, mainly at its eastern part, cutting across cultivated land, roads, houses, and even the area of the NATO Larissa airport. Most of these fissures had an opening of up to several tens of centimetres, presenting also an expansion rate of up to 30 mm/year. The maximum amplitude of opening is taking place between August and October, when the groundwater pumping is high and the water table level is low. This study also found that these large amplitude fissures observed in the area do not originate from earthquake-related effects. They should be attributed to sediment compaction resulting from excessive water pumping for irrigation purposes together with the rainfall rates during the last 40 years.

(Jones and Jefferson, 2011) mentioned that the essentially expansive soil is one that changes in volume in relation to changes in water content. Here the focus is on soils that exhibit significant swell potential, while shrinkage potential also exists. There are a number of cases where expansion can occur through chemically induced changes (e.g. swelling of lime treated sulphate soils). However, many soils that exhibit swelling and shrinking behaviour contain expansive clay minerals, such as smectite, that absorb water. The more of this clay a soil contains the higher its swell potential and the more water it can absorb. As a result, these materials swell, and thus increase in volume, when they get wet and shrink when they dry. Many towns, cities, transport routes and buildings are founded on clay-rich soils and rocks. The clays within these materials may be a significant hazard to engineering construction due to their ability to shrink or swell with changes in water content.

Results found by (Kontogianni et al., 2007) indicate that there is a dependent factor on groundwater fluctuation, which plays an important role in affecting the ground deformation; this has been explained in detail by (Mokhtari and Dehghani, 2012). As the expansive soils contain the clay mineral montmorillonite with claystone and shale, sedimentary and residual soils are capable of absorbing great amounts of water and expanding. The expansive nature of the clay is less near the ground surface, where the profile is subjected to seasonal and environmental changes. The more absorbed by the soil, the more its volume increases. Expansive soils also shrink when they dry out. Fissures can also develop in the soil. These fissures help water to penetrate into deeper layers. This produces a cycle of shrinkage and swelling that causes the soil to undergo a great amount of volume change. This movement in the soil results in structural damage, especially in lightweight structures such as sidewalks, driveways, basement floors, pipelines and foundations. The clay minerals that typically cause soil volume changes are montmorillonites, vermiculates and some mixed layer minerals. Illites and kaolinites are often inexpansive but can cause volume changes when particles are extremely fine. Consequently there is an indirect impact of groundwater level fluctuation on land deformation through its motivation of the swelling and shrinkage operation.

According to (Sgouras, 1994), the main types of clay minerals which are distributed in the eastern, western, northeastern, southern, and southwestern regions of the eastern part of northern Thessaly are montmorillonite and ellite. The percentages of montmorillonite and illite vary in the range 0–16.1% and 17.6–30.4 %, respectively. The percentage of montmorillonite is enough to influence uplift and subsidence deformation behaviour through the cycle of shrinkage and swelling that causes the ground to undergo volume changes.

3.3. Results and Discussions

3.3.1. Monthly amount of precipitation

The aim of this study, as mentioned above, is to investigate surface deformation signals associated with monthly precipitation and groundwater withdrawal and the interference between them. The study is based on monthly precipitation for the periods (1995–2008) and (1992–2010) corresponding to the RADAR images from two tracks, ascending and descending.

The monthly precipitation recorded at the meteorological station of Larissa, operated by the (Hellenic national meteorological service HNMS)**,** has been correlated to the time, the fluctuation of groundwater, and the land deformation. The station is located within the coordinates easting and northing (60,7800,106 - 43.59,983,687), as shown in preceding Figure 30. This station was selected based on its location in the middle of the study area. The elevation of the station is 73 m and its code is 16648.

The accumulation of monthly precipitation is shown in Table 18 for the period 1992–2010. The fluctuation of the precipitation over the four seasons throughout this period is evident. This table indicates that the minimum accumulation of precipitation during the summer season varied between 0 and 0.3 mm for the months June 1996, July 1999 and August 1992, whereas the maximum precipitation for this season varied between 30.6 and 93.2 mm for the months August 1997, July 2001 and June 2004.

Table18. Accumulation of monthly precipitation (mm) for the period 1992–2010, Larissa station

Months / Years	Jan.	Feb.	Mar.	Apr.	May	June	July	Aug.	Sept.	Oct.	Nov.	Dec.
1992	5.8	9.2	10.4	88.3	54.8	74.2	13.8	0	0	39.3	62	25.4
1993	16	29.2	25.3	12.4	76	3.9	1.4	3.2	6.9	9.1	148.7	24.6
1994	71.4	32.3	21.5	61.9	26.7	1.3	24.2	8.2	0	85.9	49.9	61.5
1995	56.8	5.9	32.7	18.1	32.3	34.4	31	12.3	24	7.8	22.5	92.7
1996	73.6	56	61.9	22.3	9	0.3	14.7	30.5	63.7	70	30.9	50
1997	31.4	14.5	20.8	53.4	17.6	30.7	1.4	30.6	1.4	56.1	18.1	67.7
1998	17.1	57.1	32.6	4.5	131.5	7	0.3	0.7	37.1	17.6	155	52.9
1999	45.4	55.8	80.5	30.3	5.4	5	0	6.9	23.9	57.4	63.5	61.7
2000	14.1	38	24.7	13	25.7	15.7	0.8	3.6	9.6	40.8	25.6	16
2001	32.8	20.8	8.9	49.2	66.8	11.4	61.1	18.9	0.9	2.3	15.7	57.2
2002	13.5	15.5	42.1	61.2	7.4	0.5	56.9	7.2	102.4	64.8	64.4	145.9
2003	88.8	18.3	20.1	26.4	47.9	33.2	28.4	5.3	22.8	86.1	8.3	52.8
2004	87.8	8.4	31.9	43.5	57.1	93.2	4.6	2.6	20.1	37.2	26	41.8
2005	23	47.6	64.1	5.7	26.7	3.6	5.3	16.4	44.8	10.3	60.8	66.8
2006	103.4	38.8	34.1	35.4	1.9	10.6	28	10.4	156	106.1	11.6	11.9
2007	14	29.5	26.6	19.7	36.5	39.1	0	25.1	21.9	104.5	97.8	21.4
2008	3.8	18.3	12.3	42	3.6	12.4	18.6	6.6	63.8	18.5	21.9	62.3
2009	85.8	14.4	62.6	13.5	36.6	5.4	28.8	1.9	31.2	117.2	26.6	89
2010	19.5	62.8	44.7	8.6	51.1	10.3	45.2	13.5	57.8	111.6	35.8	17.3

Additionally, the minimum amount of precipitation accumulated during the winter season varied between 3.8 and 11.9 mm for the months January 2008, February 1995 and December 2006, while the maximum accumulation of precipitation varied between 62.8 and 145.9 mm for the months February 2010, January 2006 and December 2002.

As for the spring season, the minimum accumulation of precipitation varied between 1.9 and 8.9 mm for the months May 2006, April 1998 and March 2001, whereas the maximum precipitation during this season varied between 80.5 and 131.5 mm for the months March 1999, April 1992 and May 1998.

With regard to the autumn season, the minimum precipitation varied between 0 and 8.3 mm for the months September 1992, October 2001 and November 2003, while the maximum precipitation varied between 117.2 and 156 mm for the months October 2009, November 1998 and September 2006.

The charts 32 - 50 below depict the fluctuations in the amount of precipitation over time, with one chart for each year of the period (1992–2010).

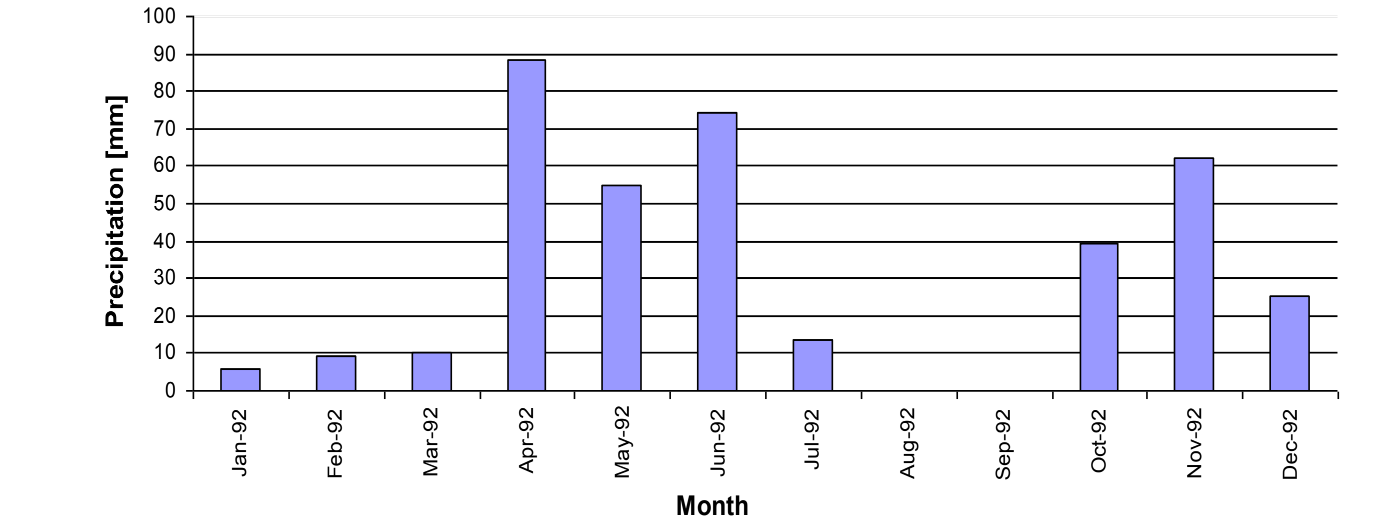

Figure.32 Accumulation of monthly precipitation for the year 1992

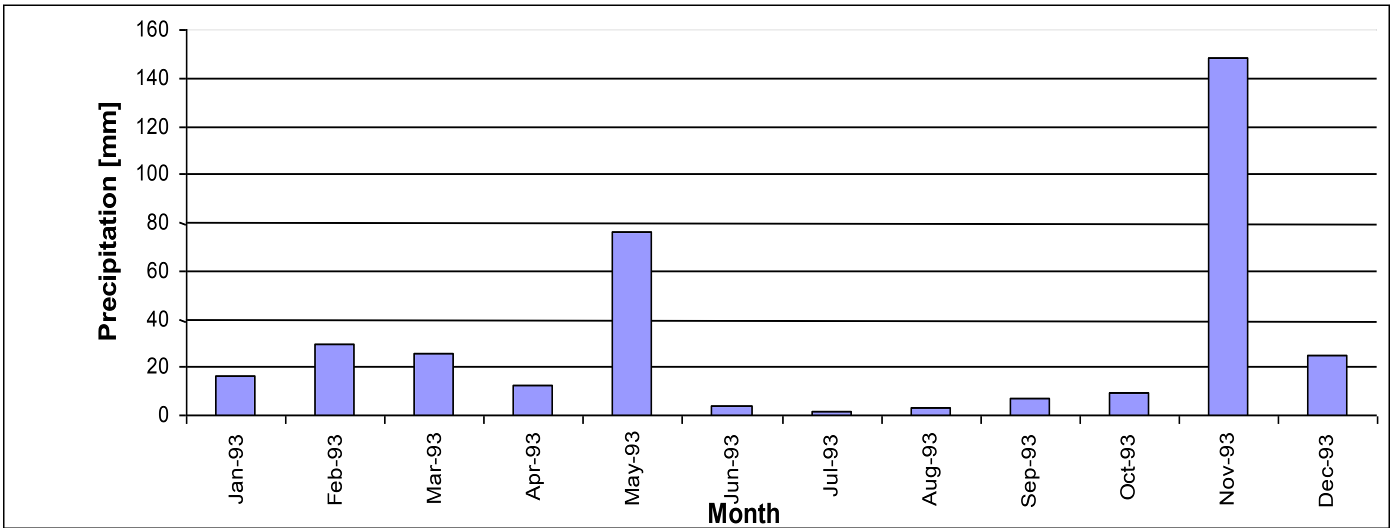

Figure 33. Accumulation of monthly precipitation for the year 1993

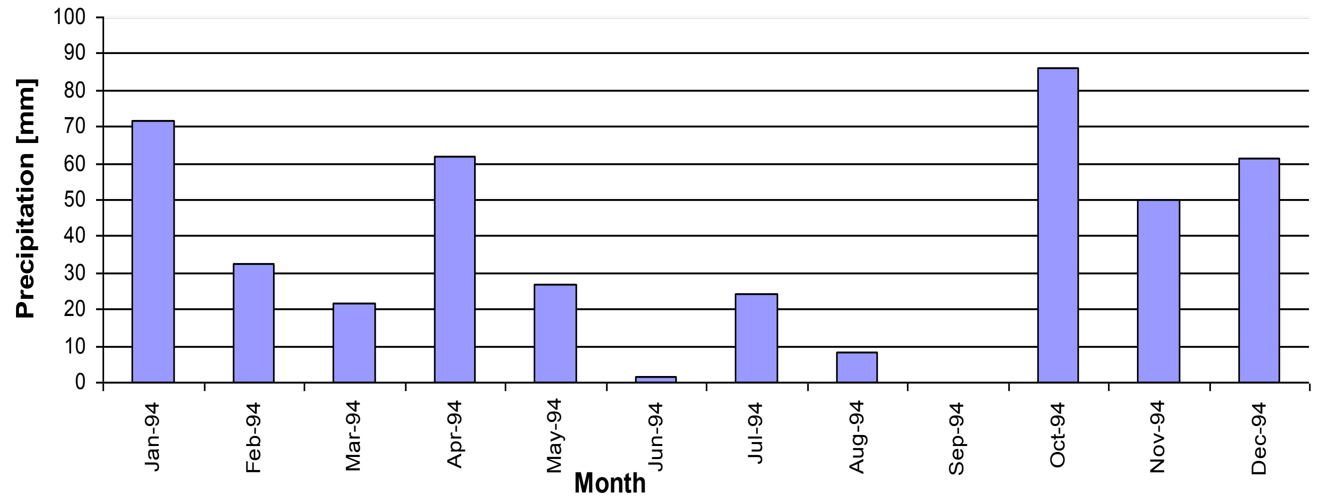

Figure 34. Accumulation of monthly precipitation for the year 1994

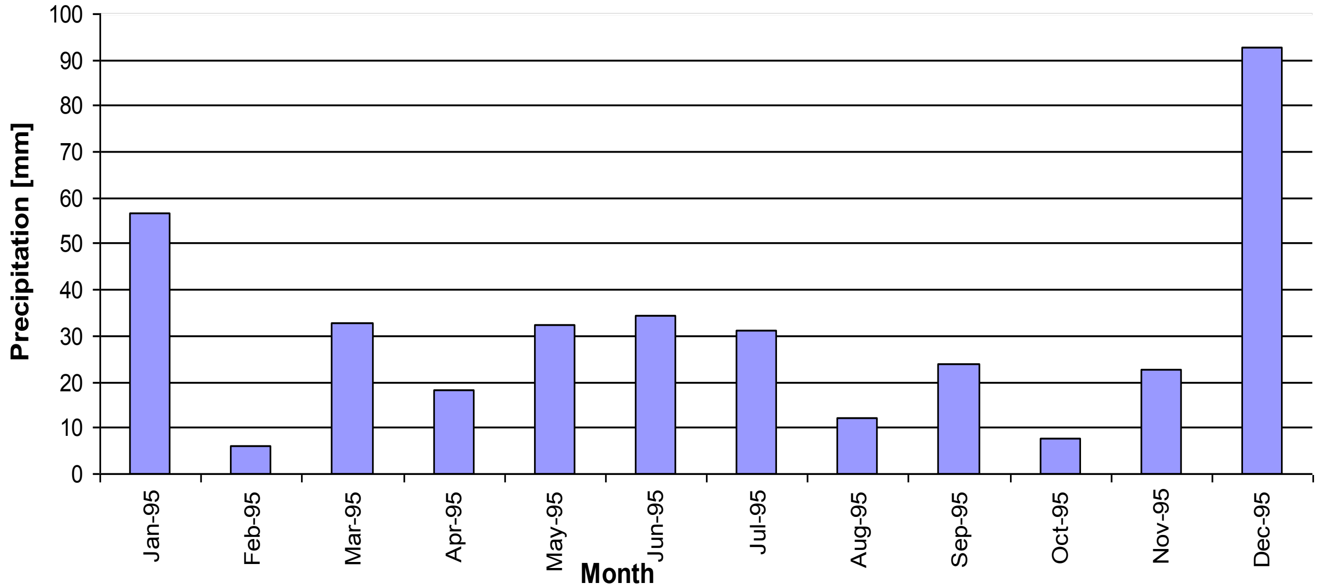

Figure.35 Accumulation of monthly precipitation for the year 1995

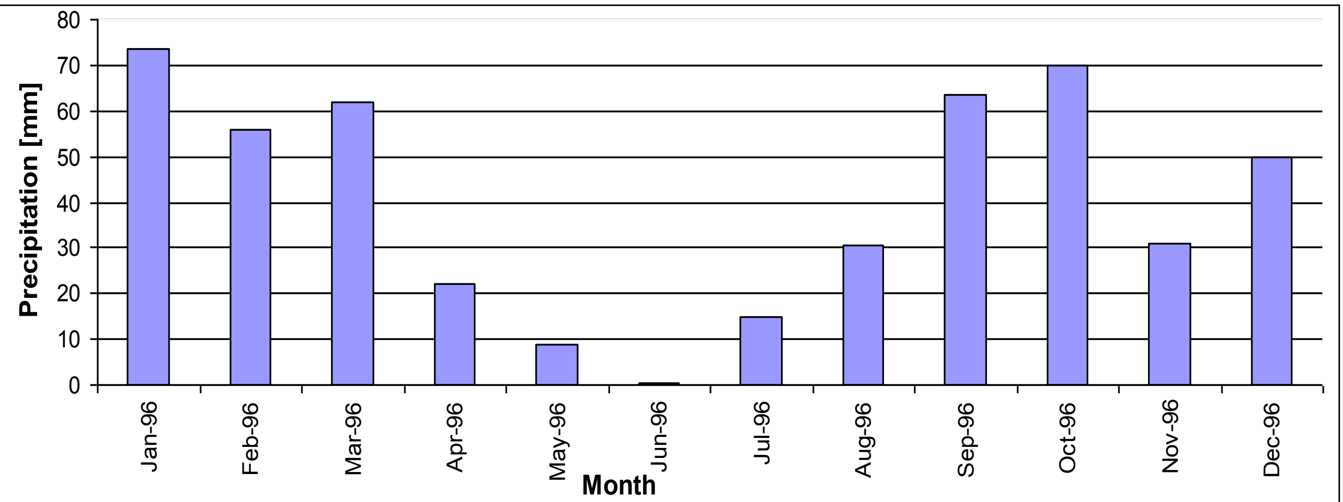

Figure 36. Accumulation of monthly precipitation for the year 1996

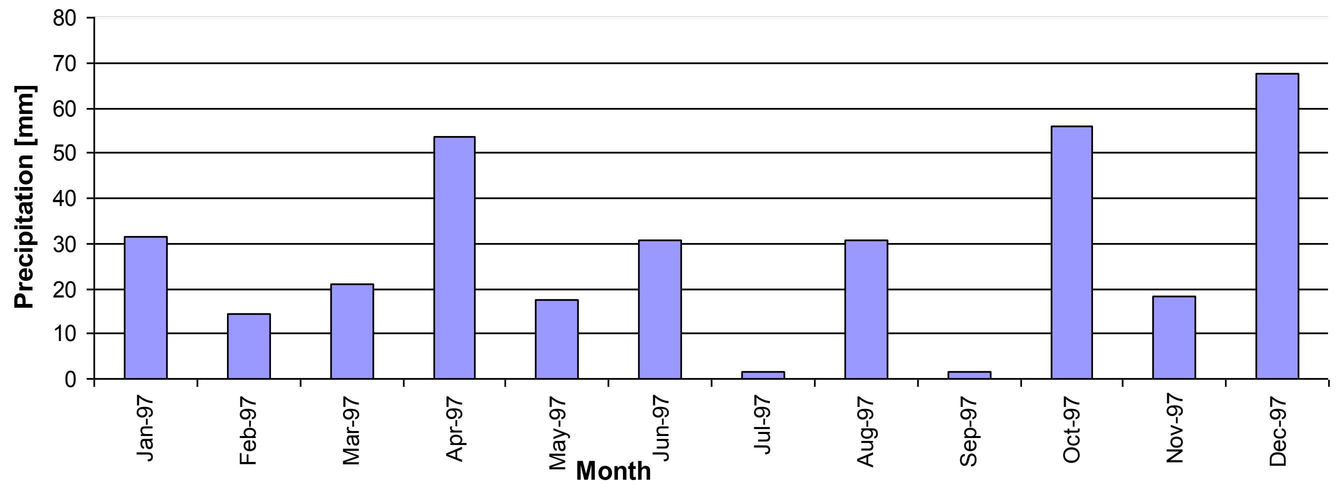

Figure. 37Accumulation of monthly precipitation for the year 1997

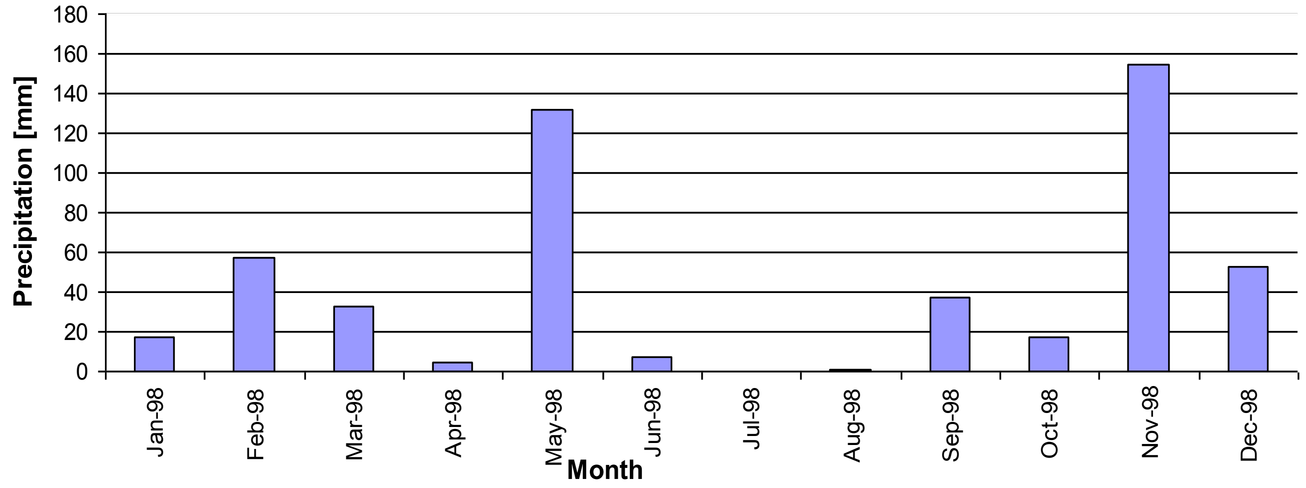

Figure 38. Accumulation of monthly precipitation for the year 1998

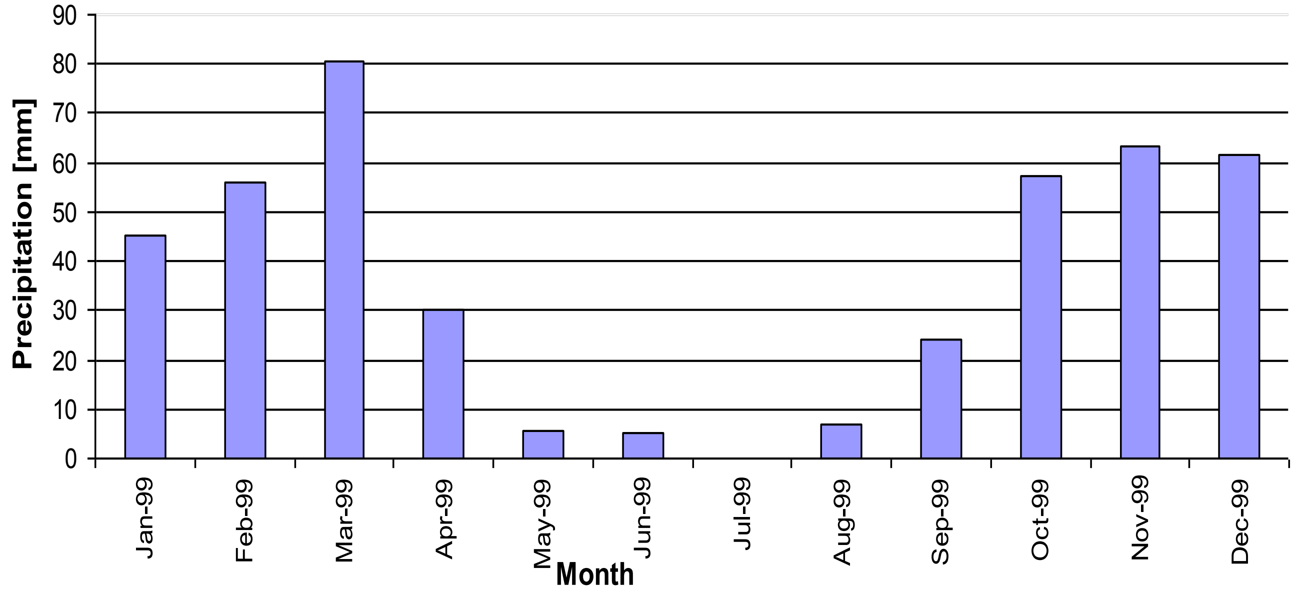

Figure 39. Accumulation of monthly precipitation for the year 1999

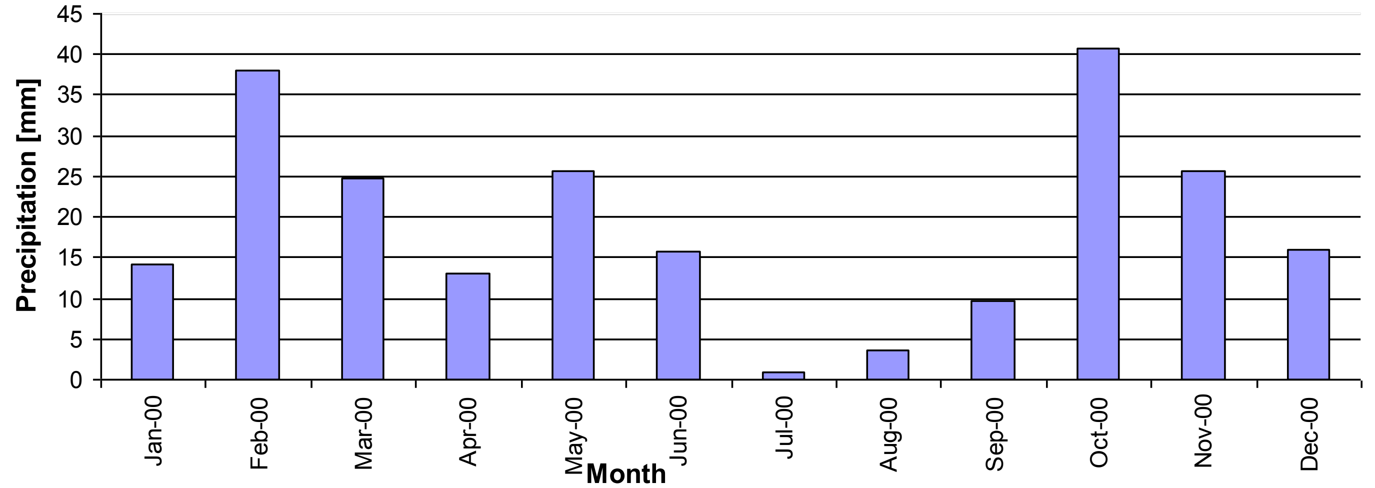

Figure 40. Accumulation of monthly precipitation for the year 2000

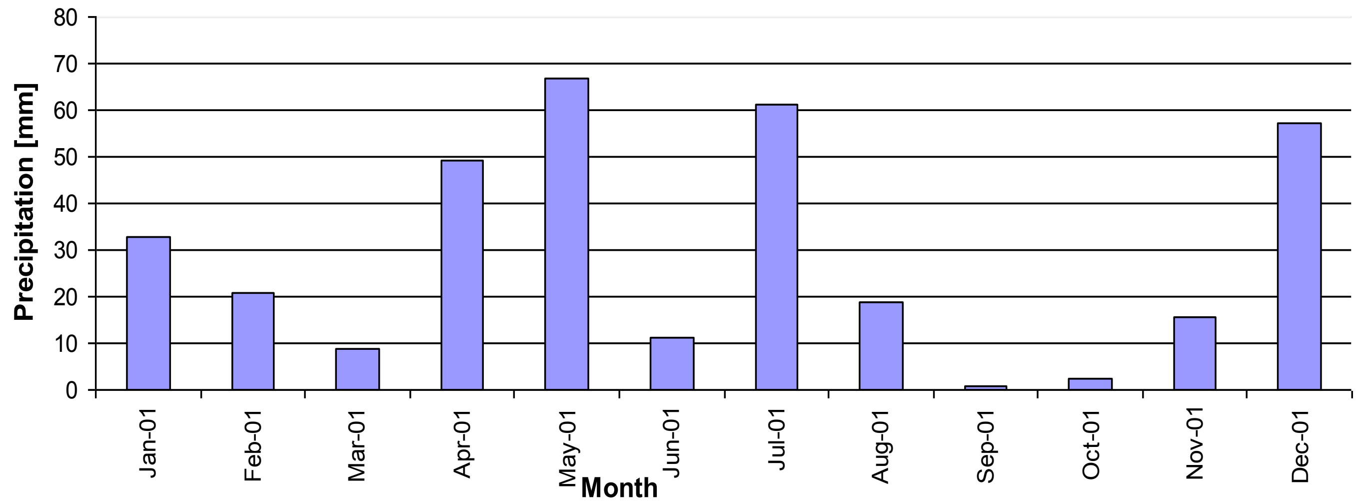

Figure.41 Accumulation of monthly precipitation for the year 2001

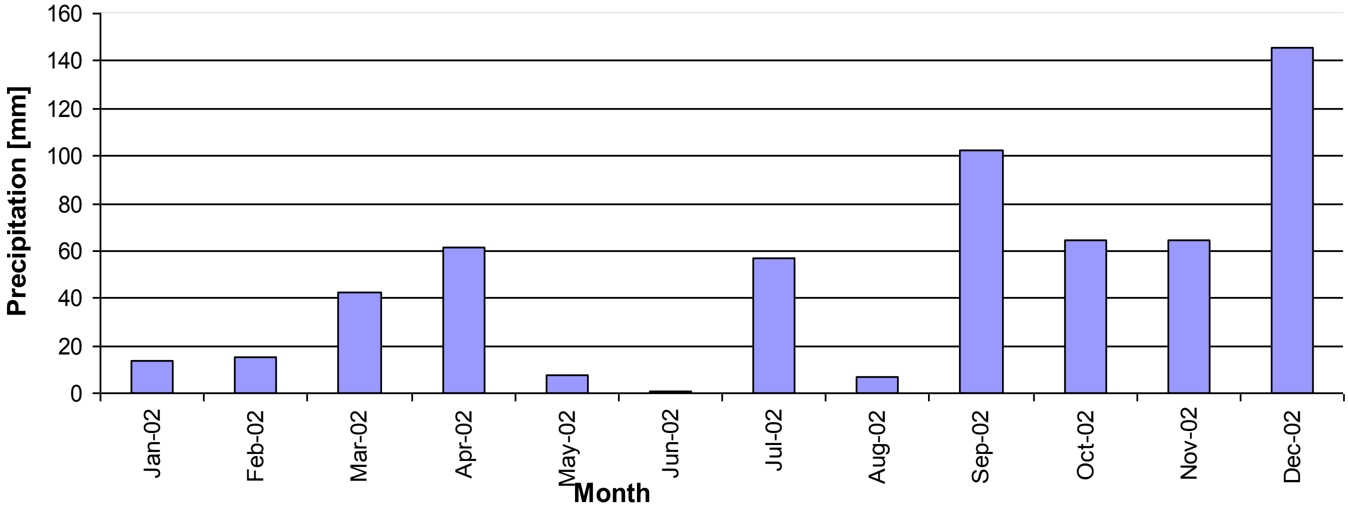

Figure 42. Accumulation of monthly precipitation for the year 2002

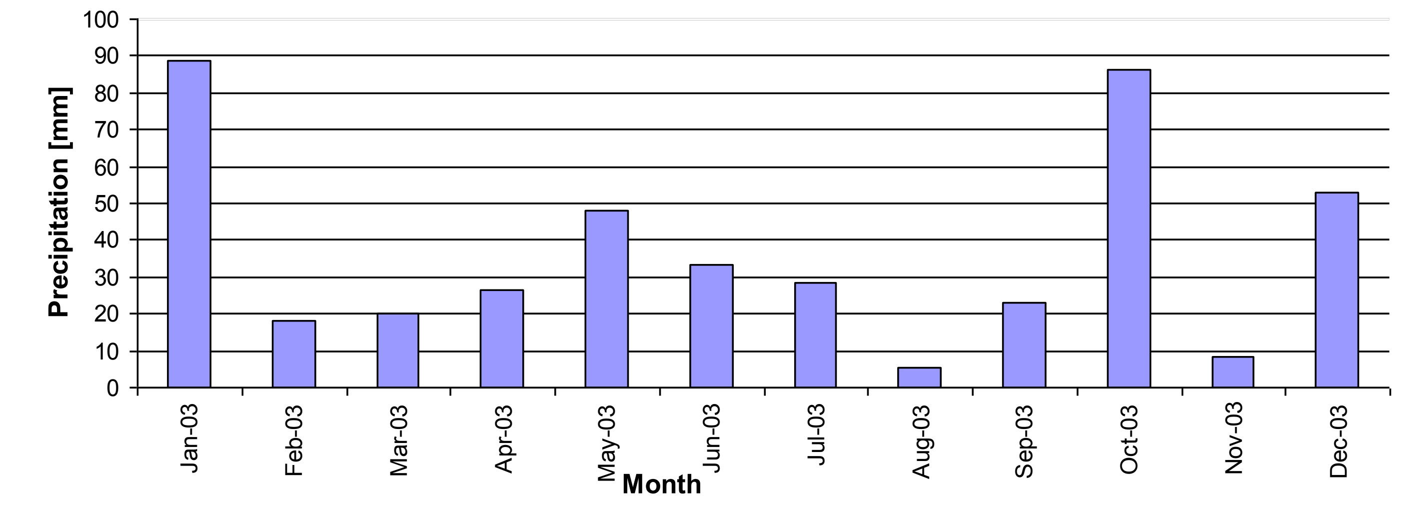

Figure 43. Accumulation of monthly precipitation for the year 2003

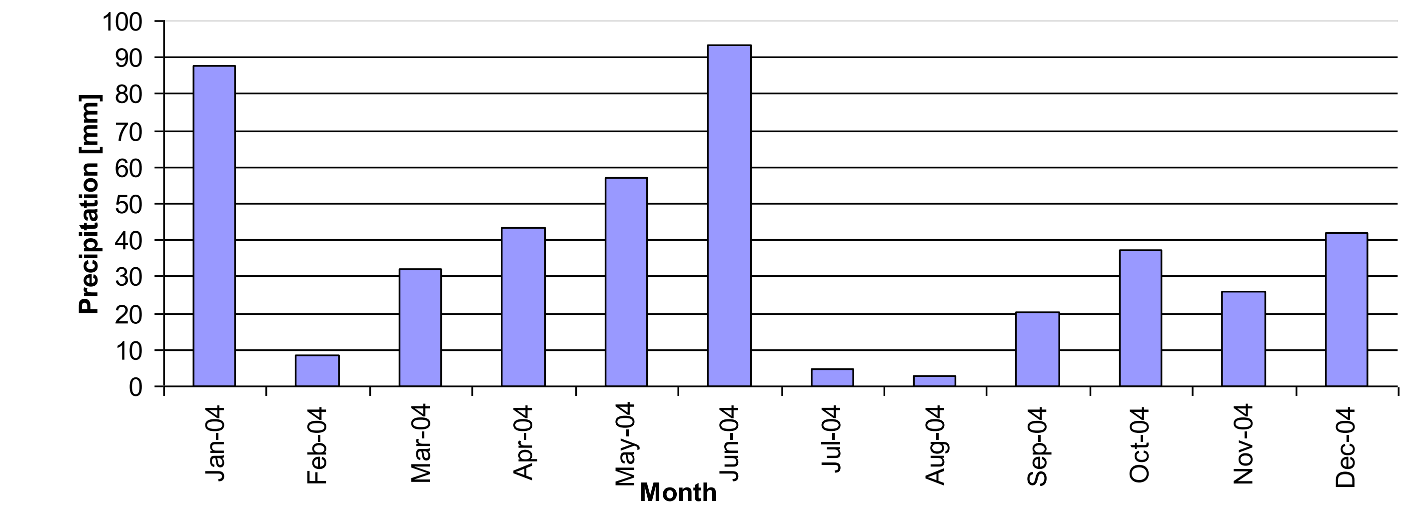

Figure 44. Accumulation of monthly precipitation for the year 2004

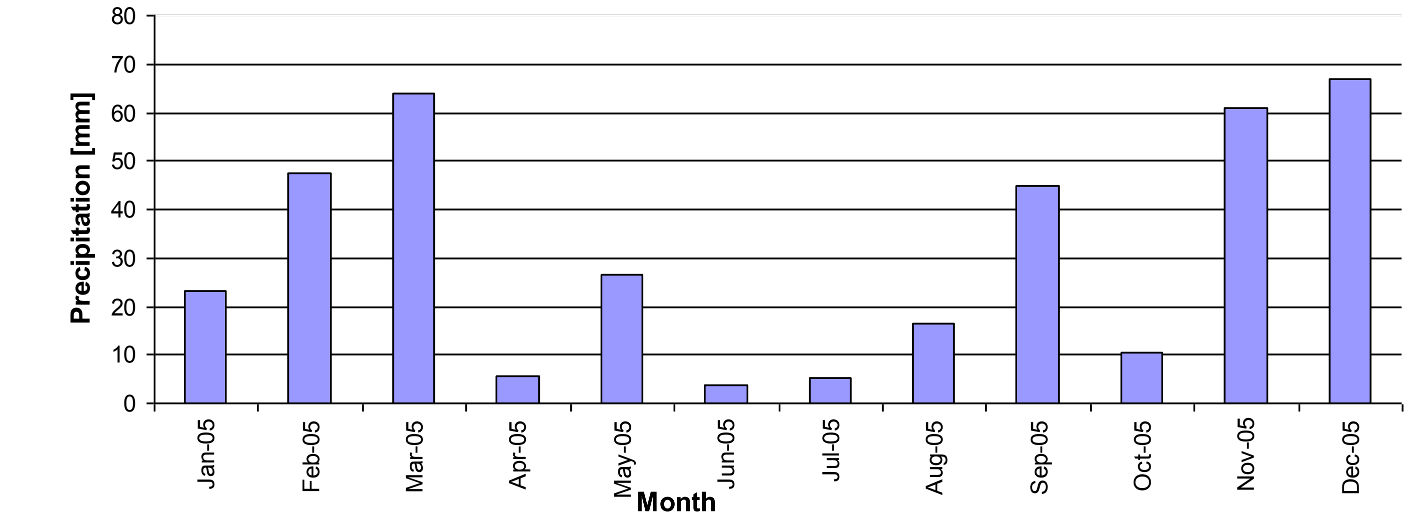

Figure45. Accumulation of monthly precipitation for the year 2005

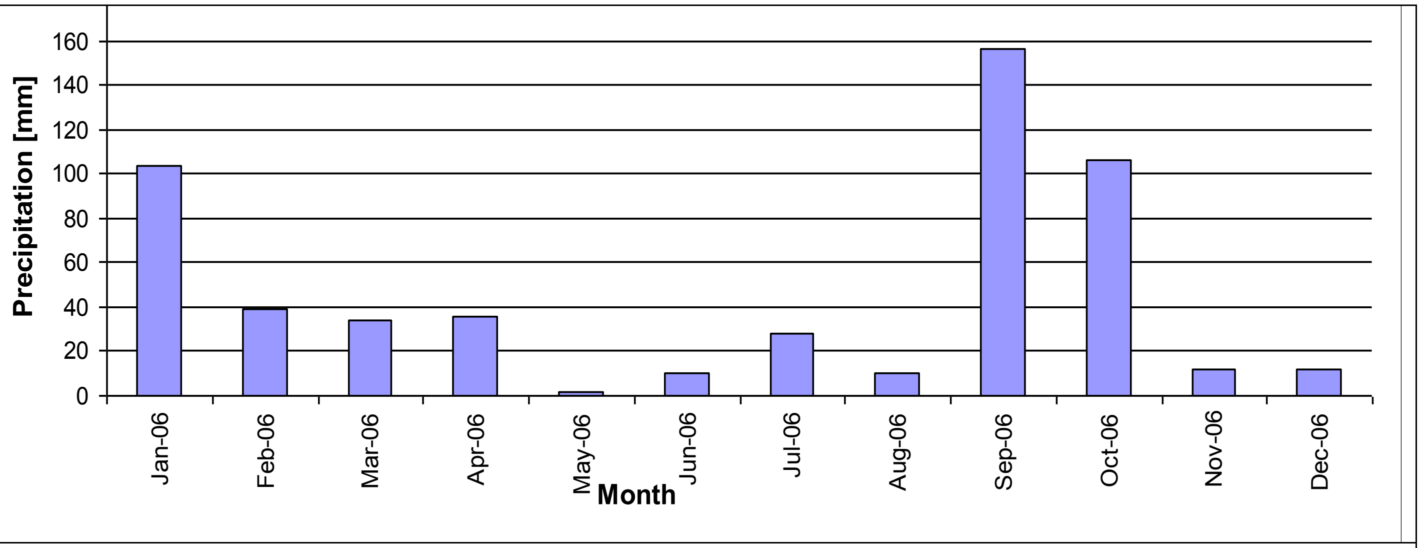

Figure.46 Accumulation of monthly precipitation for the year 2006

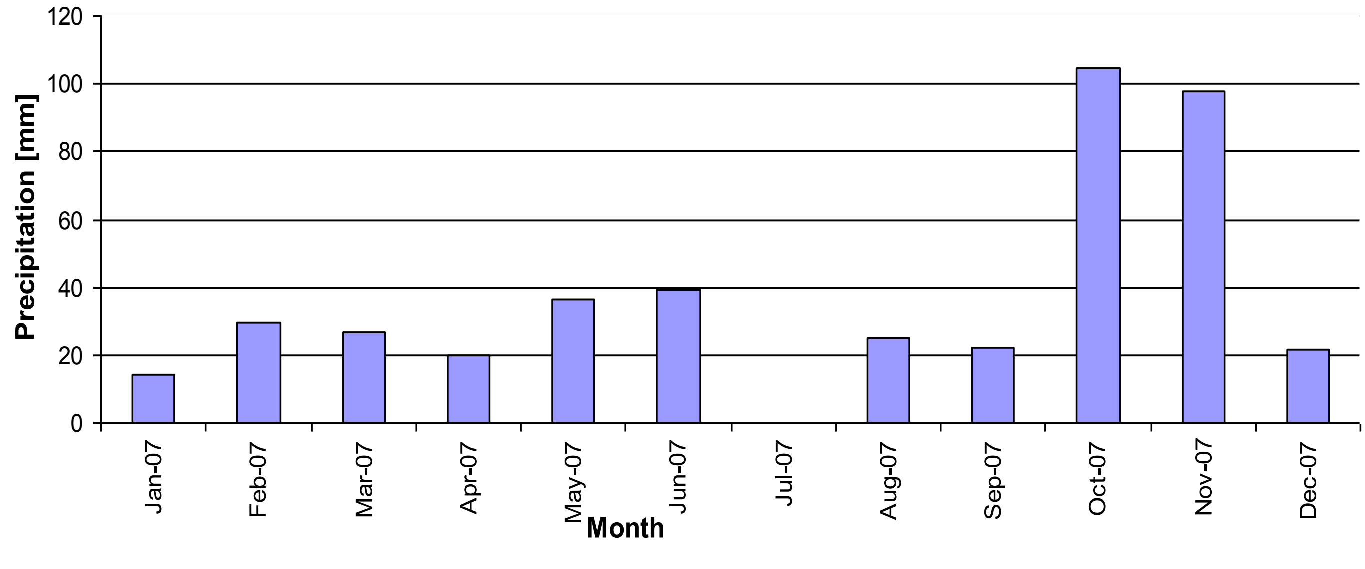

Figure.47 Accumulation of monthly precipitation for the year 2007

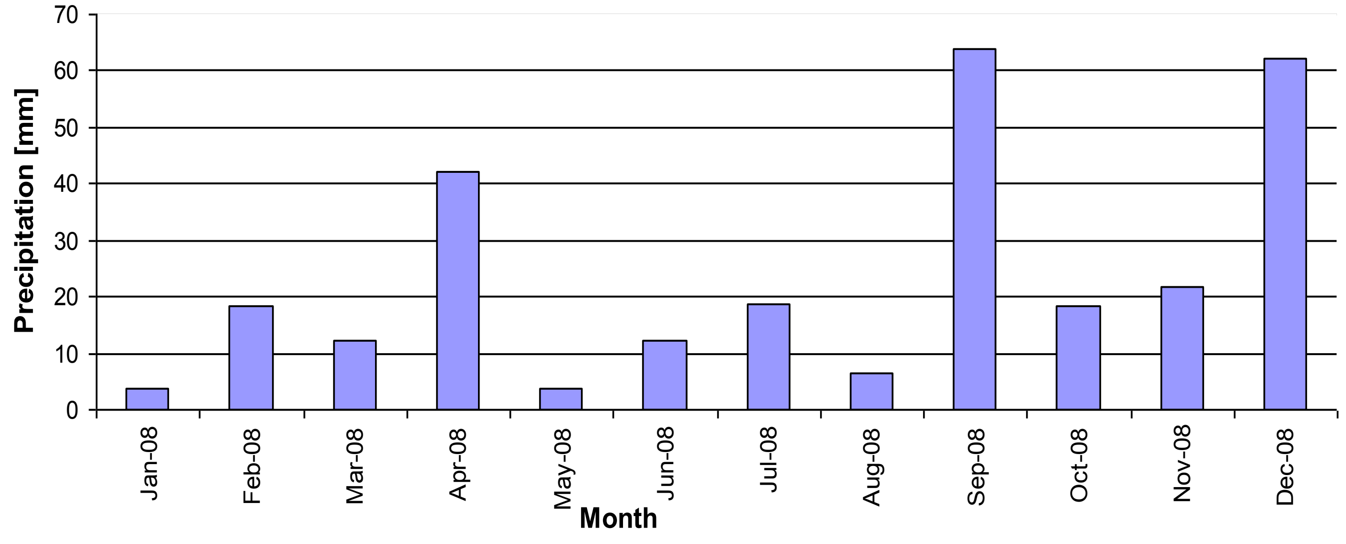

Figure .48 Accumulation of monthly precipitation for the year 2008

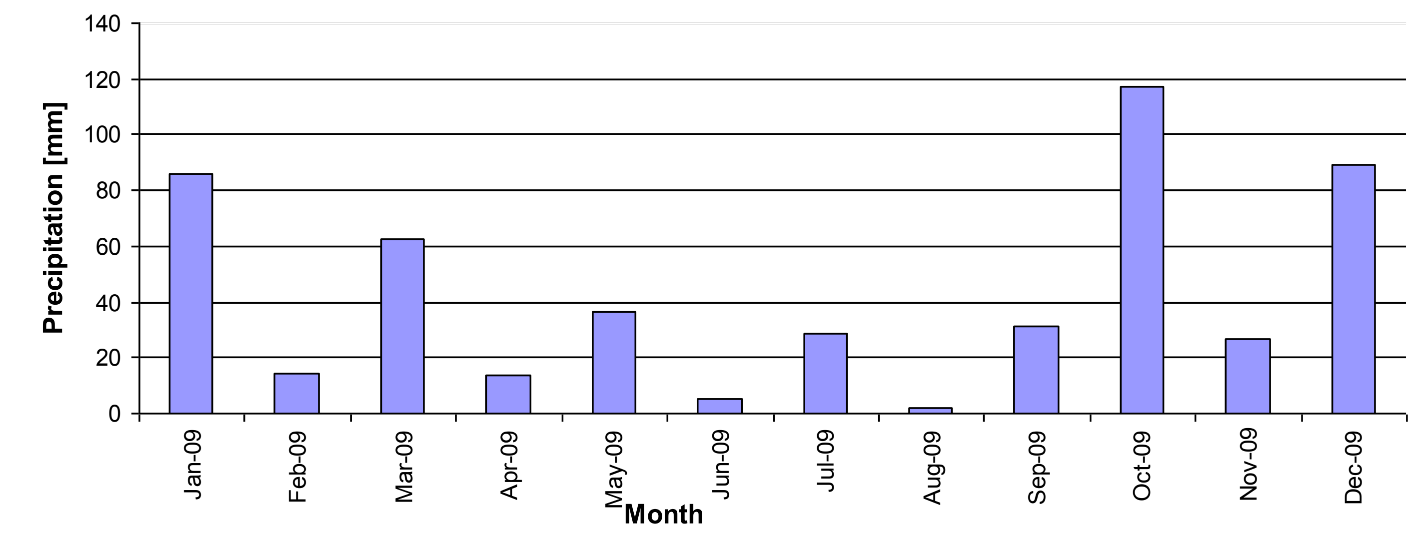

Figure .49 Accumulation of monthly precipitation for the year 2009

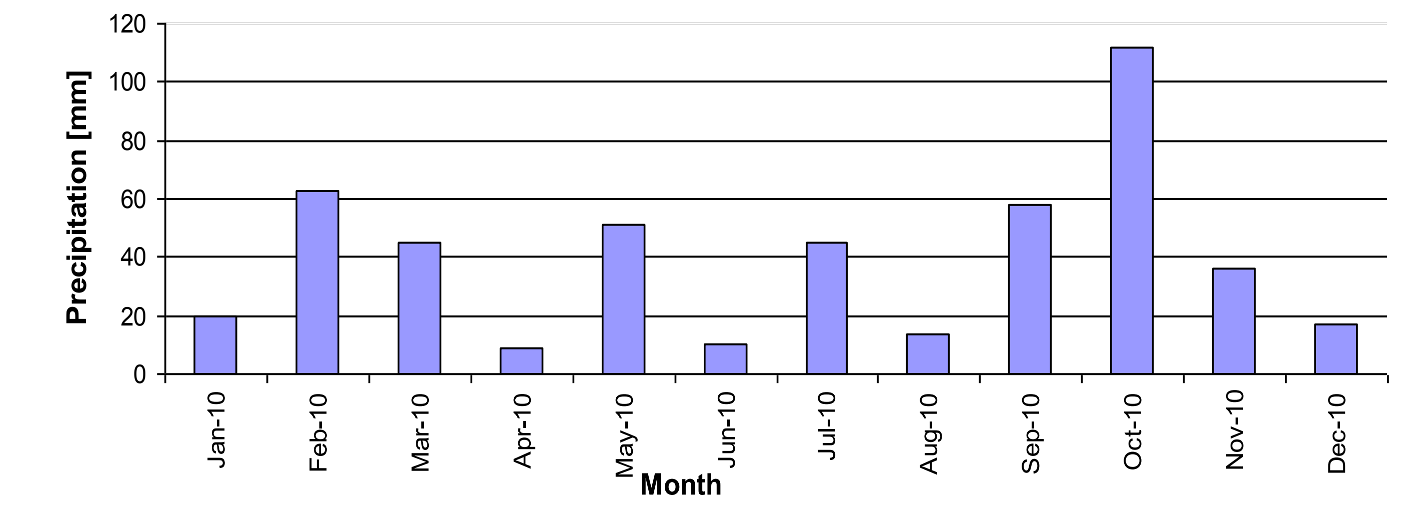

Figure .50 Accumulation of monthly precipitation for the year 2010

3.3.2. Behaviour of the groundwater level

In order to identify and to estimate the impact of groundwater level fluctuation on land deformation within the study area in the eastern part of the Larissa basin, northern Thessaly, more than 15 wells were established in the Thessaly Larissa Regional Unit by the (Decentralized Administration of Thessaly Sterea Elada). Seven of these wells were chosen because they have approximately integrated data corresponding to the time series of InSAR data, on the other hand, the selection depended on the presence of the point candidates of persistent scatters interferometry (PSI). The locations of the boreholes are depicted in Figure 51. These data were treated to construct a sequence of groundwater level fluctuations along the time axis for the period 1992–2010and to identify May and October as the wet and dry periods of each borehole.

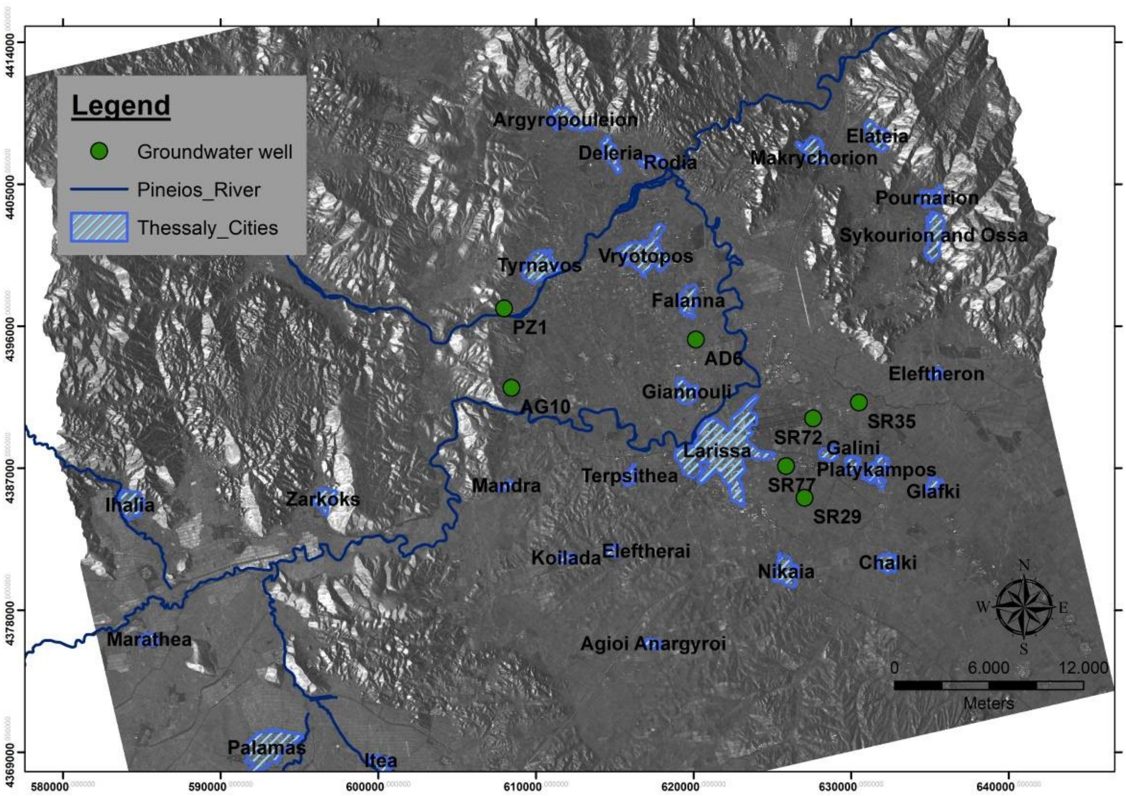

Figure 51. Location of groundwater monitoring network within study area, superimposed on SLC SAR image

3.4. Groundwater monitoring network

Fluctuation of groundwater levels in the period 1992–2010 for the boreholes AD6, AG10, PZ1, SR29, SR35, SR72 and SR77) will be explained and discussed in the following sections.

3.4.1. AD6

This borehole is located 4.98 km north of Larissa and 1.98 km west of the Pineios River. Its easting and northing coordinates are (362786, 4395151), with an elevation of 68 m. The behaviour of the groundwater level of this borehole is depicted in Figure 52. The general behaviour of the groundwater level indicates a continuous decline during the period 1992–2010. Furthermore the details of the behaviour indicate that a continuous fluctuation occurred during all the months of each year, possibly as a consequence of the recharge and discharge of the aquifer. Piezometric level monitoring data indicate that the mean annual fluctuation of the groundwater level was 9.43 m/year and the highest level was 4.21 m (April 1999). The amount of precipitation during this month was 30 mm. This high level of groundwater may be attributable to the amount of precipitation. On the other hand, the aquifer of this borehole is located west of the Pineios River, as mentioned before and consequently this high level may also be attributable to seepage of the water from the river's aquifer to the aquifer of this borehole. The low level of the groundwater was 21.1 m (May 2008), and the accumulated amount of precipitation during this month was 3.6 mm. This decline of the groundwater level may be attributable to the low rate of precipitation, which would have affected the rate of water permeability and in turn the aquifer water recharge. On the other hand, the low amount of precipitation may have been accompanied by dramatic groundwater overexploitation.

3.4.2. AG10

This borehole is located 1.60 km north of the Pineios River and its easting and northing coordinates are (350991, 4392488). The elevation of this borehole is 87 m. The time series of this borehole is from January 1995 to December 2010, and no data were recorded before this date. The behaviour of the groundwater level is depicted in Figure 53. The groundwater level of this borehole shows a continuous decline. Furthermore, fluctuation of the groundwater level during this period is evident, which may be an indicator of mutual recharge and discharge of the aquifer. Piezometric level monitoring data indicate that the mean annual groundwater level fluctuation rate was 19.17 m/year, and the high level was 15.12 m in April 1999. The monthly precipitation during this month was 30 mm, despite the location of this borehole near the Pineios River. Nevertheless there is a high probability that there is no seepage from the river to the aquifer of this borehole. On the contrary, the seepage from the aquifer of this borehole may occur towards the river's aquifer, because the elevation of the area of the borehole or its aquifer is 200 m and the elevation of the Pineios River in this location is 100 m, as depicted in the elevation map of study area (Figure 59). The lowest level of groundwater during the time series was 24.43 m in August 2008, and the accumulation of precipitation for this month was 6.6 mm. This low level may be a result of a low amount of precipitation leading to a decrease in the recharge or supply of the aquifer. Additionally, the low amount of precipitation may result in increased groundwater withdrawal to fulfil the irrigation requirement of crops.

3.4.3. PZ1

This borehole is located 452 m north of the Pineios River, and its easting and northing coordinates are (350703, 4397525). The elevation of this borehole is 93 m. The time series of the groundwater level is depicted in (Figure 54), with data from January 1992 to November 2004. The general behaviour of the groundwater level begins with a decline, followed by a rise with continuous stability until July 2000, followed by decline. Once again a rising of the groundwater level in 2002 is obvious. There is evidence of a continuous fluctuation of groundwater level, which may be attributable to the mutual recharge and discharge of the aquifer. Piezometric level monitoring data indicate that the mean annual of the groundwater level fluctuation rate was 15.94 m/year, while the highest level was 8.88 m in February 2003. The accumulation of monthly precipitation during this month was 18.3 mm, and this relatively high level may be attributable to low groundwater exploitation or withdrawal if the monthly precipitation was enough to fulfil the water irrigation requirement of crops, and simultaneously the precipitation may have contributed to supplying or recharging the aquifer. The lowest level was 21.4 m in April 2002, and the amount of precipitation this month was 61.2 mm. Despite the high amount of precipitation, this recorded level indicates that there is no high supplying of the aquifer. An accepted explanation for this situation is that seepage occurred from the aquifer of the borehole towards the Pineios River aquifer, because the elevation of the borehole (aquifer) is equal to 200 m while the elevation of the Pineios River area in this location is equal to 100 m. Additionally, an increase in groundwater withdrawal may have contributed to the decline of the groundwater level during this month, while on the other hand, surface runoff may have contributed to decreasing the water permeability and consequently decreasing the aquifer's water supply.

3.4.4. SR 29

This borehole is located 4.65 km southeast of Larissa, and its easting and northing coordinates are (369347, 4384897). The elevation of this borehole is 74 m. The time series of the groundwater level is depicted in (Figure 55). The time series is from January 1992 to December 2007. The general behaviour points to a declining trend of the water level during this period. Details of the behaviour indicate fluctuation of the groundwater level throughout this period, which may be attributable to the mutual recharge and discharge of the aquifer. Piezometric monitoring data indicate that the mean annual groundwater level fluctuation rate was 39.52 m/year. The highest level was 16.16 m in February 1992, and accumulation of the amount of precipitation this month was 9.2 mm; however, this rate of precipitation is quite low to supply or recharge the aquifer. Nevertheless there is a possibility that almost all of this amount will percolate because this area is flat. The other accepted viewpoint is that the amount of precipitation may have been enough to fulfil the water irrigation requirement of crops, leading to low groundwater withdrawal. On the other hand, this level may be attributable to the seepage of water from the high area located southwest of the area of the borehole aquifer with an elevation of 200 m towards the area of borehole (aquifer) with an elevation of 100 m. This may be an acceptable reasoning for the high level of the groundwater with this low rate of precipitation. On the other hand, maybe runoff occurred from the high to the low area. The lowest level of groundwater was 73.39 m in August 2005, and the accumulation of precipitation for this month was 16.4 mm, despite the considerable possibility of percolation of almost all of the precipitation for the same reason as mentioned above. Nevertheless, this amount of precipitation is not enough to recharge or supply the aquifer, so during this period dramatic groundwater withdrawal may have occurred to fulfil the water irrigation requirement of crops.

3.4.5. SR35

This borehole is located east of the NATO airport of Larissa. Its easting and northing coordinates are (372990, 4390822), and its elevation is 61 m. The time series of the groundwater level is depicted in Figure 56. The time series is from January 1992 to December 2010; however, no monitoring data were recorded from October 2009 to August 2010. The general behaviour of the groundwater level during this period begins with a decline, followed by a rising level with continuous stability until January 2006. Thereafter a decline occurred once again. While the details indicate continuous fluctuation of the groundwater level during the time series, this may be attributable to the mutual recharge and discharge of the aquifer. Piezometric level monitoring data indicate that the mean annual of the groundwater level fluctuation rate was 4.72 m/year. The highest level of the groundwater was 3.15 m in September 1999, and the accumulated amount of precipitation during this month was 37.1 mm. This high level of groundwater may be attributable to the percolation of approximately all of the precipitation, while on the other hand, low groundwater withdrawal may be associated with this percolation. Furthermore, there is not a high demand for water for irrigation, because this period is either the end or the beginning of the season for crops. The area of this borehole (aquifer) is located in the south of an elevated area at 200 m, and consequently there is a considerable possibility of seepage from the aquifer towards a lower aquifer with an elevation of 100 m. alternatively, there may have been runoff of water from this area towards the area of the borehole (aquifer). On the other hand, this borehole (aquifer) is located south of a water harvesting channel (tributary), which is pouring water into the watershed located 7 km east of the borehole, and consequently there may be seepage from this channel to the aquifer. The lowest level of the groundwater was 7.42 m in August 2008, and the accumulated amount of precipitation during this month was 6.6 mm, which was not enough to recharge and supply the aquifer and may have been accompanied by high groundwater withdrawal.

3.4.6. SR72

This borehole is located 100 m east of NATO airport, its easting and northing coordinates are (370056, 4389904), and it is at an elevation of 66 m. The time series is depicted in (Figure 57). Time series monitoring of the groundwater level was carried out for the period January 1992 to November 2010; however there are no data monitoring records for the period September 2009 to August 2010. The general time series behaviour of the groundwater level during the monitoring period indicates a continuous decline towards the end of the period. Fluctuation of the groundwater level is evident from the time series data, possibly resulting from the mutual recharge and discharge of the aquifer. Piezometric monitoring data indicate that the mean annual groundwater level fluctuation rate was 26.31 m/year. The highest level was 15.42 m, in February 1992, and the accumulated precipitation during this month was 9.2 mm. Despite the quite low precipitation rate to recharge the aquifer during this short period, there is still a possibility that approximately all this amount was percolated, because this area is flat. On the other hand, this level may be attributable to aquifer supplying from the Pineios River, especially given that the distance between the borehole's aquifer and the Pineios River is 3.96 km. Another acceptable reason that the water withdrawal for this month was quite low could be the low requirement of water for crops. Furthermore, this level may also be attributable to water seepage and runoff from an elevated area northeast of the borehole's aquifer. The behaviour of the groundwater level of this borehole is similar to that of borehole SR29, which may be because the two boreholes are located over the same aquifer. It is worth mentioning that the behaviour of the groundwater level of borehole SR35 is almost similar to that of borehole SR72. The distance between these two boreholes (SR72 and, SR35) is 3 km, indicating that they are located over an identical type of aquifer. The lowest groundwater level was 39.47 m, in August 2008, and the accumulated amount of precipitation during this month was 6.6 mm. This low groundwater level may be as a result of the low amount of precipitation during this month, leading to a decrease in recharging of the aquifer, while the low amount of precipitation may leading to increased groundwater withdrawal to fulfil the irrigation requirement of crops. Low groundwater level behaviour of this borehole during this month is almost similar to the low level behaviour of the groundwater of the borehole AG10.

3.4.7. SR77

This borehole is located 1.04 km east of Larissa and 2.33 km south of NATO airport, its easting and northing coordinates are (368234, 4386942), and its elevation is 72 m. The time series is depicted in (Figure 58). Groundwater level monitoring was carried out for the period January 1992 to November 2010; however, there are no data monitoring records for the period September 2009 to August 2010. The general behaviour of the groundwater level points to a declining trend over the time series, which may be attributed to the non-recharge of the lost water of the aquifer. While the monitoring data indicate continuous fluctuation of the groundwater level, this may be attributable to the mutual recharge and discharge of the aquifer. Piezometric level monitoring data indicate that the mean annual of the groundwater level fluctuation was 26.29 m/year. The highest level of groundwater was 14.02 m, in February 1992, and the monthly precipitation during this month was 9.2 mm, which is not enough to recharge the aquifer, as mentioned before for boreholes SR35 and SR72. This convergence of the behaviours of these boreholes may be attributable to their location over an identical type of aquifer. Consequently, the reason for this high level may be attributed to the low groundwater withdrawal due to the low water requirement to fulfil the irrigation demand of crops. The lowest level of groundwater was 38.88 m, in August 2008, and the accumulated precipitation during this month was 6.6 mm. The low groundwater level is a natural consequence of the low amount of precipitation, leading to low recharge of the aquifer. The other acceptable reasoning is that the high amount of groundwater withdrawal to fulfil the irrigation requirement of crops results in a dramatic decline in the groundwater level.

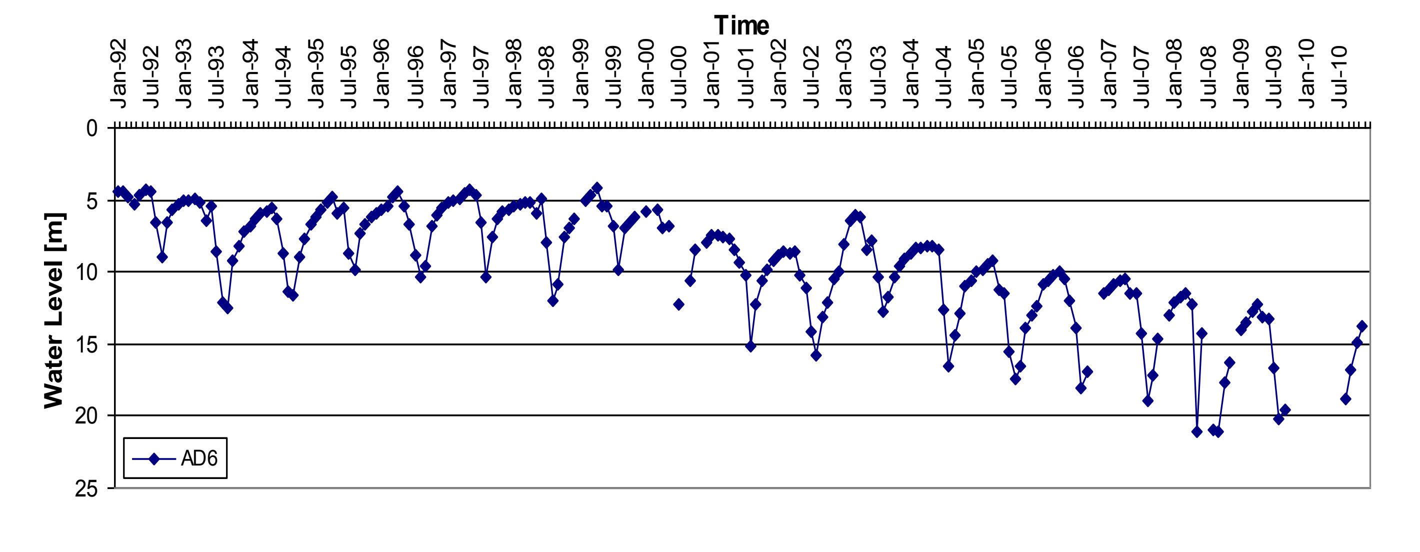

Figure .52 Groundwater level fluctuation in relation to time for borehole AD6 of the period 1992 - 2010.

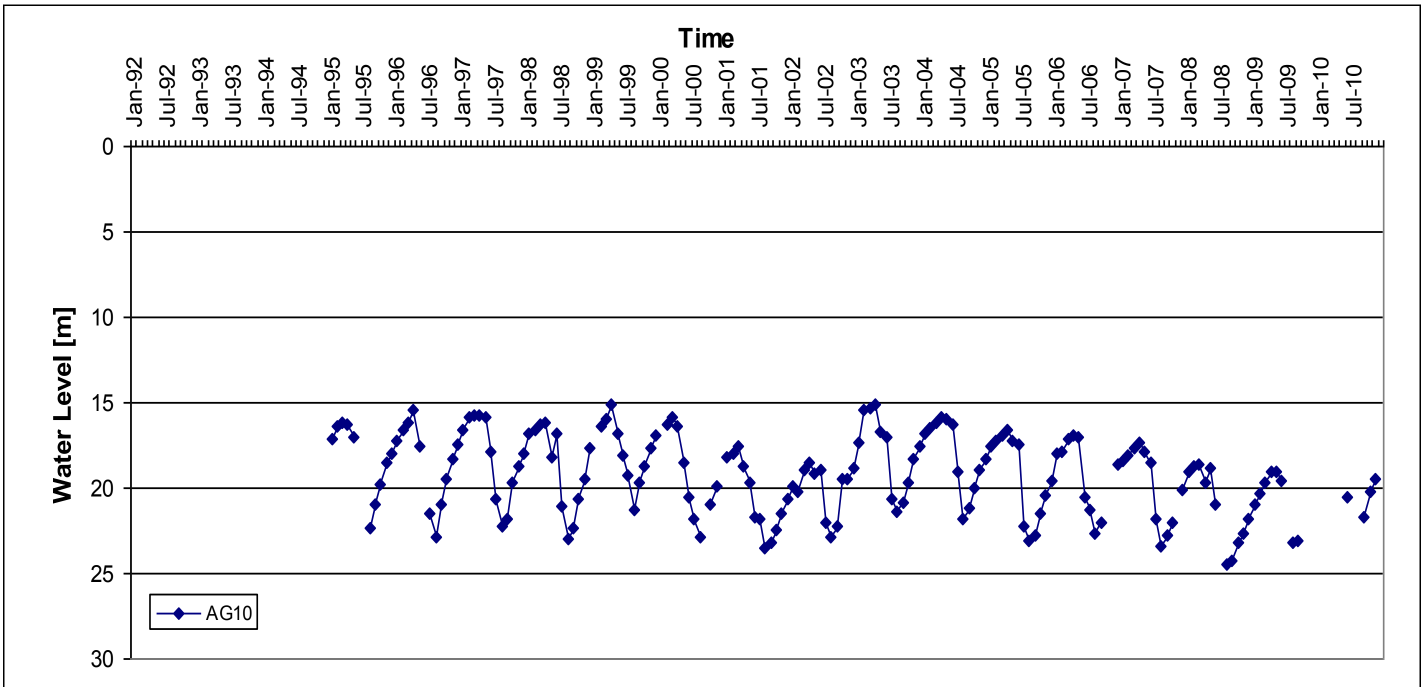

Figure 53. Groundwater level fluctuation in relation to time for borehole AG10 of the period 1992 - 2010.

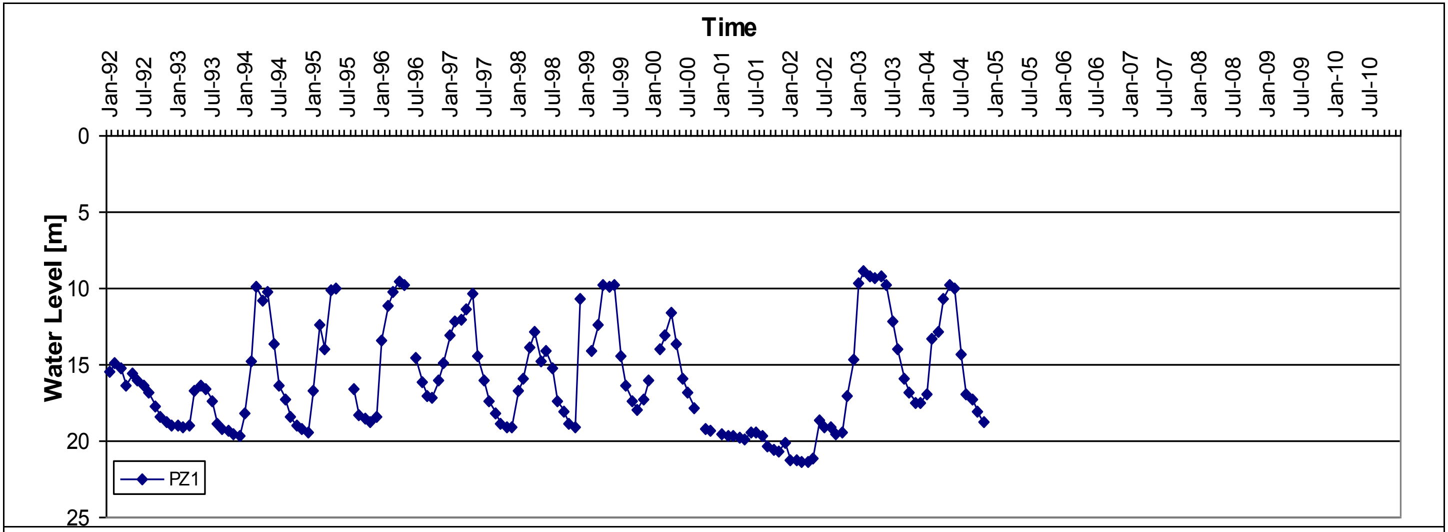

Figure 54. Groundwater level fluctuation in relation to time for borehole PZ1 of the period 1992 - 2010.

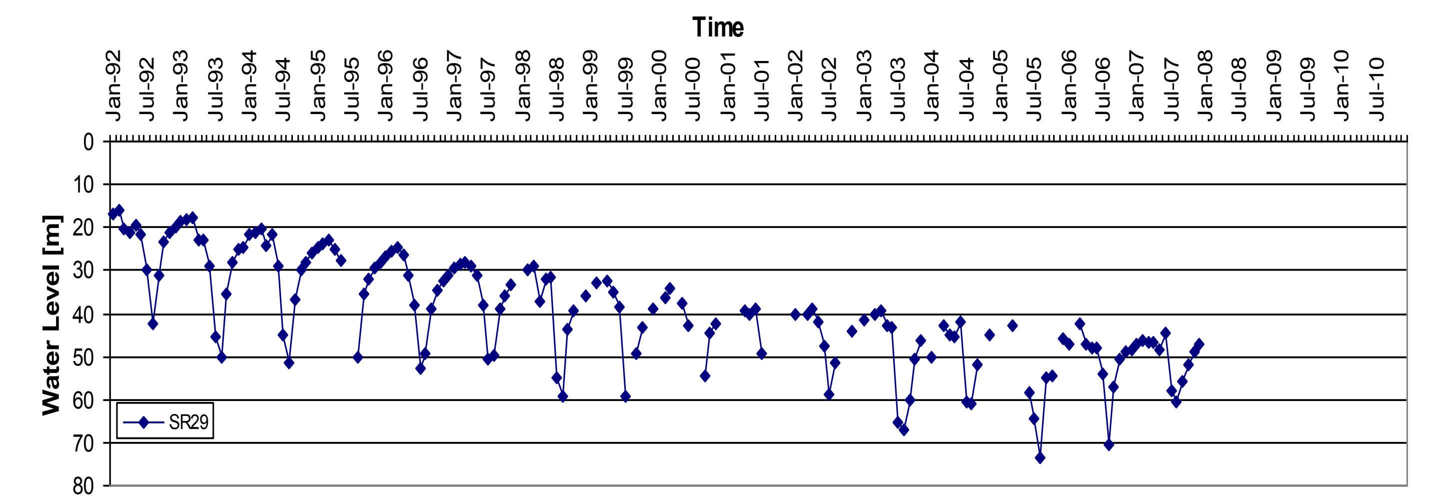

Figure .55 Groundwater level fluctuation in relation to time for borehole SR29 of the period 1992 - 2010.

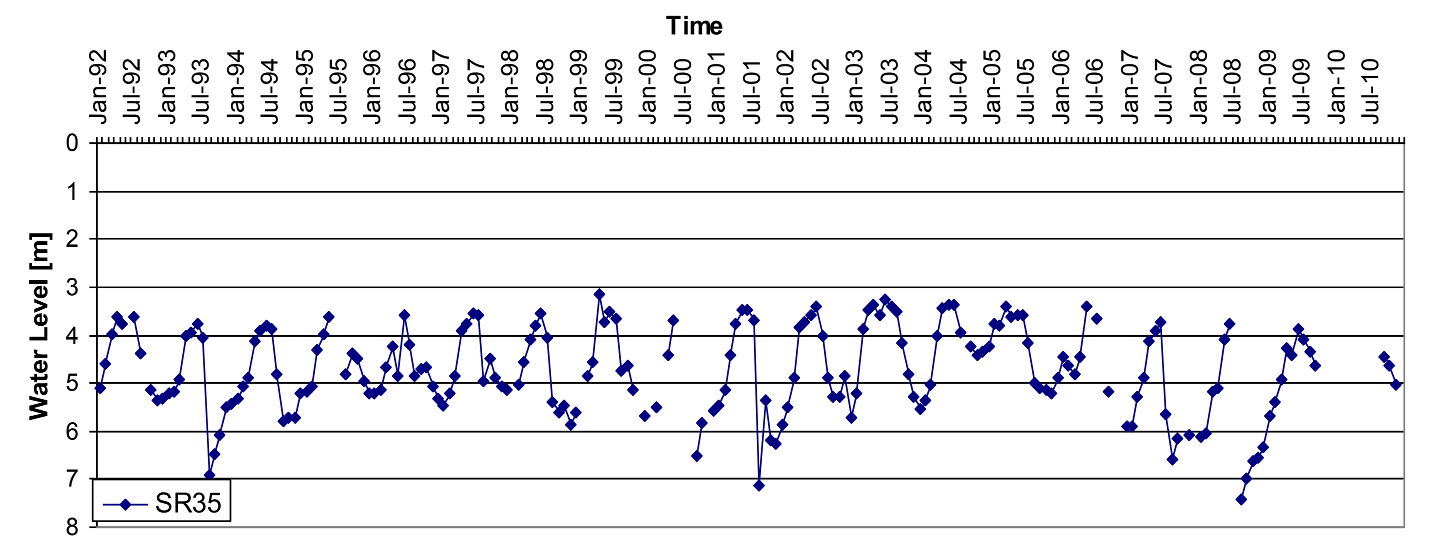

Figure .56 Groundwater level fluctuation in relation to time for borehole SR35 of the period 1992 - 2010.

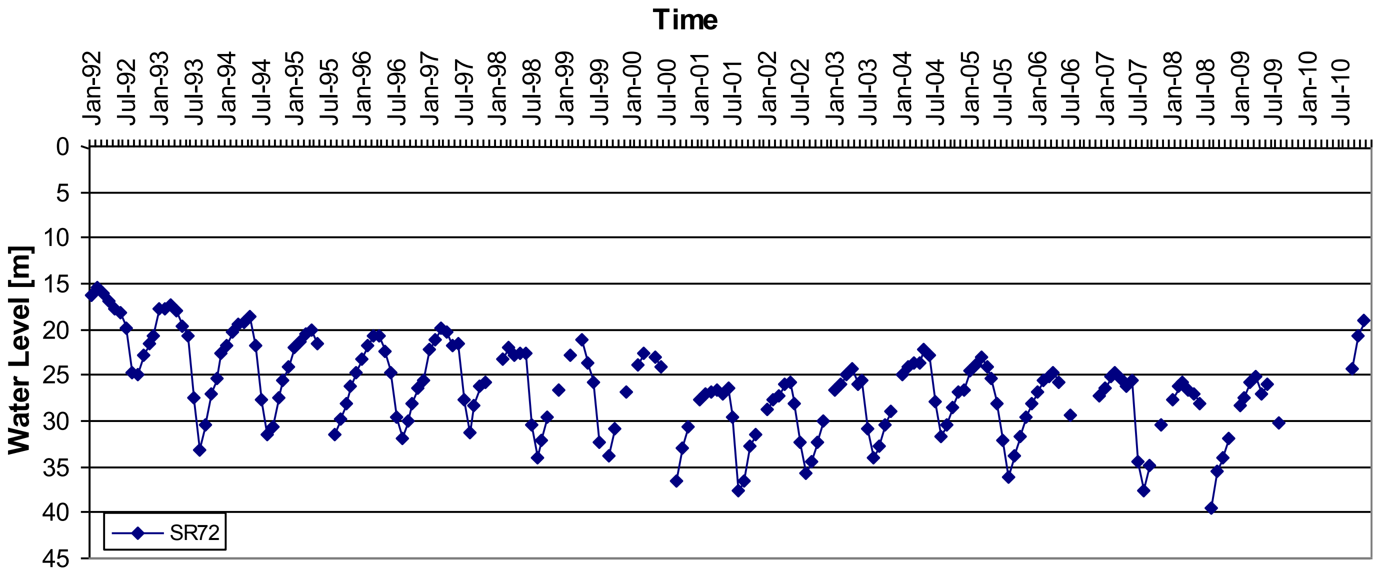

Figure 57. Groundwater level fluctuation in relation to time for borehole SR72 of the period 1992 - 2010.

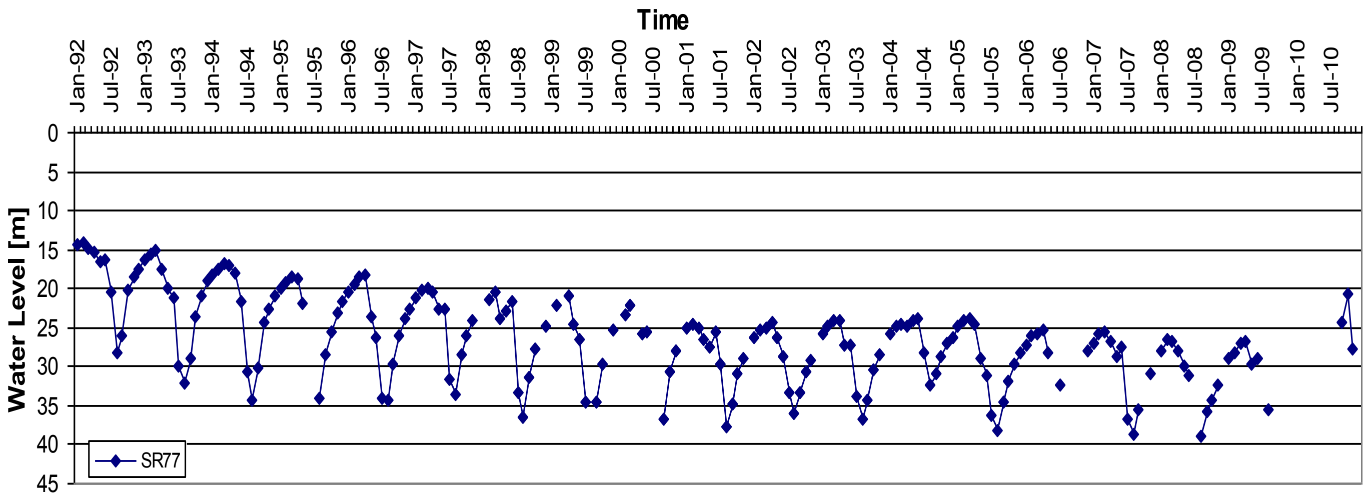

Figure .58 Groundwater level fluctuation in relation to time for borehole SR77 of the period 1992 - 2010.

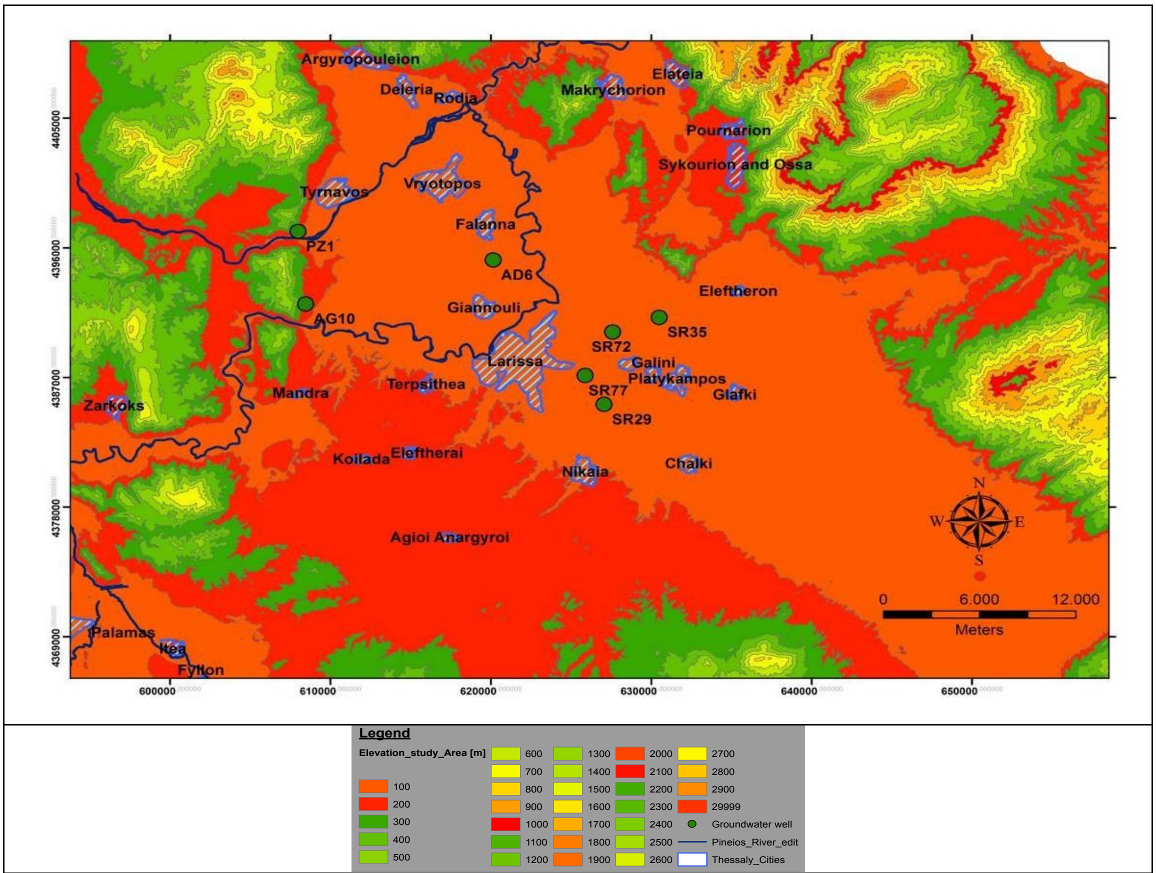

Figure 59. Elevation map of the study area depicted the location of the boreholes.

3.5. Groundwater level monitoring for May and October (wet and dry period)

With a view to identifying the behaviour of the groundwater level corresponding to the wet and dry periods, the months of May and October have been chosen as corresponding to the wet and dry periods, respectively. An interference correlation between monthly precipitation and groundwater level for May and October has been constructed to identify the impact of precipitation on the behaviour of groundwater level during these periods. The amount of groundwater withdrawal was predicted approximately, because no groundwater withdrawal records were obtained for any wells under this study. The fluctuation of groundwater level in relation to the time and precipitation during May and October for the period 1992–2010 for the boreholes AD6, AG10, PZ1, SR29, SR35, SR72 and SR77 will be explained and discussed in the following sections.

3.5.1. AD6

The behaviour of the groundwater level for this borehole during May and October is depicted in Figure 60. The general behaviour of the groundwater level during the period 1992–2010 indicates a declining trend until the end of the period. Despite the fact that the accumulation of precipitation in October is larger than the accumulation of precipitation in May, it is evident that the groundwater level in May is higher than the groundwater level in October, which may be attributable to two possible causes. Firstly, the groundwater level is not solely due to the accumulated precipitation during May but also to the precipitation of preceding months, which recharged the aquifer. Secondly, there was low groundwater withdrawal during May and the preceding months during the winter season to fulfil the irrigation requirement of crops, and there may be a compensation of water lost due to withdrawal by precipitation or from another source. The groundwater level for October is lower than the groundwater level for May despite a high amount of precipitation during this month. This may be attributable to the overexploitation of groundwater during the months preceding October, during the summer season, when there is not enough water to compensate for lost water either from precipitation or any other sources. Consequently, despite the high amount of precipitation recorded in October, it is not enough to raise the groundwater level during this month. The groundwater level of May 2008 is lower than the groundwater level of October 2008, which may be attributable to a large decrease in the amount of precipitation with an accompanying overexploitation of groundwater during this month. This indicates that precipitation has a significant impact on the groundwater level within this aquifer, as evidenced by the rise in groundwater level as a result of increased precipitation which was observed once again during May 2009.

3.5.2. AG10

The behaviour of the groundwater level at this borehole during May and October is depicted in Figure 61. Note the absence of data monitoring records for May and October during the period 1992–1994. The general groundwater level behaviour indicates a declining trend for May and October until the end of time series. It is noticeable that the groundwater level in May is close to the groundwater level in October for the year 2002, despite the considerable difference in monthly precipitation between the two months, which was 7.4 mm and 64.8mm for May and October, respectively. This may be due to the low amount of precipitation during May, while the groundwater level for October may be attributable to the overexploitation of groundwater during this month and many months before during the summer season. This is an acceptable reason for the low level of groundwater. Additionally, the high amount of precipitation is not enough to compensate for the water lost during this month. These two reasons may account for the convergence between the groundwater levels of these two months.

3.5.3. PZ1

The behaviour of the groundwater level at this borehole during May and October is depicted in Figure 62. Note the absence of data monitoring records for May and October during the period 2005–2010. The general groundwater level behaviour in May indicates a decline followed by a rise during the period 1993–1994. It is worth mentioning that this increase is not attributed to the amount of precipitation, because there was a decrease in precipitation during this period. Consequently this increase may be attributable to other sources of water supply. The increase was followed by a stable level during the period 1994–1997, which may be attributable to the low exploitation of groundwater. Afterwards, despite the high amount of precipitation, a high decline was observed during May 1998, which indicates that the groundwater level was not affected by the amount of precipitation. Maybe overexploitation of groundwater occurred during this period to fulfil the irrigation requirement of crops or for another reason. Thereafter an increase in groundwater level occurred once again in 1999, which is evidence that there was no impact of precipitation on the groundwater level of this case. Subsequently, an extreme sloping trend is observed during the period 1999–2002 followed by a high increase during May 2002–2003. This may be attributed with a high probability to the increase in precipitation. The groundwater level for October is indicated to be approximately stable during the period 1992–2001. Thereafter a rise in the groundwater level during 2001–2003 is observed, which may be attributed to the amount of precipitation. It is noticeable that the groundwater level for May 2001 is close to the level for October of the same year, despite the amount of precipitation in May and October being 66.8 and 2.3 mm, respectively. This may be attributable to the overexploitation of groundwater during May, resulting in the lost water exceeding the compensation water. Additionally, the groundwater level for May 2002 was lower than the groundwater level for October of the same year. This may be attributable to the high amount of precipitation in October (64.8 mm) in comparison with the amount of precipitation in May (7.4 mm).

3.5.4. SR29

The behaviour of the groundwater level of this borehole for May and October is depicted in Figure 63. Note the absence of monitoring data for May during the period 2005–2010 and for October during the period 2004–2010. The general behaviour of the groundwater level for the two months May and October indicates a declining trend towards the end of the time series, which may be attributable to insufficient compensation of the lost water. The groundwater level for May is higher than the groundwater level for October in the same time series. Additionally, the behaviour of the groundwater level during May and October represents normal behaviour for the wet and dry periods.

3.5.5. SR35

The behaviour of the groundwater level of this borehole for May and October is depicted in Figure 64. Note the absence of monitoring data for May 2010 and for the month of October during the periods 2006–2007 and 2009. The general behaviour of the groundwater level for May indicates stability during the period 1992–1994 followed by a sharp decline during 1995–1996. This may be attributable to the decrease in the monthly amount of precipitation. Afterwards, a small rise during 1996–1997 has been observed, followed by continuous stability. A small fluctuation, barely observable during the period 1997–2006, decline was subsequently observed during the period 2006–2009. While the behaviour of the groundwater level for October indicates a sharp decline initially during 1992–1993, thereafter a rise was observed during the period 1993–1995. It is noticeable that the groundwater level for October 1996 is approximately higher than the groundwater level for May of the same year, despite the monthly precipitation for May and October being 9 and 70 mm, respectively. Consequently this low groundwater level for May may be attributable to the low amount of precipitation during this month. Furthermore, the high groundwater level for October is, with a considerable probability, attributed to the amount of precipitation. Following a declining trend during the period 1997–2001, a rise in the groundwater level during the period 2001–2004 was observed, which may be attributable to the increase in the monthly amount of precipitation during this period. After that, a decline occurred once again during the period 2004–2008, and this also may be attributable to the decreasing amount of precipitation.

3.5.6. SR72

The behaviour of the groundwater level of this borehole for May and October is depicted in Figure 65. Note the absence of monitoring data for the month of October during 2006–2007 and for May 2010. In general, the groundwater level is higher in May than in October during the time series. of the data for the month of May indicate a slow decline during the period 1992–2001, followed by a slow rise during the period 2001–2004. This may be attributable to the impact of the monthly amount of precipitation. Subsequently a slowly decline was observed once again during the period 2004–2009, which may be attributable to increased groundwater withdrawal to fulfil the irrigation requirement of crops. Furthermore, the amount of precipitation was not enough to compensate for the lost water.

For the month of October, the data generally indicate a decline in the groundwater level during the period 1992–2005. The sharp decline during the period 1992–1993 may be attributable to the decreasing monthly precipitation. This was followed by a slow decline in the period 1994–1996 and a rise during the period 1996–1997. Subsequently, a decline was observed during the period 1998–2000, which may be attributable to insufficient water to compensate for the water lost as a result of withdrawal. After that, a slowly rising trend was observed during the period 2001–2004, which may be attributable to increasing amounts of precipitation. Immediately thereafter a decline in the groundwater level during the period 2004–2005 occurred, which may be attributable to the decreasing amount of precipitation.

3.5.7. SR77

The behaviour of the groundwater level of this borehole for May and October is depicted in Figure 66. Note the absence of monitoring data for May 2010 and for the month of October during 2006–2007. It is worth mentioning that the behaviour of the groundwater level of this borehole is similar to that of borehole SR29. This may be due to the location of these two boreholes over the same aquifer, as the distance between the two boreholes is 3.47 km. It is possible to predict a similar quantity of water withdrawal from the two boreholes because the same agricultural crops are cultivated within this area.

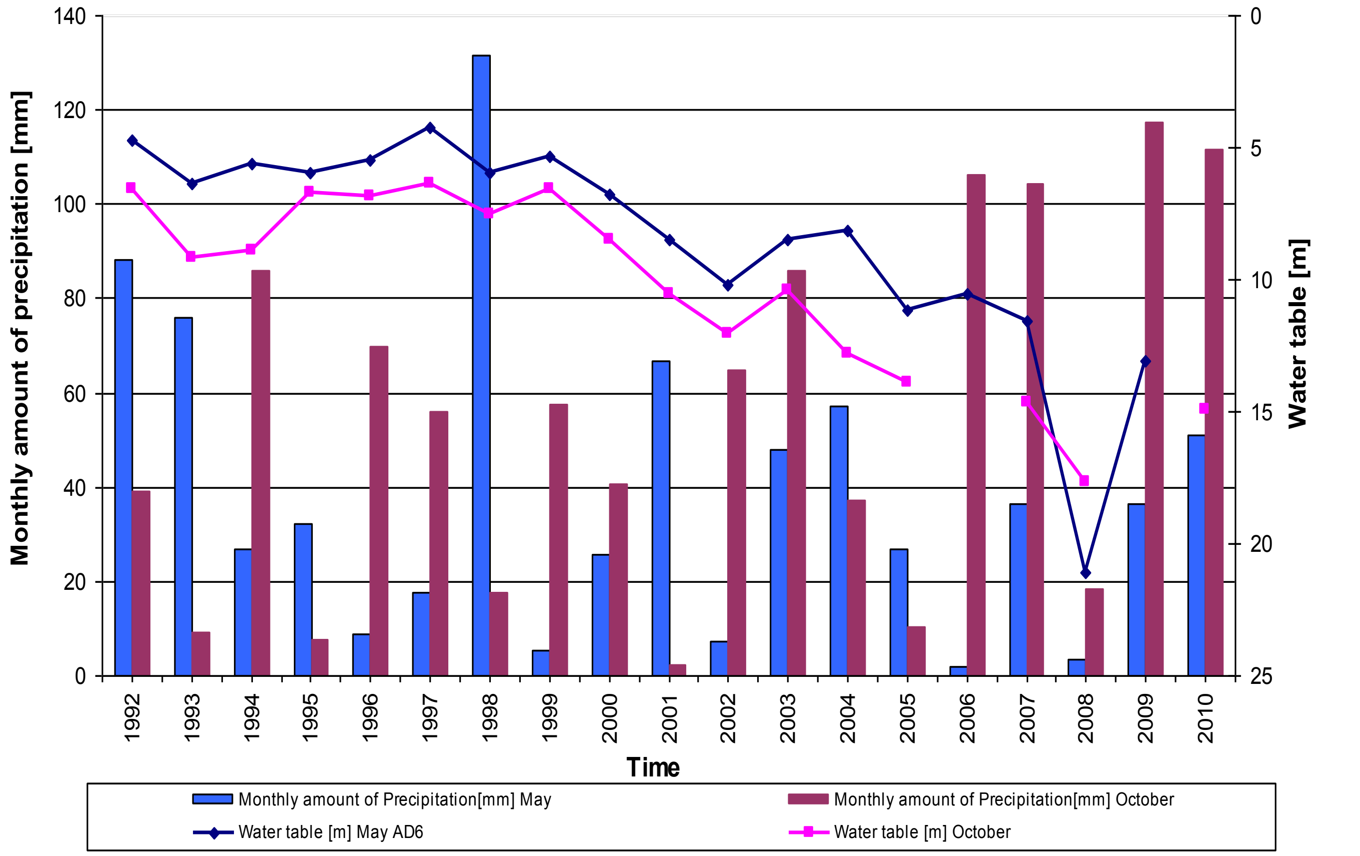

Figure.60 Groundwater level fluctuation in relation to time and monthly accumulation of precipitation during May and October for borehole AD6 during the period 1992–2010

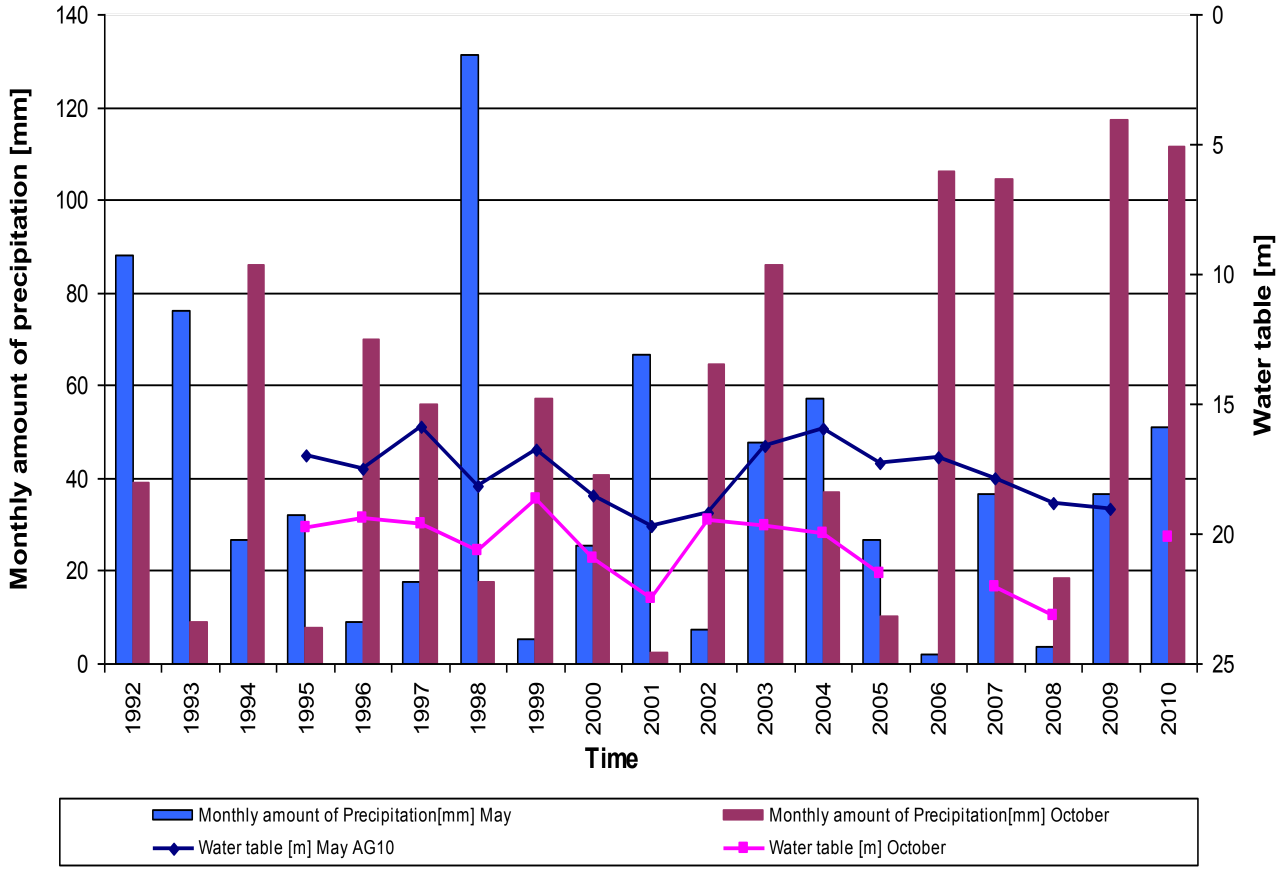

Figure.61 Groundwater level fluctuation in relation to time and monthly accumulation of precipitation during May and October for borehole AG10 during the period 1992–2010

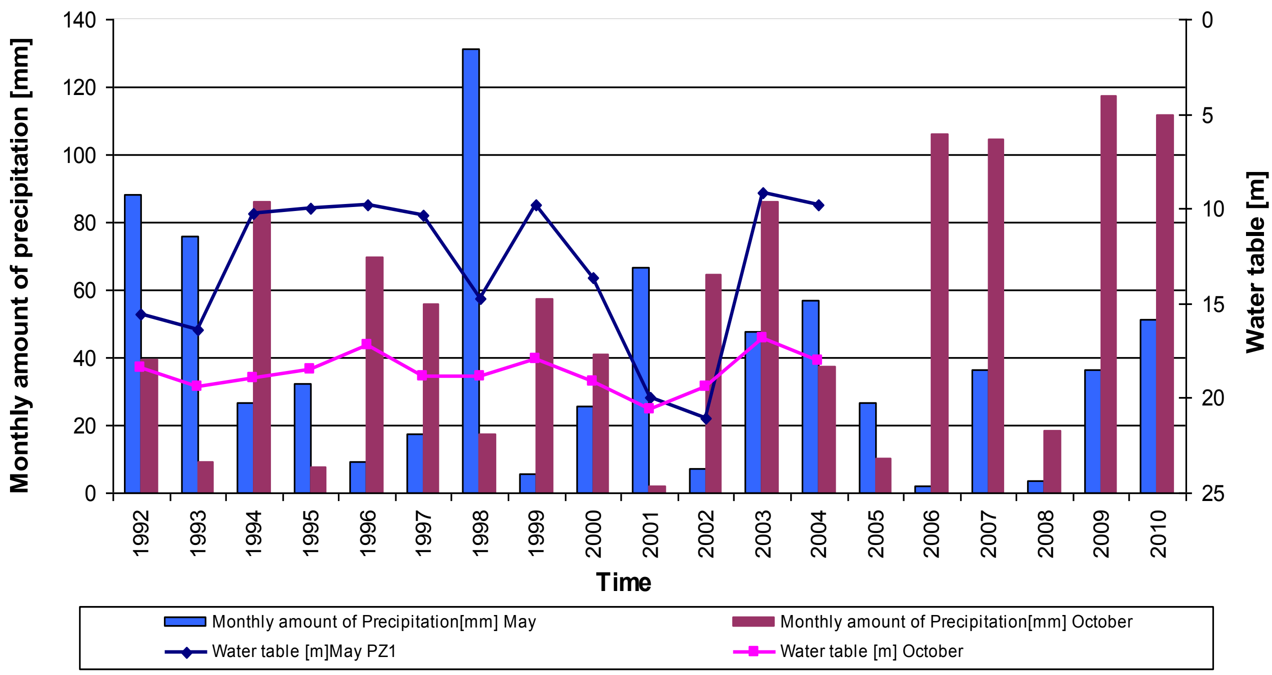

Figure 62. Groundwater level fluctuation in relation to time and monthly accumulation of precipitation during May and October for borehole PZ1 during the period 1992–2010

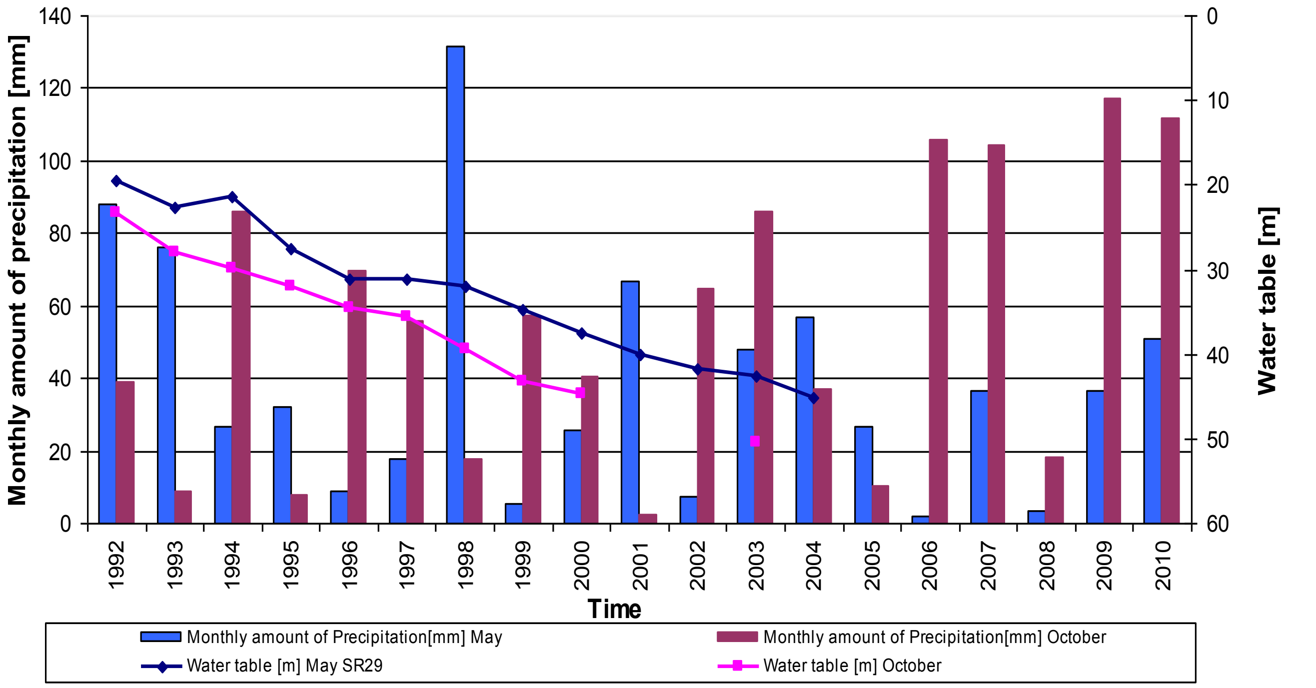

Figure . 63 Groundwater level fluctuation in relation to time and monthly accumulation of precipitation during May and October for borehole SR29 during the period 1992–2010

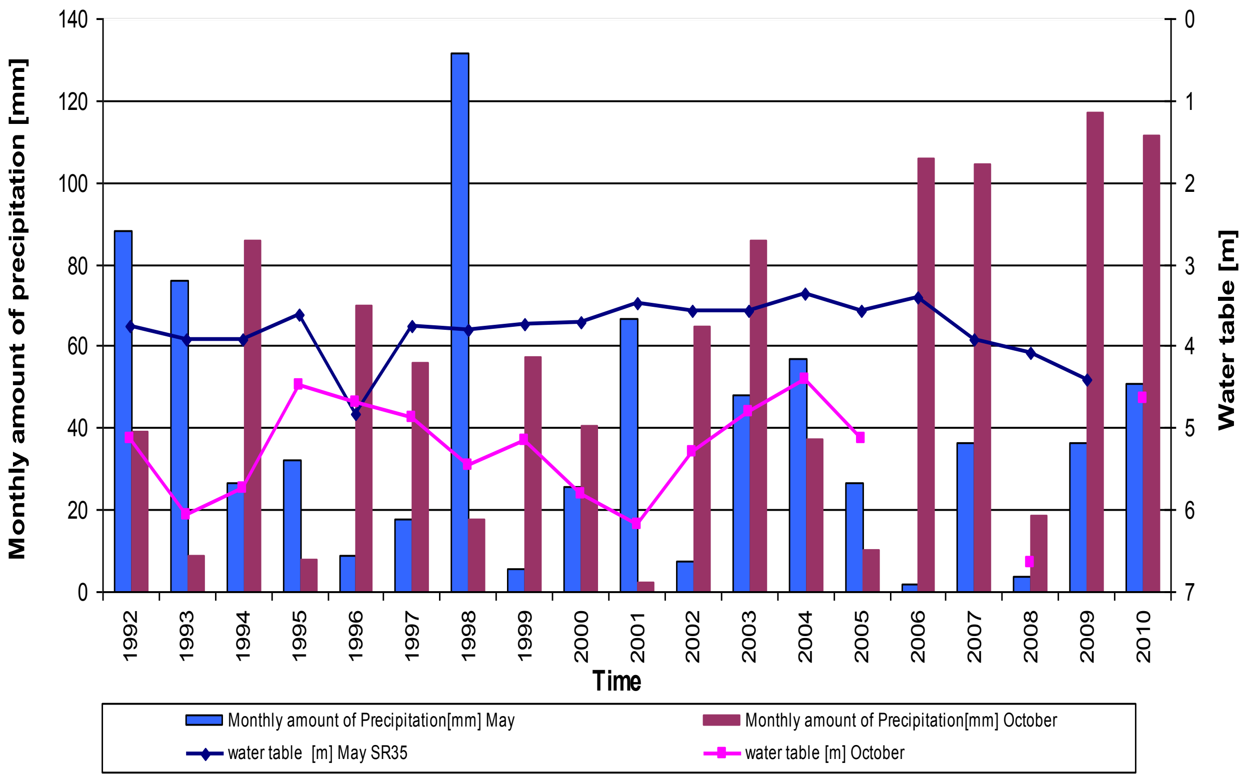

Figure 64. Groundwater level fluctuation in relation to time and monthly accumulation of precipitation during May and October for borehole SR35 during the period 1992–2010

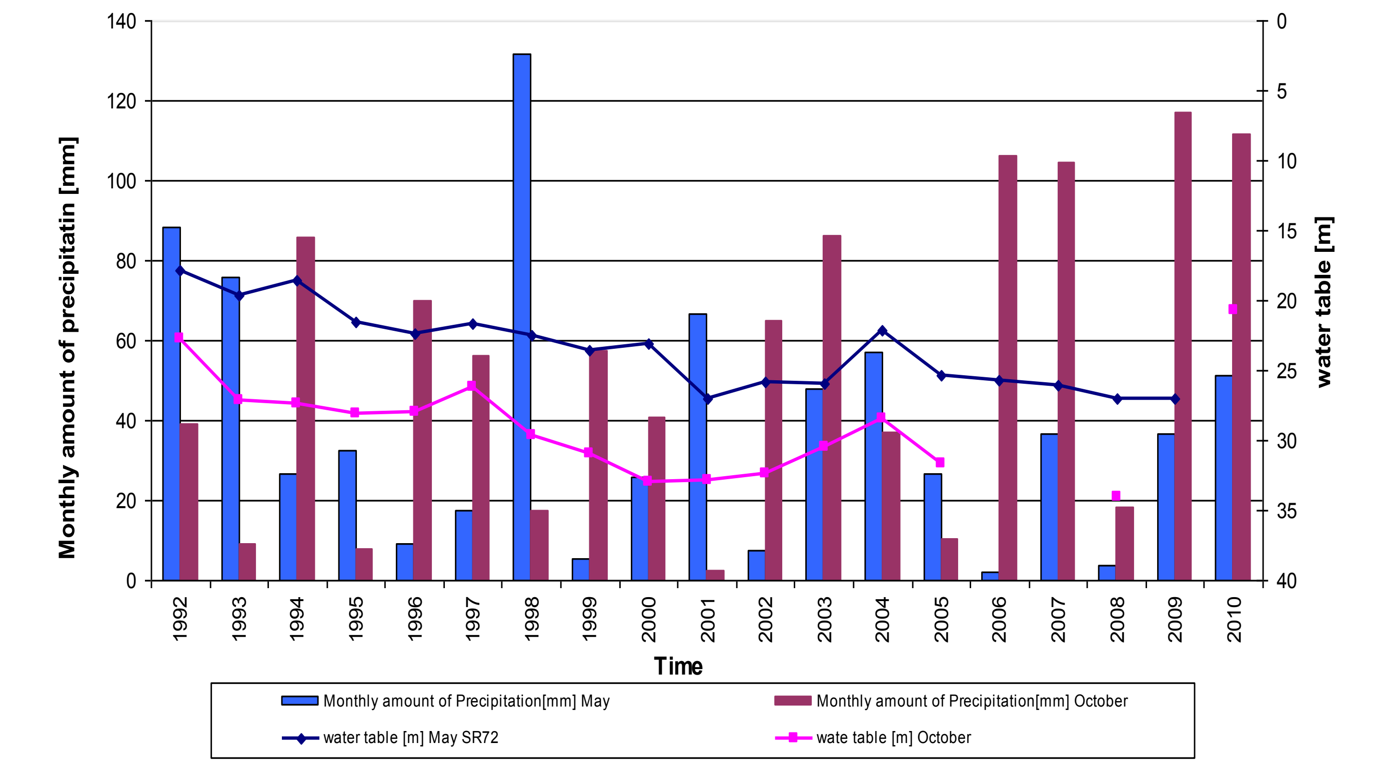

Figure 65. Groundwater level fluctuation in relation to time and monthly accumulation of precipitation during May and October for borehole SR72 during the period 1992–2010

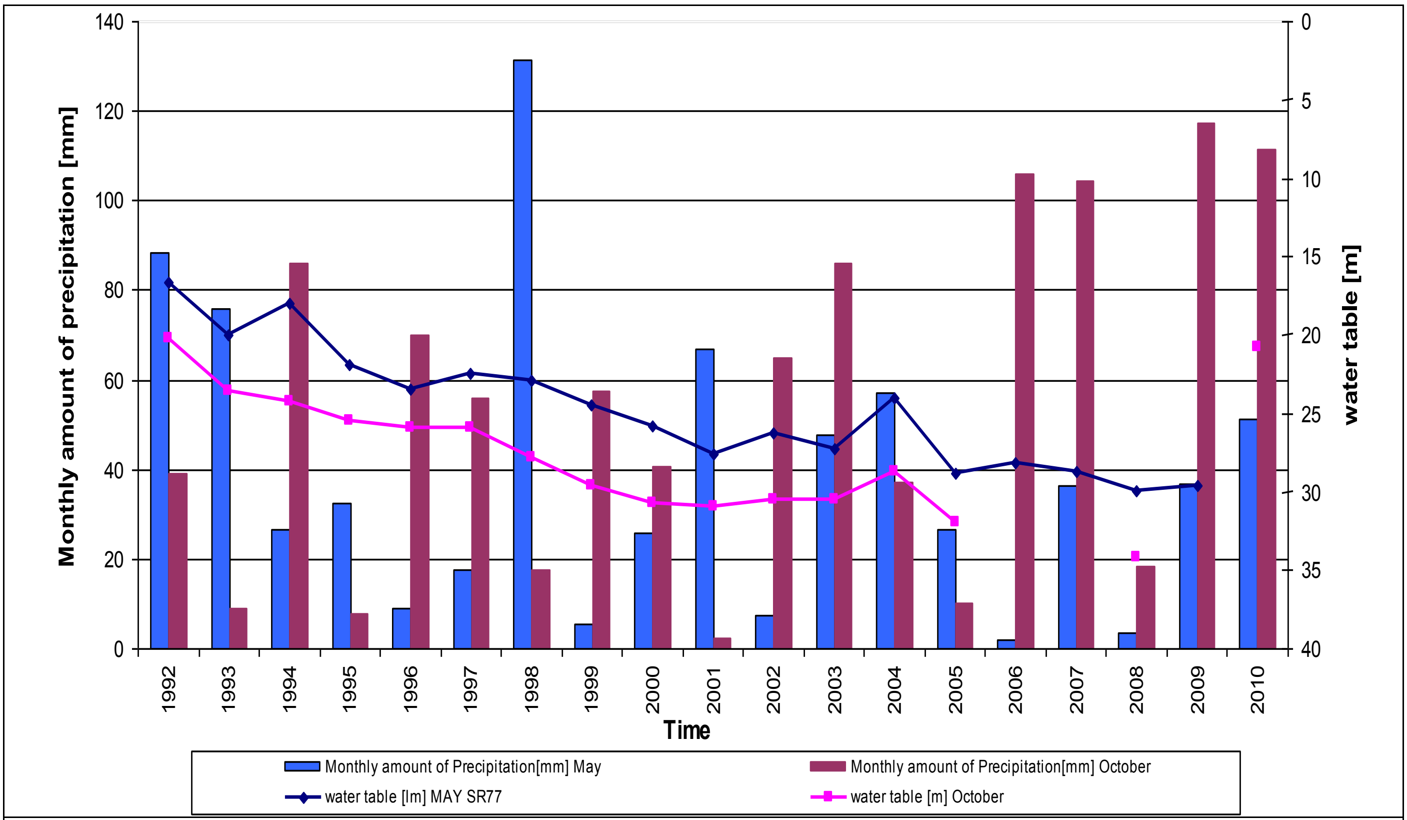

Figure 66. Groundwater level fluctuation in relation to time and monthly accumulation of precipitation during May and October for borehole SR77 during the period 1992–2010

3.6. Land–surface deformation corresponding to the seasonal groundwater fluctuation and monthly accumulation of precipitation

The selection of PSI point candidates representative of each water well (borehole) depended on the availability of signal radar targets around water well sites, taking into account the replication of each selection with three replicates point's candidates, with different distances between the borehole and each point candidate to investigate the statistical correlation between groundwater level fluctuation and ground deformation despite different distances. The information of all following selected points' candidates is depicted in appendix A.

3.7. Ascending track 143

Before explaining the impact of groundwater level fluctuation on land deformation, it is necessary to provide details of the behaviour of the groundwater level and precipitation corresponding to the time series of SAR data within this track.. First of all it is essential to explain the groundwater level behaviour of each borehole and its interference correlation with precipitation, and subsequently the interference between land deformation and the fluctuation of groundwater level, as found by (Herrera et al., 2009) in their study in the metropolitan area of Murcia City (SE Spain). In general, the piezometric level is closely related to annual precipitation, because rain infiltration and irrigation are the most important sources of recharge of the aquifer.

3.7.1. AD6

The groundwater level behaviour corresponding to the monthly accumulation of precipitation, depending on time series data of SAR PSI, is depicted in Table 19 and Figure 67. In general, the groundwater level behaviour during the period 1995–2006 points to a decline, which may be attributable to the lack of compensation of the lost water. The data indicate stability during the period June 1995–May 1997, and a subsequent sharp decline is observed during the period May 1997–August 1998, which may be attributable to the decreasing precipitation, especially during the period of December 1997–August 1998. There is an absence of monitoring data for January 1997, but thereafter stability or a slow decline of groundwater level is observed during period June 1999–April 2003. This may be attributable to the fluctuation in the amount of precipitation. Subsequently, a sharp decline occurred during April 2003–

August 2003, which may be attributable to a decrease in the amount of precipitation. Thereafter a rise in groundwater level is observed as a result of an increase in precipitation during August 2003–April 2004, followed by a sharp decline during the period April 2004–August 2004, which may be attributable to the decreasing amount of precipitation. Subsequently, a rise in the groundwater level is observed during the period August 2004–May 2005. There is a high probability that this rise is due to the increasing amount of precipitation. A sharp decline in groundwater level during the period May 2005–August 2005 is observed, followed by a rise during the period August 2005–December 2006. This rise was accompanied by a decrease in the amount of precipitation and therefore may be attributed to another source supplying groundwater.

Table19. Monthly accumulation of precipitation corresponding to the groundwater level of the borehole AD6

Time series data of SAR PSI	Monthly amount of precipitation (mm)	Groundwater level [m] of borehole AD6
Jun_1995	34.4	5.6
Dec_1995	92.7	5.93
Apr_1996	22.3	4.43
Mar_1997	20.8	4.91
May_1997	17.6	4.24
Dec_1997	67.7	5.65
Aug_1998	0.7	11.96
Jan_1999	45.4	
Jun_1999	5	5.46
Oct_1999	57.4	6.6
May_2000	25.7	6.76
Apr_2003	26.4	6.2
Aug_2003	5.3	12.74
Feb_2004	8.4	8.32
Apr_2004	43.5	8.18
Aug_2004	2.6	16.56
Sep_2004	20.1	14.38
May_2005	26.7	11.18
Aug_2005	16.4	17.39
Dec_2006	11.9	11.5

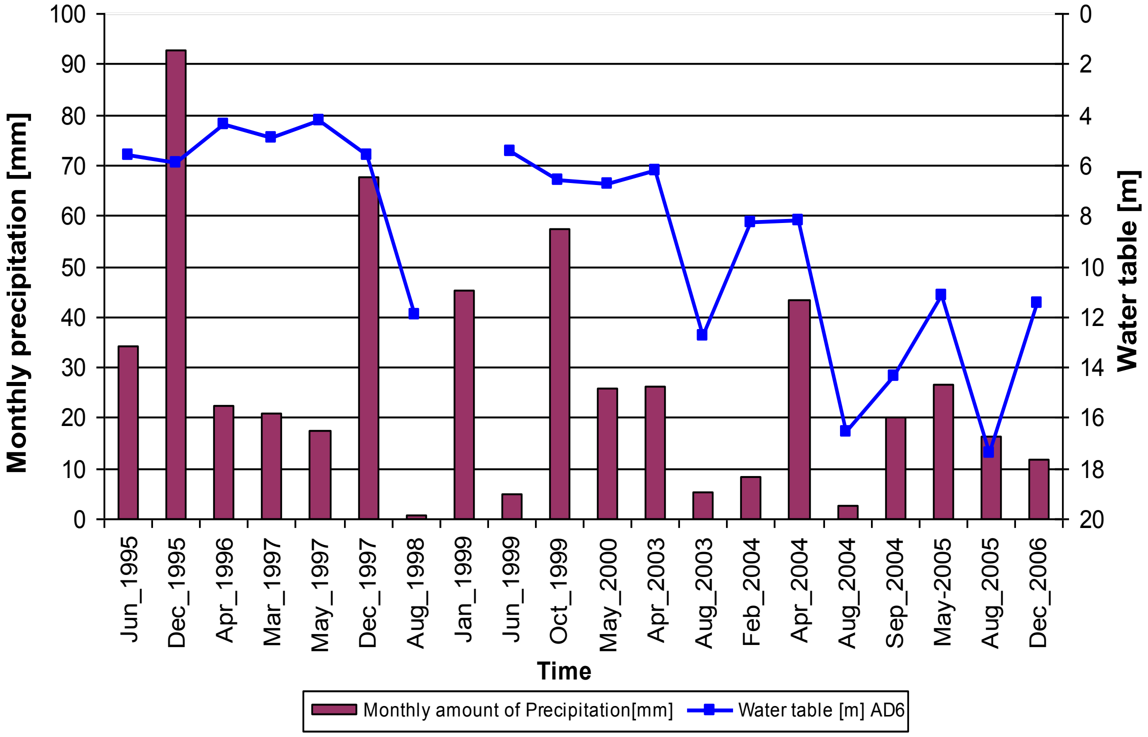

Figure 67. Monthly accumulation of precipitation corresponding to the groundwater level of the borehole AD6

3.7.1.1. Interference between land deformation and monthly precipitation as indirect impact on groundwater level (seasonal deformation) of the borehole AD6

Three point candidates resulting from the PSI technique have been chosen, with different distances between these points and the borehole, as shown in Figure 68, to correlate, identify, and examine the impact of groundwater level fluctuation on land deformation. Deformation of three point candidates at distances of 90, 179 and 219 m from the borehole, monthly precipitation, and groundwater level are shown in Table 20. Deformation of the point candidates corresponding to monthly precipitation is depicted in Figure 69. Deformation of the point candidates corresponding to groundwater level is depicted in Figure 70.

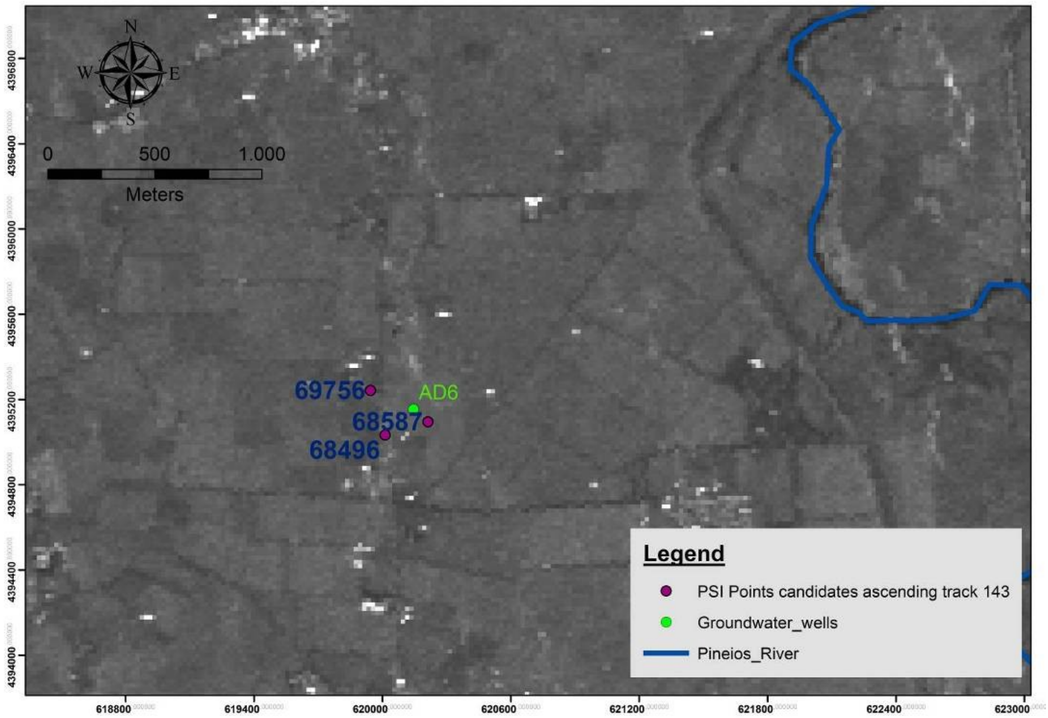

Figure 68. Three point candidates of the PSI with different distances from borehole AD6

Table20. Ground deformation of point candidates of PSI ascending track (143) corresponding to groundwater level and monthly precipitation behaviour of borehole (AD6)

Time series data of SAR PSI	LOS Displacemnt mm p (68587) 90 m	LOS Displacemnt mm p(68496) 179 m	LOS Displacemnt mm p(69756) 219 m	Groundwater level (m) Borehole AD6	Monthly precipitation (mm)
Jun_1995	32.39	-49.126	-100.847	5.6	34.4
Dec_1995	22.467	-42.593	-96.434	5.93	92.7
Apr_1996	26.09	-47.28	-93.127	4.43	22.3
Mar_1997	14.77	-41.625	-87.14	4.91	20.8
May_1997	26.666	-25.741	-82.509	4.24	17.6
Dec_1997	22.386	-34.936	-68.698	5.65	67.7
Aug_1998	24.382	-40.629	-60.376	11.96	0.7
Jan_1999	15.324	-22.307	-59.953		45.4
Jun_1999	5.299	-20.46	-51.634	5.46	5
Oct_1999	16.454	-32.256	-51.344	6.6	57.4
May_2000	7.578	-16.042	-56.279	6.76	25.7
Apr_2003	0.299	-9.977	-15.193	6.2	26.4
Aug_2003	-2.562	-4.718	-7.259	12.74	5.3
Feb_2004	-0.4	-1.903	-10.831	8.32	8.4
Apr_2004	5.812	2.472	-15.168	8.18	43.5
Aug_2004	-6.223	-9.911	-2.619	16.56	2.6
Sep_2004	3.461	1.078	-0.192	14.38	20.1
May_2005	2.237	1.731	7.312	11.18	26.7
Aug_2005	1.9	4.57	12.449	17.39	16.4
Dec_2006	-0.979	15.172	31.2	11.5	11.9

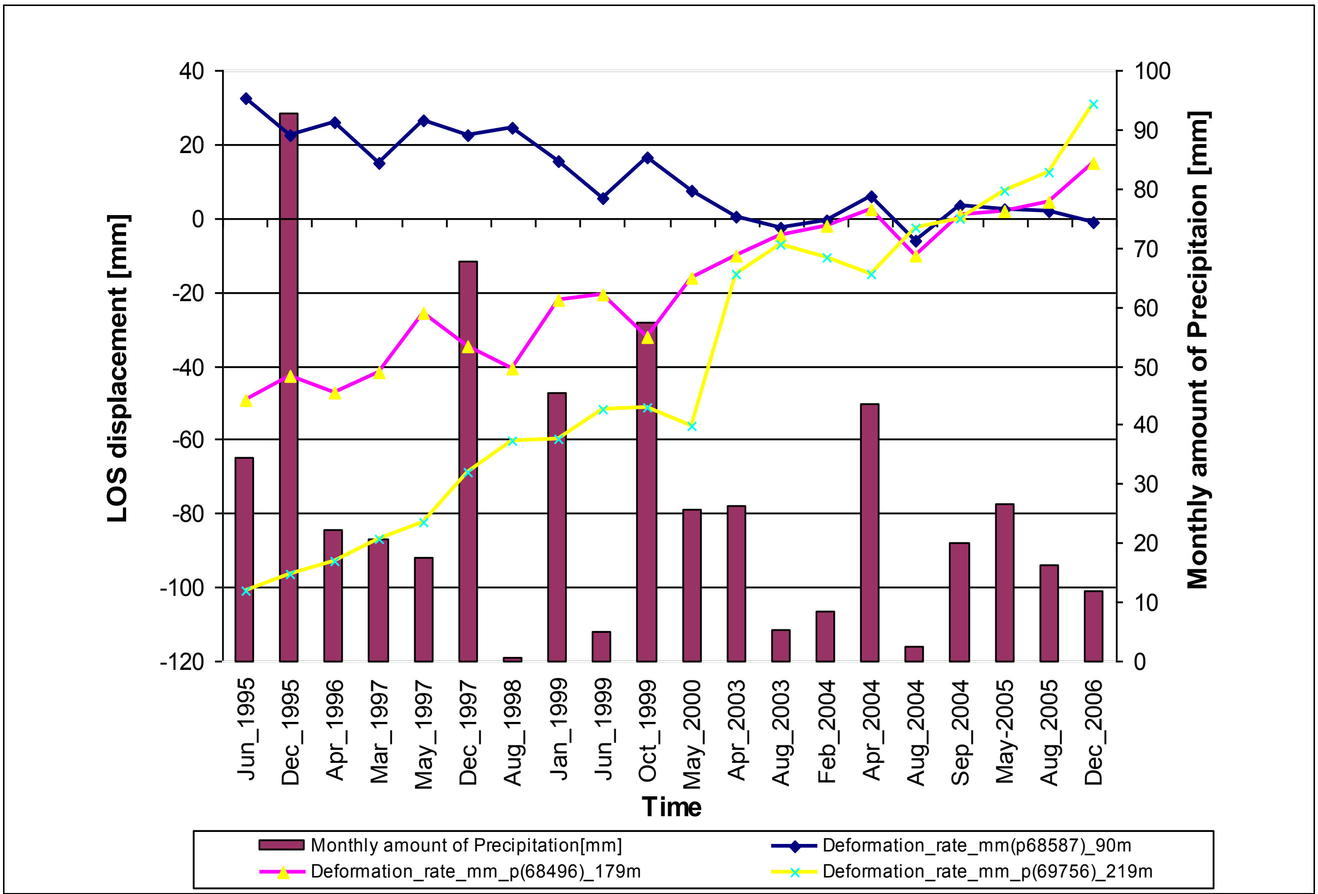

Figure 69. LOS Displacemnt of point candidates of PSI corresponding to monthly precipitation amount. Displacement time series of point candidates are rescaled to the first acquisition (i.e. 28 June 1995).

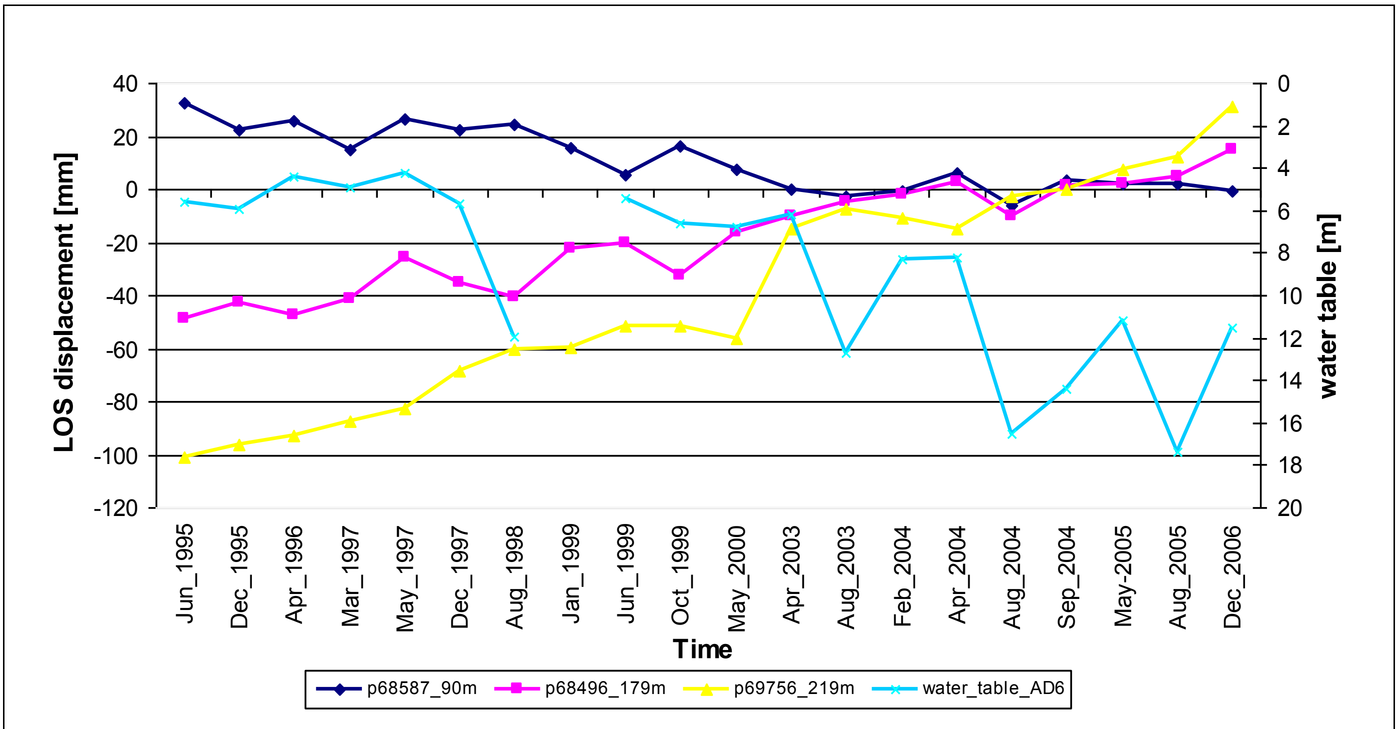

Figure.70 LOS Displacemnt of point candidates corresponding to the groundwater level of borehole AD6. Displacement time series of point candidates are rescaled to the first acquisition (i.e. 28 June 1995).

The deformation behaviour of the first point, number 68587 at 90 m from the borehole, points to a general declining trend, as the time series begins with uplift then goes into subsidence. The minimum uplift was 0.299 mm (April 2003), while the maximum uplift was 32.39 mm (June 1995). The minimum subsidence was -0.4 mm (February 2004), and the maximum subsidence was -6.22 mm (August 2004).

Minimum uplift may be attributable to the indirect impact of the precipitation amount, which was 26.4 mm, and of the groundwater level, which was 6.2 m. The maximum uplift may also be attributable to the indirect impact of the precipitation, which was 34.4 mm, and of the groundwater level, which was 5.6 m, as this amount of precipitation may have raised the groundwater level and consequently caused this uplift.

The minimum subsidence may be attributable to the low amount of precipitation (8.4 mm) and its indirect impact on the groundwater level, which was 8.32 m. Maximum subsidence may be attributable to the indirect impact of the precipitation amount (2.6 mm) on the groundwater level, which was 16.65 m, as this precipitation amount was not sufficient to raise the groundwater level and consequently caused this subsidence.

Details of the impact of groundwater level fluctuation on land deformation indicate that the decrease in uplift during the period June 1995–December 1995 was accompanied by the decline of groundwater level. An increase in uplift is observed during the period December 1995–April 1996, which was accompanied by a rise in groundwater level. This was followed by a decrease in uplift accompanied by a decline in the groundwater level during the period April 1996–March 1997. Thereafter an increase in uplift was accompanied by a rise in groundwater level during the period March 1997–May 1997, and subsequently a decrease in uplift was accompanied by a decline in groundwater level during the period May 1997–December 1997. A decrease in uplift is observed through the decline of groundwater level during the period August 1998–June 1999, followed by a decrease in uplift accompanied by the decline of the groundwater level during the period October 1999–May 2000. Noticeably, the change in status of land deformation from uplift to subsidence was accompanied a sharp trend of decline of groundwater level during the period April 2003–August 2003. Thereafter a contrary status occurred, from subsidence to uplift, during the period August 2003–April 2004, accompanied by a rise in groundwater level. A contrary case occurred once again from uplift to subsidence during the period April 2004–August 2004. This change can, with a considerable probability, be attributed to the sharp trend of decline of the groundwater level.

The deformation behaviour of the second point, number 68496 at a distance of 179 m from the borehole, shows a general rise, as the time series begins with subsidence then goes into uplift. The minimum subsidence was -1.9 mm (February 2004) and the maximum subsidence was -49.126 mm, while the minimum uplift was 1.078 mm (September 2004) and the maximum uplift was 15.172 mm (December 2006). The minimum subsidence may be attributable to the indirect influence of the precipitation, which was 8.4 mm, through its impact on the groundwater level, which was 8.32 m, as this precipitation amount was not enough to raise the groundwater level. The maximum subsidence, with considerable probability, is not attributed to the indirect impact of the precipitation on the groundwater level despite the evident correlation between the precipitation (34.4 mm) and the high groundwater level (5.6 m). Consequently there is an expectation that another parameter or factor caused this subsidence.

The minimum uplift may be attributable to the indirect impact of the precipitation, which was 20.1 mm, on land deformation through its impact on the groundwater level, which was 14.38 m, while the maximum uplift may also be attributable to the indirect impact of the precipitation, which was 11.9 mm, through its impact on the groundwater level, which was 11.5 m, despite the fact that the higher amount of precipitation was accompanied by the minimum uplift and the lower precipitation amount was accompanied by the maximum uplift. This low amount of precipitation may have been complementary to the amount of water already within the aquifer and may consequently have caused this uplift.

Details of the impact of groundwater level fluctuation on land deformation indicate that there are many correlations. A decrease in subsidence was accompanied the decline of groundwater level during the period March 1997–May 1997, followed by an increase in subsidence, which was accompanied by the decline of groundwater level, during the periods May 1997–August 1998 and June 1999–October 1999. An increase in subsidence is observed during the period May 2000–April 2003, which was accompanied by the decline of groundwater level. Additionally, a status change from uplift to subsidence accompanied the sharp declining trend of groundwater level observed during the period April 2004–August 2004, followed by a contrary status change from subsidence to uplift through the raising of groundwater level during the period August 2004–May 2005. Moreover an increase in uplift was observed through the raising of the groundwater level during the period August 2005–December 2006.

The deformation behaviour of the third point, number 69756at a distance of 219 m from the borehole, shows a general rising trend, as the time series begins with subsidence and then goes to uplift. The minimum subsidence was -0.192 mm (September 2004) and the maximum subsidence was -100.847 (June 1995), while the minimum uplift was 7.312 mm and the maximum was 31.2 mm (December 2006).

The minimum subsidence may be attributable to the indirect impact of the precipitation amount (20.1 mm) through its impact on the groundwater level (14.38 m), as this amount of precipitation was not enough to increase the groundwater level. Consequently, a large decline in groundwater level occurred, leading to this subsidence. There is a high probability that the maximum subsidence is not attributable to the indirect impact of the precipitation, which was 34.4 mm, on the groundwater level, which was 5.6 m, because this level is quite close to the surface and should therefore correspond to a smaller value of either subsidence or uplift. Therefore, some other factor has caused this subsidence. Additionally minimum and maximum uplift may not be attributable to the indirect impact of the precipitation on the groundwater level, because despite the different between the precipitation that accompanied the minimum and maximum uplift (26.7 mm and 11.9 mm, respectively), the groundwater levels for these two cases were convergent (11.8 m and 11.50 m). Consequently this uplift may be due to the impact of some other factor or parameter. There is no continuous significant correlation between deformation of this PSI point and groundwater level fluctuation for the borehole AD6. This may be attributable to the short time series (1995–2006). However, some correlations have been observed. A decrease in subsidence accompanied the rise in the groundwater level during the periods December 1995–April 1996 and March 1997–May 1997, and an increase in subsidence accompanied the decline of the groundwater level during the period October 1999–May 2000. This was followed by a decrease in subsidence through raising of the groundwater level during the period May 2000–April 2003. A status change from subsidence to uplift correlates with the rising groundwater level during the period August 2004 – May 2005, while an increase in uplift during the period August 2005 – December 2006 accompanied the rising groundwater level.

3.7.2. AG10

Groundwater level behaviour corresponding to the monthly accumulation of precipitation based on the time series data of SAR PSI is depicted in Table 21 and Figure 71. The general behaviour of the groundwater level during the time series 1995–2006 points to a decline, which may be attributable to the lack of compensation for the lost water. The data indicate a slow decline during the period April 1996–May 1997 and a subsequent sharp decline during the period May 1997–August 1998, which may be attributable to the decrease in precipitation, especially during the period December 1997–August 1998. Note the absence of monitoring data for January 1997. Stability or a slow decline followed by a rising of the groundwater level was observed during the period June 1999–May 2000, and subsequently a sharp rise occurred during May 2000–April 2003. Thereafter a sharp declining trend was observed due to decreasing precipitation during the period April 2003– August 2003, followed by a sharp rising trend during the period August 2003–April 2004 which accompanied increasing precipitation. Afterwards, a decline in the groundwater level is observed during the period April 2004–August 2004, and it is evident that this decline may be attributed with a high probability to the decrease in precipitation. The rising of the groundwater level during the period August 2004–May 2005 was accompanied by increasing precipitation and was followed by a decline of the groundwater level during the period May 2005–August 2005 and a rising of the groundwater level during August 2005–December 2006. This decline of the groundwater accompanied decreasing precipitation, while the rising of the groundwater is not, with high probability, attributable to the amount of precipitation, because it accompanied a decreasing amount of precipitation.

Table21. Monthly accumulation of precipitation corresponding to the groundwater level of the borehole AG10

Time series data of SAR PSI	Monthly amount of precipitation (mm)	Groundwater level [m] of borehole AG10
Jun_1995	34.4	
Dec_1995	92.7	17.97
Apr_1996	22.3	15.47
Mar_1997	20.8	15.76
May_1997	17.6	15.86
Dec_1997	67.7	18
Aug_1998	0.7	23.02
Jan_1999	45.40	
Jun_1999	5.00	18.04
Oct_1999	57.40	18.7
May_2000	25.70	18.55
Apr_2003	26.40	15.14
Aug_2003	5.30	21.39
Feb_2004	8.40	16.45
Apr_2004	43.50	15.87
Aug_2004	2.60	21.78
Sep_2004	20.10	21.17
May_2005	26.70	17.28
Aug_2005	16.40	23.08
Dec_2006	11.90	18.63

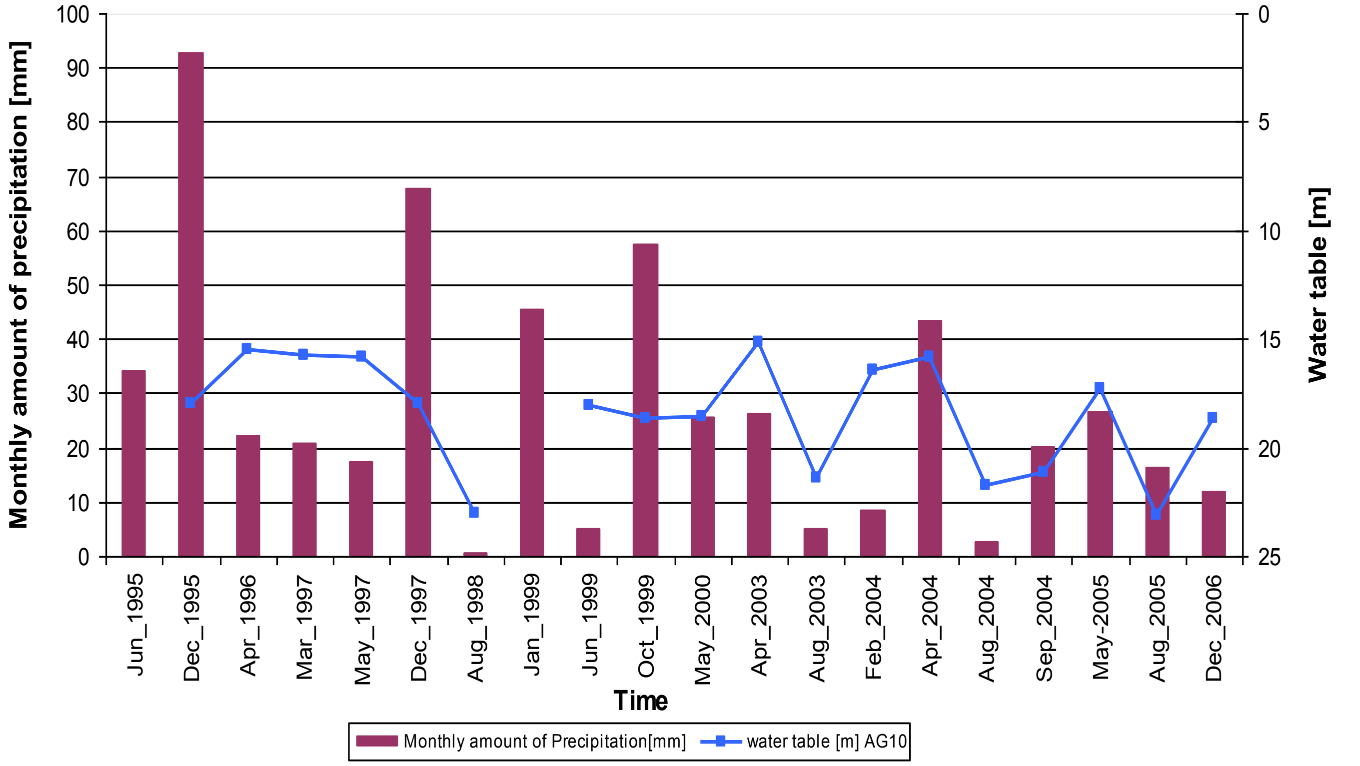

Figure 71. Monthly accumulation of precipitation corresponding to the groundwater level of the borehole AG10

3.7.2.1. Interference between land deformation and monthly precipitation as indirect impact on groundwater level (seasonal deformation) of the borehole AG10

Three point candidates resulting from the PSI technique have been chosen, with different distances between these points and the borehole, as shown in Figure 72, to correlate, identify and examine the impact of groundwater level fluctuation on land deformation. Deformation of three point candidates at distances of 178, 248 and 320 m from the borehole, monthly precipitation, and groundwater level are shown in Table 22. Deformation of the point candidates and monthly precipitation amount are depicted in Figure 73. Deformation of the point candidates and groundwater level are depicted in Figure 74.

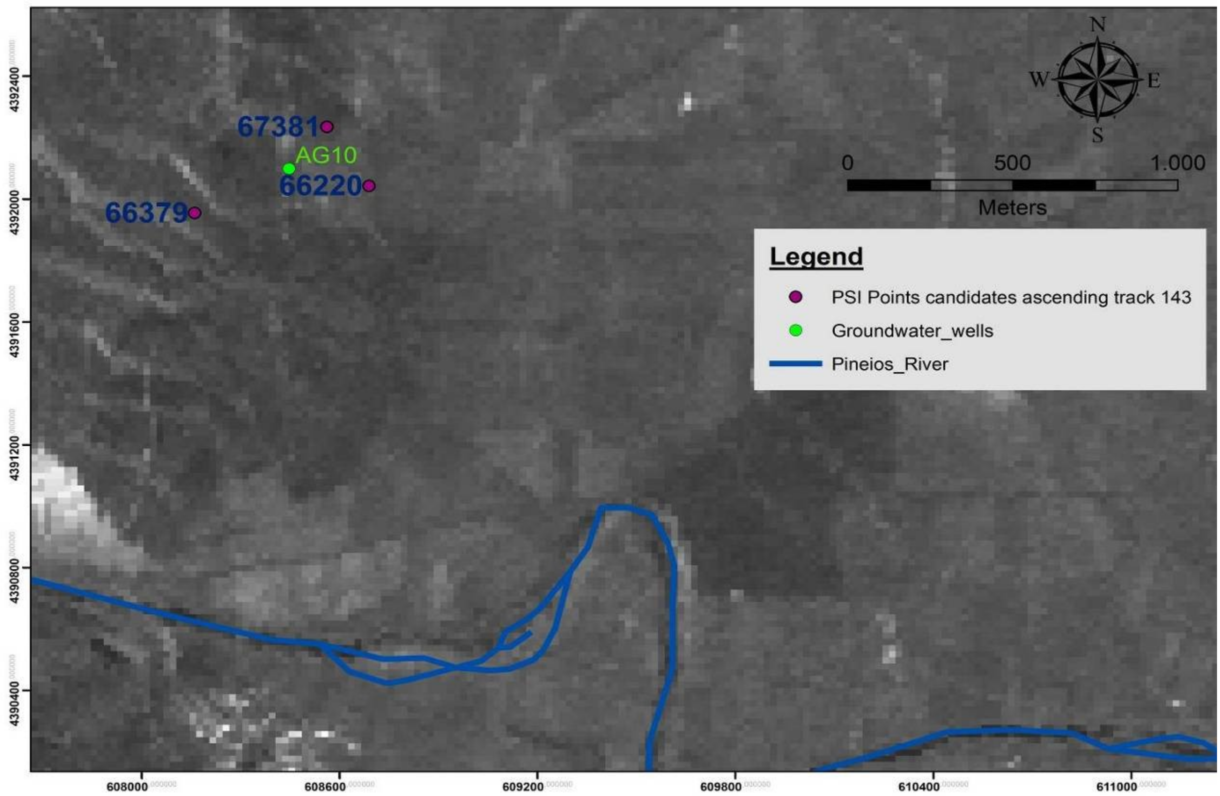

Figure72. Three point candidates of the PSI at different distances from borehole AG10

Table 22. Ground deformation of point candidates of PSI ascending track (143) corresponding to groundwater level and monthly precipitation for borehole AG10

Time series data of SAR PSI	LOS Displacemnt mm p (67381) 178.1 m	LOS Displacemnt mm p (66220) 248.39 m	LOS Displacemnt mm p (66379) 320.2 m	Groundwater level (m) borehole AG10	Monthly amount of precipitation (mm)
Jun_1995	-20.713	123.236	100.657		34.4
Dec_1995	-18.104	119.863	97.893	17.97	92.7
Apr_1996	-14.276	110.542	96.711	15.47	22.3
Mar_1997	-15.32	96.475	70.941	15.76	20.8
May_1997	-16.673	88.301	70.301	15.86	17.6
Dec_1997	-22.081	92.592	64.228	18	67.7
Aug_1998	-15.081	81.82	67.048	23.02	0.7
Jan_1999	-19.226	78.426	64.786		45.4
Jun_1999	-21.506	70.715	66.276	18.04	5
Oct_1999	-4.12	53.34	53.232	18.7	57.4
May_2000	-18.372	52.889	51.931	18.55	25.7
Apr_2003	3.535	22.725	14.098	15.14	26.4
Aug_2003	0.567	4.153	21.494	21.39	5.3
Feb_2004	-5.776	4.044	6.306	16.45	8.4
Apr_2004	-2.021	5.268	1.625	15.87	43.5
Aug_2004	-3.255	0.988	3.402	21.78	2.6
Sep_2004	-2.852	1.9	-0.476	21.17	20.1
May_2005	7.321	-8.954	-10.238	17.28	26.7
Aug_2005	2.72	0.256	-15.031	23.08	16.4
Dec_2006	3.596	-32.033	-26.546	18.63	11.9

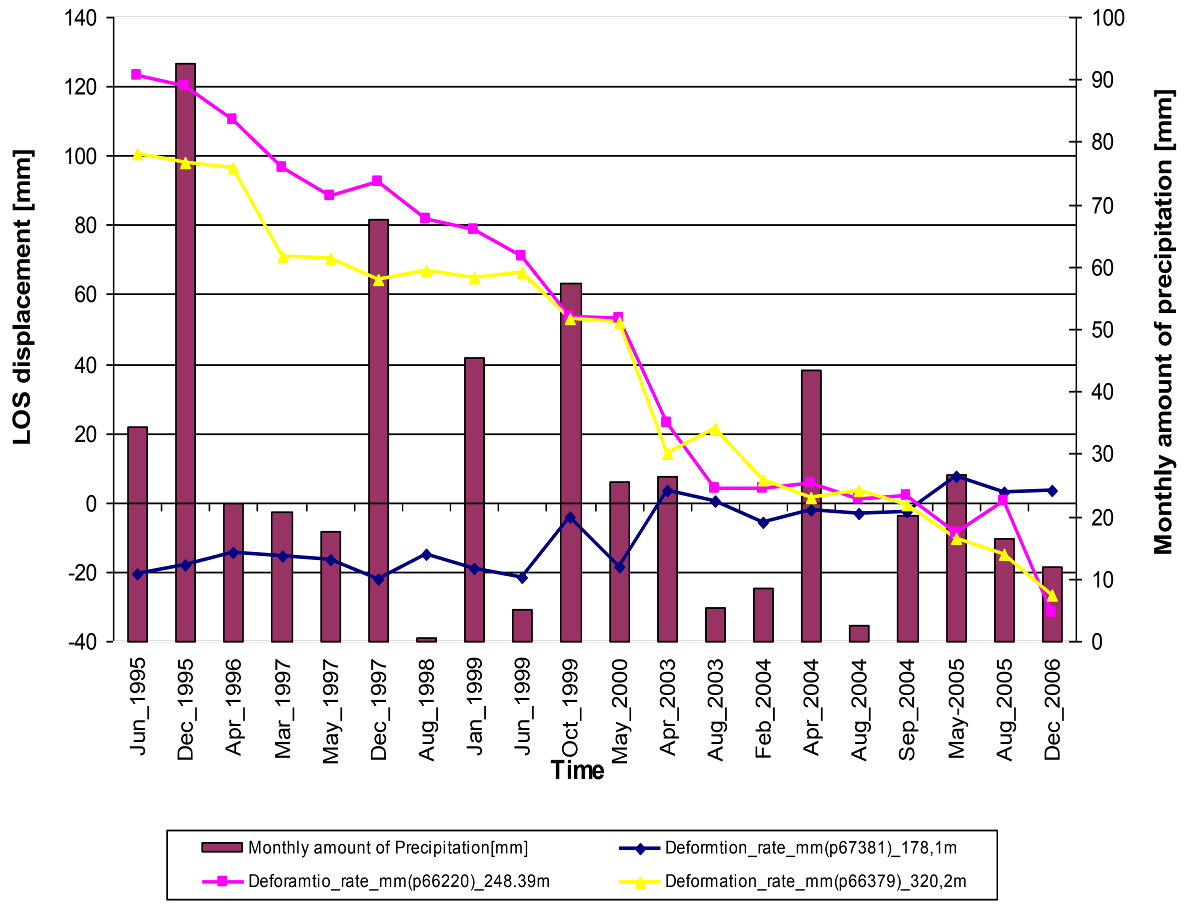

Figure 73. LOS Displacemnt of point candidates of PSI corresponding to monthly precipitation. Displacement time series of point candidates are rescaled to the first acquisition (i.e. 28 June 1995).

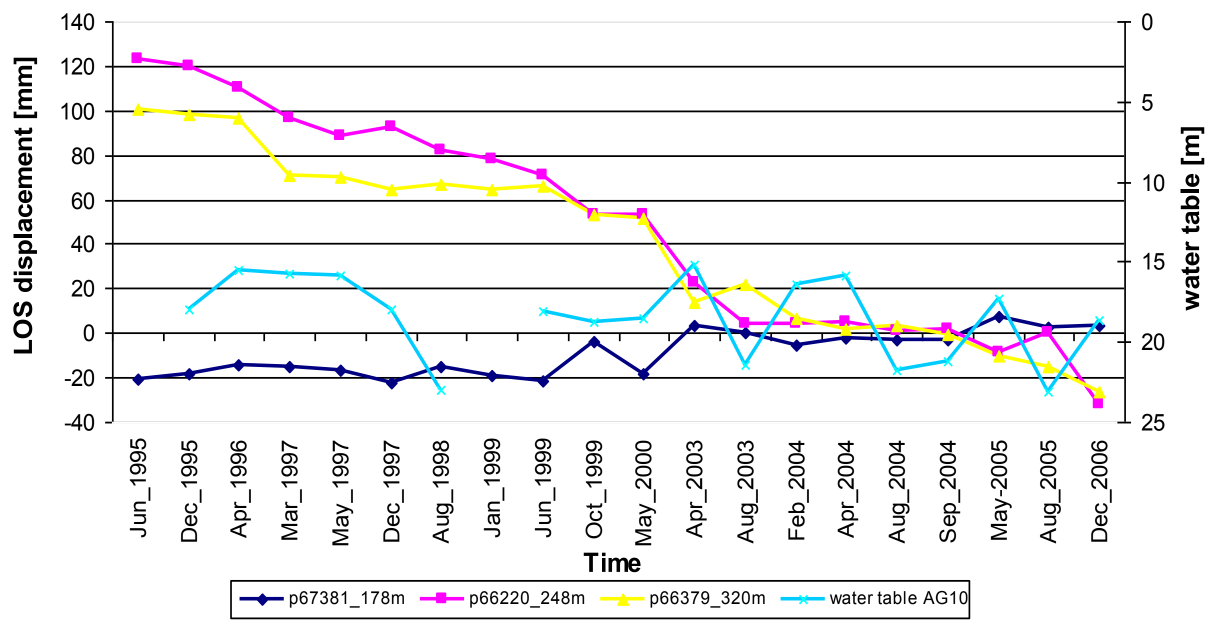

Figure 74. LOS Displacemnt of point candidates corresponding to groundwater level of borehole AG10. Displacement time series of point candidates are rescaled to the first acquisition (i.e. 28 June 1995).

The deformation behaviour of the first point (number 67381), at a distance of 178 m from the borehole, indicates a general rising trend, as the time series begins with subsidence then goes to uplift. The minimum subsidence was -2.02 mm (April 2004) and the maximum subsidence was -22.08 mm (December 1997), while the minimum uplift was 0.567 mm (August 2003) and the maximum uplift was 7.321 mm (May 2005).

The minimum subsidence may be attributable to the impact of the groundwater level; however there may have been an indirect influence of precipitation on the land deformation (subsidence) through its impact on groundwater level. The amount of precipitation was 43.50 mm and may have been enough to recharge the aquifer and raise the groundwater level to more than 15.78 m, which was found during this month. Nevertheless, an overexploitation of groundwater may have prevented the precipitation from elevating the groundwater level sufficiently to decrease the subsidence. The maximum subsidence may be attributable to the low level of groundwater, which was 18 m. Although the precipitation amount was 67.7 mm, it may not have had any indirect impact on the land deformation through its impact on the groundwater level, because it may have been sufficient to raise the groundwater level and consequently reduce the subsidence to a value lower than that found.

Minimum uplift may have been triggered by the indirect influence of precipitation on the groundwater level. The precipitation amount (5.30 mm) was not sufficient to raise the groundwater level, which was 21.39 m, and consequently there was low uplift. Furthermore, the maximum uplift may be attributable to the indirect impact of the precipitation (26.70 mm) on land deformation by raising the groundwater level, which was 17.28 m.

Details of the impact of the groundwater level on the land deformation indicate that decreasing subsidence accompanied the raising of the groundwater level during the period December 1995–April 1996, followed by increasing subsidence as a result of the decline of the groundwater level during the periods April 1996–March 1997 and March 1997–May 1997. Thereafter a sharp increasing trend of subsidence accompanied the sharp declining trend of groundwater during the period May 1997–December 1997. Additionally, a status change from subsidence to uplift is observed as a result of the rising groundwater level during the period May 2000–April 2003. A subsequent decrease in uplift accompanied the decline of the groundwater level during the period April 2003–August 2003, while a decrease in subsidence accompanied the rising groundwater level during the period February 2004–April 2004. Subsequently, an increase of subsidence accompanied the sharp decline of groundwater level during the period April 2004–August 2004, followed by a decrease in subsidence that accompanied the rising groundwater level during the period August 2004–September 2004. Thereafter a status change from subsidence to uplift is observed once again as a result of the rising groundwater level during the period September 2004–May 2005. A subsequent decrease in uplift accompanied the decline of groundwater level during the period May 2005–August 2005, and finally an increase in uplift is observed as a result of the rising groundwater level during the period August 2005–December 2006.

The deformation behaviour of the second point (number 66220), at a distance of 248 m from the borehole, indicates a general decline, as the time series begins with uplift and then goes into subsidence. The minimum uplift was 0.256 mm (August 2005), whereas the maximum uplift was 123.236 mm (June 1995); the minimum subsidence was -8.954 mm (May 2005), and the maximum subsidence was -32.033 mm (December 2006).

The minimum uplift may be attributable to the indirect impact of the precipitation (16.40 mm) on the groundwater level, which was 23.08 m. The precipitation may have been insufficient to raise the groundwater level and consequently cause this uplift. The maximum uplift accompanied precipitation of 34.4 mm which may have raised the groundwater level and consequently caused maximum uplift; however, this is an expectation because no monitoring data for groundwater level have been recorded during this month.

The minimum subsidence may be attributable to the indirect impact of the precipitation (26.70 mm), as this amount may have been enough to raise the groundwater to 17.28 m and reduce the subsidence accordingly. The maximum subsidence may also be attributable to the indirect impact of precipitation (11.90 mm), as this amount may not be enough to raise the groundwater level to 18.63 m, and consequently the decline of the groundwater level caused this subsidence.

Details of the impact of the groundwater level on land deformation indicate that the decrease in uplift accompanied the decline of the groundwater level during the periods April 1996–March 1997, March 1997–May 1997, December 1997–August 1998 and January 1999–June 1999. Many similar significant correlations are observed. The decrease in uplift accompanied the decline of the groundwater level during the period April 2003–August 2003, followed by a slow increase of uplift as the groundwater level rose during August 2003–April 2004. Subsequently, there was a decrease in uplift with the decline of the groundwater level during the period April 2004–August 2004, and thereafter a small increase in uplift is observed with rising groundwater level during the period August 2004–September 2004.

The deformation behaviour of the third point (number 66379), at a distance of 320 m from the borehole, indicates a general decline, as the time series begins with uplift and then goes into subsidence. The minimum uplift was 1.625 mm (April 2004), while the maximum uplift was 100.657 mm (June 1995). The minimum subsidence was -0.467 mm (September 2004), and the maximum subsidence was -26.546 mm (December 2006).

The minimum uplift may be attributable to the indirect impact of the precipitation, which was 43.50 mm, on the land deformation through its impact on the groundwater level, which was 15.87 m, as the precipitation may have raised the groundwater level and consequently caused this uplift. The basis for this reasoning is that the maximum uplift accompanied precipitation of 34.4 mm, and this amount, when added to the water already existing within the aquifer, may have been sufficient to raise the groundwater level and consequently cause uplift. However, this is an expectation only, because no monitoring data were recorded for groundwater level during this month. On the other hand, maybe other factors participated to affect this uplift. The acceptable reasoning being that the precipitation amount that accompanied the minimum uplift was larger than the precipitation amount that accompanied the maximum uplift.

While the minimum subsidence may also be attributable to the indirect impact of the precipitation amount, which was 20.10 mm, on the land deformation through its impact on the groundwater level, which was 21.17 m, this precipitation amount may not have been enough to raise the groundwater level and therefore the subsidence may have been caused by a decline of the groundwater level. The basis for this reasoning is that the maximum subsidence had accompanied a monthly precipitation of 11.90 mm, which may not have been enough to raise the groundwater level, which was 18.63 m, and consequently caused this subsidence. However, maybe some other factor has caused this subsidence, because the low groundwater level was accompanied by the minimum subsidence, while the high groundwater level was accompanied by the maximum subsidence.

Details of the impact of the groundwater level on land deformation indicate that there is no continuous significant correlation between groundwater level and land deformation. This may be attributable to the synchronization of the short data of the time series 1995–2006 as well as the long distance between the borehole and the point candidate of the PSI. However, there are some cases of correlation within time series: the decrease in uplift during the periods April 1996–May 1997 and June 1999–October 1999 accompanied declines in the groundwater level.

3.7.3. PZ1

Groundwater level behaviour corresponding to the monthly accumulation of precipitation based on time series data of SAR PSI is depicted in Table 23 and Figure 75. The general behaviour of the groundwater level points to continuous fluctuation, culminating in a decline at the end of the time series. The first behaviour may be attributable to the impact of fluctuation in the amount of monthly precipitation, while the decline may be attributable to the lack of compensation for the water lost during the period August 2004–September 2004 despite the increasing monthly precipitation. Note the absence of data monitoring records for groundwater level for June 1995, January 1995, and the period May 2005–December 2006. Details of the behaviour indicate rising groundwater levels during the period December 1995–April 1996, which was accompanied by a decreasing amount of precipitation. Therefore this rising level is, with high probability, attributable to another supplying source of water. A decline in the groundwater level is observed during the period April 1996–March 1997, and this may be attributable to decreasing precipitation. A subsequent rise in the groundwater level during the period March 1997–May 1997 is observed, despite the decrease in precipitation; accordingly, the rising groundwater level may be attributable to another water source. Thereafter a decline in the groundwater level accompanied increasing precipitation during the period May 1997–December 1997, and this may be attributable to an insufficient amount of precipitation to compensate for water withdrawal. Subsequent rising groundwater level and decreasing precipitation during the period December 1997–August 1998 is observed, which indicates that it was supplied from a source other than precipitation during this period. On the other hand, maybe this negative correlation between groundwater level and precipitation is attributable to the gap in the data between the two periods. A decline of the groundwater level is observed along with increasing precipitation during the period June 1999–October 1999, which is a further indication that another source is supplying the aquifer. Thereafter a rise in groundwater level along with an increase in precipitation is observed during the period May 2000–April 2003, and subsequently a decline and rise of groundwater level is observed during the periods April 2003–August 2003 and August 2003–April 2004, respectively. This fluctuation of decline and rise may be attributable to the decreasing and increasing precipitation amounts. A decline in the groundwater level during the period April 2004–August 2004 may be attributable to decreasing precipitation. The decline at the end of the time series accompanies increasing precipitation during the period August 2004–September 2004, which may be attributable to an insufficient amount of precipitation to recharge the aquifer after water withdrawal.

Table 23. Monthly accumulation of precipitation corresponding to the groundwater level of the borehole PZ1

Time series data of SAR PSI	Monthly amount of precipitation (mm)	Groundwater level (m) Borehole PZ1
Jun_1995	34.4	
Dec_1995	92.7	18.41
Apr_1996	22.3	9.55
Mar_1997	20.8	12.03
May_1997	17.6	10.33
Dec_1997	67.7	19.12
Aug_1998	0.7	17.4
Jan_1999	45.4	
Jun_1999	5	9.8
Oct_1999	57.4	17.98
May_2000	25.7	13.68
Apr_2003	26.4	9.3
Aug_2003	5.3	13.93
Feb_2004	8.4	13.25
Apr_2004	43.5	10.68
Aug_2004	2.6	16.95
Sep_2004	20.1	17.32
May_2005	26.7	
Aug_2005	16.4	
Dec_2006	11.9	

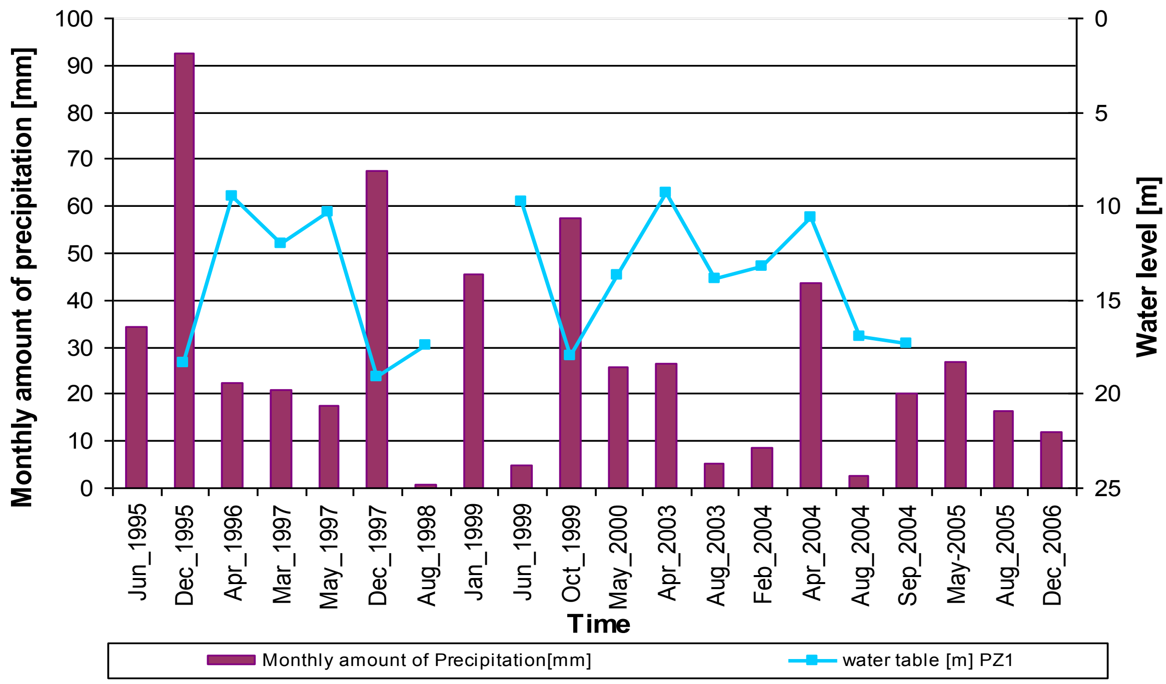

Figure 75. Monthly accumulation of precipitation corresponding to the groundwater level of the borehole PZ1

3.7.3.1. Interference between land deformation and monthly precipitation as indirect impact on groundwater level (seasonal deformation) of the borehole PZ1

Three point candidates resulting from the PSI technique have been chosen at different distances from the borehole, as shown in Figure 76, to correlate, identify and examine the impact of groundwater level fluctuation on land deformation. Deformation of three point candidates at distances of 50, 98 and 142 m from the borehole, monthly precipitation, and groundwater level are shown in Table 24. Deformation of point candidates and monthly precipitation are depicted in Figure 77. Deformation of point candidates and groundwater level are depicted in Figure 78.

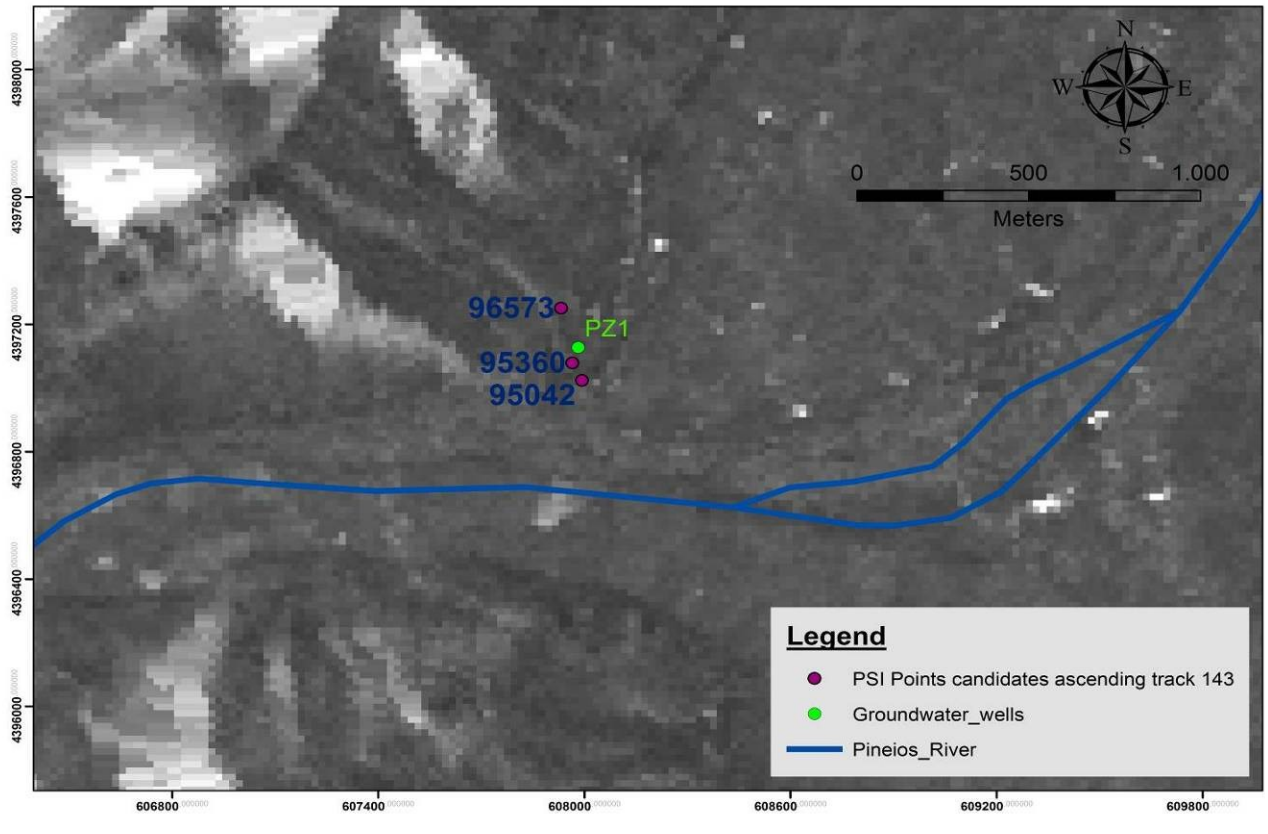

Figure .76 Three point candidates of the PSI at different distances from borehole PZ1

Table 24. Ground deformation of point candidates of PSI ascending track (143) corresponding to groundwater level and monthly precipitation behaviour of borehole PZ1

Time series data of SAR PSI	LOS Displacemnt mm p (95360) 50.77 m	LOS Displacemnt mm P (95042) 98 m	LOS Displacemnt mm p (96573) 142.27 m	Groundwater level (m) borehole PZ1	Monthly amount of precipitation (mm)
Jun_1995	134.435	140.442	68.59		34.4
Dec1995	119.834	134.122	73.786	18.41	92.7
Apr_1996	121.472	134.38	72.298	9.55	22.3
Mar_1997	115.207	110.977	52.686	12.03	20.8
May_1997	110.417	98.555	51.111	10.33	17.6
Dec_1997	84.146	103.668	56.664	19.12	67.7
Aug_1998	91.749	96.19	45.064	17.4	0.7
Jan_1999	77.472	85.607	49.601		45.4
Jun_1999	78.573	85.144	45.647	9.8	5
Oct_1999	70.093	64.521	33.726	17.98	57.4
May_2000	49.846	72.513	28.112	13.68	25.7
Apr_2003	13.465	6.105	-9.029	9.3	26.4
Aug_2003	18.213	9.608	9.659	13.93	5.3
Feb_2004	9.744	15.988	11.979	13.25	8.4
Apr_2004	3.879	21.835	14.919	10.68	43.5
Aug_2004	0.088	3.788	-0.854	16.95	2.6
Sep_2004	-1.176	3.929	-0.314	17.32	20.1
May_2005	-9.366	-37.092	-14.993		26.7
Aug_2005	-10.515	-13.766	-7.377		16.4
Dec_2006	-28.871	-10.357	-4.023		11.9

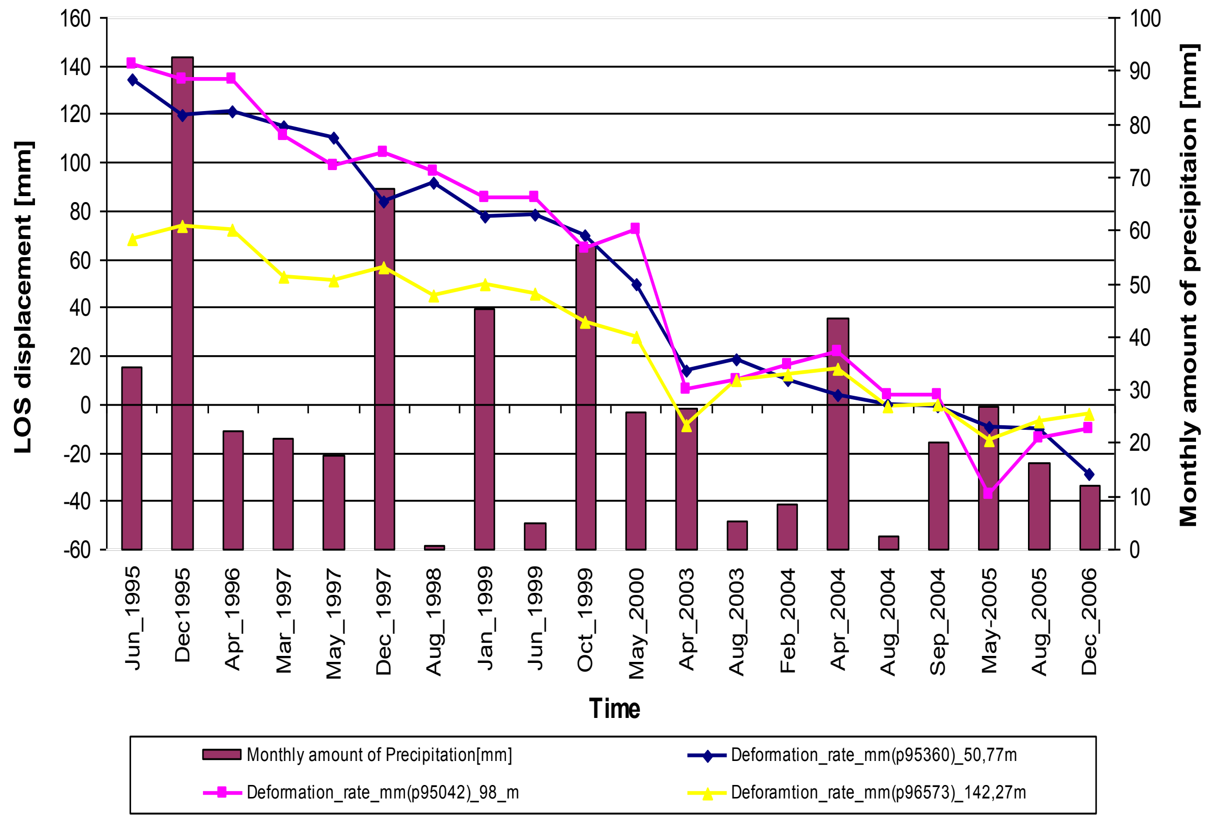

Figure 77. LOS Displacemnt of point candidates of PSI corresponding to monthly precipitation. Displacement time series of point candidates are rescaled to the first acquisition (i.e. 28 June 1995).

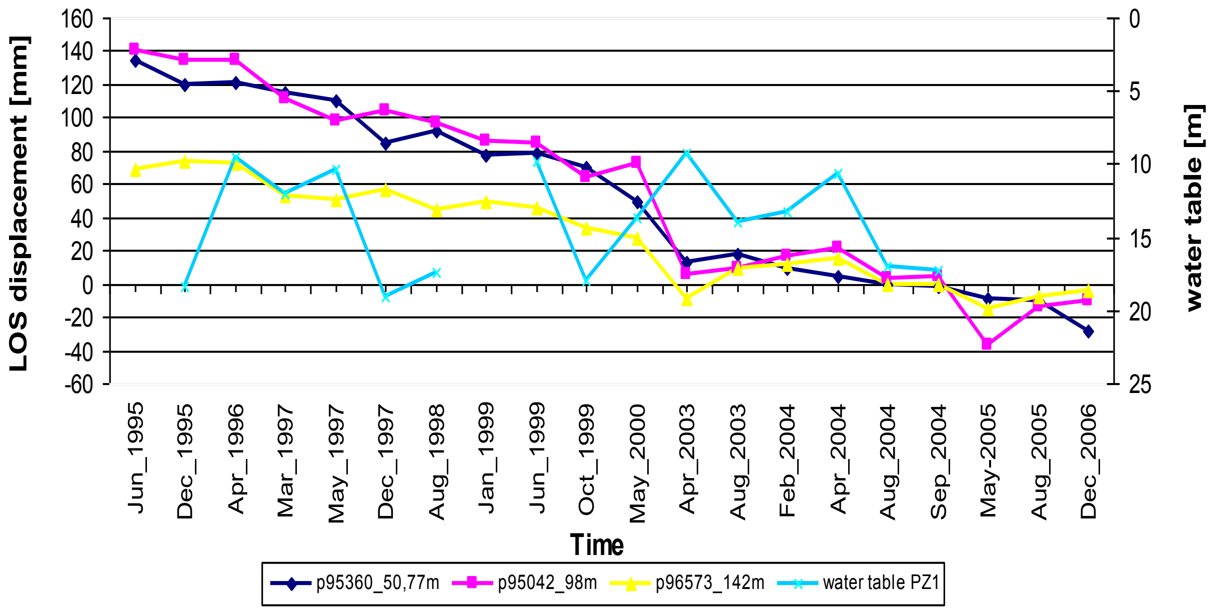

Figure 78. LOS Displacemnt of point candidates corresponding to groundwater level of borehole PZ1. Displacement time series of point candidates are rescaled to the first acquisition (i.e. 28 June 1995).

The deformation behaviour of the first point (number 95360), at a distance of 50.77 m from the borehole, indicates a general decline, as the time series begins with uplift and then goes into subsidence. The minimum uplift was 0.088 mm (August 2004) and the maximum uplift was 143.435 mm (June 1995), while the minimum subsidence was -1.176 mm (September 2004) and the maximum subsidence was -28.871 mm (December 2006).

The minimum uplift may be attributed to the indirect impact of the precipitation, which was 2.6 mm, on the land deformation through its impact on the groundwater level, which was 16.95 m. Accordingly, this precipitation amount was not enough to raise the groundwater level and consequently caused this small uplift. The basis for this reasoning is that the maximum uplift was accompanied by a precipitation amount of 34.4 mm, and this amount may have raised the groundwater level and consequently caused this high value of uplift. Nevertheless this is an expectation, because no monitoring data for groundwater level were recorded during this month.
The minimum subsidence may also be attributable to the indirect impact of the precipitation, which was 20.10 mm, on the land deformation through its impact on the groundwater level, which was 17.32 m, because the precipitation may have been insufficient to raise the groundwater level, and consequently the decline of the groundwater level caused this subsidence. The basis for this reasoning is that the maximum subsidence was accompanied by 11.90 mm precipitation. However, this is an expectation, because there are no data monitoring records for groundwater level during this month.

Details of the impact of groundwater level on land deformation indicate no continuous significant correlation between them; however, many cases of correlation within the time series are observed. A small increase in uplift accompanied a rise in groundwater level during the period December 1995–April 1996, followed by a decrease in uplift with the decline of the groundwater level during the period April 1996–March 1997. Thereafter decreasing uplift is observed with the sharp decline of groundwater level during the period May 1997–December 1997, while a subsequent increase of uplift accompanied a rise in groundwater level during the period December 1997–August 1998. This increase in uplift may not be attributable to the rise in groundwater level, because there is a data gap during this period. Additionally, a decrease in uplift is followed by a status change from uplift to subsidence coinciding with the decline of the groundwater level during the period April 2004–September 2004.

The deformation behaviour of the second point (number 95042), at a distance of 98 m from the borehole, indicates a general decline, as the time series begins with uplift and then goes into subsidence. The minimum uplift was 3.788 mm (August 2004) and the maximum uplift was 140.442 mm (June 1995), while the minimum subsidence was -10.357 mm and the maximum subsidence was -37.092 mm (May 2005).

The minimum uplift may be attributed to the indirect impact of the precipitation, which was 2.6 mm, on land deformation through its impact on the groundwater level, which was 16.95 m, as this precipitation amount was not enough to raise the groundwater level and consequently caused this small uplift. The basis for this reasoning is that the maximum uplift accompanied 34.4 mm of precipitation, which may have raised the groundwater level and consequently caused this high value of uplift; however, this is an expectation, because no monitoring data for groundwater level were recorded during this month. On the other hand, precipitation amount maybe is associated with other factor causing this uplift for the reason that the precipitation amount is not sufficient to cause this high value of uplift over this short period.

The minimum subsidence may also be attributed to the indirect impact of the precipitation (11.9 mm) on land deformation through its impact on groundwater level; however no monitoring data were recorded during this month. The precipitation may not have been enough to raise the groundwater level, and consequently subsidence occurred as a result of the decline in groundwater level.

The maximum subsidence may be attributable to the indirect impact of precipitation (26.7 mm) on land deformation through its impact on groundwater level; however, no monitoring data were recorded during this month. This amount of precipitation was not enough to raise the groundwater level, and as a result subsidence occurred; however, this is only an expectation, because no monitoring data for groundwater level were recorded during this month. Maybe some other impact factor participated in causing this subsidence, because the minimum subsidence accompanied low precipitation while the maximum subsidence accompanied a higher amount of precipitation.

Details of the impact of groundwater level on land deformation indicate that there is no continuous significant correlation between them; however, there are some cases of correlation within the time series. A decrease in uplift accompanied the decline of the groundwater level during the period April 1996–March 1997. A decrease in uplift was also observed throughout the sharp decline of the groundwater level during the period June 1999–October 1999, followed by an increase in uplift with rising groundwater level during the periods October 1999–May 2000 and August 2003–April 2004. There was a decrease in uplift with the sharp decline in groundwater level during the period April 2004–September 2004.

The deformation behaviour of the third point (number 96573), at a distance of 142 m from the borehole, indicates a general decline, as the time series begins with uplift and then goes into subsidence; however, a status change from uplift to subsidence is observed during the period May 2000–April 2003, followed by another status change from subsidence to uplift during the period April 2003–August 2003. The minimum uplift was 9.659 mm (August 2003) and the maximum uplift was 73.786 mm (December 1995), while the minimum subsidence was -0.314 mm (September 2004) and the maximum subsidence was -14.993 mm (May 2005).

The minimum uplift may not be attributable to the indirect impact of precipitation (5.3 mm) on land deformation through its impact on the groundwater level, which was 13.93 m, because the amount of precipitation was not enough to raise the groundwater level sufficiently to cause this amount of uplift. Some other factor may have contributed to causing this uplift, because such a low level of groundwater should be accompanied by either a lower value of uplift or subsidence.

The maximum uplift also may not be attributable to the indirect impact of precipitation (92.7 mm) through its impact on groundwater level, which was 18.41 m, because such a low level of groundwater should be accompanied by subsidence; therefore, this uplift may be attributable to the influence of some other factor or parameter.

While the minimum subsidence may be attributable to the indirect impact of precipitation (20.1 mm) on land deformation through its impact on the groundwater level, which was 17.32 m, this amount of precipitation was not enough to raise the groundwater level; consequently, the decline of the groundwater level caused this subsidence.

The maximum subsidence accompanied precipitation of 26.7 mm, which may not have been enough to raise the groundwater level and as a result caused subsidence; however, this is an expectation only, because no monitoring data for groundwater level were recorded during this month. Furthermore, there may be some other reason for this subsidence, because the minimum subsidence accompanied low precipitation while the maximum subsidence accompanied high precipitation; however the first opinion is more likely if the groundwater level had been known.

Details of the impact of the groundwater level on land deformation indicate that there is no continuous significant correlation between them; however, there are many correlations within the time series. A decrease in uplift accompanied the decline of groundwater level during the periods April 1996–March 1997 and June 1999–October 1999. A status change from uplift to subsidence then to uplift once again during the periods May 2000–April 2003 and April 2003–August 2003 is observed, which may be attributable to the impact of factors other than groundwater because there is no significant correlation between the fluctuation of groundwater level and land deformation. This was followed by an increase in uplift, which accompanied the rising groundwater level during the period August 2003–April 2004. Subsequently, a sharply decreasing trend of uplift followed by a status change from uplift to subsidence accompanied the decline of the groundwater level during the period April 2004–September 2004.

3.7.4. SR29

The groundwater level behaviour corresponding to the monthly accumulation of precipitation based on time series data of SAR PSI is depicted in Table 25 and Figure 79. The general behaviour of groundwater level during 1995–2006 points to a decline, which may be attributable to the lack of compensation for the lost water. Details of the behaviour indicate a slow decline of the groundwater level accompanied by decreasing precipitation during the period December 1995–May 1997. Note the absence of groundwater level data records for June 1995, December 1997, January 1997, February 2004 and May 2005. Thereafter a decline in the groundwater level was observed alongside increasing precipitation during the period June 1999 – October 1999, with a subsequent rise in groundwater level during the period October 1999–May 2000, which may be attributable to the increasing precipitation. Thereafter a decline in the groundwater level accompanied the decreasing precipitation during the periods April 2003 – August 2003 and April 2004 – August 2004. This was followed by a rise in the groundwater level with increasing precipitation during the period August 2004–September 2004.

Table 25. Monthly accumulation of precipitation corresponding to the groundwater level of the borehole SR29

Time series data of SAR PSI	Monthly amount of precipitation (mm)	Groundwater level (m) Borehole SR29
Jun_1995	34.4	
Dec_1995	92.7	28
Apr_1996	22.3	26,26
Mar_1997	20.8	28
May_1997	17.6	31,13
Dec_1997	67.7	
Aug_1998	0.7	59.3
Jan_1999	45.4	
Jun_1999	5	38.52
Oct_1999	57.4	43.2
May_2000	25.7	37.55
Apr_2003	26.4	39.46
Aug_2003	5.3	67.14
Feb_2004	8.4	
Apr_2004	43.5	44.98
Aug_2004	2.6	61
Sep_2004	20.1	51.83
May_2005	26.7	
Aug_2005	16.4	73.39
Dec_2006	11.9	48.62

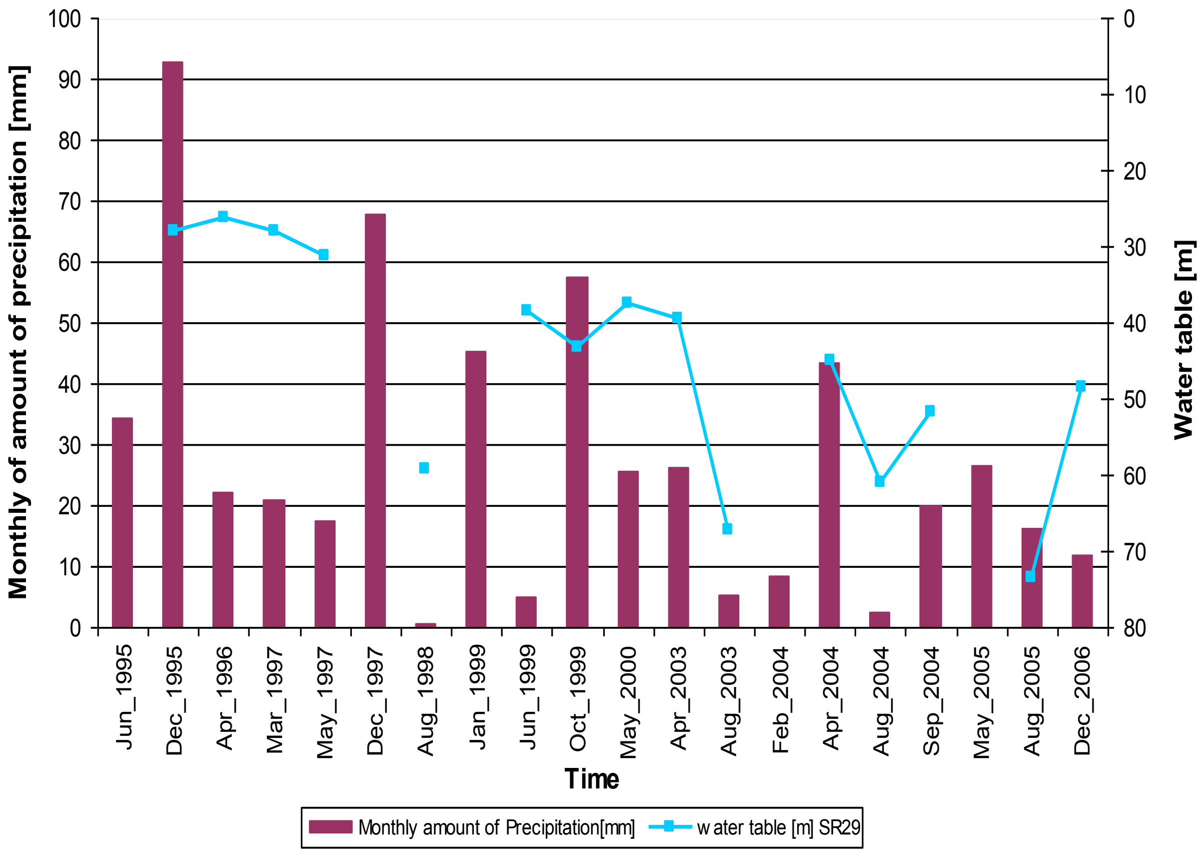

Figure 79. Monthly accumulation of precipitation corresponding to the groundwater level of the borehole SR29

3.7.4.1. Interference between land deformation and monthly precipitation as indirect impact on groundwater level (seasonal deformation) of the borehole SR29

Three point candidates resulting from the PSI technique have been chosen, with different distances between these points and borehole, as shown in Figure 80, to correlate, identify and examine the impact of groundwater level fluctuation on land deformation. Deformation of three point candidates at distances of 64, 143 and 245 m from the borehole, the monthly amount of precipitation, and the groundwater level are shown in Table 26. Deformation of the point candidates and monthly precipitation are depicted in Figure 81. Deformation of point candidates and groundwater level are depicted in Figure 82.

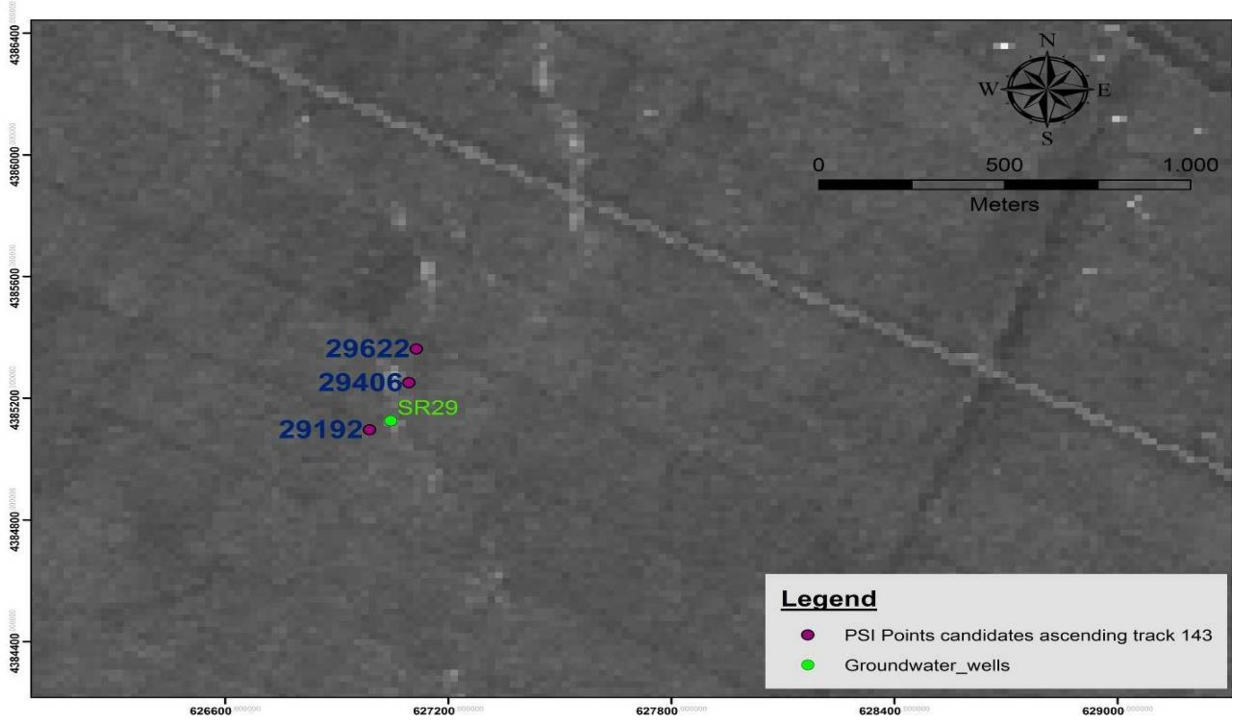

Figure 80. Three point candidates of the PSI at different distances from borehole SR29

Table 26. Ground deformation of point candidates of PSI ascending track (143) corresponding to groundwater level and monthly precipitation behaviour of borehole SR29

Time series data of SAR PSI	LOS Displacemnt mm p (29192) 64 m	LOS Displacemnt mm p (29406) 143 m	LOS Displacemnt mm p (29622) 245 m	Groundwater level (m) borehole SR29	Monthly amount of precipitation (mm)
Jun_1995	-222.716	-223.989	-80.972		34.4
Dec_1995	-219.432	-199.775	-70.422	28	92.7
Apr_1996	-200.398	-209.708	-77.486	26.26	22.3
Mar_1997	-186.021	-182.14	-68.297	28	20.8
May_1997	-167.751	-179.12	-64.564	31.13	17.6
Dec_1997	-160.44	-165.376	-56.482		67.7
Aug_1998	-147.142	-141.805	-43.27	59.3	0.7
Jan_1999	-131.74	-144.138	-42.46		45.4
Jun_1999	-138.928	-135.913	-43.497	38.52	5
Oct_1999	-124.069	-112.167	-50.985	43.2	57.4
May_2000	-107.145	-107.373	-39.632	37.55	25.7
Apr_2003	-32.476	-37.682	-10.951	39.46	26.4
Aug_2003	-31.796	-21.57	-6.09	67.14	5.3
Feb_2004	-16.769	-13.253	-4.756		8.4
Apr_2004	-4.743	-9.016	-8.746	44.98	43.5
Aug_2004	-6.627	-6.468	-6.814	61	2.6
Sep_2004	-2.357	-4.381	-1.322	51.83	20.1
May_2005	23.847	19.813	-1.183		26.7
Aug_2005	18.589	19.552	16.321	73.39	16.4
Dec_2006	61.661	62.344	22.595	48.62	11.9

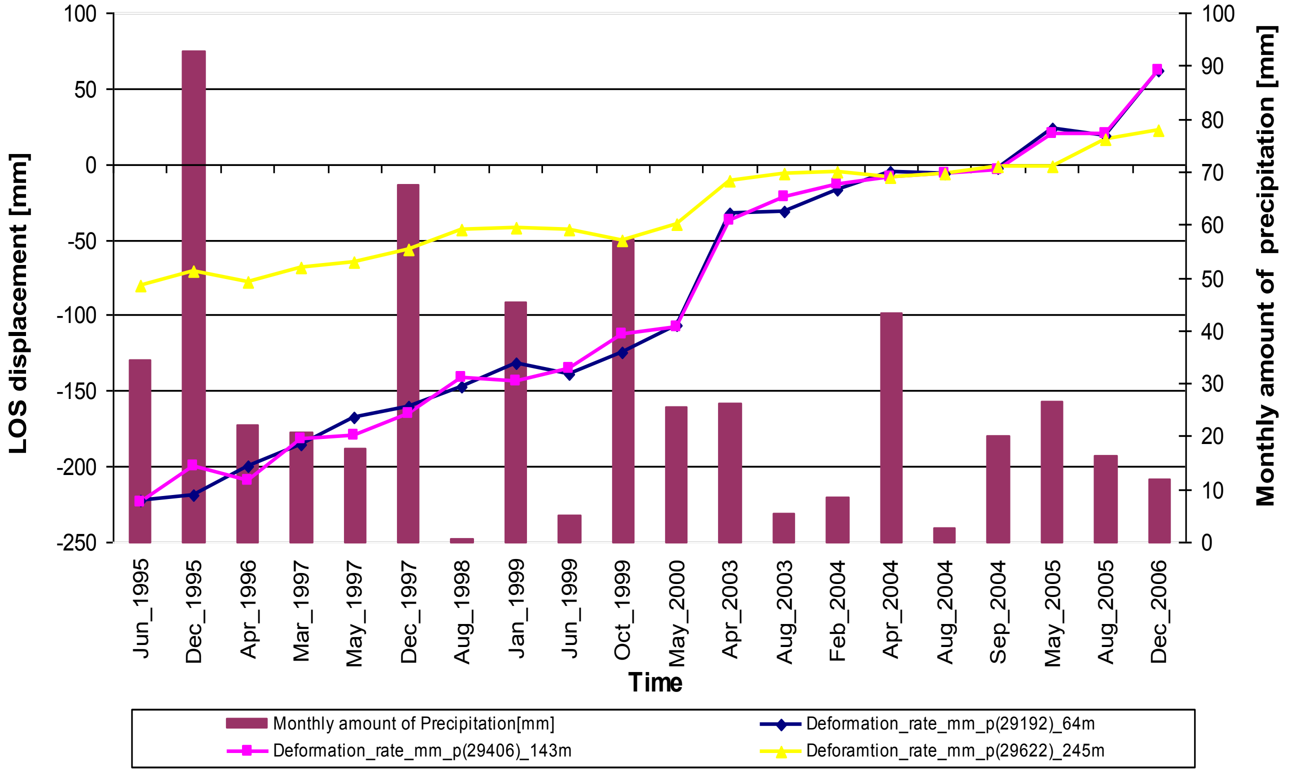

Figure.81 LOS Displacemnt of point candidates of PSI and monthly precipitation Displacement time series of point candidates are rescaled to the first acquisition (i.e. 28 June 1995).

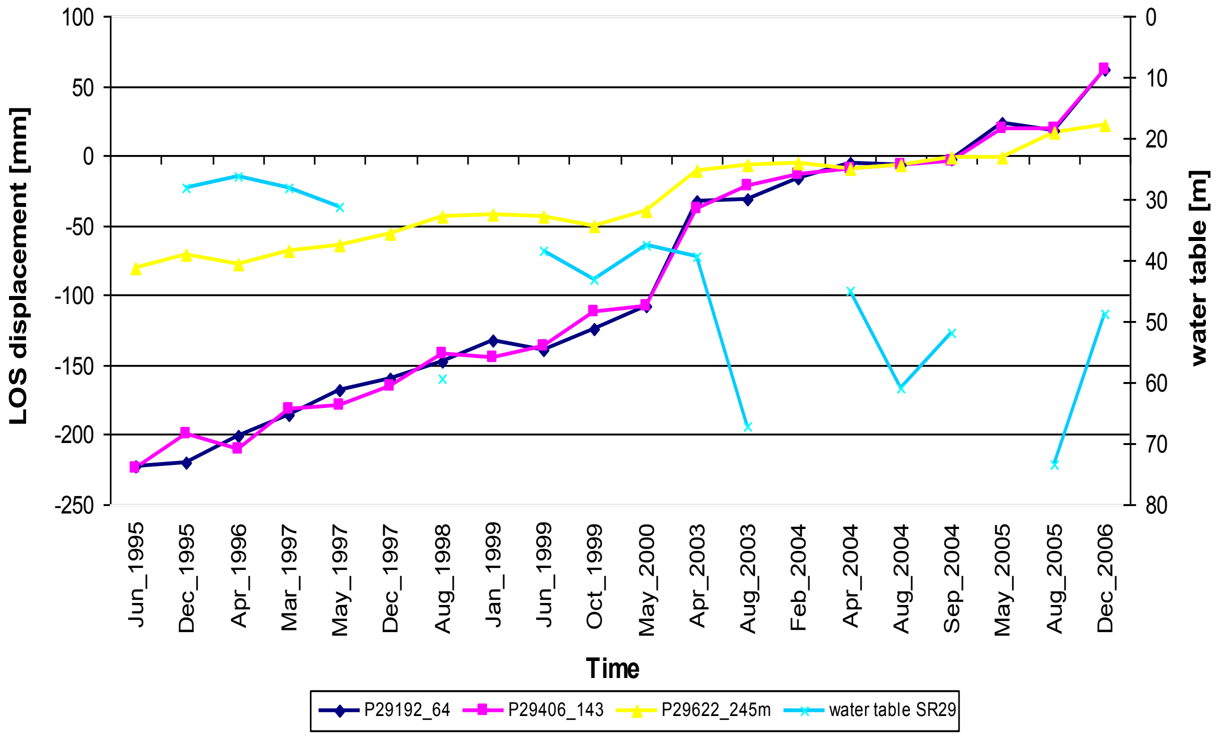

Figure 82. LOS Displacemnt of point candidates corresponding to groundwater level of borehole SR29. Displacement time series of point candidates are rescaled to the first acquisition (i.e. 28 June 1995).

The deformation behaviour of the first point (number 29192), at a distance of 64 m from borehole, indicates a general rising trend, as the time series begins with subsidence and then goes into uplift. The minimum subsidence was -2.357 mm (September 2004) and the maximum subsidence was -222.716 mm (June 1995), while the minimum uplift was 18.589 mm (August 2005) and the maximum uplift was 61.661 mm (December 2006).

The minimum subsidence may be attributable to the indirect impact of precipitation (20.1 mm) on land deformation through its impact on groundwater level (51.83 m). As it was not enough to raise the groundwater level, the decline of the groundwater level caused this subsidence. However, this low level of groundwater should probably cause more than this value of subsidence, which points to the presence of some other influencing factor that limits the continuation of subsidence. The maximum subsidence accompanied 34.40 mm of precipitation, which may not have been enough to raise the groundwater level and consequently caused this subsidence; however, no monitoring data for groundwater level were recorded during this month, so this is only an expectation. Some other factor may have participated in causing this subsidence. The acceptable reasoning for this is that the minimum subsidence accompanied low precipitation while the maximum subsidence accompanied higher precipitation amount. The minimum uplift may not be attributable to the indirect impact of precipitation, which was 16.40 mm, on the land deformation through its impact on groundwater level, which was 73.3 m, because this amount of precipitation was not enough to raise the groundwater level and consequently cause this uplift. Accordingly, this uplift may have been caused by some other factor, because this low level of groundwater should be accompanied by either a smaller value of uplift or subsidence. Indeed, it is more reasonable to expect a high value of subsidence with this low groundwater level.

The maximum uplift may be attributable to the indirect impact of precipitation (11.90 mm) on the land deformation through its impact on groundwater level (48.62 m), because the low precipitation amount may still have raised the groundwater level and consequently caused this uplift. In addition, some other factor may have participated in causing this uplift.

Details of the impact of the groundwater level on the land deformation indicate that there is no continuous significant correlation between them, which may be attributable to the non-continuation or the interruption of groundwater monitoring data during this period (June 1995–December 2006). However some cases of correlation are observed. A decrease in subsidence accompanied the raising of the groundwater level during the period October 1999–May 2000. The stability of subsidence may be attributable to the decline of the groundwater level during the period April 2003–August 2003. An increase of subsidence accompanied the decline of the groundwater level during the period April 2004–August 2004, followed by a decrease in subsidence through the raising of the groundwater level during the period August 2004–September 2004. Thereafter an increase in uplift accompanied the raising of the groundwater level during the period August 2005–December 2006.

The deformation behaviour of the second point (number 29406), at a distance of 143 m from the borehole, indicates a general rising trend, as the time series begins with subsidence and then goes into uplift. The minimum subsidence was -4.381 mm (September 2004) and the maximum subsidence was -223.989 mm (June 1995), while the minimum uplift was 19.552 mm (August 2005) and the maximum uplift was 62.344 mm (December 2006).

The minimum subsidence may be attributable to the indirect impact of precipitation, which was 20.1 mm, on land deformation through its impact on groundwater level, as it was not enough to raise the groundwater level, which was 51.83 m and consequently the decline of the groundwater level caused this subsidence. However such a low groundwater level should be expected to cause a larger value of subsidence; therefore some other factor may have limited the continuation of subsidence. The maximum subsidence accompanied 34.40 mm of precipitation, which may not have been enough to raise the groundwater level and consequently caused this subsidence. However this is only an expectation, because no groundwater level monitoring data were recorded during this month. There may be some other cause of this subsidence, based on the reasoning that the minimum subsidence accompanied low precipitation while the maximum subsidence accompanied higher precipitation amount. However the first viewpoint is more likely if the groundwater level had been known.

The minimum uplift may not be attributable to the indirect impact of precipitation (16.40 mm) on the land deformation through its impact on groundwater level, which was 73.39 m, because this amount of precipitation was not enough to raise the groundwater level and consequently cause this uplift. This uplift may have been caused by some other factor, because such a low level of groundwater should be accompanied by either a smaller value of uplift than this or subsidence; moreover, it is more likely to expect a high value of subsidence with this low groundwater level. The maximum uplift may be attributable to the indirect impact of precipitation (11.90 mm) on land deformation through its impact on groundwater level, which was 48.62 m. This low precipitation amount may nevertheless have raised the groundwater level and consequently caused this uplift. Some other factor may also have participated in causing this uplift. It is worth mentioning that the deformation and correlation behaviour of the PSI point candidate 29192 is identical to that of PSI point candidate 29406 despite the different distances between the borehole and the two point candidates, which are 64 and 143 m, respectively.

Details of the impact of the groundwater level on the land deformation indicate that there is no continuous significant correlation between them, which may be attributable to either non-continuation or the interruption of the groundwater monitoring data during the period June 1995–December 2006. However some correlations are observed. A decrease in subsidence accompanied the raising of the groundwater level during the periods October 1999–May 2000 and August 2004–September 2004. Subsequently an increase in uplift accompanied the raising of the groundwater level during the period August 2005–December 2006.

The deformation behaviour of the third point (number 29622), at a distance of 245 m from the borehole, indicates a general rising trend, as the time series begins with subsidence and then goes into uplift. The minimum subsidence was -1.183 mm (May 2005) and the maximum subsidence was -80.972 mm (June 1995), while the minimum uplift was 16.321 mm (August 2005) and the maximum uplift was 22.595 mm (December 2006).

The minimum subsidence may be attributable to the indirect impact of precipitation (26.70 mm) on land deformation through its impact on the groundwater level, as it may not have been enough to raise the groundwater level and the consequent decline of the groundwater level caused the subsidence; however no groundwater monitoring data were recorded during this month. The maximum subsidence accompanied 34.40 mm of precipitation, which may not have been enough to raise the groundwater level and consequently caused this subsidence; however this is only an expectation, because there are no data monitoring records for groundwater level during May 2005 or June 1995Some other factor may have contributed to causing this subsidence, on the basis that the minimum subsidence accompanied low precipitation amount while the maximum subsidence accompanied higher precipitation; however the first viewpoint is more likely if the groundwater level had been known.

The minimum uplift may not be attributable to the indirect impact of precipitation, which was 16.40 mm, on the land deformation through its impact on groundwater level, which was 73.39 m, because this amount of precipitation was not enough to raise the groundwater level and consequently cause this uplift. Accordingly this uplift may have been caused by some other factor, because such a low level of groundwater should be accompanied by either a smaller value of uplift or subsidence. Indeed, it is more likely to expect a high value of subsidence with this low groundwater level.
The maximum uplift may be attributable to the indirect impact of precipitation (11.90 mm) on land deformation through its impact on groundwater level, which was 48.62 m. Despite being low, this amount of precipitation may have raised the groundwater level and consequently caused this uplift. Some other factor may also have contributed to causing this uplift. It is worth mentioning that the deformation and correlation behaviour of point candidate 29192 is identical to that of point candidates 29406 and 29622, despite the fact that they are at different distances (64, 143 and 245 m, respectively) from the borehole.

Details of the impact of groundwater level on land deformation indicate that there is no continuous significant correlation between them, which may be attributable either to non-continuation or the interruption of groundwater monitoring data during the period June 1995–December 2006. However, some correlation cases are observed. An increase in subsidence accompanied the decline of groundwater level during the period June 1999–October 1999. A decrease in subsidence accompanied the raising of the groundwater level during the periods October 1999–May 2000 and August 2004–September 2004. Furthermore an increase in uplift accompanied the raising of the groundwater level during the period August 2005–December 2006.

3.7.5. SR35

The groundwater level behaviour corresponding to the monthly accumulation of precipitation based on time series data of SAR PSI is depicted in Table 27 and Figure 83. The general behaviour of the groundwater level during the period 1995–2006 points to a continuous fluctuation, and a decline is observed at the end of the time series during the period May 2005–December 2006. The decline may be attributable to the decreasing amount of precipitation and consequently the lack of compensation for the water lost from the aquifer. Note the absence of data monitoring records of groundwater level for June 1995, January 1999 and August 2004.

Details of the behaviour indicate a rising groundwater level during the period December 1995–April 1996, which accompanied decreasing precipitation amount; consequently this rise can, with high probability, be attributed to some other source of water supply. This was followed by a decline of the groundwater level during the period April 1996–March 1997, which may be attributable to a decreasing amount of precipitation. A subsequent rise of the groundwater level during the period March 1997–May 1997 is observed, which accompanied decreasing precipitation; therefore the rise of groundwater level may be attributable to some other water source. Thereafter a decline of the groundwater level accompanied increasing precipitation during the period May 1997–December 1997. This may be attributable to an insufficient amount of precipitation to compensate for water withdrawal. A subsequent decline of the groundwater level alongside decreasing precipitation is observed during the period December 1997–August 1998. Once again, a decline of the groundwater level is observed with increasing precipitation amount during the period June 1999–October 1999. This may also be attributable to an insufficient amount of precipitation to recharge the aquifer and compensate for water withdrawal. Thereafter a rise in groundwater level with increasing precipitation is observed during the period May 2000–April 2003, followed by a decline and then a rise of groundwater level during the periods April 2003–August 2003 and February 2004–April 2004, respectively. This fluctuation between decline and rise may be attributable to decreasing and increasing amounts of precipitation. A rise in groundwater level is observed during the period September 2004–May 2005, which may be attributable to the increasing amount of precipitation. Ultimately, a decline of groundwater level accompanied decreasing precipitation during the period May 2005–December 2006. It is worth mentioning that the correlation behaviour of groundwater level and precipitation amount for borehole SR35 is approximately the same as for borehole PZ1.

Table 27. Monthly accumulation of precipitation corresponding to the groundwater level of the borehole SR35

Time series data of SAR PSI	Monthly amount of precipitation (mm)	Groundwater level (m) borehole SR35
Jun_1995	34.4	
Dec_1995	92.7	5.21
Apr_1996	22.3	4.25
Mar_1997	20.8	4.85
May_1997	17.6	3.75
Dec_1997	67.7	5.14
Aug_1998	0.7	5.38
Jan_1999	45.4	
Jun_1999	5	3.5
Oct_1999	57.4	5.15
May_2000	25.7	3.71
Apr_2003	26.4	3.38
Aug_2003	5.3	3.5
Feb_2004	8.4	5.04
Apr_2004	43.5	3.44
Aug_2004	2.6	
Sep_2004	20.1	4.25
May_2005	26.7	3.57
Aug_2005	16.4	4.98
Dec_2006	11.9	5.91

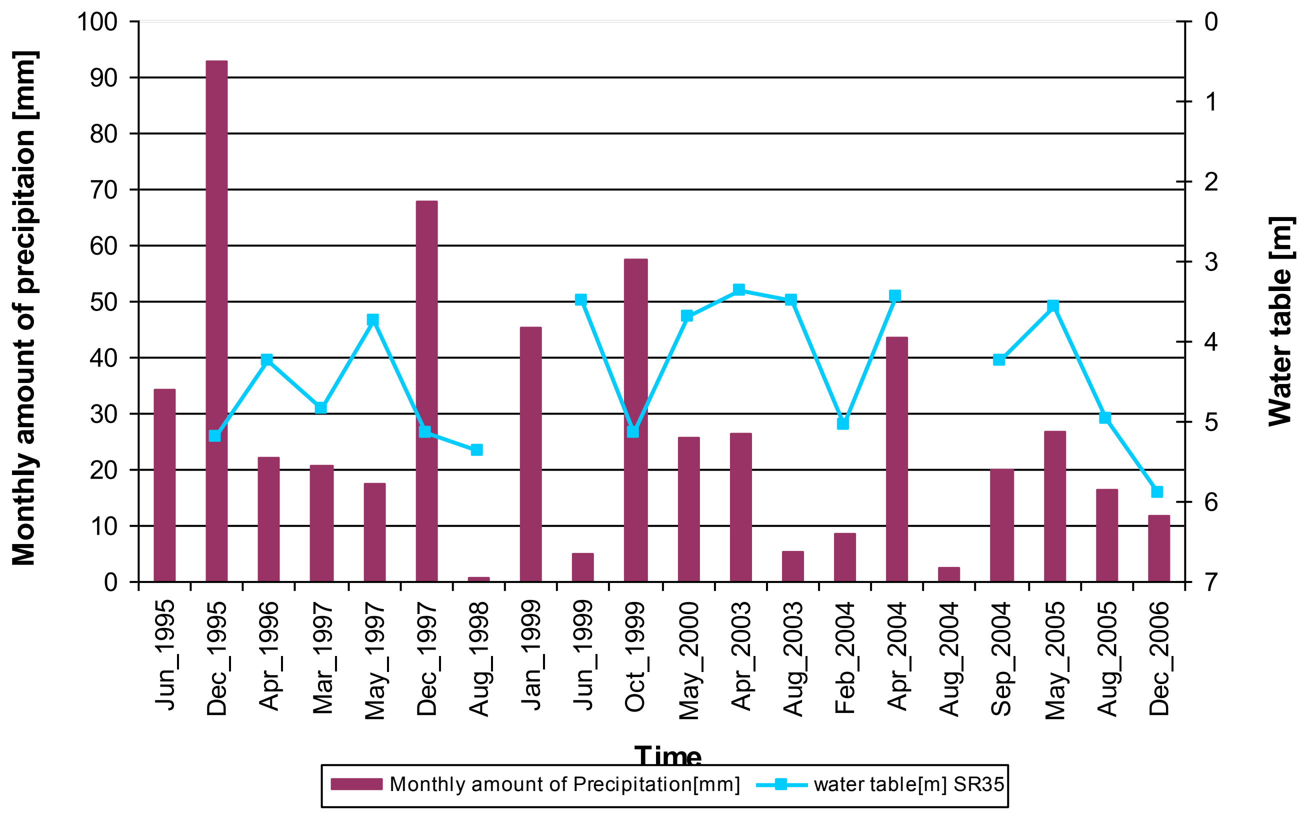

Figure 83. Monthly accumulation of precipitation corresponding to the groundwater level of the borehole SR35

3.7.5.1. Interference between land deformation and monthly precipitation as indirect impact on groundwater level (seasonal deformation) of the borehole SR35

Three point candidates resulting from the PSI technique have been chosen, with different distances between these points and the borehole, as shown in Figure 84, to correlate, identify and examine the impact of groundwater level fluctuation on land deformation. Deformation of the three point candidates, which are at distances of 183, 411 and 436 m from the borehole, monthly precipitation, and groundwater level are shown in Table 28. Deformation of the point candidates and monthly precipitation are depicted in Figure 85. Deformation of the point candidates and groundwater level are depicted in Figure 86.

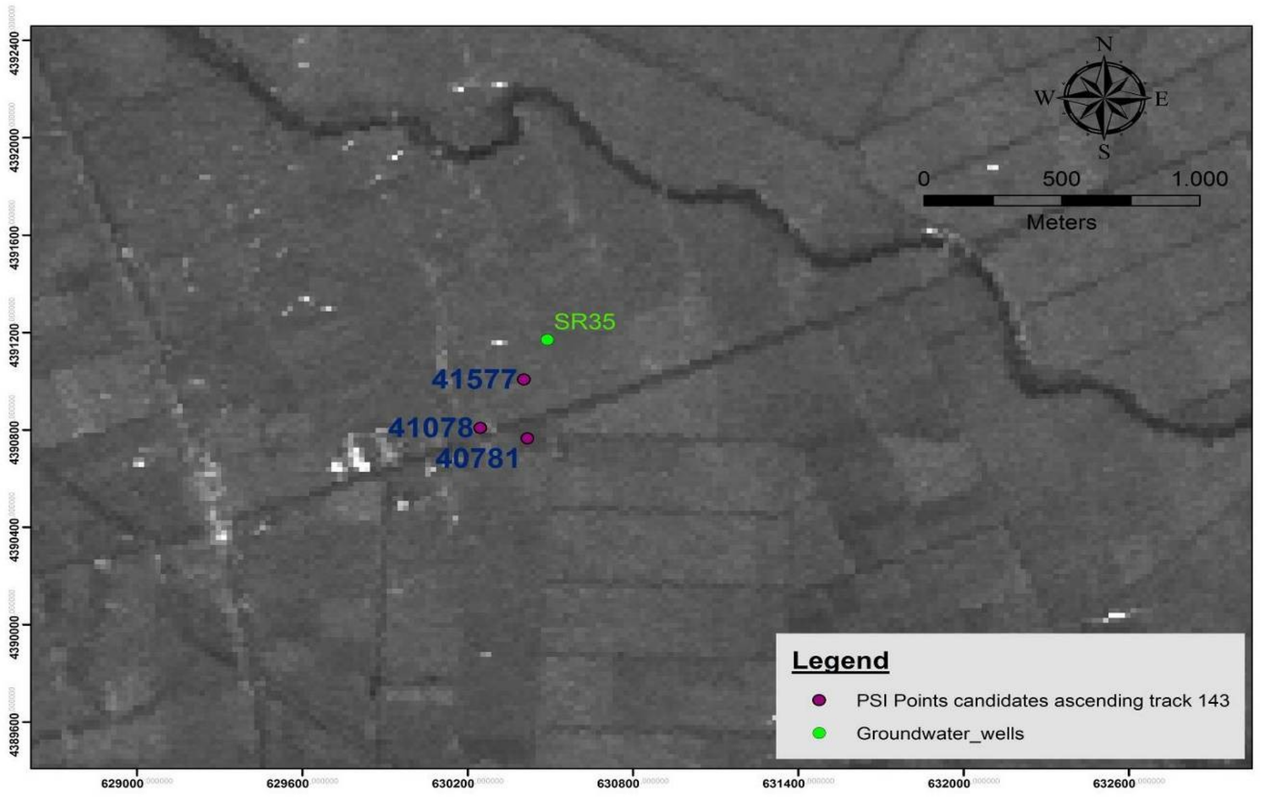

Figure84. Three point candidates of the PSI at different distances from borehole SR35

Table 28. Ground deformation of point candidates of PSI ascending track (143) corresponding to groundwater level and monthly precipitation behaviour of borehole SR35

Time series data of SAR PSI	LOS Displacemnt mm P (41577) 183 m	LOS Displacemnt mm P (40781) 411 m	LOS Displacemnt mm P (41078) 436 m	Groundwater level (m) borehole SR35	Monthly amount of precipitation (mm)
Jun_1995	-18.949	-135.849	-59.914		34.4
Dec_1995	-13.305	-130.401	-55.108	5.21	92.7
Apr_1996	-18.718	-131.161	-57.223	4.25	22.3
Mar_1997	-8.931	-116.265	-57.811	4.85	20.8
May_1997	-21.744	-120.835	-61.205	3.75	17.6
Dec_1997	-11.858	-105.532	-48.862	5.14	67.7
Aug_1998	-6.007	-94.339	-38.054	5.38	0.7
Jan_1999	-12.624	-96.434	-39.597		45.4
Jun_1999	-7.057	-86.988	-40.334	3.5	5
Oct_1999	-2.823	-70.98	-41.929	5.15	57.4
May_2000	-9.113	-70.684	-30.609	3.71	25.7
Apr_2003	-4.737	-21.787	-6.59	3.38	26.4
Aug_2003	-9.933	-13.809	-13.687	3.5	5.3
Feb_2004	-10.082	-10.555	-3.797	5.04	8.4
Apr_2004	2.348	-4.081	8.189	3.44	43.5
Aug_2004	0.434	-1.963	-2.716		2.6
Sep_2004	-0.841	3.649	1.154	4.25	20.1
May_2005	-4.698	15.414	-1.923	3.57	26.7
Aug_2005	11.096	15.444	10.624	4.98	16.4
Dec_2006	8.619	35.045	19.246	5.91	11.9

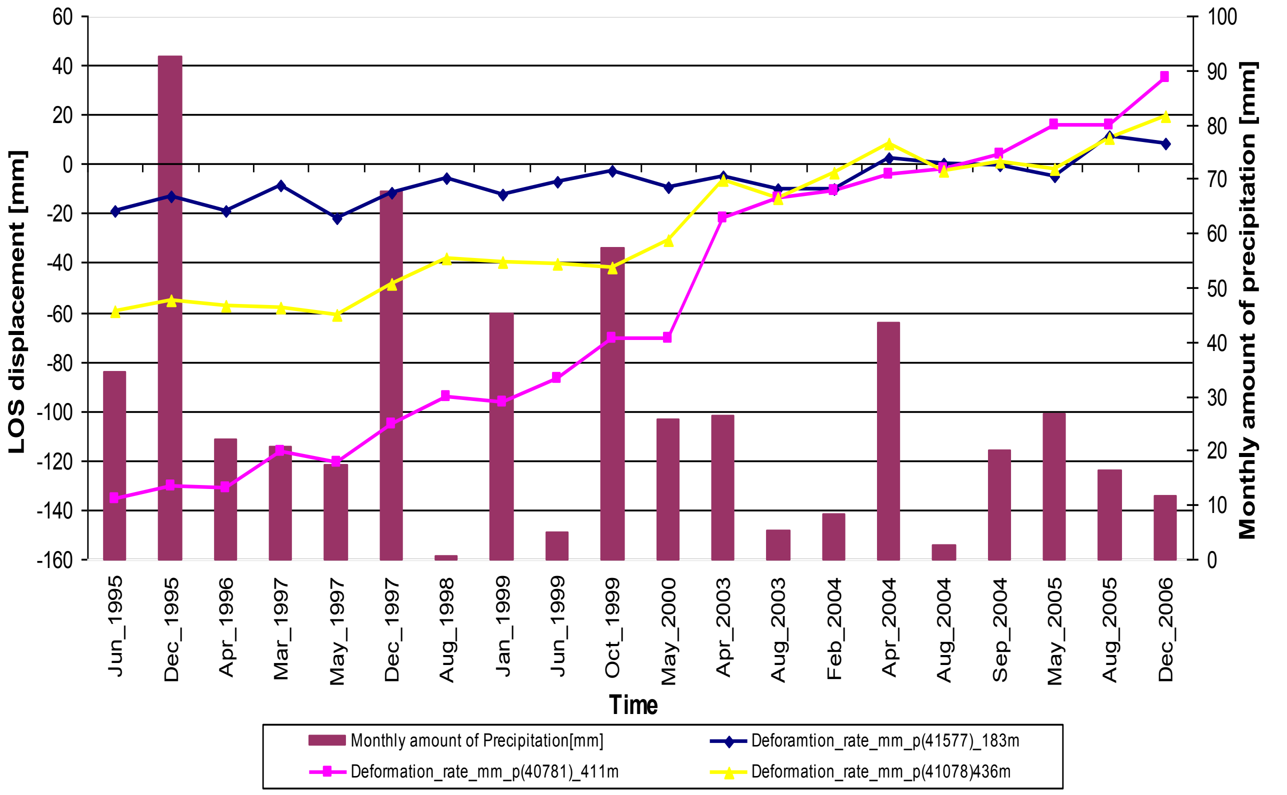

Figure.85 LOS Displacemnt of point candidates of PSI corresponding to monthly precipitation amount. Displacement time series of point candidates are rescaled to the first acquisition (i.e. 28 June 1995).

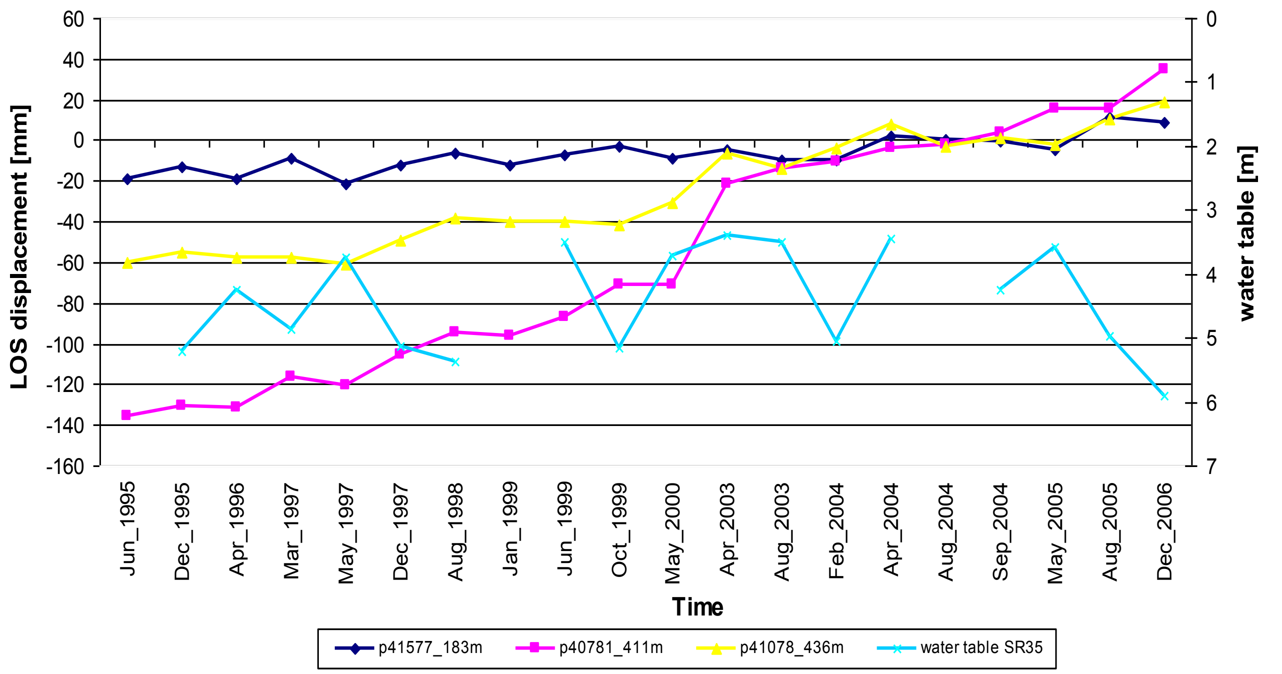

Figure 86.LOS Displacemnt of point candidates corresponding to groundwater level of borehole SR35. Displacement time series of point candidates are rescaled to the first acquisition (i.e. 28 June 1995).

The deformation behaviour of the first point (number 41577), at a distance of 183 m from the borehole, indicates a general rising trend, as the time series begins with subsidence and then goes into uplift. Eventually a swap between subsidence and uplift is observed. The minimum subsidence was -0.841 mm (September 2004) and the maximum subsidence was -21.744 mm (May 1997), while the minimum uplift was 0.434 mm (August 2004) and the maximum uplift was 11.096 mm (August 2005).

The minimum subsidence may not be attributable to the indirect impact of precipitation (20.1 mm) on land deformation through its impact on groundwater level, which was 4.25 m, despite the probability that the precipitation raised the groundwater level and consequently reduced the subsidence to this value. Nevertheless, uplift would be expected to accompany such a high groundwater level, therefore this subsidence may have been caused by some other participating factor. Moreover, the maximum subsidence may not be attributable to the indirect impact of precipitation (17.60 mm) on the groundwater level, which was 3.75 m, because such a high level of groundwater level should cause uplift; therefore this subsidence may be attributable to some other impact factor.

The minimum uplift may be attributable to the indirect impact of precipitation (2.60 mm) on land deformation through its impact on the groundwater level; however there are no monitoring records of groundwater level for this month. Nevertheless the low amount of precipitation may not have been enough to raise the groundwater level, resulting in this low uplift. The maximum uplift may also be attributable to the indirect impact of precipitation (16.40 mm) on land deformation through its effect on the groundwater level, which was 4.98 m; accordingly, this amount of precipitation may have raised the groundwater level and consequently resulted in this uplift.

Details of the impact of groundwater level on land deformation indicate that there is no continuous significant correlation between them. This may be attributed to either the long distance between the borehole and point candidate of PSI or the short time series of SAR data; however, many correlation cases are observed. Decreasing subsidence accompanied the raising of the groundwater level during the period May 2000–April 2003, followed by an increase in subsidence alongside the decline of the groundwater level during the periods April 2003–August 2003 and August 2003–February 2004. Thereafter a decrease in subsidence followed by a status change from

subsidence to uplift with rising groundwater level are observed during the period February 2004–April 2004. There was a decrease in uplift with the sharp decline of the groundwater level during the period August 2005–December 2006.
The deformation behaviour of the second point (number 40781), at a distance of 411 m from the borehole, indicates a general rising trend, as the time series begins with subsidence and then goes into uplift. The minimum subsidence was -1.963 mm (August 2004) and the maximum subsidence was -135.849 mm (June 1995), while the minimum uplift was 3.649 mm (September 2004) and the maximum uplift was 35.045 mm (December 2006).

The minimum subsidence may be attributable to the indirect impact of precipitation (2.60 mm) on land deformation through its impact on the groundwater level; however, no monitoring data were recorded during this month. The precipitation amount may not have been enough to raise the ground water level and consequently resulted in this subsidence. The maximum subsidence may not be attributable to the indirect impact of precipitation (34.40 mm) through its impact on the groundwater level; however, no monitoring data were recorded during this month. The basis for this reasoning is that this amount of precipitation should be accompanied by either a smaller amount of subsidence value than that found or uplift. Accordingly, some other factor may have participated in causing this subsidence.

The minimum uplift may be attributable to the indirect impact of precipitation (20.10 mm) on land deformation through its impact on the groundwater level, which was 4.25 m. Accordingly, this amount of precipitation may have raised the groundwater level and consequently resulted in this uplift. The maximum uplift may also be attributable to the indirect impact of precipitation (11.90 mm) on land deformation through its effect on the groundwater level, which was 5.91 m; this amount of precipitation may have raised the groundwater level and consequently resulted in this uplift. Furthermore, comparing the values of precipitation amount and groundwater level that accompanied the minimum uplift, they were higher than the values of precipitation amount and groundwater level that accompanied the maximum uplift, therefore some other factor may have affected this uplift.

Details of the impact of groundwater level on land deformation indicate that there is no continuous significant correlation between them, which may be attributable to the long distance between the borehole and the point candidate of PSI; however, many correlations are observed. The stability of subsidence following its decreasing trend may be attributable to the rising groundwater level during the period October 1999–May 2000. Thereafter a sharp decrease in subsidence accompanied the raising of the groundwater level during the period May 2003–April 2003. Another similar case is observed during the period February 2004–April 2004. Furthermore, an increase in uplift accompanied the raising of the groundwater level during the period September 2004–May 2005. The deformation behaviour of the third point (number 41078), at a distance of 436 m from the borehole, indicates a general rising trend, as the time series begins with subsidence and then goes into uplift. There is subsequently a swap from subsidence to uplift during the period February 2004–May 2005. The minimum subsidence was -1.923 mm (May 2005) and the maximum subsidence was - 61.205 mm (May 1997), while the minimum uplift was 1.154 mm (September 2004) and the maximum uplift was 19.246 mm (December 2006). The minimum and maximum subsidence may not be attributable to the indirect impact of precipitation 26.70 and 17.6 mm, respectively) on land deformation through its impact on the groundwater levels, which were 3.57 and 3.57 m, respectively.

The minimum uplift may be attributable to the indirect impact of precipitation (20.10 mm) on land deformation through its effect on the groundwater level, which was 4.25 m. The maximum uplift may also be attributable to the indirect impact of precipitation (11.90 m) on the groundwater level, which was 5.91 m; however, this groundwater level is lower than the groundwater level which accompanied the minimum uplift, leading to the conclusion that the maximum uplift may be attributable to some other factor.

Details of the impact of the groundwater level on land deformation indicate that there is no continuous significant correlation between them, which may be attributable to the long distance between the borehole and the point candidate of PSI; however many correlation cases are observed. An increase in subsidence accompanied the decline of the groundwater level during the periods April 1996–March 1997 and June 1999–October 1999, followed by a decrease in subsidence with the raising of the groundwater level during the periods October 1999–May 2000 and May 2000–April 2003. A subsequent increase in subsidence accompanied the decline of the groundwater level during the period April 2003–August 2003, followed by a status change from subsidence to uplift through the sharp rising trend of groundwater level during the period February 2004–April 2004.

3.7.6. SR72

The groundwater level behaviour corresponding to the monthly accumulation of precipitation based on the time series data of SAR PSI is depicted in Table 29 and Figure 87. The general behaviour of the groundwater level during the period 1995–2006 points to a decline, which may be attributable to non-compensation for the lost water. Note the absence groundwater level monitoring data for the periods June 1995, December 1997 and January 1999.

Details of the behaviour indicate a rise in groundwater level despite decreasing precipitation during the period December 1995–March 1997. This may be attributable either to some other source supplying the groundwater or to the gap in the data between the two monitoring records. This was followed by a decline in the groundwater level with decreasing precipitation during the period March 1997–May 1997. A subsequent decline of the groundwater level accompanied increasing precipitation during the period June 1999–October 1999, which may be attributable to insufficient precipitation to compensate for the water lost. This was followed by a rise the groundwater level that accompanied the decrease in precipitation during the period October 1999–May 2000. A decline in the groundwater level is observed with decreasing precipitation during the periods August 2003–April 2004 and April 2004–August 2004. A subsequent rise in the groundwater level accompanied increasing precipitation during the period August 2004–May 2005. This was followed by a decline in the groundwater level which accompanied decreasing precipitation during the period May 2005–August 2005.

Table 29. Monthly accumulation of precipitation corresponding to the groundwater level of the borehole SR72

Time series data of SAR PSI	Monthly amount of precipitation (mm)	Groundwater level (m) borehole SR72
Jun_1995	34.4	
Dec_1995	92.7	24.62
Apr_1996	22.3	20.6
Mar_1997	20.8	19.94
May_1997	17.6	21.7
Dec_1997	67.7	
Aug_1998	0.7	34
Jan_1999	45.4	
Jun_1999	5	25.7
Oct_1999	57.4	30.9
May_2000	25.7	23.1
Apr_2003	26.4	24.2
Aug_2003	5.3	34.08
Feb_2004	8.4	24.18
Apr_2004	43.5	23.72
Aug_2004	2.6	31.6
Sep_2004	20.1	30.32
May_2005	26.7	25.32
Aug_2005	16.4	36.04
Dec_2006	11.9	27.34

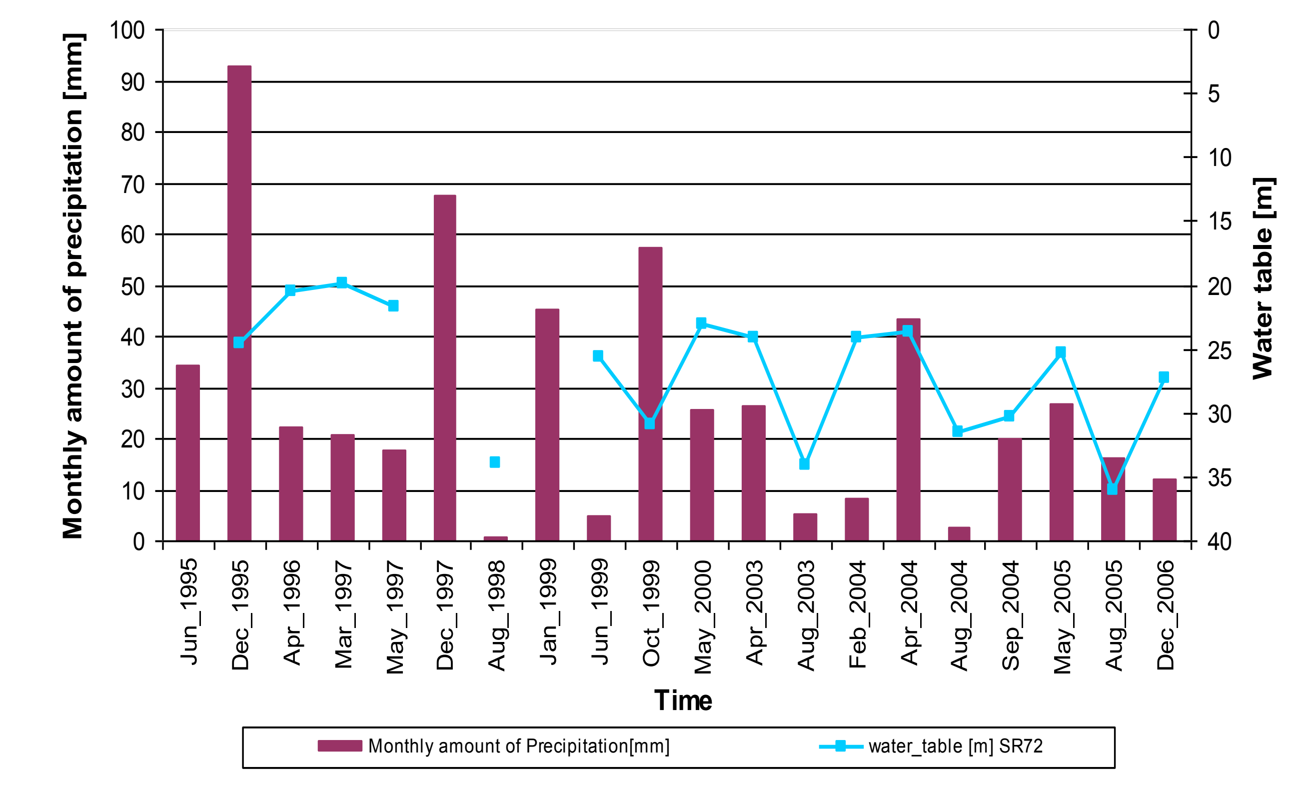

Figure 87. Monthly accumulation of precipitation corresponding to the groundwater level of the borehole SR72

3.7.6.1. Interference between land deformation and monthly precipitation as indirect impact on groundwater level (seasonal deformation) of the borehole SR72

Three point candidates resulting from the PSI technique have been chosen, with different distances between these points and borehole, as shown in Figure 88, to correlate, identify and examine the impact of groundwater level fluctuation on the land deformation. Deformation of the three point candidates, at distances of 322, 341 and 475 m from the borehole, monthly precipitation, and groundwater level are shown in Table 30. Deformation of point candidates and monthly precipitation are depicted in Figure 89. Deformation of point candidates and groundwater level are depicted in Figure 90.

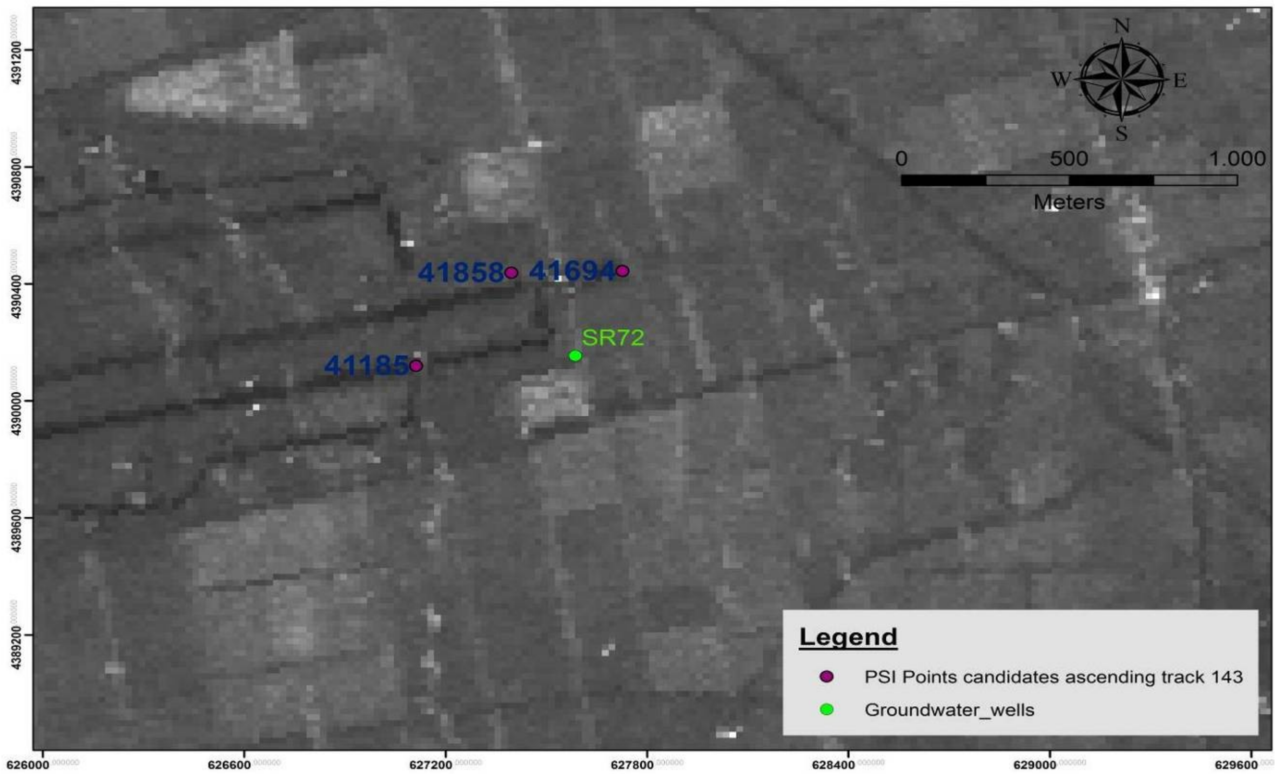

Figure 88. Three point candidates of the PSI at different distances from borehole SR72

Table 30. Ground deformation of point candidates of PSI ascending track (143) corresponding to groundwater level and monthly precipitation behaviour of borehole SR72

Time series data of SAR PSI	LOS Displacemnt mm p(41694) 322 m	LOS Displacemnt mm p(41858) 341 m	LOS Displacemnt mm p(41185) 475 m	Groundwater level (m) borehole SR72	Monthly amount of precipitation (mm)
Jun_1995	-149.104	-157.555	-71.145		34.4
Dec_1995	-141.293	-159.06	-75.945	24.62	92.7
Apr_1996	-143.183	-136.644	-62.937	20.6	22.3
Mar_1997	-130.062	-127.5	-65.038	19.94	20.8
May_1997	-115.989	-130.025	-71.573	21.7	17.6
Dec_1997	-113.706	-115.158	-60.453		67.7
Aug_1998	-101.637	-113.55	-52.816	34	0.7
Jan_1999	-99.388	-88.942	-47.388		45.4
Jun_1999	-80.519	-95.49	-46.329	25.7	5
Oct_1999	-79.505	-90.332	-41.558	30.9	57.4
May_2000	-78.529	-75.25	-29.145	23.1	25.7
Apr_2003	-21.231	-26.251	-19.265	24.2	26.4
Aug_2003	-8.196	-15.829	-14.28	34.08	5.3
Feb_2004	-14.19	-10.175	5.383	24.18	8.4
Apr_2004	-3.059	-1.419	-1.971	23.72	43.5
Aug_2004	5.669	-3.271	0.881	31.6	2.6
Sep_2004	4.243	1.863	-3.354	30.32	20.1
May_2005	3.712	16.967	5.924	25.32	26.7
Aug_2005	16.842	10.34	8.614	36.04	16.4
Dec_2006	33.334	40.273	18.254	27.34	11.9

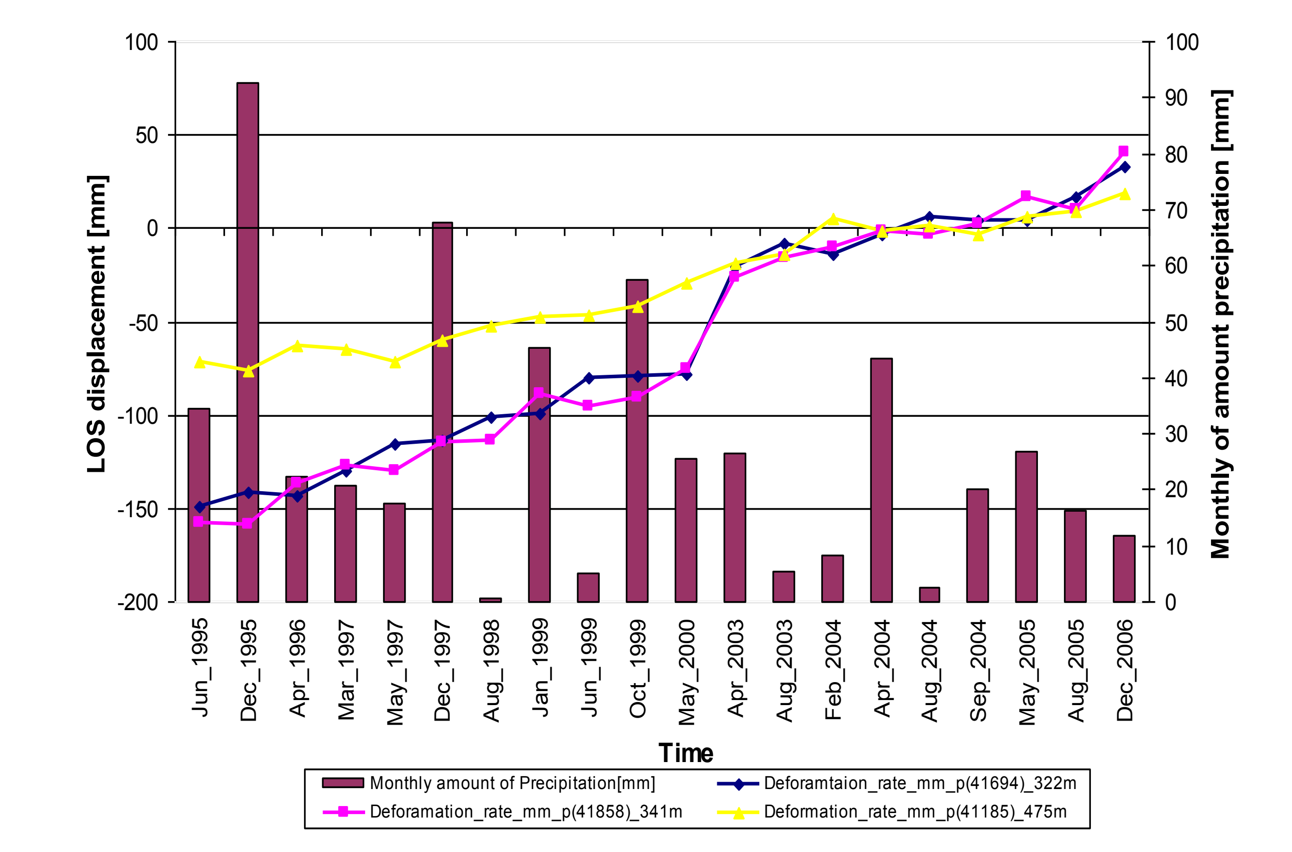

Figure.89 LOS Displacemnt of point candidates of PSI corresponding to monthly precipitation. Displacement time series of point candidates are rescaled to the first acquisition (i.e. 28 June 1995).

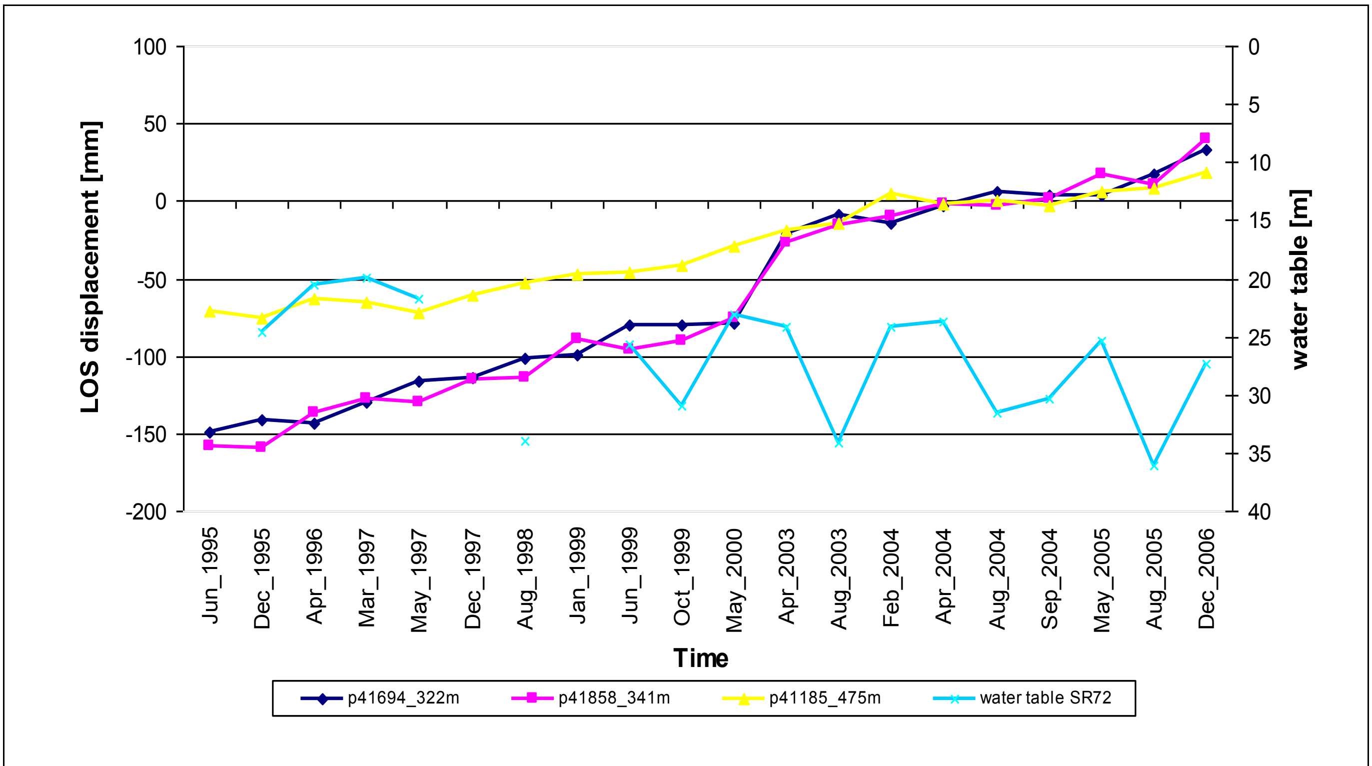

Figure 90. LOS Displacemnt of point candidates corresponding to groundwater level of borehole SR72. Displacement time series of point candidates are rescaled to the first acquisition (i.e. 28 June 1995).

The deformation behaviour of the first point (number 41694), at a distance of 322 m from the borehole, indicates to general rising trend, as the time series begins with subsidence and then goes into uplift. The minimum subsidence was -3.059 mm (April 2004) and the maximum subsidence was -149.104 mm (June 1995), while the minimum uplift was 3.712 mm (May 2005) and the maximum uplift was 33.334 mm (December 2006).

The minimum subsidence may be attributable to the indirect impact of precipitation (43.50 mm) on land deformation through its impact on the groundwater level, which was 23.72 m. Accordingly, the precipitation may have raised the groundwater level and consequently reduced the subsidence to the value found. Meanwhile the maximum subsidence may not be attributable to the indirect impact of precipitation (34.40 mm) on land deformation through its impact on the groundwater level, although no monitoring data were recorded during this month. This amount of precipitation may have been insufficient to raise the groundwater level and consequently to reduce the subsidence to a value less than that found; therefore some other factor may have participated in causing this subsidence.

The minimum uplift may not be attributable to the indirect impact of precipitation (26.70 mm) on land deformation through its impact on the groundwater level, which was 25.32 m, because this low amount of precipitation may not have been enough to raise the groundwater level accordingly. This low groundwater level should be accompanied by subsidence. Similarly, the maximum uplift may not be attributable to the indirect impact of precipitation amount (11.9 mm) on the groundwater level, which was (27.32 m), on the basis that such a low precipitation amount and this groundwater level should accompany either low uplift or subsidence; therefore, it is expected that some other factor has caused this uplift.

Details of the impact of groundwater level on land deformation indicate that there is no continuous significant correlation between them, which may be due to the long distance between the borehole and point candidate of PSI; however, many correlation cases are observed. A decrease in subsidence accompanied the raising of the groundwater level during the period April 1996–March 1997. Another correlation is between the slow decrease in subsidence and the sharp rise of groundwater level during the period October 1999–May 2000. Additionally, a decrease in subsidence accompanied the raising of the groundwater level during the period February 2004–April 2004, and ultimately an increase in uplift is observed with the raising of the groundwater level during the period August 2005–December 2006.

The deformation behaviour of the second point (number 41858), at a distance of 341 m from the borehole, indicates a general rising trend, as the time series begins with subsidence and then goes into uplift. The minimum subsidence was -1.419 mm (April 2004) and the maximum subsidence was -159.06 mm (December 1995), while the minimum uplift was 1.863 mm (September 2004) and the maximum uplift was 40.237 mm (December 2006).

The minimum subsidence may be attributable to the indirect impact of precipitation (43.50 mm) on land deformation through its impact on the groundwater level, which was 23.72 m; the precipitation may have raised the groundwater level and consequently reduced the subsidence to the value found. The maximum subsidence may not be attributable to the indirect impact of precipitation amount (92.70 mm) on the groundwater level, which was 24.62 m; this reasoning is on the basis that accompanying this high amount of precipitation should be either uplift or a low value of subsidence. The amount of precipitation may not have been enough to raise the groundwater level, indicating that some other factor may have caused this subsidence.

The minimum uplift may not be attributable to the indirect impact of precipitation (20.10 mm) on land deformation through its impact on the groundwater level, which was 30.32 m, because such a low level of groundwater should be accompanied by subsidence. Accordingly, this uplift may have been induced by the participation of some other factor. Similarly, the maximum uplift may not be attributable to the indirect impact of precipitation amount (11.9 mm) on the groundwater level, which was 27.34 m, because such a low groundwater level should be accompanied by subsidence; therefore, there is a high probability this uplift was caused by the participation of some other factor.

Details of the impact of groundwater level on land deformation indicate that there is no continuous significant correlation between them, which may be due to the long distance between the borehole and point candidate of PSI; however many correlation cases are observed—more than the correlation cases for the first point, at distance 322

m. A decrease in subsidence accompanied the raising of the groundwater level during the period December 1995–March 1997, followed by an increase in subsidence as the groundwater level declined during the period March 1997–May 1997. Also observed was a decrease in subsidence with the raising of the groundwater level during the periods October 1999–May 2000 and February 2004–April 2004, followed by an increase in subsidence with a sharp decline in the groundwater level during the period April 2004–August 2004. Thereafter a status change from subsidence to uplift followed by increasing uplift accompanied the raising of the groundwater level during the periods August 2004–September 2004 and September 2004–May 2005. This was followed by a decrease in uplift with the decline of the groundwater level during the period May 2005–August 2005 and, ultimately, an increase in uplift with the raising of the groundwater level during the period August 2005–December 2006.

The deformation behaviour of the third point (number 41185), at a distance of 475 m from the borehole, indicates a general rising trend, as the time series curve begins with subsidence and then goes into uplift. There was a swap between subsidence and uplift during the period April 2004–May 2005 and eventually uplift is observed. The minimum subsidence was -1.971 mm (April 2004) and the maximum subsidence was -75.945 mm (December 1995), while the minimum uplift was 0.881 mm (August 2004) mm and the maximum uplift was 18.254 mm (December 2006).

The minimum subsidence may be attributable to the indirect impact of precipitation (43.50 mm) on land deformation through its impact on the groundwater level, which was 23.72 m. The precipitation may have raised the groundwater level and consequently reduced the subsidence to the value found. The maximum subsidence may not be attributable to the indirect impact of precipitation (92.70 mm) on the groundwater level, which was 24.62 m, because such a high amount of precipitation should be accompanied by either uplift or a low value of subsidence; on the other hand, there is high probability that this precipitation amount was enough to raise the groundwater level, so some other factor may have caused this subsidence.

The minimum uplift may be attributable to the indirect impact of precipitation (2.60 mm) on land deformation through its impact on the groundwater level, which was 27.34 m. This low amount of precipitation may not have been enough to raise the groundwater level and consequently has caused this minimum uplift. Additionally, the maximum uplift may not be attributable to the indirect impact of precipitation (11.9 mm) on the groundwater level, which was 27.34 m, because such a low groundwater level should be accompanied by subsidence. Therefore there is a high probability that this uplift was caused by the participation of some other factor. It is worth mentioning that the behaviours of minimum and maximum subsidence and maximum uplift of the second point candidate (number 41858) are identical to those of the third point (number 41185).

Details of the impact of groundwater level on land deformation indicate that there is no continuous significant correlation between them, which may be due to the long distance between the borehole and the point candidate of PSI; however, many correlation cases are observed. A decrease in subsidence accompanied the raising of the groundwater level during the period December 1995–April 1996, and an increase in subsidence accompanied the decline of the groundwater level during the period March 1997–May 1997. A decrease in subsidence along with the raising of the groundwater level is observed during the period October 1999–May 2000. There is another correlation between the status change from subsidence to uplift and the raising of the groundwater level during the period August 2003–February 2004, and there is a subsequent status change from subsidence to uplift with the raising of the groundwater level during the period September 2004–May 2005. Ultimately an increase in uplift accompanied the raising of the groundwater level during the period August 2005–December 2006.

3.7.7. SR77

The groundwater level behaviour corresponding to the monthly accumulation of precipitation based on the time series data of SAR PSI is depicted in Table 31 and Figure 91. The general behaviour of the groundwater level during 1995–2006 points to a decline, which may be due to the lack of compensation for the water lost. Note the absence of groundwater monitoring data for June 1995, December 1997 and January 1999. Details of the behaviour indicate a decline of the groundwater level with decreasing precipitation amount during the period December 1995–May 1997, while a decline of the groundwater level during the period June 1999–October 1999 accompanied an increasing amount of precipitation. This was followed by a rise in the groundwater level with increasing precipitation during the period May 2000–April

2003, and a subsequent decline of the groundwater level accompanied decreasing precipitation during the period April 2003–August 2003. Thereafter a rise in the groundwater level accompanied increasing precipitation during the period August 2003–April 2004, and subsequently a decline of the groundwater level accompanied the decreasing precipitation during the period April 2004–August 2004. A rise in the groundwater level accompanied increasing precipitation during the period August 2004–May 2005, and ultimately a decline of groundwater level was observed with the decrease in precipitation during the period May 2005–August 2005.

Table 31. Monthly accumulation of precipitation corresponding to the groundwater level of the borehole SR77

Time series data of SAR PSI	Monthly amount of precipitation (mm)	Groundwater level (m) borehole SR77
Jun_1995	34.4	
Dec_1995	92.7	21.68
Apr_1996	22.3	18.18
Mar_1997	20.8	19.88
May_1997	17.6	22.51
Dec_1997	67.7	
Aug_1998	0.7	36.43
Jan_1999	45.4	
Jun_1999	5	26.55
Oct_1999	57.4	29.64
May_2000	25.7	25.8
Apr_2003	26.4	24.1
Aug_2003	5.3	36.62
Feb_2004	8.4	24.88
Apr_2004	43.5	24.9
Aug_2004	2.6	32.42
Sep_2004	20.1	30.94
May_2005	26.7	28.83
Aug_2005	16.4	38.28
Dec_2006	11.9	27.9

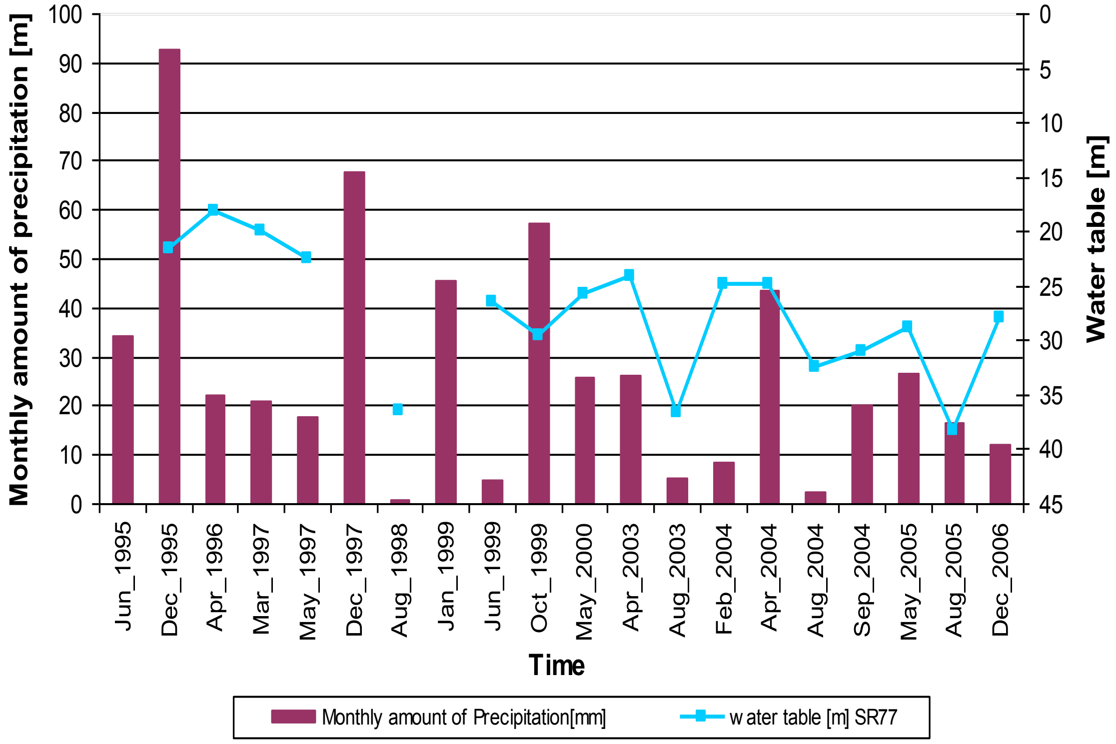

Figure 91. Monthly accumulation of precipitation corresponding to the groundwater level of the borehole SR77

3.7.7.1. Interference between land deformation and monthly precipitation as indirect impact on groundwater level (seasonal deformation) of the borehole SR77

Three point candidates resulting from the PSI technique have been chosen, with different distances between these points and the borehole, as shown in Figure 92, to correlate, identify and examine the impact of groundwater level fluctuation on the land deformation. Deformation of three point candidates, at distances of 293, 385 and 404 m from the borehole, the monthly amount of precipitation, and the groundwater level are shown in Table 32. The deformation of point candidates and the monthly precipitation are depicted in Figure 93. The deformation of point candidates and the groundwater level are depicted in Figure 94.

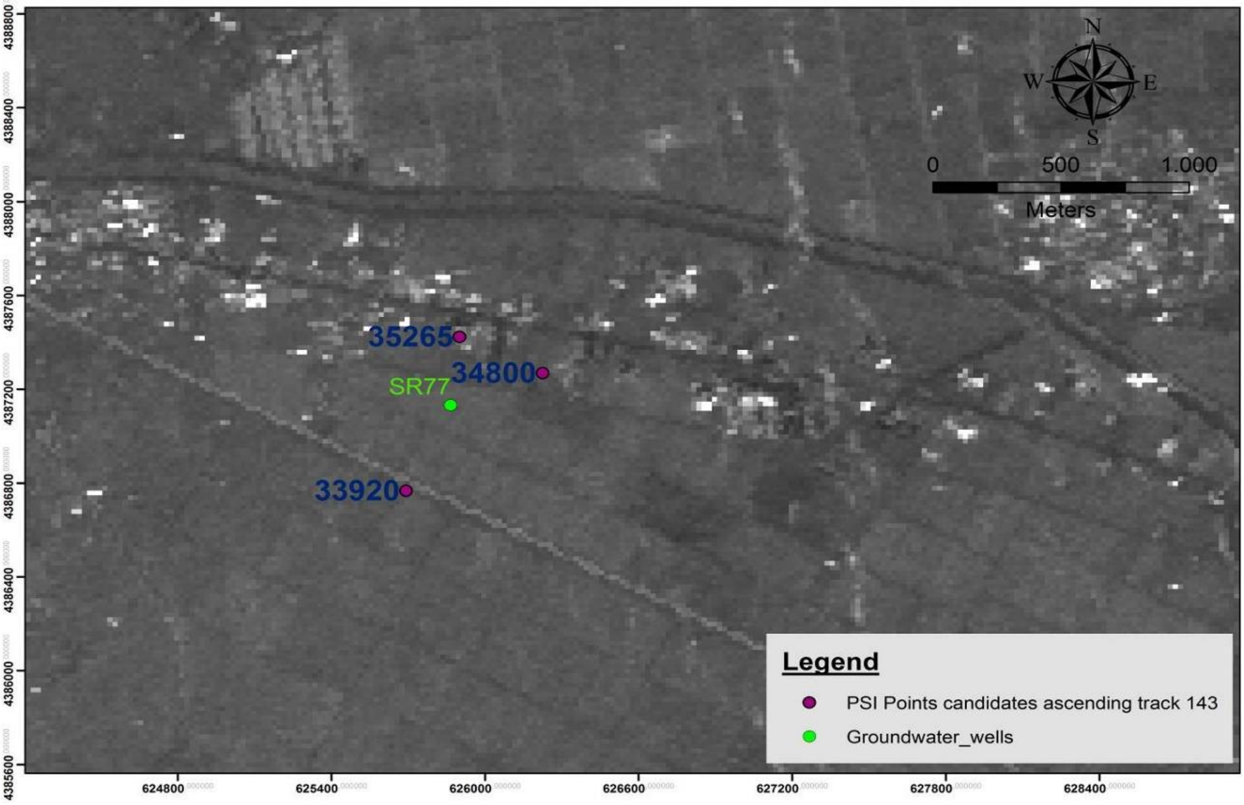

Figure .92 Three point candidates of the PSI at different distances from borehole SR77

Table 32. Ground deformation of point candidates of PSI ascending track (143) corresponding to groundwater level and monthly precipitation behaviour of borehole SR77

Time series data of SAR PSI	LOS Displacemnt mm p(35265) 293 m	LOS Displacemnt mm p(34800) 385 m	LOS Displacemnt mm p(33920) 404 m	Groundwater level (m) borehole SR77	Monthly amount of precipitation (mm)
Jun_1995	-169.359	-114.591	-231.129		34.4
Dec_1995	-150.87	-96.644	-217.016	21.68	92.7
Apr_1996	-157.328	-107.773	-207.436	18.18	22.3
Mar_1997	-132.53	-89.011	-186.302	19.88	20.8
May_1997	-124.532	-84.527	-175.443	22.51	17.6
Dec_1997	-109.571	-74.073	-172.73		67.7
Aug_1998	-98.985	-67.012	-151.508	36.43	0.7
Jan_1999	-92.682	-63.004	-151.643		45.4
Jun_1999	-99.151	-65.435	-129.893	26.55	5
Oct_1999	-93.806	-57.073	-118.338	29.64	57.4
May_2000	-77.929	-55.01	-107.695	25.8	25.7
Apr_2003	-26.344	-15.514	-32.363	24.1	26.4
Aug_2003	-13.199	-22.749	-27.73	36.62	5.3
Feb_2004	-10.508	-5.329	-7.613	24.88	8.4
Apr_2004	-11.573	-16.381	-5.116	24.9	43.5
Aug_2004	0.166	4.872	-11.792	32.42	2.6
Sep_2004	-1.393	0.548	-1.32	30.94	20.1
May_2005	6.314	13.385	19.025	28.83	26.7
Aug_2005	22.248	16.136	21.699	38.28	16.4
Dec_2006	38.909	25.684	58.088	27.9	11.9

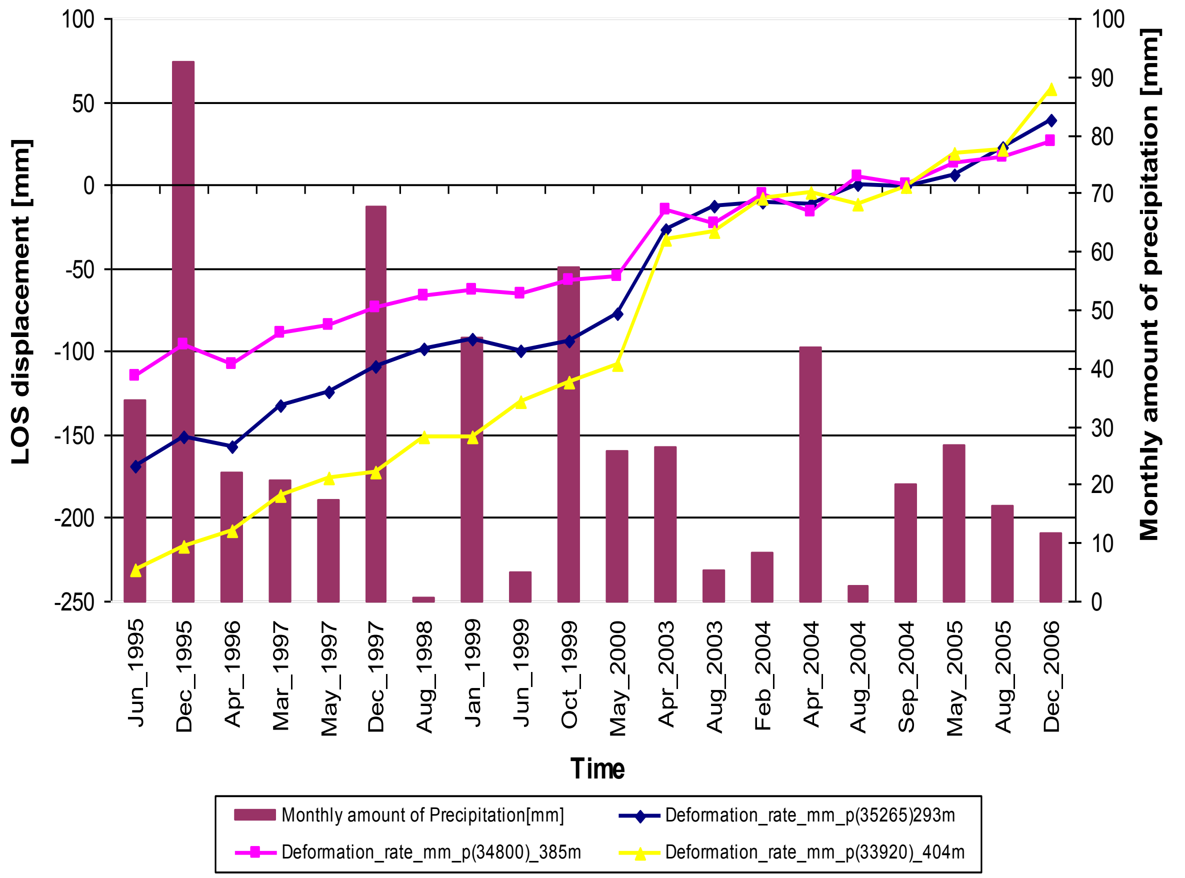

Figure 93. LOS Displacemnt of point candidates of PSI corresponding to monthly precipitation. Displacement time series of point candidates are rescaled to the first acquisition (i.e. 28 June 1995).

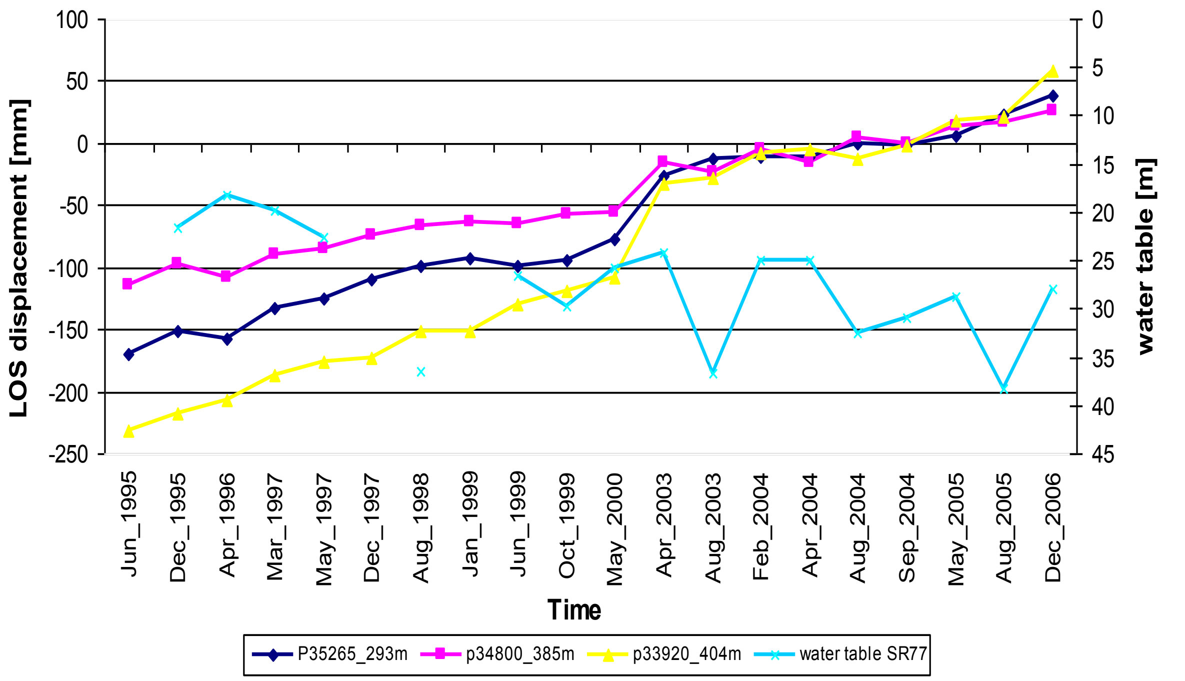

Figure 94. LOS Displacemnt of point candidates corresponding to groundwater level of borehole SR77. Displacement time series of point candidates are rescaled to the first acquisition (i.e. 28 June 1995).

The deformation behaviour of the first point (number 35265), at a distance of 293 m from the borehole, indicates to general rising trend, as the time series begins with subsidence and then goes into uplift. The minimum subsidence was -1.393 mm (September 2004) and the maximum subsidence was -169.359 mm (June 1995), while the minimum uplift was 0.166 mm (August 2004) and the maximum uplift was 38.909 mm (December 2006).

The minimum subsidence may be attributable to the indirect impact of precipitation (20.10 mm) on land deformation through its impact on the groundwater level, which was 30.94 m; accordingly, this amount of precipitation may have raised the groundwater level and consequently reduced the subsidence to the value found. The maximum subsidence may not be attributable to the indirect impact of precipitation (34.40 mm) on the groundwater level; however, there are no monitoring data records for this month. This amount of precipitation may have been enough to raise the groundwater level sufficiently to reduce subsidence to a value less than that found; accordingly, there is a probability that some other factor caused this high value of subsidence.

The minimum uplift may not be attributable to the indirect impact of precipitation (2.60 mm) on land deformation through its impact the on groundwater level, which was 32.40 m. It is probable that this low amount of precipitation was not enough to raise the groundwater level, and such a low groundwater level should be accompanied by subsidence. The maximum uplift may not be attributable to the indirect impact of precipitation 11.9 mm) on the groundwater level, which was 27.90 m, despite the fact that this amount of precipitation may have been enough to raise the groundwater level. However, this low groundwater level should have been accompanied by subsidence, not uplift. The uplift may have been caused by the participation of some other factor.
Details of the impact of groundwater level on land deformation indicate that there is no continuous significant correlation between them, which may be attributable to the long distance between the borehole and the point candidate of PSI; however many correlation cases are observed. Decreasing subsidence is observed with the raising of the groundwater level during the periods October 1999–May 2000 and May 2000–April 2003. The stability or the slowly decreasing subsidence may be attributable to the stability of the groundwater level during the period February 2004–April 2004.

Another correlation case is observed in the status change from subsidence to uplift through the raising of the groundwater level during the period September 2004–May 2005, and ultimately an increase in uplift is observed through the raising of the groundwater level during the period August 2005–December 2006.

The deformation behaviour of the second point (number 34800), at a distance of 385 m from the borehole, indicates a general rising trend, as the time series begins with subsidence and then goes into uplift. The minimum subsidence was -5.329 mm (February 2004) and the maximum subsidence was -114.591 mm (June 1995), while the minimum uplift was 0.548 mm (September 2004) and the maximum uplift was 25.684 mm (December 2006).

The minimum subsidence may not be attributable to the indirect impact of precipitation (8.40 mm) on land deformation through its impact on the groundwater level, which was 24.88 m. Accordingly, this amount of precipitation may not have been enough to raise the groundwater level and consequently caused the subsidence found The maximum subsidence may not be attributable to the indirect impact of precipitation (34.40 mm) on the groundwater level; however, there is an absence groundwater monitoring data records for this month. Nevertheless this amount of precipitation may have been enough to raise the groundwater level and consequently reduce the subsidence to a value less than that found; therefore there is considerable probability that some other factor participated in causing this high value of subsidence.

The minimum uplift may not be attributable to the indirect impact of precipitation (20.10 mm) on land deformation through its impact on the groundwater level, which was 30.94 m, because there is a considerable probability that this amount of precipitation was enough to raise the groundwater level more than was found. On the other hand, this groundwater level should be accompanied by subsidence. The maximum uplift also may not be attributable to the indirect impact of precipitation (11.9 mm) on the groundwater level, which was 27.90 m, because these values of precipitation amount and groundwater level should be accompanied by subsidence; therefore, some other factor may have participated in causing this uplift.

The details of the impact of groundwater level on land deformation indicate that there is no continuous significant correlation between them, which may be attributable to the long distance between the borehole and point candidate of PSI; however, many correlation cases are observed. Decreasing subsidence accompanied the raising of the groundwater level during the periods October 1999–May 2000 and May 2000–April 2003. This was followed by an increase in subsidence with the sharp declining trend of the groundwater level during the period April 2003–August 2003. An increase in uplift accompanied the raising of the groundwater level during the periods September 2004–May 2005 and August 2005–December 2006.

The deformation behaviour of the third point (number 33920), at a distance of 404 m from the borehole, indicates a general rising trend, as the time series begins with subsidence and then goes into uplift. The minimum subsidence was -1.32 mm (September 2004) and the maximum subsidence was -231.129 mm (June 1995), while the minimum uplift was 19.025 mm (May 2005) and the maximum uplift was 58.088 mm (December 2006).

The minimum subsidence may be attributable to the indirect impact of precipitation (20.10 mm) on land deformation through its impact on the groundwater level, which was 30.94 m. This amount of precipitation may not have been enough to raise the groundwater level and consequently caused the subsidence found. The maximum subsidence may not be attributable to the indirect impact of precipitation (34.40 mm) on the groundwater level; however, there are no groundwater level data monitoring records for this month. This amount of precipitation may have been enough to raise the groundwater level sufficiently to reduce the subsidence to a value less than that found; accordingly, it is probable that some other factor participated in causing this high value of subsidence.

The minimum uplift may not be attributable to the indirect impact of precipitation (26.70 mm) on land deformation through its impact on the groundwater level, which was 28.83 m, because this amount of precipitation was probably enough to raise the groundwater to a level higher than that found; therefore, some other factor may have participated in causing this uplift. The maximum uplift also may not be attributable to the indirect impact of precipitation (11.9 mm) on the groundwater level, which was 27.90 m, because this amount of precipitation may not have been enough to raise the groundwater level, and such a low groundwater level should be accompanied by subsidence. Some other factor may have participated in causing this uplift. It is worth mentioning that the correlation behaviour of point candidates and groundwater level is approximately identical for the three points, despite the difference in the distance of each point candidate from the borehole.

The details of the impact of groundwater level on land deformation indicate that there is no continuous significant correlation between them, which may be attributable to the long distance between the borehole and point candidate of PSI; however, many correlation cases are observed. Decreasing subsidence accompanied the raising of the groundwater level during the periods December 1995–April 1996, October 1999–May 2000, May 2000–April 2003 and August 2003–February 2004. This was followed by slowly decreasing subsidence which accompanied the stable groundwater level during the period February 2004–April 2004. Subsequently, an increase in subsidence is observed with the decline of the groundwater level during the period April 2004–August 2004. Thereafter decreasing subsidence followed by a status change from subsidence to uplift accompanied the rising groundwater level during the periods August 2004–September 2004 and September 2004–May 2005. Ultimately, an increase in uplift accompanied the raising of the groundwater level during the period August 2005–December 2006.

3.8. Descending track 279

Within this track the fluctuation of the groundwater level of just two boreholes has been correlated with the time series of ground deformation of the point candidates of PSI around these boreholes. No point candidates of PSI are observed around the other boreholes that have been examined within the ascending track. The two boreholes examined and correlated with land deformation within this track are SR72 and SR77.

3.8.1. SR72

The groundwater level behaviour corresponding to the monthly accumulation of precipitation based on the time series data of SAR PSI is depicted in Table 33 and Figure 95. The general behaviour of the groundwater level during 1992–2010 points to decline, which may be attributable to the non-compensation for the water lost. Note the absence of groundwater monitoring data records for June 1995, July 1995, January

1998, January 2000, October 2006, July 2008, and December 2008. Details of the behaviour of groundwater level point to decline and rising through the increasing and decreasing amounts of precipitation during the period November 1992–April 1995. Raising of the groundwater level is observed with the increasing amount of precipitation during the period August 1995–March 1996, followed by a decline of the groundwater level with decreasing precipitation during the period April 1996–June 1996. A subsequent rise of the groundwater level accompanied increasing precipitation during the period September 1996–December 1996. An increase in groundwater level, followed by stability, during the period January 1997–June 1997 may not be attributable to the impact of precipitation amount. This was followed by a decline of the groundwater level with a decrease in the amount of precipitation during the period July 1997–September 1997. Thereafter a rise in groundwater level accompanied the increase in precipitation amount during the period September 1997–May 1998. Subsequently, a decline and rise of the groundwater level are observed during the periods May 1998–September 1998 and September 1998–February 1999. A decline of the groundwater level accompanied decreasing precipitation during the periods February 1999–June 1999, September 1999–October 1999 and June 2003–November 2003, followed by a rise in groundwater level with increasing precipitation during the period November 2003–March 2005. Subsequently, a decline of the groundwater level with decreasing precipitation is observed during the period March 2005–April 2005; however, a decline in the groundwater level during the period May 2005–September 2005 is not attributable to the fluctuation of precipitation amount during this period. This was followed by raising of the groundwater level with increasing precipitation during the period September 2005–December 2005. Thereafter a decline of the groundwater level with decreasing precipitation is observed during the period February 2006–July 2006. Note that the correlation behaviour between groundwater level and precipitation amount is more obvious within the time series 1992–2010 than within the time series 1995–2006 for the same borehole. This may be attributable to the large number of data within this time series (1992–2010).

Table 33. Monthly accumulation of precipitation corresponding to the groundwater level of the borehole SR72

Time series data of SAR PSI	Monthly amount of precipitation (mm)	Groundwater level (m) borehole SR 72
Nov_1992	62	21.58
Oct_1993	9.1	27.12
Mar_1995	32.7	20.47
Apr_1995	18.1	20.16
Jun_1995	34.4	
Jul_1995	31	
Aug_1995	12.3	31.55
Sep_1995	24	29.78
Oct_1995	7.8	28.05
Dec_1995	92.7	24.62
Mar_1996	61.9	20.62
Apr_1996	22.3	20.6
May_1996	9	22.4
Jun_1996	0.3	24.78
Sep_1996	63.7	30.08
Oct_1996	70	28.03
Nov_1996	30.9	26.39
Dec_1996	50	25.46
Jan_1997	31.4	22.22
Feb_1997	14.5	21.05
May_1997	17.6	21.7
Jun_1997	30.7	21.62
Jul_1997	1.4	27.62
Sep_1997	1.4	28.21
Nov_1997	18.1	25.76
Jan_1998	17.1	
May_1998	131.5	22.51
Jun_1998	7	22.52
Sep_1998	37.1	32.09
Feb_1999	55.8	22.9
Jun_1999	5	25.7
Sep_1999	23.9	33.76
Oct_1999	57.4	30.9
Jan_2000	14.1	
Mar_2003	20.1	25
Jun_2003	33.2	25.6
Nov_2003	8.3	29
Feb_2005	47.6	23.89
Mar_2005	64.1	23.1
Apr_2005	5.7	24.13
May_2005	26.7	25.32
Sep_2005	44.8	33.7
Dec_2005	66.8	28.2
Feb_2006	38.8	25.6
Jul_2006	28	29.45
Oct_2006	106.1	

Supplement of Table 33. Monthly accumulation of precipitation corresponding to the groundwater level of the borehole SR72

Time series data of SAR PSI	Monthly amount of precipitation (mm)	Groundwater level (m) borehole SR 72
Feb_2007	29.5	25.12
Aug_2007	25.1	37.55
Apr_2008	42	26.68
Jul_2008	18.6	
Dec_2008	62.3	
Jan_2009	85.8	28.22
Feb_2009	14.4	27.48
Oct_2010	111.6	20.73

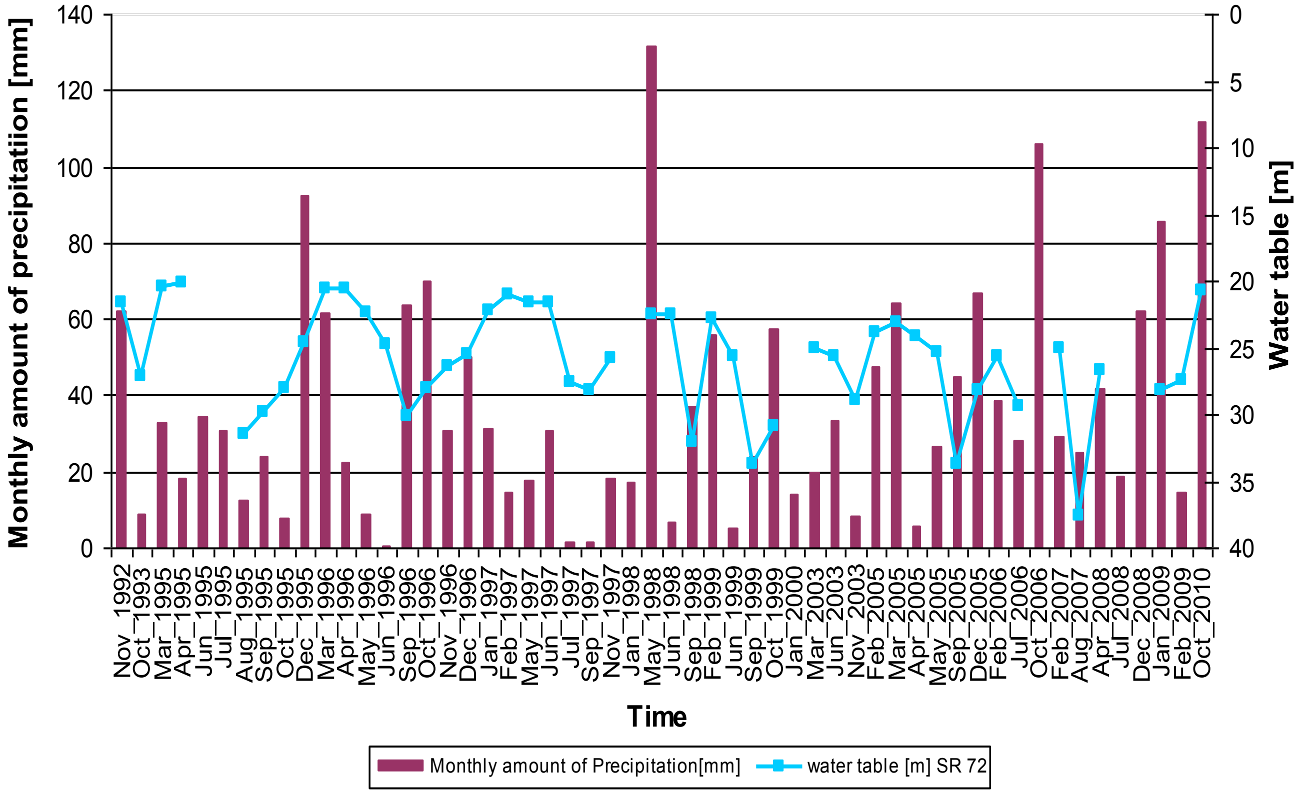

Figure 95. Monthly accumulation of precipitation corresponding to the groundwater level of the borehole SR72

3.8.1.1. Interference between land deformation and monthly amount of precipitation as indirect impact on groundwater level (seasonal deformation) of the borehole SR72

Three point candidates resulting from the PSI technique have been chosen, with different distances between these points and the borehole, as shown in Figure 96, to correlate, identify and examine the impact of groundwater level fluctuation on the land deformation. The deformation of three point candidates, at distances of 0.799, 1.864 and 2.584 km from the borehole, monthly amount of precipitation, and groundwater level are shown in Table 34. The deformation of point candidates and monthly precipitation amount are depicted in Figure 97. The deformation of point candidates and the groundwater level are depicted in Figure 98.

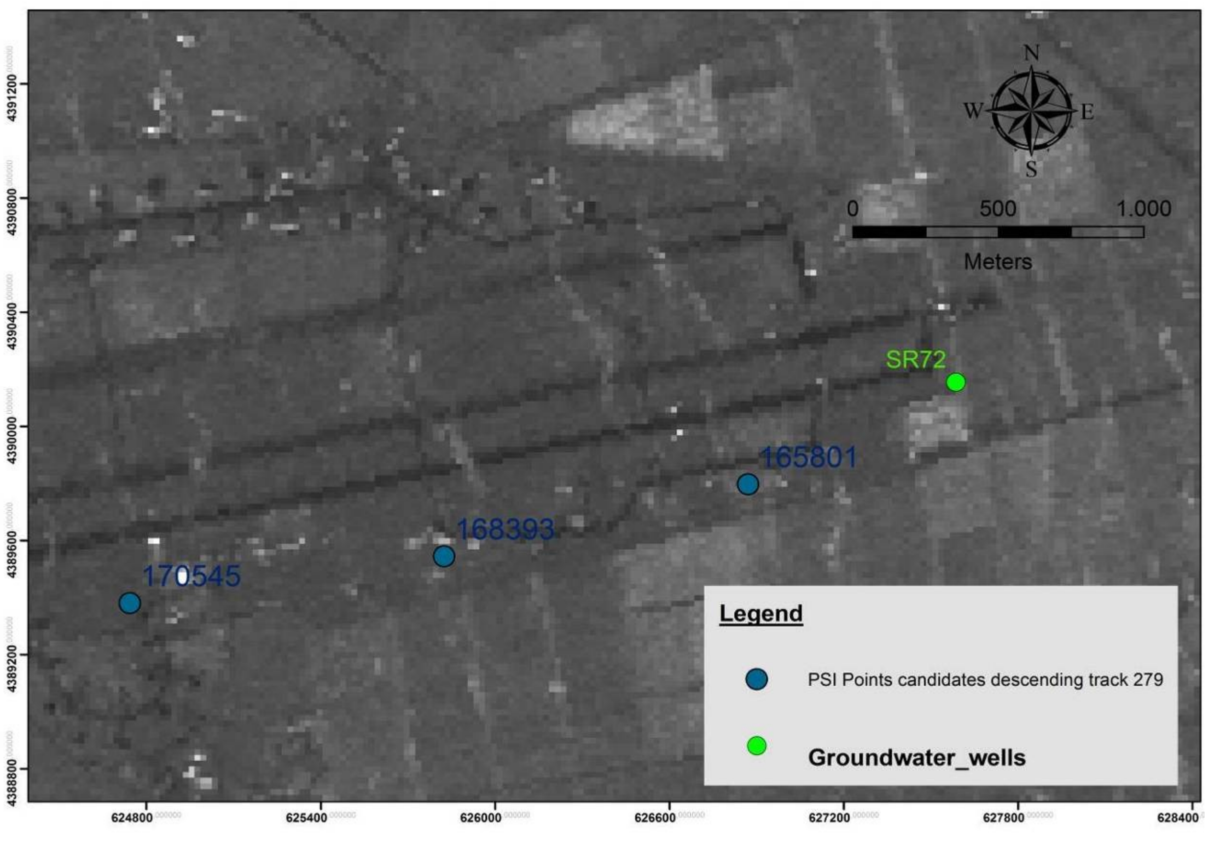

Figure.96 Three point candidates of the PSI at different distances from borehole SR72

Table 34. Ground deformation of point candidates of PSI descending track (279) corresponding to groundwater level and monthly precipitation behaviour of borehole SR72

Time series data of SAR PSI	LOS Displacemnt mm p (165801) 799.17 m	LOS Displacemnt mm p (168393) 1.864 m	LOS Displacemnt mm p (170545) 2.548 m	Groundwater level (m) borehole SR72	Monthly amount of precipitation (mm)
Nov_1992	-80.92	-88.87	95.275	21.58	62
Oct_1993	-78.952	-79.903	80.175	27.12	9.1
Mar_1995	-72.17	-72.435	76.872	20.47	32.7
Apr_1995	-64.074	-69.946	81.156	20.16	18.1
Jun_1995	-63.155	-60.672	78.94		34.4
Jul_1995	-73.224	-68.867	80.345		31
Aug_1995	-61.486	-67.553	70.273	31.55	12.3
Sep_1995	-63.295	-70.396	75.643	29.78	24
Oct_1995	-76.387	-58.474	77.888	28.05	7.8
Dec_1995	-57.464	-69.078	78.059	24.62	92.7
Mar_1996	-74.666	-69.523	71.027	20.62	61.9
Apr_1996	-68.955	-60.897	73.322	20.6	22.3
May_1996	-72.879	-61.475	78.697	22.4	9
Jun_1996	-67.79	-60.702	66.32	24.78	0.3
Sep_1996	-72.565	-57.663	61.314	30.08	63.7
Oct_1996	-73.28	-56.384	60.084	28.03	70
Nov_1996	-63.577	-65.366	59.787	26.39	30.9
Dec_1996	-65.545	-50.285	65.126	25.46	50
Jan_1997	-70.279	-66.155	66.378	22.22	31.4
Feb_1997	-62.327	-56.286	70.803	21.05	14.5
May_1997	-56.07	-50.144	70.538	21.7	17.6
Jun_1997	-68.38	-56.153	62.027	21.62	30.7
Jul_1997	-57.917	-67.659	59.372	27.62	1.4
Sep_1997	-49.168	-63.056	55.503	28.21	1.4
Nov_1997	-61.554	-53.289	58.754	25.76	18.1
Jan_1998	-60.168	-55.692	57.811		17.1
May_1998	-48.964	-66.826	56.837	22.51	131.5
Jun_1998	-56.917	-50.872	47.189	22.52	7
Sep_1998	-57.332	-48.327	63.607	32.09	37.1
Feb_1999	-45.585	-55.395	40.771	22.9	55.8
Jun_1999	-55.653	-47.234	52.464	25.7	5
Sep_1999	-50.446	-51.415	51.316	33.76	23.9
Oct_1999	-45.815	-49.652	50.769	30.9	57.4
Jan_2000	-46.189	-45.374	56.432		14.1
Mar_2003	-23.095	-22.67	33.888	25	20.1
Jun_2003	-27.792	-29.593	32.523	25.6	33.2
Nov_2003	-29.884	-27.966	27.64	29	8.3
Feb_2005	-29.942	-23.959	23.52	23.89	47.6
Mar_2005	-19.65	-20.54	29.604	23.1	64.1
Apr_2005	-15.611	-18.921	22.3	24.13	5.7
May_2005	-23.456	-26.895	21.731	25.32	26.7
Sep_2005	-20.147	-10.901	12.604	33.7	44.8
Dec_2005	-9.93	-16.296	8.024	28.2	66.8
Feb_2006	-9.325	-13.309	20.875	25.6	38.8
Jul_2006	-13.815	-6.275	16.351	29.45	28
Oct_2006	0.628	-16.693	6.328		106.1

Supplement of Table 34. Ground deformation of point candidates of PSI descending track (279) corresponding to groundwater level and monthly precipitation behaviour of borehole SR72

Time series data of SAR PSI	LOS Displacemnt mm p (165801) 799.17 m	LOS Displacemnt mm p (168393) 1.864 m	LOS Displacemnt mm p (170545) 2.548 m	Groundwater level (m) borehole SR72	Monthly amount of precipitation (mm)
Feb_2007	-7.463	-2.272	8.158	25.12	29.5
Aug_2007	-5.017	-7.252	-0.041	37.55	25.1
Apr_2008	7.298	0.949	6.237	26.68	42
Jul_2008	1.184	4.509	-2.439		18.6
Dec_2008	-7.309	5.548	-8.56		62.3
Jun_2009	-3.691	-1.572	-0.883	28.22	85.8
Feb_2009	9.645	12.003	-0.06	27.48	14.4
Oct_2010	15.839	14.039	-19.971	20.73	111.6

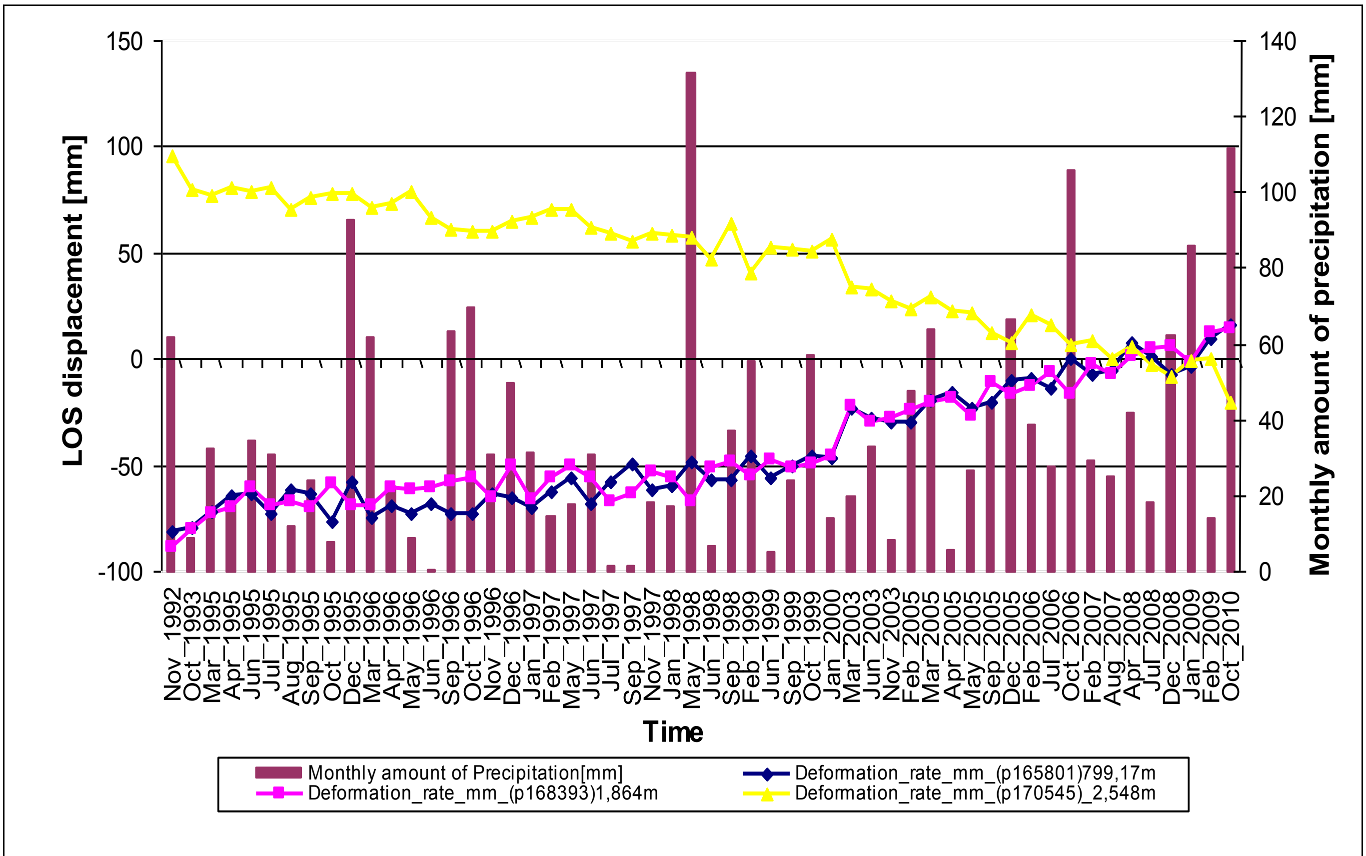

Figure 97. LOS Displacemnt of point candidates of PSI corresponding to monthly precipitation. Displacement time series of point candidates are rescaled to the first acquisition (i.e. 12 Nov 1992).

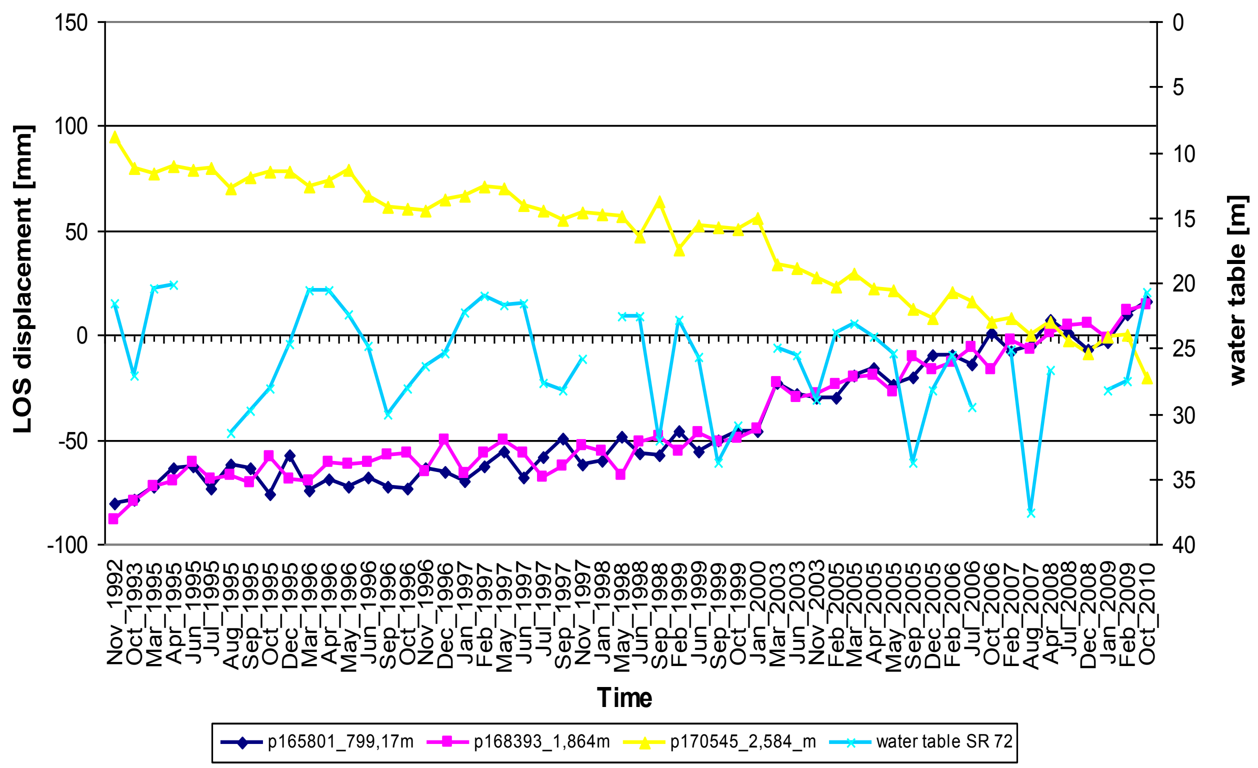

Figure .98 LOS Displacemnt of point candidates corresponding to groundwater level of borehole SR72. Displacement time series of point candidates are rescaled to the first acquisition (i.e. 12 Nov 1992).

The deformation behaviour of the first point (number 165801), at a distance of 799 m from the borehole, indicates a general rising trend, as the time series begins with subsidence and then goes into uplift; however, a swap between subsidence and uplift is observed during the period August 2007–October 2010. The minimum subsidence was -3.69 mm (January 2009) and the maximum subsidence was -80.92 mm (November 1992), while the minimum uplift was 0.628 mm (October 2006) and the maximum uplift was 15.839 mm (October 2010).

The minimum subsidence may not be attributable to the indirect impact of precipitation (85.80 mm) on land deformation through its impact on the groundwater level, which was 28.22 m, because this amount of precipitation may have been enough to raise the groundwater level higher than the level found; however, groundwater withdrawal may have exceeded the precipitation amount, and consequently it was not enough to recharge the aquifer or to raise the groundwater level. Consequently, the decline of groundwater caused this subsidence. The maximum subsidence may not be attributable to the indirect impact of precipitation

(62 mm) on the groundwater level, which was 21.28 m, because this precipitation amount may have been enough to raise the groundwater level sufficiently to reduce subsidence to a value less than that found. Accordingly, there is a considerable probability that some other factor participated in causing this high value of subsidence.

The minimum uplift may be attributable to the indirect impact of precipitation (106.10 mm) on land deformation through its impact on the groundwater level; however, there are no groundwater level monitoring data records for this month. Nevertheless, there is a considerable probability that this precipitation amount may have raised the groundwater level and consequently caused this uplift. The maximum uplift may not be attributable to the indirect impact of precipitation (111.6 mm) on the groundwater level, which was 20.73 m, because this precipitation amount may have been enough to raise the groundwater to a level higher than that found. Accordingly, some other factor may have participated in causing this uplift. Another acceptable reasoning is that this low groundwater level should be accompanied by a smaller amount of uplift than that found or subsidence.

Details of the impact of groundwater level on land deformation indicate a non-continuous significant correlation between them, which may be attributable to the long distance between the borehole and the point candidate of PSI; nevertheless, many correlation cases are observed, which may be attributable to the large expansion in the number of data within this time series (1992–2010). Decreasing subsidence is observed with the raising of the groundwater level during the period October 1995–December 1995. Thereafter an increase in subsidence accompanied the decline of the groundwater level during the periods April 1996–May 1996 and June 1996–September 1996. A subsequent decrease in subsidence accompanied the raising of the groundwater level during the periods October 1996–November 1996 and January 1997–February 1997. A small increase in subsidence accompanied the sharp decline of the groundwater level during the period June 1998–September 1998, followed by a decrease in subsidence with the raising of the groundwater level during the period September 1998–February 1999. An increase in subsidence accompanied the decline of the groundwater level during the period February 1999–June 1999, followed by a decrease in subsidence with the raising of the groundwater level during the period September 1999–October 1999. There was another increase in subsidence with the decline of the groundwater level during the periods March 2003–June 2003, June 2003–November 2003 and April 2005–May 2005, while a decrease in subsidence accompanied the raising of the groundwater level during the periods September 2005–December 2005 and December 2005–February 2006. A subsequent increase in subsidence is observed with the decline of the groundwater level during the period February 2006–July 2006, and a status change from uplift to subsidence is observed with the sharp decline of the groundwater level during the period October 2006–February 2007. Another status change from subsidence to uplift is observed with the raising of the groundwater level during the period August 2007–April 2008, while a decrease in subsidence followed by a status change form subsidence to uplift and a subsequent increase in uplift are observed with the raising of the groundwater level during the periods January 2009–February 2009 and February 2009–October 2010.

The deformation behaviour of the second point (number 168393), at a distance of 1.680 km from the borehole, indicates a general rising trend, as the time series begins with subsidence and then goes into uplift; however, a swap between subsidence and uplift is observed during the period April 2008–October 2010.

The minimum subsidence was -1.572 mm (January 2009) and the maximum subsidence was -88.87 mm (November 1992), while the minimum uplift was 0.949 mm (April 2008) and the maximum uplift was 14.039 mm (October 2010).

The minimum subsidence may not be attributable to the indirect impact of precipitation (85.80 mm) on land deformation through its impact on the groundwater level, which was 28.22 m, because this amount of precipitation may have been enough to raise the groundwater to a higher level than that found and consequently reduce the subsidence to a value less than that or cause uplift. However, groundwater withdrawal may have exceeded the precipitation amount, resulting in this subsidence. The maximum subsidence also may not be attributable to the indirect impact of precipitation (62 mm) on the groundwater level, which was 21.58 m, because this amount of precipitation may have been enough to raise the groundwater level and consequently reduce subsidence to a value less than that found. It is possible that groundwater withdrawal exceeded the precipitation amount, consequently resulting in subsidence; nevertheless, there is considerable probability that this high value of subsidence during this short period was caused by the participation of some other factor.

The minimum uplift may not be attributable to the indirect impact of precipitation (42 mm) on land deformation through its impact on the groundwater level, which was 26.68 m, because although this amount of precipitation may have been enough to raise the groundwater level, groundwater withdrawal exceeded this precipitation amount and consequently the groundwater level declined. This groundwater level should be accompanied by subsidence or a smaller amount of uplift; therefore, some other factor may have participated in causing this uplift. The maximum uplift also may not be attributable to the indirect impact of precipitation (111.6 mm) on the groundwater level, which was 20.73 m, because although this amount of precipitation may have been enough to raise the groundwater level to a higher level than was found, groundwater withdrawal may have exceeded this precipitation amount resulting in an overall decline in groundwater level. Consequently some other factor may have participated in causing this uplift. It is worth mentioning that the minimum and maximum subsidence and uplift behaviour is identical to that of the first point candidate (number 165801).

Details of the impact of groundwater level on land deformation indicate the non-continuous significant correlation between them, which may be attributable to the long distance between the borehole and the point candidate of PSI; however, many correlation cases are observed, which may be attributable to the large expansion in the number of data within the time series 1992–2010. An increase in uplift accompanied the raising of the groundwater level during the periods March 1995–April 1995, September 1995–October 1995, September 1996–October 1996, and November 1996–December 1996, followed by an increase in subsidence with the decline of the groundwater level during the period June 1997–July 1997. Subsequently, a decrease in subsidence accompanied the raising of the groundwater level during the period September 1997–November 1997, and an increase in subsidence accompanied the decline of the groundwater level during the period June 1999–September 1999. This was followed by a decrease in subsidence with the raising of the groundwater level during the period September 1999–October 1999 and a subsequent increase in subsidence with the decline of the groundwater level during the period March 2003–June 2003. Thereafter a decrease in subsidence accompanied the raising of the groundwater level during the periods November 2003–February 2005 and February 2005–March 2005. An increase in subsidence accompanied the decline of the groundwater level during the period April 2005–May 2005, followed by a decrease in subsidence with the raising of the groundwater level during the period December 2005–February 2006. A status change from subsidence to uplift is observed with the raising of the groundwater level during the period August 2007–April 2008, and a similar case is observed during the period January 2009–February 2009. Ultimately, an increase in uplift accompanied the raising of the groundwater level during the period February 2009–October 2010.

The deformation behaviour of the third point (number 170545), at a distance of 2.584 km from the borehole, indicates a general declining trend, as the time series begins with uplift and then goes into subsidence; however, a swap between uplift and subsidence is observed during the period April 2008–October 2010. The minimum uplift was 6.237 mm (April 2008) and the maximum uplift was 95.275 mm (November 1992), while the minimum subsidence was -0.041 mm (August 2007) and the maximum subsidence was -19.971 mm (October 2010).

The minimum uplift may not be attributable to the indirect impact of precipitation (42 mm) on land deformation through its impact on the groundwater level, which was 26.68 m, because although this amount of precipitation may have been enough to raise the groundwater level, groundwater withdrawal may have exceeded this precipitation amount resulting in a decline of the groundwater; consequently, this groundwater level should be accompanied by subsidence or a smaller amount of uplift. Some other factor may have participated in causing this uplift. The maximum uplift also may not be attributable to the indirect impact of precipitation (62 mm) on land deformation through its impact on the groundwater level, which was 21.58 m, because although this amount of precipitation may have been enough to raise the groundwater level higher than the level recorded, groundwater withdrawal may have exceeded this precipitation amount, resulting in a decline in the groundwater level. Consequently, some other factor may have participated in causing this uplift.

The minimum subsidence may be attributable to the indirect impact of precipitation (25.10 mm) on land deformation through its impact on the groundwater level, which was 37.55 m. This amount of precipitation may not have been enough to raise the groundwater level, and consequently the decline of the groundwater level caused this subsidence. On the contrary, the maximum subsidence may not be attributable to the indirect impact of precipitation (111.60 mm) on land deformation through its impact on the groundwater level, which was 20.73 m, despite the probability that groundwater withdrawal exceeded the precipitation amount and resulted in subsidence. There is considerable probability that such a high value of subsidence during this short period was caused by the participation of some other factor.

Details of the impact of the groundwater level on land deformation indicate a non-continuous significant correlation between them, which may be attributable to the long distance between the borehole and the point candidate of PSI; however, many correlation cases are observed, which may be due to the large expansion in the number of data within this time series (1992–2010). A decrease in uplift accompanied the decline of the groundwater level during the period November 1992–October 1993, while a subsequent increase in uplift is observed through the raising of the groundwater level during the periods March 1995–April 1995, August 1995–September 1995, and October 1995–December 1995. This was followed by a decrease in uplift, which accompanied the decline of the groundwater level during the periods May 1996–June 1996 and June 1996–September 1996. Thereafter an increase in uplift accompanied the raising of the groundwater level during the periods November 1996–December 1996 and January 1997–February 1997, followed by a decrease in uplift with the decline of the groundwater level during the periods February 1997–May 1997, June 1997–July 1997 and July 1997–September 1997. An increase in uplift is observed once again with the raising of the groundwater level during the period September 1997–November 1997, while a subsequent decrease in uplift accompanied the decline of the groundwater level during the periods June 1999–September 1999, March 2003–June 2003 and June 2003–November 2003. Thereafter an increase in uplift is observed with the raising of the groundwater level during the period February 2005–March 2005, followed by a decrease in uplift with the decline of the groundwater level during the periods March 2005–April 2005 and May 2005–September 2005. An increase in uplift accompanied the raising of the groundwater level during the period December 2005–February 2006, followed by a decrease in uplift with the decline of the groundwater level during the period February 2006–July 2006. A status change from uplift to subsidence is observed with the sharp decline in the groundwater level during the period February 2007–August 2007, followed by another status change from subsidence to uplift with the sharp raising of the groundwater level during the period August 2007–April 2008. Ultimately, a decrease in subsidence is observed with the raising of the groundwater level during the period January 2009–February 2009.

3.8.2. SR77

The groundwater level behaviour corresponding to the monthly accumulation of precipitation based on the time series data of SAR PSI is depicted in Table 35 and Figure 99. The general behaviour of the groundwater level during 1992–2010 points to a decline, which may be attributable to non-compensation for the water lost through withdrawal of groundwater. Note the absence of groundwater data for June and July 1995, January 1998 and 2000, October 2006, and July and December 2008. It is worth mentioning that the behaviour of this borehole is identical to that of borehole SR72.

Table 35. Monthly accumulation of precipitation corresponding to the groundwater level of the borehole SR77

Time series data of SAR PSI	Monthly amount of precipitation (mm)	Groundwater level (m) borehole SR 77
Nov_1992	62	18.48
Oct_1993	9.1	23.6
Mar_1995	32.7	18.45
Apr_1995	18.1	18.68
Jun_1995	34.4	
Jul_1995	31	
Aug_1995	12.3	34.03
Sep_1995	24	28.48
Oct_1995	7.8	25.52
Dec_1995	92.7	21.68
Mar_1996	61.9	18.5
Apr_1996	22.3	18.18
May_1996	9	23.48
Jun_1996	0.3	26.17
Sep_1996	63.7	29.75
Oct_1996	70	25.96
Nov_1996	30.9	23.77
Dec_1996	50	22.6
Jan_1997	31.4	21.05
Feb_1997	14.5	20.22
May_1997	17.6	22.51
Jun_1997	30.7	22.62
Jul_1997	1.4	31.7
Sep_1997	1.4	28.48
Nov_1997	18.1	24.13
Jan_1998	17.1	
May_1998	131.5	22.91
Jun_1998	7	21.74
Sep_1998	37.1	31.26
Feb_1999	55.8	22.25
Jun_1999	5	26.55
Sep_1999	23.9	34.53
Oct_1999	57.4	29.64
Jan_2000	14.1	
Mar_2003	20.1	24.15
Jun_2003	33.2	27.36
Nov_2003	8.3	28.58
Feb_2005	47.6	24.16
Mar_2005	64.1	23.72
Apr_2005	5.7	24.47
May_2005	26.7	28.83
Sep_2005	44.8	34.54

Supplement of Table 35. Monthly accumulation of precipitation corresponding to the groundwater level of the borehole SR77

Time series data of SAR PSI	Monthly amount of precipitation (mm)	Groundwater level (m) borehole SR 77
Dec_2005	66.8	28.2
Feb_2006	38.8	26.03
Jul_2006	28	32.43
Oct_2006	106.1	
Feb_2007	29.5	25.88
Aug_2007	25.1	38.63
Apr_2008	42	27.95
Jul_2008	18.6	
Dec_2008	62.3	
Jan_2009	85.8	28.98
Feb_2009	14.4	28.2
Oct_2010	111.6	20.73

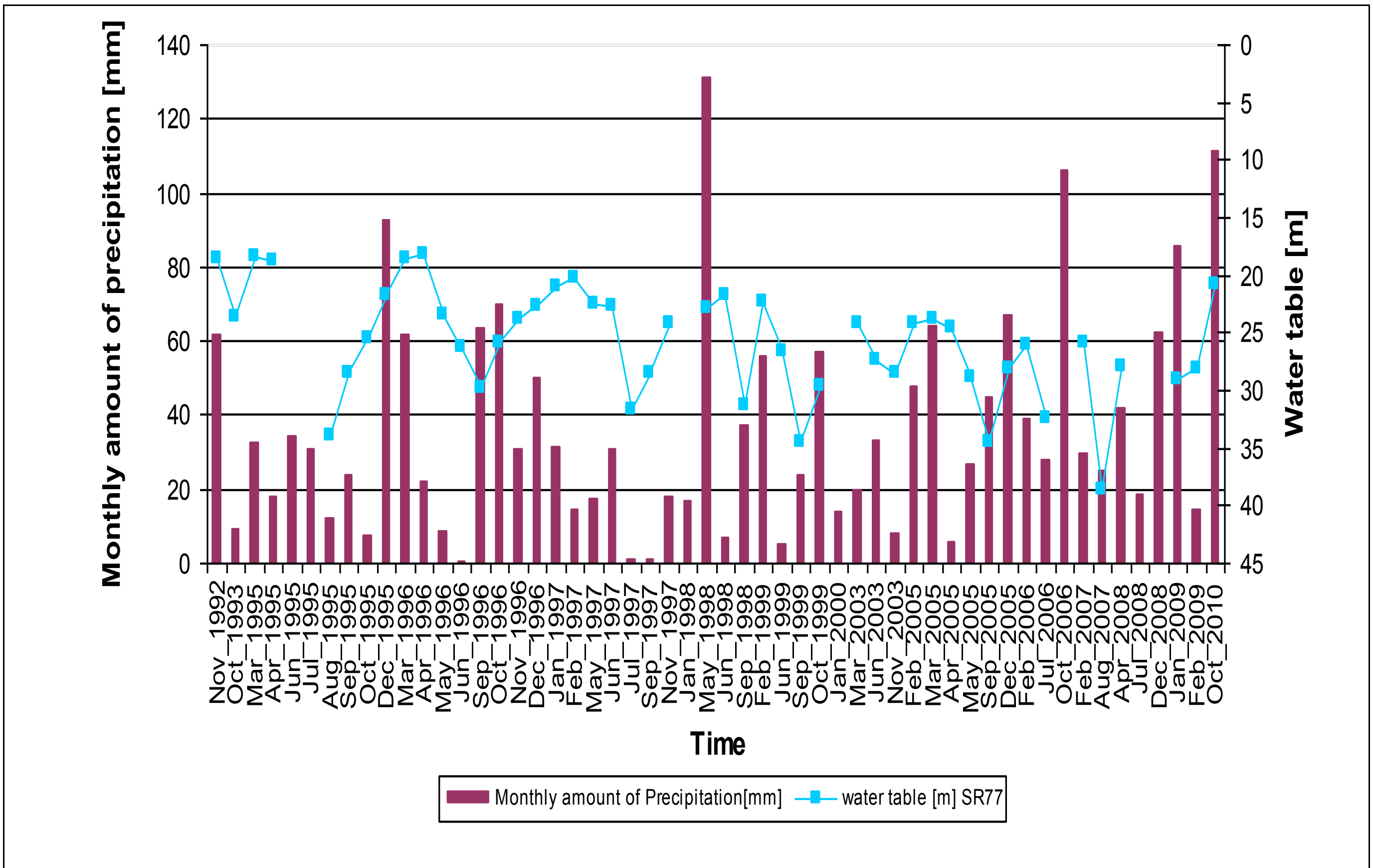

Figure 99. Monthly accumulation of precipitation corresponding to the groundwater level of the borehole SR77

3.8.2.1. Interference between land deformation and monthly precipitation as indirect impact on groundwater level (seasonal deformation) of the borehole SR77

Three point candidates resulting from the PSI technique have been chosen, at different distances from the borehole, as shown in Figure 100, to correlate, identify and examine the impact of groundwater level fluctuation on land deformation. The deformation of three point candidates, at distances of 289, 373 and 385 m from the borehole, monthly precipitation, and groundwater level are shown in Table 36. The deformation of point candidates and monthly precipitation are depicted in Figure 101. The deformation of point candidates and groundwater level are depicted in Figure 102.

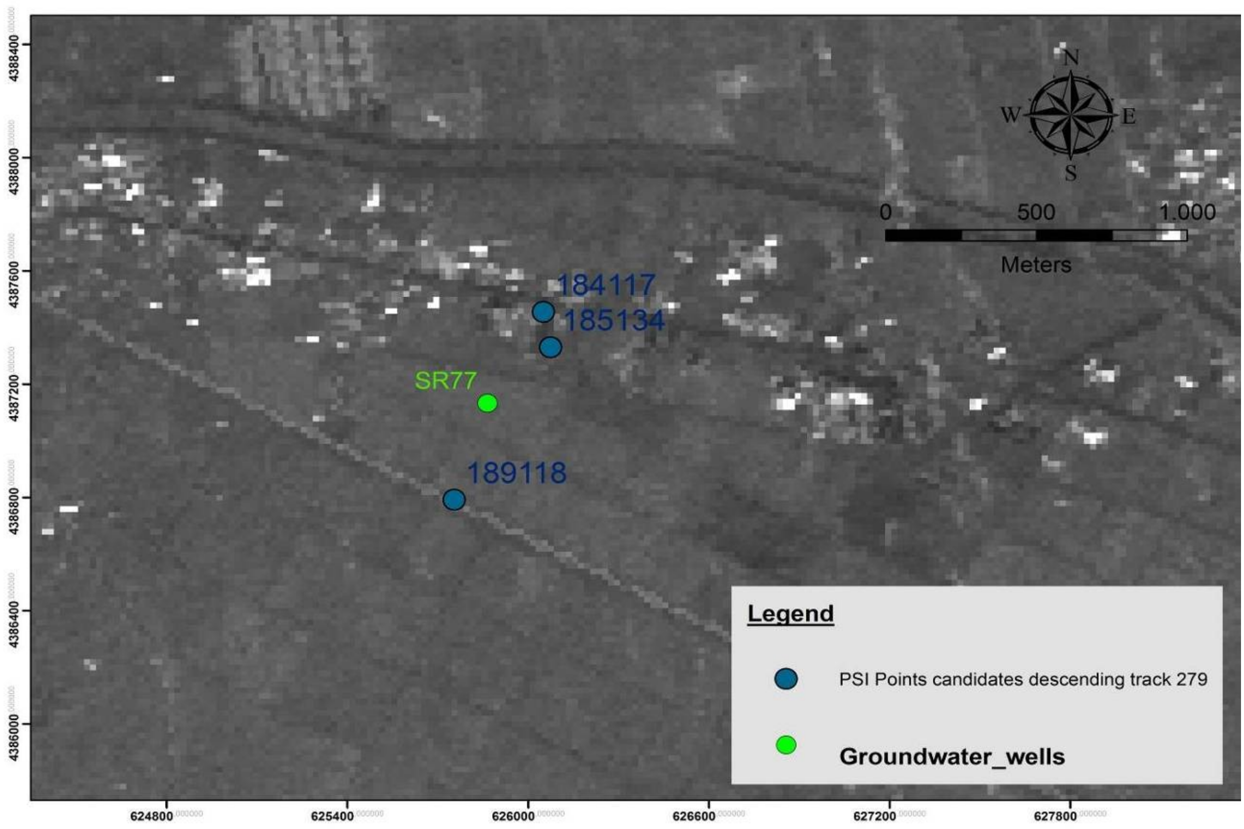

Figure.100 Three point candidates of the PSI at different distances from borehole SR77

Table 36. Ground deformation of point candidates of PSI descending track (279) corresponding to groundwater level and monthly precipitation behaviour of borehole SR77

Time series data of SAR PSI	LOS Displacemnt mm p (185134) 289 m	LOS Displacemnt mm p (184117) 373 m	LOS Displacemnt mm p (189118) 385 m	Groundwater level (m) borehole SR77	Monthly amount of precipitation (mm)
Nov_1992	-88.562	-128.705	6.49	18.48	62
Oct_1993	-77.542	-122.228	4.61	23.6	9.1
Mar_1995	-66.82	-102.619	13.505	18.45	32.7
Apr_1995	-81.83	-94.15	10.523	18.68	18.1
Jun_1995	-69.937	-98.372	18.75		34.4
Jul_1995	-68.911	-98.627	6.17		31
Aug_1995	-78.516	-105.934	4.391	34.03	12.3
Sep_1995	-64.748	-105.066	11.572	28.48	24
Oct_1995	-76.213	-101.498	4.827	25.52	7.8
Dec_1995	-72.175	-94.421	12.695	21.68	92.7
Mar_1996	-65.13	-95.357	10.684	18.5	61.9
Apr_1996	-62.625	-95.389	19.087	18.18	22.3
May_1996	-64.105	-90.119	7.745	23.48	9
Jun_1996	-53.94	-98.169	15.376	26.17	0.3
Sep_1996	-63.449	-94.786	14.685	29.75	63.7
Oct_1996	-61.721	-95.823	12.867	25.96	70
Nov_1996	-65.32	-87.793	13.117	23.77	30.9
Dec_1996	-61.429	-90.362	11.039	22.6	50
Jan_1997	-65.947	-85.979	7.285	21.05	31.4
Feb_1997	-62.942	-96.248	15.932	20.22	14.5
May_1997	-68.163	-100.354	8.425	22.51	17.6
Jun_1997	-64.897	-97.812	18.194	22.62	30.7
Jul_1997	-57.209	-85.796	17.944	31.7	1.4
Sep_1997	-63.903	-88.268	5.801	28.48	1.4
Nov_1997	-52.407	-80.912	13.58	24.13	18.1
Jan_1998	-62.197	-90.353	-0.624		17.1
May_1998	-48.738	-78.656	4.231	22.91	131.5
Jun_1998	-59.88	-89.33	11.985	21.74	7
Sep_1998	-48.976	-79.659	1.834	31.26	37.1
Feb_1999	-56.872	-66.031	13.615	22.25	55.8
Jun_1999	-55.696	-64.044	10.015	26.55	5
Sep_1999	-47.552	-65.235	14.599	34.53	23.9
Oct_1999	-50.444	-77.168	1.466	29.64	57.4
Jan_2000	-56.191	-75.461	7.084		14.1
Mar_2003	-23.98	-37.055	-1.608	24.15	20.1
Jun_2003	-28.187	-41.488	5.469	27.36	33.2
Nov_2003	-33.275	-31.343	2.061	28.58	8.3
Feb_2005	-13.109	-30.627	-8.528	24.16	47.6
Mar_2005	-13.48	-28.88	-3.567	23.72	64.1

Supplement of Table 36. Ground deformation of point candidates of PSI descending track (279) corresponding to groundwater level and monthly precipitation behaviour of borehole SR77

Time series data of SAR PSI	LOS Displacemnt mm p (185134) 289 m	LOS Displacemnt mm p (184117) 373 m	LOS Displacemnt mm p (189118) 385 m	Groundwater level (m) borehole SR77	Monthly amount of precipitation (mm)
Apr_2005	-17.622	-37.869	10.967	24.47	5.7
May_2005	-16.842	-13.032	15.029	28.83	26.7
Sep_2005	-14.932	-18.941	0.278	34.54	44.8
Dec_2005	-20.089	-24.616	-5.084	28.2	66.8
Feb_2006	-3.888	-21.157	-2.033	26.03	38.8
Jul_2006	-13.644	-16.504	7.157	32.43	28
Oct_2006	-16.041	-3.64	0.996		106.1
Feb_2007	-6.412	-13.048	-5.799	25.88	29.5
Aug_2007	7.158	-13.721	-6.308	38.63	25.1
Apr_2008	-2.888	1.361	6.805	27.95	42
Jul_2008	1.028	1.839	0.644		18.6
Dec_2008	-3.939	-3.289	-4.706		62.3
Jan_2009	-3.671	4.484	3.658	28.98	85.8
Feb_2009	-0.049	1.767	6.82	28.2	14.4
Oct_2010	17.665	21.069	-1.625	20.73	111.6

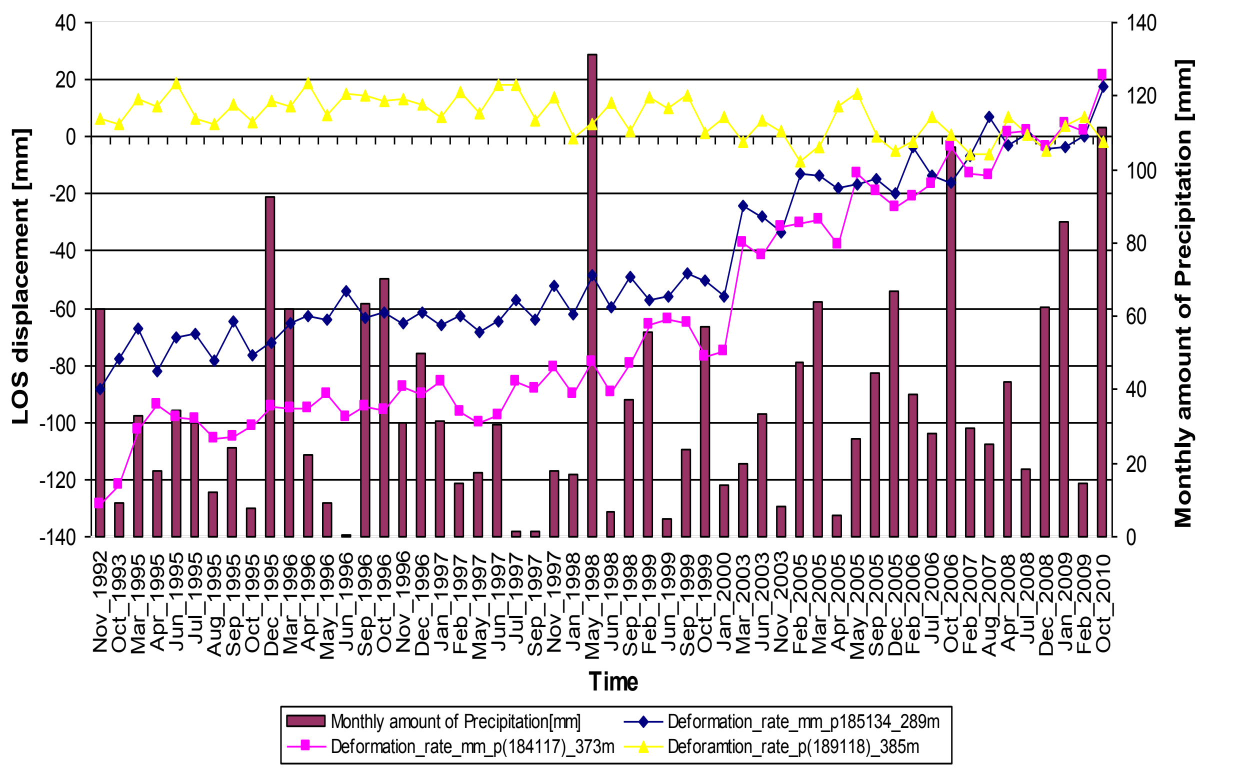

Figure.101 LOS Displacemnt of point candidates of PSI corresponding to monthly precipitation. Displacement time series of point candidates are rescaled to the first acquisition (i.e. 12 Nov 1992).

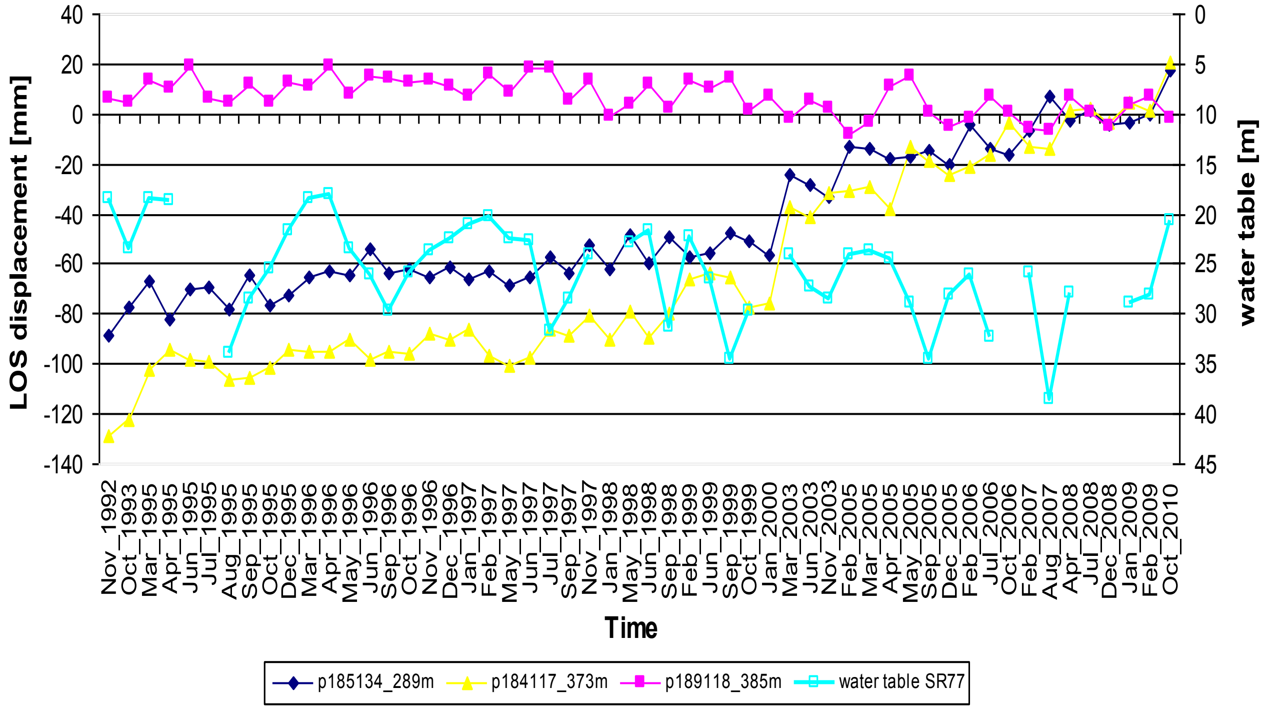

Figure.102 LOS Displacemnt of point candidates corresponding to groundwater level of borehole SR77. Displacement time series of point candidates are rescaled to the first acquisition (i.e. 12 Nov 1992).

The deformation behaviour of the first point (number 185134), at a distance of 289 m from the borehole, indicates general rising trend, as the time series begins with subsidence and then goes into uplift; however, a swap between subsidence and uplift is observed during the period April 2008–October 2010. The minimum subsidence was -0.049 mm (February 2009) and the maximum subsidence was -88.562 mm (November 1992), while the minimum uplift was 1.028 mm (July 2008) and the maximum uplift was 17.665 mm (October 2010).

The minimum subsidence may not be attributable to the indirect impact of precipitation (14.4 mm) on land deformation through its impact on the groundwater level, which was 28.2 m. This amount of precipitation was not enough to raise the groundwater level and consequently the groundwater level declined; however, this low level of groundwater should be accompanied by a larger amount of subsidence. Moreover, the maximum subsidence may not be attributable to the indirect impact of precipitation (62 mm) on land deformation through its impact on the groundwater level, which was 18.48 m, because this amount of precipitation was enough to raise the groundwater to this level or higher, which should be accompanied by a lower amount of subsidence; consequently, this subsidence is probably due to the participation of some other factor.

The minimum uplift may be attributable to the indirect impact of precipitation (18.6 mm) on land deformation through its impact on the groundwater level; however, there are no data monitoring records of groundwater level during this month. This amount of precipitation may have raised the groundwater level and consequently caused this uplift. The maximum uplift may not be attributable to the indirect impact of precipitation (111.6 mm) on land deformation through its impact on the groundwater level, which was 20.73 m, because groundwater withdrawal may have exceeded precipitation resulting in a decline in the groundwater level, which should be accompanied by subsidence. Consequently, this uplift is probably due to the participation of some other factor.

Details of the impact of groundwater level on land deformation indicate non-continuous significant correlation between them despite the short distance between the borehole and the point candidates of PSI; however, many correlation cases are observed, which may be attributable to the large number of data within this time series (1992–2010). Decreasing subsidence accompanied the raising of the groundwater level during the period October 1993–March 1995, followed by an increase in subsidence with the decline of the groundwater level during the period March 1995–April 1995. Thereafter a decrease in subsidence accompanied the raising of the groundwater level during the period August 1995–September 1995, and an increase in subsidence accompanied the decline of the groundwater level during the periods April 1996–May 1996 and June 1996–September 1996. This was followed by a decrease in subsidence with the raising of the groundwater level during the periods September 1996–October 1996, November 1996–December 1996, and January 1997–February 1997. Subsequently, an increase in subsidence accompanied the decline of the groundwater level during the period February 1997–May 1997. A decrease in subsidence is observed with the raising of the groundwater level during the period September 1997–November 1997, and an increase in subsidence is observed with the decline of the groundwater level during the periods March 2003–June 2003 and June 2003–November 2003. This was followed by a decrease in subsidence with the raising of the groundwater level during the period November 2003–February 2005. Subsequently, an increase in subsidence is observed with the decline of the

groundwater level during the period March 2005–April 2005. A decrease in subsidence once again accompanied the raising of the groundwater level during the period December 2005–February 2006, followed by an increase in subsidence with the decline of the groundwater level during the period February 2006–July 2006. Ultimately, a decrease in subsidence followed by a status change from subsidence to uplift is observed with the raising of the groundwater level during the periods January 2009–February 2009 and February 2009–October 2010.
The deformation behaviour of the second point (number 184117), at a distance of 373 m from the borehole, indicates a general rising trend, as the time series begins with subsidence and then goes into uplift; however, a swap between subsidence and uplift is observed during the period December 2008–October 2010. The minimum subsidence was -3.289 mm (December 2008) and the maximum subsidence was -128.705 mm (November 1992), while the minimum uplift was 1.361 mm (April 2008) and the maximum uplift was 21.069 mm (October 2010).

The minimum subsidence may not be attributable to the indirect impact of precipitation (62.3 mm) on land deformation through its impact on the groundwater level, although no monitoring data for groundwater level were recorded during this month. This amount of precipitation may have been enough to raise the groundwater level, and consequently an uplift status should have occurred; therefore, some other factor has caused this subsidence. However, this is merely an expectation, because there is no groundwater level monitoring data. Alternatively, the precipitation may have raised the groundwater level from a lower to a low level has and consequently caused this low value of subsidence.

The maximum subsidence also may not be attributable to the indirect impact of precipitation (62 mm) on land deformation through its impact on the groundwater level, which was 18.48 m, because this amount of precipitation may have been enough to raise the groundwater level to a higher level than that found and one that should be accompanied by a lower amount of subsidence. Consequently, this subsidence is probably due to the participation of some other factor, particularly during this short period.

The minimum uplift may not be attributable to the indirect impact of precipitation (42 mm) on land deformation through its impact on the groundwater level, which was

27.2 m. This amount of precipitation may have been enough to raise the groundwater to a level higher than that found; however, groundwater withdrawal may have exceeded the precipitation amount. This low groundwater level should be accompanied by subsidence; therefore, this uplift is probably due to the participation of some other factor. The maximum uplift also may not be attributable to the indirect impact of precipitation (111.6 mm) on land deformation through its impact on the groundwater level, which was 20.73 mm. This amount of precipitation may have been enough to raise the groundwater to a level higher than that found; however, groundwater withdrawal may have exceeded the precipitation amount. This low groundwater level should be accompanied by subsidence; therefore, this uplift is probably due to the participation of some other factor.

Details of the impact of groundwater level on land deformation indicate that there is no continuous significant correlation between them, despite the short distance between borehole and point candidate of PSI; however, many correlation cases are observed, which may be attributable to the large number of data within this time series (1992–2010). Decreasing subsidence is observed with the raising of the groundwater level during the periods August 1995–September 1995 and October 1995–December 1995. An increase in subsidence accompanied the decline of the groundwater level during the period May 1996–June 1996. Thereafter a decrease in subsidence accompanied the raising of the groundwater level during the periods October 1996–November 1996 and December 1996–January 1997. Subsequently, an increase in subsidence accompanied the decline of the groundwater level during the period February 1997–May 1997, followed by a decrease in subsidence once again with the raising of the groundwater level during the periods September 1997–November 1997 and September 1998–February 1999. Thereafter an increase in subsidence accompanied the decline of the groundwater level during the periods June 1999–September 1999 and March 2003–June 2003. A decrease in subsidence is observed with the raising of the groundwater level during the periods November 2003–February 2005 and February 2005–March 2005, followed by an increase in subsidence with the decline of the groundwater level during the period March 2005–April 2005. A decrease in subsidence is observed with the raising of the groundwater level during the period December 2005–February 2006. Thereafter an increase in subsidence accompanied the decline of the groundwater level during the period February 2007–

August 2007, followed by a status change from subsidence to uplift with the sharp raising of the groundwater level during the period August 2007–April 2008. Ultimately, an increase in uplift accompanied the raising of the groundwater level during the period February 2009–October 2010.

The deformation behaviour of the third point (number 189118), at a distance of 385 m from the borehole, indicates a general declining trend, as the time series begins with uplift and then goes into subsidence; however, a fluctuation between subsidence and uplift is observed during the period January 1998–October 2010. Although there is no difference in the distances of the second and third point candidate of PSI from the borehole SR77, nevertheless the third point candidate indicates different deformation behaviour from the two previous point candidates.
The minimum uplift was 0.278 mm (September 2005) and the maximum uplift was 19.087 mm (April 1996), while the minimum subsidence was -0.624 mm (January 1998) and the maximum subsidence was -8.528 mm (February 2005).

The minimum uplift may not be attributable to the indirect impact of precipitation (44.8 mm) on land deformation through its impact on the groundwater level, which was 34.54 m, because although the precipitation may have been sufficient to raise the groundwater to a higher level than that found, groundwater withdrawal may have exceeded the precipitation amount; therefore, this low groundwater level should be accompanied by subsidence. Consequently, this uplift may have been caused by the participation of some other factor. The maximum uplift also may not be attributable to the indirect impact of precipitation (22.3 mm) on the groundwater level, which was 18.18 m, because this amount of precipitation was not enough to raise the groundwater level. Therefore, this amount of precipitation and groundwater level should be accompanied by subsidence, and accordingly this uplift may have been caused by the participation of some other factor.

The minimum subsidence may be attributable to the indirect impact of precipitation (17.1 mm) on land deformation through its impact on the groundwater level; although there are no monitoring data records for groundwater level during this month. This amount of precipitation was not enough to raise the groundwater level, and the decline of the groundwater level caused this subsidence. The maximum subsidence may also be attributable to the indirect impact of precipitation (47.6 mm) through its impact on the groundwater level, which was 24.16 m. Although this precipitation may have been enough to raise the groundwater level, the groundwater withdrawal exceeded the precipitation amount. Consequently, the decline of the groundwater level caused this subsidence.

Details of the impact of groundwater level on land deformation indicate a non-continuous significant correlation between them, despite the short distance between the borehole and the point candidate of PSI; however, many correlation cases are observed, which may be attributable to the large number of data within this time series (1992–2010). A decrease in uplift accompanied the decline of the groundwater level during the period November 1992–October 1993, followed by an increase in uplift with the raising of the groundwater level during the period October 1993–March 1995. Subsequently, a decrease in uplift is observed with the decline of the groundwater level during the period March 1995–April 1995. Thereafter an increase in uplift accompanied the raising of the groundwater level during the periods August 1995–September 1995, October 1995–December 1995 and March 1996–April 1996, followed by a decrease in uplift with the decline of the groundwater level during the period April 1996–May 1996. An increase in uplift is observed with the raising of the groundwater level during the period January 1997–February 1997, followed by a decrease in uplift with the decline of the groundwater level during the period February 1997–May 1997. Another correlation case observed during the time series is the increase in uplift with the raising of the groundwater level during the periods September 1997–November 1997 and May 1998–June 1998. This was followed by a decrease in uplift with the decline of the groundwater level during the period June 1998–September 1998. Subsequently, an increase in uplift is observed once again with the raising of the groundwater level during the period September 1998–February 1999, followed by a decrease in uplift with the decline of the groundwater level during the periods February 1999–June 1999 and June 2003–November 2003. A decrease in subsidence accompanied the raising of the groundwater level during the period February 2005–March 2005, followed by a sharp decrease in uplift that accompanied the decline of the groundwater level during the period May 2005–September 2005. A subsequent decrease in subsidence is observed with the raising of the groundwater level during the period December 2005–February 2006, and an increase in subsidence accompanied the decline of the groundwater level during the period February 2007–August 2007. This was followed by a status change from subsidence to uplift with the raising of the groundwater level during the period August 2007–April 2008. Ultimately, an increase in uplift is observed with the raising of the groundwater level during the period January 2009–February 2009.

3.9. Conventional SAR Interferometry

The conventional technique of SAR Interferometry has been implemented to investigate and emphasise the seasonal impact of groundwater level fluctuation on land deformation within the same part of the study area which was examined using PSI, using the same two tracks, ascending and descending.

3.9.1. Ascending track 143

One interferogram has been chosen within this track, as is depicted previously in Figure 9 in chapter of processing which covers the period 19960228_19960403, for the reason that the accuracy of the deformation estimated from an individual differential interferogram is mainly limited by the atmospheric path delay term (Wegmuller et al., 2006). Additionally, the non-continuous stable signal or objects within agricultural fields constitute obstacles using this technique. From 29 differential interferograms, one single interferogram has been selected which does not exhibit any of the problems mentioned before, especially within agricultural fields. It is worth mentioning that the wrapped phase plays an important role in selecting the number of interferograms by implementing a conventional technique. In this case study, many interferograms have the problem of wrapped phase, especially within the agricultural fields. In addition, the impact of time decorrelation, especially within agricultural fields, is one of many important determinant parameters. Furthermore, the interferogram pair has been selected according to its perpendicular baseline, which might be small to avoid residual topographic effects and geometric decorrelation. The baseline was lower than 200 m. Parameters of the interferogram pair are depicted in Table 5 in chapter of processing. Moreover, this differential interferogram has been chosen according to its time period, which covers part of the wet period, represented by March, in order to examine one of the temporal characteristics of displacement, related to the groundwater level fluctuation of the many boreholes distributed within part of the study area during this period. Additionally, a coherence map of this period is depicted in Figure 8 in chapter of processing. Coherence varies between 0.12 and

0.99; however, coherence is good approximately all over the study area. The good quality of the coherence may be attributable to the low temporal interval, which is 35 days.

The correlation information of interferometric phases related to the fluctuation of groundwater level is shown in Table 37. However, results of interferometric correlation were different within the same interferogram because of differences in the groundwater level fluctuation of each borehole, as explained presently.

It is worth mentioning that the wrapped phase plays an important role in selecting the number of interferograms within the conventional technique. Many interferograms have the problem of wrapped phase, especially within agricultural fields. In addition, the impact of time decorrelation, especially within agricultural fields, is one of many important determinant parameters.

Table 37. Groundwater level and interferometric fringe of boreholes

Borehole	Groundwater level (m)	Interferometric fringes
AD6	4.8	High Significant
AG10	16.4	Low Significant
PZ1	10.19	Low Significant
SR29	24.44	Significant
SR35	4.67	High Significant
SR72	20.62	Significant
SR77	18.50	High Significant

Clear high significant interferometric fringes are observed around the borehole AD6 during March, which indicates uplift due to the high groundwater level, as shown in Figure 103. Low significant interferometric fringes are observed north, west and south of the borehole AG10 during the same period, which indicates subsidence due to the low groundwater level, as depicted in Figure 104. Low significant interferometric fringes are also observed around the borehole PZ1 (Figure 105). Fringes of subsidence, represented by red colour points, are evident around the northeast and south of the borehole because of the low groundwater level during this period. Regarding borehole SR29, significant interferometric fringes of subsidence are observed south and east of the borehole due to the low groundwater level, as depicted in Figure 106. It is worth mentioning that the interferometric fringes, which indicate subsidence phase due to low groundwater level in many boreholes within the study area, are not observed close to the boreholes. This may be attributable to the impact of groundwater withdrawal, which may cause uplift close to the boreholes during the implementation of this operation.

Regarding the borehole SR35, significant interferometric fringes are observed, which indicate uplift due to high groundwater level during March, as shown in Figure 107. For the borehole SR72, high significant interferometric fringes are observed, as depicted in Figure 108. The subsidence phase around the borehole is evident, and especially the density of the subsidence phase to the north and east of the borehole during this period due to low groundwater level. High significant interferometric fringes are also observed for the borehole SR77, as shown in Figure 109, as subsidence phase is observed around the borehole due to low groundwater level during this period.

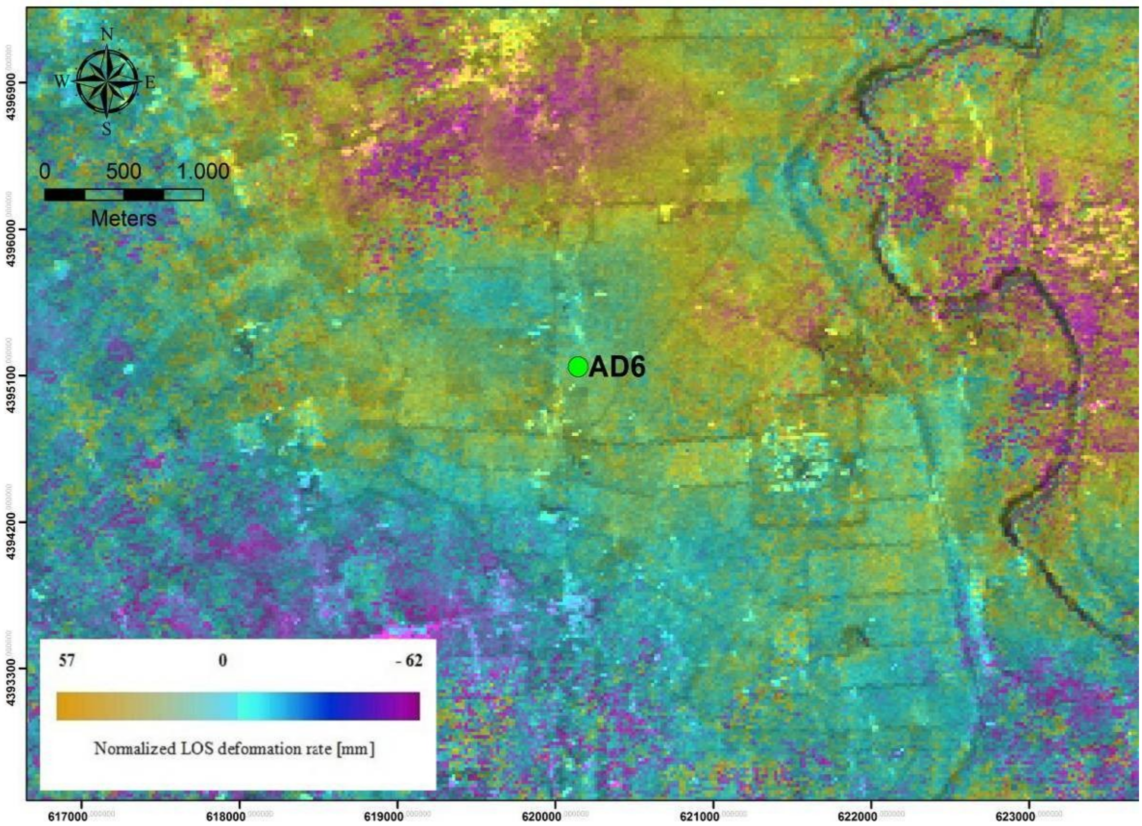

Figure.103 Differential interferogram of the area around borehole AD6, time interval 19960228–19960403. The green point is the location of the borehole.

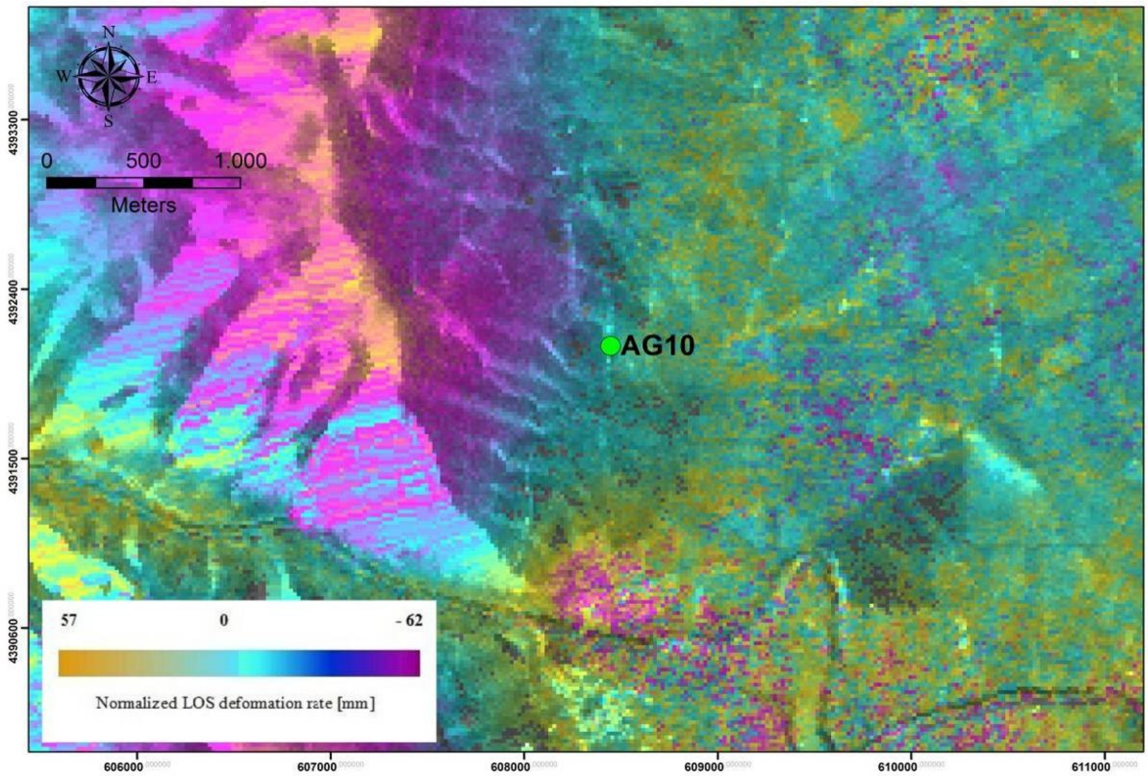

Figure.104 Differential interferogram of the area around borehole AG10, time interval 19960228–19960403. The green point is the location of the borehole.

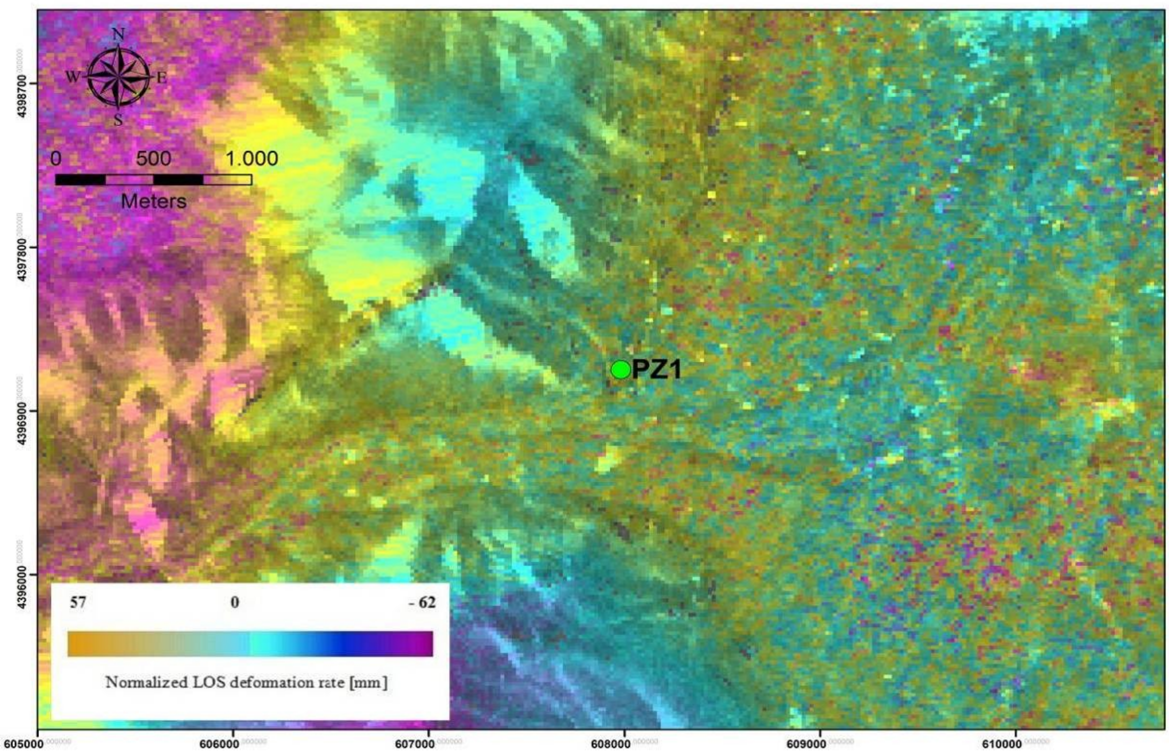

Figure.105 Differential interferogram of the area around borehole PZ1, time interval 19960228–19960403. The green point is the location of the borehole.

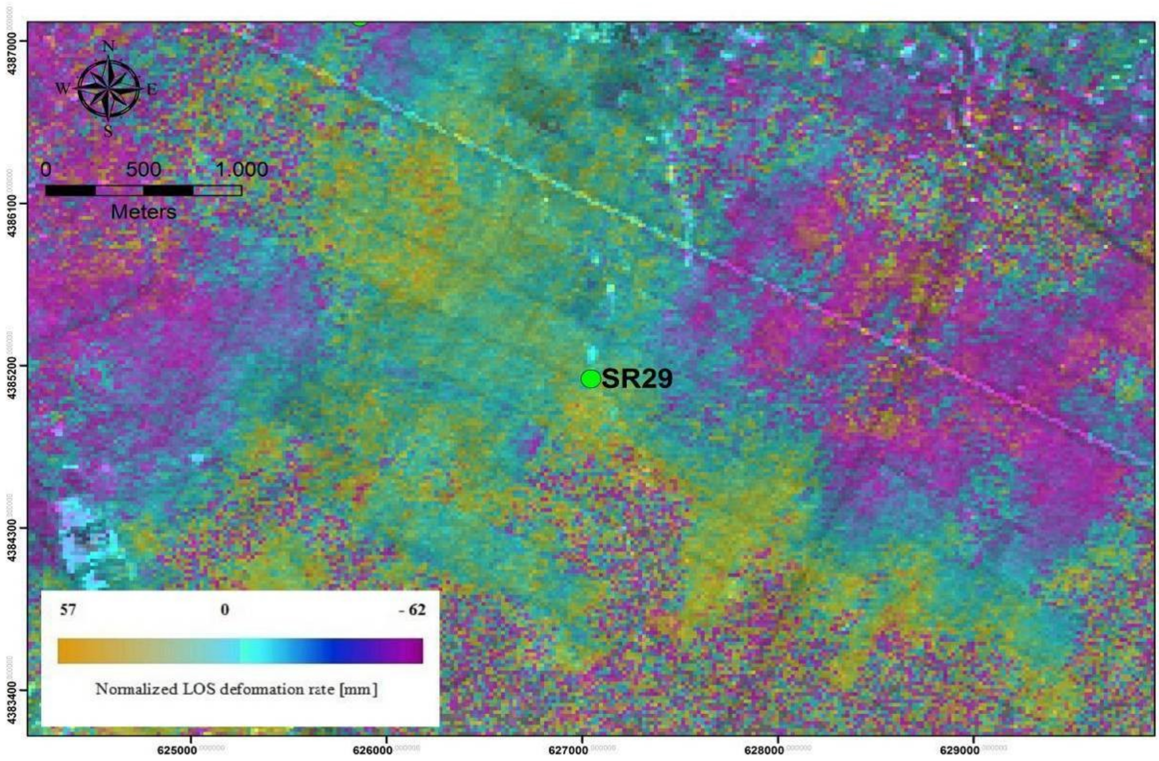

Figure.106 Differential interferogram of the area around borehole SR29, time interval 19960228–19960403. The green point is the location of the borehole.

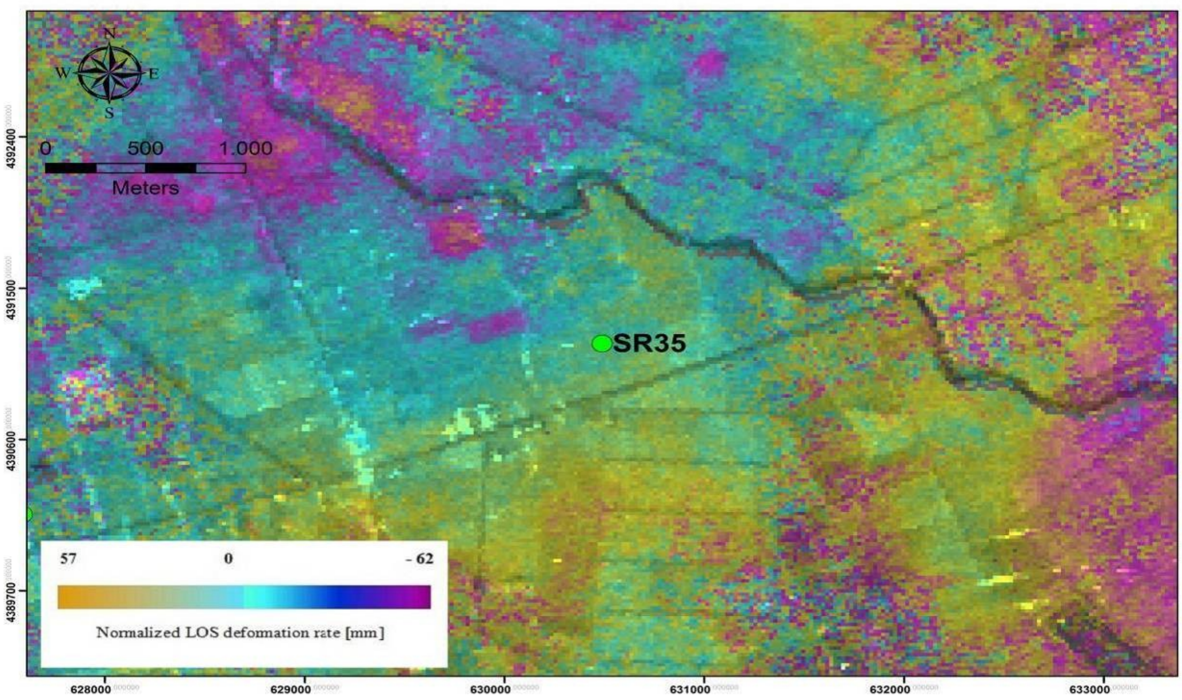

Figure.107 Differential interferogram of the area around borehole SR35, time interval 19960228–19960403. The green point is the location of the borehole.

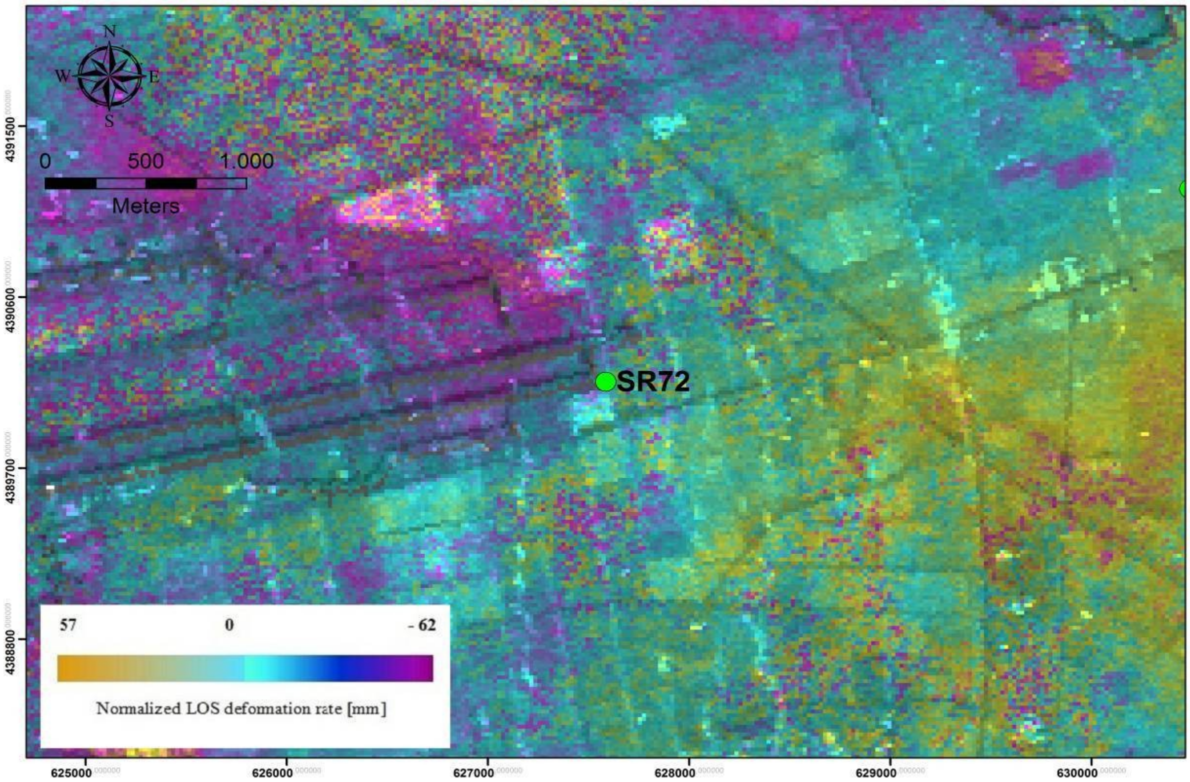

Figure.108 Differential interferogram of the area around borehole SR72, time interval 19960228–19960403. The green point is the location of the borehole.

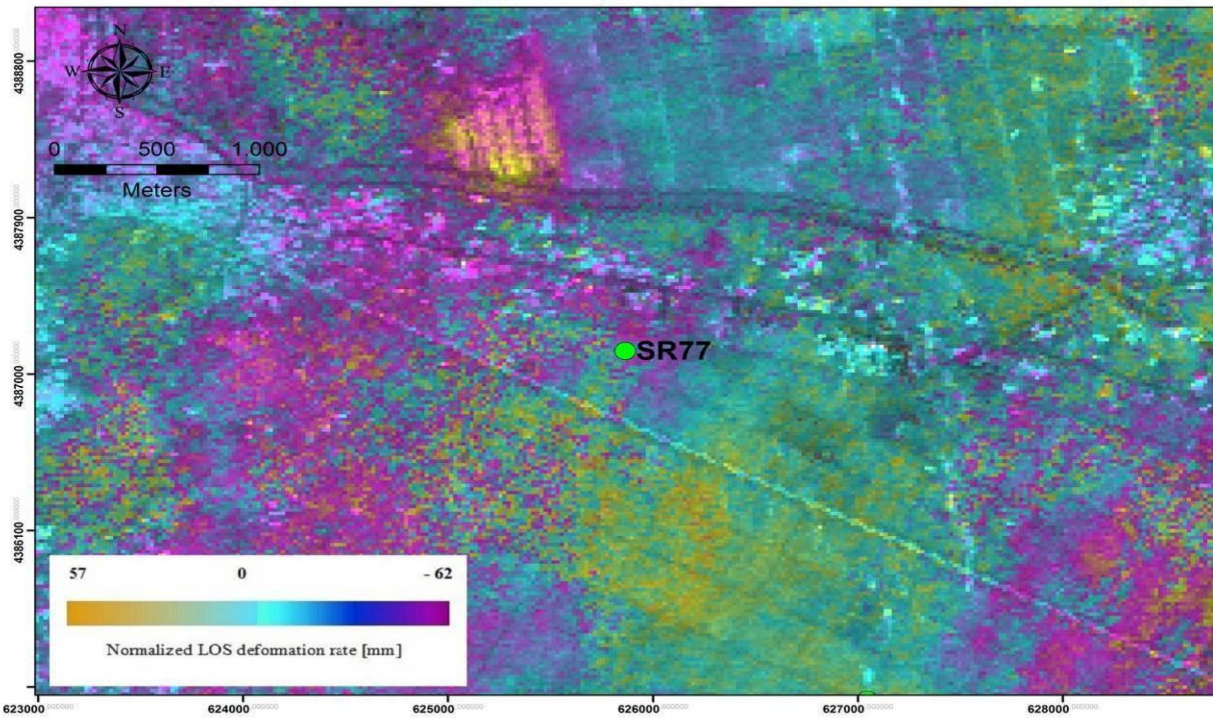

Figure109. Differential interferogram of the area around borehole SR77, time interval 19960228–19960403. The green point is the location of the borehole.

3.9.2. Descending track 279

One interferogram has been chosen within this track during the period 19980802–19980906, as depicted previously in Figure 21 in chapter of processing, for the same reasons mentioned above for the ascending track. Consequently, from 70 differential interferograms, only one pair of interferograms does not have any of the problems mentioned previously, especially within agricultural fields. Furthermore, the interferogram pair has been selected according to its perpendicular baseline, which might be small to avoid residual topographic effects and geometric decorrelation, which was lower than 150 m. Parameters of the differential interferogram pair are depicted previously in Table 14 in chapter of processing, Moreover, this pair has been chosen according to the time period, which covers part of the dry period, represented by August and a few days at the start of September, in order to examine temporal characteristics of displacement related to the groundwater level fluctuation of many boreholes distributed within part of the study area.

A coherence map of this period is depicted previously in Figure 20 in chapter of processing. Coherence varies between 0.10 and 0.99; however, there is good coherence approximately all over the scene, except in agricultural fields located in the mid–north, mid-east and mid- southeast and southwest of the scene. The good quality of coherence may be attributable to the low temporal interval, which is 35 days. The correlation information of interferometric phases, related to the fluctuation of the groundwater level, is shown in Table 38.

Table 38. Groundwater level and interferometric fringe of boreholes.

Borehole	Groundwater level (m)	Interferometric fringes
AD6	11.96	High Significant
AG10	23.02	High Significant
PZ1	17.40	Low Significant
SR29	59.30	Significant
SR35	5.38	Low Significant
SR72	34.00	High Significant
SR77	36.43	High Significant

High significant interferometric fringes are observed around the borehole AD6, as shown in Figure 110, which indicates a subsidence phase due to low groundwater level. In addition, clear high significant interferometric fringes are observed around the borehole AG10, as shown in Figure 111, which indicates subsidence due to low groundwater level. Concerning the borehole PZ1, low significant interferometric fringes are observed around the borehole, which indicates uplift despite the low groundwater level. This may be attributable to the impact of groundwater withdrawal, which may have caused uplift close to the borehole position during the implementation of this operation. Nevertheless there is subsidence to the west, north and northeast of the borehole at distances of 125–300 m as shown in figure 112. Other clear significant interferometric fringes are observed around the borehole SR29, as shown in Figure 113, which indicates subsidence phase due to low groundwater level. Low significant interferometric fringes are observed around the borehole SR35, as shown in Figure 114, which indicates uplift due to high groundwater level. High clear significant interferometric fringes are observed around the borehole SR72, as shown in Figure 115, which indicates subsidence due to low groundwater level during the part of the dry period which is covered, mainly August and a few days at the start of September. In relation to the borehole SR77, high clear significant interferometric fringes are observed around it, as is shown in Figure 116, which indicates subsidence due to low groundwater level.

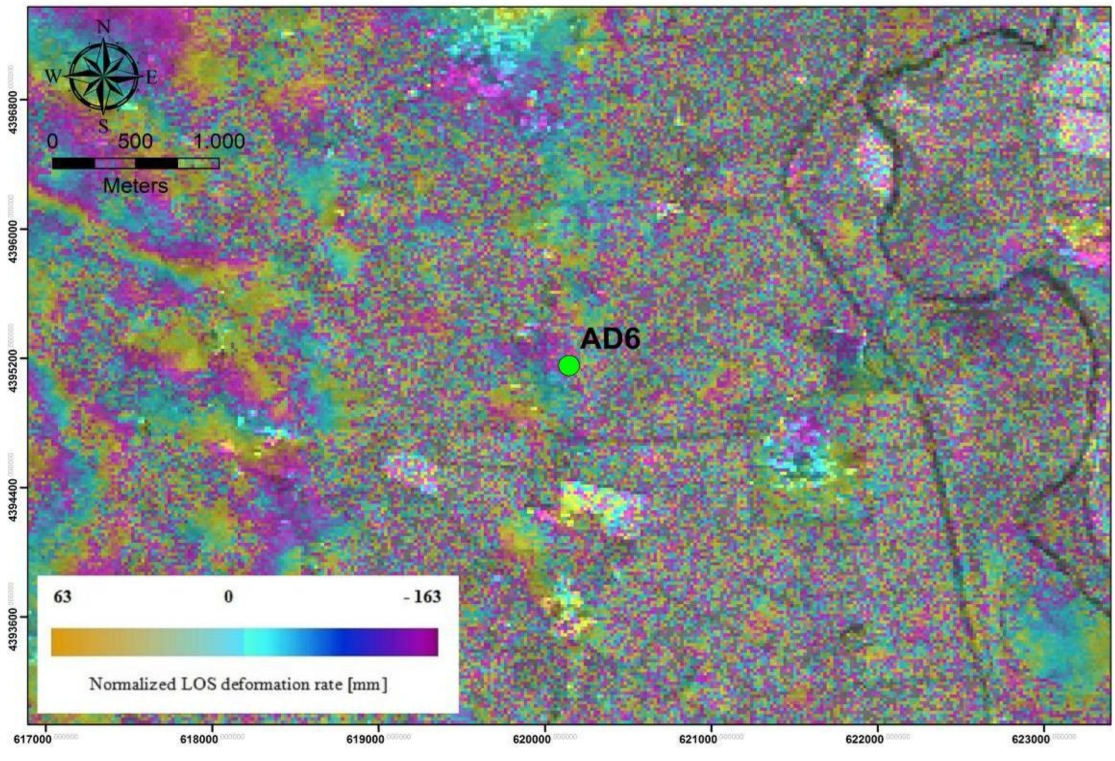

Figure.110 Differential interferogram of the area around borehole AD6, time interval 19980802–19980906. The green point is the location of the borehole.

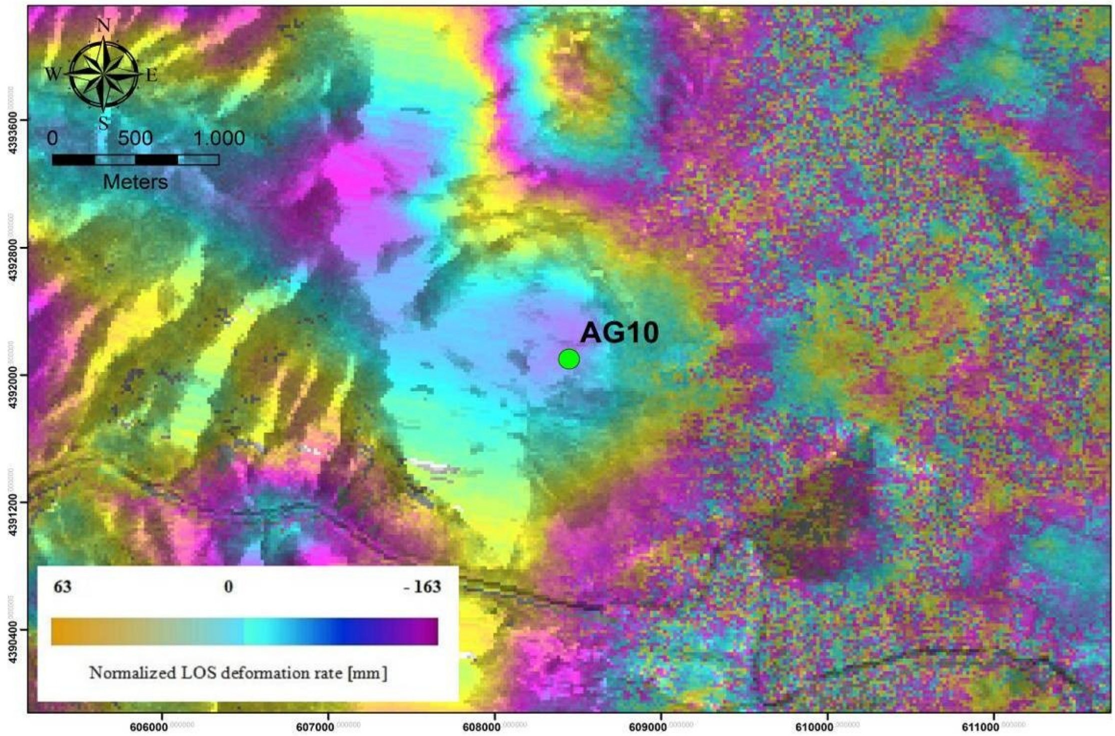

Figure.111 Differential interferogram of the area around borehole AG10, time interval 19980802–19980906. The green point is the location of the borehole.

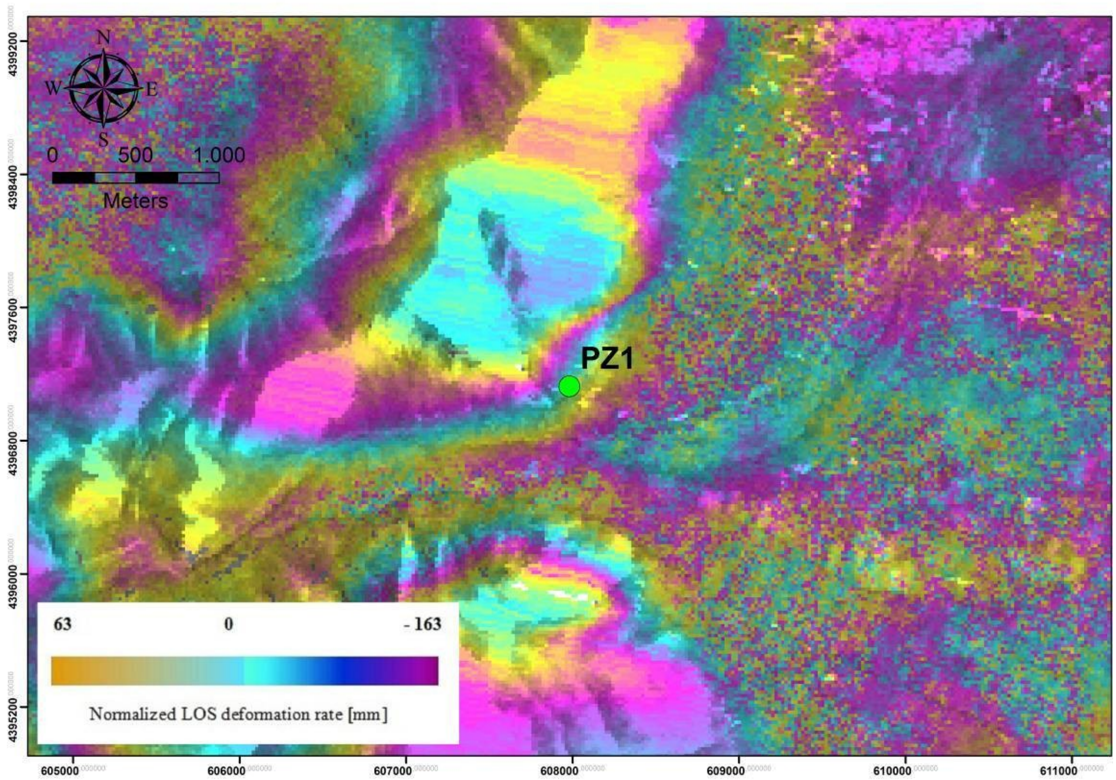

Figure.112 Differential interferogram of the area around borehole PZ1, time interval 19980802–19980906. The green point is the location of the borehole.

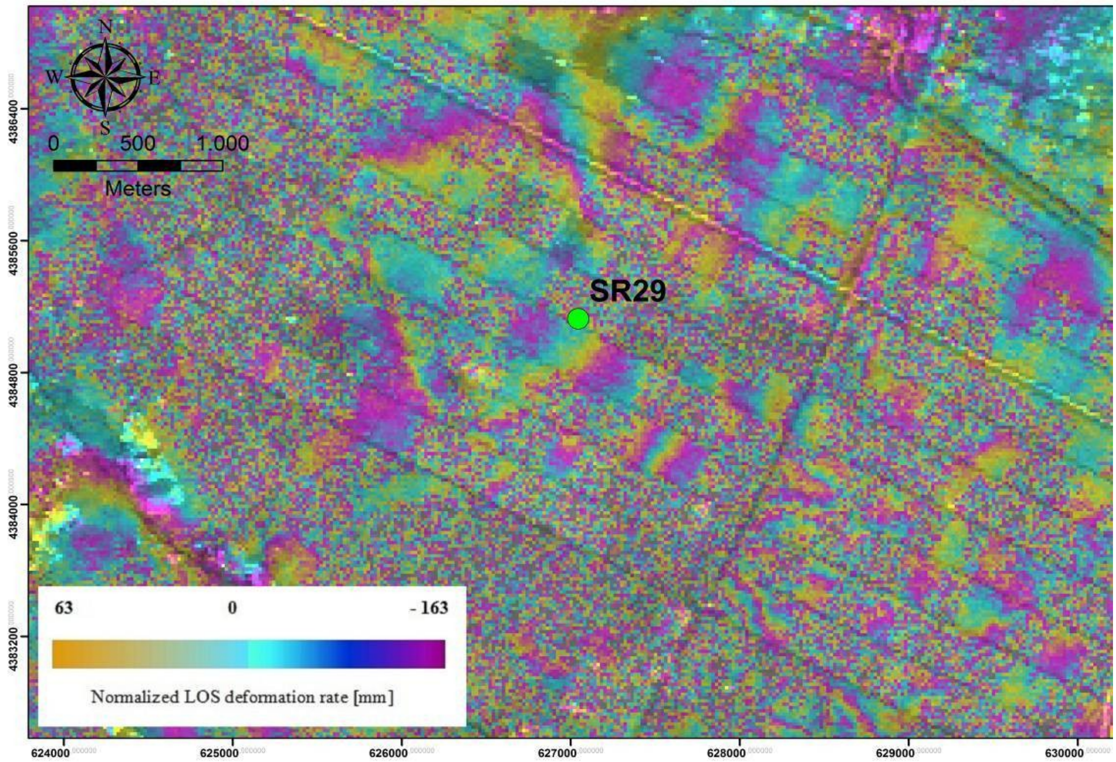

Figure.113 Differential interferogram of the area around borehole SR29, time interval 19980802–19980906. The green point is the location of the borehole.

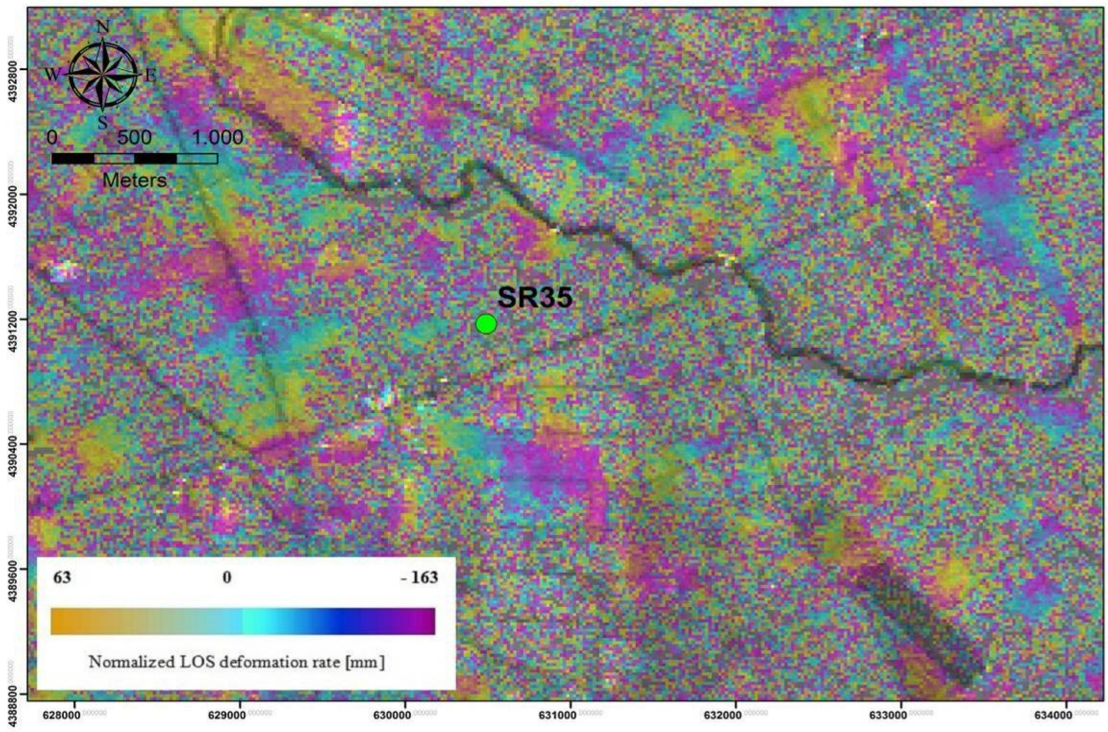

Figure.114 Differential interferogram of the area around borehole SR35, time interval 19980802–19980906. The green point is the location of the borehole.

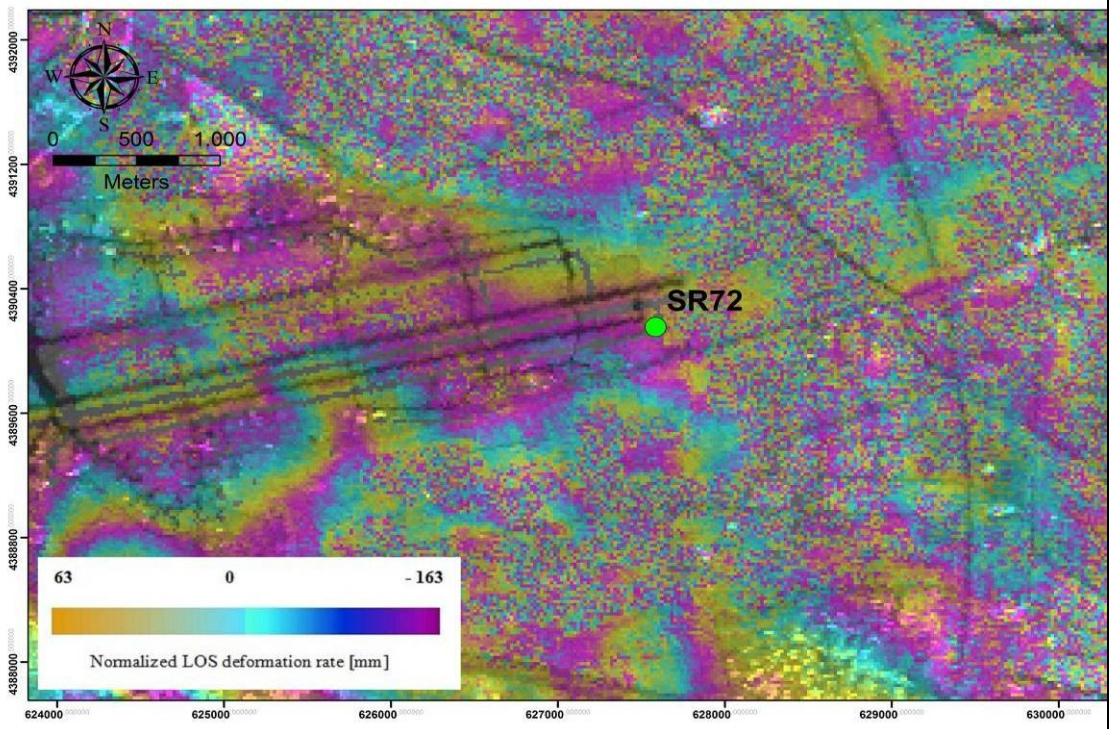

Figure.115 Differential interferogram of the area around borehole SR72, time interval 19980802–19980906. The green point is the location of the borehole.

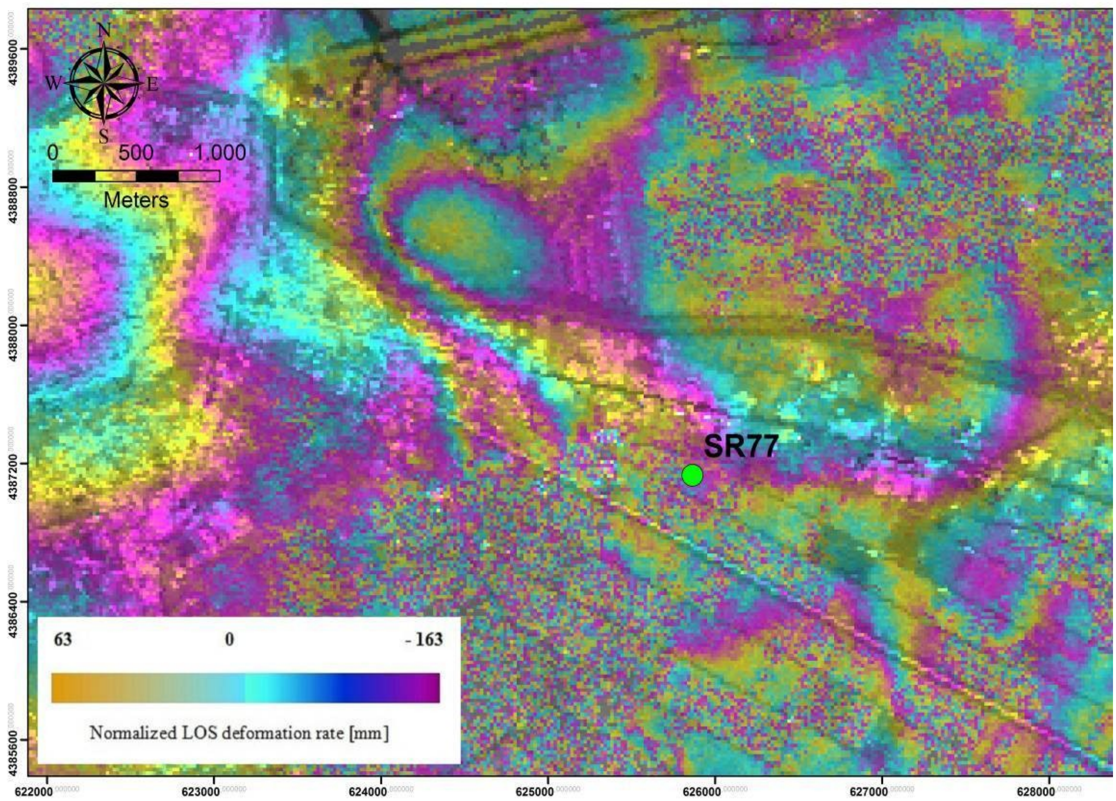

Figure.116 Differential interferogram of the area around borehole SR77, time interval 19980802–19980906. The green point is the location of the borehole.

3.10. Impact and interference type of clay minerals with fluctuation of groundwater level on land deformation

A montmorillonite is one of many clay minerals that have the ability to swell and shrink. However, it is considered as a dependent factor affected by the fluctuation of groundwater. Consequently, this factor plays an important role in impacting ground deformation through the mutual cycling of swelling and shrinking operations. The influence of such types of clay minerals on ground deformation is summarised in the flowchart in Figure 117. The swelling and shrinking cycle in this case study causes compaction of materials which is resulted by water pumping. A continuous cycle of clay minerals swelling and shrinkage maybe are caused earthquakes with microseismic (3–4) magnitude.

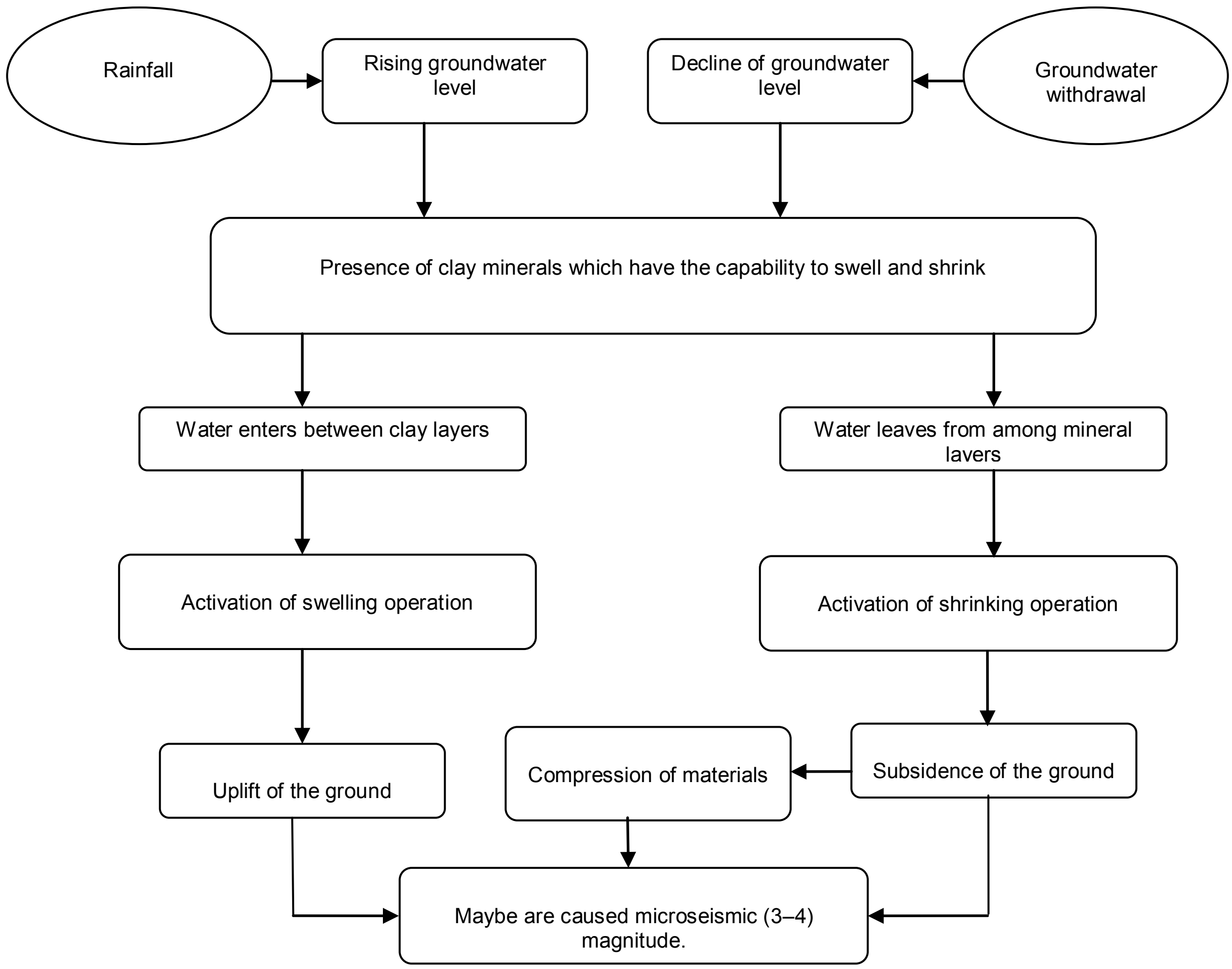

Figure.117 Cycle of swelling and shrinking of clay minerals

3.11. Impact and interference of faults movement with fluctuation of groundwater level on land deformation

The effect of the groundwater level on land deformation has been discussed in detail previously; however, many other parameters may play an important role in land deformation and should be discussed separately. One of these parameters is the movement of faults, and although this parameter has been discussed in detail in the chapter on impact faults and earthquakes, the interference of this factor with groundwater level fluctuation and its' impact on land deformation should be discussed, because movement on faults, whether slow (fault creep) or sudden (earthquake), represents a serious problem (Tocher, 1958). It is worth mentioning that many normal faults are distributed within the study area. The interference effects of these faults on land deformation will be discussed using a probability approach, because no statistical correlation or model building has been done between land deformation and fault movement. Consequently land deformation behaviour may be attributable to fault movement behaviour. The same point candidates of PSI which were discussed previously in relation to the effect of groundwater level fluctuation of two tracks, ascending and descending, will be discussed in a theoretical correlation with the fault movement effect.

3.11.1.Ascending track 143

The name of each borehole will be mentioned, representing the point candidates of PSI which are located around it.

3.11.1.2. AD6

The behaviour of three point candidates in relation to groundwater level has been mentioned previously (Figure 70) Subsidence phase behaviour is evident from the time series of the three point candidates, and this subsidence phase, either at the beginning or the end of the time series, may be attributable to the location of these points east of the hanging wall side of the normal fault, with distances varying between 1.73 and 1.95 km between the three point candidates and the normal fault trace, as shown in Figure 118.

3.11.1.3. AG10

The behaviour of three point candidates in relation to groundwater level has been mentioned previously (Figure 74). Subsidence phase behaviour is evident from the time series of the three point candidates, and this subsidence phase, either at the beginning or the end of the time series, may be attributable to the location of these points north of the hanging wall side of the normal fault, with distances varying between 1.72 and 2.0 km between three point candidates and the normal fault trace, as shown in Figure 119.

3.11.1.4. PZ1

The behaviour of three point candidates in relation to groundwater level has been mentioned previously (Figure 78). Subsidence phase behaviour is evident from the time series of the three point candidates, and this subsidence phase is observed at the end of the time series and may be attributable to the location of these points north of the hanging wall side of the normal fault, with distances varying between 0.24 and 0.47 km between three point candidates and the normal fault trace, as shown in Figure 120.

3.11.1.5. SR29

The behaviour of three point candidates in relation to groundwater level has been mentioned previously (Figure 82). Subsidence and uplift phase behaviour is evident from the time series of the three point candidates. The subsidence phase may be attributable to the location of point candidates northeast of the hanging wall side of the normal fault, with distances varying between 2.8 and 3.10 km between three point candidates and the normal fault trace. The uplift phase may be attributable to the location of point candidates southwest of the footwall side of the normal fault, with distances varying between 0.49 and 0.75 km between three point candidates and the normal fault trace, as shown in Figure 121.

3.11.1.6. SR35

The behaviour of three point candidates in relation to groundwater level has been mentioned previously (Figure 86). Subsidence and uplift phase behaviour is evident from the time series of the three point candidates. For the point candidate with number

41577, the subsidence phase may be attributable to the location of the point candidate north of the hanging wall side of the normal fault, with a distance of 0.1 km between the point candidate and the normal fault trace. The subsidence may also be attributable to the location of the point candidate southwest of the hanging wall side of the normal fault, at a distance of 2.8 km between the point candidate and the normal fault trace. However, the uplift phase of the same point may also be attributable to the location of the point candidate south of the footwall side of the normal fault, with a distance of 2.7 km between the point candidate and the normal fault trace.

Concerning the point candidates with numbers 41078 and 40781, the subsidence phase may be attributable to the location of the point candidates north of the hanging wall side of the normal fault, at distances varying between 2.85 and 2.89 km between the point candidates and the normal fault trace. However, the uplift phase of the same points may also be attributable to the location of the point candidates south of the footwall side of the normal fault, at distances varying between 0.1 and 0.14 km between the point candidates and the normal fault trace, as shown in Figure 122.

3.11.1.7. SR72

The behaviour of three point candidates in relation to groundwater level has been mentioned previously (Figure 90). Subsidence and uplift phase behaviour is evident from the time series of the three point candidates. The subsidence phase may be attributable to the location of the point candidates northeast of the hanging wall side of the normal fault, with distances varying between 3.0 and 3.77 km between the three point candidates and the normal fault trace, as shown in Figure 123.

3.11.1.8. SR77

The behaviour of three point candidates in relation to groundwater level has been mentioned previously (Figure 94). Subsidence and uplift phase behaviour is evident from the time series of the three point candidates. For the point candidates with numbers 35265 and 34800, the subsidence phase may be attributable to the location of the point candidates east of the hanging wall side of the normal fault, with distances varying between 0.34 and 0.44 km between the point candidates and the normal fault trace. For the point candidate with number 33920, the subsidence phase may be attributable to the location of the point candidate north of the hanging wall side of the normal fault, with a distance of 0.40 km between the point candidate and the normal fault trace. However, the uplift phase of the same point may also be attributable to the location of the point candidate southwest of the footwall side of the normal fault, with a distance of 0.45 km between the point candidate and the normal fault trace, as shown in Figure 124.

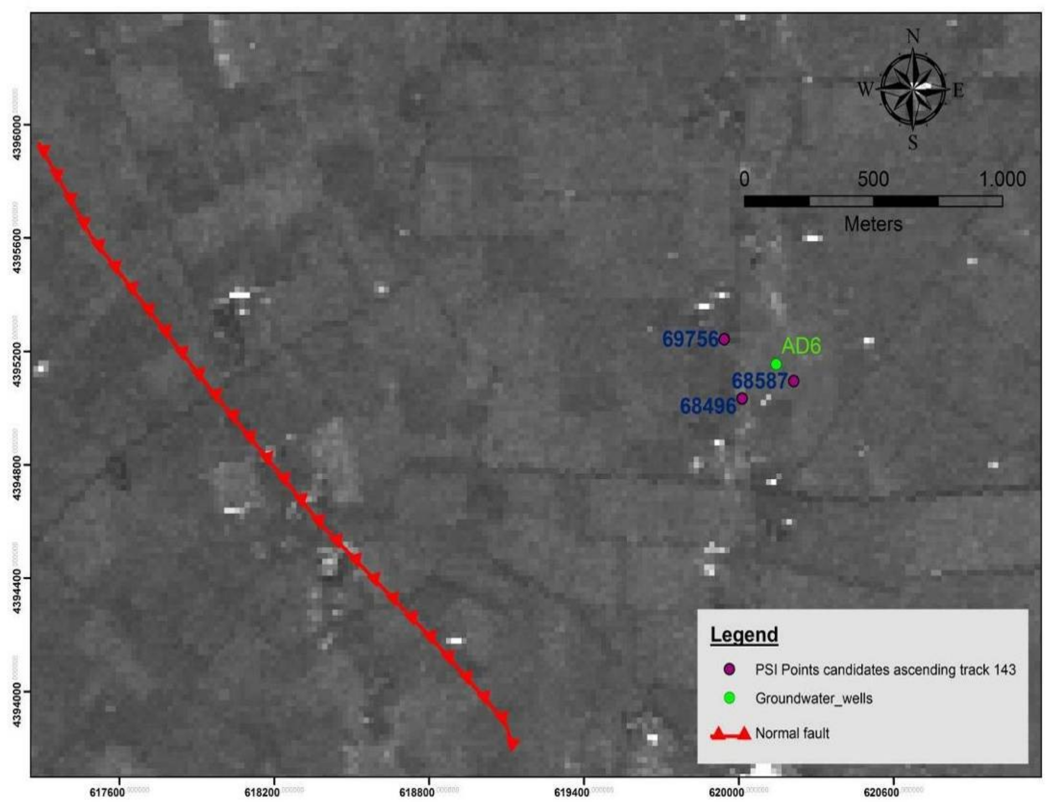

Figure.118 Location of point candidates of PSI of the borehole AD6 corresponding to the normal fault

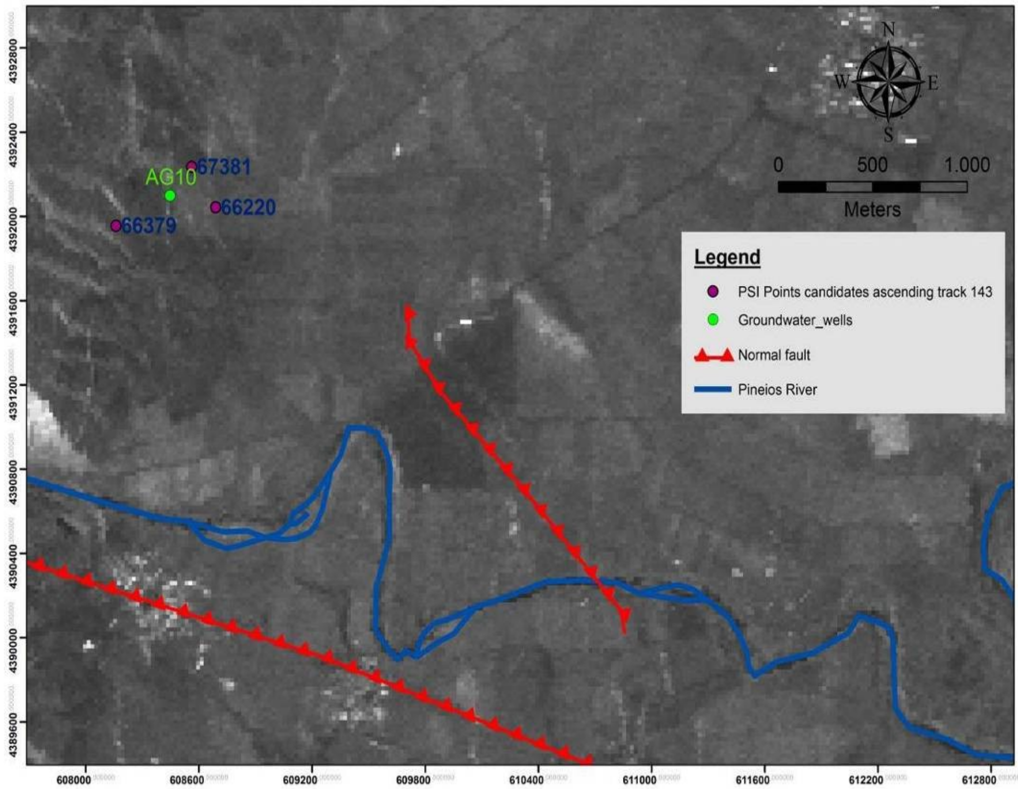

Figure.119 Location of point candidates of PSI of the borehole AG10 corresponding to the normal fault

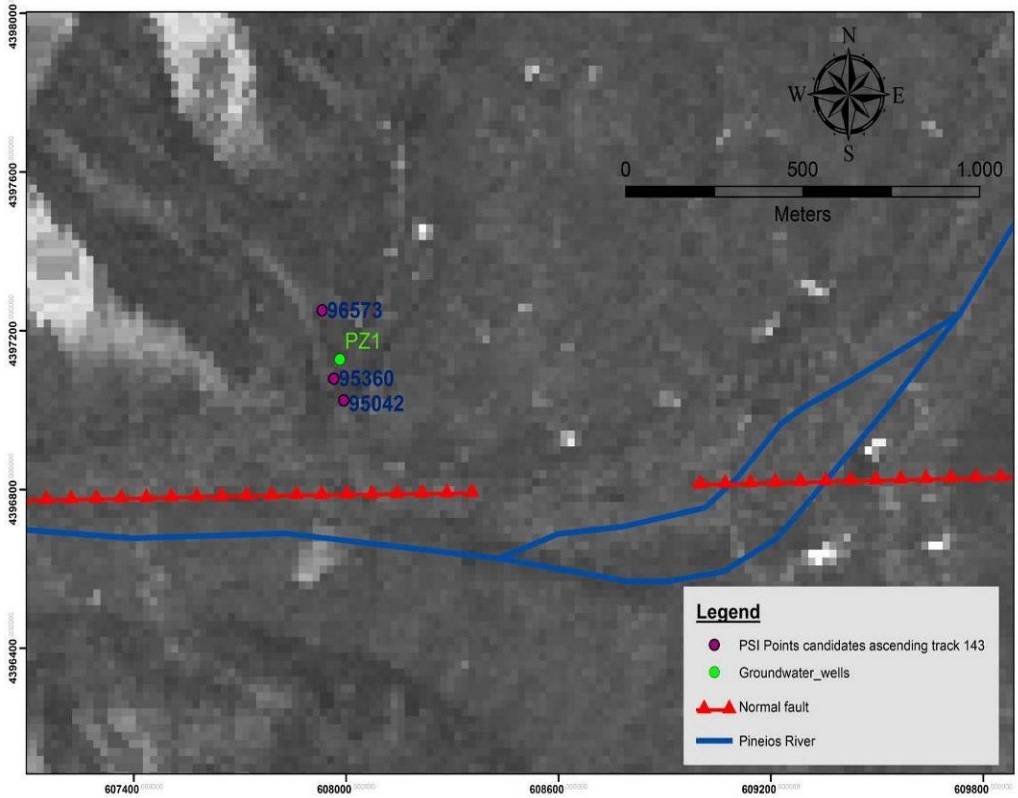

Figure120. Location of point candidates of PSI of the borehole PZ1 corresponding to the normal fault

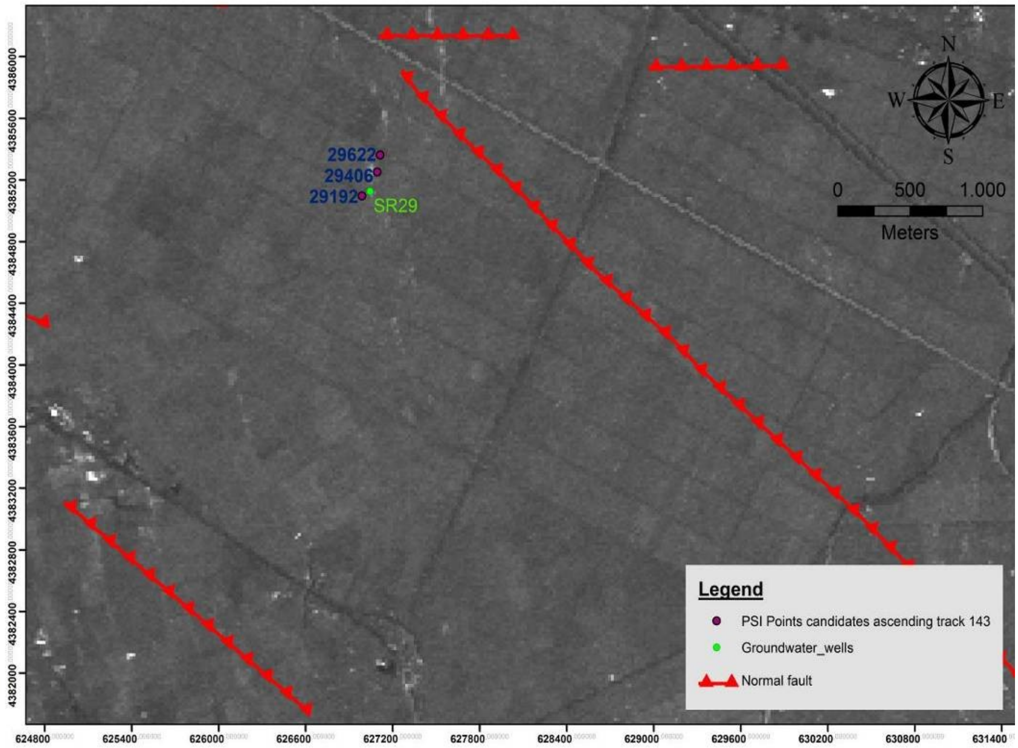

Figure.121 Location of point candidates of PSI of the borehole SR29 corresponding to the normal fault

Figure.122 Location of point candidates of PSI of the borehole SR35 corresponding to the normal fault

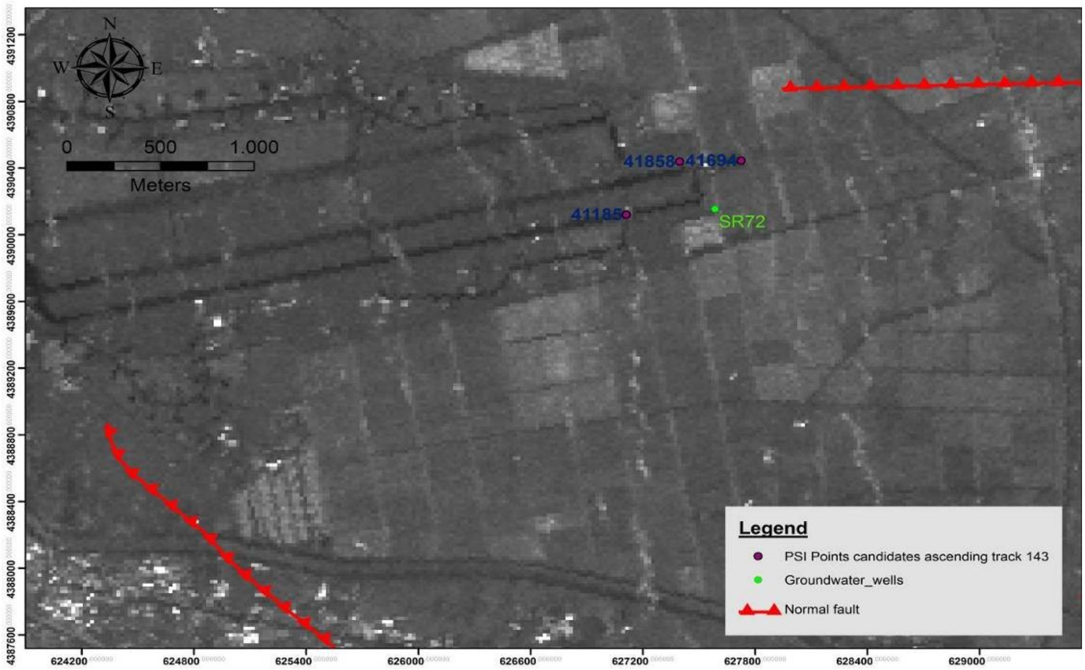

Figure123. Location of point candidates of PSI of the borehole SR72 corresponding to the normal fault

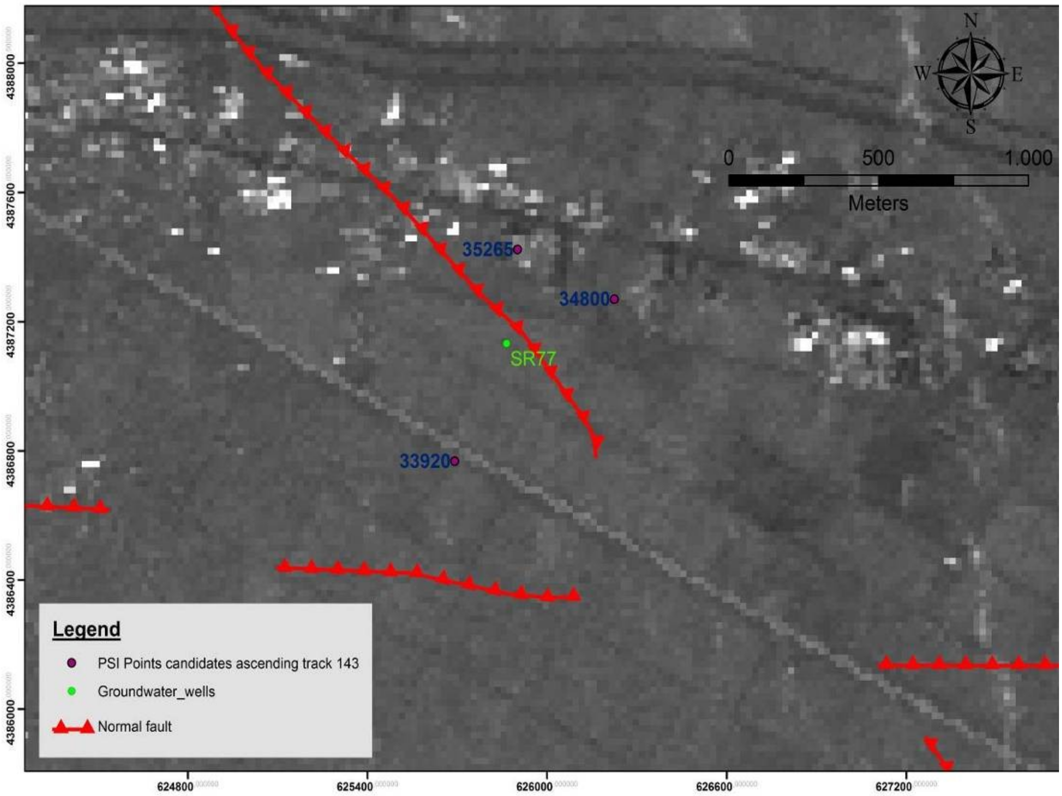

Figure124. Location of point candidates of PSI of the borehole SR77 corresponding to the normal fault

3.11.2.Descending track 279

The name of each borehole will be mentioned, representing the point candidates of PSI which are located around it.

3.11.2.1. SR72

The behaviour of three point candidates in relation to groundwater level has been mentioned previously (Figure 98). Subsidence and uplift phase behaviour is evident from the time series of the three point candidates. The subsidence phase may be attributable to the location of the point candidates east of the hanging wall side of the normal fault, with distances varying between 1.15 and 3.31 km between the three point candidates and the normal fault trace, as shown in Figure 125.

3.11.2.2. SR77

The behaviour of three point candidates in relation to groundwater level has been mentioned previously (Figure 102). Subsidence and uplift phase behaviour is evident from the time series of the three point candidates. For the point candidates with numbers 184117 and 185134, the subsidence phase may be attributable to the location of the point candidates east of the hanging wall side of the normal fault, with distances varying between 0.33 and 0.42 km between the point candidates and the normal fault trace. For the point candidate with number 189118, the subsidence phase may be attributable to the location of the point candidate north of the hanging wall side of the normal fault, with a distance of 0.41 km between the point candidate and the normal fault trace. However, the uplift phase of the same point may also be attributable to the location of the point candidate south of the footwall side of the normal fault, with a distance of 0.50 km between the point candidate and the normal fault trace, as shown in Figure 126.

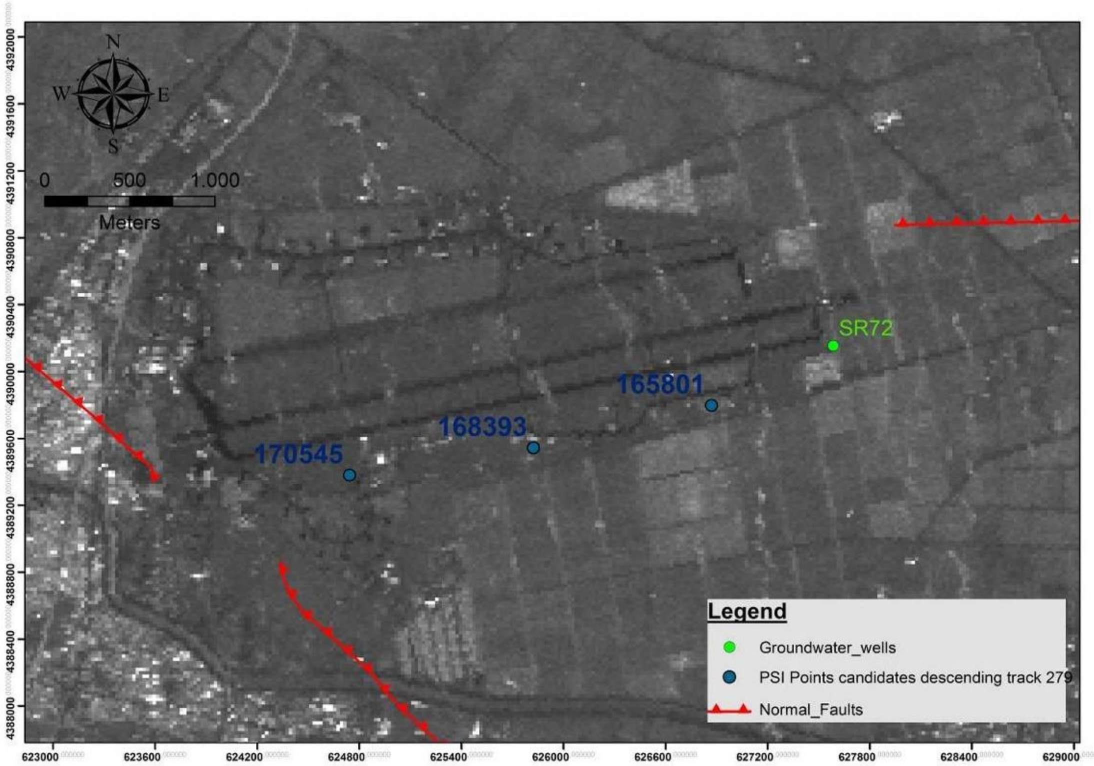

Figure.125 Location of point candidates of PSI of the borehole SR72 corresponding to the normal fault

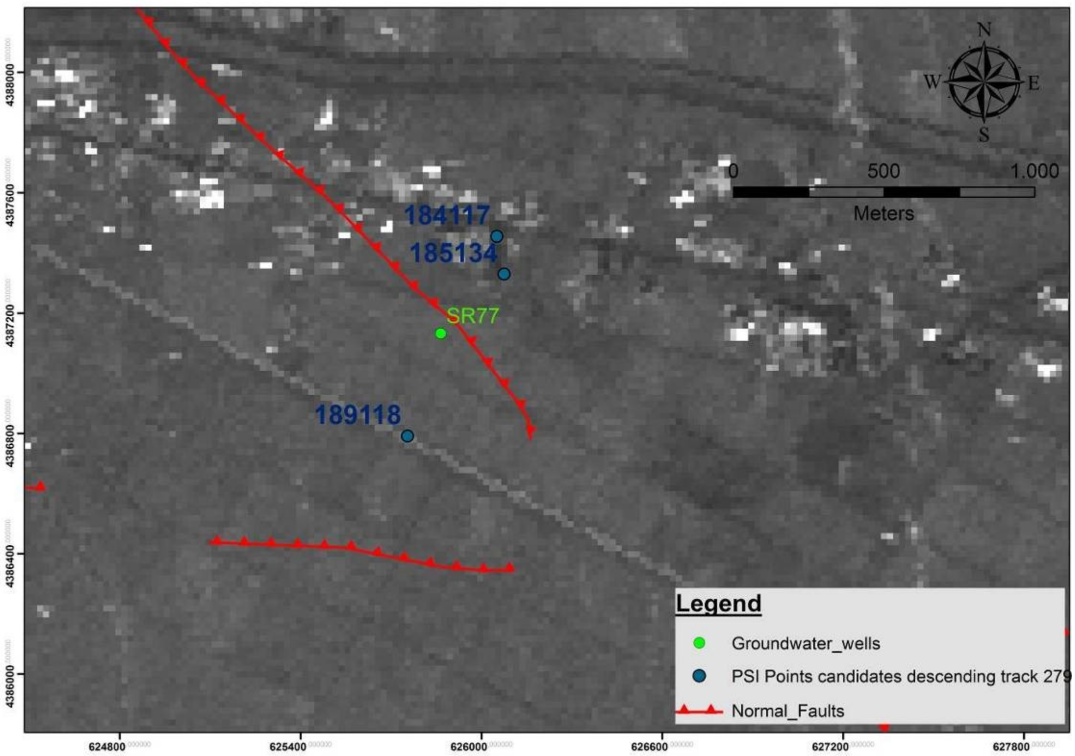

Figure126. Location of point candidates of PSI of the borehole SR77 corresponding to the normal fault

3.12. Interference impact of lithology with groundwater level fluctuation on land deformation

The effect of groundwater level on land deformation has been discussed in detail previously; however, many other parameters apart from groundwater level fluctuation and fault movement may play an important role in land deformation and should be discussed separately. One such parameter is the type of lithology; however, this has been discussed in detail in chapter on the impact of lithology on land deformation. Nevertheless, the interference of this factor with groundwater level fluctuation on land deformation should be discussed. The influence of lithology type will be discussed theoretically, because no statistical correlations have been built or created.

3.12.1. Ascending track 143

Point candidates located around boreholes AD6, SR29, SR35, SR77 and SR72 overlie alluvial deposits. This formation consists mostly of loose fluvial material, and consequently these deposits are particularly prone to subsidence. Subsidence phase behaviour may be attributable to the influence of lithology type, aside from the influence of other factors such as groundwater level and fault movement; however, it is not straightforward to determine the influence of lithology separately from that of other factors within this study due to the absence of statistical correlation between ground deformation and lithology.

Regarding the point candidates of PSI which are located around the borehole AG10, each one overlies a different lithology type. The point candidates with numbers 67381 and 66220 are located over old talus, scree and torrent terraces, usually with carbonate cement of the Pleistocene age. This type of lithology may appear to be resistant to subsidence or uplift due to the presence of the cemented material; nevertheless subsidence and uplift phases are evident from the time series behaviour of ground deformation of these two point candidates. This may be evidence of the influence of groundwater level fluctuation on land deformation or fault movement. Point candidate number 66379 overlies the middle Triassic Jurassic. This lithology type, depending on its material, may appear to be resistant to subsidence and uplift; however, the behaviour of two deformation phases is evident from the time series of ground deformation of the point candidate. This may be attributable to the influence of groundwater level fluctuation on land deformation and fault movement.

The point candidates located around the borehole PZ1 overlie a lithology of old talus cones, scree and torrent terraces of the Pleistocene age. This type of lithology may appear to be resistant to subsidence or uplift due to the presence of cemented material; nevertheless subsidence and uplift phases are evident from the time series behaviour of ground deformation of these point candidates. This may be evidence of the influence of groundwater level fluctuation or fault movement on land deformation.

3.12.2.Descending track 279

The point candidates located around boreholes SR72 and SR77 overlie alluvial deposits. This formation consists mostly of loose fluvial material; therefore these deposits are particularly prone to subsidence. Consequently, the subsidence phase behaviour may be attributable to the influence of lithology type, aside from the influence of other factors such as groundwater level and fault movement.

Chapter Four: Impact of faults movement and earthquakes on ground deformation

4.1. Introduction to faults movement and earthquakes

Faults and earthquakes as results of fault movements have an important influence on ground deformation, concerning natural hazards. These parameters may play an important role in influencing ground deformation within the study area, and in consequence should be discussed separately. The reason is that movement on faults, whether slow (fault creep) or sudden (earthquake), represents a serious problem (Tocher, 1958).

Thessaly region is characterised by considerable neo-tectonic activity. The known active faults are normal and WNW-trending, indicating a NNE extension. The Rodia fault system is composed of several segments characterized by different directions and ages that are described and tentatively analysed here; the fault zone has a general E-W to ESE-WNW direction and bounds to the north the Tyrnavos Low, where the Palaeozoic substratum is in direct contact with Pliocene and mainly Quaternary deposits (Caputo, 1993).

(Caputo and Pavlides, 1993) found that the palaeogeography persisted until the Late Pliocene (Early Pleistocene), when the NE-SW-oriented extension broke up the area and created the Thessalian System, which is a NW-SE trending basin and range system. It consists of a series of structural highs and lows, bounded by major normal faults. The fault pattern of the region is much more complicated, because the area has suffered several different tectonic events, both compression and extensional. Probably because both the latest tectonic events have been extensional, most of the large mapped faults are normal and several of them are active. This bias could also be due to the fact that normal faults usually create more prominent and persistent morphological features than a reverse fault or a thrust. Normal faulting and structural blocks are widespread in Thessaly. They have two principal trends. The NW-SE trend is the most dominant on a regional scale, but it is not so well defined by major faults and just a few of the NW-SE trending major faults can be clearly mapped in the field. Nevertheless, the basin and range-like Thessalian System is generated by this fault set. In contrast, the E-W to ESE-WNW trending fault system is easily observed in the field. Its large-scale morphological features are much less prominent then the NW-SE trending ones, but equally evident. Examples are the Almyros and the Vasilika Basins, the Trikala and the Tyrnavos Lows and the Chalkodoni High. Additionally, (Caputo and Pavlides, 1993) noted that the density and distribution patterns of Thessaly faults in the northern and southern sectors do not differ significantly. Also, if we consider the important parameter of the long-term slip-rate which has been estimated for most of the faults, the recent morphotectonic activity of the region seems uniform and similar for the two sectors.

(Caputo et al., 2004) carried out a palaeoseismological investigation along the Tyrnavos Fault, an ESE–WNW trending, north-dipping normal fault representing one of the major tectonic structures bordering the Late Pleistocene–Holocene Tyrnavos Basin of northern Thessaly in central Greece. According to their geological, structural, morphotectonic and geophysical researches, the Tyrnavos Fault can be geometrically and kinematically characterised as a typical Aegean-type active fault.

(Caputo and Helly, 2005) mentioned that the Rodia Fault is one of the major Middle-Late Quaternary faults separating the Tyrnavos Basin from the Gonnoi Horst, Thessaly. In addition, they mentioned that the important aspects to be taken into account are firstly, that it is noteworthy that Larissa town, which is the third largest in Greece, is located only (15–20) km from the possible future epicentre of a strong earthquake; secondly, many houses were constructed before the 1970s and 1980s, and therefore earlier than any major antiseismic criteria were introduced in 1953. As a direct consequence, the vulnerability of these buildings is potentially high. Finally, they suggest that the seismic risk in this sector of Thessaly is probably very high.

(Caputo et al., 2011) have found that most of the faults affecting the Tyrnavos basin are capable of producing damage to the Great Theatre of Larissa, though not all of them are capable of generating the same distribution of cumulative gaps openings in the walls.

The palaeoseismological investigation substantiates the Late Pleistocene to Holocene morphogenic activity of the Tyrnavos Fault, showing a seismotectonic evolution characterized by numerous morphogenic earthquakes during the latest Pleistocene–Holocene times. According to the available data, the recurrence interval for major earthquakes capable of producing some tens of centimetres of vertical displacement along this sector of the fault is in the range of some thousands of years, say 2–4 ka (Caputo et al., 2006).

(Caputo, 1995) mentioned that, taking into account the epicentral distribution of the present century, an apparent anomaly is evident for Thessaly. In the southern sector, seismic activity is widespread, while in the northern sector it is almost completely absent. It is also important to note that both large (M > 6.0) and moderate (4.0 < M ~ 6.0) size earthquakes follow this distribution. Therefore, two possible and alternative solutions may be proposed to explain this pattern. First, a northern rigid, independent and non-deforming block exists or, second, the northern region represents a large seismic gap. In particular, if we take into account major shocks which have occurred during the last decades, and who's associated morphogenic faults have been identified, the same geographically N-S diversified seismic behaviour is manifest. With the exception of the 1941 Larissa earthquake (Ms = 6.1), all the seismic events with magnitude higher than (6.0) occurred in the southern sector.

(Caputo et al., 2011) mentioned that the instrumental record starts in 1911 and lists nine earthquakes with magnitudes of 6.0 or above. The strongest among these was the 1954 Sophades earthquake, with a surface wave magnitude of Ms = 6.7. In addition, regarding the Larissa settlement, they mentioned that Larissa, the capital of Thessaly, is located in the eastern part of Central Greece, at the southern border of a Late Quarternary graben, the Tyrnavos Basin. Palaeoseismological, morphotectonic, and geophysical investigations as well as historical and instrumental records show evidence of seismic activity in this area. Previous investigations have documented the occurrence of several moderate to strong earthquakes during the Holocene time on active faults, with recurrence intervals of a few thousand years.

4.2. Results and Discussions

In order to examine and investigate the correlation between fault movements and ground deformation by implementing three techniques, conventional SAR interferometric, interferometric stacking and persistent scatterers interferometry (PSI), fault traces which are distributed within the study area of the eastern part of northern Thessaly were digitized from the papers by (Caputo, 1993), (Caputo and Pavlides, 1993), (Caputo et al., 1994), (Caputo et al., 2004), (Caputo and Helly, 2005) and

(Caputo et al., 2006). Thereafter these were corrected and rectified depending on 7 geological maps of Thessaly at a scale of 1:50,000 issued by the Greek Institute of Geology and Mineral Exploration, which were used along with field observations. The maps cover Larissa, Farkadona, Platykampos, Gonnoi, Trikala, Rapsani, and Sofades. In addition, by using a seismotectonic map of Greece with seismogeological data at a scale of 1:500,000, a shape file was consequently created and identified utilizing GIS software ArcGIS 9.3. Table 39 shows the surface location and principal geometrical parameters of the active faults.

According to the Greek Seismic Code (EAK, 2000), Greece is divided into three seismic hazard zones. The study area is located in the second zone, where the design acceleration on seismic bedrock is assigned as 0.24g. Figure 127 shows the New Seismic Hazard Map of Greece.

Note that it is necessary also to map the earthquake events which have occurred within the study area in order to recognize the activity of faults, since without the presence of faults there would be no earthquake events, and furthermore to correlate and forecast the influence of fault movements and earthquakes on ground deformation.

Earthquake events data within the study area were collected by utilizing the earthquake catalogue of the (Institute of Geodynamics), National Observatory of Athens, and an attribute table was then created from this catalogue. Consequently, a shape file of earthquake events was created utilizing Arc GIS 9.3 for the period 1964 – 2010 with magnitude M >= 3 and depth varying between 0 – 30 km. The distribution of faults and earthquake epicentres within the study area is depicted in Figure 128. It can be seen that within the study area the eastern part of northern Thessaly has not experienced earthquakes with magnitude M > 4, as shown in Table 40.

Table 39. Fault parameters from (Caputo et al., 2011)

Fault	Latitude	Longitude	Length (km)	Width (km)	Dip	strike
Rodia RF	39.83◦N	22.25◦E	15	10	50 ◦ S	109◦
Ghyrtoni GF	39.74◦N	22.44◦E	12	8	60 ◦ S	101◦
Tyrnavos TF	39.73◦N	22.16◦E	13	9	50 ◦ N	282◦
Larissa LF	39.66◦N	22.23◦E	18	12	60 ◦ N	285◦
Asmaki AF	39.66◦N	22.49◦E	10	7	60 ◦ N	272◦
Dimitra DF	39.69◦N	22.49◦E	10	7	60 ◦ N	276◦
Kastri KF	39.63◦N	22.53◦E	12	8	60 ◦ N	269◦

Surface location and principal geometrical parameters of the active faults in the simplified seismotectonic model of the Tyrnavos Basin. Latitude and longitude are referred to the western corner of the fault trace. Dip and strike are in the convention of Aki and Richards' (1980) source orientation for all earthquakes.

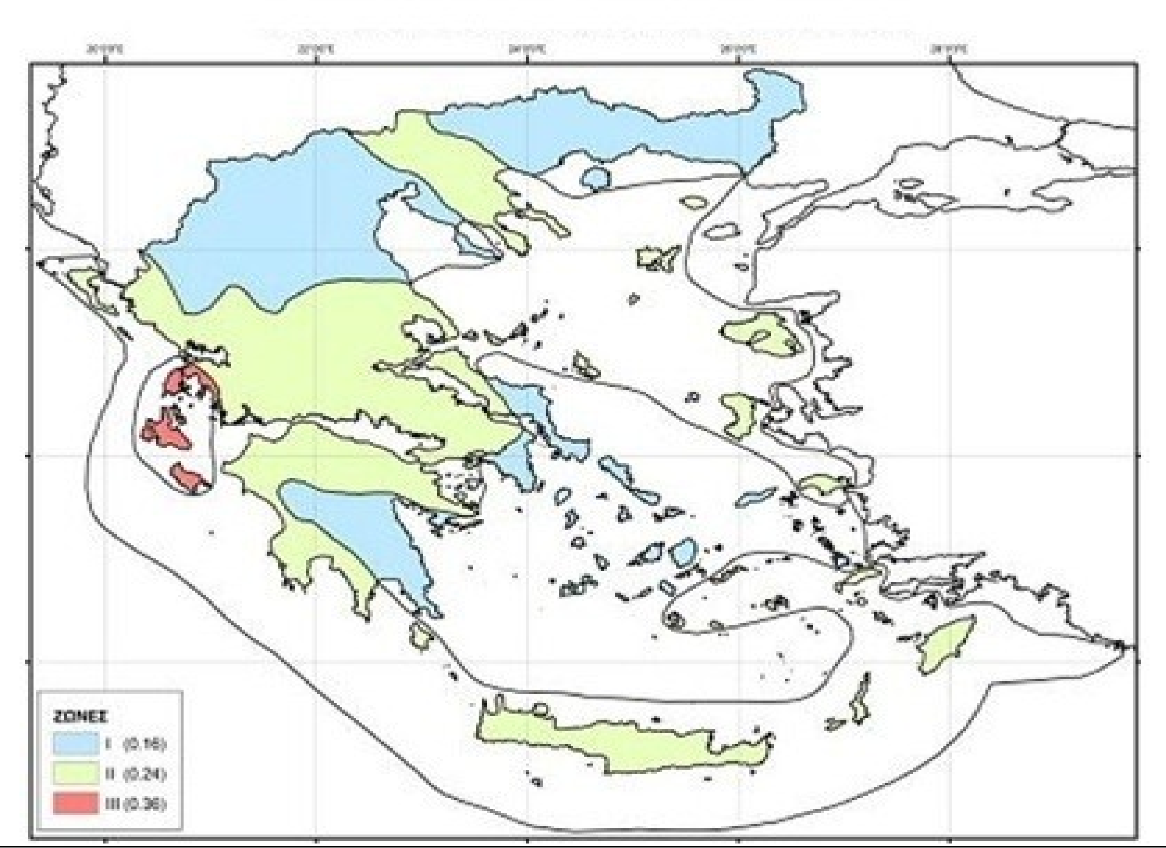

Figure.127 Map of New Seismic Hazard of Greece (EAK, 2000)

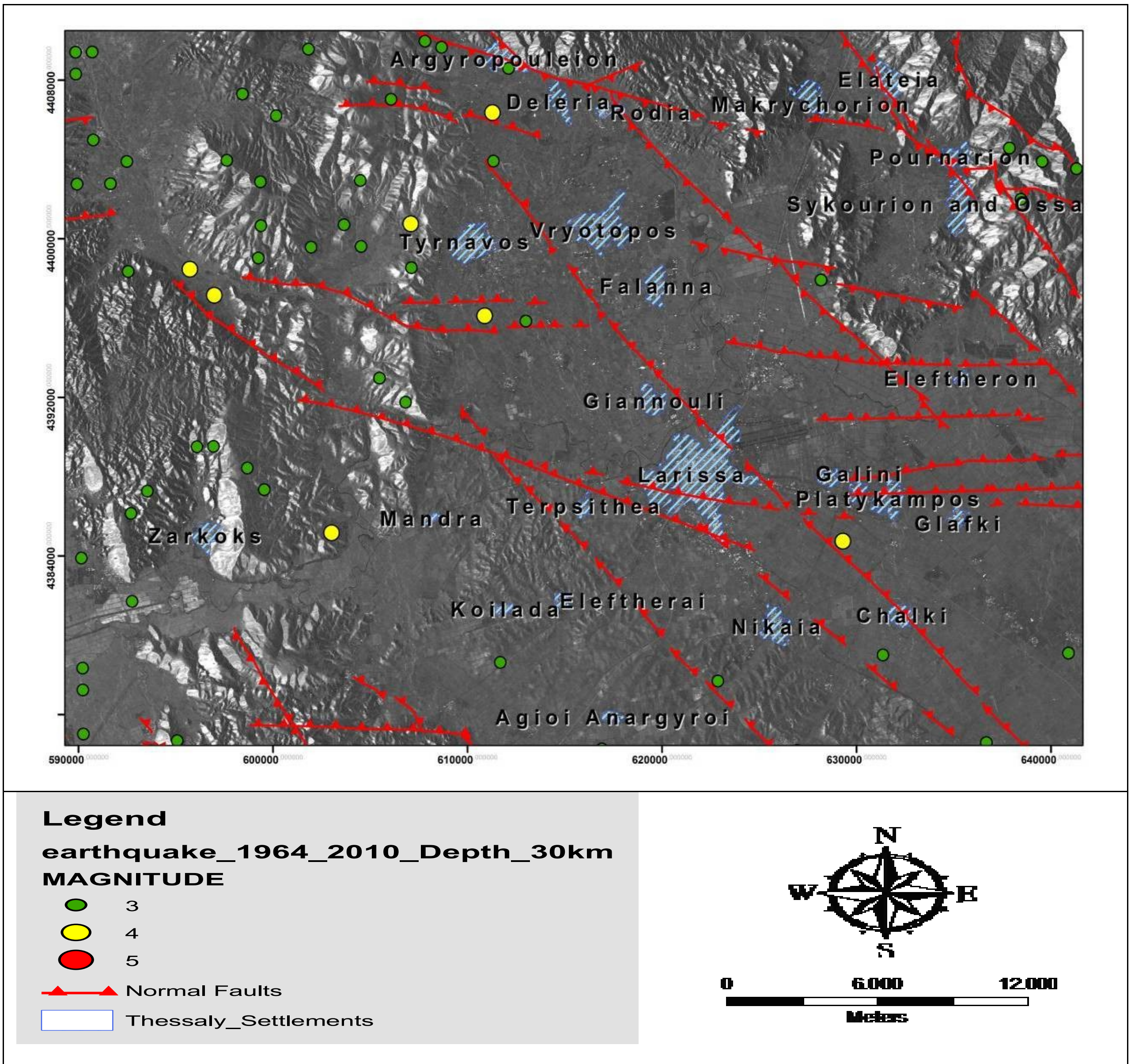

Figure.128 Distribution of faults and earthquakes within study area

Table 40. List of earthquakes which occurred from 1964 – 2010 in the northern part of eastern Thessaly data from (Institute of Geodynamics), National Observatory of Athens

Time	Latitude	Longitude	Depth	Magnitude
19 58 3.0	39,80	22,30	0	4
16 16 58.7	39,60	21,90	0	4
23 16 11.0	39,75	22,00	0	3
03 38 34.0	39,75	22,50	0	3
10 57 6.0	39,70	22,10	0	4
05 33 5.0	39,75	22,25	0	4
22 12 48.0	39,50	22,20	0	3
00 14 40.0	39,40	22,40	0	3
20 26 46.0	39,50	22,10	0	3
06 00 24.0	39,70	22,30	0	4
02 58 11.0	39,60	22,70	0	3
06 31 22.0	39,40	22,40	0	4
10 05 24.0	39,50	22,30	0	3
07 56 18.0	39,60	21,90	0	3
20 09 55.0	39,60	22,70	0	3
07 07 46.0	39,60	22,00	0	3
12 02 51.0	39,40	22,20	0	5
22 44 40.0	39,40	22,00	0	4
12 31 42.0	39,90	22,10	0	3
15 46 9.0	39,40	22,30	0	3
20 27 41.4	39,40	22,00	0	3
19 28 22.7	39,50	22,50	10	4
18 24 33.3	39,40	22,20	10	3
06 34 4.0	39,40	22,00	0	4
17 25 42.0	39,50	22,00	0	3
13 37 27.0	39,70	21,90	0	4
13 07 39.0	39,60	22,00	0	3
23 10 13.5	39,85	22,68	5	3
04 14 55.9	39,53	21,88	6	3
11 11 9.5	39,45	22,65	1	3
08 41 19.0	39,47	22,51	1	3
12 04 53.1	39,91	22,38	1	4
06 44 24.5	39,87	22,28	1	3
10 48 32.7	39,81	22,00	28	3
10 49 20.0	39,82	22,05	15	3
03 31 40.0	39,77	22,07	9	3
01 20 33.3	39,77	22,05	10	3
02 02 3.6	39,73	22,25	10	3
00 15 59.7	39,63	22,09	8	3
15 32 31.8	39,40	22,08	4	3
03 57 40.2	39,86	22,30	5	3
20 20 24.6	39,89	22,21	5	4
10 14 3.5	39,95	22,03	27	4
16 00 36.9	39,92	22,06	5	3
09 12 6.9	39,85	22,14	5	3
14 44 9.7	39,42	22,18	5	3
11 53 1.1	39,56	22,53	10	3
13 16 49.0	39,84	22,26	5	3

Supplement Table 40. List of earthquakes which occurred from 1964 – 2010 in the northern part of eastern Thessaly data from (Institute of Geodynamics), National Observatory of Athens

Time	Latitude	Longitude	Depth	Magnitude
18 00 21.2	39,87	22,26	5	3
20 30 39.4	39,76	21,89	5	4
23 25 23.7	39,82	21,90	5	3
03 25 7.3	39,97	22,01	5	3
23 05 25.5	39,73	21,89	5	3
23 10 52.7	39,70	21,91	5	3
23 20 30.9	39,74	21,97	5	3
17 35 27.2	39,54	22,43	5	3
21 43 30.7	39,39	22,63	29	3
22 30 33.8	39,55	22,30	5	3
20 15 18.0	39,53	21,98	10	3
21 043	39,60	22,05	5	3
11 08 36.7	39,54	22,05	5	3
20 22 8.1	39,55	22,05	5	3
04 31 55.3	39,87	22,03	1	3
04 57 2.9	39,96	22,45	1	3
07 02 10.9	39,37	22,54	20	3
12 34 36.5	39,92	22,56	6	4
23 22 34.0	39,95	22,49	25	3
10 00 6.4	39,97	22,54	7	3
05 24 5.9	39,97	22,45	5	3
03 56 33.6	39,52	22,05	17	3
17 36 58.0	40,00	22,00	5	3
17 32 35.6	40,00	22,00	5	3
12 08 42.9	40,00	23,00	10	4
04 48 30.2	40,00	22,00	5	3
15 30 36.7	40,00	22,00	10	3
21 42 5.2	40,00	22,00	5	3
20 03 2.9	39,00	22,00	9	3
03 54 2.3	39,49	22,67	10	3
20 32 9.6	39,42	22,55	5	3
15 22 31.8	39,55	22,64	5	3
20 28 55.7	39,93	22,38	30	3
03 52 58.2	39,92	22,43	13	3
00 07 38.7	39,91	22,55	5	3
00 33 30.7	39,92	22,51	5	3
12 18 41.7	39,91	22,45	10	3
20 05 40.3	39,38	22,64	5	3
00 15 5.6	39,61	22,20	12	4
23 56 54.8	39,71	21,95	5	3
19 57 43.9	39,48	22,23	5	3
03 03 6.7	39,46	21,85	26	3
01 40 21.2	39,33	22,61	5	3
18 48 44.1	39,38	22,27	10	3
04 58 31.9	39,91	22,03	5	3
21 12 50.2	39,42	22,31	10	3
03 41 53.5	39,91	22,16	10	3
08 28 4.4	39,90	22,48	8	3
19 18 58.8	39,80	22,24	5	3
21 00 18.9	39,66	22,24	25	3
19 46 58.2	39,93	22,49	7	3

Supplement Table 40. List of earthquakes which occurred from 1964 – 2010 in the northern part of eastern Thessaly data from (Institute of Geodynamics), National Observatory of Athens

Time	Latitude	Longitude	Depth	Magnitude
07 06 40.7	39,94	22,35	18	5
07 27 58.7	39,94	22,37	5	3
07 30 19.1	39,82	22,31	5	3
12 29 40.3	39,69	22,32	25	3
21 04 12.7	39,95	21,96	10	3
11 39 36.9	39,42	22,45	5	3
23 51 48.2	39,94	22,43	25	3
19 00 07.8	39,78	21,99	10	3
12 41 15.4	39,71	22,09	10	4
00 45 53.6	39,81	22,15	28	3
00 54 55.5	39,78	22,14	28	3
00 58 41.3	39,76	21,99	28	3
01 30 22.6	39,80	22,17	27	3
03 50 29.0	39,74	22,02	30	3
04 34 40.5	39,63	22,69	21	3
23 59 11.5	39,69	21,90	10	3
20 16 23.1	39,36	22,35	24	3
16 47 02.4	39,72	22,68	10	3
17 15 33.3	39,42	21,98	10	3
23 46 09.3	39,79	22,06	24	3
15 14 25.7	39,96	22,44	17	3
11 34 30.8	39,52	21,90	26	3
17 52 44.0	39,70	21,85	10	3
14 40 07.4	39,89	21,98	25	3
06 23 12.1	39,96	22,45	24	4
13 13 07.2	39,58	22,08	15	3
09 28 28.8	39,76	21,90	24	4
01 25 37.9	39,56	21,82	5	3
22 52 21.7	39,91	21,93	3	3
06 02 46.1	39,91	21,93	5	3
00 20 53.7	39,90	21,99	15	3
00 13 27.7	39,78	22,08	10	3
02 32 48.3	39,89	21,90	4	3
12 43 04.6	39,46	22,60	23	3
09 56 39.5	39,90	21,89	5	3
11 21 43.7	39,90	21,90	19	3
06 01 24.6	39,95	22,16	4	3
12 13 28.9	39,74	22,22	4	3
09 01 30.7	39,91	21,97	5	3
09 56 52.3	39,90	21,93	5	3
00 29 50.7	39,75	21,87	20	3
13 30 50.3	39,91	21,94	5	3
04 31 43.6	39,78	22,29	5	3
01 37 09.8	39,62	22,08	17	3
14 48 35.8	39,35	22,41	19	3
22 19 44.4	39,91	22,00	4	3
18 20 57.0	39,88	21,89	3	3
12 04 07.9	39,74	21,91	8	3
03 15 24.3	39,88	22,05	4	3
23 34 05.0	39,85	22,01	6	3

Supplement Table 40. List of earthquakes which occurred from 1964 – 2010 in the northern part of eastern Thessaly data from (Institute of Geodynamics), National Observatory of Athens

Time	Latitude	Longitude	Depth	Magnitude
16 26 42.6	39,76	21,96	10	3
06 29 45.1	39,38	22,37	3	3
08 00 00.8	39,86	22,62	25	4
03 05 35.5	39,91	22,01	10	3
08 11 11.2	39,39	22,02	25	3
08 14 27.9	39,36	22,60	19	3
02 35 52.5	39,36	22,62	23	3
00 51 23.9	39,34	22,60	17	3
10 20 52.0	39,35	22,60	22	3
12 52 31.7	39,38	22,61	4	3
19 16 28.0	39,38	22,61	21	3
12 34 24.7	39,37	22,46	17	3
18 58 06.9	39,37	22,45	20	3
01 13 54.7	39,36	22,47	17	3
12 54 08.8	39,75	22,21	15	3
18 13 34.7	39,65	22,12	17	3
13 36 27.3	39,76	22,61	15	3
23 28 36.4	39,77	22,65	22	3
00 50 06.6	39,51	22,08	17	3
14 34 11.7	39,74	22,19	7	3
01 01 21.0	39,48	22,09	5	3
07 28 15.4	39,73	22,14	5	3
14 42 43.3	39,56	21,96	24	3
02 40 07.9	39,77	22,22	19	3
03 09 08.9	39,77	22,16	9	3
13 41 44.0	39,43	22,60	21	3
18 42 09.6	39,45	22,61	22	3
12 34 28.3	39,43	22,61	25	3
18 39 48.2	39,40	22,62	19	3
10 33 03.0	39,83	22,72	21	3
01 59 32.1	39,51	22,59	3	3
02 09 30.4	39,50	22,60	16	3
03 39 37.4	39,68	22,23	5	3
20 01 09.9	39,94	22,46	22	3
17 10 44.8	39,63	22,16	15	3
20 21 40.2	39,65	22,13	15	3
20 45 58.9	39,64	22,15	10	3
03 58 56.5	39,94	22,46	13	3
23 03 21.2	39,85	22,08	5	3
12 22 36.6	39,40	22,60	21	3
21 11 50.2	39,39	22,01	29	3
21 20 59.3	39,38	22,01	29	3
20 01 11.6	39,90	22,50	6	3
18 27 15.0	39,83	22,05	12	3
23 56 54.5	39,83	22,06	4	3
01 23 53.3	39,83	22,27	20	3
18 57 59.9	39,83	22,19	10	3
22 48 17.0	39,78	22,61	16	3
00 21 20.3	39,78	22,63	21	3
06 54 52.5	39,73	22,08	12	3

Supplement Table 40. List of earthquakes which occurred from 1964 – 2010 in the northern part of eastern Thessaly data from (Institute of Geodynamics), National Observatory of Athens

Time	Latitude	Longitude	Depth	Magnitude
02 10 14.6	39,42	22,03	20	3
19 47 46.9	39,43	22,01	23	3
11 25 14.6	39,51	22,36	23	3
11 45 17.9	39,75	22,16	4	3
18 55 08.3	39,71	21,94	12	3
18 59 31.2	39,75	21,93	25	3
19 02 25.9	39,73	21,90	14	3
19 22 41.9	39,75	22,00	18	3
19 38 49.5	39,70	21,95	11	3
07 12 43.9	39,33	22,59	28	3
13 37 57.8	39,75	22,00	9	3
00 24 30.9	39,49	21,99	13	3
15 12 55.3	39,36	22,51	23	3
17 53 12.6	39,82	22,75	10	3
23 42 04.5	39,54	22,71	24	3
23 47 50.0	39,57	22,67	3	3
08 17 36.8	39,76	21,90	24	3
11 39 25.5	39,76	21,89	24	3
19 42 32.7	39,77	21,87	16	3
03 40 22.5	39,55	22,68	8	3
04 37 49.2	39,53	22,69	6	3
19 26 37.4	39,54	22,67	5	3
18 40 01.6	39,96	22,59	7	3
18 41 22.3	39,96	22,59	5	3

The interference effects of fault movement on ground deformation will be discussed and interpreted in a probability approach depending on spatial correlation, for the reason that no statistical correlation or model-building has been done between ground deformation and fault movement. In other words, in deformation either subsidence or uplift may be attributable to the influence of faults movements. Three techniques have been implemented to identify and investigate the impact of fault movements on ground deformation using two tracks, ascending and descending.

4.2.1. Ascending track 143

4.2.1.1. Interferometric stacking

The results of the interferometric stacking technique, using an ascending track, were depicted previously in Figure 10 in the processing chapter. Interferometric stacking patterns results are confined to the settlements of the study area, without any results for interferometric patterns within agricultural lands, which is the reverse of the single interferogram results. Since interferometric stacking patterns were observed within all the settlements in the study area, the patterns within each settlement were isolated and superimposed utilizing an ArcGIS environment to extract statistical results of ground deformation. Thirty settlements were identified, but just 19 of them were selected to examine and investigate the influence of faults movement on land deformation. The reason for selecting these settlements is based on the type of lithology, since each of the nineteen overlies just one type of lithology, whereas the others all overlie more than one type of lithology. The minimum and maximum rates of ground deformation, subsidence and uplift, of each settlement are depicted in Table 41.

Table 41. Minimum and maximum deformation rates in LOS of interferometric stacking, 1995-2008

I.d	Settlements	Minimum Subsidence mm	Maximum Subsidence mm	Mean	Minimum Uplift mm	Maximum Uplift mm	Mean
1	Larissa	-0.46	-2.961	-1.710	0.545	6.636	3.276
2	Giannouli	-0.131	-3.574	-1.852	0.729	4.171	2.450
3	Chalki	-0.208	-2.842	-1.494	0.42	4.317	2.039
4	Eleftheron	-0.225	-0.225	-0.224	0.56	3.526	2.066
5	Falanna	-0.05	-2..4	-1.048	0.539	3.691	1.832
6	Melissochorion	-0.126	-1.713	-0.859	0.567	3.278	1.657
7	Galini	-0.10	-0.11	-0.105	0.694	3.692	1.973
8	Platykampos	-0.138	-3.027	-1.441	0.527	3.463	1.770
9	Glafki	-0.874	-0.9	-0.84	0.146	3.67	1.855
10	Itea	-0.131	-4.313	-1.947	0.463	2.946	1.575
11	Fyllon	-0. 01	-1.108	-0.551	0.326	3.502	1.598
12	Palamas	-0.216	-1.676	-0.945	0.348	3.306	1.497
13	Marathea	-0.664	-1.545	-1.104	0.211	2.891	1.371
14	Nikaia	-0.75	-0.8	-0.77	0.217	4.269	1.850
15	Terpsithea	Null	Null	Null	0.218	4.384	2.688
16	Tyrnavos	-0.178	-1.447	-0.735	0.14	2.504	1.052
17	Rodia	-0.036	-0.752	-0.393	0.284	3.109	1.254
18	Mandra	-0.086	-1.587	-0.681	0.127	1.316	0.665
19	Eleftherai	-0.34	-0.35	-0.345	0.267	3.365	1.552

In the following, the ground deformation of each settlement will be discussed separately.

4.2.1.1.1. Larissa

The results of interferometric stacking patterns and total deformation rate estimation during the period June 1995 – March 2008 for Larissa are shown in Figure 129. Ground deformation results within the settlement of Larissa indicate that the subsidence varies in the range - 0.46 – - 2.961 mm/year, while uplift varies in the range 0.545 – 6.636 mm/year. Two phase's patterns for subsidence and uplift are distributed through the settlement of Larissa. Three big fault traces pass through the settlement, the first one crossing from the northeast side of the settlement, the second crossing from the south side, and the third one crossing from south of the settlement's border. Interferometric patterns of subsidence are distributed over the northern, middle and southern parts of the settlement. Subsidence within Larissa may be attributed to its location, which is on the side of the hanging walls of normal fault traces in the northern, middle and southern parts of the settlement. Furthermore, subsidence in the northern part of the settlement may be attributed to the liquefaction hazard, as found by (Papathanassiou and Christaras, 2008), who found that the northern part of the city, taking a probability approach of 50%, can be defined as the boundary between the occurrence and non-occurrence of liquefaction-induced ground disruption, and in two areas surface evidence of liquefaction is likely to occur for these earthquake parameters. It is worth mentioning that this applies to all the following results for subsidence in the northern part of the settlement, in all techniques and tracks. In addition, the uplift patterns which are distributed in the northern, middle and southern parts of the settlement may also be attributed to their location, which is at the side of the footwalls of the normal fault traces.

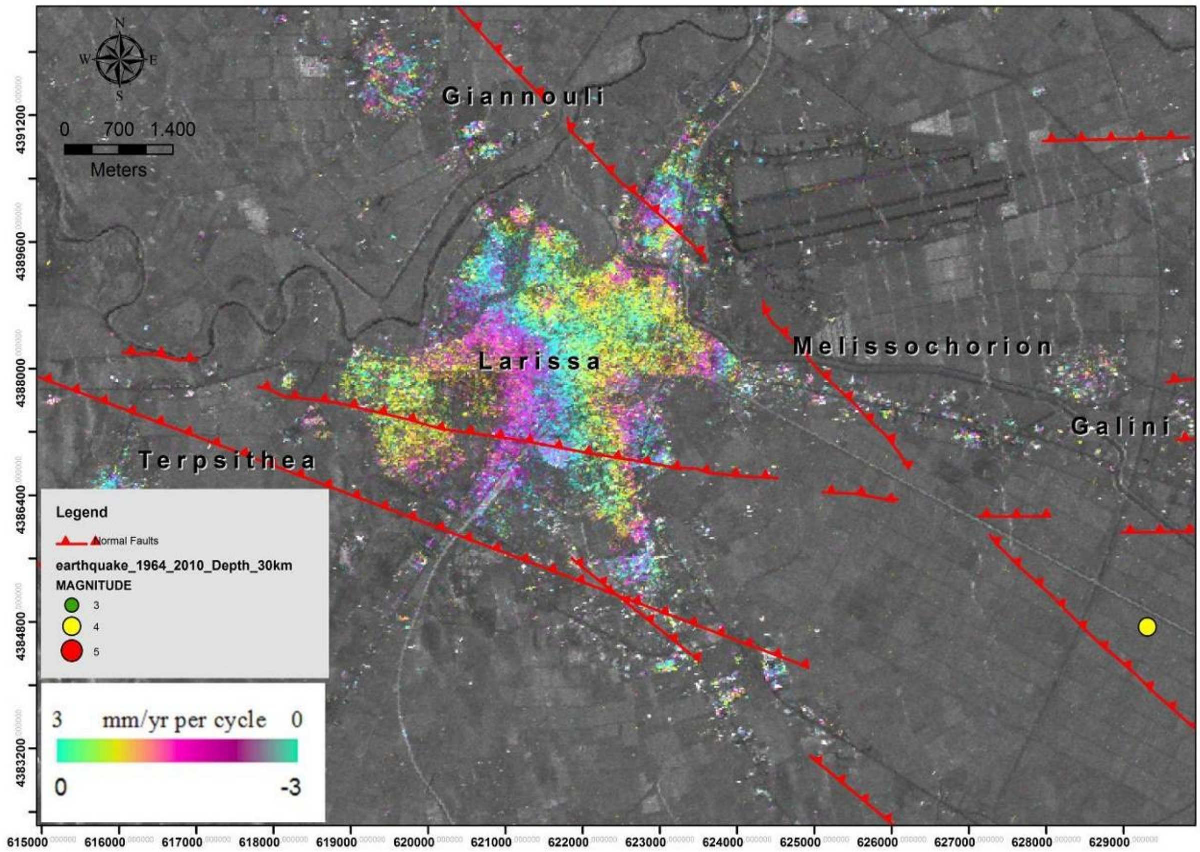

Figure.129 Total deformation at Larissa estimated with interferometric stacking technique, June 1995-March 2008

4.2.1.1.2. Giannouli

The results of interferometric stacking patterns and total deformation rate estimation during the period June 1995 – March 2008 for Giannouli are shown in Figure 130. Ground deformation results within Giannouli settlement indicate that the subsidence varies in the range -0.131 – -3.574 mm/year, while the uplift varies in the range 0.729 – 4.171 mm/year. Two phase patterns for subsidence and uplift are observed distributed all over the settlement, which is located southwest of a normal fault trace. The interferometric pattern of subsidence is distributed over the northern, western and southern parts of the settlement, whereas slight subsidence patterns are observed in the southeastern and central eastern parts. Uplift patterns are concentrated along the eastern, northeastern, and southeastern parts of the settlement. Subsidence may be attributed to the impact of other effects of fault movement, while uplift may be attributed to the location of the settlement 1.13 km southeast of the footwall of a normal fault trace, and possibly for that reason the uplift patterns are observed on the opposite side of the footwall.

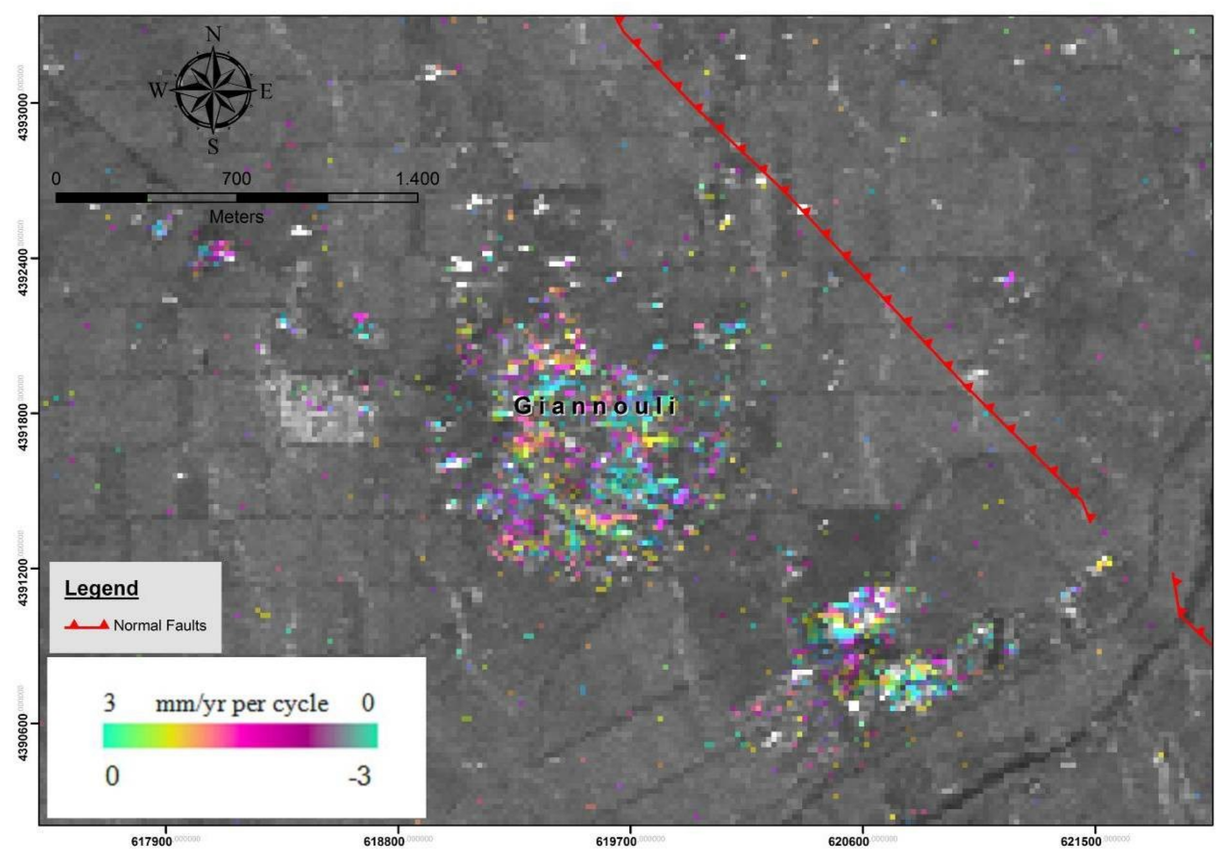

Figure130. Total deformation at Giannouli estimated with interferometric stacking technique, June 1995-March, 2008

4.2.1.1.3. Chalki

The results of interferometric stacking patterns and total deformation rate estimation during the period June 1995 – March 2008 for Chalki are shown in Figure 131. Ground deformation results within the settlement of Chalki indicate that the subsidence varies in the range -0.208 – -2.842 mm/year, while uplift varies in the range 0.42 – 4.317 mm/year. A normal fault is crossed and interrupted by the settlement from the northwest to the southeast. Two phase patterns for subsidence and uplift are observed distributed over the whole settlement. Subsidence is observed in the northeastern and eastern parts of the settlement, which may be attributed to the location of these parts in the side of the hanging wall of a normal fault trace. The uplift patterns which are observed distributed in the northern, central and southern parts of the settlement may be attributed to the location of these parts in the side of the footwall of the same normal fault trace. The patterns of subsidence which are observed in the eastern and central parts of the settlement may be attributed to the location of the settlement 3.5 km east of the hanging wall of another normal fault trace.

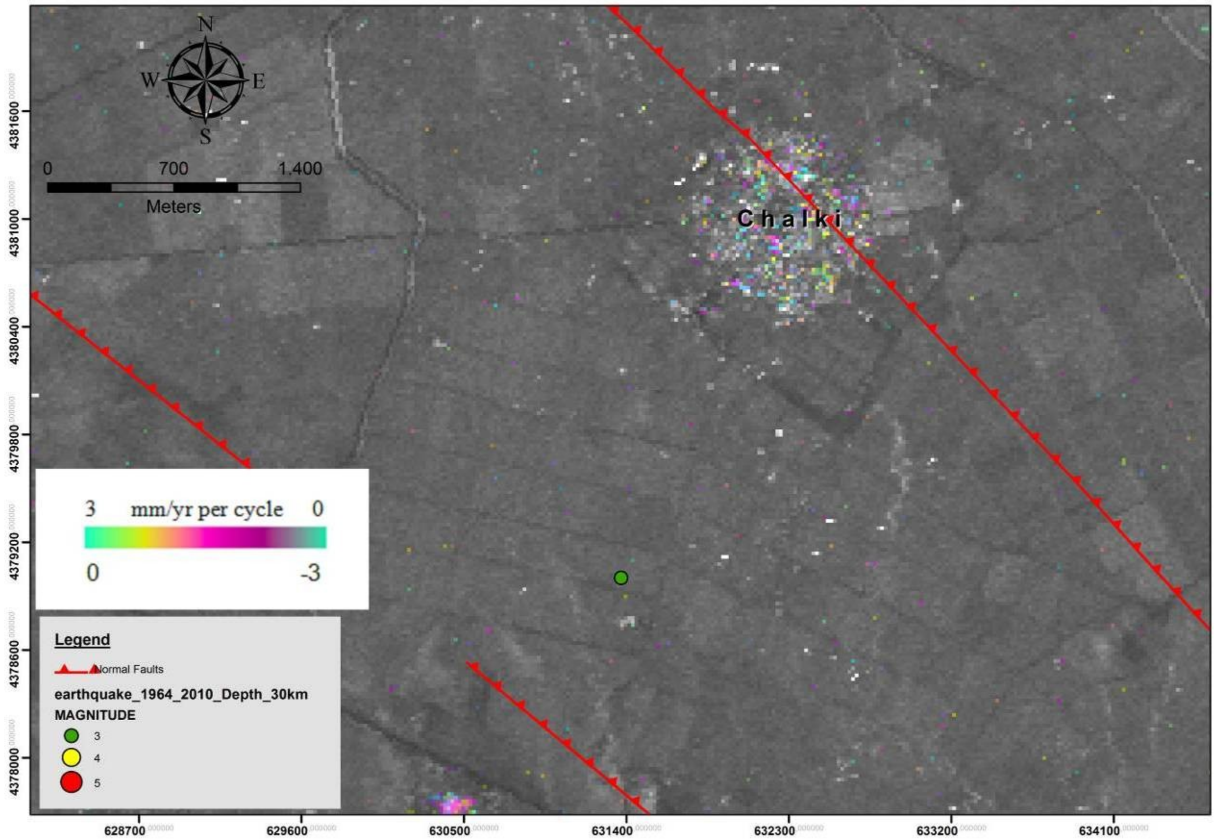

Figure131. Total deformation at Chalki estimated with interferometric stacking technique, June 1995-March 2008

4.2.1.1.4. Eleftheron

The results of interferometric stacking patterns and total deformation rate estimation during the period June 1995 – March 2008 for Eleftheron are shown in Figure 132. Ground deformation results within Eleftheron settlement indicate that the subsidence varies in the range -0.225 – -0.225 mm/year, while uplift varies in the range 0.556 – 3.526. The settlement is located in the middle of four normal faults; the first is located 0.33 km to the north, the second is 1.66 km to the south, and the third and fourth faults are located 2.4 km west and 4.7 km east respectively. Subsidence patterns are observed on the southwestern side as well as appearing slightly in the middle of the settlement. Subsidence in the southwestern part of the settlement may be attributed to its location south of the hanging wall of a normal fault trace, as mentioned above, while the subsidence observed in the middle and northwest of the settlement may be attributed to other impact factors, because this part of the settlement is located south of the footwall of a normal fault trace. Uplift is observed along the northeastern and southwestern border of the settlement, which may be attributed to the location of the settlement south of the footwall of a normal fault trace.

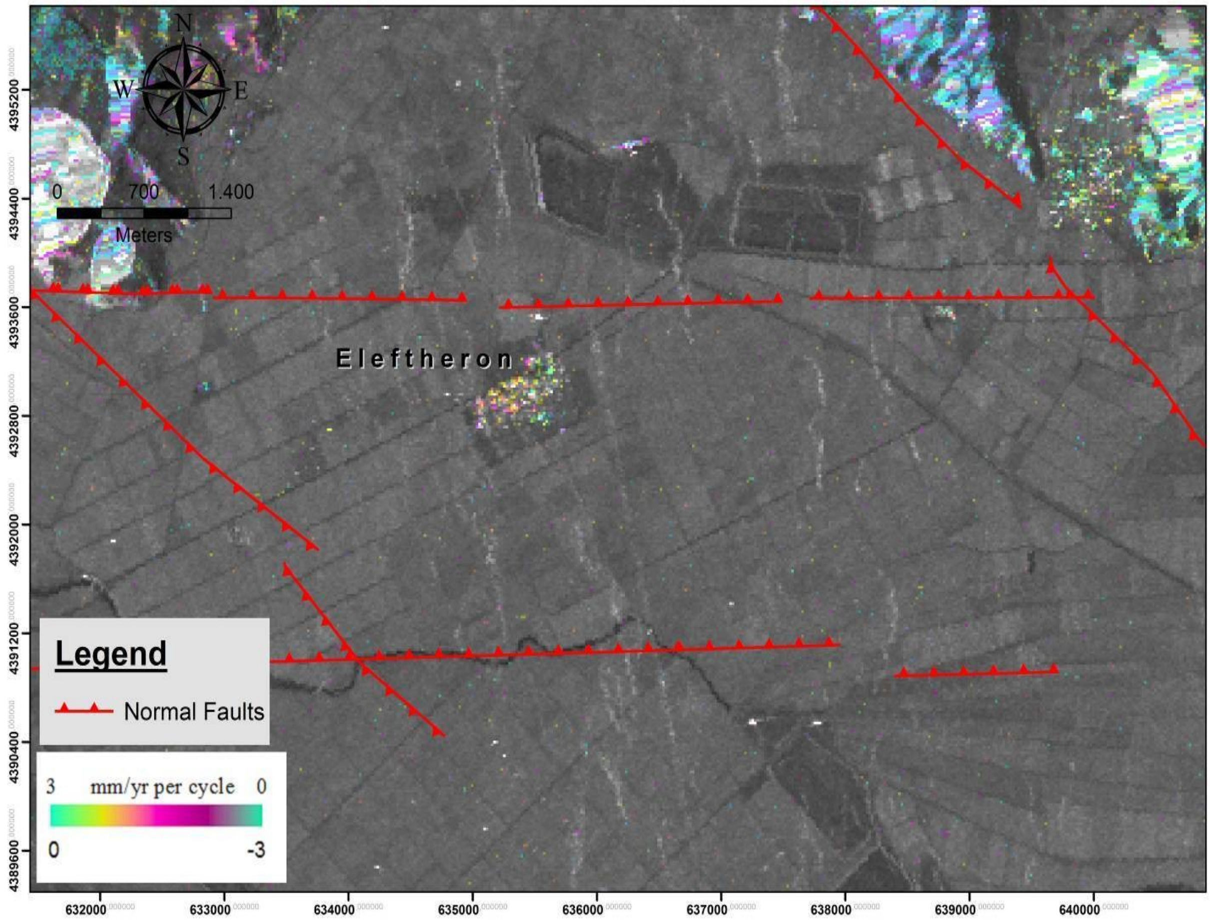

Figure.132 Total deformation at Eleftheron estimated with interferometric stacking technique, June 1995-March 2008

4.2.1.1.5. Falanna

The results of interferometric stacking patterns and total deformation rate estimation during the period June 1995 – March 2008 for Falanna are shown in Figure 133. Ground deformation results within Falanna settlement indicate that the subsidence varies in the range -0.05 – -2.34 mm/year while the uplift varies in the range 0.539 – 3.691 mm/year. The settlement is located 3.17 km east of a normal fault trace, and is furthermore located northeast of another normal fault trace. Subsidence patterns are concentrated in the middle, middle-east and middle-west of the settlement and slight subsidence also appears in the northern part of the settlement. Uplift patterns are observed in the northern and southern parts of the settlement. Subsidence in the middle of the settlement may be attributed to the location of the settlement in the eastern part of the hanging wall of a normal fault trace, as mentioned above, whereas the uplift may be attributed to other impact factors.

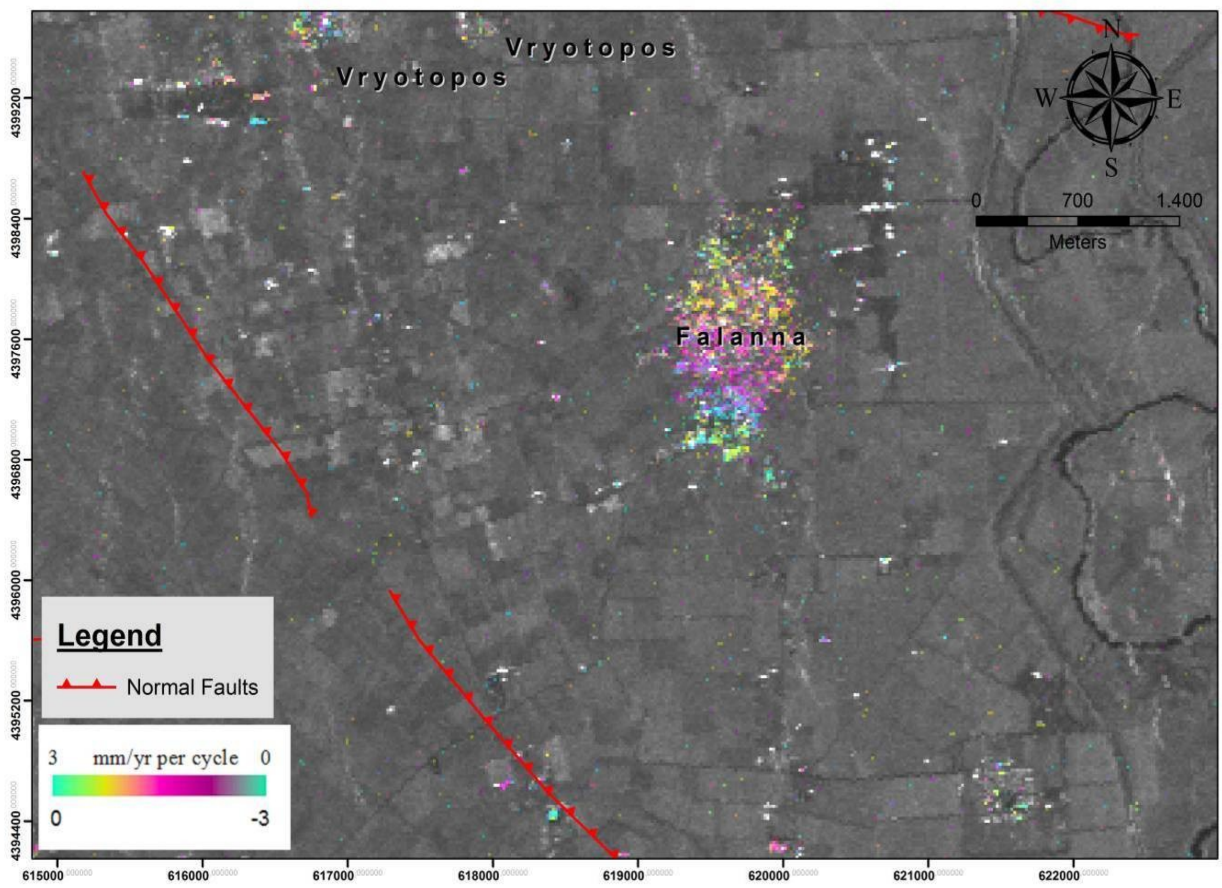

Figure.133 Total deformation at Falanna estimated with interferometric stacking technique, June 1995-March 2008

4.2.1.1.6. Melissochorion

The results of interferometric stacking patterns and total deformation rate estimation during the period June 1995 – March 2008 for Melissochorion are shown in Figure 134. Ground deformation results within Melissochorion settlement indicate that the subsidence varies in the range -0.126 – -1.713 mm/year, while uplift varies in the range 0.567 – 3.278 mm/year. The settlement is located 2.7 km south of a normal fault trace, and is furthermore located 2.6 km east of another normal fault trace. Subsidence patterns are concentrated in the western, middle, and northeastern parts of the settlement, while uplift patterns are distributed northwest and southwest of the settlement. Subsidence may be attributed to the location of the settlement east of the hanging wall of a normal fault trace, whereas uplift may be attributed to the location of the settlement at the southern part of the footwall of a normal fault trace, as mentioned above.

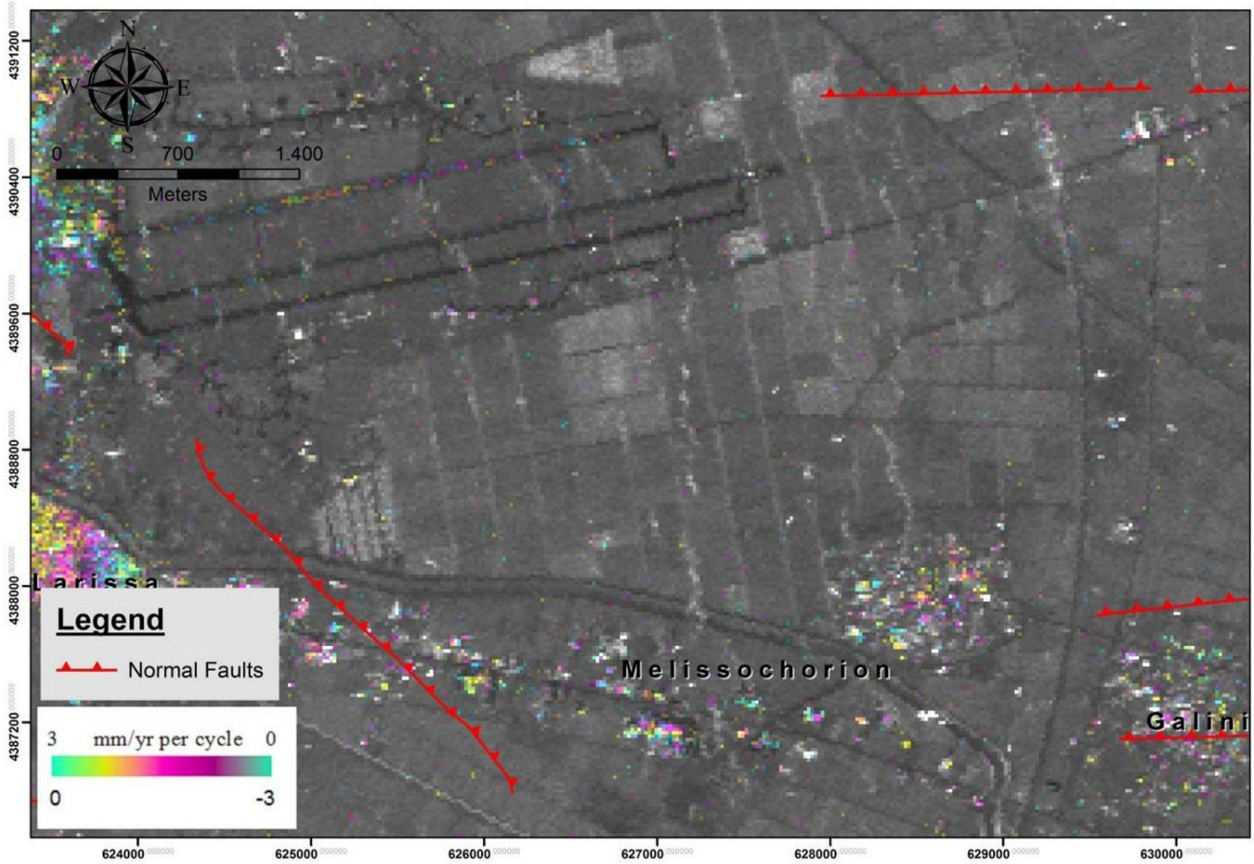

Figure.134 Total deformation at Melissochorion estimated with interferometric stacking technique, June 1995- March 2008

4.2.1.1.7. Galini

The results of interferometric stacking patterns and total deformation rate estimation during the period June 1995 – March 2008 for Galini are shown in Figure 135. Ground deformation results within Galini settlement indicate that the subsidence varies in the range -0.10 – -0.11 mm/year, while uplift varies in the range 0.694 – 3.692 mm/year. The settlement is located 0.17 km south of a normal fault, while another normal fault trace crosses the settlement from the southeast to the southwest. Subsidence patterns are concentrated in the middle and southern parts of the settlement, while slight subsidence patterns are observed in the northern part. Uplift patterns are distributed along the northern border of the settlement, as well as in the middle-east and middle-west and southeastern parts of the settlement. Subsidence may be attributed to the location of the affected area in the side of the hanging wall of a normal fault trace. However, subsidence in the side of the footwall of the normal fault trace which crosses the settlement from the south may be attributed to another impact factor. Uplift along the northern part of the settlement may be attributed to its location south of the footwall of a normal fault trace, and the same applies to the uplift which is observed in the southeastern part of the settlement.

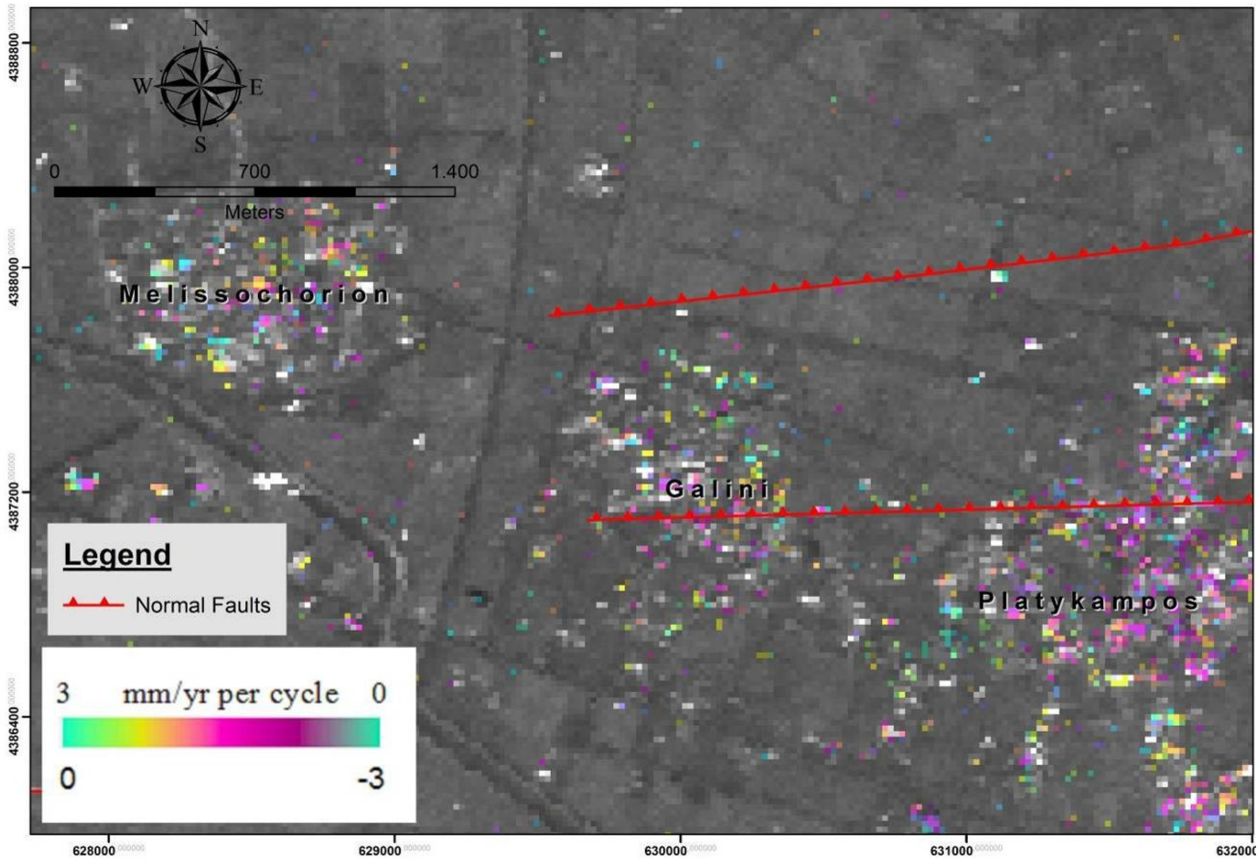

Figure.135 Total deformation at Galini estimated with interferometric stacking technique, June 1995 - March 2008

4.2.1.1.8. Platykampos

The results of interferometric stacking patterns and total deformation rate estimation during the period June 1995 – March 2008 for Platykampos are shown in Figure 136. Ground deformation results within Platykampos settlement indicate that the subsidence varies in the range -0.138 – -3.027 mm/year, while uplift varies in the range 0.527 – 3.463 mm/year. The settlement is located 0.35 km south of a normal fault trace, while another normal fault trace crosses the settlement from the upper middle-east to the west of the settlement. Subsidence patterns are distributed through the whole settlement, while slight uplift patterns are observed in the northern, northeastern, western and middle, and southern parts of the settlement. Subsidence in the northern part may be attributed to the location of the affected area in the side of the hanging wall of a normal fault trace, but subsidence in the middle and southern parts of the settlement, although observed in the side of the footwall of a normal fault trace which crosses the settlement from the east, may nevertheless be attributed to another impact factor. Whereas uplift in the northern, northeastern and middle parts of the settlement may be attributed to its location south of the footwall of a normal fault trace which is located north of the settlement, as mentioned above, the uplift in the southern part of the settlement may be attributed to its location on the side of the footwall of a normal fault trace which crosses the settlement from the east.

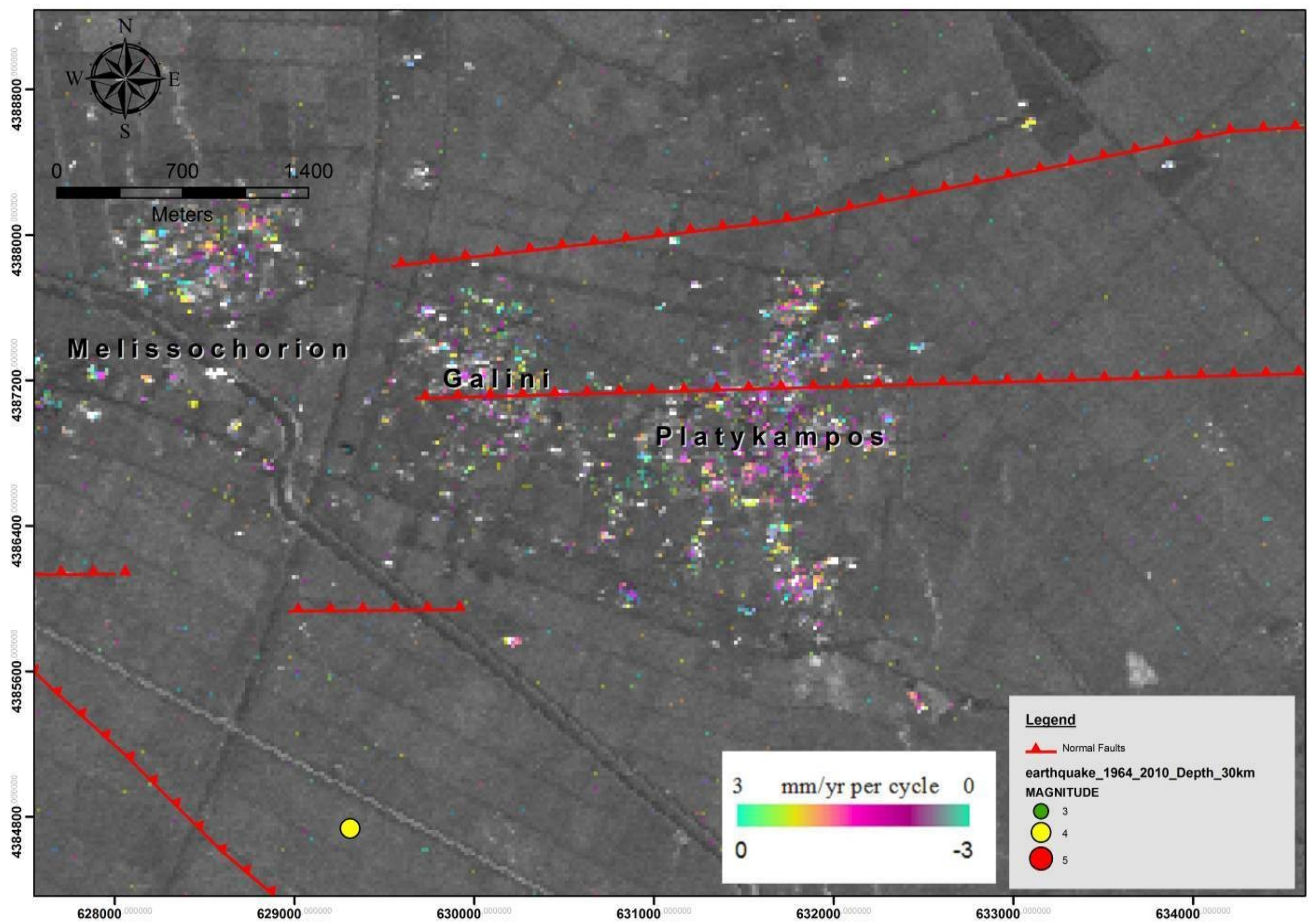

Figure136. Total deformation at Platykampos estimated with interferometric stacking technique, June 1995-, March 2008

4.2.1.1.9. Glafki

The results of interferometric stacking patterns and total deformation rate estimation during the period June 1995 – March 2008 for Glafki_are shown in Figure 137. Ground deformation results within Glafki_settlement indicate that the subsidence varies in the range -0.874 – -0.9 mm/year, while uplift varies in the range 0.146 – 3.67 mm/year. The settlement is located 0.88 km south of a normal fault trace. Slight subsidence patterns are observed in the northern, western, eastern and southern parts of the settlement, whereas uplift patterns are concentrated in the northern, middle and middle-western parts of the settlement. Uplift may be attributed to the location of the settlement on the southern part of the footwall of a normal fault trace. However, subsidence may be attributed to another impact factor.

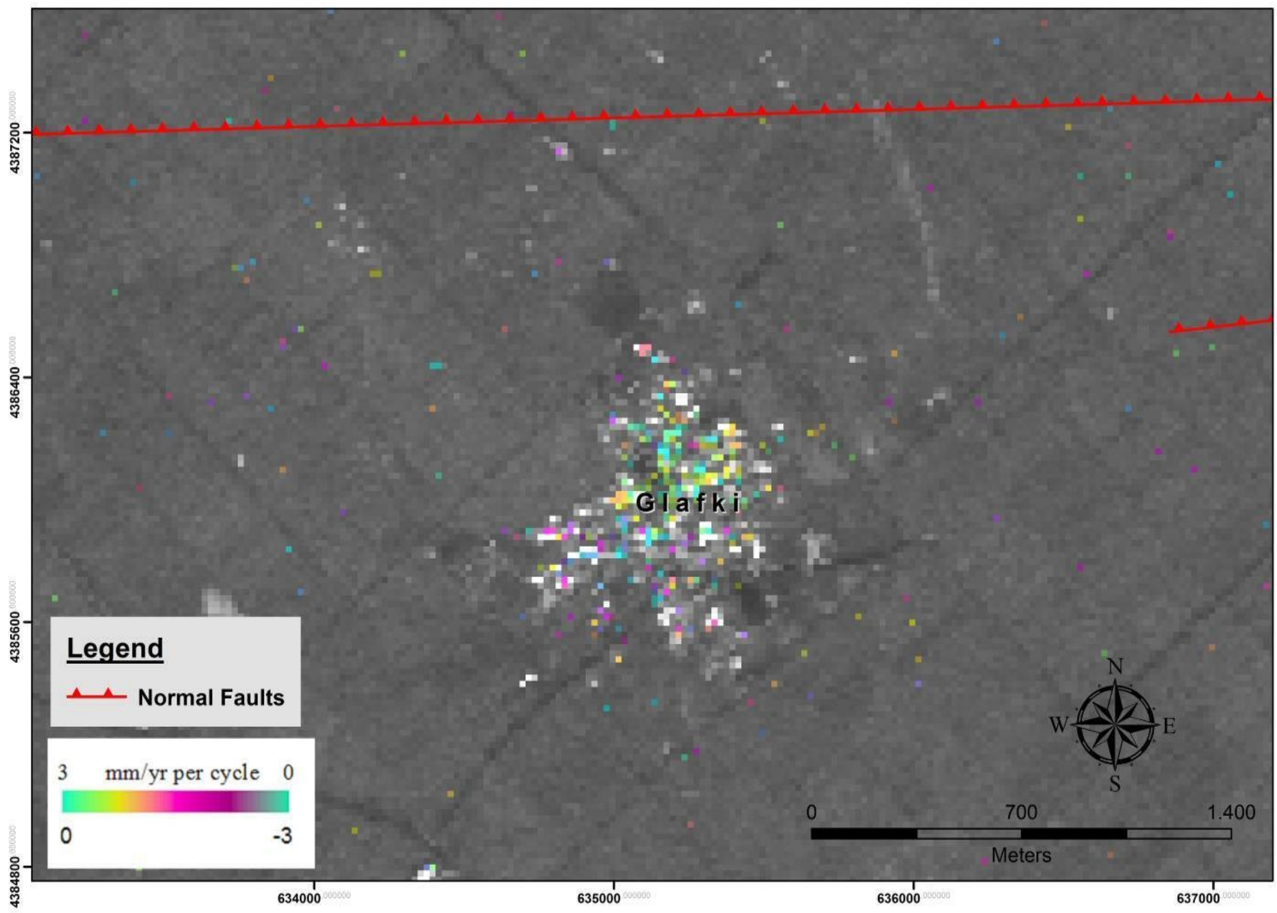

Figure137. Total deformation at Glafki estimated with interferometric stacking technique, June 1995 - March 2008

4.2.1.1.10. Itea

The results of interferometric stacking patterns and total deformation rate estimation during the period June 1995 – March 2008 for Itea are shown in Figure 138. Ground deformation results within Itea settlement indicate that the subsidence varies in the range -0.131 – -4.313 mm/year, while uplift varies in the range 0.463 – 2.946 mm/year. The settlement is located 2.3 km southwest of a normal fault. Subsidence patterns are distributed through all parts of the settlement. Furthermore, uplift patterns are also observed over almost all of the settlement. Subsidence may be attributed to its location southwest of the hanging wall of a normal fault trace, as mentioned above. However, uplift may be attributed to another impact factor.

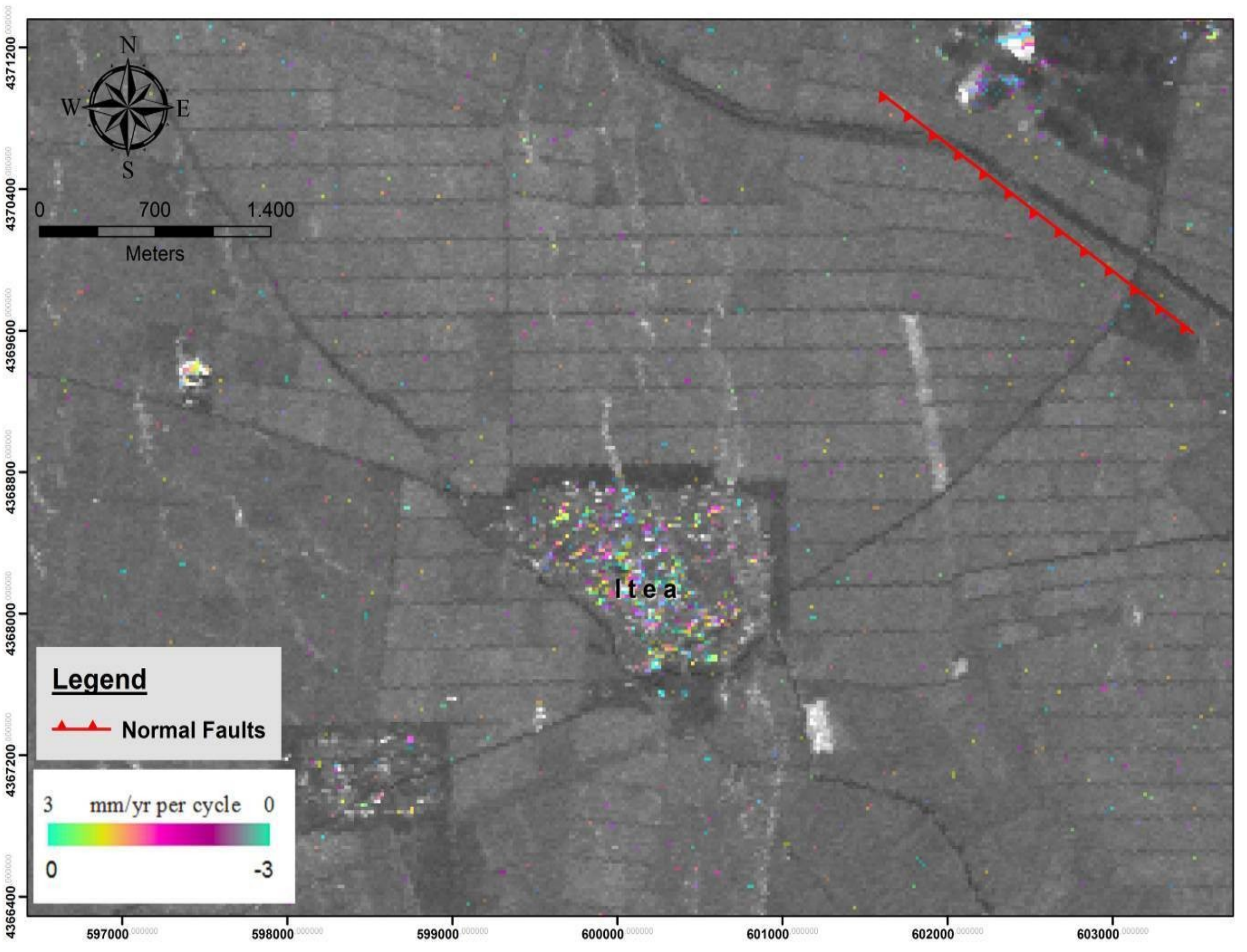

Figure. 138 Total deformation at Itea estimated with interferometric stacking technique, June 1995 - March 2008

4.2.1.1.11. Fyllon

The results of interferometric stacking patterns and total deformation rate estimation during the period June 1995 – March 2008 for Fyllon are shown in Figure 139. Ground deformation results within Fyllon settlement indicate that the subsidence varies in the range -0.01 – -1.108 mm/year, while uplift varies in the range 0.326 – 3.502 mm/year. No fault traces have been observed around this settlement; in other words, this settlement has not been affected by fault movements. Slight patterns of subsidence and uplift can be observed distributed within the settlement: these may be attributed to another impact factor.

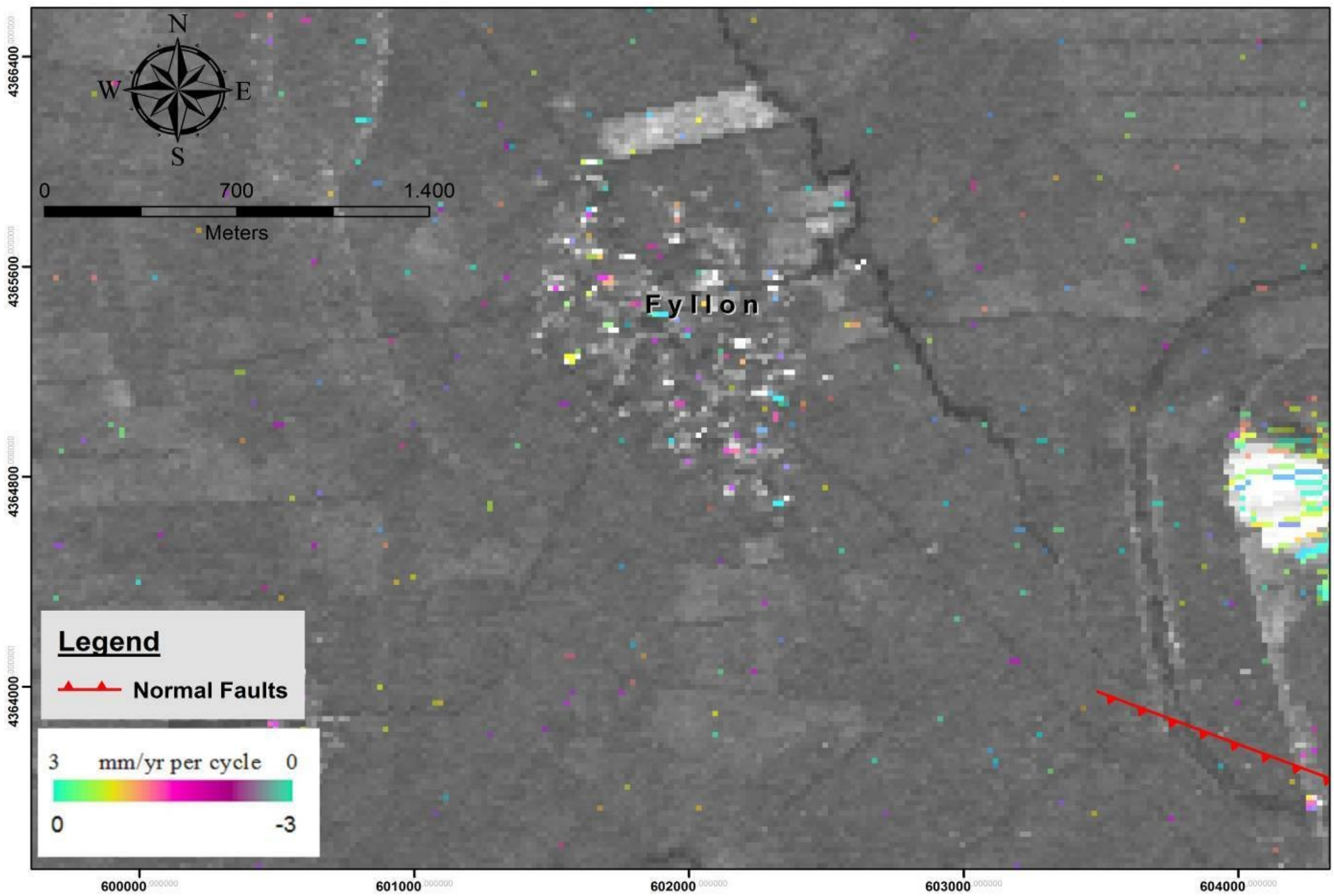

Figure. 139 Total deformation at Fyllon estimated with interferometric stacking technique, June 1995 - March 2008

4.2.1.1.12. Palamas

The results of interferometric stacking patterns and total deformation rate estimation during the period June 1995 – March 2008 for Palamas are shown in Figure 140. Ground deformation results within Palamas settlement indicate that the subsidence varies in the range -0.216 – -1.676 mm/year, while uplift varies in the range 0.348 – 3.306 mm/year. No fault traces have been observed around this settlement; in other words, this settlement has not been affected by fault movements. Subsidence patterns can be observed over almost all the settlement. Uplift patterns are observed in the northeast and less clearly in the middle and northwestern parts of the settlement. Subsidence and uplift are not attributed to the impact of fault movement; consequently, this deformation is attributed to some other impact factor.

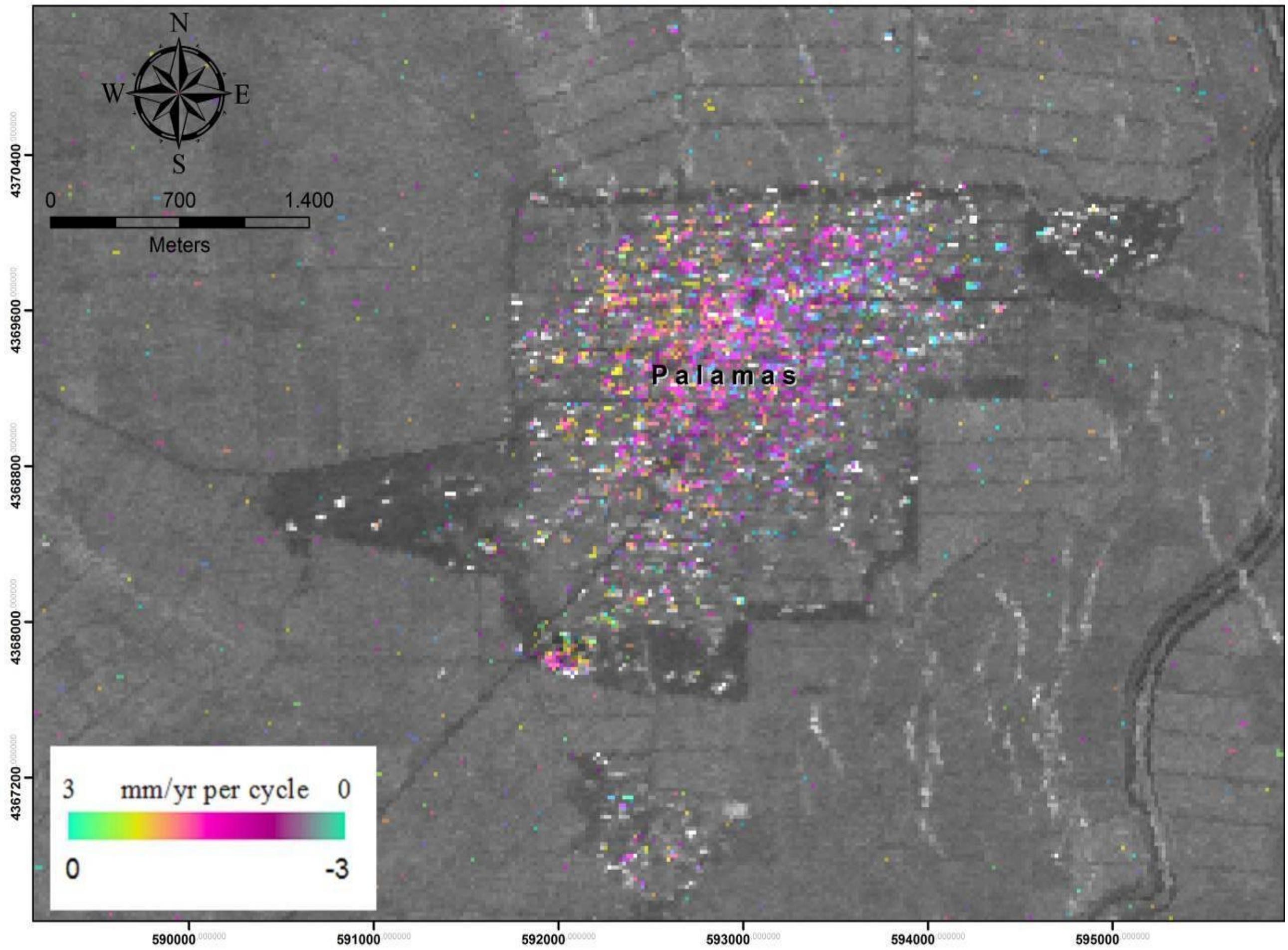

Figure. 140 Total deformation at Palamas estimated with interferometric stacking technique, June 1995 - March 2008

4.2.1.1.13. Marathea

The results of interferometric stacking patterns and total deformation rate estimation during the period June 1995 – March 2008 for Marathea are shown in Figure 141. Ground deformation results within Marathea settlement indicate that the subsidence varies in the range -0.664 – -1.545 mm/year, while uplift varies in the range 0.211 – 2.891 mm/year. The settlement is located 2.6 km west of a normal fault trace.

Subsidence patterns are observed across the whole settlement, while uplift patterns are slightly observed in the middle-north, eastern, western and southern parts of the settlement. Uplift may be attributed to the location of the settlement west of the footwall of a normal fault trace, as mentioned above, whereas subsidence may be attributed to another impact factor.

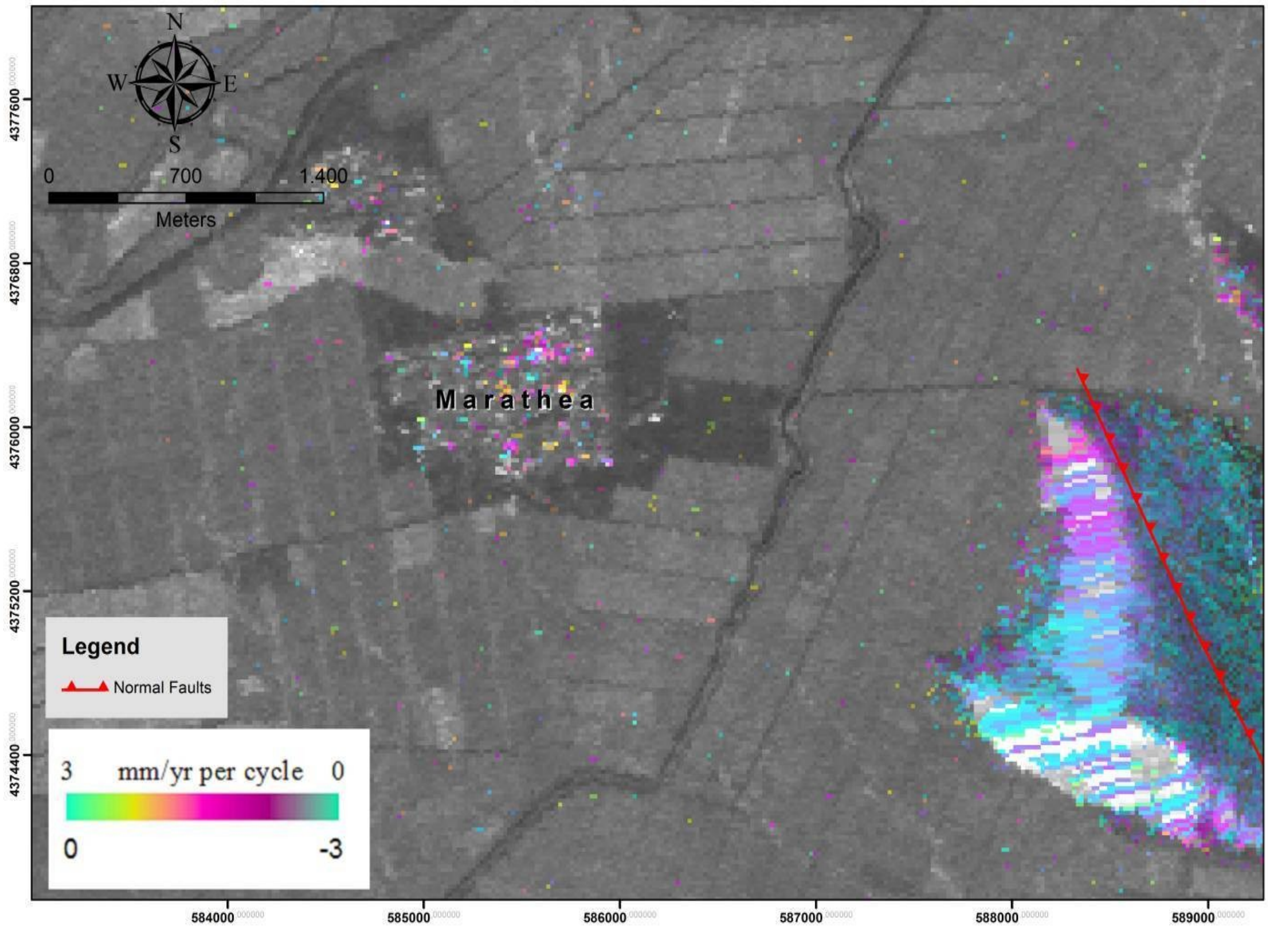

Figure.141 Total deformation at Marathea estimated with interferometric stacking technique, June 1995 - March 2008

4.2.1.1.14. Nikaia

The results of interferometric stacking patterns and total deformation rate estimation during the period June 1995 – March 2008 for Nikaia are shown in Figure 142. Ground deformation results within Nikaia settlement indicate that the subsidence varies in the range -0.75 – -0.8 mm/year, while uplift varies in the range 0.217 – 4.269 mm/year. The settlement is located 0.9 km southwest and 1.68 km west of two normal faults. It is additionally located 4.0 km northeast of another normal fault, although the potential impact of this fault may be low, given the greater distance between the settlement and the fault trace. Subsidence patterns are distributed across the north, middle, middle-east and middle-west of the settlement, whereas uplift patterns are distributed across the northeast and northwest of the settlement, in addition to which they are concentrated in the southern part of the settlement. Subsidence may be attributed to another impact factor of fault movements. However, the uplift particularly in the northern part of the settlement may be attributed to the location of the settlement southwest of the footwall of a normal fault, as mentioned above.

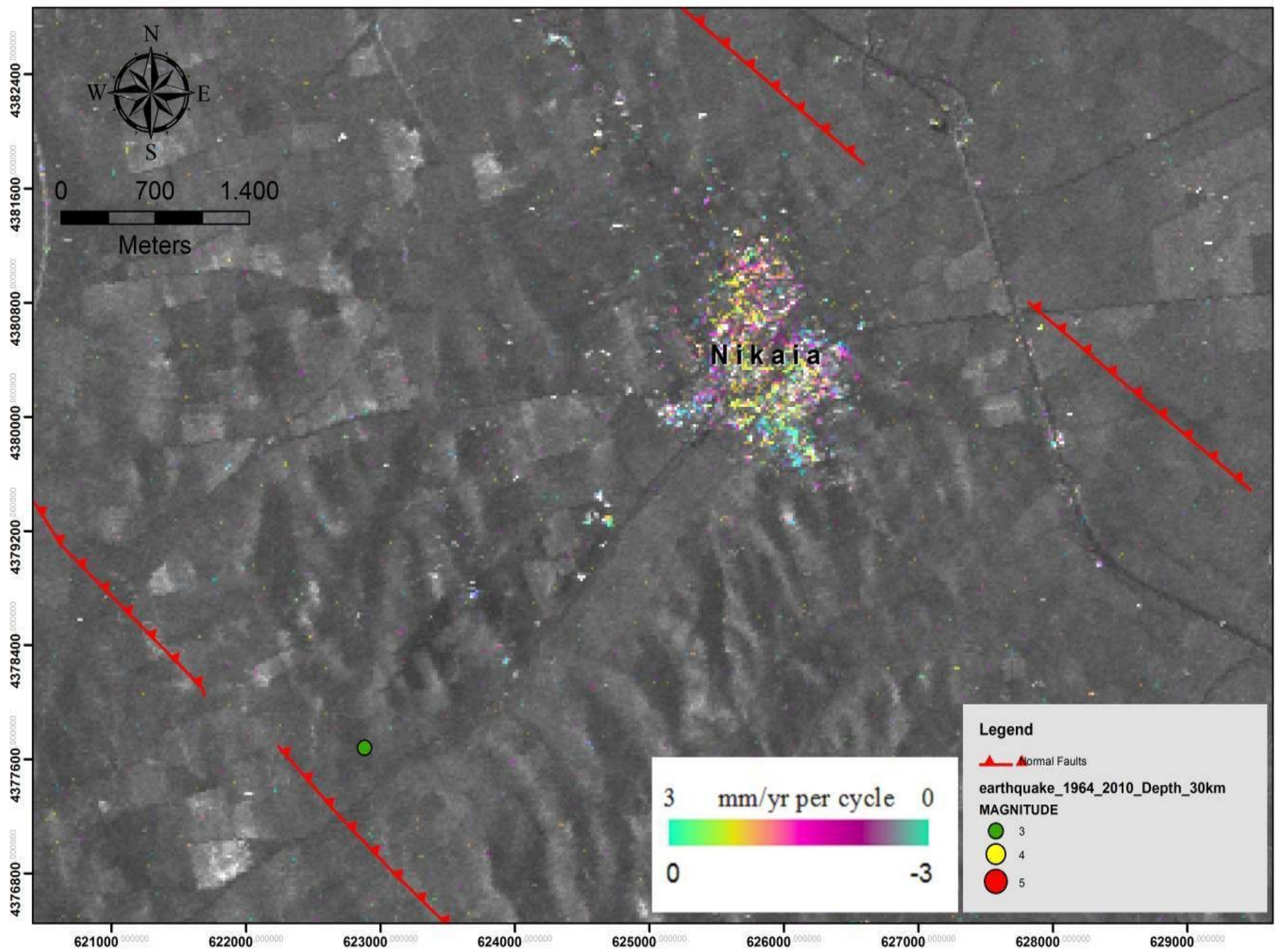

Figure.142 Total deformation at Nikaia estimated with interferometric stacking technique, June 1995 - March 2008

4.2.1.1.15. <u>Terpsithea</u>

The results of interferometric stacking patterns and total deformation rate estimation during the period June 1995 – March 2008 for Terpsithea are shown in Figure 143. Ground deformation results within Terpsithea settlement indicate that there is no subsidence, while uplift varies in the range 0.218 – 4.384 mm/year. The settlement is located 0.77 km south of a normal fault, and 0.86 km northeast of another normal fault. Although the rate of subsidence is nil, nevertheless patterns are slightly visible distributed over the northern, middle and southern western parts of the settlement, which may indicate the activity of a fault which is located southwest of the settlement. Uplift patterns are observed over the whole settlement, which may be attributed to the location of the settlement south of the footwall of a normal fault trace, as mentioned above.

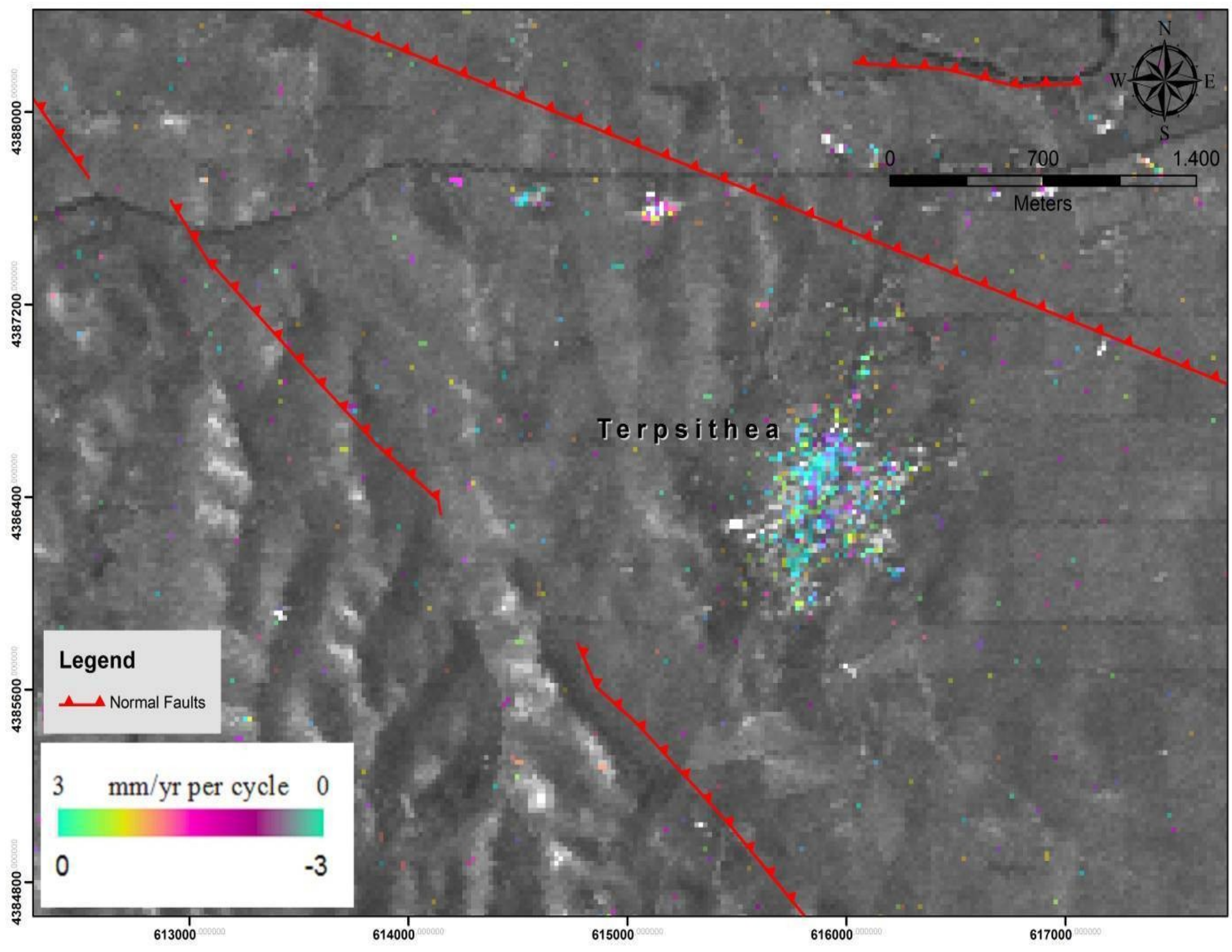

Figure 143 Total deformation at Terpsithea estimated with interferometric stacking technique, June 1995 - March 2008

4.2.1.1.16. Tyrnavos

The results of interferometric stacking patterns and total deformation rate estimation during the period June 1995 – March 2008 for Tyrnavos are shown in Figure 144. Ground deformation results within Tyrnavos settlement indicate that the subsidence varies in the range -0.178 – -1.447 mm/year, while uplift varies in the range 0.14 – 2.504 mm/year. The settlement is located 3.5 km north and 2.57 km southwest of two normal faults respectively. Subsidence patterns are distributed over the middle, northern, western and southwestern parts of the settlement. Uplift patterns are concentrated in the eastern and southeastern parts of the settlement, but are also observed in the northern and northwestern parts of the settlement. Subsidence may be attributed to the location of the settlement north of the hanging wall of a normal fault trace, while uplift may be attributed to the location of the settlement southwest of the footwall of another normal fault trace, as mentioned above.

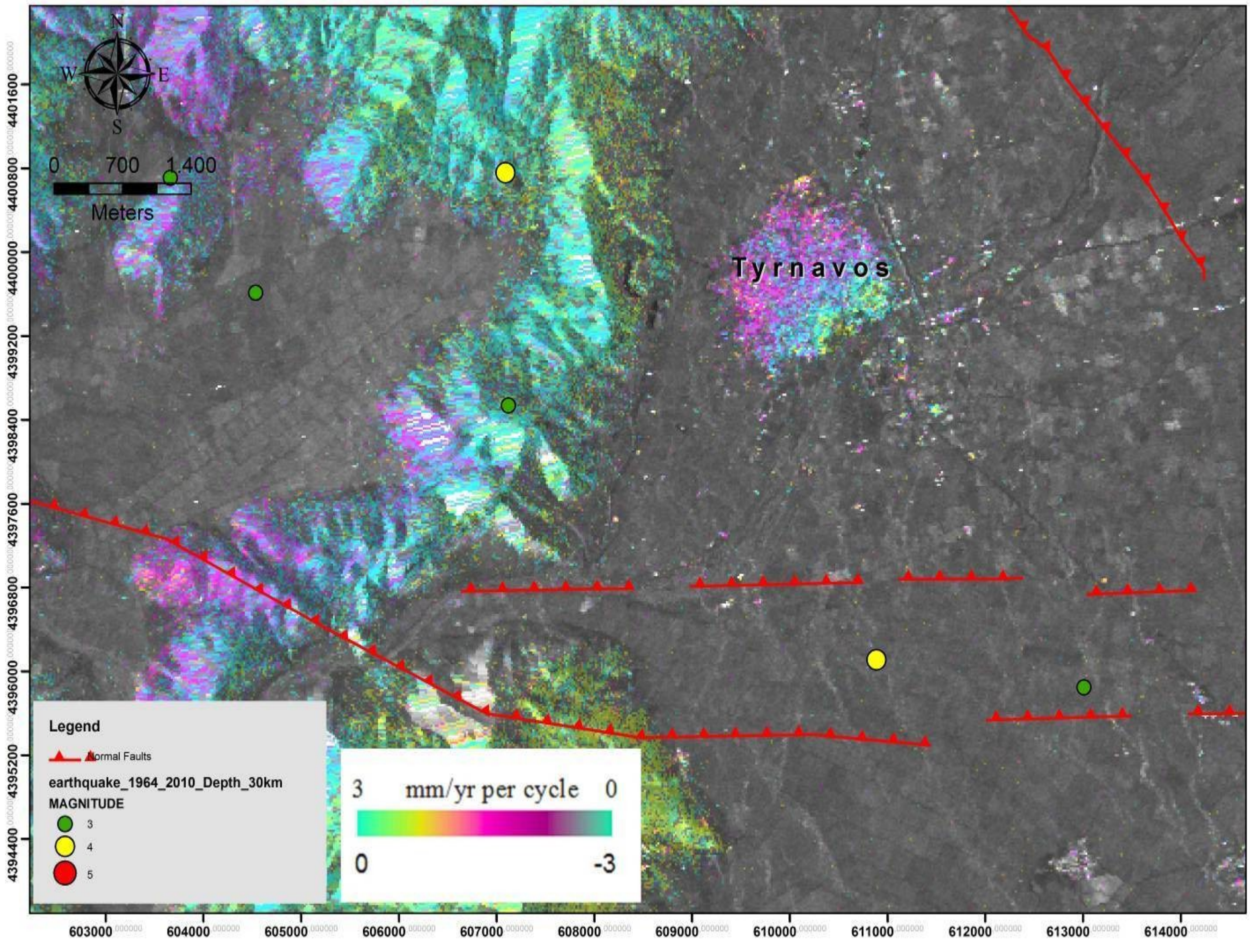

Figure144. Total deformation at Tyrnavos estimated with interferometric stacking technique, June 1995 - March 2008

4.2.1.1.17. <u>Rodia</u>

The results of interferometric stacking patterns and total deformation rate estimation during the period June 1995 – March 2008 for Rodia are shown in Figure 145.

Ground deformation results within Rodia settlement indicate that the subsidence varies in the range -0.036 – -0.752 mm/year, while uplift varies in the range 0.284 – 3.109 mm/year. The settlement is located 0.995 km south and 0.123 km west of two normal faults respectively. Subsidence patterns are approximately distributed over the whole settlement, in the eastern, northeastern, southeastern, and less so in the northwestern parts of the settlement, whereas uplift patterns are slightly observed in the northeastern, northwestern and eastern parts of the settlement, and are in addition more visible in the southeastern, middle and southwestern parts. Subsidence may be attributed to the location of the settlement south and west of the hanging walls of two normal fault traces, while uplift may be attributed to another impact factor.

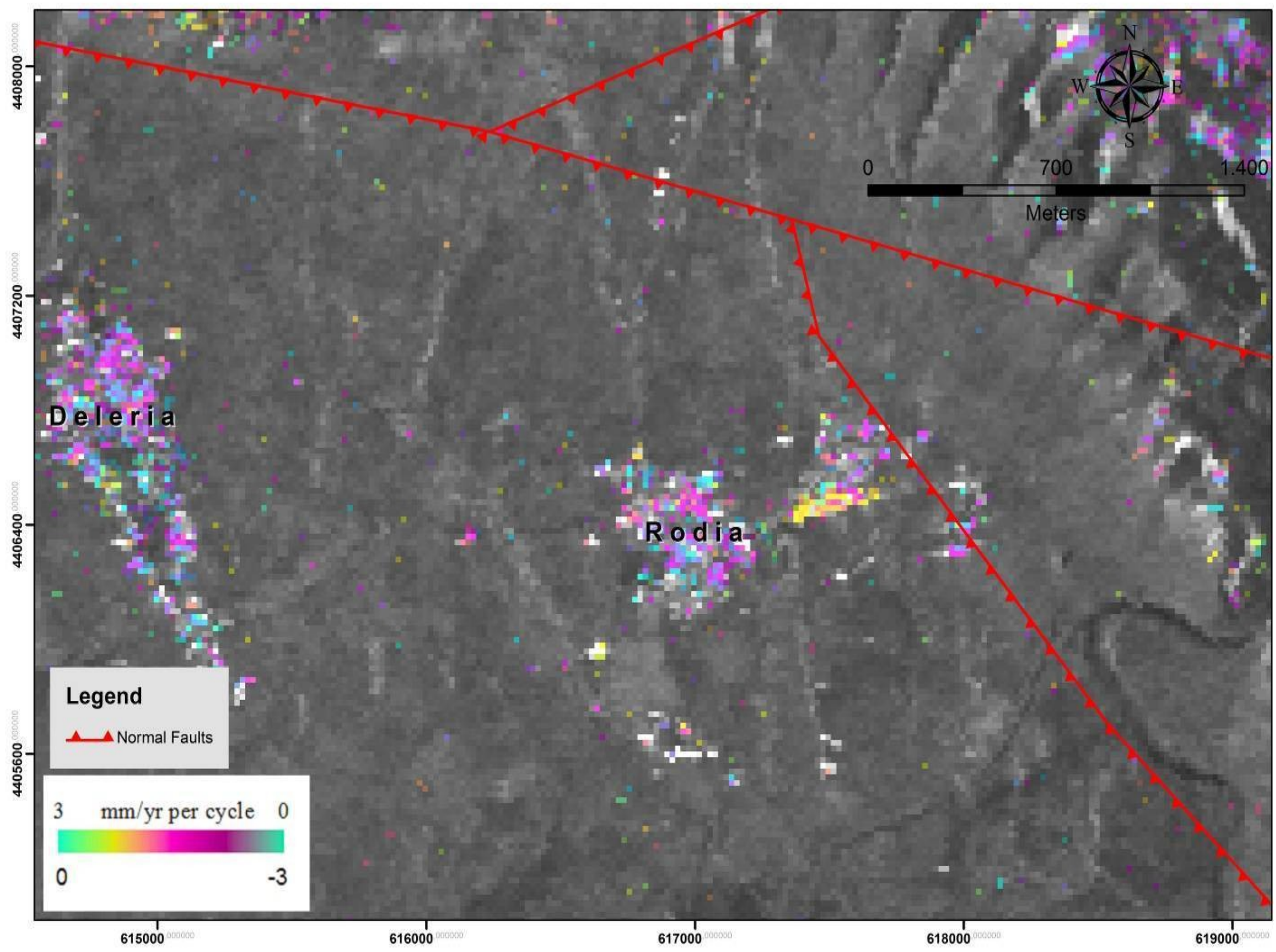

Figure.145 Total deformation at Rodia estimated with interferometric stacking technique, June 1995 - March 2008

4.2.1.1.18. Mandra

The results of interferometric stacking patterns and total deformation rate estimation during the period June 1995 – March 2008 for Mandra are shown in Figure 146. Ground deformation results within Mandra settlement indicate that the subsidence varies in the range -0.086 – -1.587 mm/year, while uplift varies in the range 0.127 – 1.316 mm/year. The settlement is located 4.12 km south and 4.57 km west of two normal faults. Subsidence patterns are slightly observed in the northern, northwestern, and northeastern parts of the settlement. Uplift patterns are distributed approximately all over the settlement. Subsidence may be attributed to another impact factor, while uplift may be attributed to the location of the settlement to the south and west of the footwalls of two normal fault traces, as mentioned above.

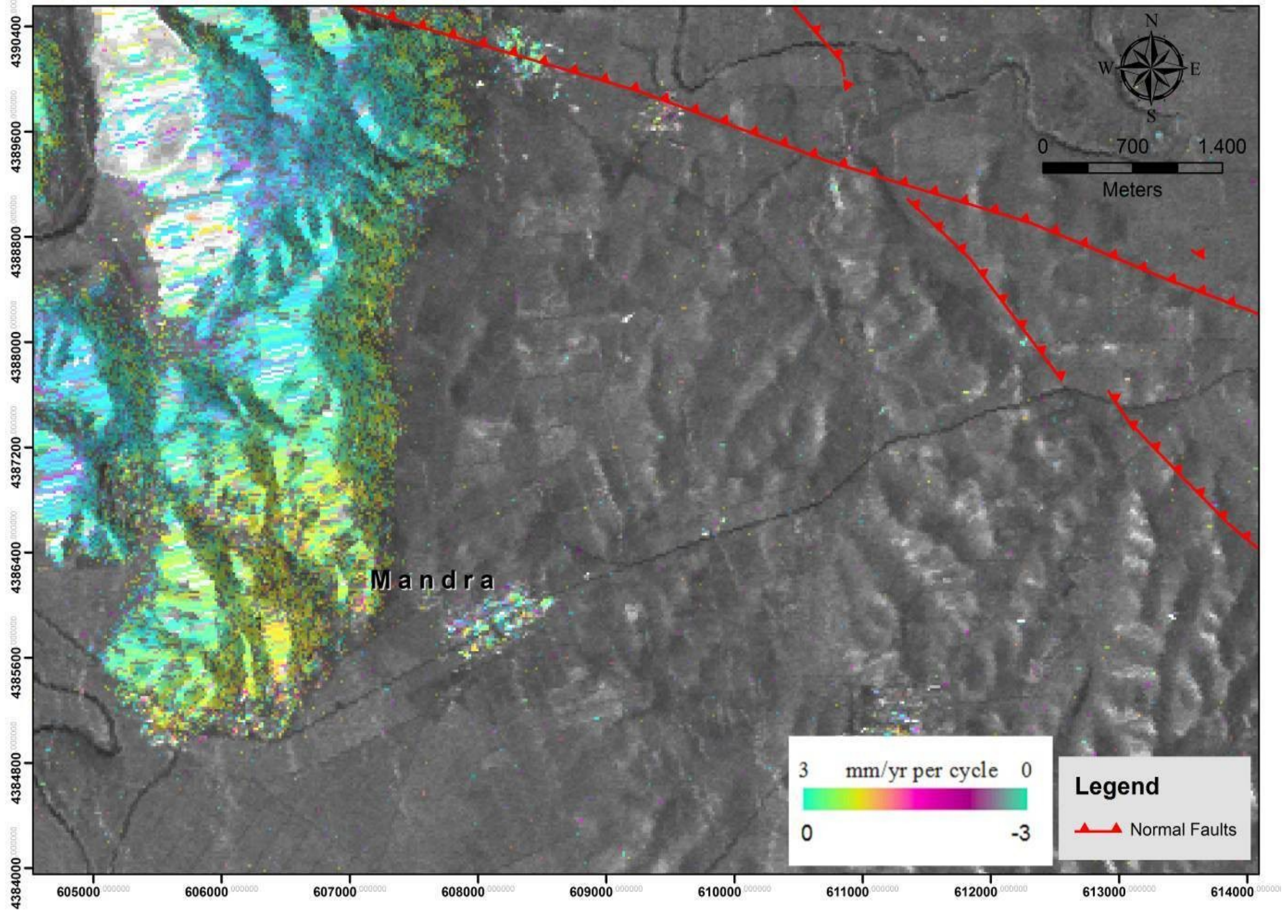

Figure146. Total deformation at Mandra estimated with interferometric stacking technique, June 1995 - March 2008

4.2.1.1.19. Eleftherai

The results of interferometric stacking patterns and total deformation rate estimation during the period June 1995 – March 2008 for Eleftherai are shown in Figure 147. Ground deformation results within Eleftherai settlement indicate that the subsidence varies in the range -0.34 – -0.35 mm/year, while uplift varies in the range 0.267 – 3.365 mm/year. The settlement is located 2.45 km southwest of a normal fault. Subsidence patterns are observed distributed all over the settlement. Uplift patterns are observed also. Subsidence may be attributed to some other impact factor, while uplift may be attributed to the location of the settlement southwest of the footwall of a normal fault trace, as mentioned above.

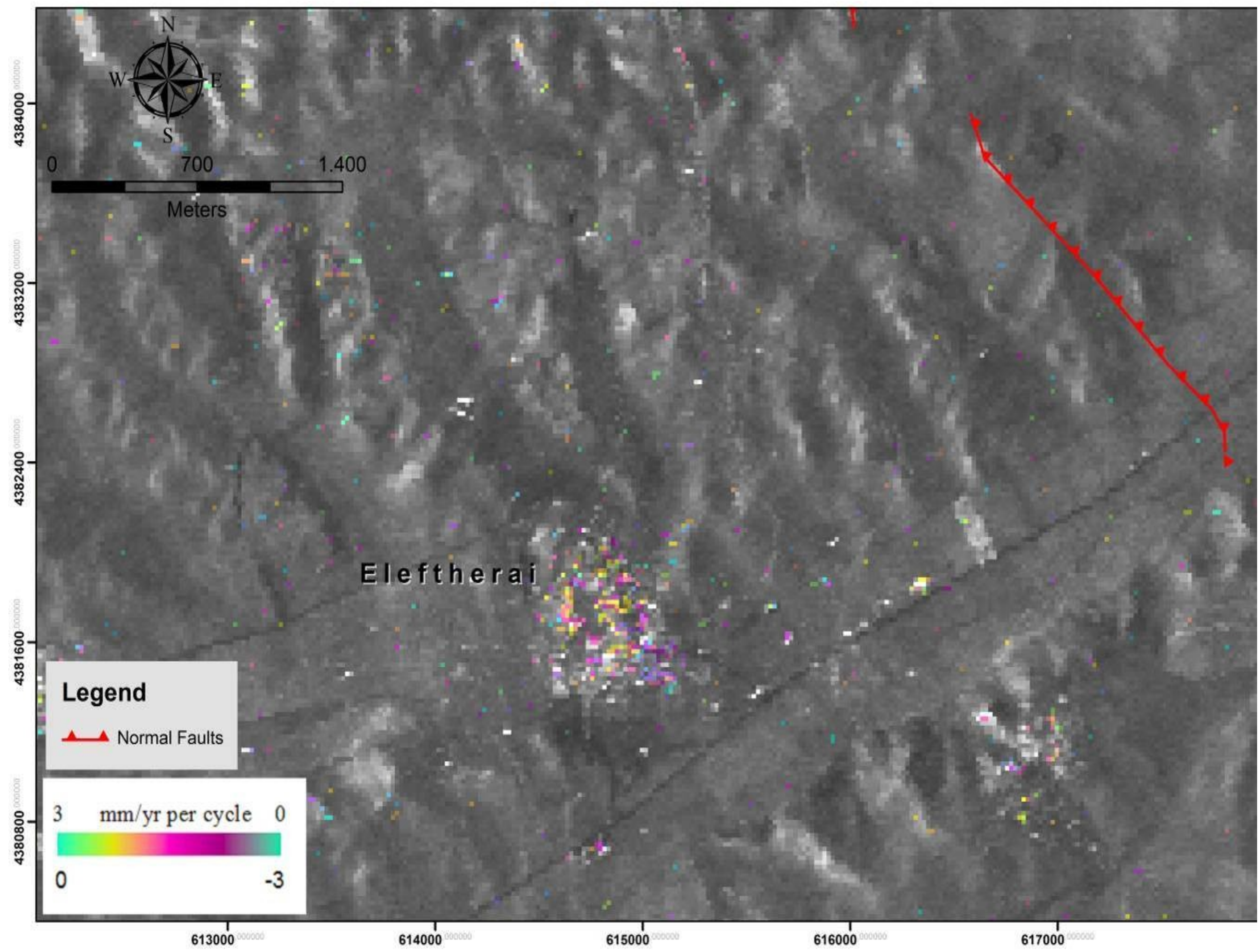

Figure147. Total deformation at Eleftherai estimated with interferometric stacking technique, June 1995 - March 2008

4.2.1.2. Conventional SAR Interferometry

A conventional technique of SAR interferometry was implemented to investigate the deformation and to ascertain whether it is attributable to the impact of fault movements or to the seasonal impact which results from any other impact factor, taking into account the short temporal period.

A single differential interferogram with a short temporal period (19960228_19960403) was chosen within this track, as depicted previously in Figure 9, additionally the parameters of this interferogram are depicted in Table 5 in the chapter on processing. The settlement of Larissa was selected to verify the impact of fault movements on ground deformation. The reason for this is that the settlement is the largest one in the study area, and furthermore three normal faults cross the settlement, as mentioned before. A 7 km cross-section was created across the settlement from northeast to southwest. This additionally crosses the three normal faults so as to be able to extract the ground deformation along the cross-section, and thereafter to create a histogram by correlating the displacement with distance for each 0.5 km along the section. Figure 148 shows the single differential interferogram, indicating the settlement of Larissa relative to the cross-section. Table 42 shows the displacement and distance along the cross-section.

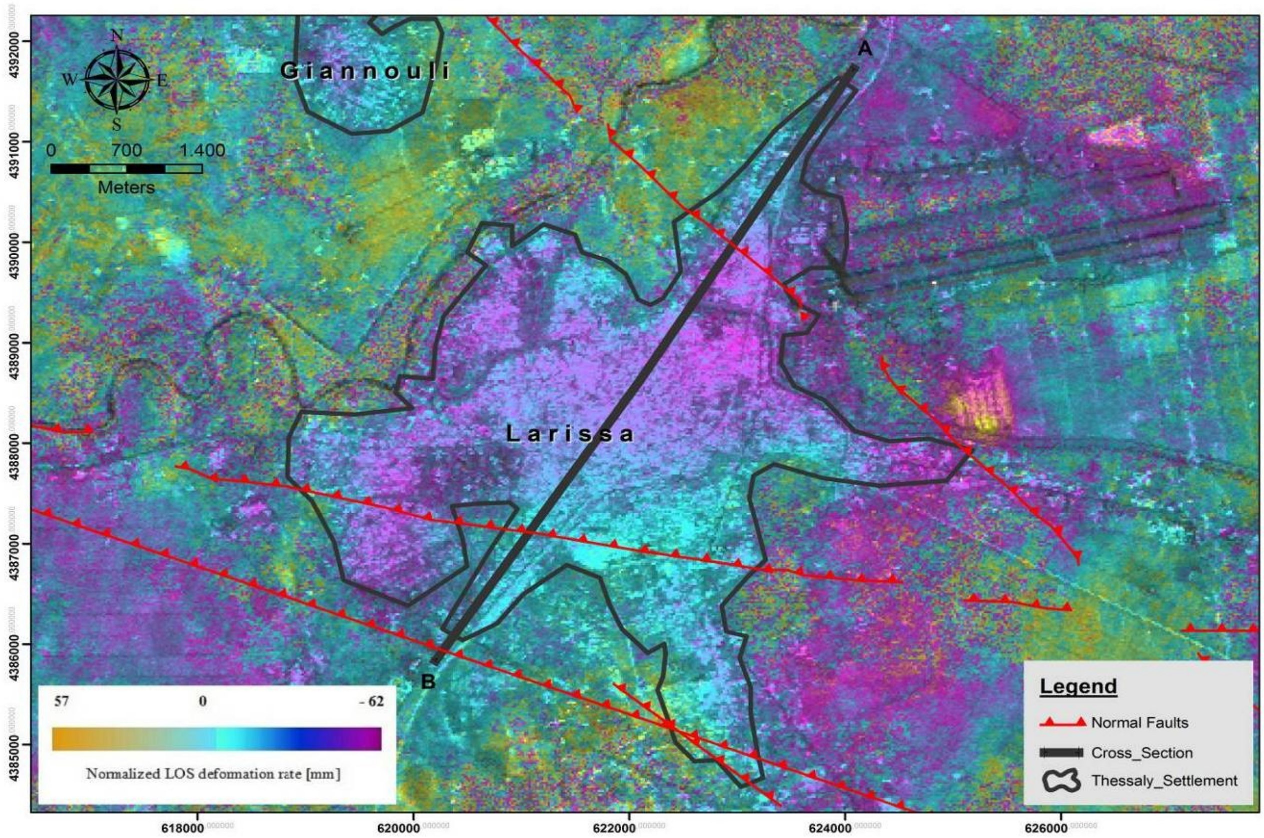

Figure148. Conventional interferogram corresponding to a 7 km cross-section of Larissa in the period 19960228_19960403

Table 42 Displacement field as observed by conventional interferometry within a 7 km Larissa cross-section, in the period 19960228_19960403 (35 days)

I.d	Distance (km)	Displacement (mm)
1	0.5	-1.004
2	1	1.212
3	1.5	1.639
4	2	2.03
5	2.5	2.252
6	3	2.804
7	3.5	1.857
8	4	2.109
9	4.5	1.378
10	5	1.022
11	5.5	0.752
12	6	5.739
13	6.5	0.967
14	7	0.529

The behavior of the ground displacement along the cross-section is depicted in Figure 149. The behavior of ground displacement with distance along the cross-section begins with subsidence then changes to uplift; however, fluctuation of the ground displacement is evident in between the fault traces. Subsidence can be observed to the side of the hanging wall of the first normal fault trace, which is located northeast of Larissa. Subsequently, a change in status from subsidence to uplift is observed, followed by an increase of the uplift that can be observed in the side of the footwall of the same fault trace. Gradually the uplift displacement decreases towards the hanging wall of the second normal fault trace, which crosses Larissa from the southern part. Thereafter an abrupt increase of uplift is observed in the side of the footwall of the same fault trace, followed by a sharp decline of uplift in the side of the hanging wall of the third normal fault trace.

The change of status from subsidence to uplift and the fluctuation of uplift along the cross-section in between the three normal fault traces very probably indicate the influence of fault movement, in spite of the short period.

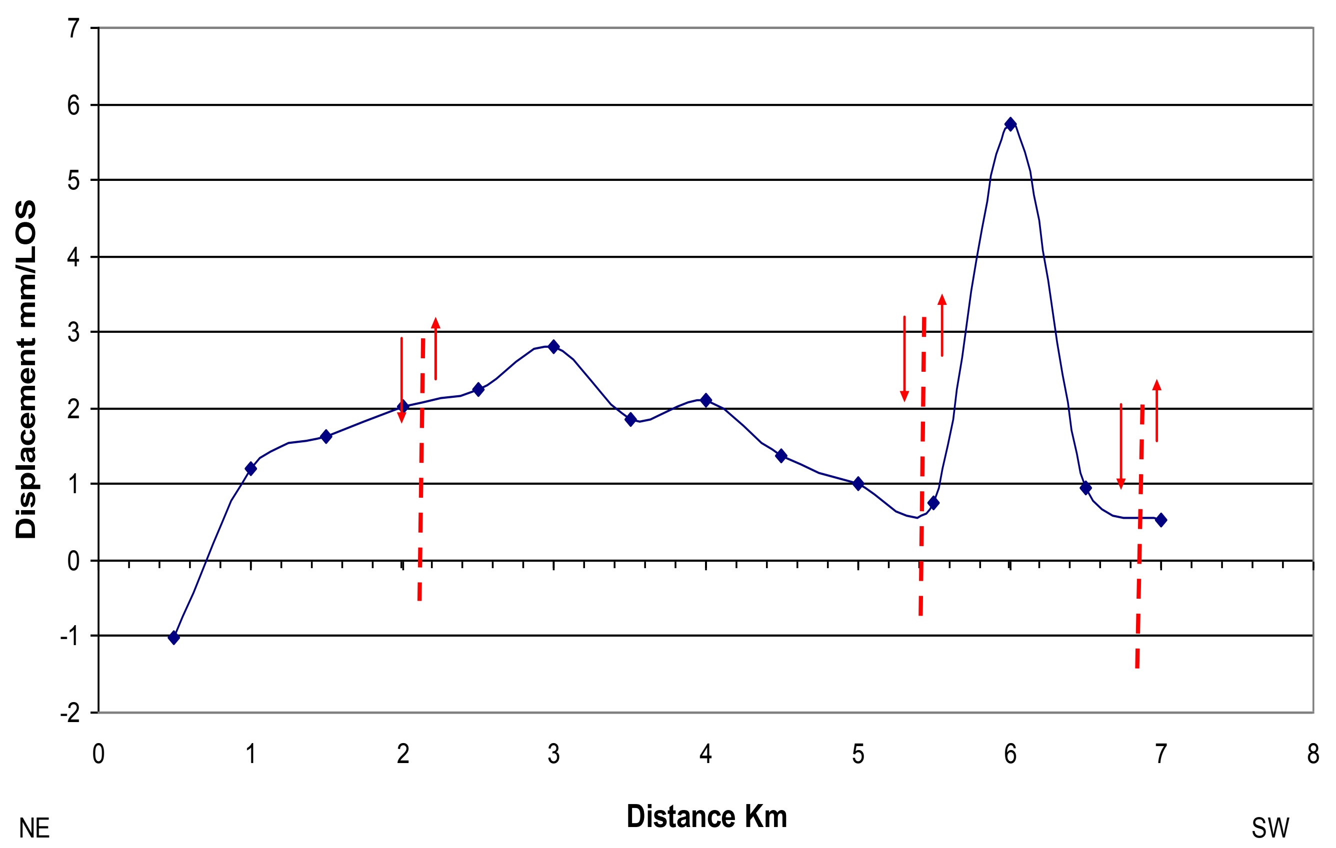

Figure149. Spatial profile showing the displacement field as observed by conventional interferometry within a 7 km cross-section of Larissa, in the period 19960228_19960403 red lines correspond to the faults

4.2.1.3. Persistent Scatterers Interferometry (PSI)

The technique of Persistent Scatterers Interferometry was also implemented to verify the impact of fault movements on ground deformation. However, a difficulty confronted in using the results of this technique was the huge number of candidate points that resulted within this track, as mentioned earlier in the chapter on processing.

Consequently, the decision was made to select two candidate points within each settlement, depending on the minimum and maximum deformation rate of the points within each settlement. However, it can be seen that not all the settlements were covered by the results of candidate points within this track. Therefore just 13 settlements from the total of 30 were covered with candidate points, while many other points are observed outside the settlements.

The minimum and maximum deformation rate in LOS and the number of candidate points within each settlement are depicted in Table 43. All the points were superimposed in an ArcGIS environment to create spatial correlation between each candidate point and the fault movements. The information of all following selected points' candidates is depicted in appendix B.

Table 43. Minimum and maximum deformation rate in LOS and the number of PSI targets within urban areas of Thessaly prefecture, 1995-2006

Settlements	Number of targets	Minimum rate (mm)	Maximum rate (mm)	Mean
Larissa	4099	-2	33	22
Giannouli	317	-3	30	20
Falanna	390	-6	16	4
Melissochorion	128	-1	36	12
Galini	181	-2	3	11
Platykampos	400	-1	20	8
Glafki	140	-3	11	11
Nikaia	230	-10	33	24
Terpsithea	185	-7	29	17
Tyrnavos	836	-2	3	9
Rodia	183	-13	7	2
Mandra	68	-2	17	9
Eleftherai	107	-4	15	5

4.2.1.3.1. Minimum deformation rate

4.2.1.3.1.1. Larissa

Candidate point number 46536 was been selected as representative of the minimum deformation rate. It is located northeastern of Larissa, 1.10 km from a normal fault trace in the side of the hanging wall. A plot of this point is depicted in Figure 150. The deformation behavior of this candidate point through its time series begins with subsidence then changes to uplift, and thereafter further changing of status between subsidence and uplift was observed during April 2004 – December 2006. The minimum subsidence was -0.364 mm (August 2005) while the maximum subsidence was -24.579 mm (June 1995). The minimum and maximum uplift were 0.771 and 5.914 mm in December 2006 and August 2003 respectively. Subsidence may be attributed to the impact of fault movement. However, uplift may be attributed to another impact factor. The location of the selected point's minimum and maximum deformation rate is shown in Figure 151.

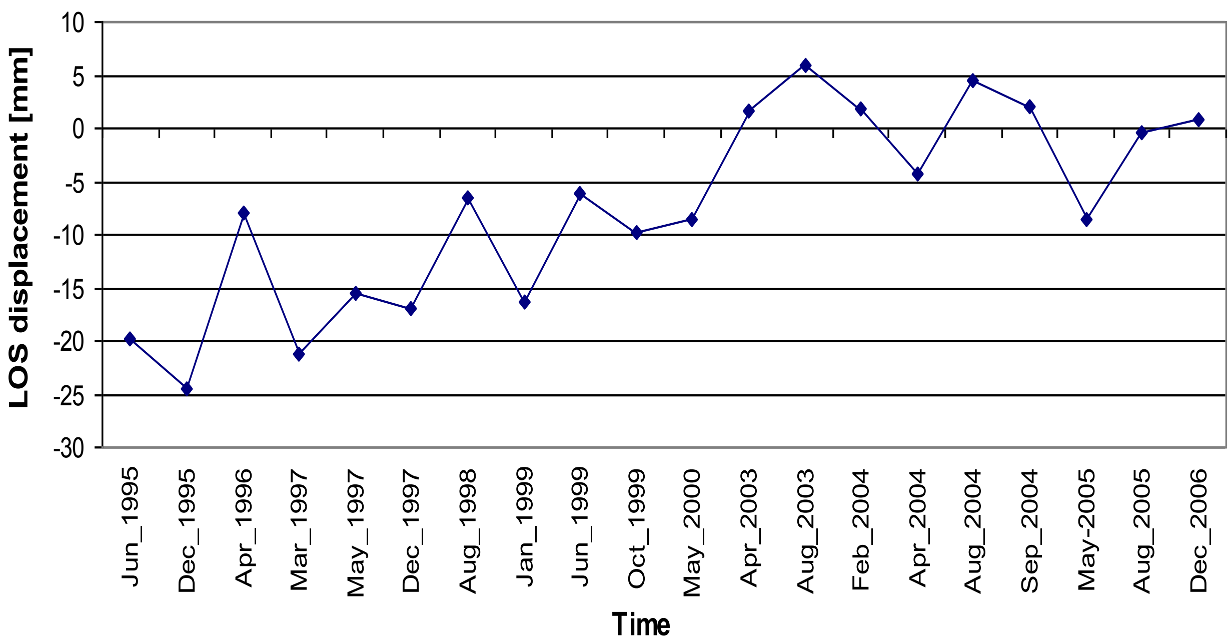

Figure150. LOS displacement time series (1995-2006) of the minimum deformation rate of PSI of Larissa. Point number 46536. Time series are rescaled to the first acquisition (28 June 1995)

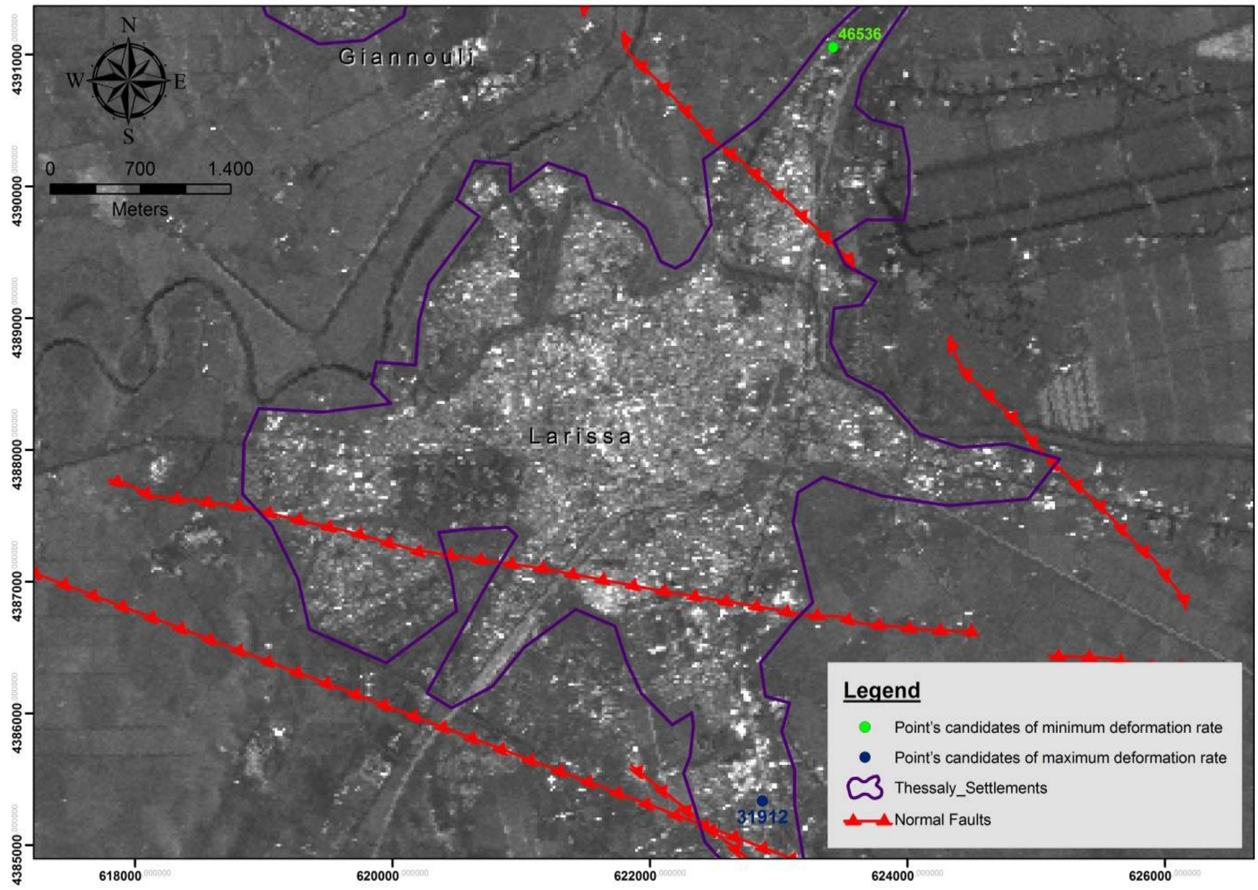

Figure151. Location of selected candidate points minimum and maximum deformation rate ascending track 143, settlement of Larissa.

4.2.1.3.1.2. Giannouli

Candidate point number 55991 was selected as representative of the minimum deformation rate. It is located northwest of Giannouli 1.144 km from a normal fault in the side of the footwall. A plot of this point is depicted in Figure 152. The deformation behavior of this point through its time series begins with subsidence then changes to uplift, and thereafter further changing of status between subsidence and uplift was observed during February 2004 – December 2006. The minimum subsidence was -2.318 mm (April 2004) while maximum subsidence was -43.143 mm (April 1996). The minimum and maximum uplift were 2.724 mm and 10.084 mm in September 2004 and December 2006 respectively. Subsidence may be attributed to another impact factor than fault movement, because of the presence of the candidate point in the side of the footwall, as mentioned above. However, uplift may be attributed to the impact of the fault movement. It is worth mentioning that the fluctuation or change of status between subsidence and uplift during February 2004 –

December 2006 may be attributed to the disparity of fault activity with other impact factors during this period. The location of the selected point's minimum and maximum deformation rate is shown in Figure 153.

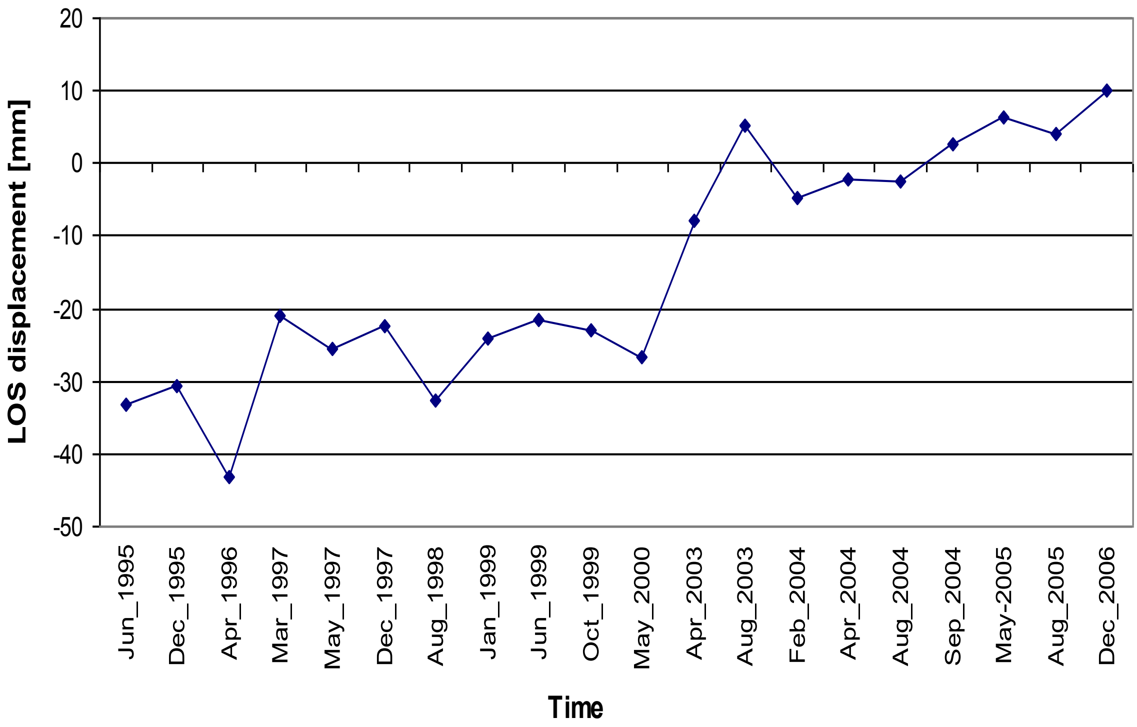

Figure.152 LOS displacement time series (1995-2006) of the minimum deformation rate of PSI of Giannouli. Point number 55991. Time series are rescaled to the first acquisition (28 June 1995)

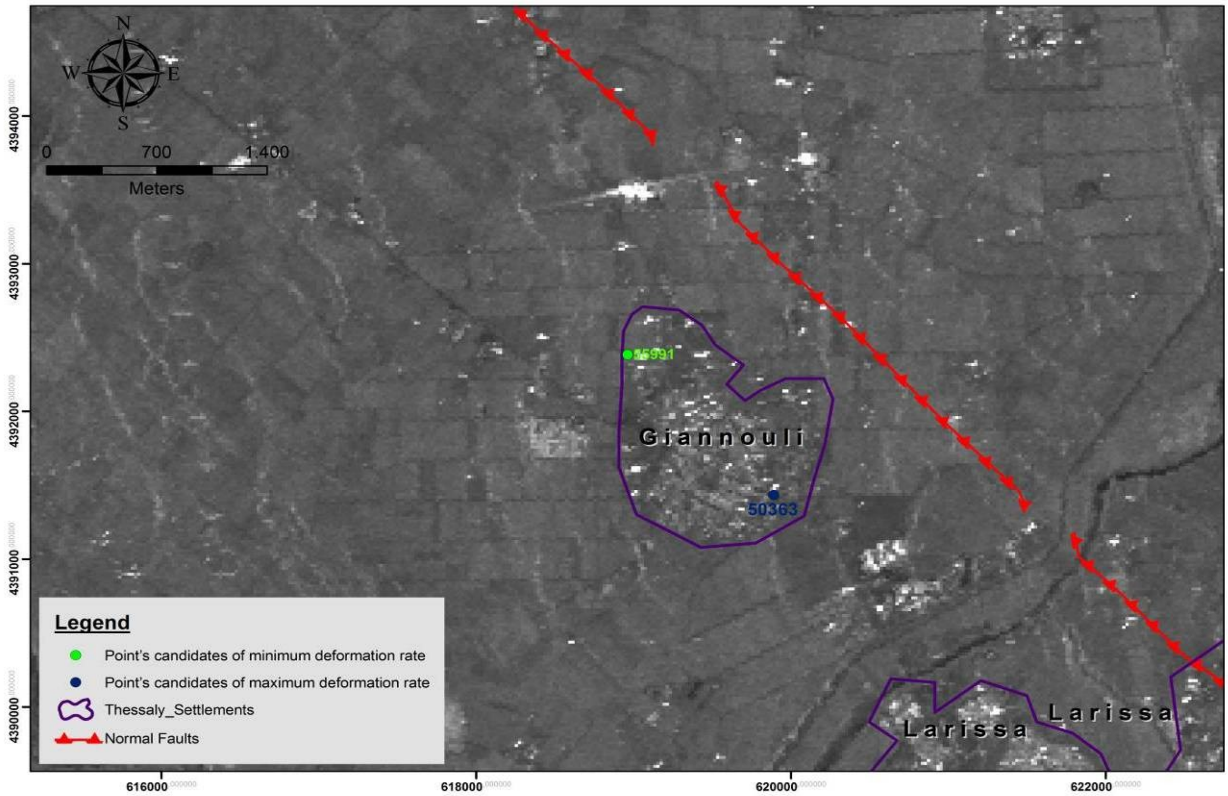

Figure153. Location of selected candidate points minimum and maximum deformation rate, ascending track 143, settlement of Giannouli

4.2.1.3.1.3. Falanna

Candidate point number 80781 was selected as representative of the minimum deformation rate. It is located in southwestern Falanna, 2.906 km east of a normal fault in the side of the hanging wall. A plot of this point is depicted in Figure 154. The deformation behavior of this candidate point through its time series begins with subsidence then changes to uplift. The minimum subsidence was -0.382 mm (August 2004) while the maximum subsidence was -43.033 mm (June 1995). The minimum and maximum uplift were 5.936 and 10.438 mm in May 2005 and December 2006 respectively. Subsidence may be attributed to the location of the point in the side of the hanging wall; in other words, it may be attributed to the impact of fault movement. However, the uplift may be attributed to another impact factor. The location of the selected point's minimum and maximum deformation rate is shown in Figure 155.

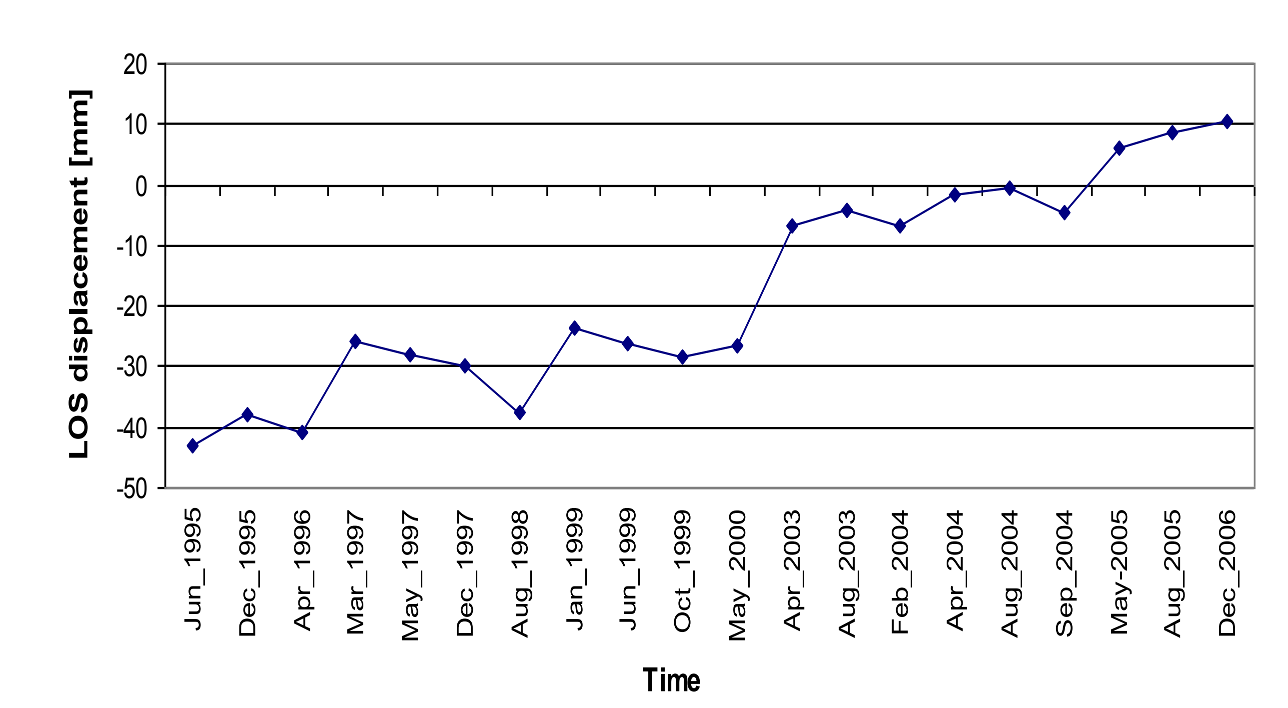

Figure.154 LOS displacement time series (1995-2006) of the minimum deformation rate of PSI of Falanna. Point number 80781. Time series are rescaled to the first acquisition (28 June 1995)

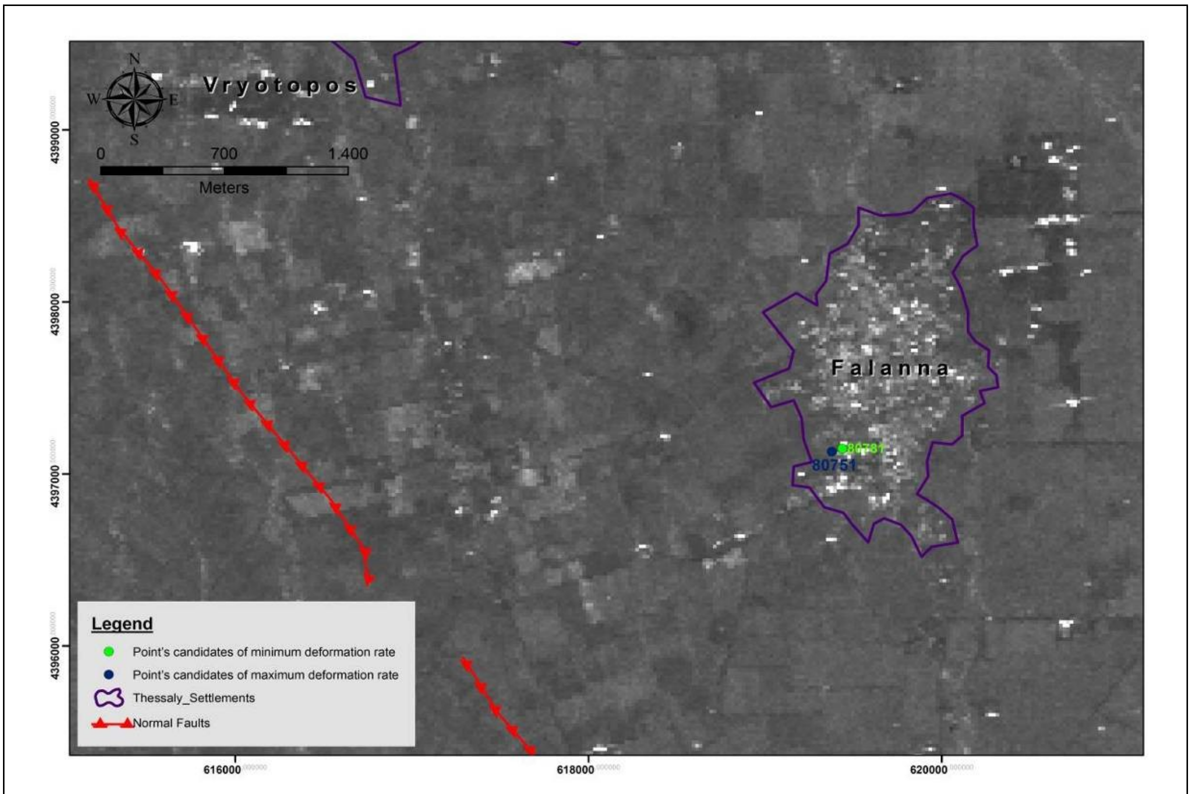

Figure.155 Location of selected candidate points minimum and maximum deformation rate, ascending track 143, settlement of Falanna.

4.2.1.3.1.4. Melissochorion

Candidate point number 35637 was selected as representative of the minimum deformation rate. It is located northwest of the settlement, and 2.725 km south of a normal fault in the side of the footwall as well as 3.4 km east of another normal fault in the side of the hanging wall. A plot of this point is depicted in Figure 156. The deformation behavior of this candidate point through its time series begins with subsidence then changes to uplift, and thereafter changing status between subsidence and uplift is observed during August 2003 – December 2006. The minimum subsidence was -0.796 mm (August 2005) while the maximum subsidence was -24.967 mm (December 1995). The minimum and maximum uplift were 4.871 and 11.115 mm in May 2005 and August 2004 respectively. Subsidence may be attributed to the location of the point on the eastern side of the hanging wall, while uplift may be attributed to the location of point south of a normal fault in the side of the footwall. It is worth mentioning that the fluctuation or change in status between subsidence and uplift during August 2003 – December 2006 may be attributed to the disparity in the impact of the faults' activity during this period. The location of the selected point's minimum and maximum deformation rate is shown in Figure 157.

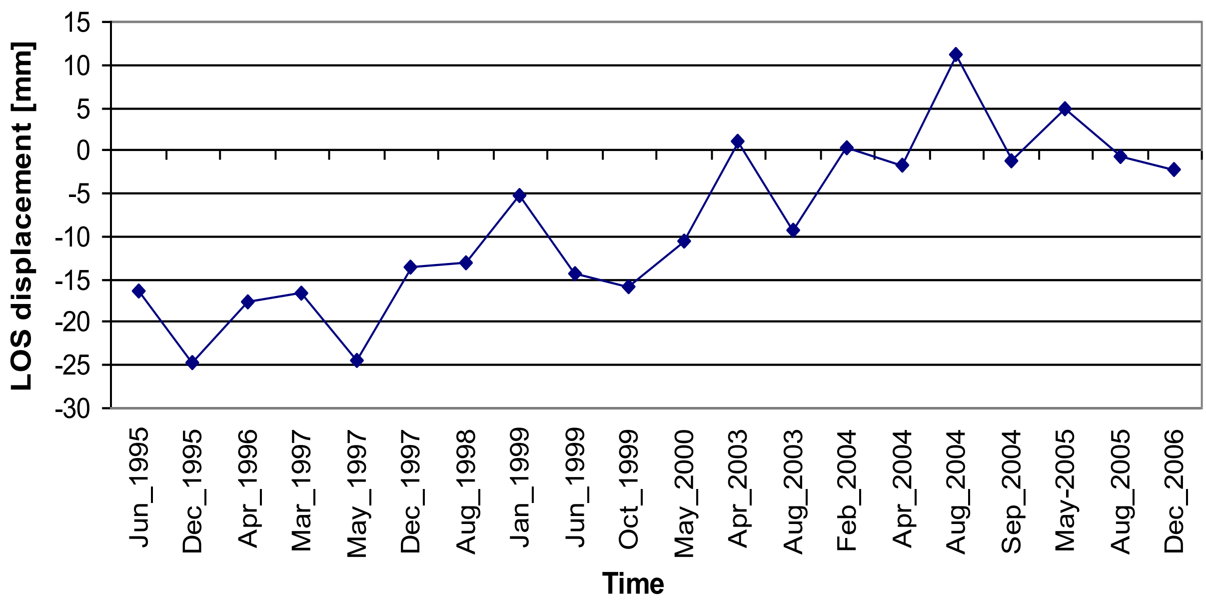

Figure156. LOS displacement time series (1995-2006) of the minimum deformation rate of PSI of Melissochorion. Point number 35637. Time series are rescaled to the first acquisition (28 June 1995)

Figure157. Location of selected candidate points minimum and maximum deformation rate, ascending track 143, settlement of Melissochorion.

4.2.1.3.1.5. Galini

Candidate point number 31580 was selected as representative of the minimum deformation rate. It is located southwest of the settlement, and 0.240 km south of a normal fault in the side of the footwall. A plot of this point is depicted in Figure 158. The deformation behavior of this candidate point through its time series showed continuous fluctuation between subsidence and uplift. The minimum subsidence was -0.292 mm (September 2004) while the maximum subsidence was -13.592 mm (January 1999). The minimum and maximum uplift were 0.442 and 10.444 mm in February 2004 and April 2004 respectively. Subsidence may be attributed to another impact factor. However, uplift may be attributed to the fault movement, since the candidate point is located in the side of the footwall, as mentioned above. The evidence of this impact is the increasing uplift during the two months of February and April 2004. The location of the selected point's minimum and maximum deformation rate is shown in Figure 159.

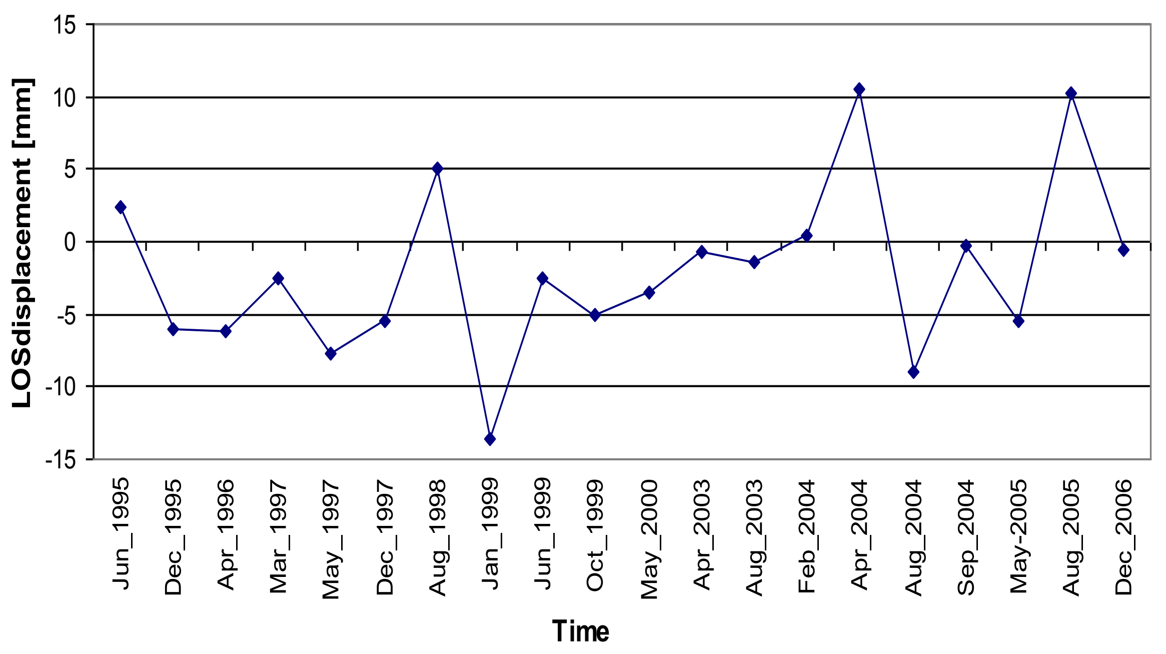

Figure158. LOS displacement time series (1995-2006) of the minimum deformation rate of PSI of Galini. Point number 31580. Time series are rescaled to the first acquisition (28 June 1995)

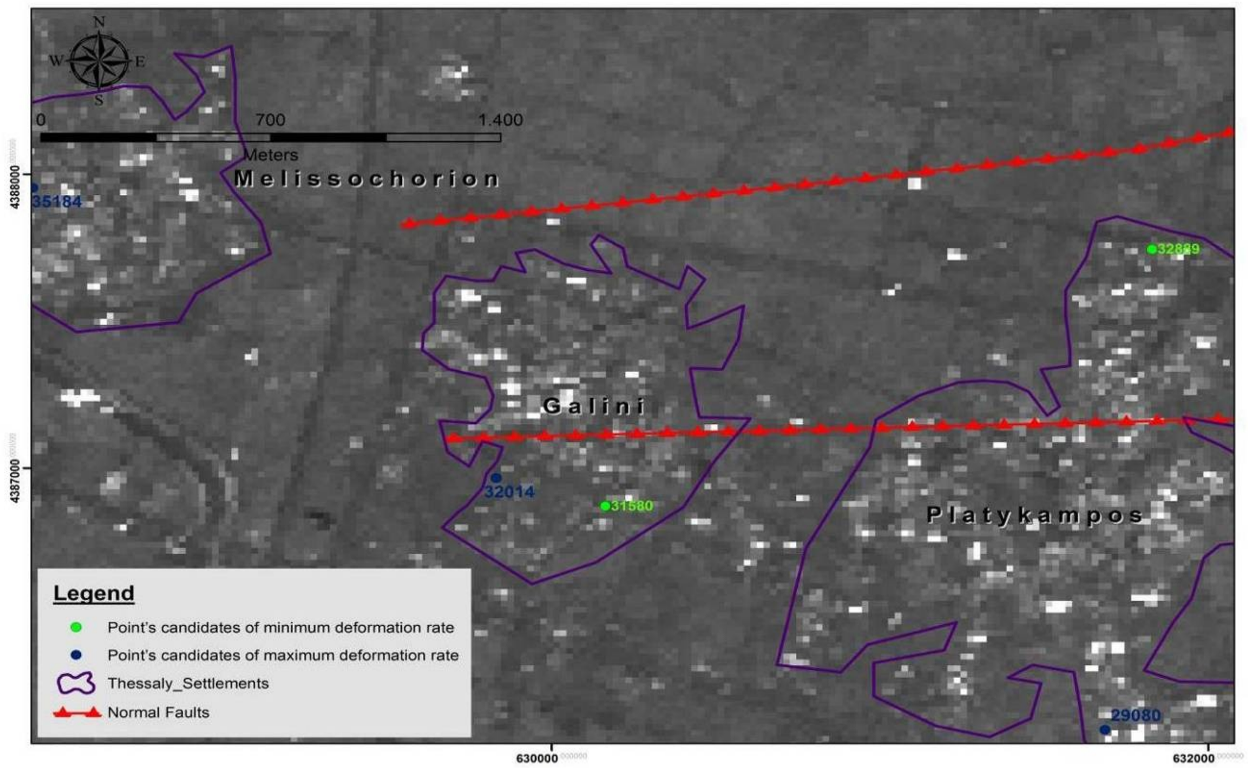

Figure.159 Location of selected candidate points minimum and maximum deformation rate, ascending track 143, settlement of Galini.

4.2.1.3.1.6. Platykampos

Candidate point number 32889 was selected as representative of the minimum deformation rate. It is located north of the settlement and 0.337 km south of a normal fault in the side of footwall, and additionally 0.585 km north of another normal fault trace in the side of the hanging wall. A plot of this point is depicted in Figure 160. The deformation behavior of this candidate point through its time series begins with uplift then changes to subsidence, and thereafter changing status between subsidence and uplift is observed during April 2003 – December 2006. The minimum subsidence was -2.049 mm (December 2006) while the maximum was -7.729 mm (August 2003). The minimum and maximum uplift were 0.035 and 16.281 mm in May 2005 and August 1998 respectively. Uplift may be attributed to the impact of the fault movement at the footwall north of the candidate point. However, subsidence may be attributed to the fault movement also at the hanging wall south of the point. Moreover, the changing status may be attributed to the disparity between the activities of the two normal faults. The location of the selected point's minimum and maximum deformation rate is shown in Figure 161.

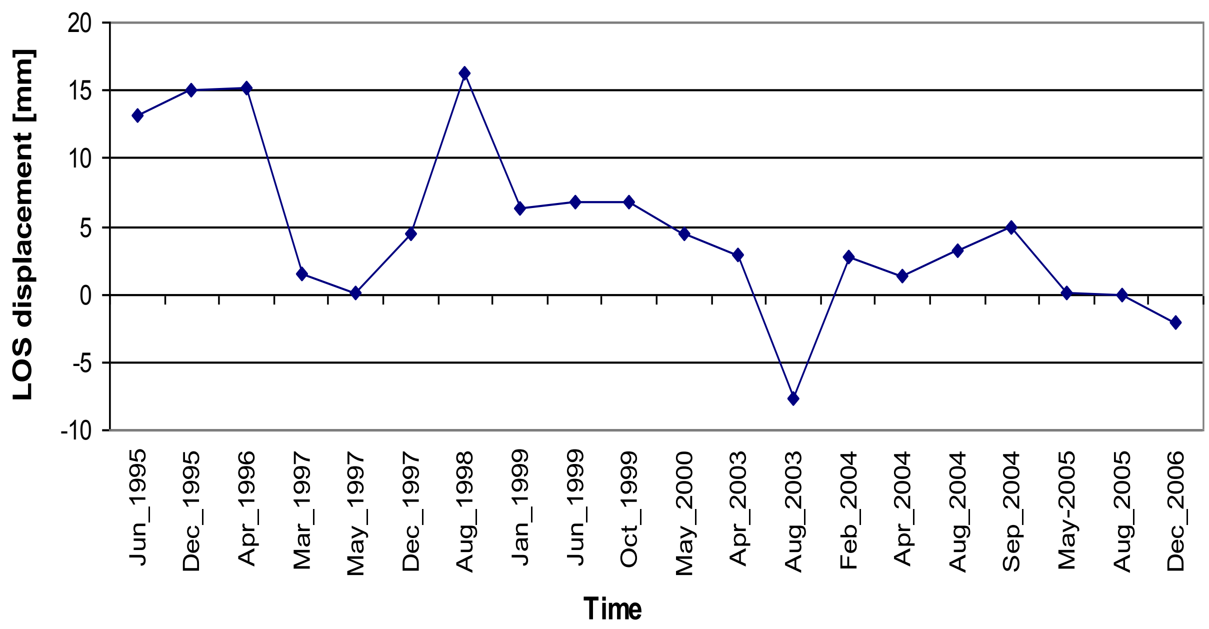

Figure160. LOS displacement time series (1995-2006) of the minimum deformation rate of PSI of Platykampos. Point number 32889. Time series are rescaled to the first acquisition (28 June 1995)

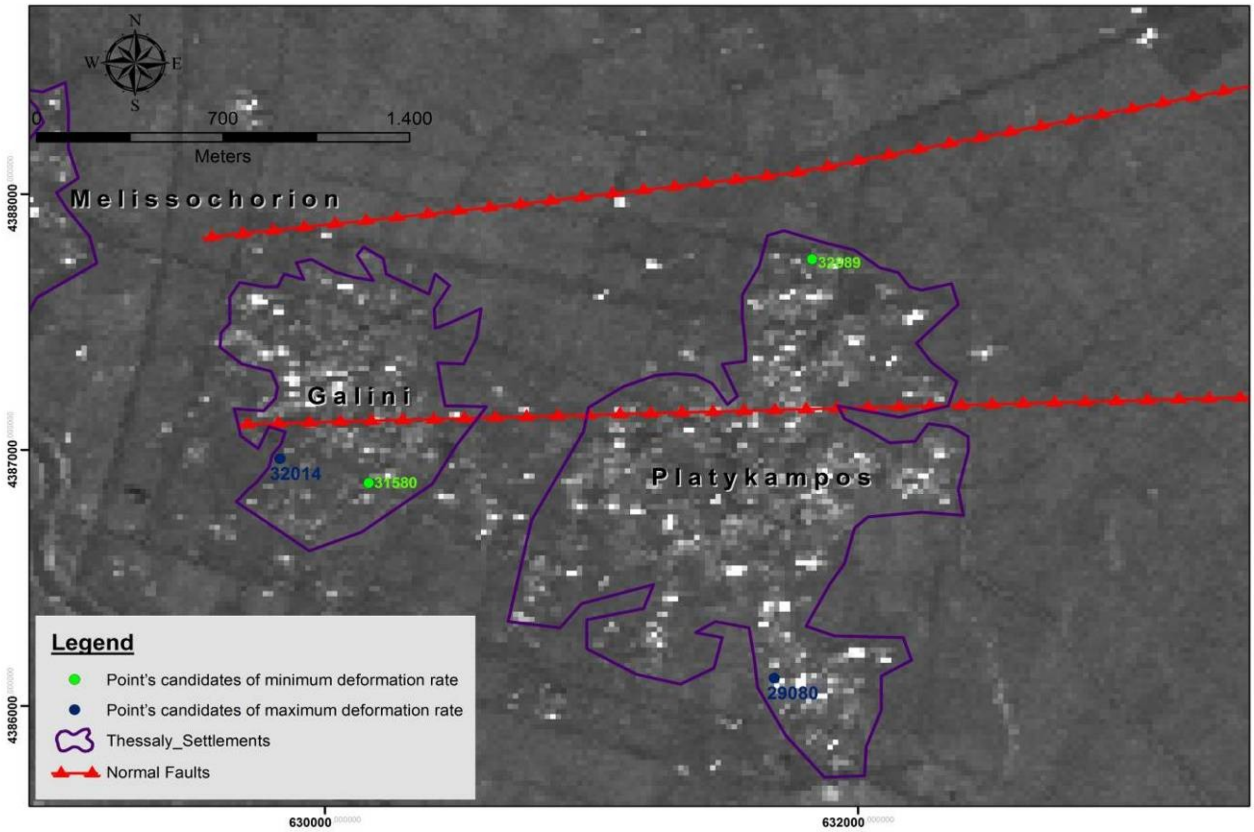

Figure161. Location of selected candidate points minimum and maximum deformation rate, ascending track 143, settlement of Platykampos.

4.2.1.3.1.7. Glafki

Candidate point number 26115 was selected as representative of the minimum deformation rate. It is located south of the settlement and 1.78 km south of a normal fault in the side of the footwall. A plot of this point is depicted in Figure 162. The deformation behavior of this candidate point through its time series begins with subsidence then changes to uplift; however, fluctuation between subsidence and uplift is observed during May 2000 – September 2004. The minimum subsidence was -1.881 mm (May 2005) while the maximum was -20.778 mm (June 1995). The minimum and maximum uplift were 0.254 and 6.099 mm in August 2005 and October 1999 respectively. Subsidence may be attributed to another impact factor than the fault movement. However, uplift may be attributed to the location of the point in the side of the footwall of the normal fault. The location of the selected point's minimum and maximum deformation rate is shown in Figure 163.

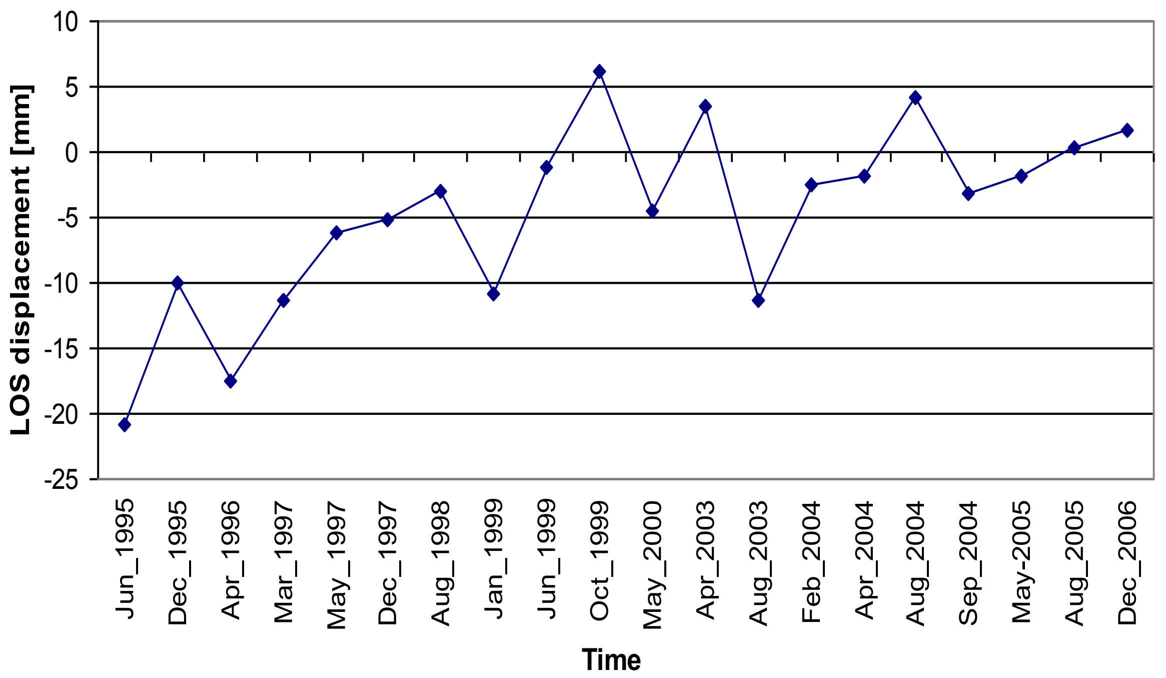

Figure.162 LOS displacement time series (1995-2006) of the minimum deformation rate of PSI of Glafki. Point number 26115. Time series are rescaled to the first acquisition (28 June 1995)

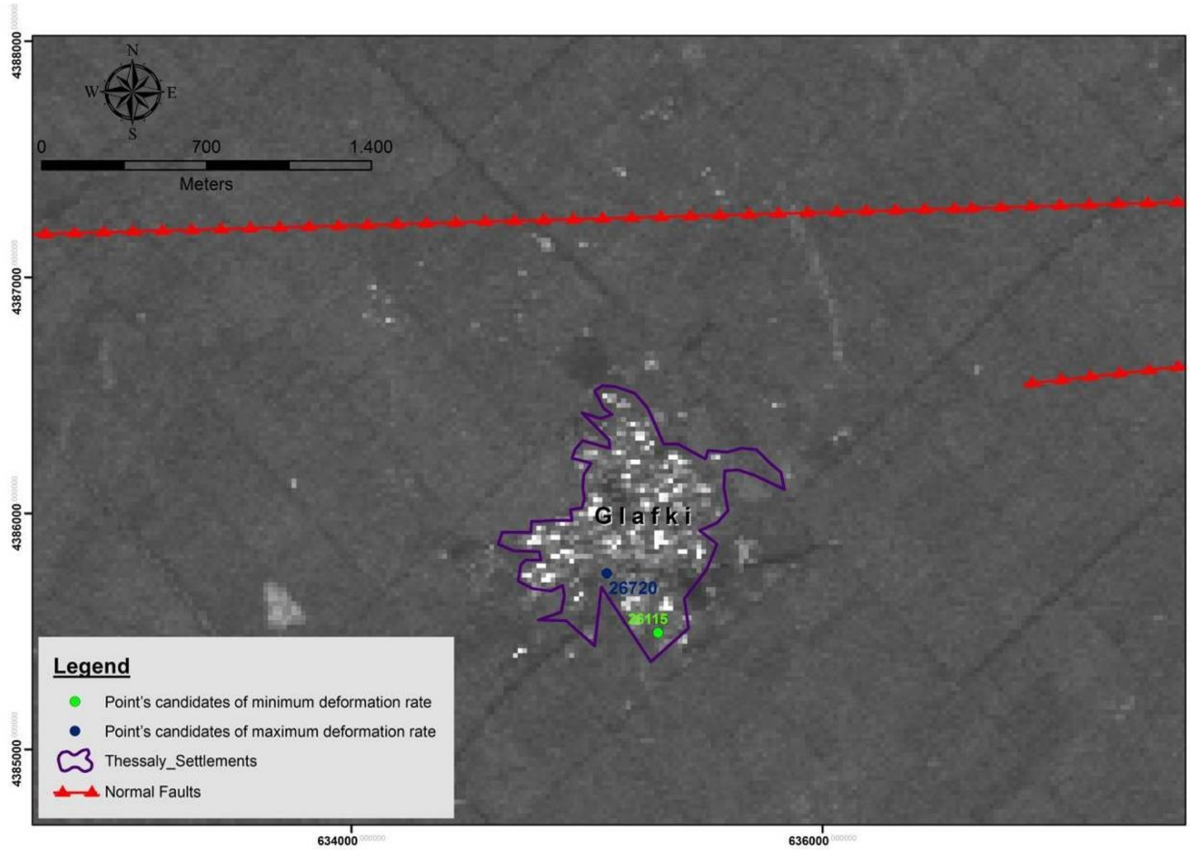

Figure.163 Location of selected candidate points minimum and maximum deformation rate, ascending track 143, settlement of Glafki.

4.2.1.3.1.8. Tyrnavos

Candidate point number 116381 was selected as representative of the minimum deformation rate It is located in the northern part of the settlement, and 2.78 km west of a normal fault in the side of the footwall as well as 5 km north of another normal fault in the side of the hanging wall. A plot of this point is depicted in Figure 164. The deformation behavior of this candidate point through its time series begins with subsidence then changes to uplift, but changing status between subsidence and uplift is observed during September 2004 – December 2006. The minimum subsidence was -2.025 mm (April 2004) while the maximum subsidence was -35.901 mm (June 1995). The minimum and maximum uplift were 5.919 and 6.608 mm in December 2006 and August 2005 respectively.

Subsidence may be attributed to the impact of fault movement of the fault trace which is located south of the candidate point, and uplift may be attributed also to the impact of fault movement of the fault east of the candidate point, as mentioned above. The location of the selected point's minimum and maximum deformation rate is shown in Figure 165.

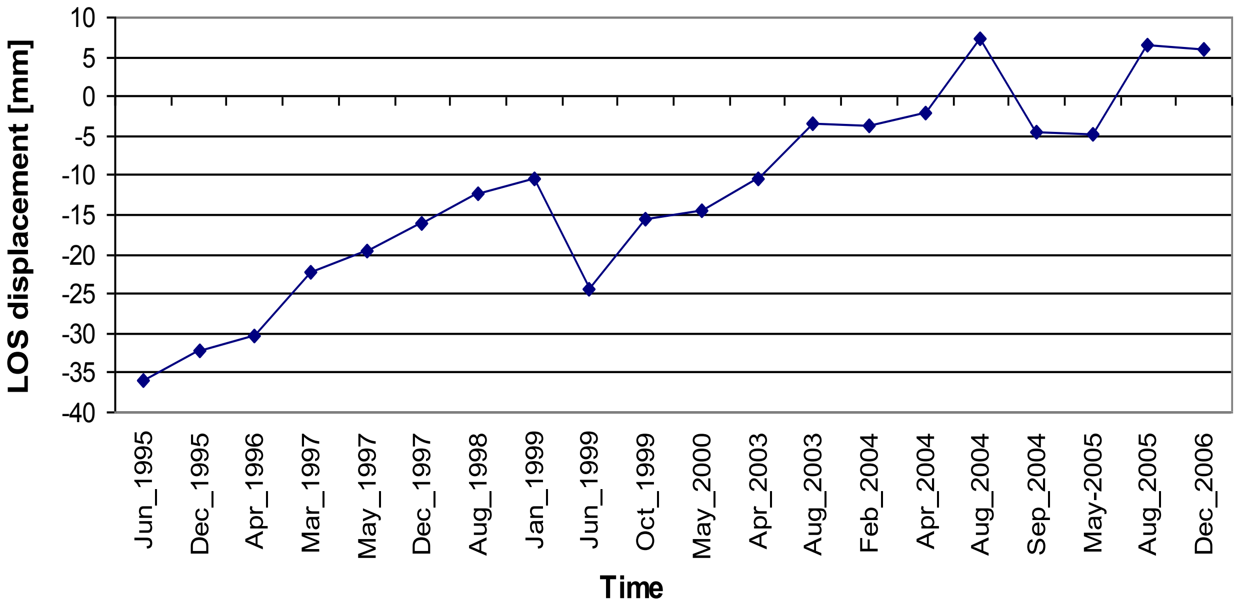

Figure164. LOS displacement time series (1995-2006) of the minimum deformation rate of PSI of Tyrnavos. Point number 116381. Time series are rescaled to the first acquisition (28 June 1995)

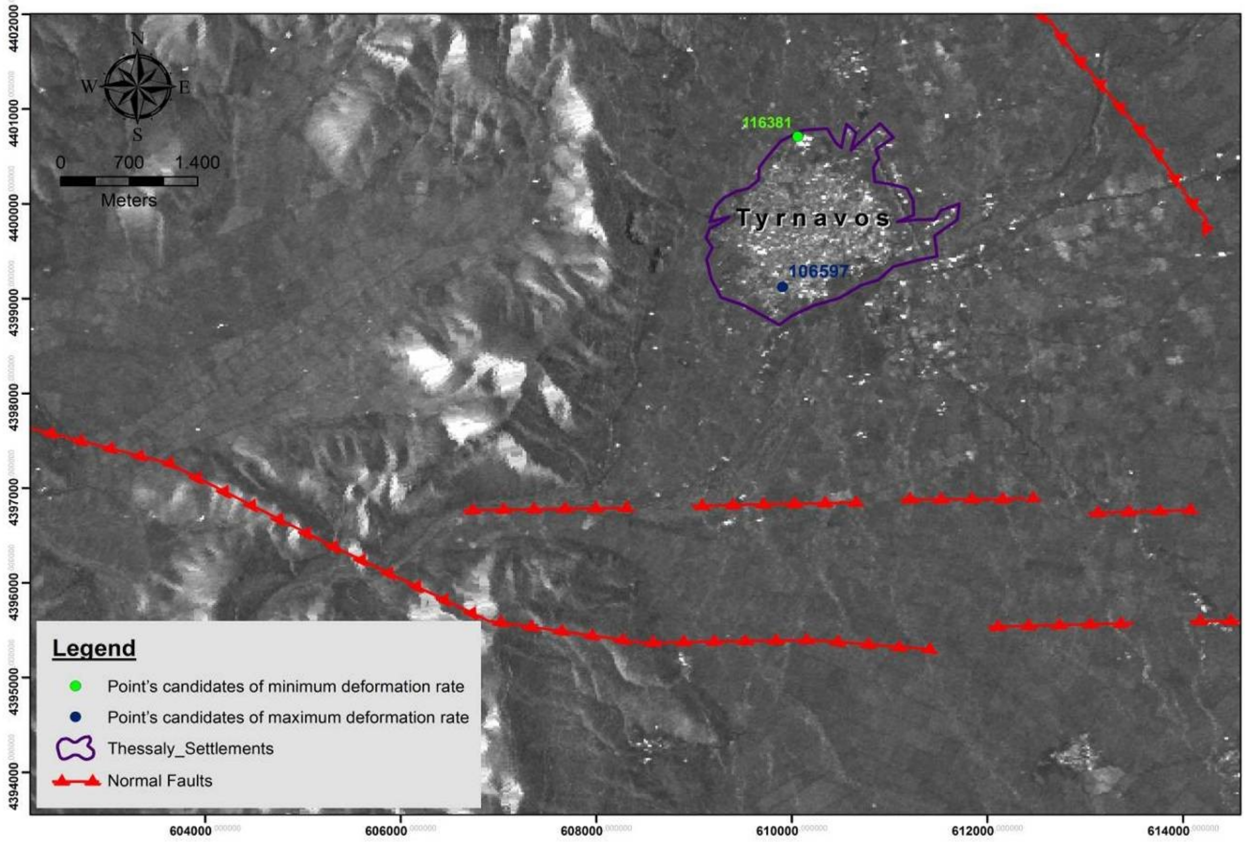

Figure.165 Location of selected candidate points minimum and maximum deformation rate, ascending track 143, settlement of Tyrnavos.

4.2.1.3.1.9. Rodia

Candidate point number 142796 was selected as representative of the minimum deformation rate. It is located to the far west of the settlement, and between two normal faults in the side of the hanging walls, the first one 1.10 km east of the point and the second one 1.1186 km to the north. A plot of this point is depicted in Figure 166. The deformation behavior of this candidate point through its time series begins with subsidence then changes to uplift. The minimum subsidence was -0.174 mm (August 2004) while the maximum was -64.326 mm (December 1995). The minimum and maximum uplift were 4.539 and 10.297 mm in September 2004 and December 2006 respectively. Subsidence may be attributed to another impact factor. However, uplift may be attributed to the impact of fault movement. The location of the selected point's minimum and maximum deformation rate is shown in Figure 167.

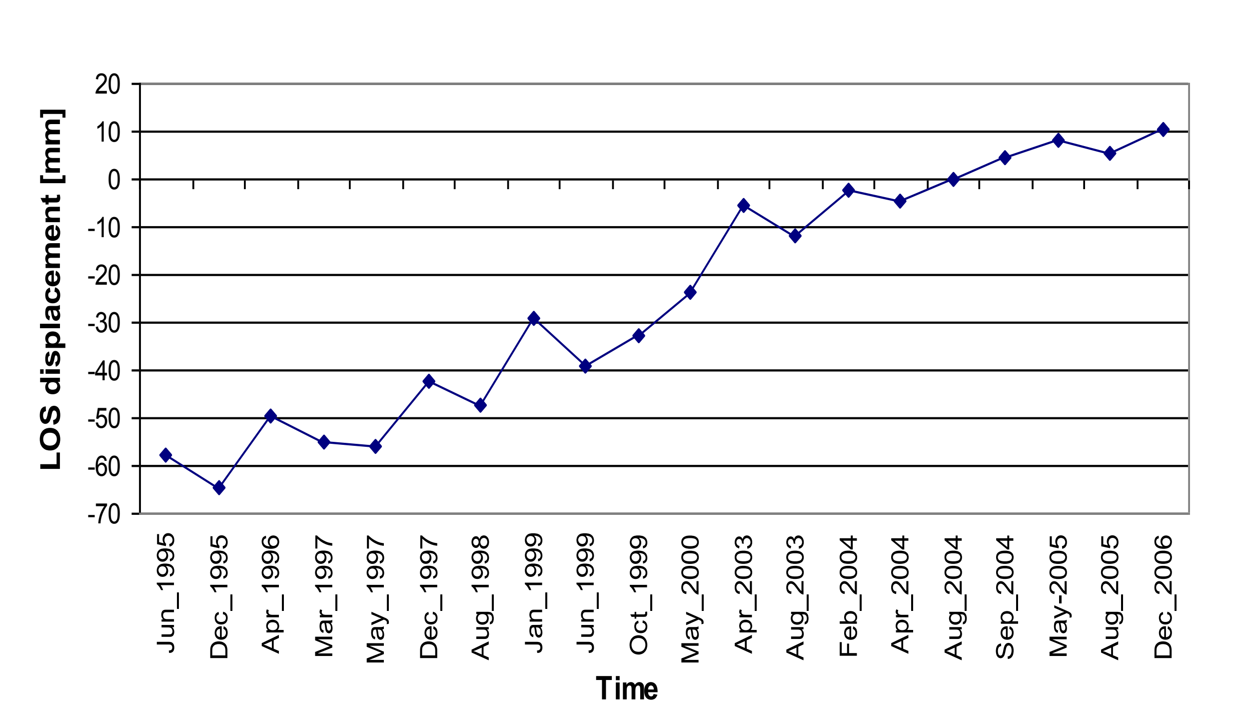

Figure166. LOS displacement time series (1995-2006) of the minimum deformation rate of PSI of Rodia. Point number 142796. Time series are rescaled to the first acquisition (28 June 1995)

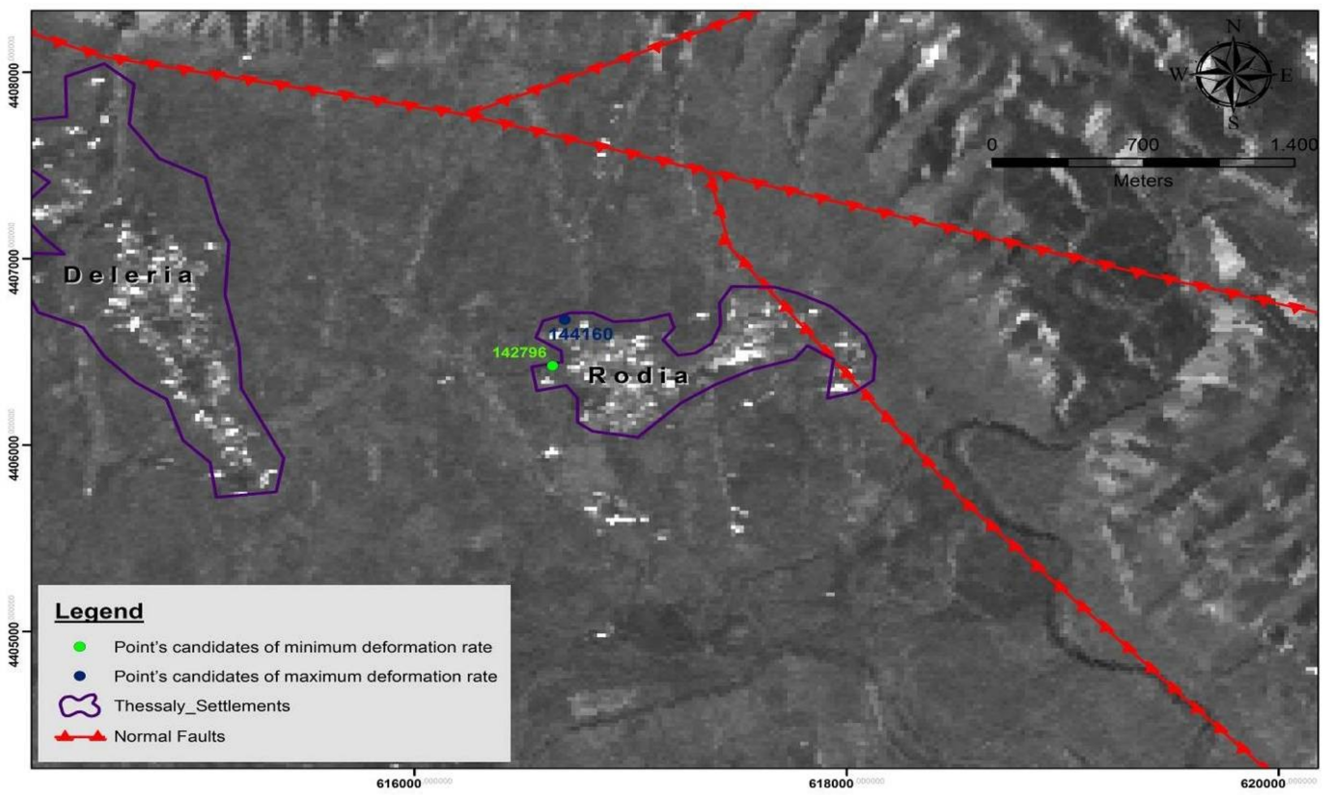

Figure167. Location of selected candidate pointsminimum and maximum deformation rate, ascending track 143, settlement of Rodia.

4.2.1.3.1.10. Mandra

Candidate point number 41227 was selected as representative of the minimum deformation rate. It is located southwest of the settlement, and southwest of two normal faults in the side of the footwalls at distances of 4.337 and 4.896 km respectively. A plot of this point is depicted in Figure 168. The deformation behavior of this candidate point through its time series begins with uplift then changes to subsidence. The minimum uplift was 0.420 mm (April 2004) while the maximum uplift was 27.553 mm (June 1995). The minimum and maximum subsidence were -0.13 and -5.982 mm in August 2005 and May 2005 respectively. Uplift may be attributed to the impact of fault movement. However, subsidence may be attributed to another impact factor. The location of the selected point's minimum and maximum deformation rate is shown in Figure 169.

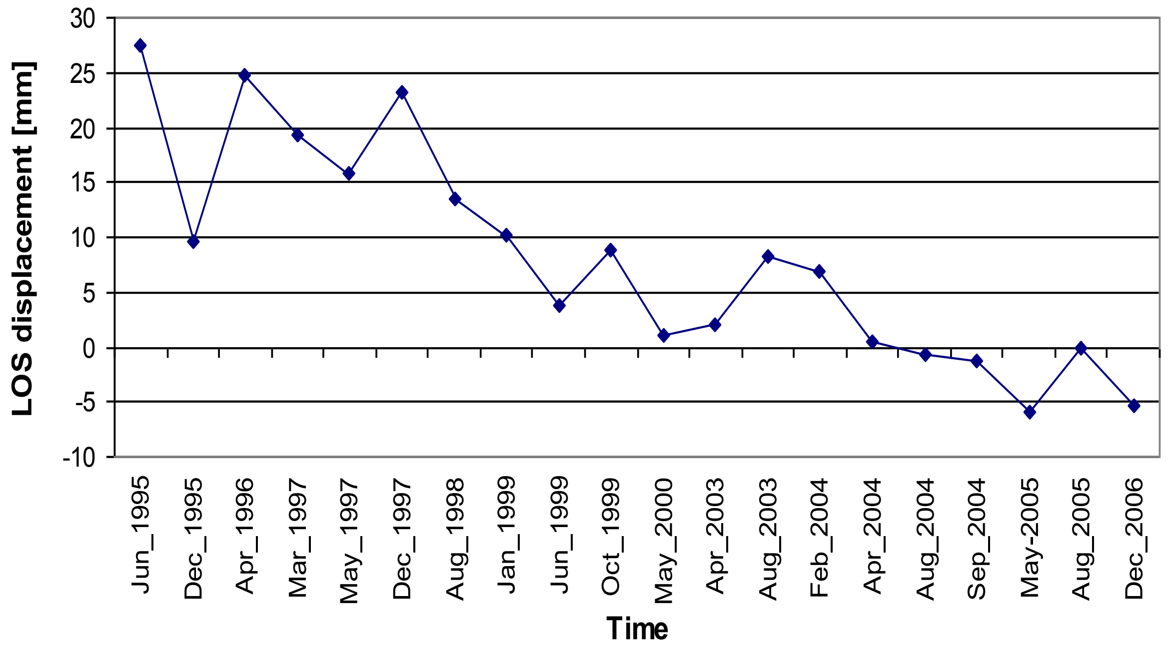

Figure.168 LOS displacement time series (1995-2006) of the minimum deformation rate of PSI of Mandra. Point number 41227. Time series are rescaled to the first acquisition (28 June 1995)

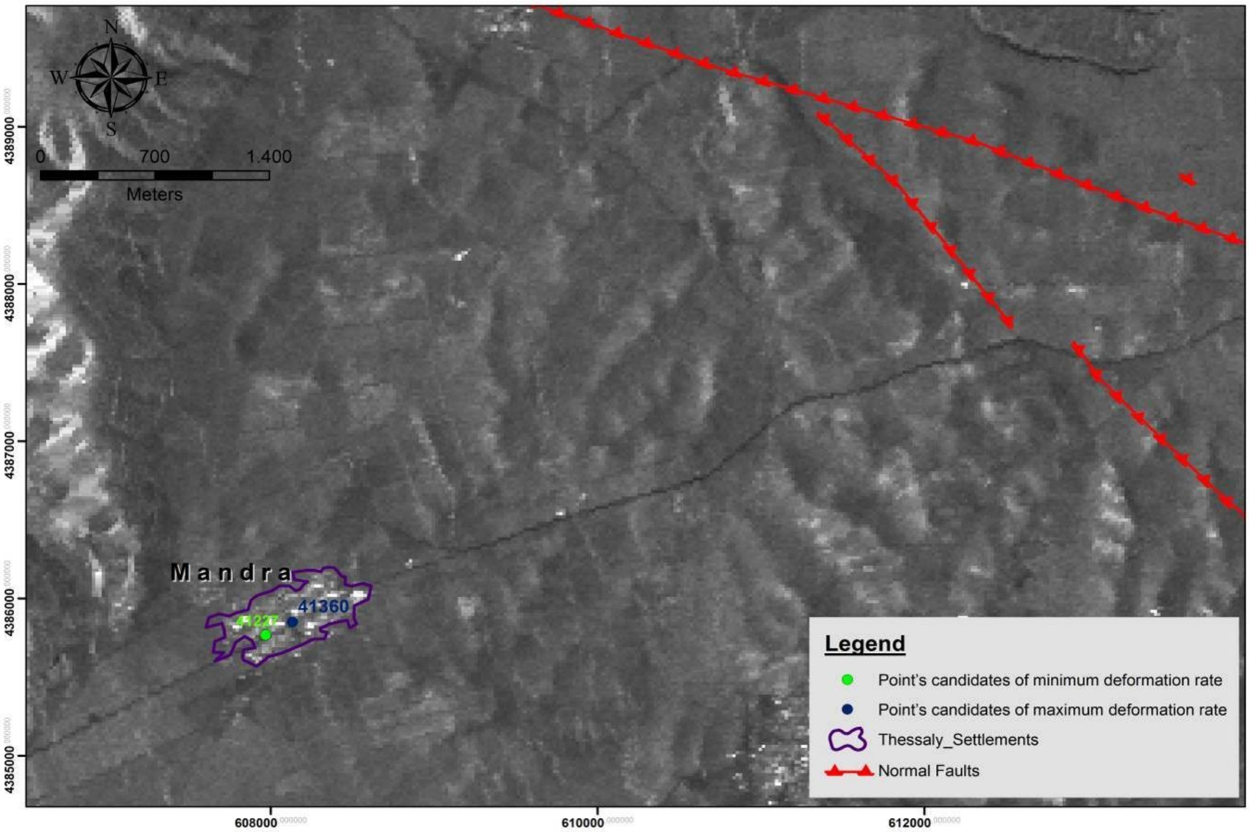

Figure169. Location of selected candidate points minimum and maximum deformation rate, ascending track 143, settlement of Mandra

4.2.1.3.1.11. <u>Eleftherai</u>

Candidate point number 28093 was selected as representative of the minimum deformation rate. It is located west of the settlement, and 3.0 km southwest of a normal fault in the side of the footwall. A plot of this point is depicted in Figure 170. The deformation behavior of this candidate point through its time series begins with uplift then changes to subsidence. The minimum uplift was 0.331 mm (August 2004) while the maximum uplift was 35.828 mm (June 1995). The minimum and maximum subsidence was -2.675 and -9.063 mm in May 2005 and December 2006 respectively. Uplift may be attributed to the impact of fault movement. However, subsidence towards the end of the time series may be attributed to decreasing fault movement activity, as a result of which one or more parameters have begun to motivate subsidence deformation. The location of the selected point's minimum and maximum deformation rate is shown in Figure 171.

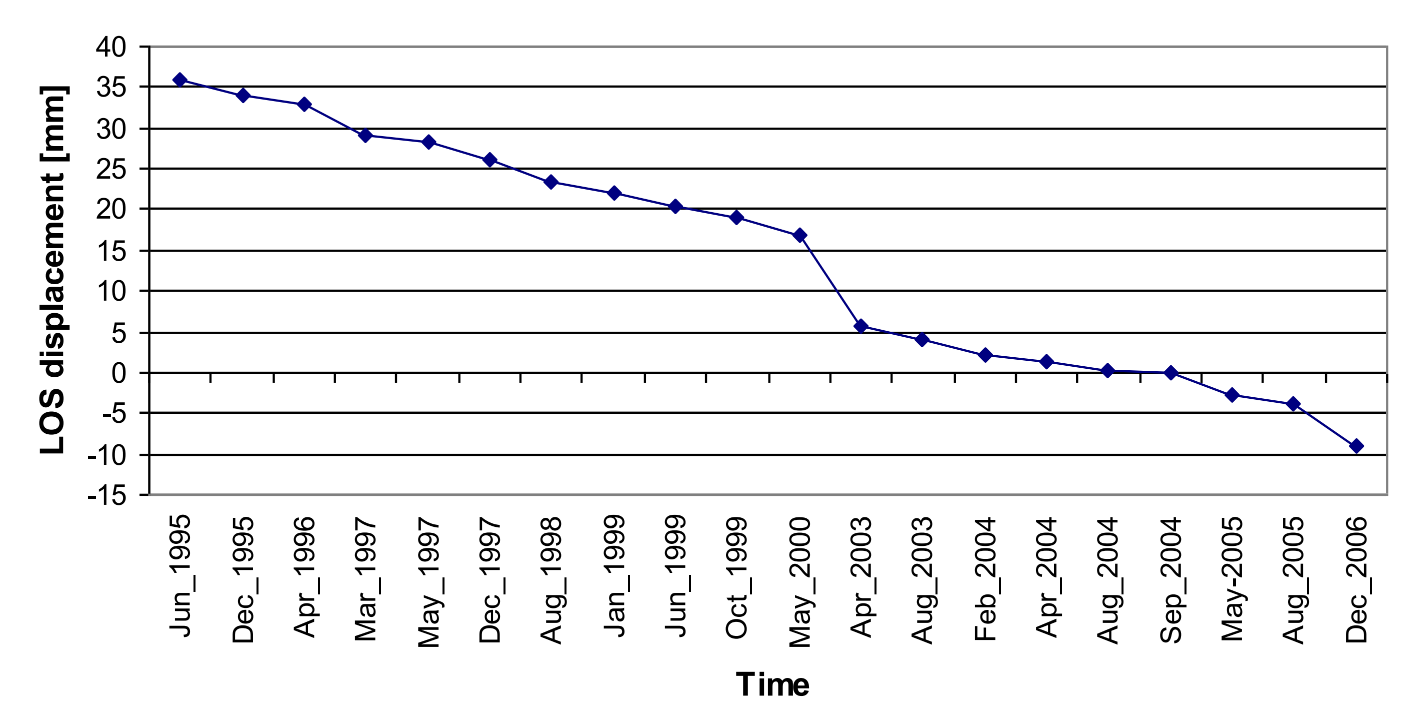

Figure170. LOS displacement time series (1995-2006) of the minimum deformation rate of PSI of Eleftherai. Point number 28093. Time series are rescaled to the first acquisition (28 June 1995)

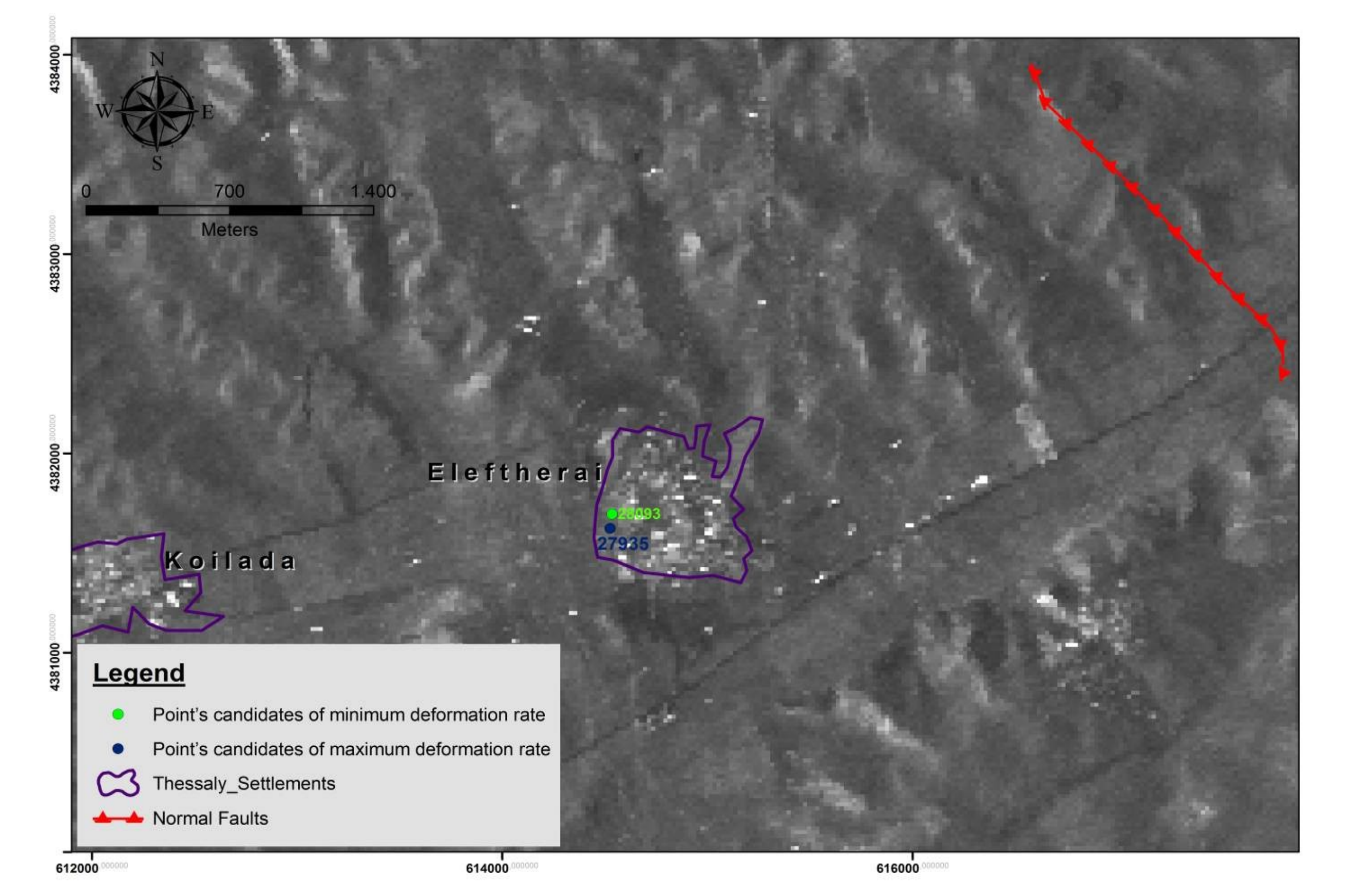

Figure171. Location of selected candidate points minimum and maximum deformation rate, ascending track 143, settlement of Eleftherai

4.2.1.3.1.12. Terpsithea

Candidate point number 36831 was selected as representative of the minimum deformation rate. It is located southwest of the settlement, and 1.611 km south of a normal fault in the side of the footwall, as well as 0.77 km northeast of a normal fault trace in the side of the hanging wall. A plot of this point is depicted in Figure 172. The deformation behavior of this candidate point through its time series begins with subsidence then changes to uplift. The minimum subsidence was -1.086 mm (April 2004) while the maximum was -66.174 mm (June 1995). The minimum and maximum uplift were 1.416 and 13.511 mm in August 2005 and December 2006 respectively. Subsidence and uplift may be attributed to the impact of fault movements, through the disparity in the activity of the two faults. Since the point is located between a footwall and a hanging wall, as mentioned above, it seems that after a decrease in the activity of the hanging wall the activity of the footwall of other normal fault trace began. The location of the selected point's minimum and maximum deformation rate is shown in Figure 173.

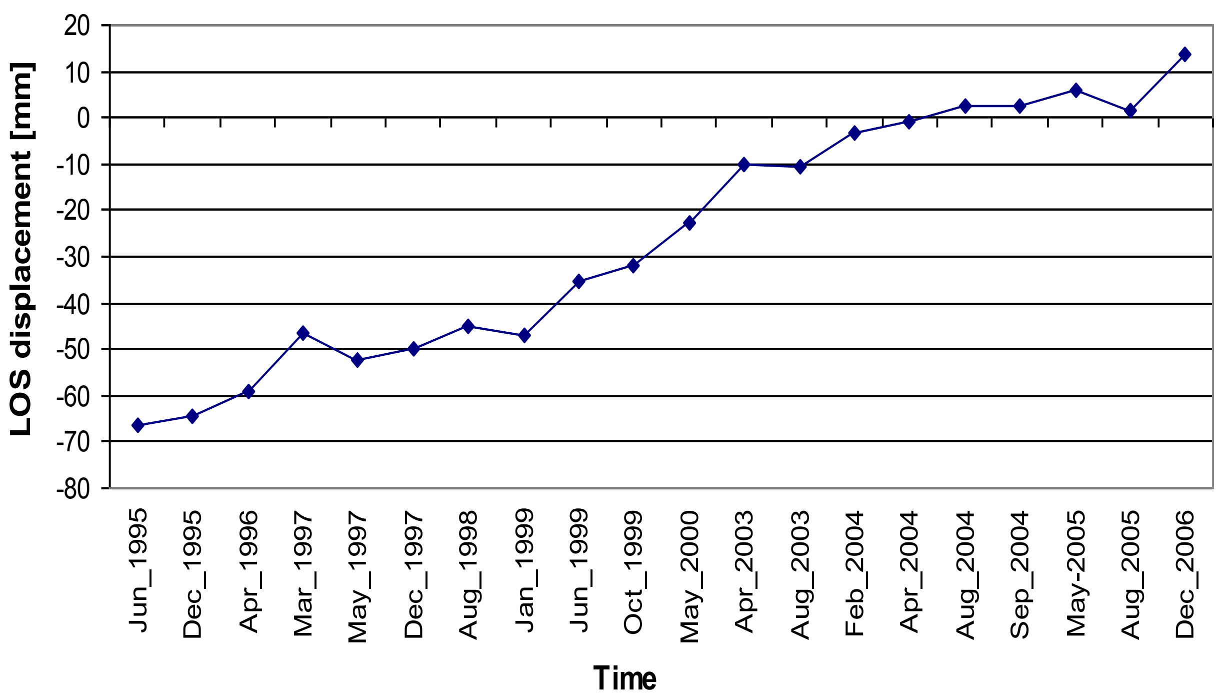

Figure172. LOS displacement time series (1995-2006) of the minimum deformation rate of PSI of Terpsithea. Point number 36831. Time series are rescaled to the first acquisition (28 June 1995)

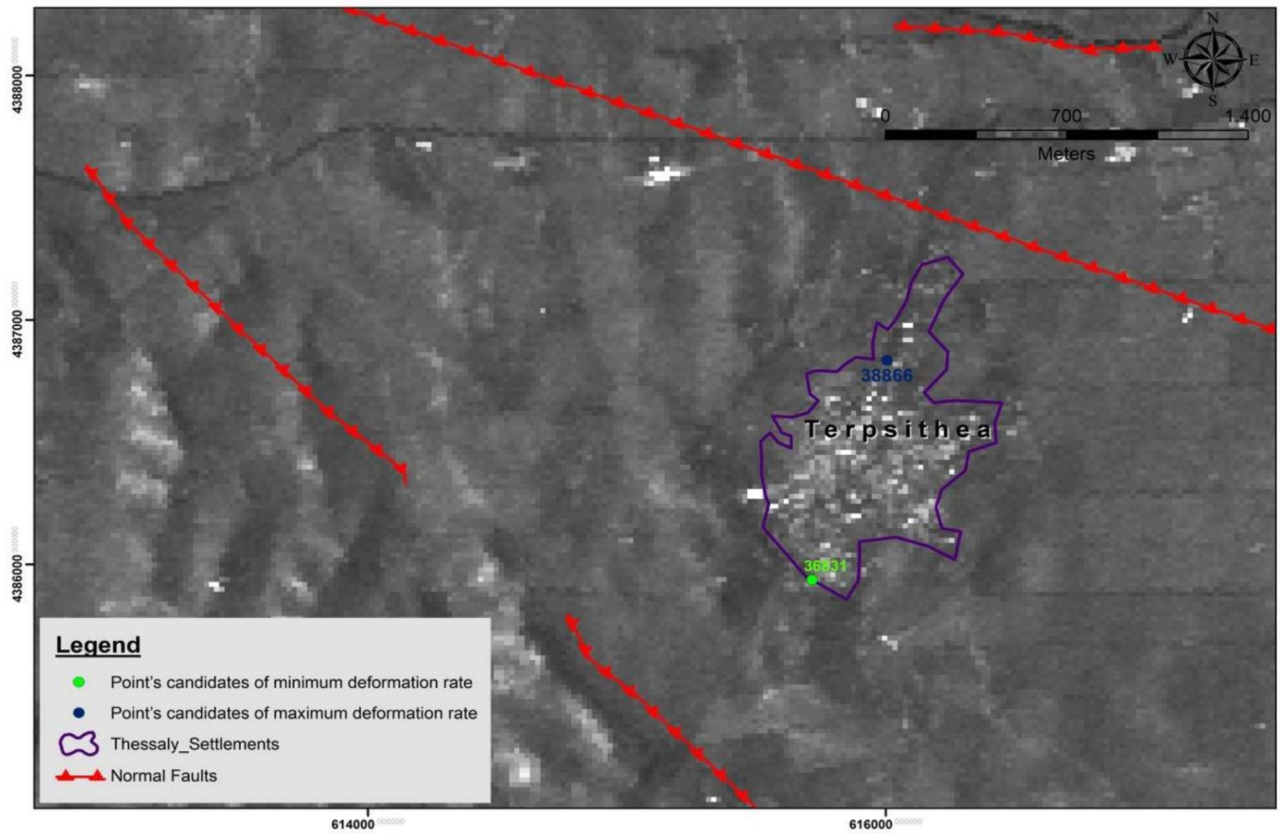

Figure173. Location of selected candidate points minimum and maximum deformation rate, ascending track 143, settlement of Terpsithea

4.2.1.3.1.13. Nikaia

Candidate point number 19557 was selected as representative of the minimum deformation rate. It is located east of the settlement, and 1.52 km south of a normal fault in the side of the footwall, as well as 5.1 km northeast of another normal fault in the side of the hanging wall. A plot of this point is depicted in Figure 174. The deformation behavior of this candidate point through its time series begins with subsidence then changes to uplift. The minimum subsidence was -0.983 mm (February 2004) while the maximum was -103.023 mm (June 1995). The minimum and maximum uplift were 3.509 and 31.033 mm in May 2005 and December 2006 respectively. Subsidence may be attributed to the impact of fault movement. However, uplift may be attributed to the disparity of faults activity, since the location of the point is between a footwall and a hanging wall, as mentioned above, so after a decrease in the activity of the hanging wall the activity of the footwall of the other normal fault trace began. The location of the selected point's minimum and maximum deformation rate is shown in Figure 175.

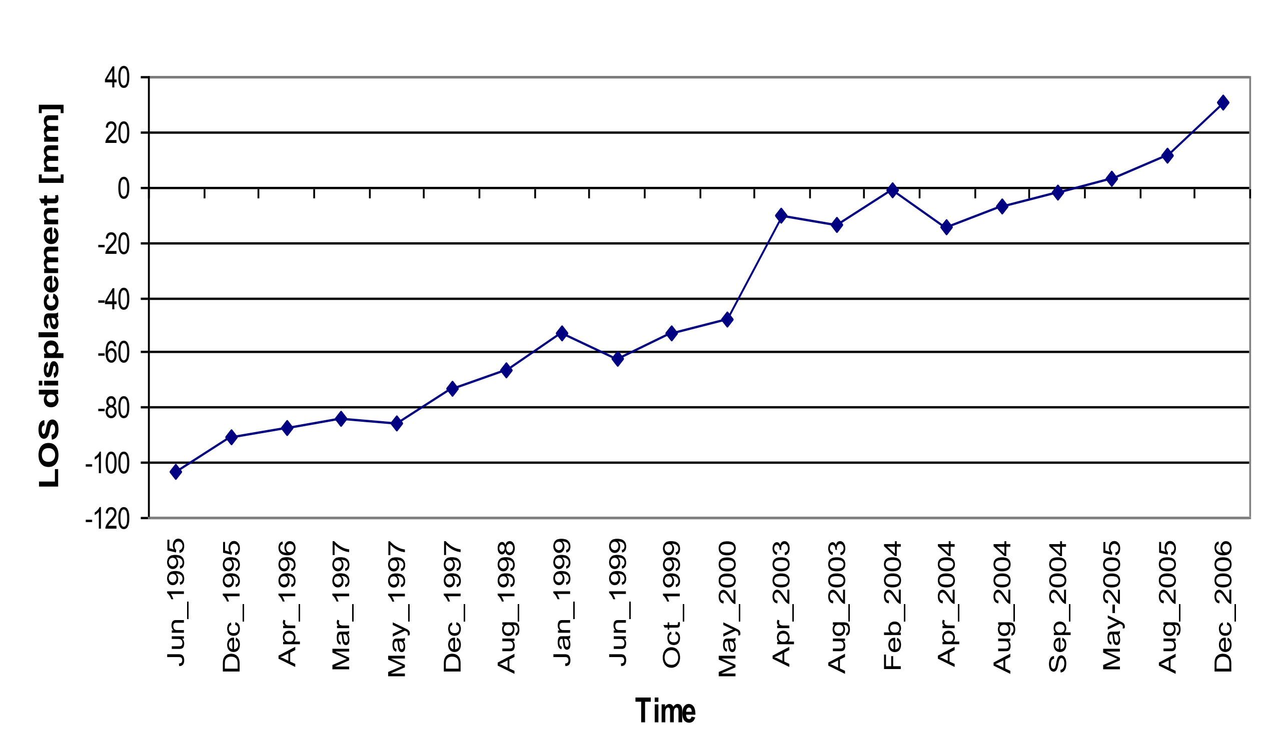

Figure174. LOS displacement time series (1995-2006) of the minimum deformation rate of PSI of Nikaia. Point number 19557. Time series are rescaled to the first acquisition (28 June 1995)

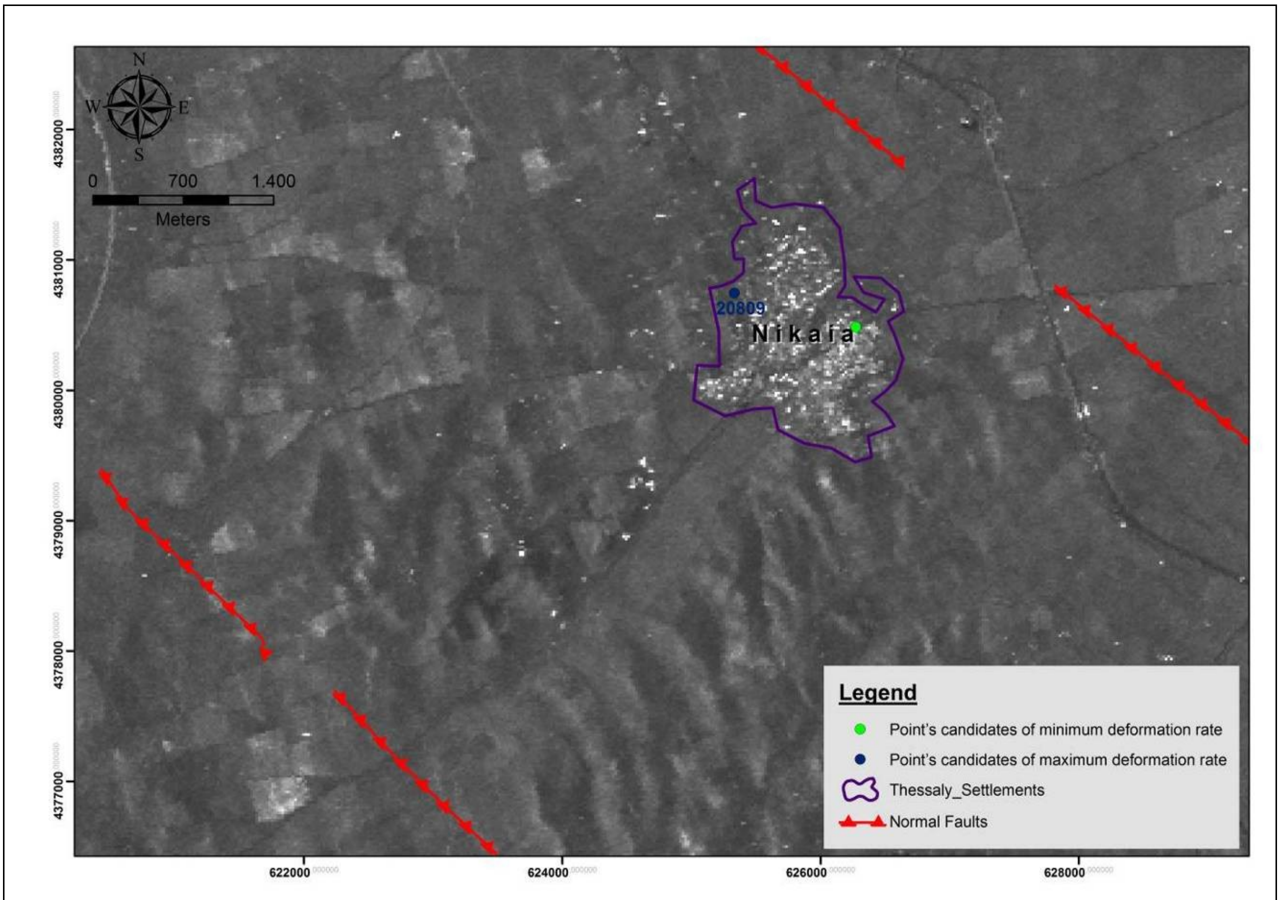

Figure.175 Location of selected candidate points minimum and maximum deformation rate, ascending track 143, settlement of Nikaia

4.2.1.3.2. Maximum deformation rate

An identical context has been implemented to that previously used with the minimum deformation rate to interpret the deformation behaviour of each candidate point; relating the spatial correlation of the candidate point location with faults traces will enable the maximum deformation rate to be verified, reflecting the impact of fault movement on the ground deformation.

4.2.1.3.2.1. <u>Larissa</u>

Candidate point number 31912 was selected as representative of the maximum deformation rate. It is located southeast of Larissa, and 0.402 km north of a normal fault in the side of the hanging wall, as well as 1.49 km south of another normal fault in the side of the footwall. A plot of this point is depicted in Figure 176. The deformation behavior of this candidate point through its time series begins with subsidence then changes to uplift. The minimum subsidence was -3.185 mm (September 2004) while the maximum was -301.818 mm (June 1995). The minimum and maximum uplift were 1.048 and 67.334 mm in August 2004 and December 2006 respectively. Subsidence may be attributed to the impact of fault movement. Uplift towards the end of the time series for the candidate point may be attributed also to the disparity in faults activity, since the location of the point is between the hanging wall and the footwall of two normal faults, as mentioned above. The location of the selected point's minimum and maximum deformation rate was shown previously in Figure 151.

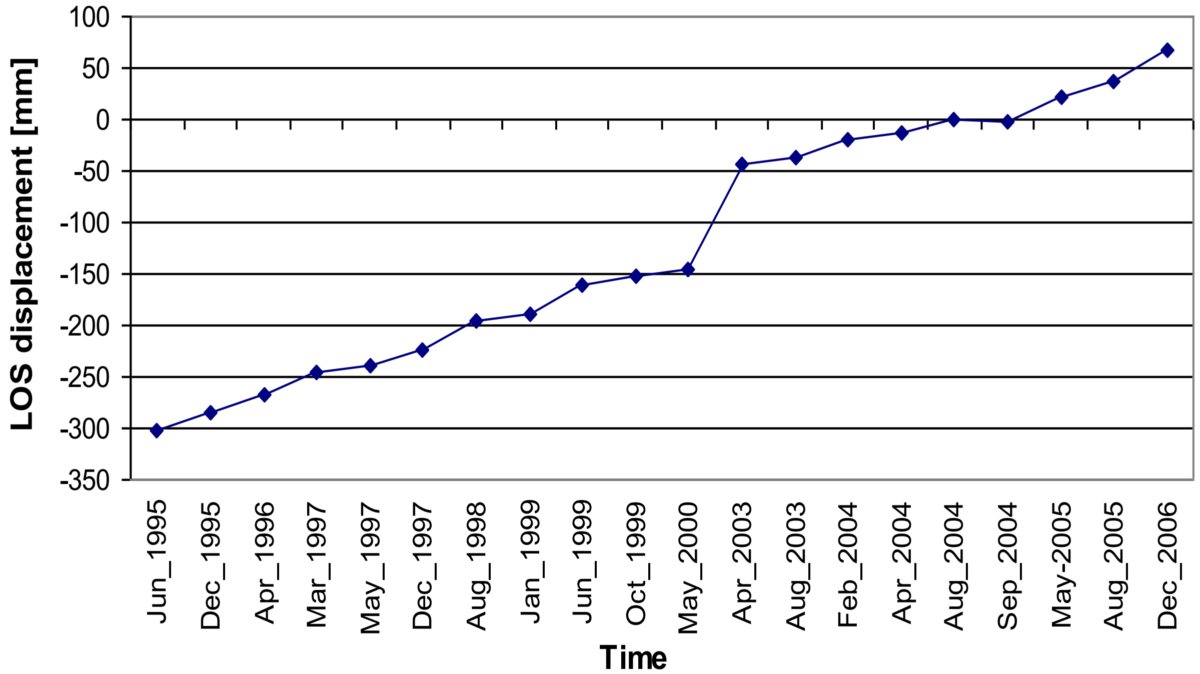

Figure176. LOS displacement time series (1995-2006) of the maximum deformation rate of PSI of Larissa. Point number 31912. Time series are rescaled to the first acquisition (28 June 1995)

4.2.1.3.2.2. Giannouli

Candidate point number 50363 was selected as representative of the maximum deformation rate. It is located southeast of the settlement, and 1.149 km west of a normal fault trace in the side of the footwall. A plot of this point is depicted in Figure 177. The deformation behavior of this candidate point through its time series begins with subsidence then changes to uplift. The minimum subsidence was -2.538 mm (September 2004) and the maximum subsidence was -278.597 mm (June 1995). The minimum and maximum uplift were 1.465 and 22.588 mm in August 2004 and May 2005 respectively. Subsidence may be attributed to an impact factor other than fault movement, because of the presence of the point in the side of the footwall, as mentioned above. However, uplift may be attributed to the impact of fault movement. The location of the selected point's minimum and maximum deformation rate was shown previously in Figure 153.

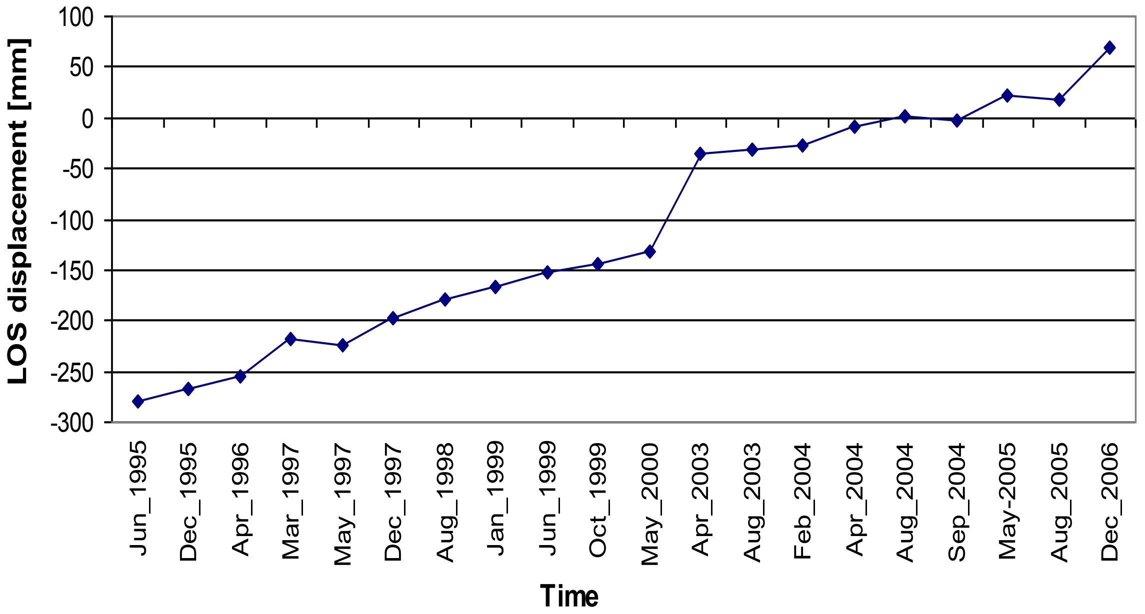

Figure177. LOS displacement time series (1995-2006) of the maximum deformation rate of PSI of Giannouli. Point number 50363. Time series are rescaled to the first acquisition (28 June 1995)

4.2.1.3.2.3. <u>Falanna</u>

Candidate point number 80751 was selected as representative of the maximum deformation rate. It is located southwest of the settlement, and 2.38 km east of a normal fault trace in the side of the hanging wall. A plot of this point is depicted in Figure 178. The deformation behavior of the candidate point through its time series begins with subsidence then changes to uplift, and changing status from uplift to subsidence was observed in August 2004. The minimum subsidence was -3.918 mm (April 2004) while the maximum was -54.374 mm (April 1996). The minimum and maximum uplift were 1.408 and 14.376 mm in August 2004 and December 2006 respectively. Subsidence may be attributed to the location of the point in the side of the hanging wall; in other words, it is attributed to the impact of fault movement. However, uplift may be attributed to another impact factor. The location of the selected point's minimum and maximum deformation rate was shown previously in Figure 155.

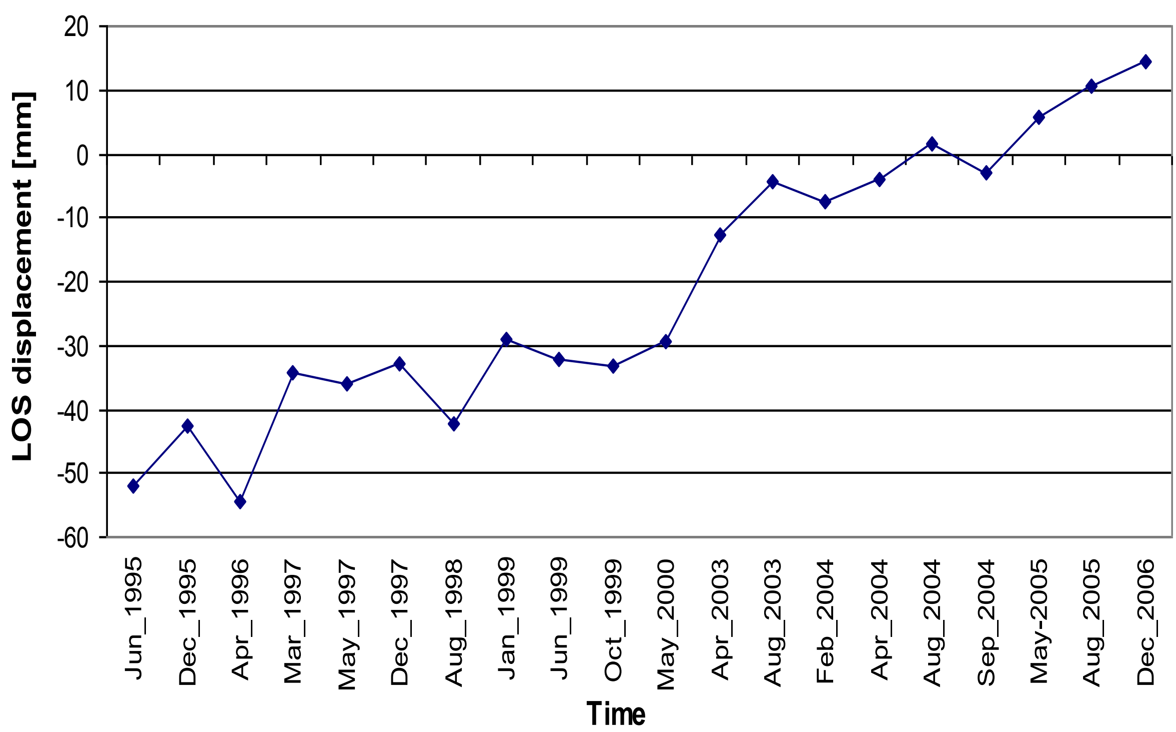

Figure178. LOS displacement time series (1995-2006) of the maximum deformation rate of PSI of Falanna. Point number 80751. Time series are rescaled to the first acquisition (28 June 1995)

4.2.1.3.2.4. Melissochorion

Candidate point number 35184 was selected as representative of the maximum deformation rate. It is located in the middle-west of the settlement, and 2.94 km south of a normal fault trace in the side of the footwall, as well as 3.48 km east of another normal fault trace in the side of the hanging wall. A plot of this point is depicted in Figure 179. The deformation behavior of this candidate point through its time series begins with subsidence then changes to uplift. The minimum subsidence was -3.547 mm (August 2004) while the maximum subsidence was -334.301 mm (June 1995). The minimum and maximum uplift were 24.470 and 84.008 mm in May 2005 and December 2006 respectively. Subsidence and uplift may be attributed to the impact of fault movement, given the candidate points location between the hanging wall and footwall of two normal faults, as mentioned above. The location of the selected point's minimum and maximum deformation rate was shown previously in Figure 157.

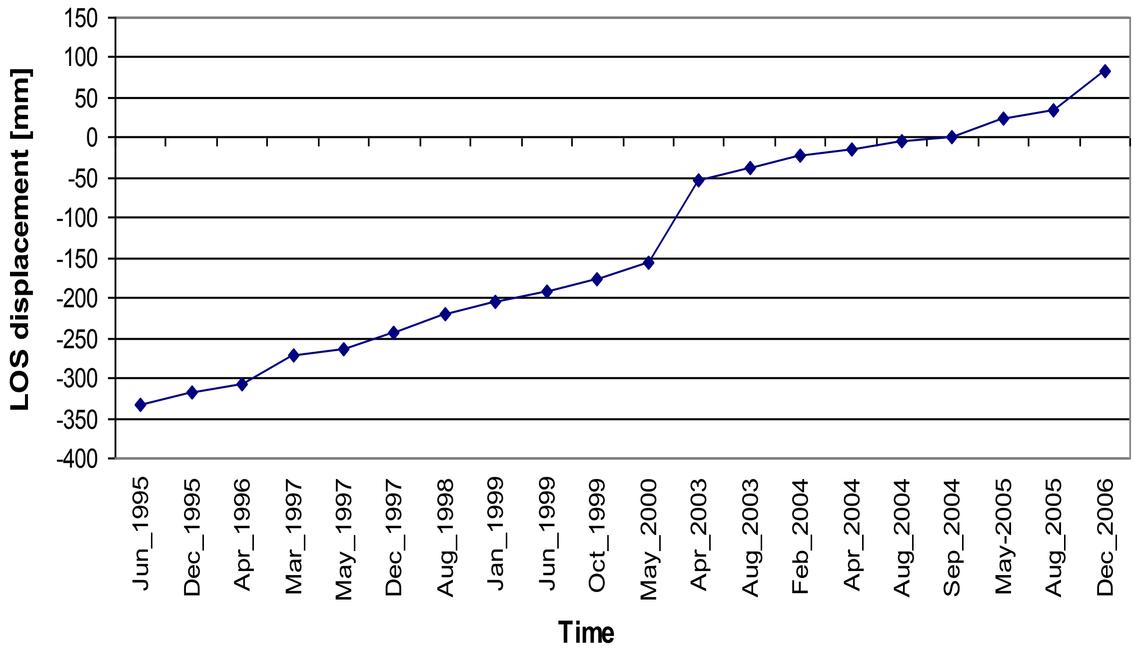

Figure179. LOS displacement time series (1995-2006) of the maximum deformation rate of PSI of Melissochorion. Point number 35184. Time series are rescaled to the first acquisition (28 June 1995)

4.2.1.3.2.5. Galini

Candidate point number 32014 was selected as representative of the maximum deformation rate. It is located southwest of the settlement, and 1.04 km north of a normal fault trace in the side of the hanging wall, as well as 0.137 km south of another normal fault trace in the side of the footwall. A plot of this point is depicted in Figure 180. The deformation behavior of the candidate point through its time series begins with subsidence then changes to uplift. The minimum subsidence was -1.924 mm (September 2004) while the maximum was -192.557 mm (December 1995). The minimum and maximum uplift were 14.064 and 54.073 mm in May 2005 and December 2006 respectively. Subsidence and uplift may be attributed to the impact of fault movement. The noticeable increase of uplift during May 2005 – December 2006 may be attributed to the disparity of fault activities. The location of the selected point's minimum and maximum deformation rate was shown previously in Figure 159.

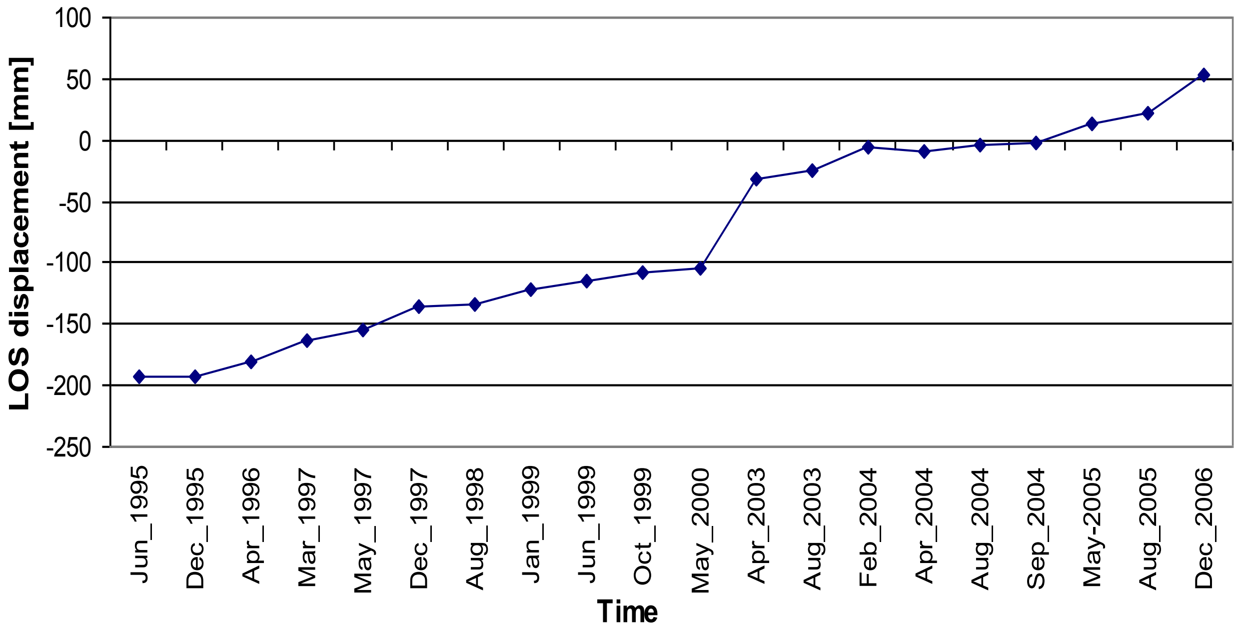

Figure180. LOS displacement time series (1995-2006) of the maximum deformation rate of PSI of Galini. Point number 32014. Time series are rescaled to the first acquisition (28 June 1995)

4.2.1.3.2.6. Platykampos

Candidate point number 29080 was selected as representative of the maximum deformation rate. It is located south of the settlement and 1.0383 km south of a normal fault trace in the side of the footwall as well as 3.236 km northeast of another normal fault trace in the side of the hanging wall. A plot of this point is depicted in Figure 181. The deformation behavior of the candidate point through its time series begins with subsidence then changes to uplift. The minimum subsidence was -0.236 mm (August 2004) while the maximum was -179.972 mm (June 1995). The minimum and maximum uplift were 2.942 and 45.814 mm in September 2004 and December 2006 respectively. Subsidence and uplift may be attributed to the impact of fault movements, given the candidate points location, and evidence of this impact is the increasing uplift during the three years from September 2004 – December 2006. The location of the selected point's minimum and maximum deformation rate was shown earlier in Figure 161.

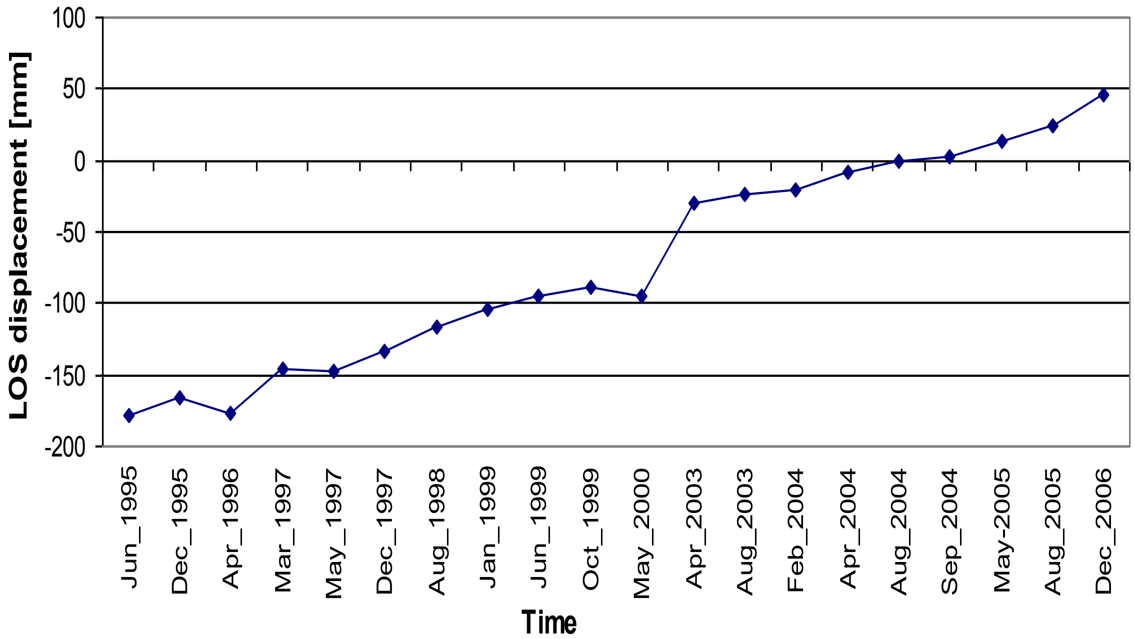

Figure181. LOS displacement time series (1995-2006) of the maximum deformation rate of PSI of Platykampos. Point number 29080. Time series are rescaled to the first acquisition (28 June 1995)

4.2.1.3.2.7. Glafki

Candidate point number 26720 was selected as representative of the maximum deformation rate. It is located southwest of the settlement and 1.505 km south of a normal fault in the side of the footwall. A plot of the point is depicted in Figure 182. The deformation behavior of this candidate point during its time series begins with subsidence then changes to uplift. The minimum subsidence was -2.035 mm (September 2004) while the maximum was -184.707 mm (June 1995). The minimum and maximum uplift were 0.908 and 41.900 mm in August 2004 and December 2006 respectively. Subsidence may be attributed to an impact factor other than fault movement. However, uplift may be attributed to the impact of fault movement. Evidence for this interpretation is the increasing uplift during the two years May 2005 – December 2006. The location of the selected point's minimum and maximum deformation rate was shown earlier in Figure 163.

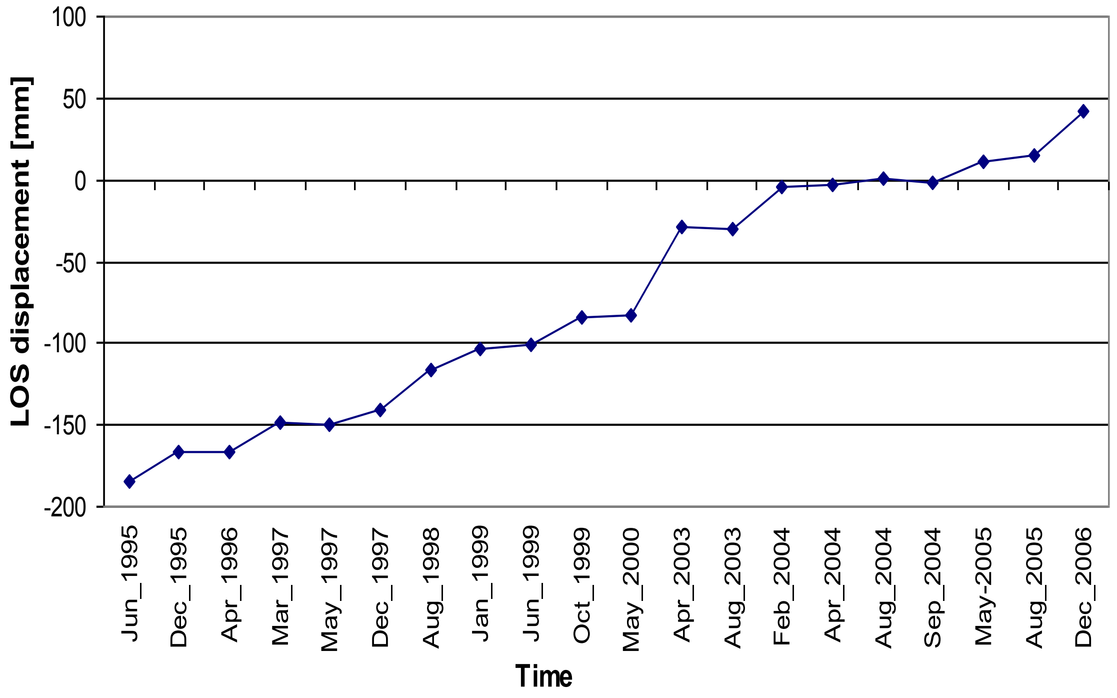

Figure182. LOS displacement time series (1995-2006) of the maximum deformation rate of PSI of Glafki. Point number 26720. Time series are rescaled to the first acquisition (28 June 1995)

4.2.1.3.2.8. Tyrnavos

Candidate point number 106597 was selected as representative of the maximum deformation rate. It is located south of the settlement, and 3.7 km north of a normal fault trace in the side of the hanging wall, as well as 3.94 km southwest of another normal fault trace in the side of the footwall. A plot of this point is depicted in Figure 183. The deformation behavior of this candidate point through its time series begins with uplift then changes to subsidence. The minimum uplift was 4.583 mm (September 2004) while the maximum uplift was 157.538 mm (June 1995). The minimum and maximum subsidence were -0.635 and -33.408 mm in August 2004 and December 2006 respectively. Uplift may be attributed to the impact of fault movement. Furthermore, subsidence at the end of the time series may be attributed as well to the disparity in fault activities, given that this point is located between two faults, as mentioned above. The location of the selected point's minimum and maximum deformation rate was shown earlier in Figure 165.

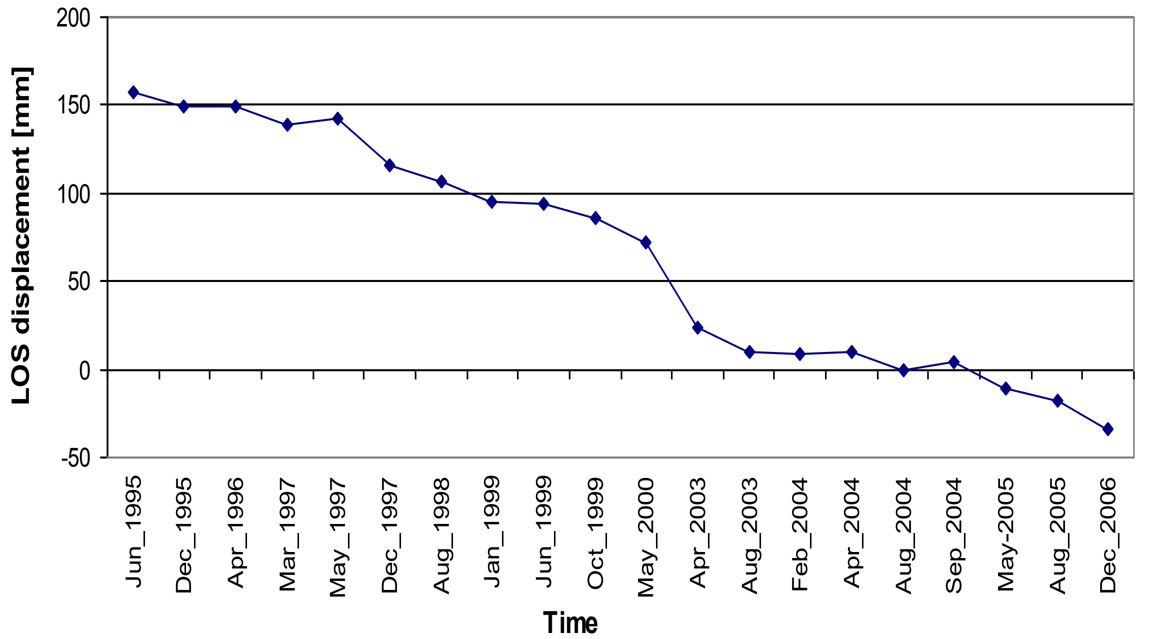

Figure183. LOS displacement time series (1995-2006) of the maximum deformation rate of PSI of Tyrnavos. Point number 106597. Time series are rescaled to the first acquisition (28 June 1995)

4.2.1.3.2.9. <u>Rodia</u>

Candidate point number 144160 was selected as representative of the maximum deformation rate. It is located northwest of the settlement and is located between the hanging walls of two normal fault traces, the first one 1.065 km east of the point, and the second one 0.970 km north of the point. A plot of the point is depicted in Figure 184. The deformation behavior of the candidate point through its time series begins with uplift then changes to subsidence. The minimum uplift was 1.008 mm (September 2004) while the maximum uplift was 94.15 mm (June 1995). The minimum and maximum subsidence were -4.883 and -35.91 mm in August 2005 and December 2006 respectively. Subsidence may be attributed to the impact of fault movement. However, uplift may be attributed to another impact factor, for the reason that the deformation behavior should be subsidence, based on the location of the point between two hanging walls, as mentioned above. The location of the selected point's minimum and maximum deformation rate was shown earlier in Figure 167.

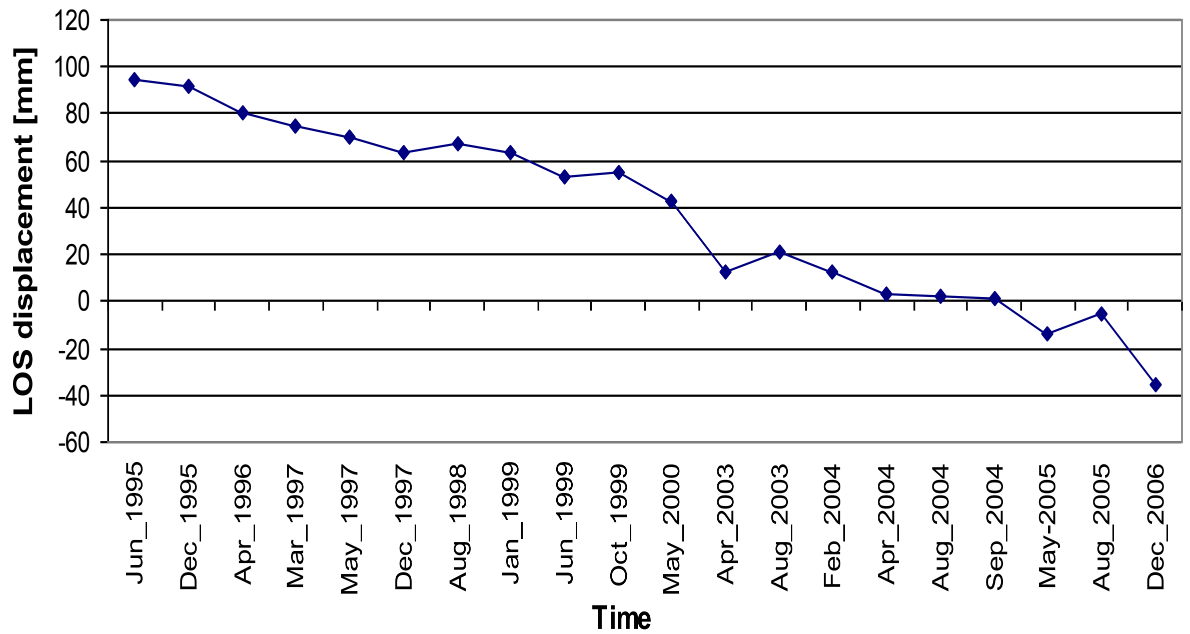

Figure184. LOS displacement time series (1995-2006) of the maximum deformation rate of PSI of Rodia. Point number 144160. Time series are rescaled to the first acquisition (28 June 1995)

4.2.1.3.2.10. Mandra

Candidate point number 41360 was selected as representative of the maximum deformation rate. It is located in the middle of the settlement and 4.431 km south and 5.346 km west of two normal faults in the side of the footwall. A plot of this point is depicted in Figure 185. The deformation behavior of this candidate point through its time series begins with subsidence then changes to uplift. The minimum subsidence was -1.381 mm (August 2004) while the maximum was -151.649 mm (April 1996). The minimum and maximum uplift were 17.349 and 40.023 mm in May 2005 and December 2006 respectively. Subsidence may be attributed to another impact factor, while uplift may be attributed to the impact of fault movement. The location of the selected point's minimum and maximum deformation rate was shown earlier in Figure 169.

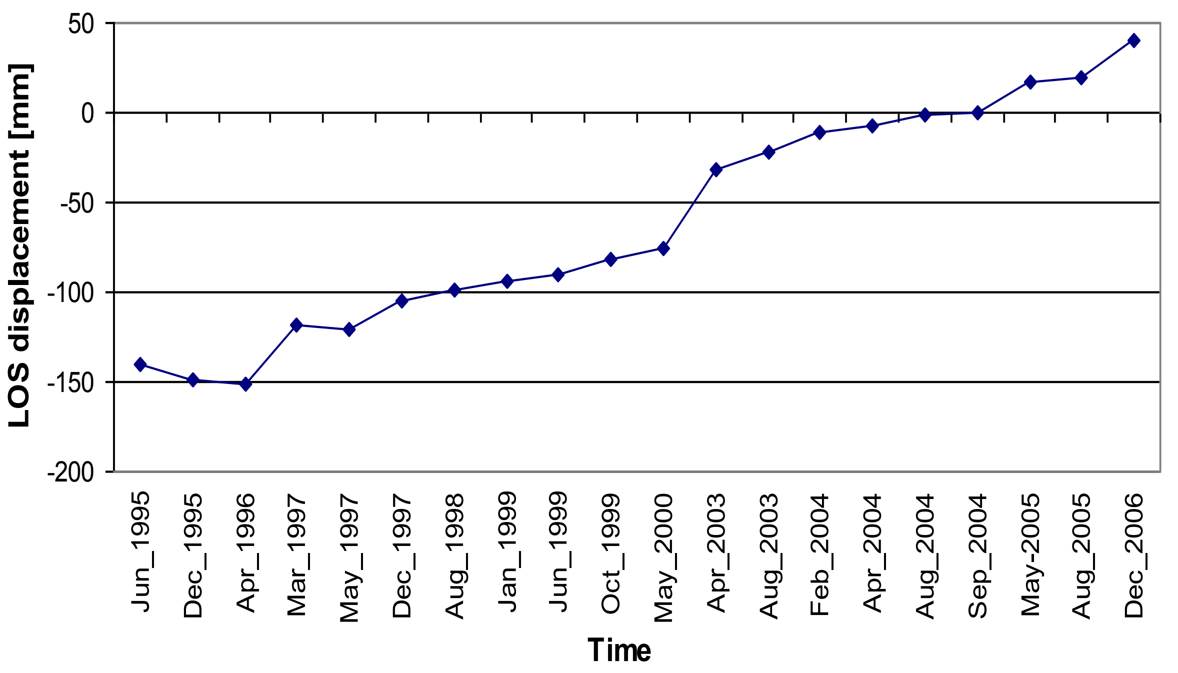

Figure.185 LOS displacement time series (1995-2006) of the maximum deformation rate of PSI of Mandra. Point number 41360. Time series are rescaled to the first acquisition (28 June 1995)

4.2.1.3.2.11. Eleftherai

Candidate point number 27935 was selected as representative of the maximum deformation rate. It is located southwest of the settlement and 3.01 km southwest of a normal fault trace in the side of the footwall. A plot of this point is depicted in Figure 186. The deformation behavior of this candidate point through its time series begins with subsidence then changes to uplift. The minimum subsidence was -0.176 mm (September 2004) while the maximum was -151.518 mm (June 1995). The minimum and maximum uplift were 8.409 and 37.188 mm in May 2005 and December 2006 respectively. Subsidence may be attributed to another impact factor. However, uplift may be attributed to the impact of fault movements since it began through the decrease in the impact of some other factor. The location of the selected point's minimum and maximum deformation rate was shown earlier in Figure 171.

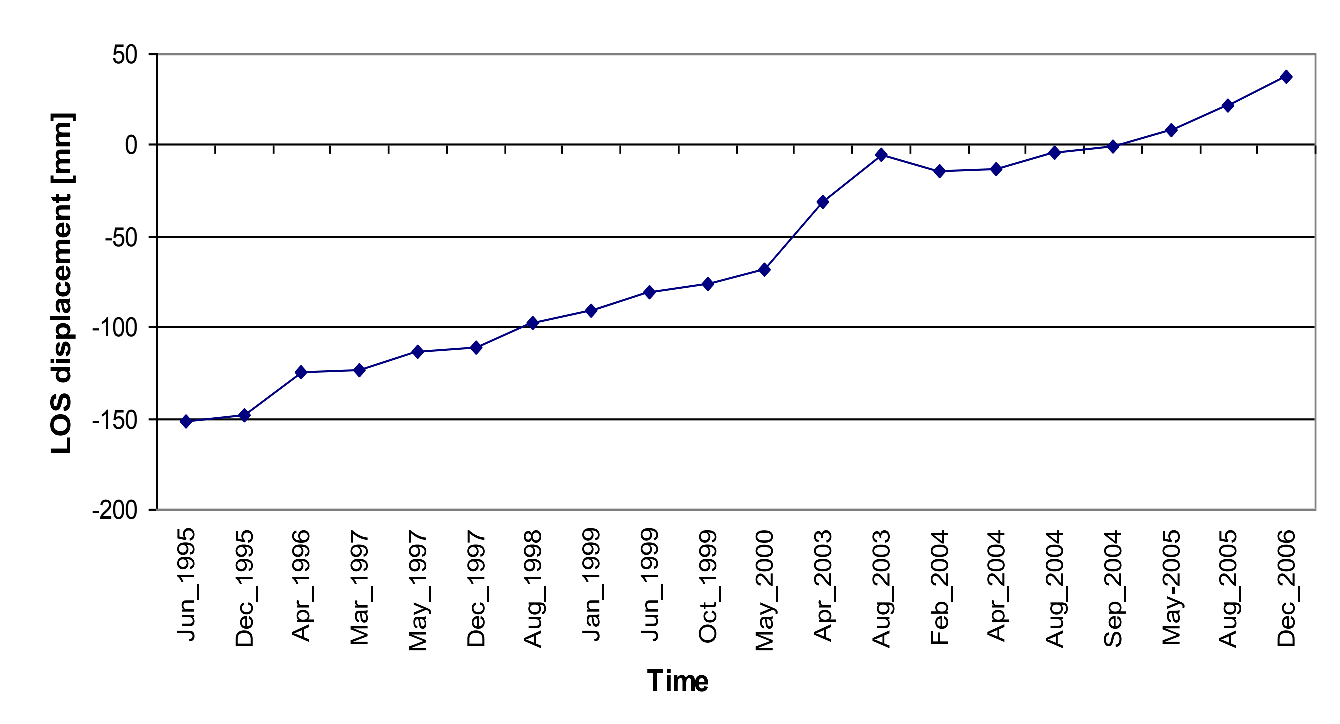

Figure186. LOS displacement time series (1995-2006) of the maximum deformation rate of PSI of Eleftherai. Point number 27935. Time series are rescaled to the first acquisition (28 June 1995)

4.2.1.3.2.12. Terpsithea

Candidate point number 38866 was selected as representative of the maximum deformation rate. It is located north of the settlement and 0.625 km south of a normal fault trace in the side of the footwall, as well as 2.5 km east of another normal fault trace in the side of the hanging wall. A plot of this point is depicted in Figure 187. The deformation behavior of the candidate point through its time series begins with subsidence then changes to uplift. The minimum subsidence was -1.058 mm (September 2004) while the maximum was -271.024 mm (June 1995). The minimum and maximum uplift were 1.784 and 62.075 mm in August 2004 and December 2006 respectively. Subsidence may be attributed to the impact of fault movement. Furthermore, uplift may be attributed to the disparity of fault activities, given the location of the point between the sides of a footwall and hanging wall, as mentioned above. Consequently, after the decrease in hanging wall activity, activity of the footwall of the other normal fault trace began, which may be the reason that the time series begins with subsidence then moves to uplift. The location of the selected point’s minimum and maximum deformation rate was shown earlier in Figure 173.

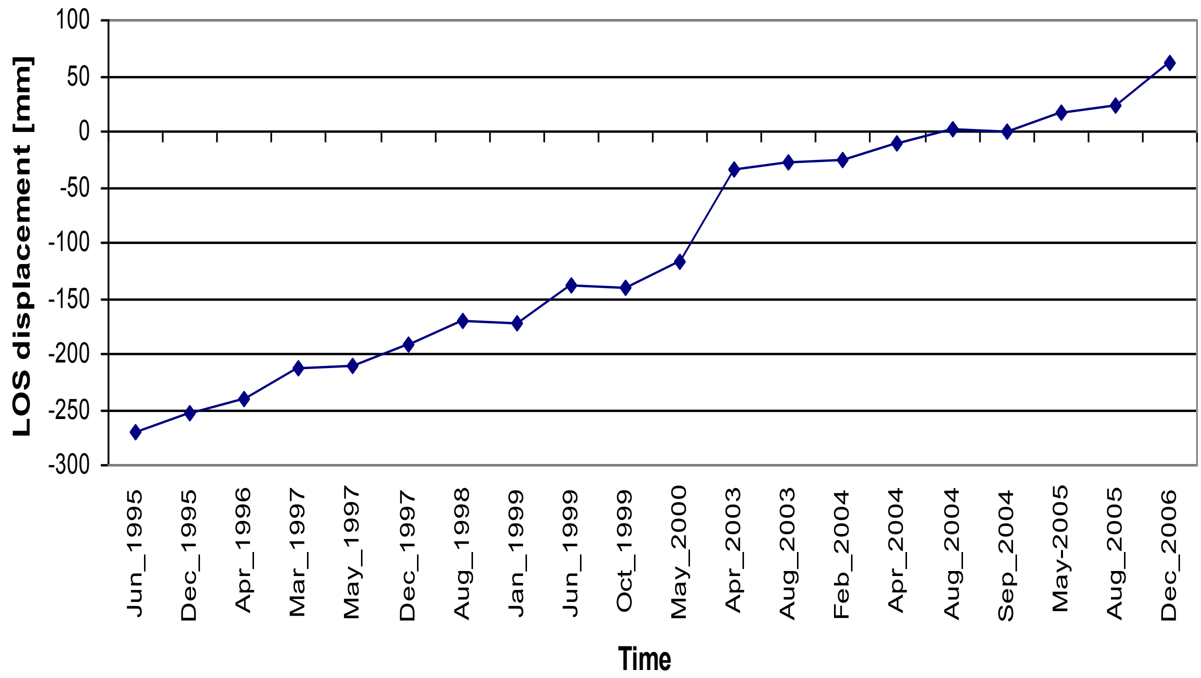

Figure187. LOS displacement time series (1995-2006) of the maximum deformation rate of PSI of Terpsithea. Point number 38866. Time series are rescaled to the first acquisition (28 June 1995)

4.2.1.3.2.13. Nikaia

Candidate point number 20809 was selected as representative of the maximum deformation rate. It is located northwest of the settlement and 3.79 km south of a normal fault trace in the side of the footwall, as well as 4.44 km northeast of another normal fault trace in the side of the hanging wall. A plot of the point is depicted in Figure 188. The deformation behavior of this candidate point through its time series begins with subsidence then changes to uplift. The minimum subsidence was -4.755 mm (September 2004) while the maximum was -301.321 mm (June 1995). The minimum and maximum uplift were 21.717 and 75.157 mm in May 2005 and December 2006 respectively. Subsidence and uplift may be attributed to the impact of fault movement. After a decrease in the hanging wall activity, activity of the footwall of the other normal fault trace began, which may be the reason that the time series begins with subsidence then changes to uplift. The location of the selected point's minimum and maximum deformation rate was shown earlier in Figure 175.

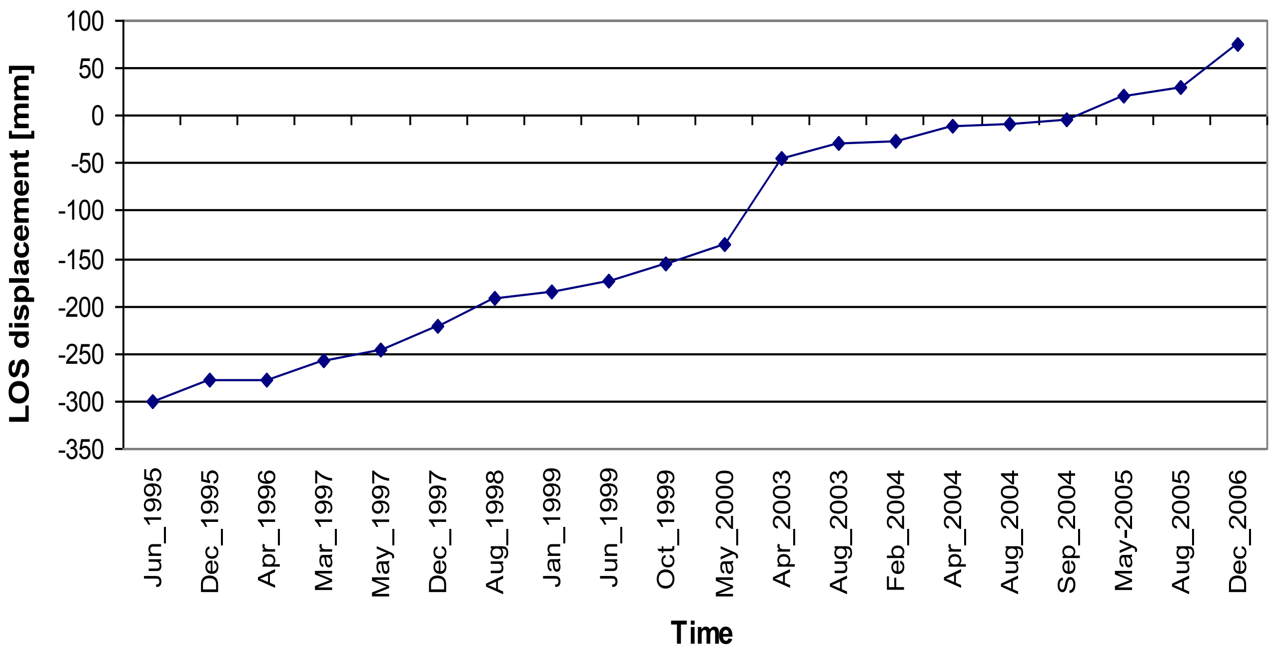

Figure.188 LOS displacement time series (1995-2006) of the maximum deformation rate of PSI of Nikaia. Point number 20809. Time series are rescaled to the first acquisition (28 June 1995)

4.2.2. Descending track 279

4.2.2.1. Interferometric stacking

The result of the interferometric stacking technique of the descending track was depicted previously in Figure 22 in the chapter on processing. The interferometric pattern results are confined to within settlements, and do not cover agricultural lands. The patterns within each settlement have been isolated and superimposed within the ArcGIS environment to extract the statistics on ground deformation. Thirty settlements were identified by implementing the interferometric stacking technique. However, just 19 settlements were selected to examine the influence of fault movements on ground deformation. The reason for choosing these settlements is that each of them overlies just one type of lithology. The other settlements each overlie more than one type of lithology. The minimum and maximum rate of ground deformation of each settlement is depicted in Table 44.

Table 44. Minimum and maximum deformation rates in LOS of interferometric stacking, 1992- 2010

I.d	Settlements	Minimum subsidence (mm)	Maximum subsidence (mm)	Mean	Minimum uplift (mm)	Maximum uplift (mm)	Mean
1	Larissa	-0.385	-3.048	-1.716	0.276	3.442	1.859
2	Giannouli	-0.432	–4.580	-5.012	0.06	0.612	0.336
3	Chalki	-0.518	-1.342	-0.927	0.50	0.524	0.512
4	Eleftheron	-0.086	-0.862	-0.474	0.044	0.365	0.204
5	Falanna	-0.09	-2.524	-1.307	0.191	0.957	0.574
6	Melissochorion	-0.02	-1.286	-0.653	0.065	0.86	0.462
7	Galini	-0.321	-0.969	-0.645	0.087	0.319	0.203
8	Platykampos	0	-1.859	-0.929	0.52	0.53	0.525
9	Glafki	-0.23	-1.336	-0.391	Null	Null	Null
10	Itea	-0.7	-3.744	-2.222	0.671	1.338	1.00
11	Fyllon	-0.219	-1.009	-1.228	Null	Null	Null
12	Palamas	-0..,11	-2.205	-1.157	0.58	0.6	0.59
13	Marathea	-0.058	-1.054	-0.556	Null	Null	Null
14	Nikaia	-0.018	-2.142	-1.08	0.445	0.784	0.614
15	Terpsithea	-0.088	-0.849	-0.468	0.046	0.358	0.202
16	Tyrnavos	-0.195	-2.157	-1.167	0.36	0.37	0.365
17	Rodia	-0.003	-1.425	-0.714	0.348	1.28	0.814
18	Mandra	-0.58	-1.731	-1.155	Null	Null	Null
19	Eleftherai	-0.273	-1.207	-0.74	0.028	0.303	0.165

In the following section the deformation of each settlement will be discussed separately.

4.2.2.1.1. Larissa

Results of interferometric stacking patterns and total deformation rate estimation during the period November 1992 – October 2010 for Larissa are shown in Figure 189. Two phase patterns of both subsidence and uplift are observed distributed through the settlement. Subsidence varies in the range - 0.385 – -3.048 mm/year. Uplift varies in the range 0.276 – 3.442 mm/year.

Three normal fault traces pass through the settlement, as mentioned before, with the ascending track. Interferometric patterns of subsidence can be observed in the middle, middle-east, northwest and southwest parts of the settlement, and are less clearly observed in the northern part of the settlement. Uplift patterns can be observed also in the northwestern border, east, and southwestern parts of the settlement; in addition less clear patterns are observed in the northern part of the settlement. Subsidence patterns within Larissa may be attributed to their location in the side of the hanging walls of normal fault traces in the northern, middle and southeastern parts of the settlement. Uplift patterns in the northwestern borders and eastern and southwestern parts of the settlement may be attributed also to their location in the side of footwalls of the normal fault traces. However, faint uplift patterns which are observed in the northern part of the settlement in the side of hanging wall of a normal fault trace may be attributed to another impact factor.

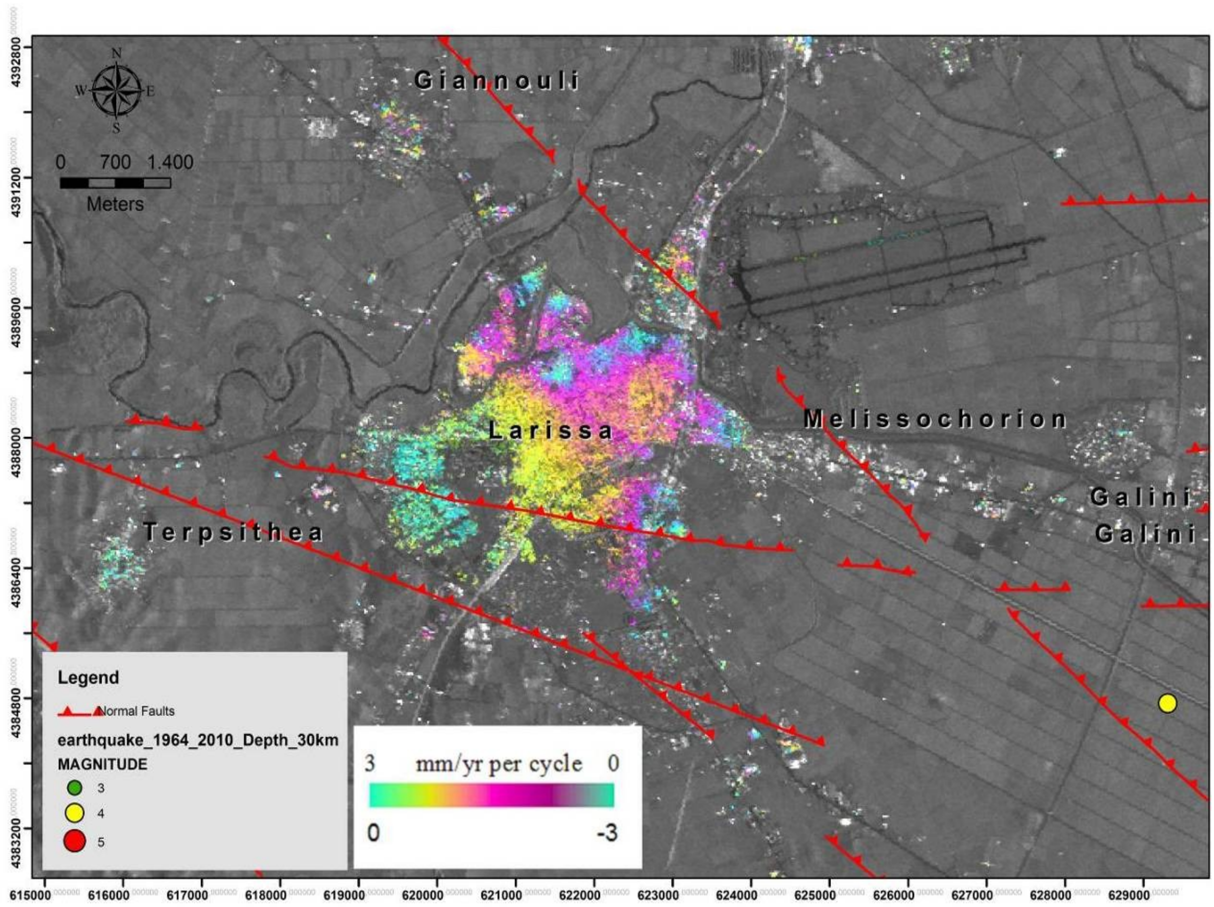

Figure.189 Total deformation at Larissa estimated with interferometric stacking technique, November 1992 – October 2010

4.2.2.1.2. Giannouli

Results of interferometric stacking patterns and total deformation rate estimation during the period November 1992 – October 2010 for Giannouli are shown in Figure 190. Two phase patterns of both subsidence and uplift are observed distributed through the whole settlement. Subsidence varies in the range -0,432 – -4,580 mm/year, while uplift varies in the range 0.06 – 0.612 mm/year. Interferometric patterns of subsidence can be slightly observed in the northwestern, northeastern parts of the settlement. However, uplift patterns are distributed in the northwestern, northeastern and eastern parts of the settlement, in addition to which a very few patterns are distributed in the western and southern parts of the settlement.

Subsidence may be attributed to another impact factor. Uplift may be attributed to the location of the settlement southeast of the footwall of a normal fault trace. Note that the density of the patterns distribution for both subsidence and uplift is less than the density of the patterns distribution of the two phases which are observed within the ascending track within the same settlement.

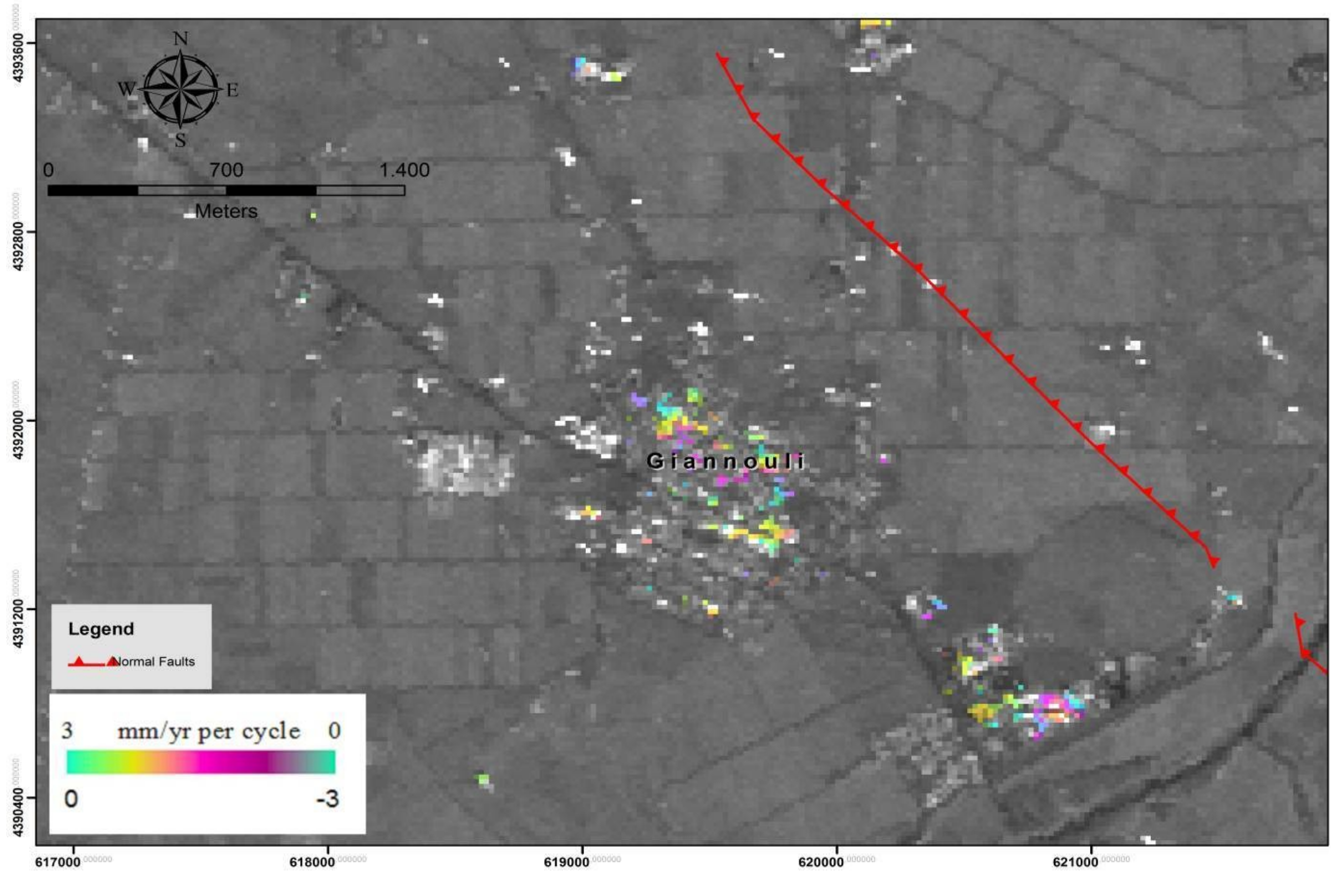

Figure.190 Total deformation at Giannouli estimated with interferometric stacking technique, November 1992 – October 2010

4.2.2.1.3. Chalki

Results of interferometric stacking patterns and total deformation rate estimation during the period November 1992 – October 2010 for Chalki are shown in Figure 191. Two phase patterns of subsidence and uplift are observed; however, the density of the subsidence patterns is very slightly observed in the southern part of the settlement. Additionally, uplift patterns can be slightly observed also in the southern and northeastern parts of the settlement.

On the whole the density of patterns distribution of both subsidence and uplift is less than the density of patterns distribution of the two phases which are observed within the ascending track within the same settlement. This may be because the number of interferograms with the descending track is more than the number of interferograms with the ascending track (70 and 29 items respectively), which affects the wrapped phase of interferometric stacking.

The deformation results within Chalki indicate that the subsidence varies in the range -0.518 – -1.342 mm/year, while uplift varies in the range 0.50 – 0.524 mm/year. Subsidence may be attributed to another impact factor, given that it is located in the side of the footwall of a normal fault trace, whereas uplift may be attributed to the location of this part in the side of the footwall of a normal fault trace.

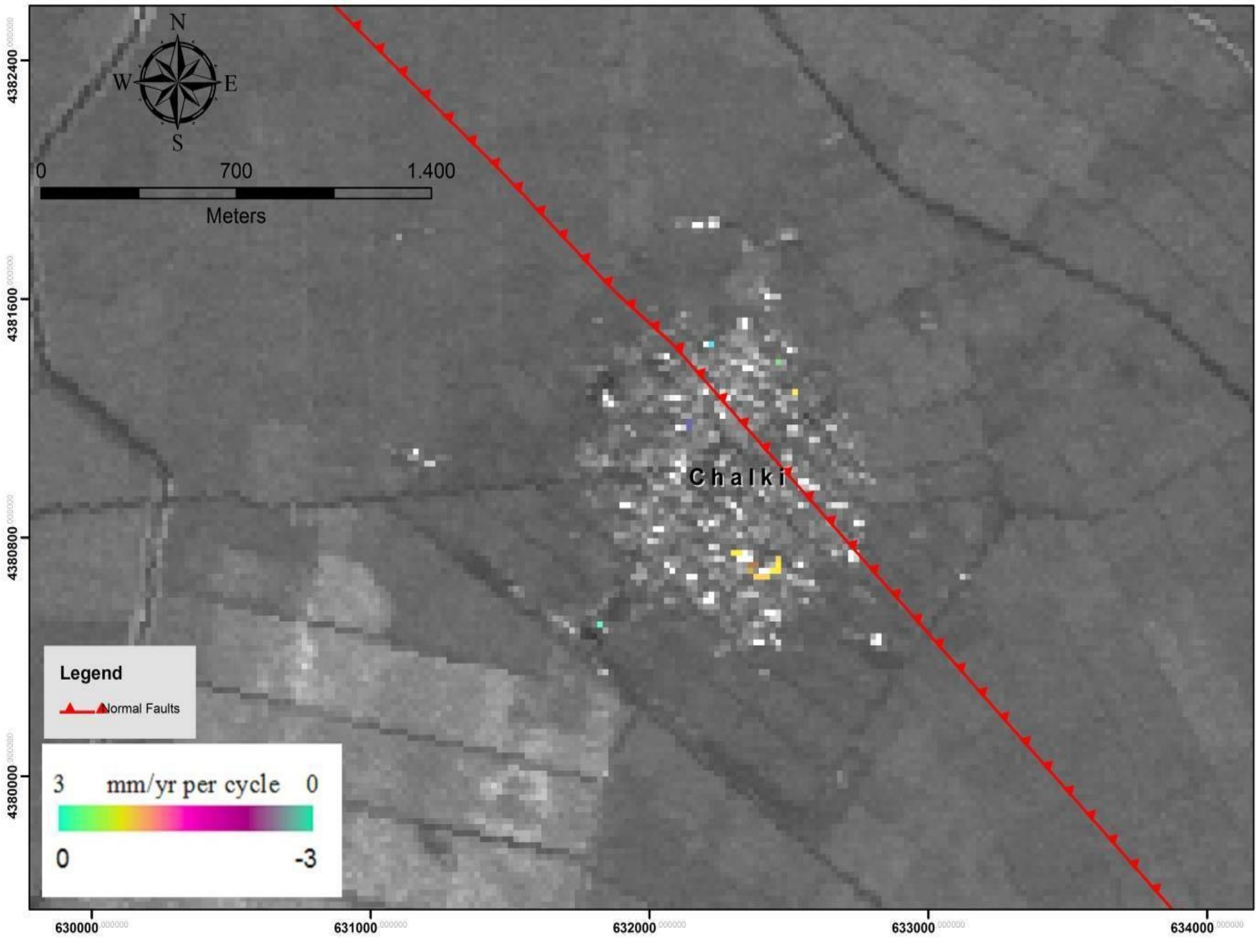

Figure191. Total deformation at Chalki estimated with interferometric stacking technique, November 1992 – October 2010

4.2.2.1.4. Eleftheron

Results of interferometric stacking patterns and total deformation rate estimation during the period November 1992 – October 2010 for Eleftheron are shown in Figure 192. Slight patterns of subsidence are observed distributed in the south of the settlement, whereas uplift patterns are observed in the northern, eastern and western parts of the settlement. Note that the density of patterns distribution of both subsidence and uplift is less than the density of patterns distribution of the two phases which are observed within the ascending track within the same settlement.

Subsidence varies in the range -0.086 – -0.862 mm/year, while uplift varies in the range 0.044 – 0.365 mm/year. Subsidence may be attributed to the location of the settlement north of the hanging wall of a normal fault trace. Furthermore, uplift may be attributed to the location of the settlement south and east of the footwalls of two normal fault traces.

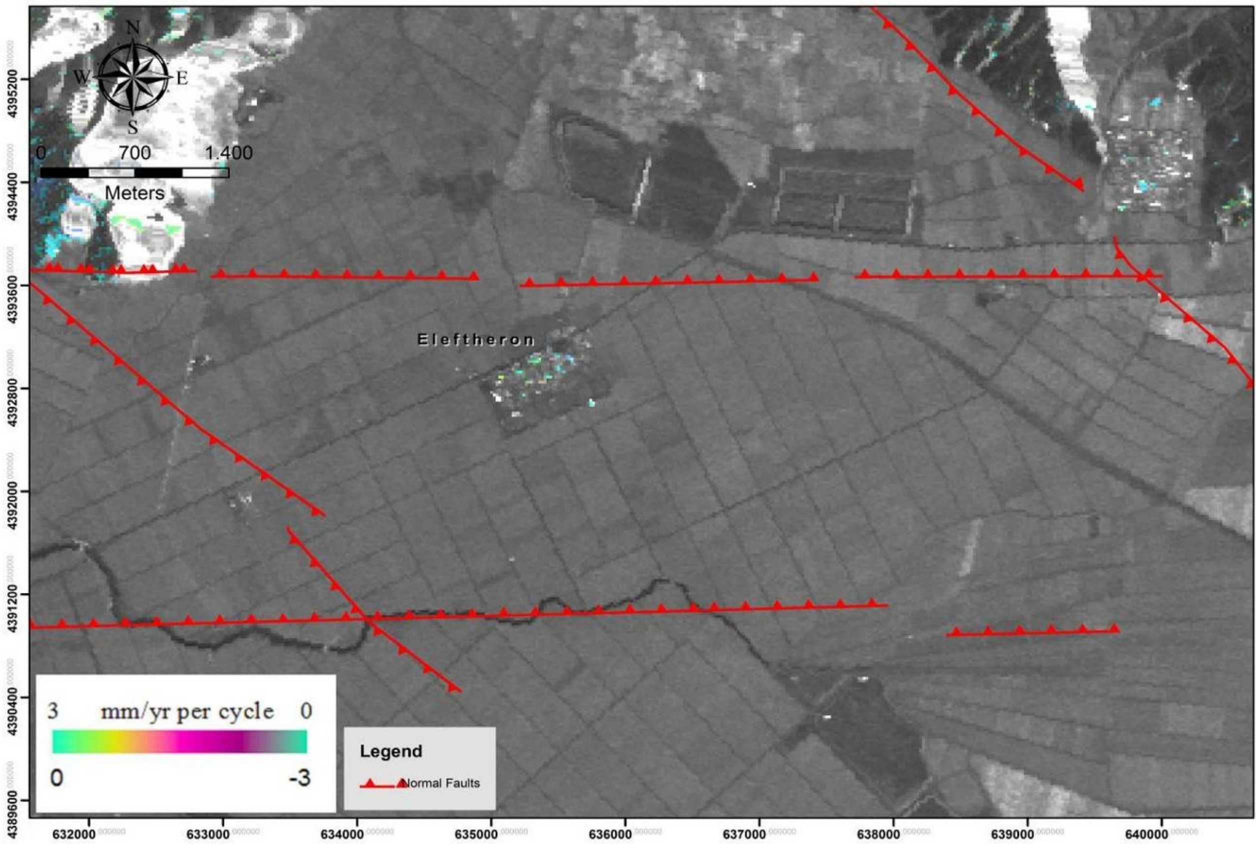

Figure.192 Total deformation at Eleftheron estimated with interferometric stacking technique, November 1992 – October 2010

4.2.2.1.5. Falanna

Results of interferometric stacking patterns and total deformation rate estimation during the period November 1992 – October 2010 for Falanna are shown in Figure 193. Ground deformation results within Falanna settlement indicate that the subsidence varies in the range -0.09 – -2.524 mm/year, while uplift varies in the range 0.191 – 0.957 mm/year.

Subsidence patterns are concentrated in the northern part. However, slight subsidence patterns can be observed in the northern, southeastern and western parts of the settlement. Uplift patterns are distributed over almost all parts of the settlement. Subsidence may be attributed to the location of the settlement in the eastern part of the hanging wall of a normal fault trace, while uplift may be attributed to some other impact factor.

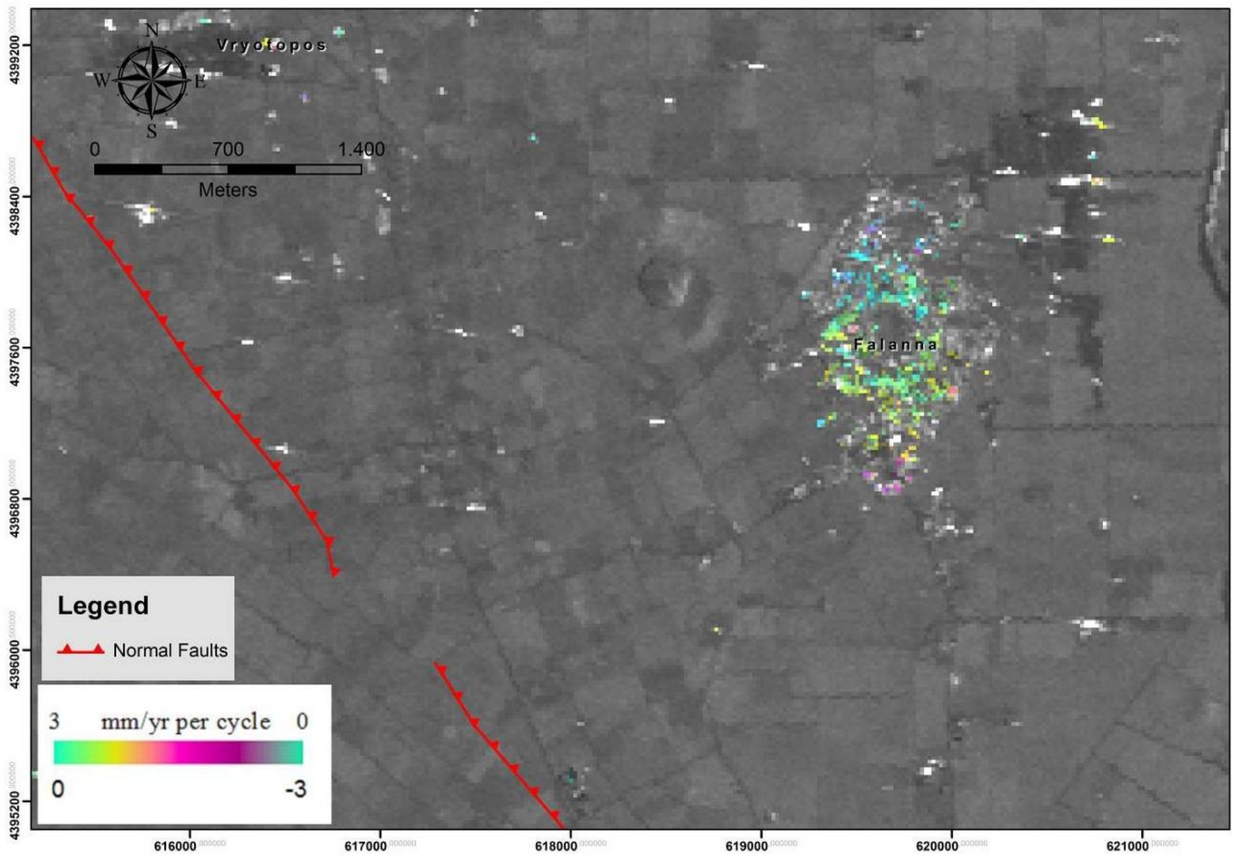

Figure.193 Total deformation at Falanna estimated with interferometric stacking technique, November 1992 – October 2010

4.2.2.1.6. <u>Melissochorion</u>

Results of interferometric stacking patterns and total deformation rate estimation during the period November 1992 – October 2010 for Melissochorion are shown in Figure 194. Ground deformation results within the settlement indicate that the subsidence varies in the range -0.02 – -1.286 mm/year, while uplift varies in the range

0.065 – 0.86 mm/year. A very low density of patterns distribution of both subsidence and uplift is observed within this settlement compared with the density of patterns distribution within the same settlement in the ascending track. Subsidence patterns are slightly observed in the southwestern part of the settlement, whereas uplift is observed in the northeastern part of the settlement. Subsidence may be attributed to the location of the settlement east of the hanging wall of a normal fault trace. Uplift may be attributed to the location of the settlement in the southern part of the footwall of a normal fault trace.

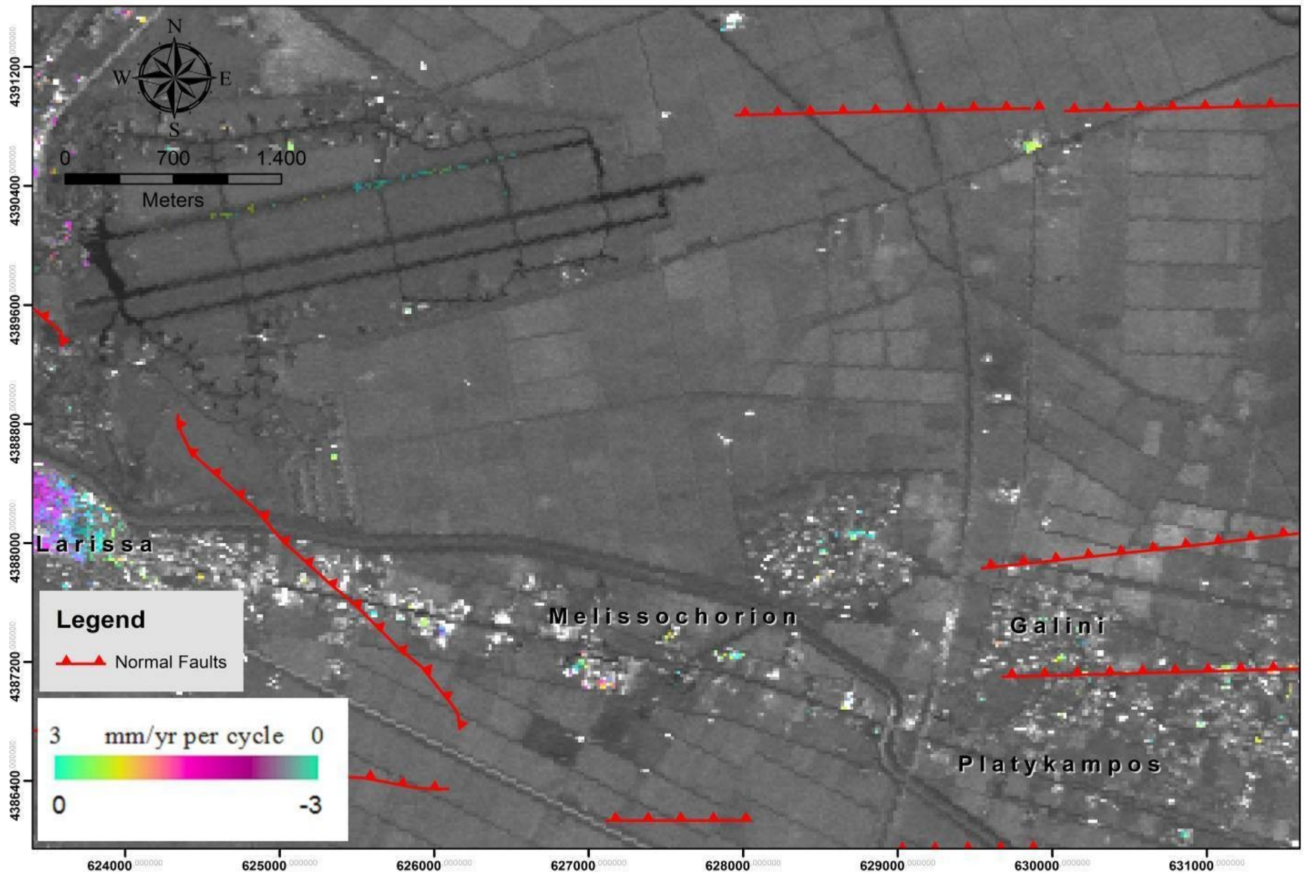

Figure.194 Total deformation at Melissochorion estimated with interferometric stacking technique, November 1992 – October 2010

4.2.2.1.7. Galini

Results of interferometric stacking patterns and total deformation rate estimation during the period November 1992 – October 2010 for Galini are shown in Figure 195. Ground deformation results for the settlement indicate that the subsidence varies in the range -0.321 – -0.969 mm/year, while uplift varies in the range 0.087 – 0.319 mm/year. A very low density of patterns distribution of both subsidence and uplift can be observed within this settlement compared with the density of patterns distribution at the same settlement with the ascending track. Slight subsidence patterns are observed in the southwestern part of the settlement, while uplift patterns are observed in the north, northeastern and southeastern parts of the settlement. Subsidence may be attributed to the location of the area in the side of the hanging wall of a normal fault trace, whereas uplift may be attributed to the location of the area in the footwalls of two normal faults, one located in the northern and the other in the southern part of the settlement.

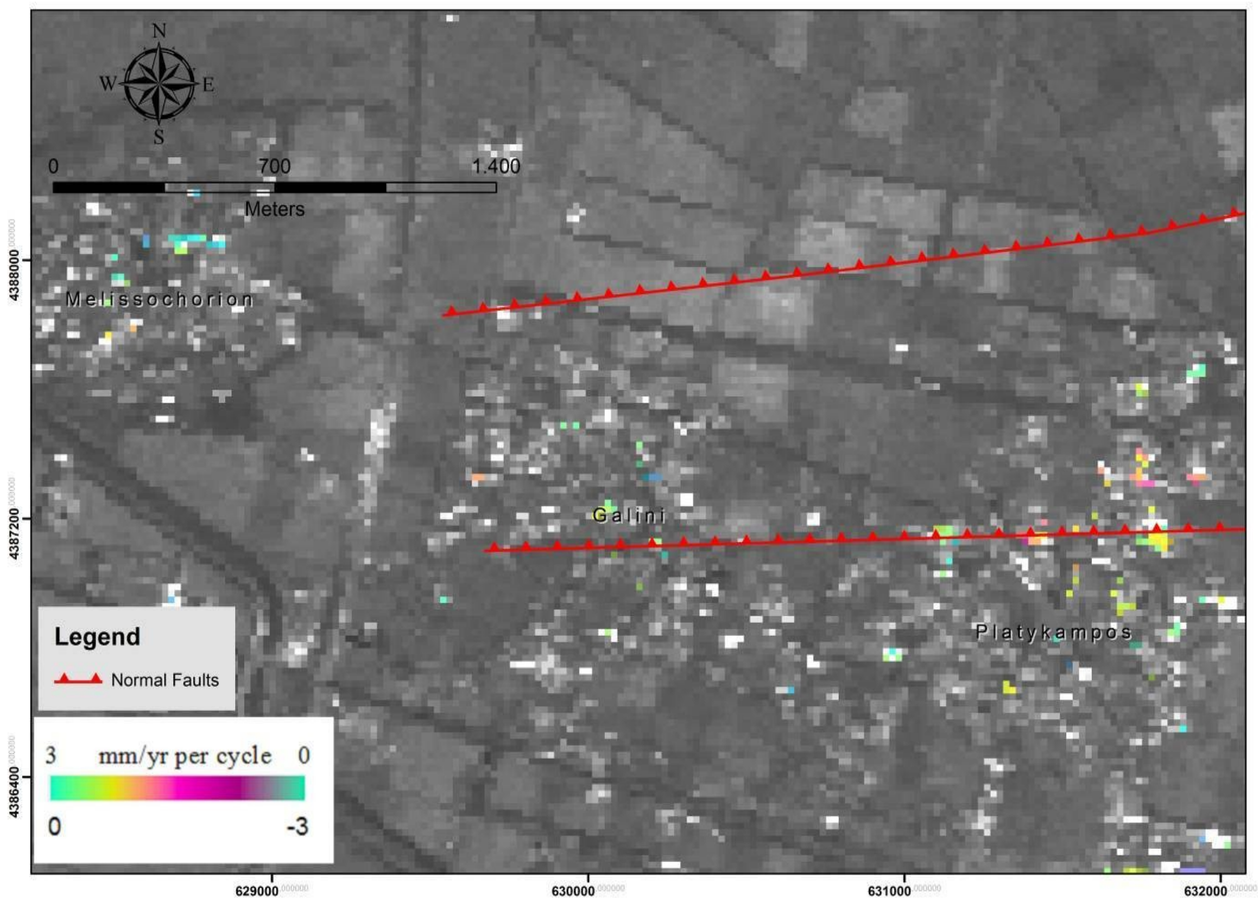

Figure195. Total deformation at Galini estimated with interferometric stacking technique, November 1992 – October 2010

4.2.2.1.8. Platykampos

Results of interferometric stacking patterns and total deformation rate estimation during the period November 1992 – October 2010 for Platykampos are shown in Figure 196. Ground deformation results within the settlement indicate that the subsidence varies in the range 0 – -1.859 mm/year, while uplift varies in the range

0.52 – 0.53 mm/year. A very low density of patterns distribution of both subsidence and uplift can be observed within this settlement compared with the patterns density of the same settlement with the ascending track. Subsidence patterns are observed in the northern middle, southwestern and western parts of the settlement. Uplift patterns are slightly distributed in the northern and southern parts of the settlement. Subsidence may be attributed to the location of the area in the side of the hanging wall of a normal fault trace. However, slight subsidence can be observed in the southwestern part of the settlement in the side of the footwall of a normal fault trace, which may be attributed to another impact factor, given that on this side of the fault there should be an uplift phase. Uplift may be attributed to the location of this area in the side of the footwall of a normal fault trace.

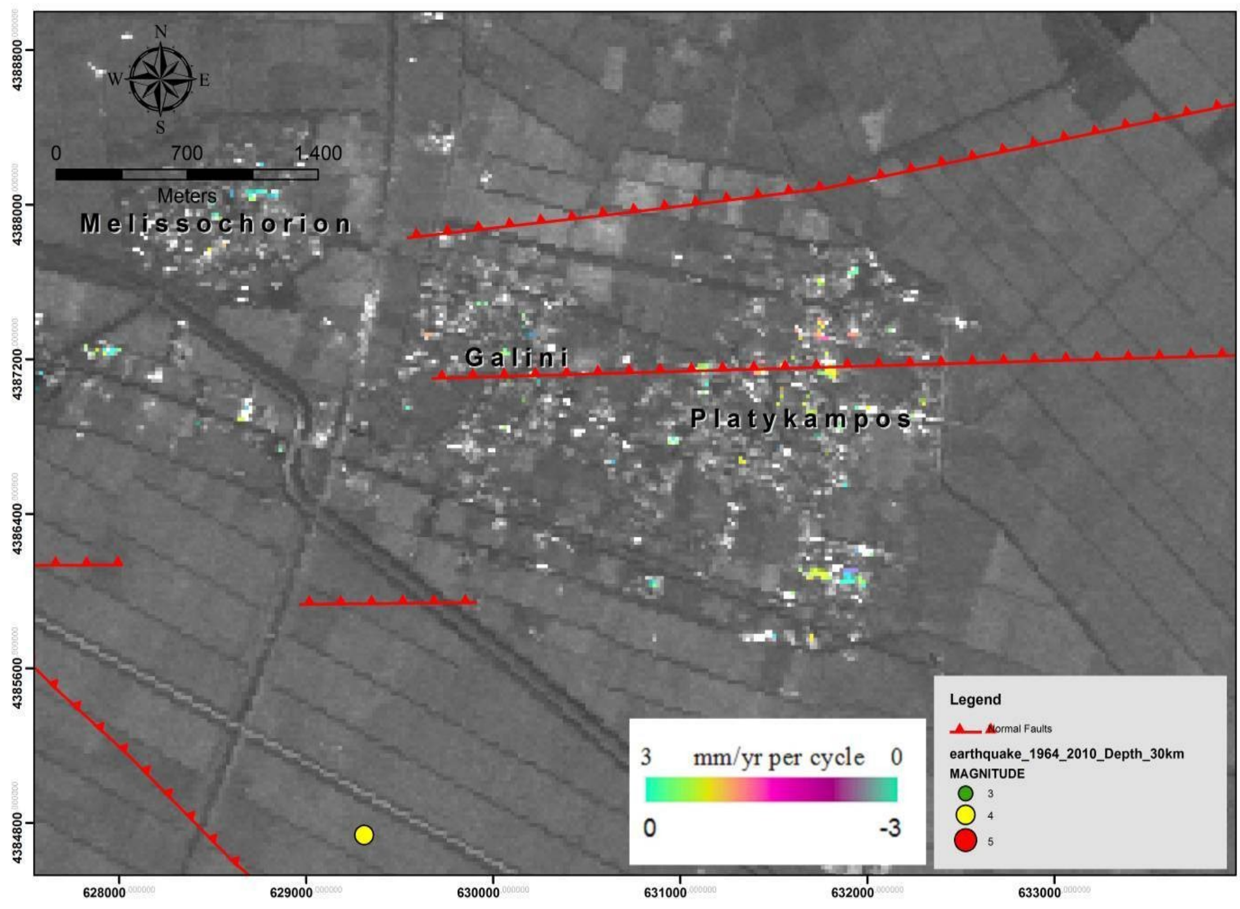

Figure.196 Total deformation at Platykampos estimated with interferometric stacking technique, November 1992 – October 2010

4.2.2.1.9. Glafki

Results of interferometric stacking patterns and total deformation rate estimation during the period November 1992 – October 2010 for Glafki are shown in Figure 197. Ground deformation results within the settlement indicate that the subsidence varies in the range -0.23 – -1.336 mm/year, while uplift was null, although it is observed as pattern phenomena. A very low density of patterns distribution of both subsidence and uplift can be observed within this settlement compared with the patterns density of the same settlement with the ascending track. Slight subsidence patterns are observed in the middle part of the settlement, whereas uplift patterns are observed southwest of the settlement. Subsidence may be attributed to another impact factor. The absence of uplift may be attributed to the footwall of the normal fault trace which is located north of the settlement.

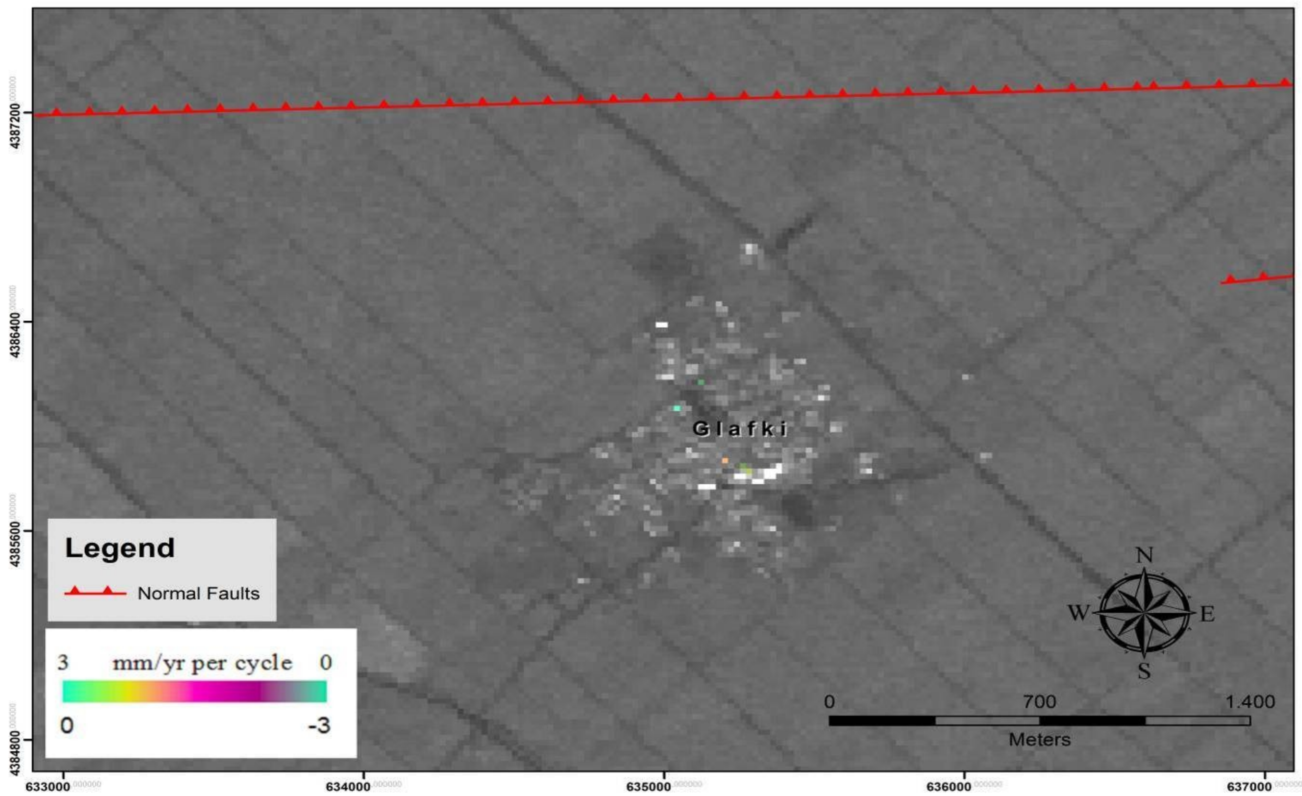

Figure197. Total deformation at Glafki estimated with interferometric stacking technique, November 1992 – October 2010

4.2.2.1.10. Itea

Results of interferometric stacking patterns and total deformation rate estimation during the period November 1992 – October 2010 for Itea are shown in Figure 198.

Ground deformation results within Itea settlement indicate that the subsidence varies in the range -0.7 – -3.744 mm/year, while uplift varies in the range 0.671 – 1.338 mm/year. A low density of patterns distribution of both subsidence and uplift has been observed within this settlement. Subsidence and uplift patterns are distributed through many parts of the settlement.

Subsidence may be attributed to the location of the settlement southwest of the hanging wall of a normal fault trace, while uplift may be attributed to another impact factor.

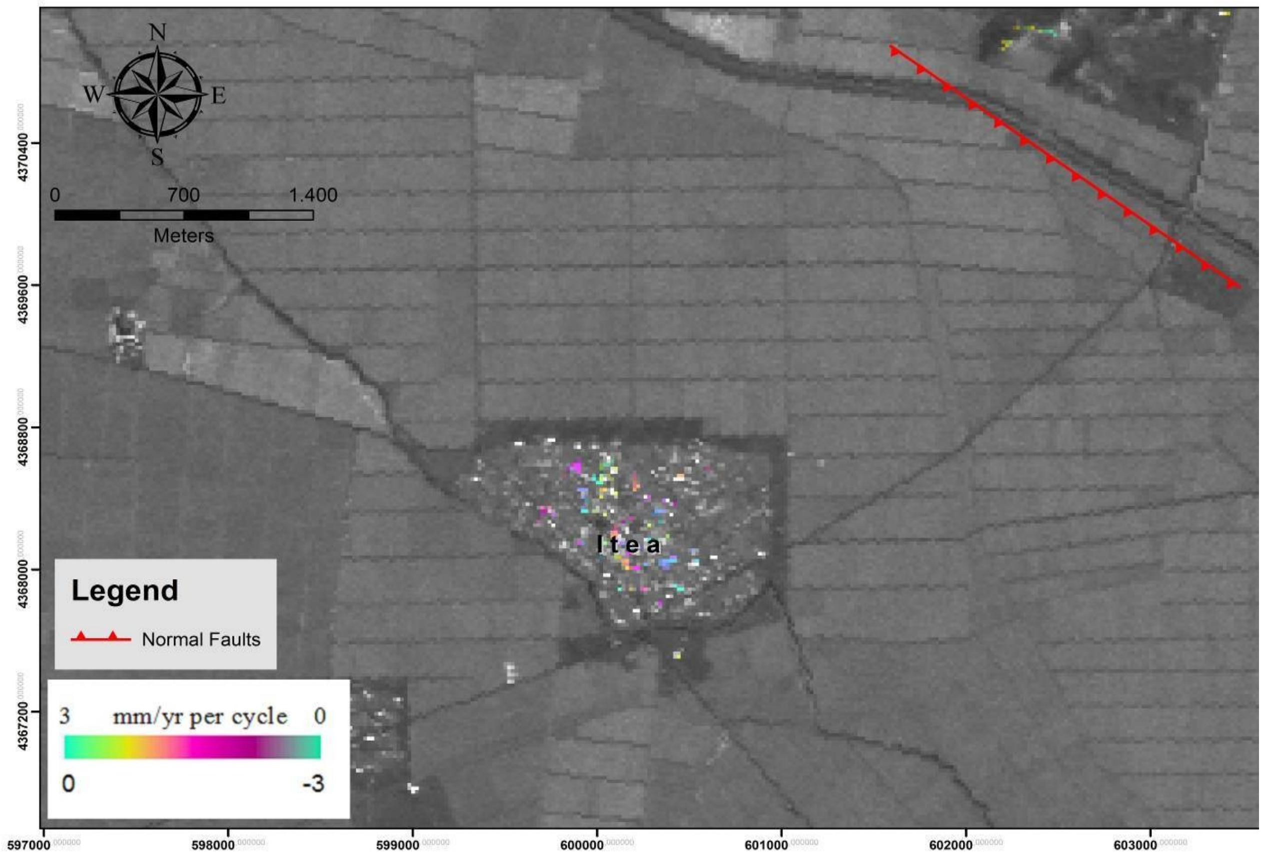

Figure198. Total deformation at Itea estimated with interferometric stacking technique, November 1992 – October 2010

4.2.2.1.11. <u>Fyllon</u>

Results of interferometric stacking patterns and total deformation rate estimation during the period November 1992 – October 2010 for Fyllon are shown in Figure 199. Ground deformation results within the settlement indicate that the subsidence varies in the range -0.219 – -1.009 mm/year, while uplift was null. However, it is observed as pattern phenomena. A very low density of patterns distribution of both subsidence and uplift can be observed within this settlement compared with the patterns density at the same settlement with the ascending track. Subsidence patterns can be observed in the middle and southern parts of the settlement, whereas uplift patterns can be observed in the northern part of the settlement. This settlement has not been affected by fault movements, so subsidence and uplift may be attributed to other impact factors.

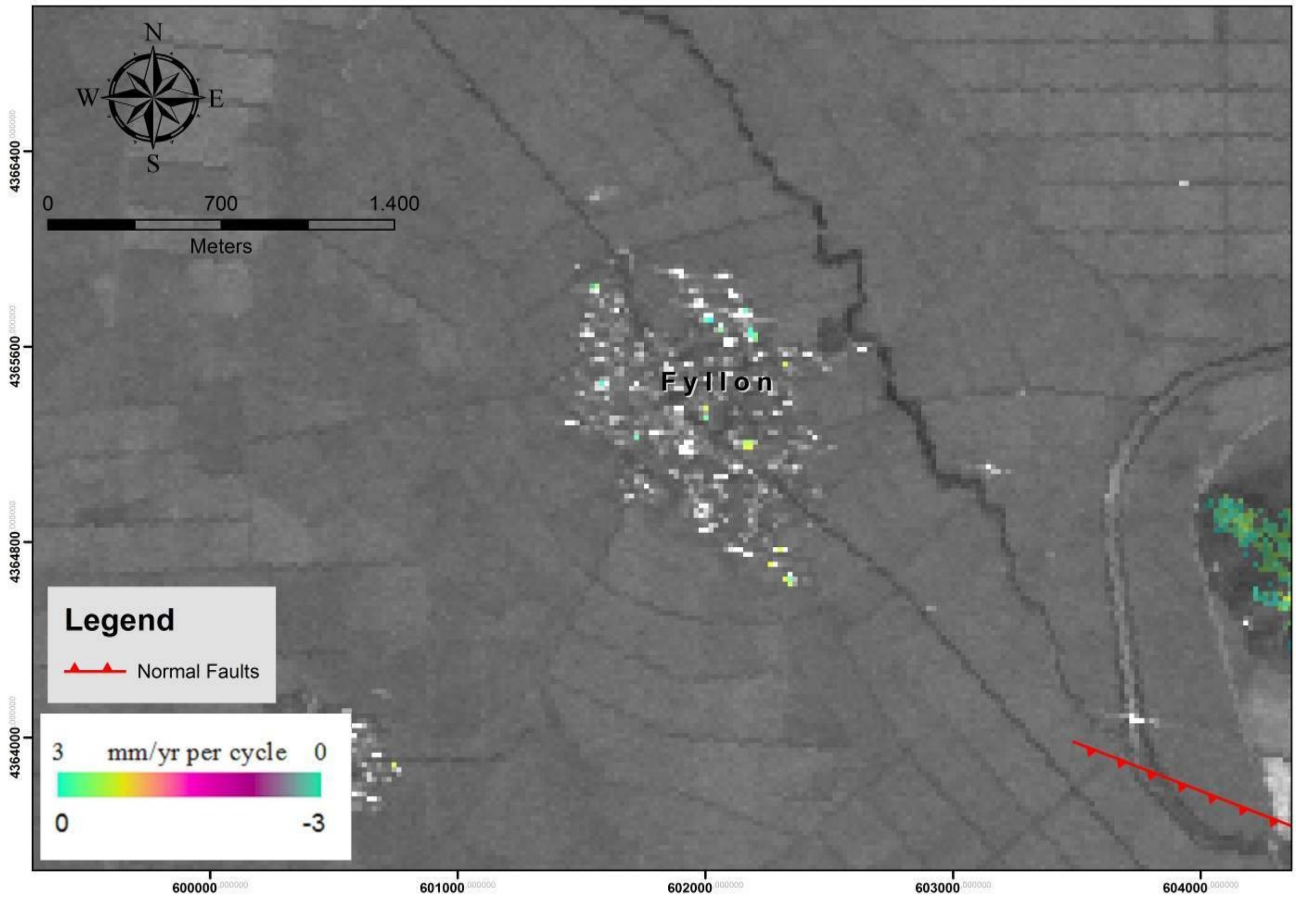

Figure199. Total deformation at Fyllon estimated with interferometric stacking technique, November 1992 – October 2010

4.2.2.1.12. Palamas

Results of interferometric stacking patterns and total deformation rate estimation during the period November 1992 – October 2010 for Palamas are shown in Figure 200. Ground deformation results within the settlement indicate that the subsidence varies in the range -0.11 – -2.205 mm/year, while uplift varies in the range 0.58 – 0.6 mm/year. A low density of patterns distribution of both subsidence and uplift can be observed within the settlement compared with the patterns density at the same settlement with the ascending track. Subsidence patterns are observed through almost all the settlement. Uplift patterns are observed in the northwestern, western and southwestern parts of the settlement. This settlement has not been affected by fault movements, so this subsidence and uplift are attributed to another impact factor.

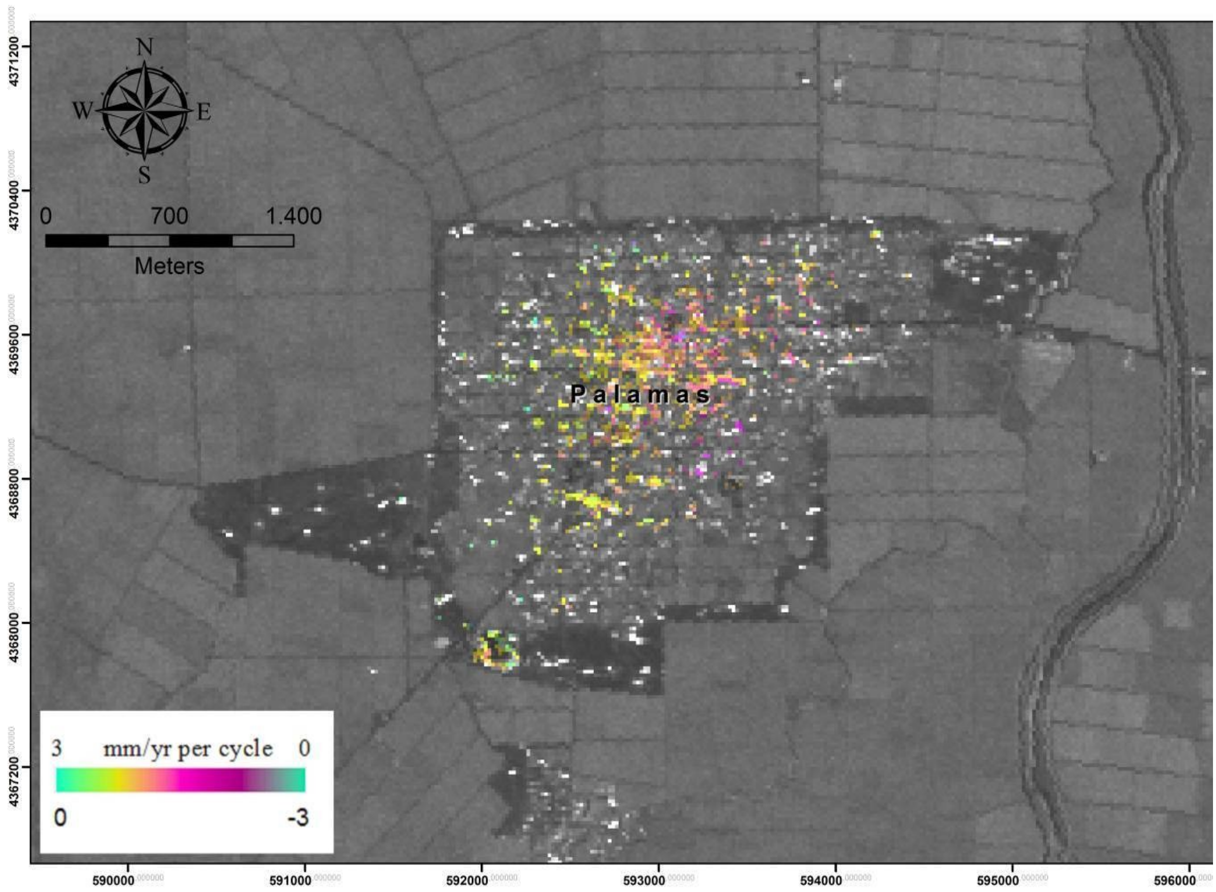

Figure.200 Total deformation at Palamas estimated with interferometric stacking technique, November 1992 – October 2010

4.2.2.1.13. Marathea

Results of interferometric stacking patterns and total deformation rate estimation during the period November 1992 – October 2010 for Marathea are shown in Figure 201. Ground deformation results within the settlement indicate that the subsidence varies in the range -0.058 – -1.054 mm/year, while uplift is null, although it is observed as pattern phenomena. A very low density of patterns distribution of both subsidence and uplift can be observed within this settlement compared with the patterns density at the same settlement with the ascending track. Slight subsidence patterns are observed in the northern and southern parts of the settlement, while uplift patterns have been observed in the southwestern part of the settlement. The null result for uplift may be attributed to the location of the settlement west of the footwall of a normal fault trace, whereas subsidence may be attributed to another impact factor.

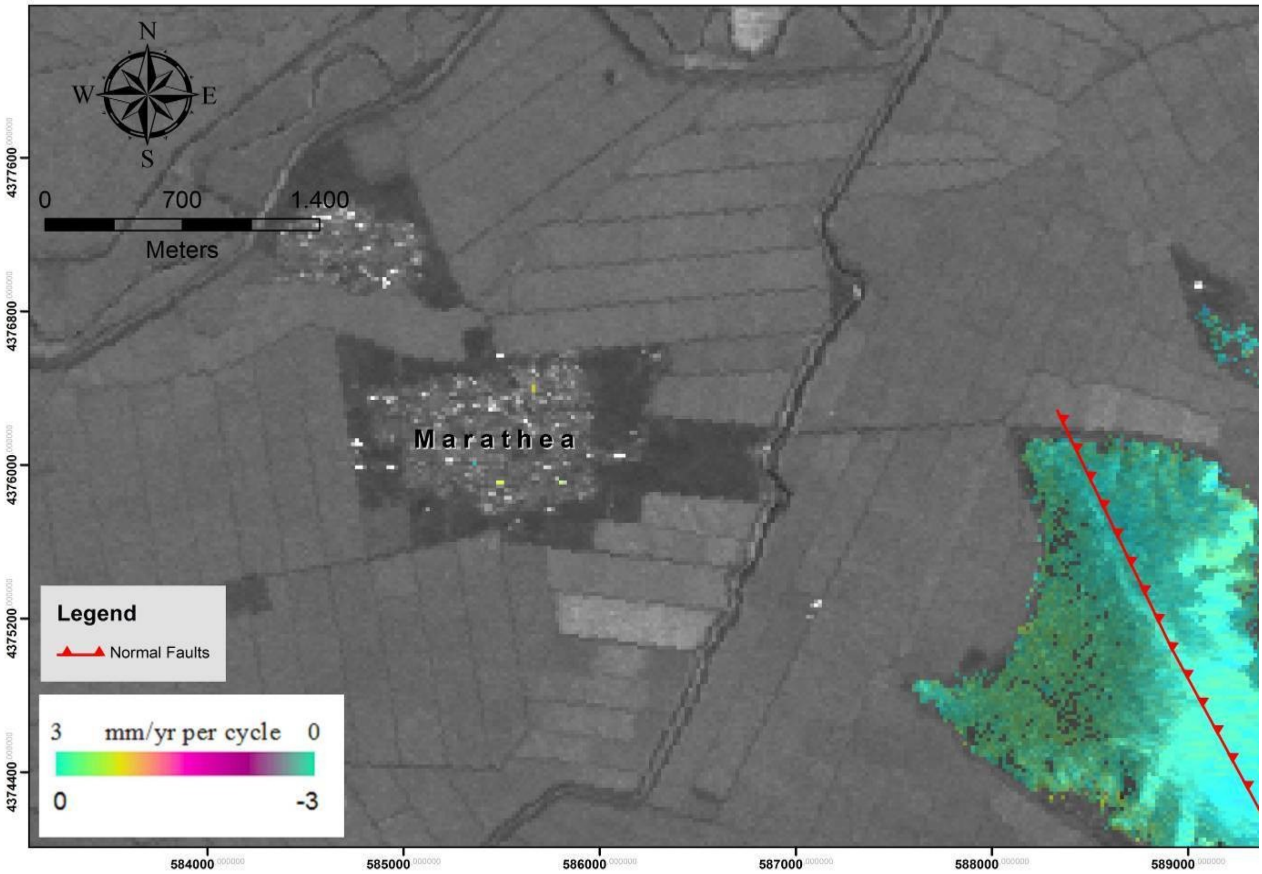

Figure201. Total deformation at Marathea estimated with interferometric stacking technique, November 1992 – October 2010

4.2.2.1.14. <u>Nikaia</u>

Results of interferometric stacking patterns and total deformation rate estimation during the period November 1992 – October 2010 for Nikaia are shown in Figure 202. Ground deformation results within the settlement indicate that the subsidence varies in the range -0.018 – -2.142 mm/year, while uplift varies in the range 0.445 – 0.784 mm/year. A low density of patterns distribution for both subsidence and uplift can be observed within this settlement compared with the patterns density of the same settlement with the ascending track. Subsidence patterns can be observed in the northern, middle, and southern parts and less marked patterns can be observed in the eastern parts of the settlement. Uplift patterns are concentrated in the southeast and slight patterns can be observed in the northwestern, middle and western parts of the settlement. Subsidence may be attributed to the impact of fault movement. However, uplift particularly in the northeastern part of the settlement may be attributed to its location east of the footwall of a normal fault trace.

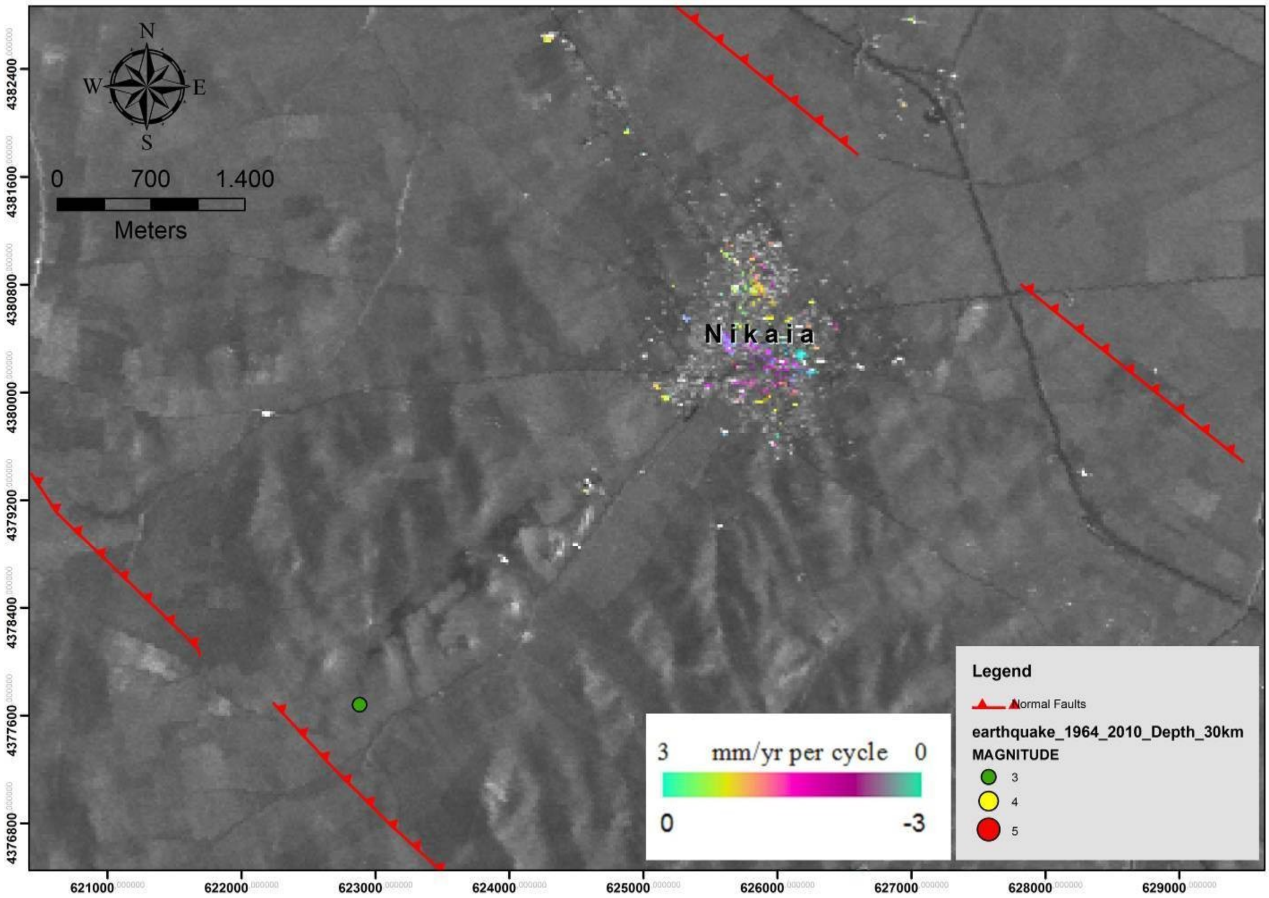

Figure.202 Total deformation at Nikaia estimated with interferometric stacking technique, November 1992 – October 2010

4.2.2.1.15. Terpsithea

Results of interferometric stacking patterns and total deformation rate estimation during the period November 1992 – October 2010 for Terpsithea are shown in Figure 203. Ground deformation results within the settlement indicate that the subsidence varies in the range -0.088 – -0.849 mm/year, while the uplift varies in the range 0.046 – 0.358 mm/year. Slight subsidence patterns can be observed in the northern, southeastern, western, and southwestern parts of the settlement. However, uplift patterns are observed over almost all of the settlement. Subsidence may be attributed to the location of the settlement northeast of the hanging wall of a normal fault trace.

Uplift may be attributed to its location south of the footwall of another normal fault trace.

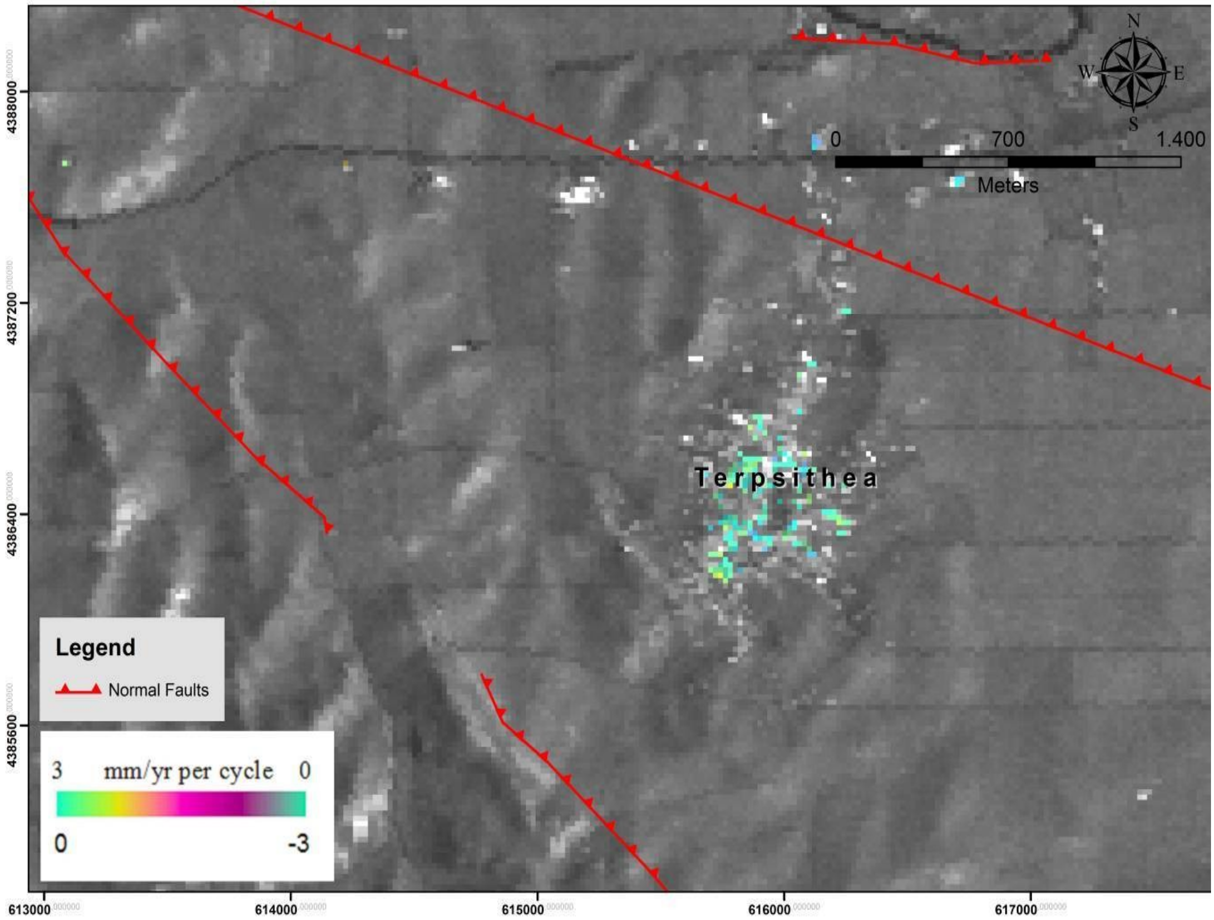

Figure203. Total deformation at Terpsithea estimated with interferometric stacking technique, November 1992 – October 2010

4.2.2.1.16. Tyrnavos

Results of interferometric stacking patterns and total deformation rate estimation during the period November 1992 – October 2010 for Tyrnavos are shown in Figure 204. Ground deformation results within the settlement indicate that the subsidence varies in the range -0.195 – -2.157 mm/year, while uplift varies in the range 0.36 – 0.37 mm/year. Subsidence patterns are distributed over the middle, eastern, and southeastern parts, and less clearly in the northern and southern parts of the settlement. Uplift patterns are distributed over the middle, northern, southern and eastern parts of the settlement. Subsidence may be attributed to the location of the settlement north of the hanging wall of a normal fault trace. However, uplift may be attributed to the location of the settlement southwest of the footwall of another normal fault trace.

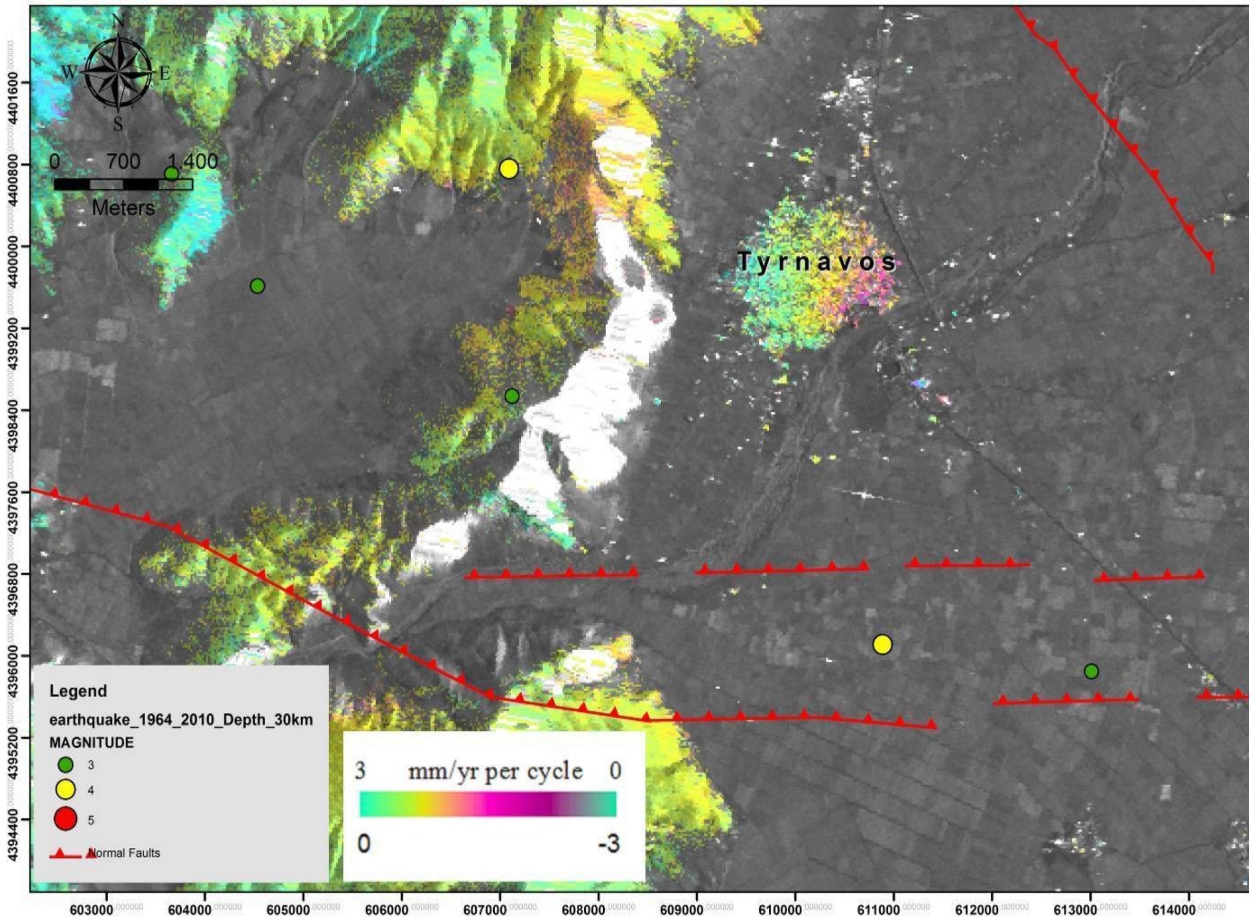

Figure204. Total deformation at Tyrnavos estimated with interferometric stacking technique, November 1992 – October 2010

4.2.2.1.17. Rodia

Results of interferometric stacking patterns and total deformation rate estimation during the period November 1992 – October 2010 for Rodia are shown in Figure 205. Ground deformation results within the settlement indicate that the subsidence varies in the range -0.003 – -1.425 mm/year, while the uplift varies in the range 0.348 – 1.28 mm/year. A low density of patterns distribution for both subsidence and uplift can be observed within this settlement compared with the patterns density of the same settlement with the ascending track. Slight subsidence patterns are observed in the eastern, far northeastern, middle, and southwestern parts of the settlement. Uplift patterns are concentrated in the northern part and less clearly observed in the eastern, western, southwestern, and far northwestern parts of the settlement. Subsidence may be attributed to the location of the settlement south and west of the hanging walls of two normal fault traces. However, uplift may be attributed to another impact factor.

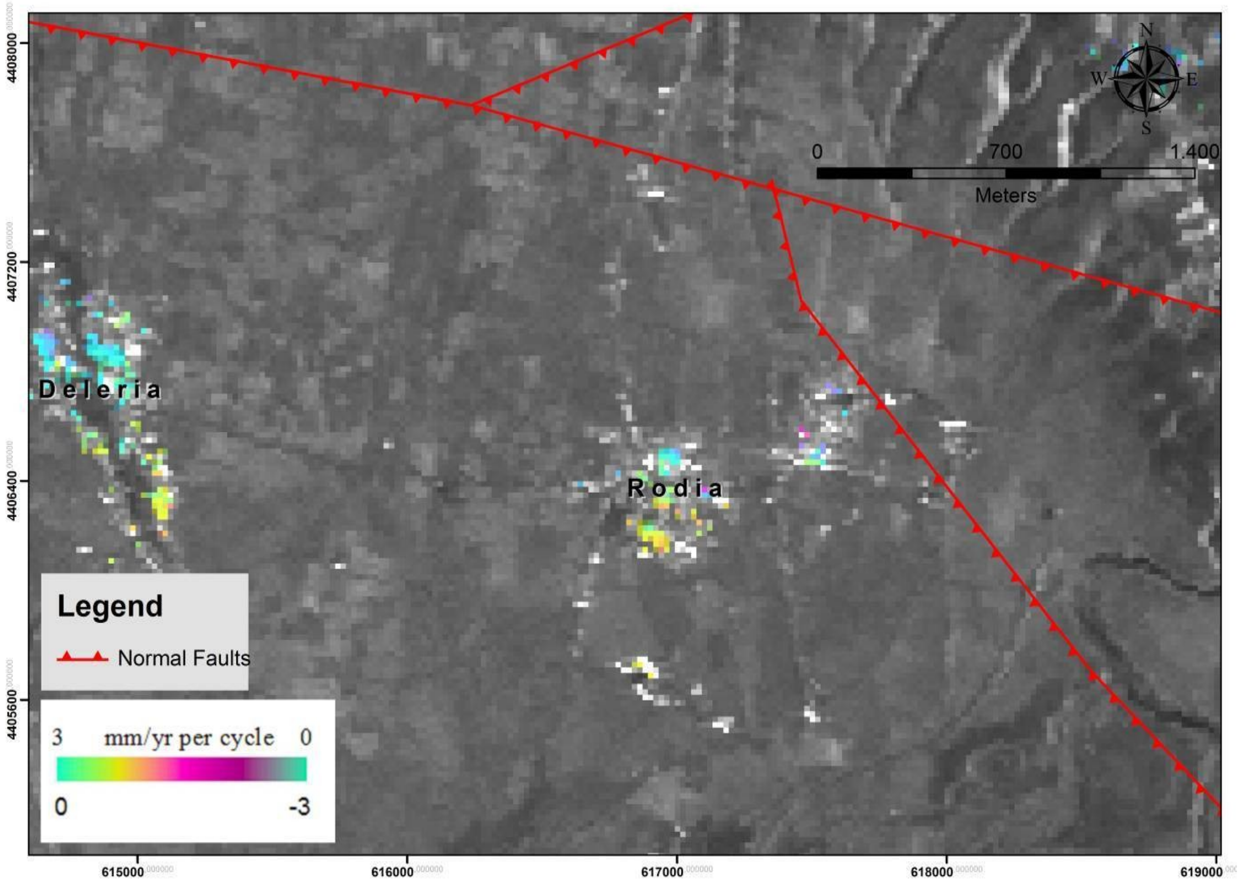

Figure.205 Total deformation estimated with interferometric stacking technique of Rodia between November, 1992 – October, 2010

4.2.2.1.18. Mandra

Results of interferometric stacking patterns and total deformation rate estimation during the period November 1992 – October 2010 for Mandra are shown in Figure 206. Ground deformation results within the settlement indicate that the subsidence varies in the range -0.58 – -1.731 mm/year, while uplift is null. A very low distribution of patterns density for both subsidence and uplift can be observed within this settlement compared with the patterns density of the same settlement with the ascending track. Subsidence patterns are distributed throughout the whole settlement, which may be attributed to another impact factor, given the settlement’s location south and west of the footwalls of two normal fault traces.

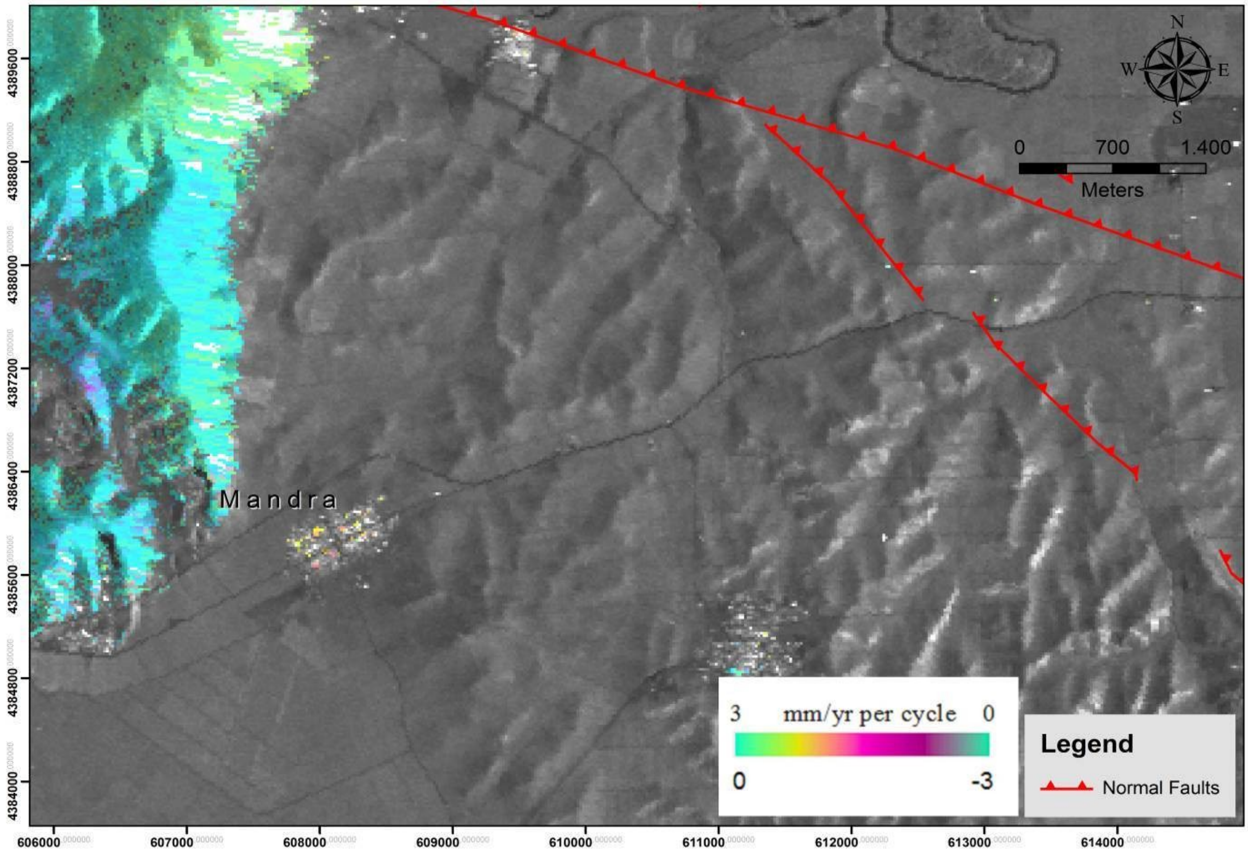

Figure.206 Total deformation at Mandra estimated with interferometric stacking technique,November 1992 – October 2010

4.2.2.1.19. Eleftherai

Results of interferometric stacking patterns and total deformation rate estimation during the period November 1992 – October 2010 for Elftherai are shown in Figure 207. Ground deformation results within the settlement indicate that the subsidence varies in the range -0.273 – -1.207 mm/year, while uplift varies in the range 0.028 – 0.303 mm/year. The distribution of patterns density observed for both subsidence and uplift within this settlement is low compared with the patterns density of the same settlement with the ascending track. Subsidence patterns are concentrated in the southern parts of the settlement. Uplift patterns are observed in the northwestern, eastern, middle, western and southern parts of the settlement. Subsidence may be attributed to some other impact factor. However, uplift may be attributed to the location of the settlement southwest of the footwall of a normal fault trace.

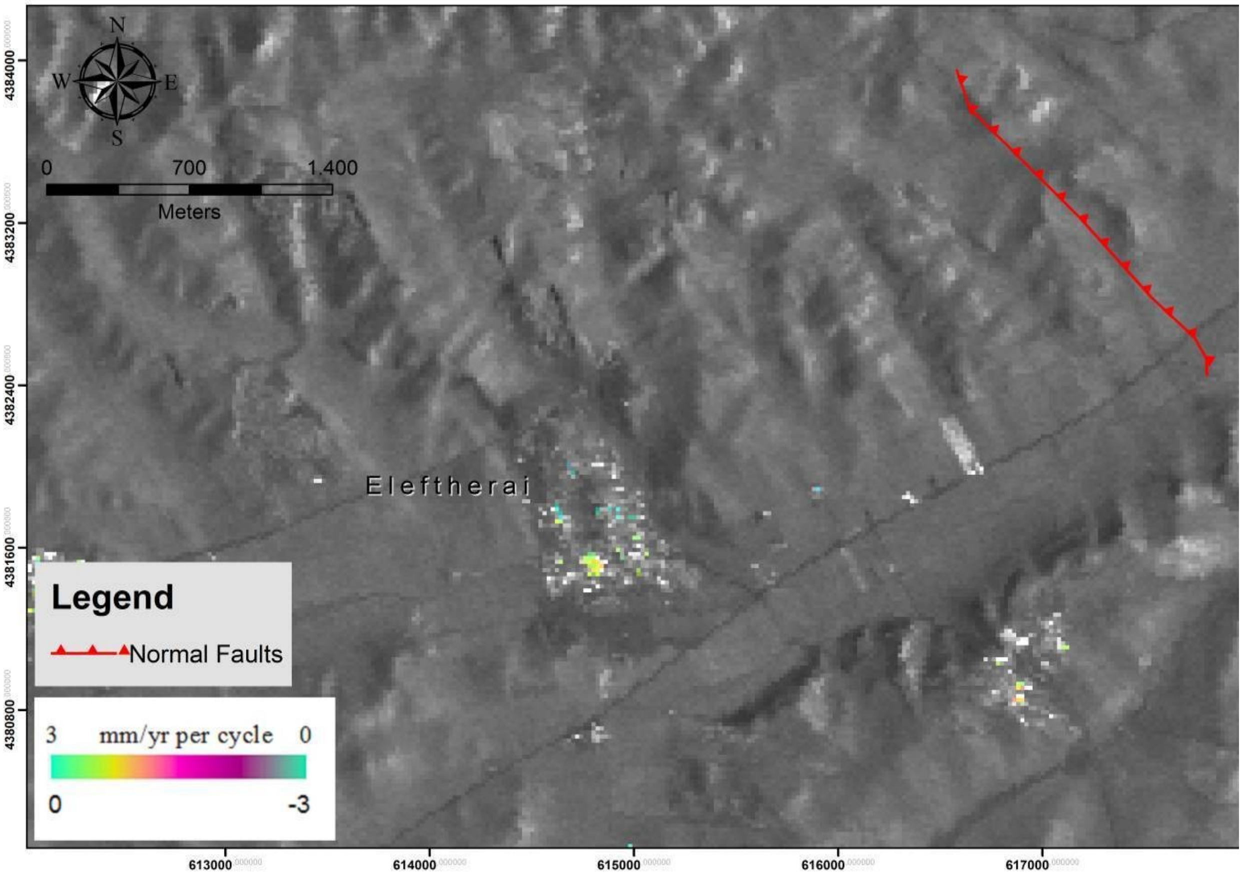

Figure.207 Total deformation at Eleftherai estimated with interferometric stacking technique, November 1992 – October 2010

4.2.2.2. Conventional SAR Interferometry

A single interferogram with a short temporal period (19980802_19980906) was chosen within this track, as depicted previously in Figure 21, additionally the parameters of this interferogram are depicted in Table 14 in the chapter on processing. The settlement of Larissa was selected in order to verify the impact of fault movements on ground deformation. Figure 208 shows the interferogram of Larissa corresponding to the cross-section. Table 45 shows the displacement and the distance along the cross-section.

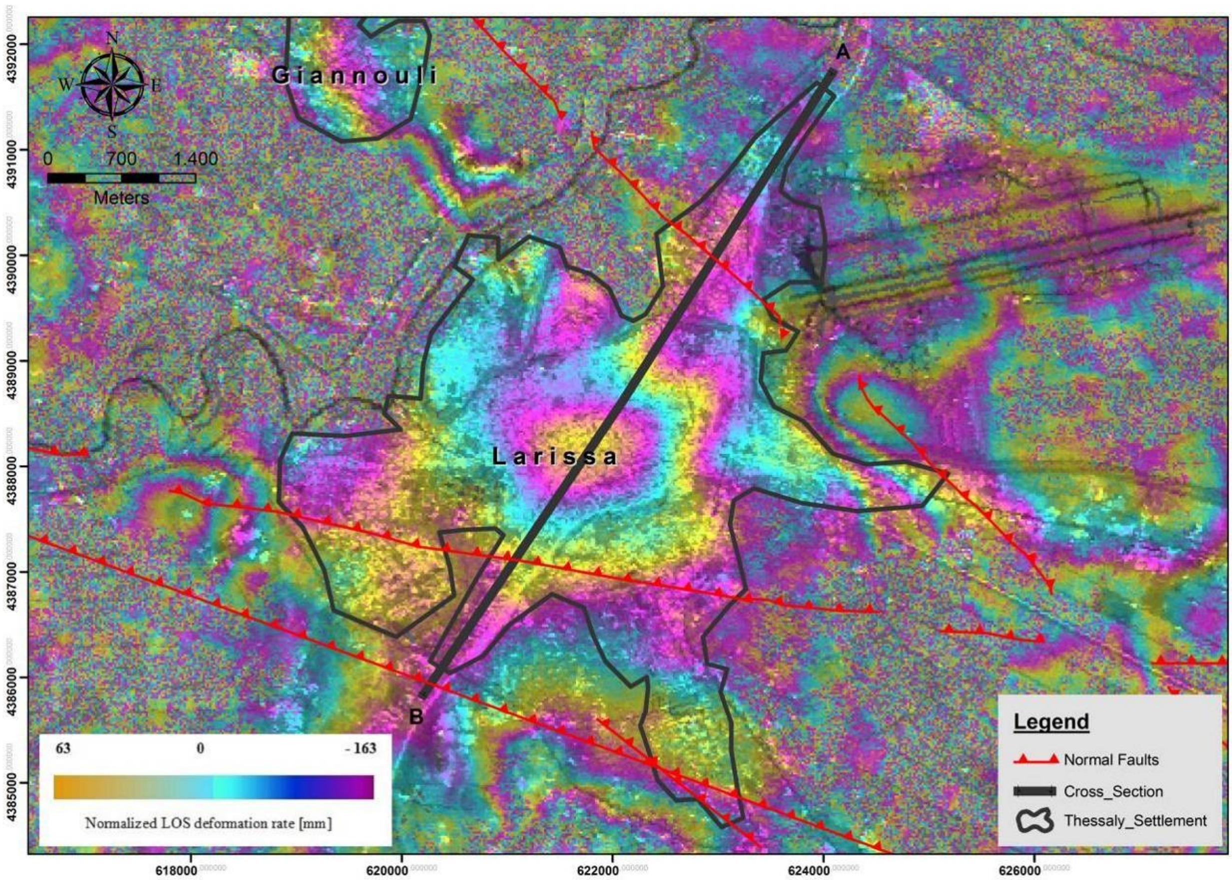

Figure.208 Conventional interferogram corresponding to 7 km cross-section of Larissa in the period 19980802_19980906

Table 45. Displacement field as observed by conventional interferometry within 7 km cross- section of Larissa in the period 19980802_19980906

I.d	Distance (km)	Displacement (mm)
1	0.5	-30.221
2	1	-30.424
3	1.5	-30.617
4	2	-30.28
5	2.5	-30.163
6	3	-20.882
7	3.5	-20.721
8	4	-20.49
9	4.5	-20.774
10	5	-20.898
11	5.5	-30.086
12	6	-30.212
13	6.5	-30.427
14	7	-30.213

Ground displacement along the cross-section is depicted in Figure 209. The behavior of the ground displacement along the cross-section indicates subsidence. Furthermore, the stability of the subsidence can be seen at the beginning of the cross-section and for 2.0 km, but thereafter a decrease in subsidence is observed in the side of footwall of the first normal fault trace, northeast of the settlement. Subsequently, the stability of the subsidence is observed once again throughout the distance 3.0 – 5.0 km, followed by increasing subsidence in the side of the hanging wall of the second normal fault trace. Thereafter, subsidence stability is once again observed until the third normal fault southwest of the settlement. This fluctuation of subsidence may be attributed to the impact of fault movement, in spite of the short time period.

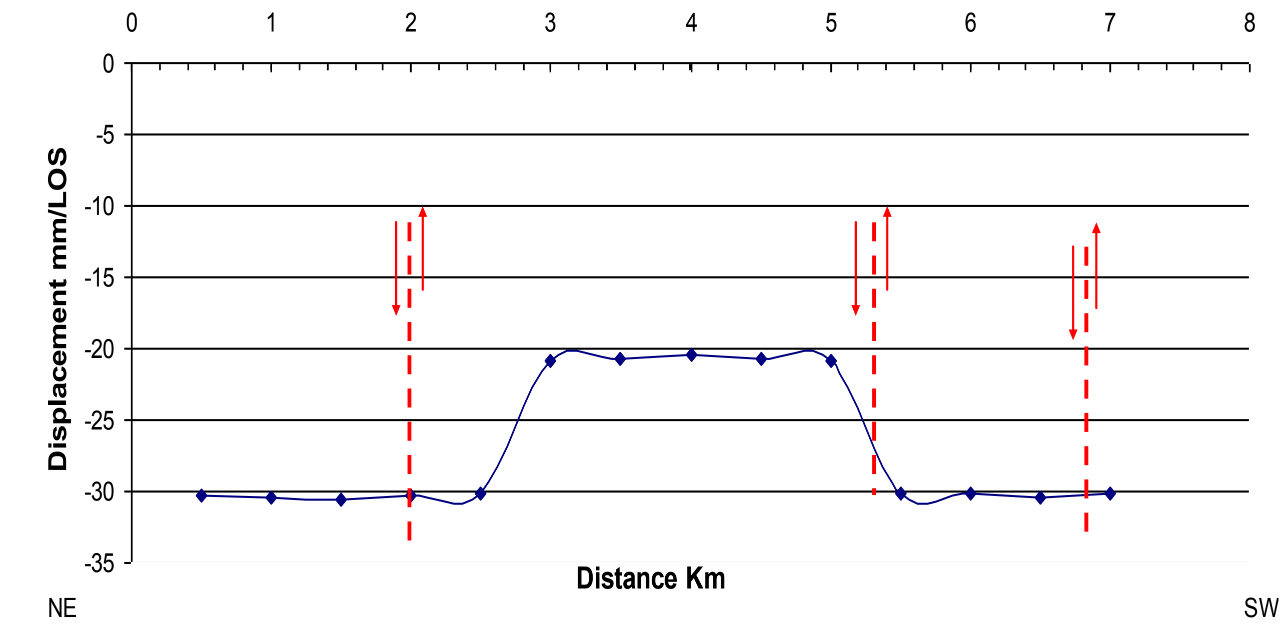

Figure.209 Spatial profile showing the displacement field as observed by conventional interferometry within a 7 km cross-section of Larissa, in the period 19980802_19980906 red lines correspond to the faults

4.2.2.3. Persistent Scatterers Interferometry (PSI)

Note that not all settlements were covered with the results of candidate points within this track. Consequently, just four settlements out of the total of 30 were covered. The less marked distribution of other candidate points can be observed outside the respective settlements. The mminimum and maximum deformation rate in LOS and the number of candidate points within each settlement are depicted in Table 46. All the candidate points have been superimposed within an ArcGIS environment to create a spatial correlation between each point candidate and fault movements.

Table 46. Minimum and maximum deformation rate in LOS and the number of PSI targets within urban areas of Thessaly prefecture, 1992-2010

Settlements	Number of targets	Minimum rate (mm)	Maximum rate (mm)	Mean
Larissa	3850	- 1	12	1
Giannouli	25	- 1	9	2
Nikaia	11	- 1	10	1
Terpsithea	122	- 1	9	2

4.2.2.3.1. Minimum deformation rate

4.2.2.3.1.1. Larissa

Candidate point number 171091 was selected as representative of the minimum deformation rate. It is located northwest of the settlement and 1.163 km southwest of a normal fault trace in the side of the footwall, as well as 2.848 km north of another normal fault trace in the side of the hanging wall. A plot of this point is depicted in Figure 210. The ground deformation behavior of this candidate point through its time series begins with uplift then changes to subsidence. The minimum uplift was 1.226 mm (July 2008) while the maximum was 134.964 mm (November 1992). The minimum and maximum subsidence were -9.772 and -23.687 mm in November 2008 and October 2010 respectively. Uplift may be attributed to the impact of fault movement, given the location of the point in the side of the footwall, as mentioned above. However, subsidence at the end of the time series may be attributed to the impact of the hanging wall of the other fault which is located south of the point.

An acceptable reason for this deformation behavior from uplift to subsidence through the time series of the candidate point in this case may be the disparity of fault activity. The location of the selected point's minimum and maximum deformation rate is shown in Figure 211.

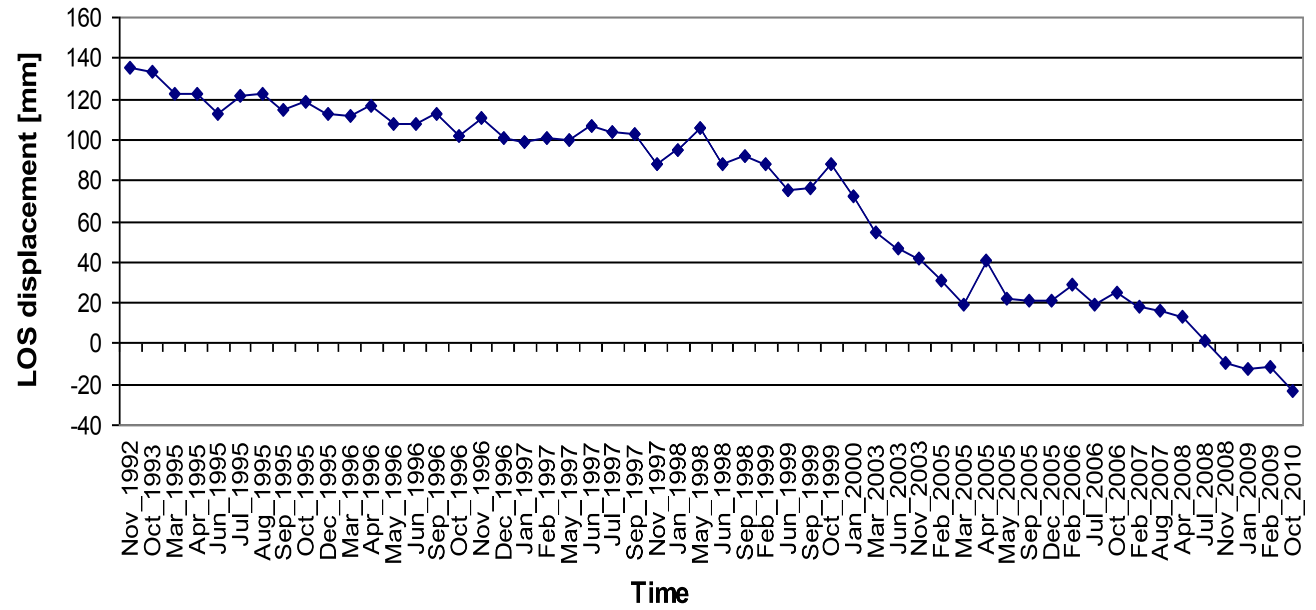

Figure210. LOS displacement time series (1992-2010) of the minimum deformation rate of PSI of Larissa. Point number 171091. Time series are rescaled to the first acquisition (12 November 1992)

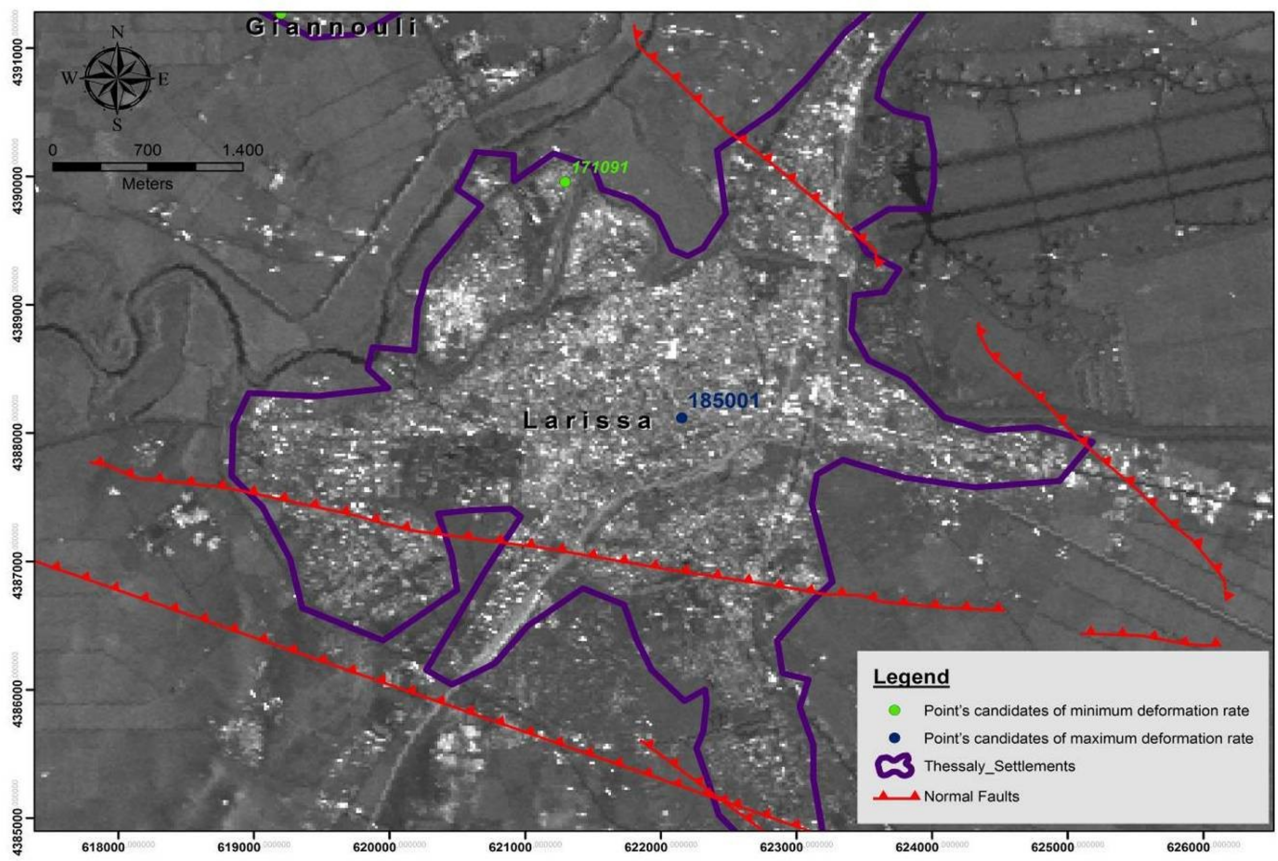

Figure.211 Location of selected candidate points minimum and maximum deformation rate, descending track 279. Settlement of Larissa.

4.2.2.3.1.2. Giannouli

Candidate point number 166001 was selected as representative of the minimum deformation rate. It is located southwest of the settlement and 1.765 km southwest of a normal fault trace in the side of the footwall. A plot of this point is depicted in Figure 212. The ground deformation behavior of the candidate point through its time series begins with uplift then changes to subsidence. The minimum uplift was 9.5015 mm (August 2007) while the maximum uplift was 104.942 mm (November 1992). The minimum and maximum subsidence were -0.322 and -17.124 mm in July 2008 and October 2010 respectively. Uplift may be attributed to the impact of fault movement, given the location of the point in the side of the footwall, as mentioned above. Subsidence may be attributed to another impact factor. The location of the selected point's minimum and maximum deformation rate is shown in Figure 213.

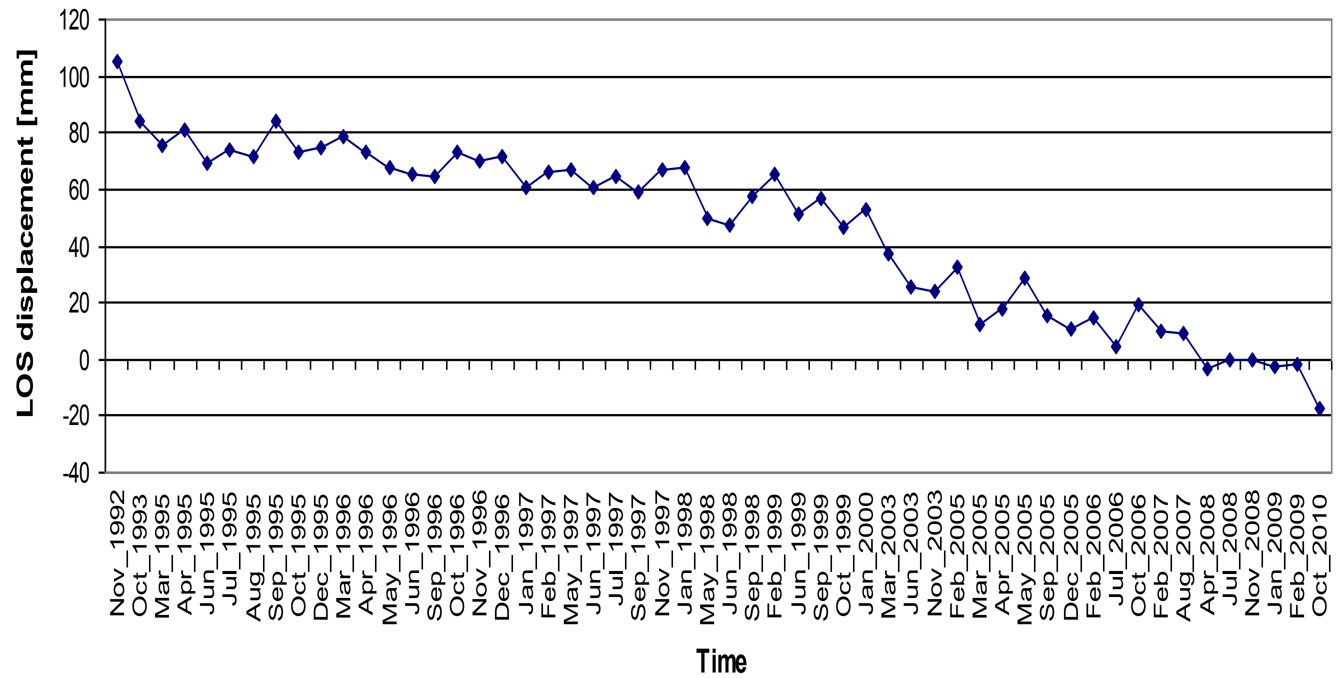

Figure212. LOS displacement time series (1992-2010) of the minimum deformation rate of PSI of Giannouli. Point number 166001. Time series are rescaled to the first acquisition (12 November 1992)

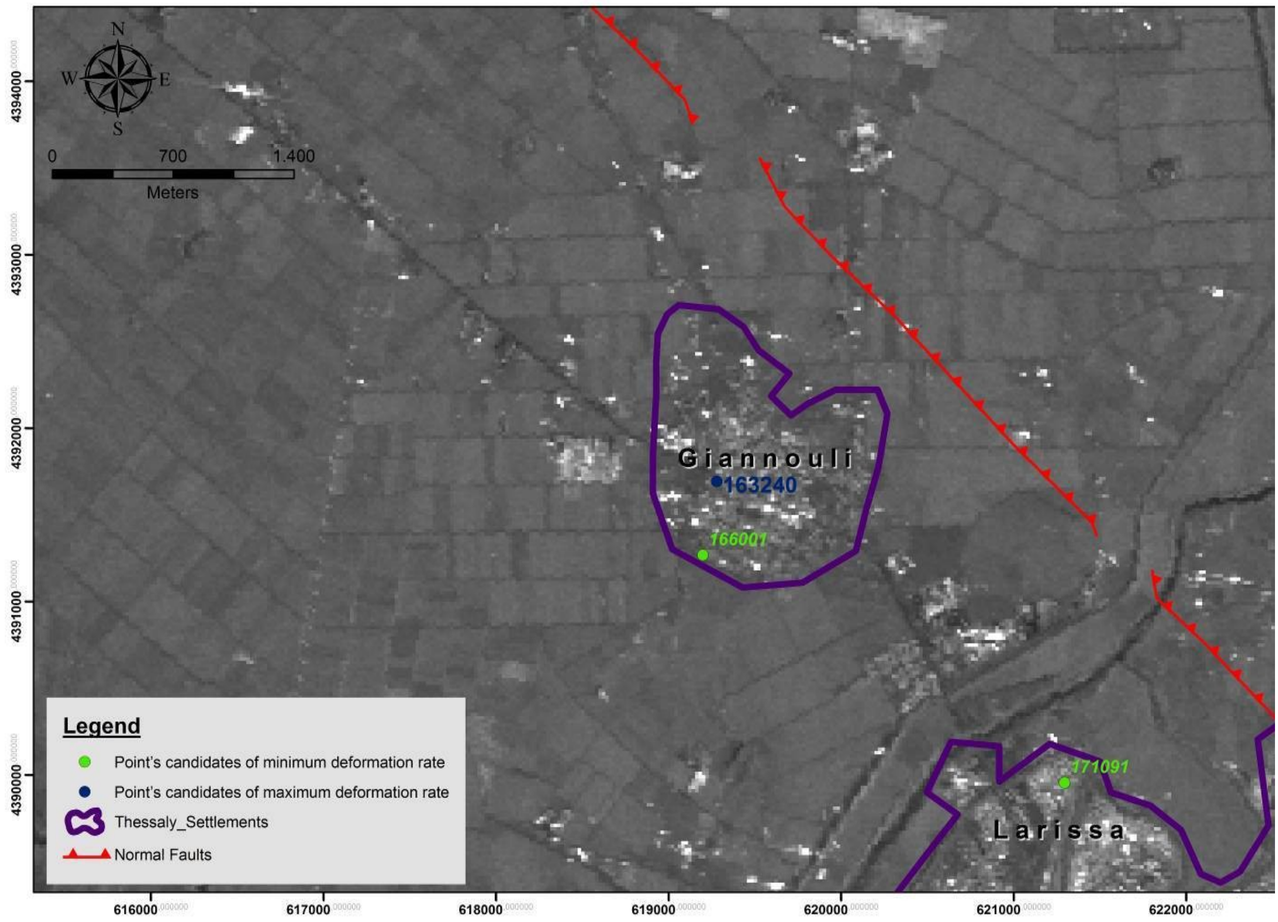

Figure213. Location of selected candidate points minimum and maximum deformation rate, descending track 279. Settlement of Giannouli

4.2.2.3.1.3. Nikaia

Candidate point number 225264 was selected as representative of the minimum deformation rate. It is located northeast of the settlement and 1.42 km south of a normal fault in the side of the footwall, as well as 5.1 km northeast of another normal fault in the side of the hanging wall. A plot of this point is depicted in Figure 214. The ground deformation behavior of this candidate point through its time series begins with uplift then changes to subsidence. The minimum uplift was 2.071 mm (July 2008) while the maximum uplift was 125.798 mm (November 1992). The minimum and maximum subsidence were -0.775 and -26.967 mm in November 2008 and October 2010 respectively. Uplift may be attributed to the impact of fault movement, given the location of the point in the side of the footwall, as mentioned above. Subsidence may be attributed to the impact of the hanging wall southwest of the point, in spite of the long distance between them. The location of the selected point's minimum and maximum deformation rate is shown in Figure 215.

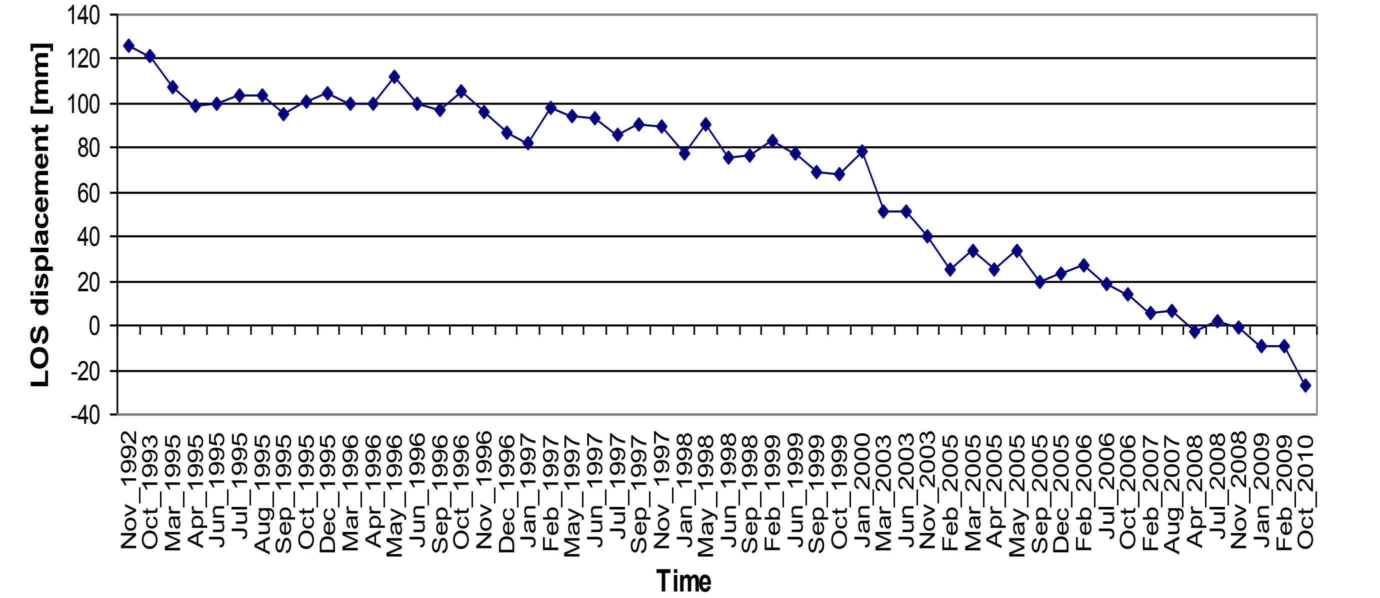

Figure.214 LOS displacement time series (1992-2010) of the minimum deformation rate of PSI of Nikaia. Point number 225264. Time series are rescaled to the first acquisition (12 November 1992)

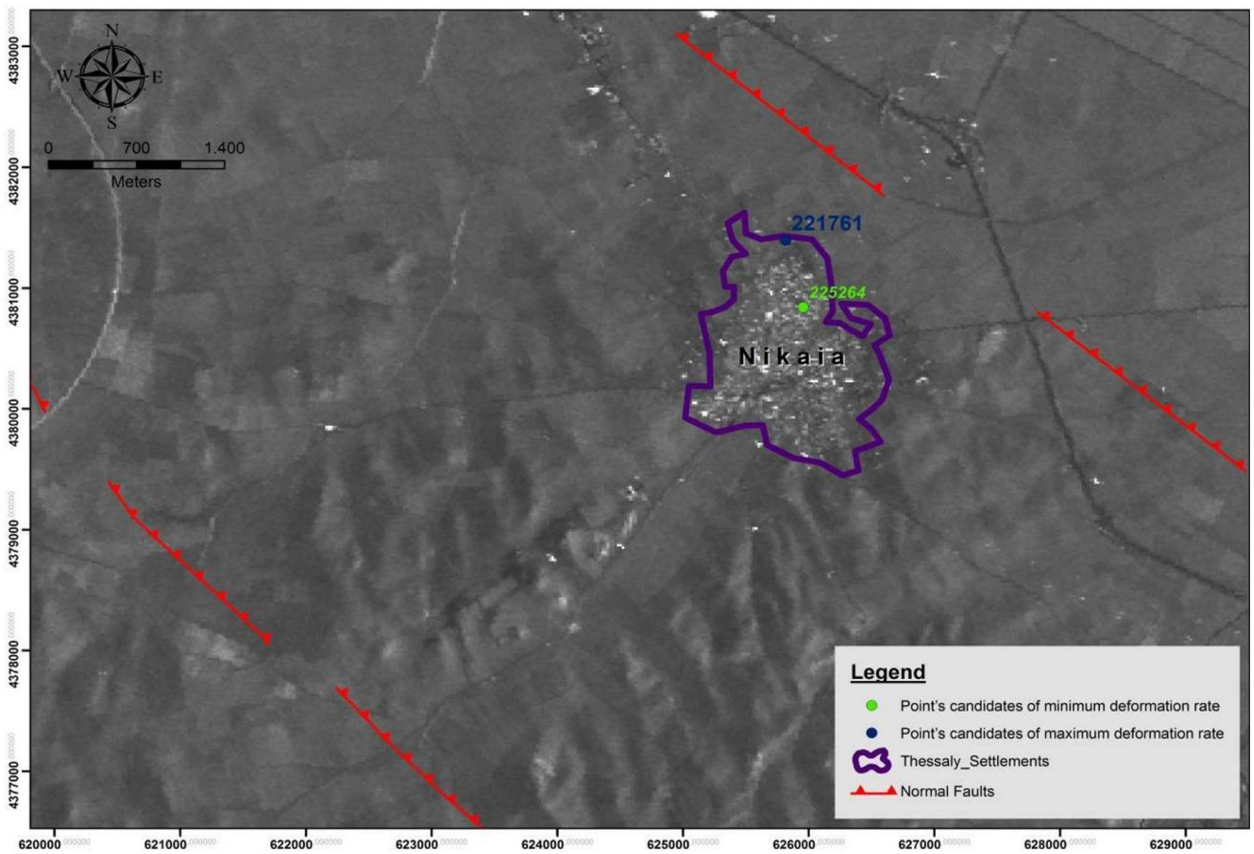

Figure215. Location of selected candidate points minimum and maximum deformation rate, descending track 279. Settlement of Nikaia

4.2.2.3.1.4. Terpsithea

Candidate point number 202683 was selected as representative of the minimum deformation rate. It is located southwest of the settlement and 1.351 km southwest of a normal fault in the side of the footwall, as well as 0.960 km northeast of another normal fault in the side of the hanging wall. A plot of this point is depicted in Figure 216. The ground deformation behavior of the candidate point through its time series begins with uplift then changes to subsidence. The minimum uplift was 0.887 mm (July 2008) while the maximum uplift was 108.817 mm (October 1993). The minimum and maximum subsidence were -1.111 and -21.807 mm in April 2008 and October 2010 respectively. Both uplift and subsidence may be attributed to disparities in the impact of fault movements, although the side of the footwall is more proactive than the side of the hanging wall. The location of the selected point's minimum and maximum deformation rate is shown in Figure 217.

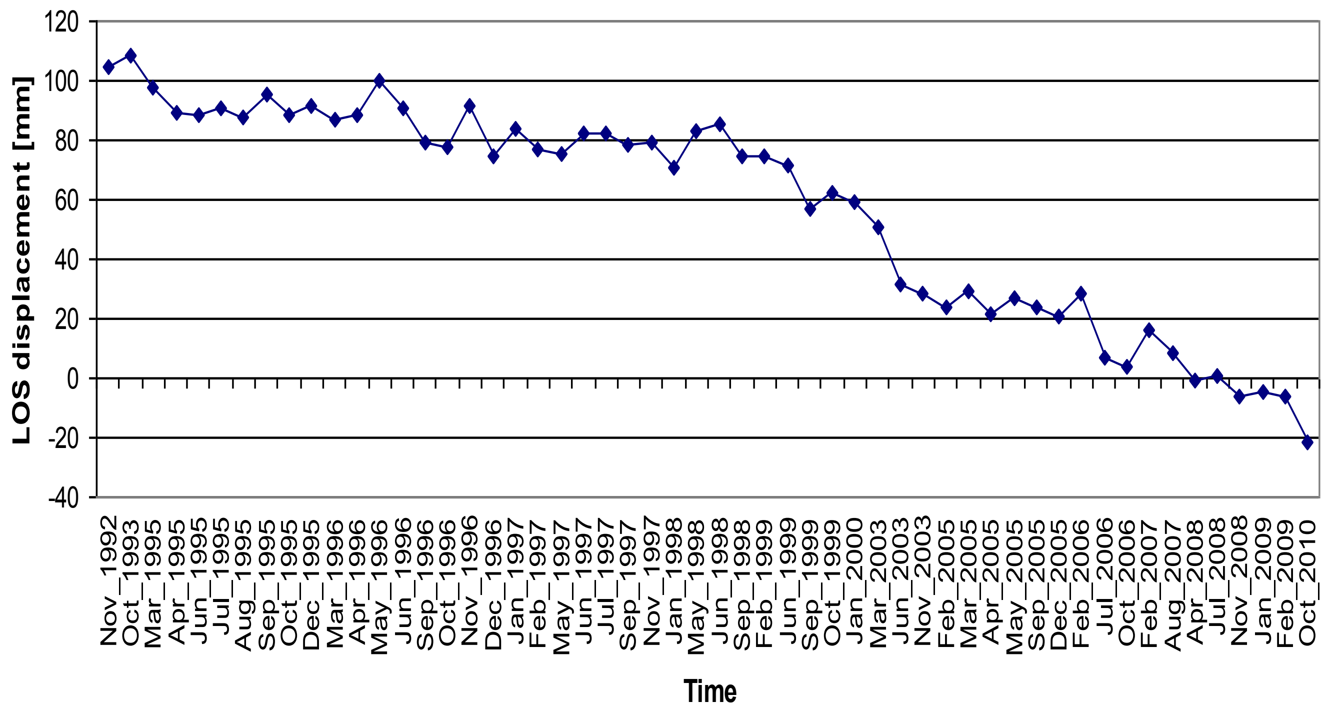

Figure216. LOS displacement time series (1992-2010) of the minimum deformation rate of PSI of Terpsithea. Point number 202683. Time series are rescaled to the first acquisition (12 November 1992)

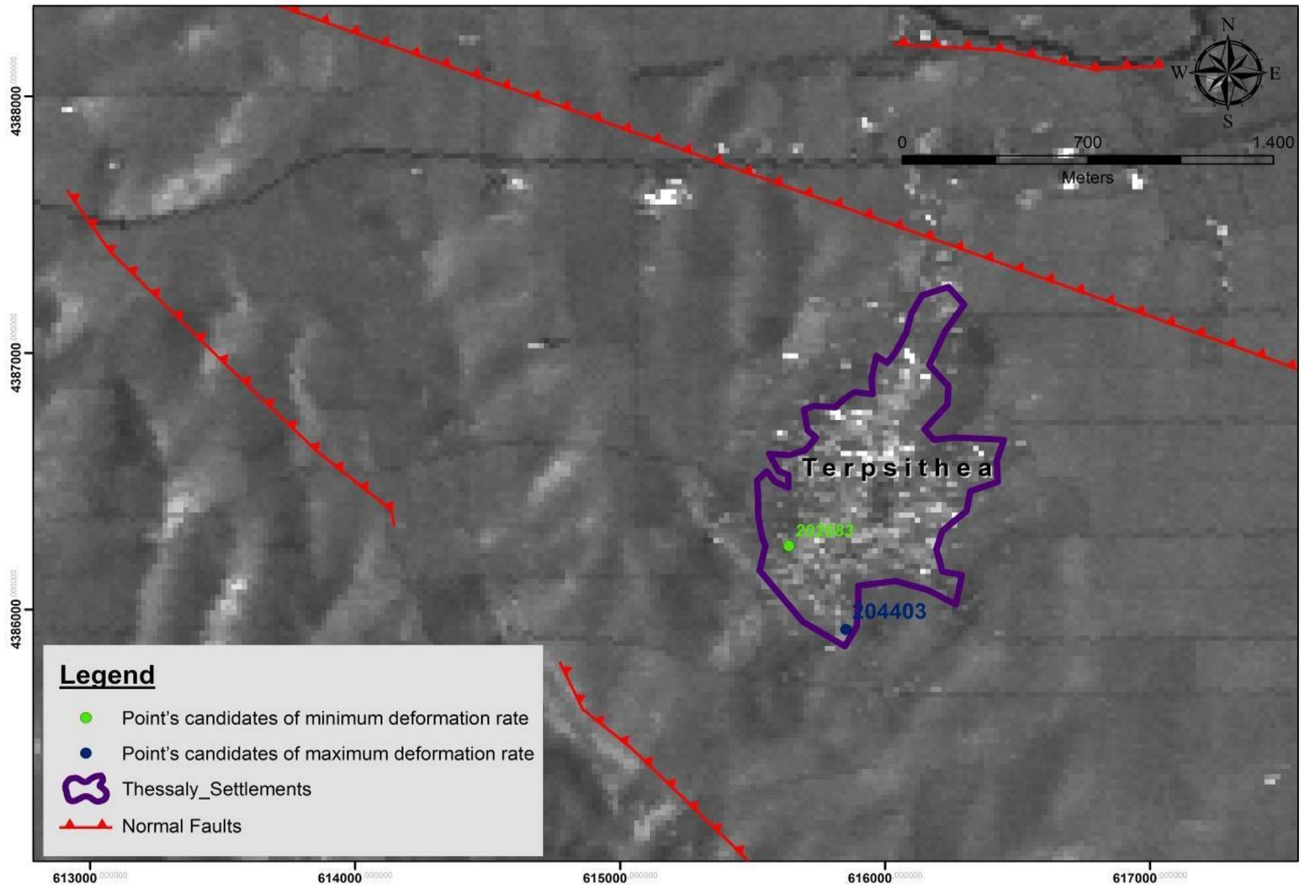

Figure217. Location of selected candidate points minimum and maximum deformation rate, descending track 279. Settlement of Terpsithea

4.2.2.3.2. Maximum deformation rate

4.2.2.3.2.1. Larissa

Candidate point number 185001 was selected as representative of the maximum deformation rate. It is located in the centre of the settlement and 2.3 km south of a normal fault in the side of the footwall, as well as 1.10 km north of another normal fault in the side of the hanging wall. A plot of the point is depicted in Figure 218. The ground deformation behavior of this candidate point through its time series begins with subsidence then changes to uplift. The minimum subsidence was -0.150 mm (January 2009) while the maximum was -187.556 mm (November 1992). The minimum and maximum uplift were 0.788 and 30.802 mm in July 2008 and October 2010 respectively. Subsidence may be attributed to the impact of fault movement. Furthermore, uplift at the end of the time series may be attributed also to disparity in the fault movement activity. The location of the selected point's minimum and maximum deformation rate was shown earlier in Figure 211.

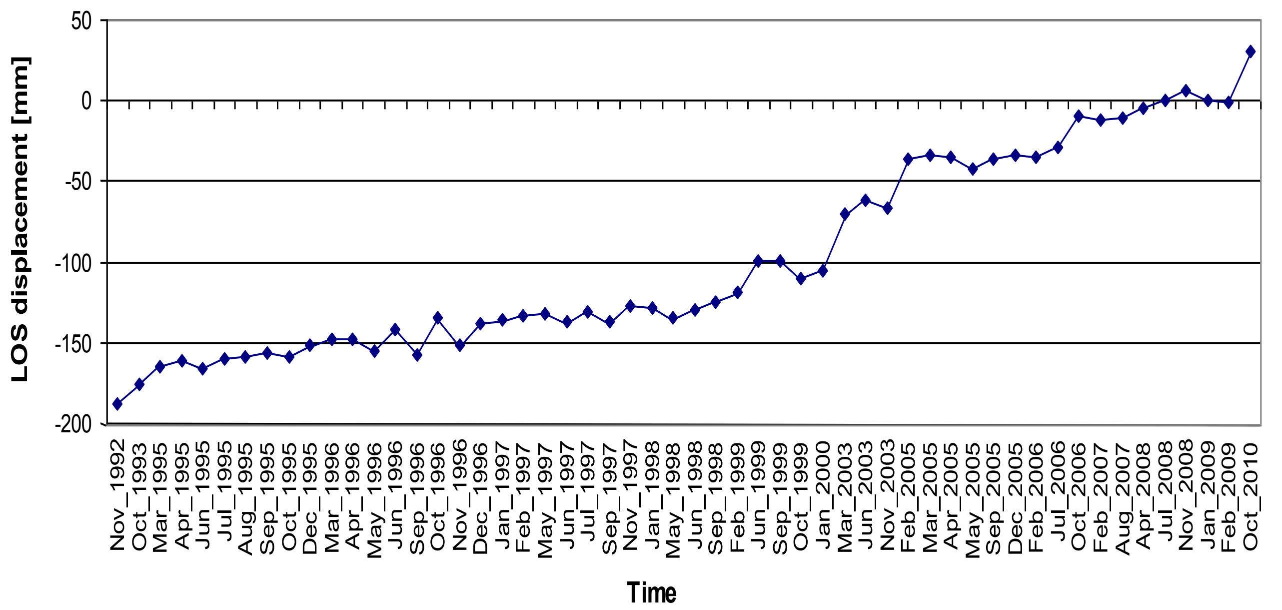

Figure.218 LOS displacement time series (1992-2010) of the maximum deformation rate of PSI of Larissa. Point number185001. Time series are rescaled to the first acquisition (12 November 1992)

4.2.2.3.2.2. Giannouli

Candidate point number 163240 was selected as representative of the maximum deformation rate. It is located in the middle-west of Giannouli and 1.417 km southwest of a normal fault trace in the side of the footwall. A plot of this point is depicted in Figure 219. The ground deformation behavior of the candidate point through its time series begins with subsidence then changes to uplift. The minimum subsidence was -9.556 mm (August 2007) while the maximum was -137.145 mm (November 1992). The minimum and maximum uplift were 2.228 and 19.329 mm in April 2008 and October 2010 respectively. Subsidence may be attributed to another impact of fault movement. However, uplift may be attributed to the impact of fault movement. The location of the selected point's minimum and maximum deformation rate was shown earlier in Figure 213.

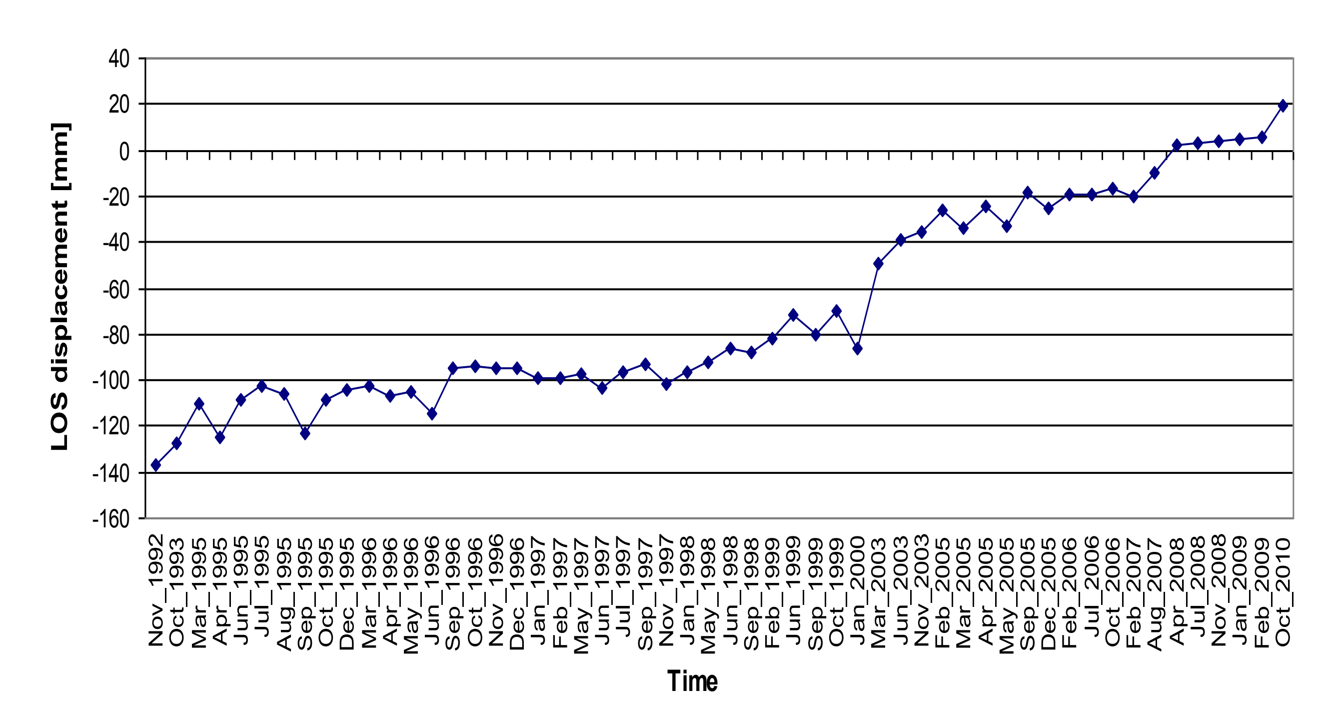

Figure.219 LOS displacement time series (1992-2010) of the maximum deformation rate of PSI of Giannouli. Point number163240. Time series are rescaled to the first acquisition (12 November 1992)

4.2.2.3.2.3. Nikaia

Candidate point number 221761 was selected as representative of the maximum deformation rate. It is located north of the settlement and 5.3 km northeast of a normal fault trace in the side of the hanging wall, as well as 1.1 km south of another normal fault trace in the side of the footwall. A plot of this point is depicted in Figure 220. The ground deformation behavior of this candidate point through its time series begins with subsidence then changes to uplift. The minimum subsidence was -1.863 mm (July 2008) while the maximum was -145.412 mm (November 1992). The minimum and maximum uplift were 0.804 and 16.11 mm in April 2008 and October 2010 respectively. Both subsidence and uplift may be attributed to disparity in the impact of fault movements in the hanging wall and footwall on the two sides. The location of the selected point's minimum and maximum deformation rate was shown earlier in Figure 215.

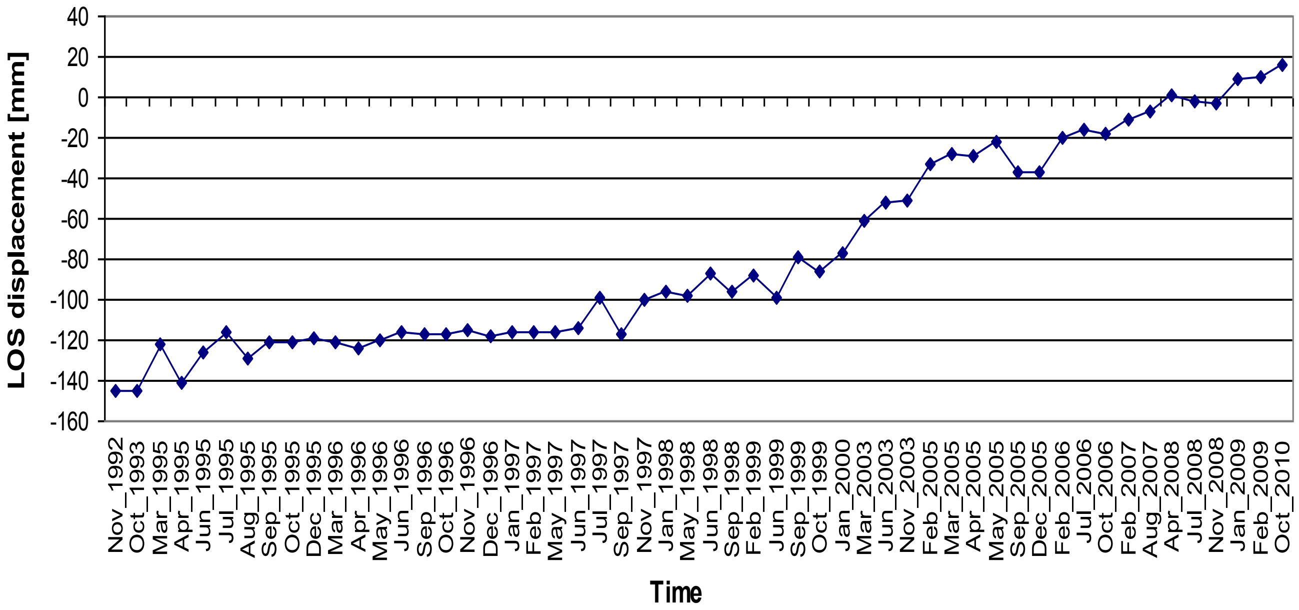

Figure220. LOS displacement time series (1992-2010) of the maximum deformation rate of PSI of Nikaia. Point number 221761. Time series are rescaled to the first acquisition (12 November 1992)

4.2.2.3.2.4. **Terpsithea**

Candidate point number 204403 was selected as representative of the maximum deformation rate. It is located south of the settlement and 0.879 km northeast of a normal fault in the side of the hanging wall, as well as 1.612 km south of another normal fault trace in the side of the footwall. A plot of this point is depicted in Figure 221. The ground deformation behavior of this candidate point through its time series begins with subsidence then changes to uplift. The minimum subsidence was -1.549 mm (July 2008) while the maximum subsidence was -142.923 mm (November 1992). The minimum and maximum uplift were 5.487 and 15.834 mm in November 2008 and October 2010 respectively. Both subsidence and uplift may be attributed to the disparity in the impact of fault movements. Evidence of this is the increasing uplift during the period November 2008 – October 2010. The location of the selected point's minimum and maximum deformation rate was shown earlier in Figure 217.

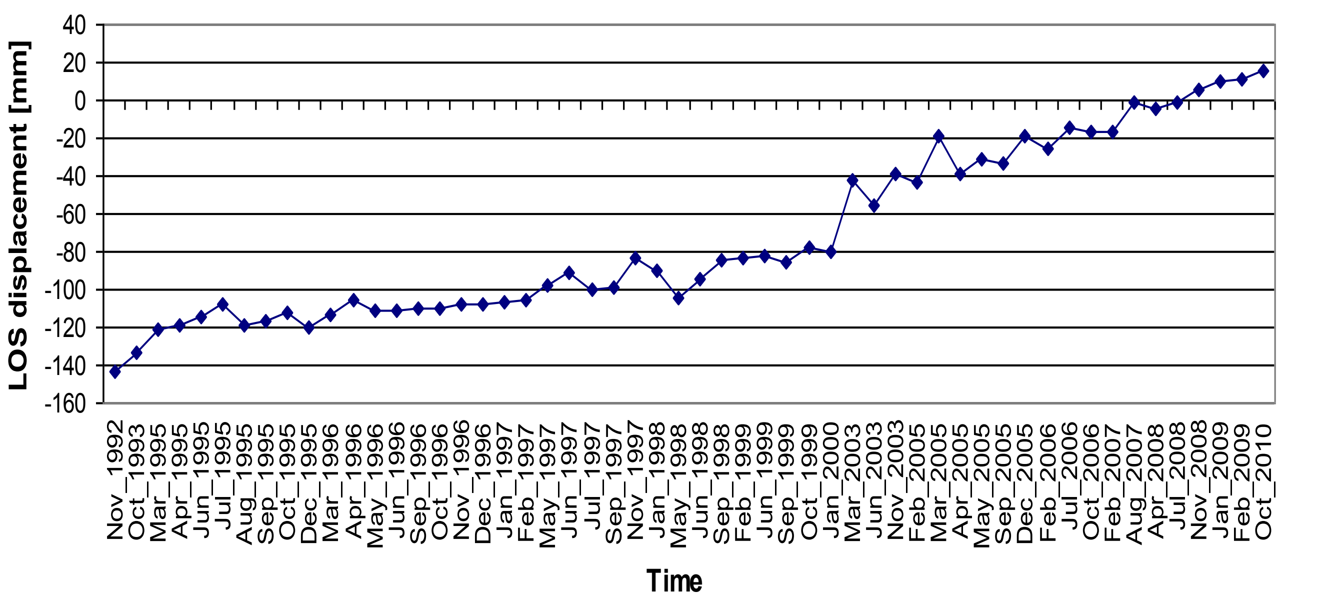

Figure.221 LOS displacement time series (1992-2010) of the maximum deformation rate of PSI of Terpsithea. Point number 204403. Time series are rescaled to the first acquisition (12 November 1992)

Chapter Five: Impact of lithology types on ground deformation

5.1. Introduction to the lithology

The type of lithology has an important impact on ground deformation for the reason that any physical or chemical change of shape or size of materials will be reflected in the stability of objects above the ground.

(Caputo and Helly, 2005) found that in Thessaly in general and particularly the sector corresponding to the Tyrnavos Basin most of the villages are settled on thick Quaternary fluvio-lacustrine deposits and therefore on the worst geological conditions for the possible occurrence of site effects. Spatial correlation between lithology type and ground deformation has been created to verify the impact of lithology on ground deformation, taking into account the general type of lithology within the study area.

5.2. Results and Discussion

Spatial correlation has been created between the lithology type of geological formations and ground deformation within the study area.

Ground deformation was assessed by implementing three techniques of SAR interferometry: interferometric stacking, conventional interferometry and Persistent Scatterers Interferometry.

Seven geological maps of Thessaly at a scale of 1:50,000 issued by the Greek Institute of Geology and Mineral Exploration, covering Larissa, Farkadwn, Platykampos, Gonnoi, Trikala, Rapsani, and Sofades, were used along with field observations.

Thirty settlements were identified. However, just 19 were selected to examine and investigate the influence of lithology type on ground deformation. The reason for selecting these settlements, as mentioned previously in the chapter on fault movements, was dependent on the type of lithology, since each one of the 19 settlements overlies just one type of lithology, while the others each overlie more than one type of lithology.

The geological formations cropping out on the surface of the broader area of the settlements were identified and mapped, and consequently a shape file was created and identified utilizing GIS software ArcGIS 9.3, as depicted in Figure 222. The intersection of the geological formation and the settlement layers revealed the geological formations of the surface of the cities and villages under investigation.

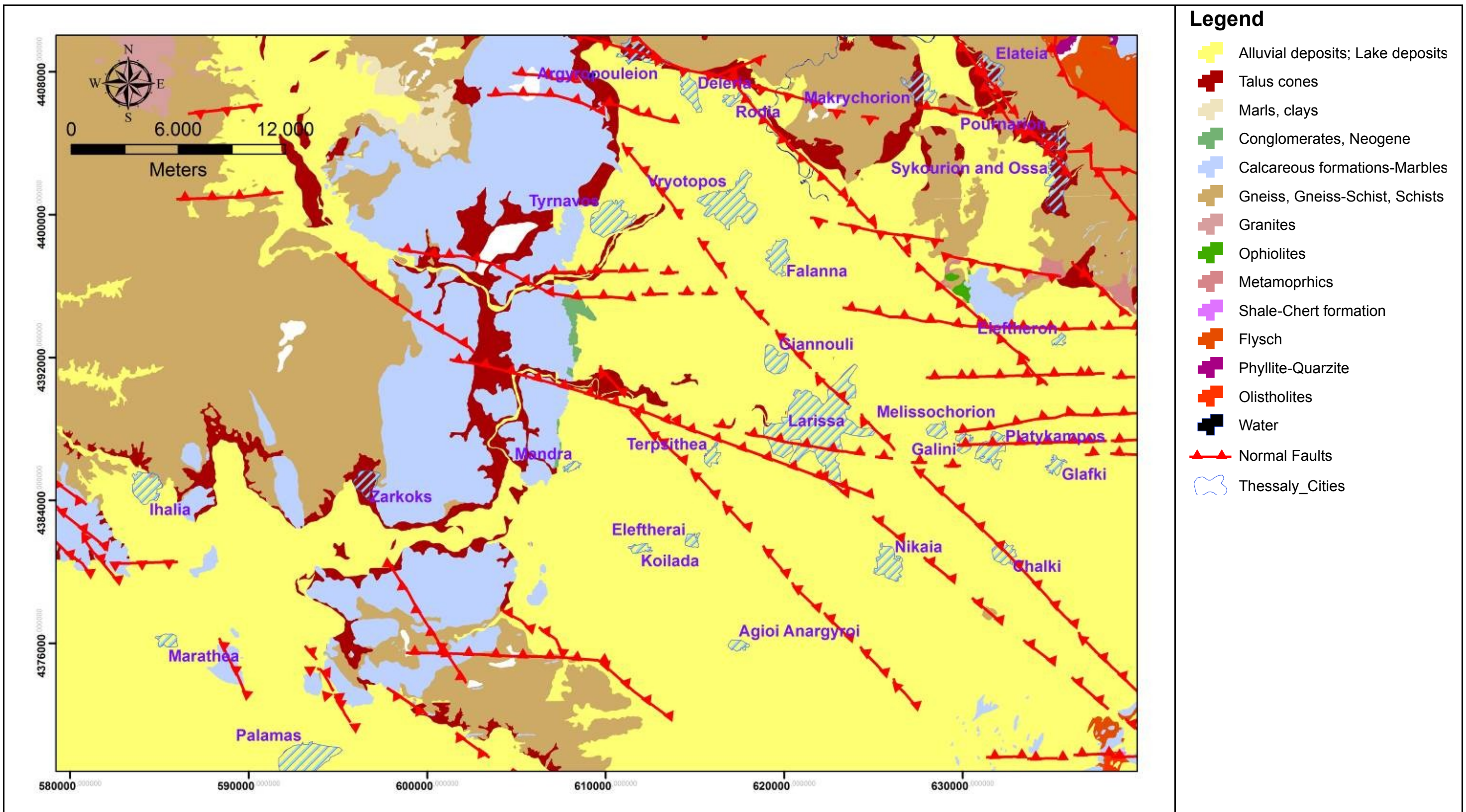

Figure222. Geological map of Thessaly, map is modified from IGME. Faults are modified from the results of previous studies.

5.2.1. The role of lithology type

The formations of the study area can generally be grouped into two categories; the first includes recent Post-Alpine deposits while the second concerns old Paleozoic rocks.

The geological formations are then grouped into three classes taking into account their lithology, consolidation, origin and age.

The first class includes recent loose alluvial deposits of Quaternary age. The second class consists of old consolidated talus cones, scree and torrent terraces material of Pleistocene and Miocene age. The third class is composed of middle Triassic, Jurassic and metamorphic systems, and old (Paleozoic) massif metamorphic rocks such as schists, gneisses and amphibolites of the metamorphic system of the Pelagoniki geotectonic zone.

5.2.1.1. First class

Alluvial deposits (al), Quaternary age. This formation consists mostly of loose fluvial material derived from the erosion over the Pinios River and its tributaries' catchments and deposited at the Thessaly alluvial plain. The thickness of this formation is not the same over the entire plain. Probably close to the borders with the older rocks of Palaeozoic and Neogene age the thickness is less. Alluvial deposits are particularly prone to subsidence due to the fact that they consist mostly of recent loose river-transported and deposited sediments. This formation occupies the southwestern part, and an extensive area of the central part of the study area.

Fluvio-lacustrine deposits (Pt2), Larissa basin. These consist mainly of clays and sands with intercalation of coarse-grained material of various thicknesses. The age of these deposits is Pleistocene. They occur at the northwestern settlements of the study area. It is considered that fine-grained deposits (clays and sand) show a trend of subsidence.

Terrestrial fluvio-torrential deposits (Pl-Pt), Pontio Pliocene-Pleistocene age. These overlie lacustrine and fluvio-lacustrine deposits consisting of sandy-clay material and loam with dispersed angular and rounded pebbles of different origin with intercalation of loose/semi-loose breccio conglomerates. Lacustrine deposits consist of marls, marl sandstones, micro- and macro-breccio conglomerates. The maximum thickness of this formation according to the geological mapping of IGME is approximately 100 m.

5.2.1.2. Second class

Old talus cones, scree and torrent terraces material (Qsc-CS, Ms) Pleistocene age. This formation occurs mainly at the borders of the alluvial plains and rarely on mountain massifs. It consists of coarse-grained material with pebbles of various sizes, consolidated, usually with carbonate cement. Terrace heights range up to approximately 20 m. Transgressive polygenic compact conglomerates pass upwards to thick-bedded micro-brecciated grey limestone.

5.2.1.3. Third class

Middle Triassic, Jurassic (Tm-J.mr). Marbles, crystalline, coarse, medium or fine-grained, overlie the rocks of the metamorphic system, with a thickness of approximately 30 m.

Mica schists (Pz-Tm.sch) of Paleozoic Middle Triassic age belong to the Pelagonian geotectonic zone. They constitute the upper members of the neopaleozoic-lower-middle Triassic formations.
Mica-schists, gneiss schists and amphibolites (Pzn-Tm-sch.mi) of Lower-Middle Triassic age of the Pelagonian geotectonic zone.

Gneisses (mainly bimicaceous) (Pz.gn), Pelagonian geotectonic zone, Paleozoic (Precarboniferous) age. These occur in the form of compact banks with a strong gneissic character and locally granitic texture. Usually, they are light-colored, greenish to whitish with a milky appearance of the feldspar components and sometimes presenting an augen structure. The proportion of femic minerals fluctuates widely from place to place and from bank to bank. Therefore, they sometimes appear to be leucocratic and sometimes Socratic.

Blue schists, gneiss-schists, gneisses and prasinites (Sch) of the blue schists class which belongs to the Pelagonian geotectonic zone. These petrographic types alternate vertically and laterally, with local predominance of either one of them.

Crystalline mica, chlorite, schist gneisses, intercalations, marbles and quartzites (Pt sh). The age of this formation is Triassic and it belongs to the metamorphic system of Geopaliagoniki geotectonic zone.

5.2.2. Ascending track 143

A similar context of discussion to that used to discuss the spatial correlation between fault movements and ground deformation will be used here also to create and discuss the impact of lithology type on ground deformation.

5.2.2.1. Interferometric stacking

Results of the interferometric stacking technique, ascending track, were depicted previously in Figure 10 within the processing chapter. The type of lithology, minimum and maximum rate of ground deformation subsidence and uplift for each settlement are depicted in Table 47.

Table 47. Type of lithology and minimum and maximum deformation rates in LOS of interferometric stacking, 1995- 2008

I.d	Settlements	Type of lithology	Minimum Subsidence mm	Maximum Subsidence mm	Mean	Minimum Uplift mm	Maximum Uplift mm	Mean
1	Larissa	al	-0.46	-2.961	-1.710	0.545	6.636	3.276
2	Giannouli	al	-0.131	-3.574	-1.852	0.729	4.171	2.450
3	Chalki	al	-0.208	-2.842	-1.494	0.42	4.317	2.039
4	Eleftheron	al	-0.225	-0.225	-0.224	0.556	3.526	2.066
5	Falanna	al	-0.05	-2.34	-1.048	0.539	3.691	1.832
6	Melissochorion	al	-0.126	-1.713	-0.859	0.567	3.278	1.657
7	Galini	al	-0.10	-0.11	-0.105	0.694	3.692	1.973
8	Platykampos	al	-0.138	-3.027	-1.441	0.527	3.463	1.770
9	Glafki	al	-0.874	-0.9	-0.84	0.146	3.67	1.855
10	Itea	al	-0.131	-4.313	-1.947	0.463	2.946	1.575
11	Fyllon	al	-0.01	-1.108	-0.551	0.326	3.502	1.598
12	Palamas	al	-0.216	-1.676	-0.945	0.348	3.306	1.497
13	Marathea	al	-0.664	-1.545	-1.104	0.211	2.891	1.371
14	Nikaia	al	-0.75	-0.8	-0.77	0.217	4.269	1.850
15	Terpsithea	pl-pt	Null	Null	Null	0.218	4.384	2.688
16	Tyrnavos	Pt2	-0.178	-1.447	-0.735	0.14	2.504	1.052
17	Rodia	Pt2	-0.036	-0.752	-0.393	0.284	3.109	1.254
18	Mandra	Pl-Pt	-0.086	-1.587	-0.681	0.127	1.316	0.665
19	Eleftherai	Pl-Pt	-0.34	-0.35	-0.345	0.267	3.365	1.552

al= Alluvial. Pt2= Fluvio-lacustrine deposits. pl-pt= Terrestrial fluvio-torrential deposit.

Figure 223 shows the correlation between lithology type and minimum and maximum deformation rate in LOS. The plot indicates that no significant differences were observed between uplifts for settlements which overlie the same type of lithology (alluvial). However, significant differences between the rate of uplift of the same lithology type, and the terrestrial fluvio-torrential deposits of the settlements of Mandra and Eleftherai are clearly observed. Additionally, the plot points to significant differences between the subsidences at settlements which have the same type of lithology (alluvial). Furthermore, the rate of subsidence at settlements which overlie a lithology of fluvio-lacustrine deposits and the terrestrial fluvio-torrential deposits at the settlements of Tyrnavos, Rodia, Mandra and Elftherai is less than the rate of subsidence at settlements which overlie the alluvial type of lithology. The greatest subsidence is observed within the settlements of Itea, Larissa, Giannouli and Platykampos.

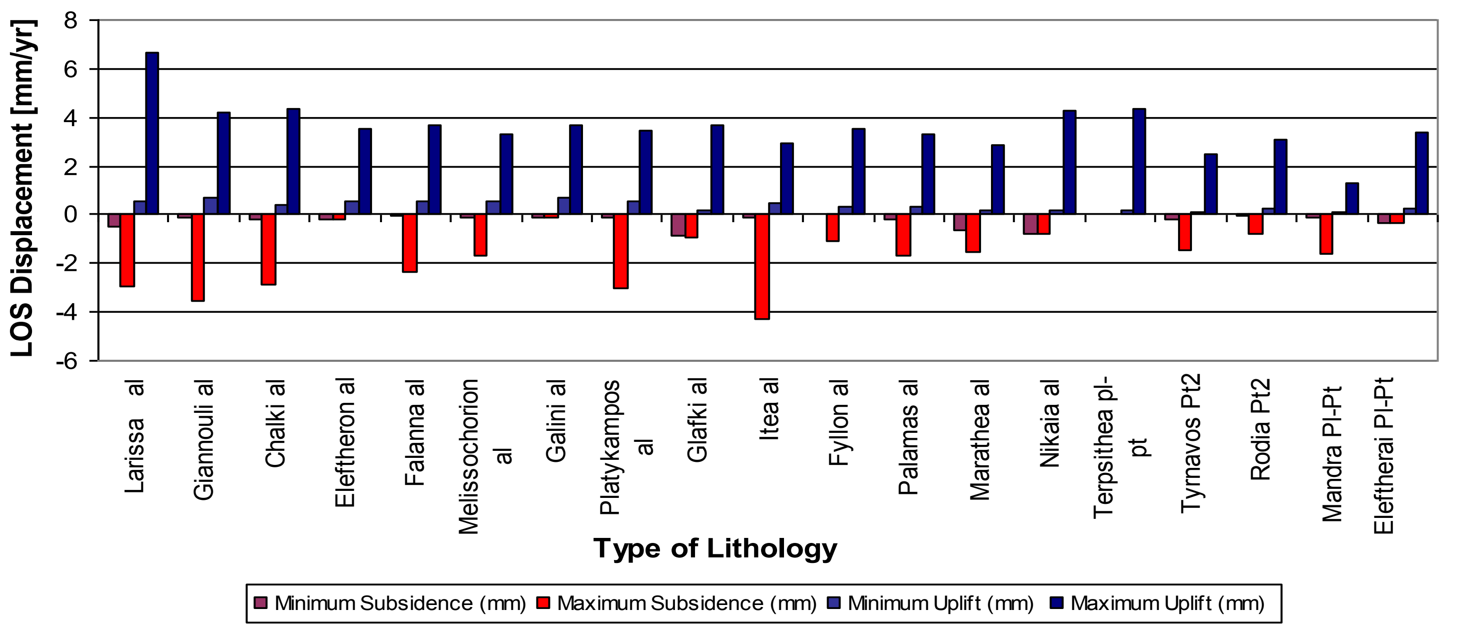

Figure.223 Minimum and maximum deformation rates in LOS of interferometric stacking 1995-2008 of 19 settlements corresponding to type of lithology.

The impact of lithology type on ground deformation will be discussed separately for each settlement.

5.2.2.1.1. Larissa

Results of interferometric stacking patterns and total deformation rate estimation during the period June 1995 – March 2008 for Larissa were shown previously in Figure 129.

Ground deformation results within the settlement of Larissa indicate that the subsidence varies in the range -0.46 – -2.961 mm/year, while uplift varies in the range 0.545 – 6.636 mm/year.

Subsidence within Larissa settlement may be attributed to the impact of the lithology type, which is alluvial, since it consists mostly of loose fluvial material, which is less coherent than other types of material and consequently shows more vulnerability. However, the impact of the hanging walls of the normal fault traces, as mentioned before, should not be ignored.

5.2.2.1.2. Giannouli

Results of interferometric stacking patterns and total deformation rate estimation during the period June 1995 – March 2008 for Giannouli were shown earlier in Figure 130.

Ground deformation results within Giannouli settlement indicate that the subsidence varies in the range -0.131 – -3.574 mm/year, while uplift varies in the range 0.729 – 4.171 mm/year.

Subsidence may be attributed to the impact of the lithology type, which is alluvial. Evidence for this explanation is the location of the settlement southwest of a normal fault trace in the side of the footwall.

5.2.2.1.3. Chalki

Results of interferometric stacking patterns and total deformation rate estimation during the period June 1995 – March 2008 for Chalki were shown earlier in Figure 131.

Ground deformation results within the settlement of Chalki indicate that the subsidence varies in the range -0.208 – -2.842 mm/year, while uplift varies in the range0.42 and 4.317 mm/year.

Subsidence may be attributed to the alluvial lithology. However, the impact of the hanging wall of a normal fault trace should not be ignored.

5.2.2.1.4. Eleftheron

Results of interferometric stacking patterns and total deformation rate estimation during the period June 1995 – March 2008 for Eleftheron were shown in Figure 132.

Ground deformation results within Eleftheron settlement indicate that the subsidence varies in the range -0.225 – -0.225 mm/year, while uplift varies in the range 0.556 – 3.526 mm.

Subsidence in the southwestern part of the settlement may be attributed either to the alluvial lithology or to its location south of the hanging wall of a normal fault trace.

The subsidence deformation which is observed in the middle and northwest of the settlement may be attributed to the alluvial lithology for the fact that this part of the settlement is located south of the footwall of a normal fault trace.

5.2.2.1.5. Falanna

Results of interferometric stacking patterns and total deformation rate estimation during the period June 1995 – March 2008 for Falanna were shown in Figure 133.

Ground deformation results within Falanna settlement indicate that the subsidence varies in the range -0.05 – -2.34 mm/year, while the uplift varies in the range 0.539 – 3.691 mm/year.
Subsidence may be attributed to the impact of the alluvial lithology. However, the location of the settlement in the eastern part of the hanging wall of a normal fault trace should not be ignored.

5.2.2.1.6. Melissochorion

Results of interferometric stacking patterns and total deformation rate estimation during the period June 1995 – March 2008 for Melissochorion were shown in Figure 134.

Ground deformation results within Melissochorion settlement indicate that the subsidence varies in the range -0.126 – -1.713 mm/year, while uplift varies in the range 0.567 – 3.278 mm/year.

Subsidence may be attributed to the alluvial lithology. However, the location of the settlement east of the hanging wall of a normal fault trace should not be ignored.

5.2.2.1.7. Galini

Results of interferometric stacking patterns and total deformation rate estimation during the period June 1995 – March 2008 for Galini were shown in Figure 135.

Ground deformation results within Galini settlement indicate that the subsidence varies in the range -0.10 – - 0.11 mm/year, while uplift varies in the range 0.694 – 3.692 mm/year.

Subsidence may be attributed to the impact of the alluvial lithology. The evidence for this is the existence of subsidence in the side of the footwall of a normal fault trace which crosses the settlement from the south. However, the location of the area affected by this type of deformation in the side of the hanging wall of a normal fault trace, in addition to the impact of the alluvial type of lithology, should not be ignored.

5.2.2.1.8. Platykampos

Results of interferometric stacking patterns and total deformation rate estimation during the period June 1995 – March 2008 for Platykampos were shown in Figure 136.

Ground deformation results within Platykampos settlement indicate that the subsidence varies in the range -0.138 – -3.027 mm/year, while uplift varies in the range 0.527 – 3.463 mm/year.

Subsidence in the northern part may be attributed to the impact of the alluvial lithology type. However, the impact of the hanging wall of a normal fault trace should not be ignored. Additionally, the evidence of the influence the alluvial lithology is the existence of subsidence in the middle and southern parts of the settlement in the side of the footwall of a normal fault trace.

5.2.2.1.9. Glafki

Results of interferometric stacking patterns and total deformation rate estimation during the period June 1995 – March 2008 for Glafki were shown in Figure 137.

Ground deformation results within Glafki settlement indicate that the subsidence varies in the range -0.874 – -0.9 mm/year, while uplift varies in the range0.146 – 3.67 mm/year.
Subsidence may be attributed to the impact of the alluvial lithology type.

5.2.2.1.10. Itea

Results of interferometric stacking patterns and total deformation rate estimation during the period June 1995 – March 2008 for Itea were shown in Figure 138.

Ground deformation results within Itea settlement indicate that the subsidence varies in the range -0.131 – -4.313 mm/year, while uplift varies in the range 0.463 – 2.946 mm/year.

Subsidence may be attributed to the impact of the alluvial lithology type. However, the location of the settlement southwest of the hanging wall of a normal fault trace should not be ignored.

5.2.2.1.11. Fyllon

Results of interferometric stacking patterns and total deformation rate estimation during the period June 1995 – March 2008 for Fyllon were shown in Figure 139.

Ground deformation results within Fyllon settlement indicate that the subsidence varies in the range -0.01 – -1.108 mm/year, while uplift varies in the range 0.326 – 3.502 mm/year.
Subsidence may be attributed to the impact of the alluvial lithology.

5.2.2.1.12. Palamas

Results of interferometric stacking patterns and total deformation rate estimation during the period June 1995 – March 2008 for Palamas were shown in Figure 140.

Ground deformation results within Palamas settlement indicate that the subsidence varies in the range -0.216 – -1.676 mm/year, while uplift varies in the range 0.348 – 3.306 mm/year.

Subsidence patterns are observed over almost all the settlement may be attributed to the impact of the alluvial lithology.

5.2.2.1.13. Marathea

Results of interferometric stacking patterns and total deformation rate estimation during the period June 1995 – March 2008 for Marathea were shown in Figure 141.

Ground deformation results within Marathea settlement indicate that the subsidence varies in the range -0.664 – -1.545 mm/year, while uplift varies in the range 0.211 – 2.891 mm/year.

Subsidence patterns are observed distributed all over the settlement. Subsidence may be attributed to the impact of the alluvial lithology.

5.2.2.1.14. Nikaia

Results of interferometric stacking patterns and total deformation rate estimation during the period June 1995 – March 2008 for Nikaia were shown in Figure 142.

Ground deformation results within Nikaia settlement indicate that the subsidence varies in the range -0.5 – -0.8 mm/year, while uplift varies in the range 0.217 – 4.269 mm/year.
Subsidence may be attributed to the impact of the alluvial lithology.

5.2.2.1.15. Terpsithea

Results of interferometric stacking patterns and total deformation rate estimation during the period June 1995 – March 2008 for Terpsithea were shown in Figure 143.

Ground deformation results within Terpsithea settlement indicate that the subsidence is null, while uplift varies in the range 0.218 – 4.384 mm/year.

The low deformation rate of subsidence may be attributed to the type of lithology, since it is terrestrial fluvio-torrential deposits consisting of sandy-clay material and loam with dispersed angular and rounded pebbles of different origin with intercalation of loose/semi-loose breccio conglomerates. In consequence, this type of material may be more resistant to subsidence, although the previous reasoning relating to the impact of the footwall of a normal fault trace is more likely.

5.2.2.1.16. Tyrnavos

Results of interferometric stacking patterns and total deformation rate estimation during the period June 1995 – March 2008 for Tyrnavos were shown in Figure 144.

Ground deformation results within Tyrnavos settlement indicate that the subsidence varies in the range -0.178 – -1.447 mm/year, while uplift varies in the range 0.14 – 2.504 mm/year.

The settlement overlies fluvio-lacustrine deposits and this lithology type may be more resistant to subsidence. In consequence, the previous reasoning relating to the impact of the hanging wall of a normal fault trace is more likely. Additionally, the low deformation rate of subsidence of the following settlement of Rodia may support this reasoning.

5.2.2.1.17. Rodia

Results of interferometric stacking patterns and total deformation rate estimation during the period June 1995 – March 2008 of Rodia were shown in Figure 145.

Ground deformation results within Rodia settlement indicate that the subsidence varies in the range -0.036 – -0.752 mm/year, while uplift varies in the range 0.284 – 3.109 mm/year.

Note the low deformation rate of subsidence in spite of the location of the settlement south and west of the hanging walls of two normal fault traces. This may be attributed to the fluvio-lacustrine deposits lithology which may be more resistant to subsidence.

5.2.2.1.18. Mandra

Results of interferometric stacking patterns and total deformation rate estimation during the period June 1995 – March 2008 for Mandra were shown in Figure 146.

Ground deformation results within Mandra settlement indicate that the subsidence varies in the range -0.086 – -1.587 mm/year, while uplift varies in the range 0.127 – 1.316 mm/year.

Subsidence may be attributed to the impact of the terrestrial fluvio- torrential deposits lithology type.

5.2.2.1.19. Eleftherai

Results of interferometric stacking patterns and total deformation rate estimation during the period June 1995 – March 2008 for Eleftherai were shown in Figure 147.

Ground deformation results within Eleftherai settlement indicate that the subsidence varies in the range -0.34 – -0.35 mm/year, while uplift varies in the range 0.267 – 3.365 mm/year.
Subsidence may be attributed to the impact of the terrestrial fluvio- torrential deposits lithology type.

5.2.2.2. Conventional SAR Interferometry

The results of the conventional technique of SAR interferometry, which was discussed previously to reveal the impact of fault movement, were used once again to reveal the impact of lithology type on ground deformation. A single interferogram with a short temporal period (19960228_19960403) was chosen within this track, as depicted previously in Figure 148. However, within this case we will not discuss the deformation rate along the cross-section but will discuss the distribution of subsidence deformation patterns across the settlement of Larissa corresponding to the impact of the alluvial deposits lithology type.

Subsidence patterns have been observed to the east, north-east, and south-west. The subsidence deformation rate is -62 mm/LOS during this period. Subsidence could not be attributed to the impact of the single factor of the lithology type during this short temporal period. This is because there are several nested and interconnected factors such as lithology, fault movements, type of clay minerals and amount of precipitation during this period. However, the lithology of alluvial deposits may constitute an essential co-factor that activates other factors in spite of the short period. Figure 224 shows the amount of precipitation during 1996, indicating the precipitation during the period of the interferogram, which varies in the range 56 – 61.9 mm.

It is worth mentioning that the amount of precipitation plays an important role by causing a swelling process in clay minerals, as mentioned before in the chapter on groundwater. In consequence, although the type of lithology under discussion is alluvial deposits, nevertheless the observed distribution of subsidence patterns does not cover the whole settlement, which may be attributed to the activation of the swelling process of clay minerals during this period. Evidence for this explanation is the greater distribution of subsidence patterns observed in the summer interferogram of the descending track. Furthermore, the largest rate of subsidence is shown in the following.

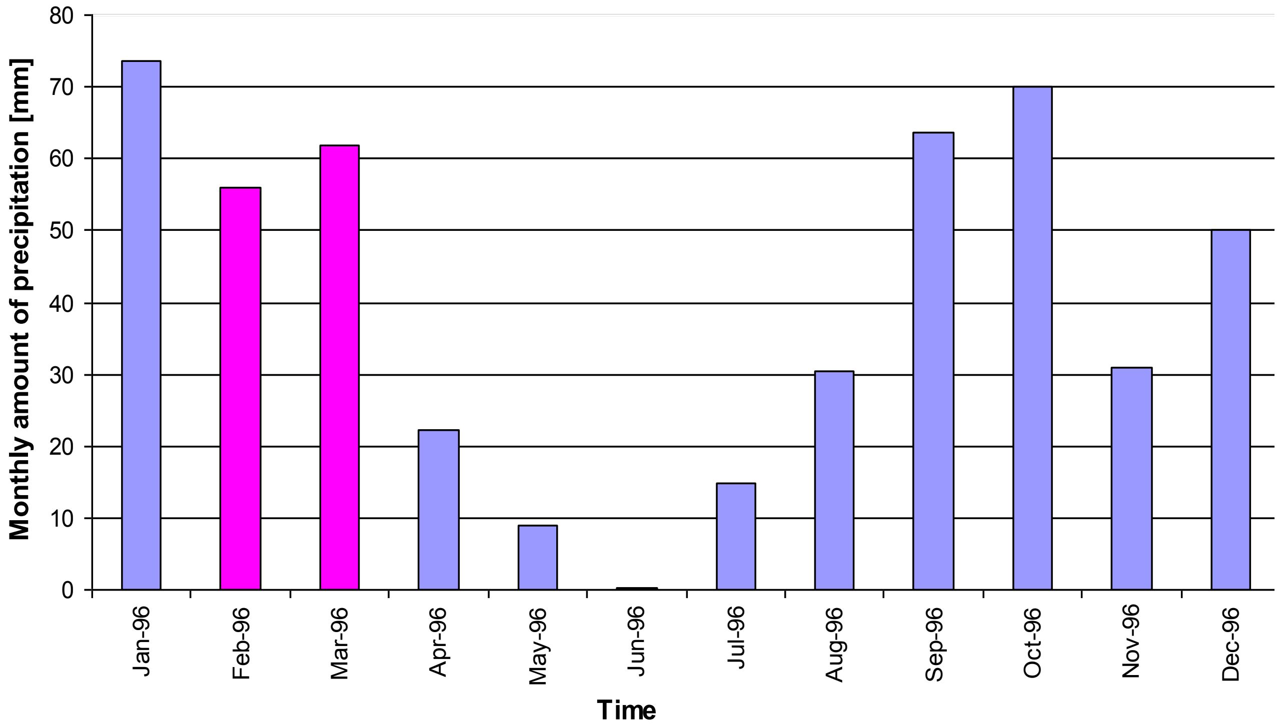

Figure.224 Monthly amount of precipitation during 1996 including precipitation during the period of the interferogram.

5.2.2.3. Persistent Scatterers Interferometry (PSI)

The same candidate points and a similar context to that used previously in discussion of the impact of fault movements on ground deformation will be used here to verify the impact of lithology type on ground deformation.

5.2.2.3.1. Minimum deformation rate

5.2.2.3.1.1. Larissa

Candidate point number 46536 was selected as representative of the minimum deformation rate. A plot of this point was depicted previously in Figure 150.

The deformation behavior of this candidate point through its time series begins with subsidence then changes to uplift, and thereafter changing status between subsidence and uplift is observed during April 2004 – December 2006. Subsidence may be attributed to the impact of the alluvial deposit lithology on ground deformation of this point. However, the location of the point in the side of the hanging wall of a normal fault trace should not be ignored.

5.2.2.3.1.2. Giannouli

Candidate point number 55991 was selected as representative of the minimum deformation rate. A plot of this point was depicted in Figure 152.

The deformation behavior of this point through its time series begins with subsidence then changes to uplift, and thereafter changing status between subsidence and uplift is observed during February 2004 – December 2006.

Subsidence may be attributed to the impact of the alluvial deposit lithology. A reasonable interpretation of this case is the location of the point in the side of the footwall of a normal fault trace.

5.2.2.3.1.3. Falanna

Candidate point number 80781 was selected as representative of the minimum deformation rate. A plot of this point was depicted in Figure 154.

The deformation behavior of this point through its time series begins with subsidence then changes to uplift.

Subsidence may be attributed to the impact of the alluvial deposit lithology on ground deformation through the behavior of this point. However, the location of the point in the side of the hanging wall of a normal fault trace should not be ignored.

5.2.2.3.1.4. Melissochorion

Candidate point number 35637 was selected as representative of the minimum deformation rate. A plot of this point was depicted in Figure 156.

The deformation behavior of this point through its time series begins with subsidence then changes to uplift, and thereafter changing status between subsidence and uplift is observed during August 2003 – December 2006.

Subsidence may be attributed to the impact of the alluvial deposit lithology type on ground deformation. However, the location of the point in the side of the hanging wall of a normal fault trace should not be ignored.

5.2.2.3.1.5. Galini

Candidate point number 31580 was selected as representative of the minimum deformation rate. A plot of this point was depicted in Figure 158.

The deformation behavior of this point through its time series shows continuous fluctuation between subsidence and uplift.

Subsidence may be attributed to the impact of the alluvial deposit lithology. Evidence for this reasoning is the location of the point in the side of the footwall of a normal fault trace. Additionally, the continuous fluctuation between subsidence and uplift during the time series may be attributed to the influence of the footwall activity of the normal fault trace and other factors, one of which is the type of lithology.

5.2.2.3.1.6. Platykampos

Candidate point number 32889 was selected as representative of the minimum deformation rate. A plot of this point was depicted in Figure 160.

The deformation behavior of this point through its time series begins with uplift then changes to subsidence, and changing status between subsidence and uplift is observed during April 2003 – December 2006.

Subsidence may be attributed to the impact of the alluvial deposit lithology type. However, the location of point in the side of the hanging wall of a normal fault trace should not be ignored. It is worth mentioning that the fluctuation of the histogram may be attributed to not only the impact of the lithology but also the influence of the hanging wall on one side and the footwall on the other.

5.2.2.3.1.7. Glafki

Candidate point number 26115 was selected as representative of the minimum deformation rate. A plot of this point was depicted in Figure 162.

The deformation behavior of this point through its time series begins with subsidence then changes to uplift, but fluctuation between subsidence and uplift can be observed during May 2000 – September 2004.

Subsidence may be attributed to the impact of the alluvial deposit lithology type. In addition, the fluctuation between subsidence and uplift may be attributed to the respective influence of the footwall of the normal fault trace activity and the type of lithology.

5.2.2.3.1.8. Tyrnavos

Candidate point number 116381 was selected as representative of the minimum deformation rate. A plot of this point was depicted in Figure 164.

The deformation behavior of this point through its time series begins with subsidence then changes to uplift, but a changing status between subsidence and uplift can be observed during September 2004 – December 2006.

Subsidence may be attributed to the impact of the fluvio-lacustrine deposits lithology. However, this type of lithology may be more resistant to subsidence. Furthermore, the location of the point in the side of the hanging wall of a normal fault trace should not be ignored.

5.2.2.3.1.9. Rodia

Candidate point number 142796 was selected as representative of the minimum deformation rate. A plot of this point was depicted in Figure 166.

The deformation behavior of this point through its time series begins with subsidence then changes to uplift.

Subsidence may be attributed to the fluvio-lacustrine deposits lithology. However, this type of lithology may be more resistant to subsidence. Furthermore, the location of the point south and west of the hanging walls of two normal fault traces should not be ignored.

5.2.2.3.1.10. Mandra

Candidate point number 41227 was selected as representative of the minimum deformation rate. A plot of this point was depicted in Figure 168.

The deformation behavior of this point through its time series begins with uplift then changes to subsidence.

Subsidence may be attributed to the impact of the terrestrial fluvio- torrential deposits lithology type. The appearance of subsidence at the end of the time series may be attributed to the decreasing or fading of the impact of the footwall, as a consequence of which the impact of that lithology type has begun.

5.2.2.3.1.11. Eleftherai

Candidate point number 28093 was selected as representative of the minimum deformation rate. A plot of this point was depicted in Figure 170.

The deformation behavior of this point through its time series begins with uplift then changes to subsidence.

Subsidence may be attributed to the impact of the terrestrial fluvio- torrential deposits lithology type. The appearance of subsidence at the end of the time series may be attributed to the decreasing or fading of the impact of the footwall, as a consequence of which the impact of that lithology type has begun. It is worth mentioning that the deformation behavior of this point is similar to that of the selected point at Mandra.

5.2.2.3.1.12. Terpsithea

Candidate point number 36831 was selected as representative of the minimum deformation rate. A plot of this point was depicted in Figure 172.

The deformation behaviour of this point through its time series begins with subsidence then changes to uplift.

Subsidence may be attributed to the lithology of terrestrial fluvio-torrential deposits. However, the impact of the hanging wall of a normal fault trace to the southwest should not be ignored.

5.2.2.3.1.13. Nikaia

Candidate point number 19557 was selected as representative of the minimum deformation rate. A plot of this point was depicted in Figure 174.

The deformation behavior of this point through its time series begins with subsidence then changes to uplift.
Subsidence may be attributed to the impact of the alluvial lithology type.

5.2.2.3.2. Maximum deformation rate

5.2.2.3.2.1. Larissa

Candidate point number 31912 was selected as representative of the maximum deformation rate. A plot of this point was depicted in Figure 176.

The deformation behavior of this point through its time series begins with subsidence then changes to uplift.

Subsidence may be attributed to the impact of the alluvial deposit lithology type. However, the location of the point in the side of the hanging wall of a normal fault trace should not be ignored.

5.2.2.3.2.2. Giannouli

Candidate point number 50363 was selected as representative of the maximum deformation rate. A plot of this point was depicted in Figure 177.

The deformation behavior of this point through its time series begins with subsidence then changes to uplift.

Subsidence may be attributed to the impact of the alluvial deposit lithology type. An acceptable reason for this is the location of the point in the side of the footwall of a normal fault trace.

5.2.2.3.2.3. Falanna

Candidate point number 80751 was selected as representative of the maximum deformation rate. A plot of this point was depicted in Figure 178.

The deformation behavior of the point through its time series begins with subsidence then changes to uplift, and changing status from uplift to subsidence can be observed in August 2004.
Subsidence may be attributed to the impact of the alluvial deposit lithology type. However, the location of the point in the side of the hanging wall of a normal fault

trace should not be ignored. It is worth mentioning that the behavior of the point's minimum deformation rate is similar to the behavior of its maximum deformation rate. This may confirm the impact of the lithology type on the ground deformation.

5.2.2.3.2.4. Melissochorion

Candidate point number 35184 was selected as representative of the maximum deformation rate. A plot of this point was depicted in Figure 179.
The deformation behavior of this point through its time series begins with subsidence then changes to uplift.

Subsidence may be attributed to the impact of the alluvial deposit lithology. However, the location of the point in the side of the hanging wall of a normal fault trace should not be ignored. It is worth mentioning that the behavior of the point's minimum deformation rate is similar to the behavior of its maximum deformation rate. This may confirm the impact of the lithology type on the ground deformation.

5.2.2.3.2.5. Galini

Candidate point number 32014 was selected as representative of the maximum deformation rate. A plot of this point was depicted in Figure 180.

The deformation behavior of the point through its time series begins with subsidence then changes to uplift.

Subsidence may be attributed to the impact of the alluvial deposit lithology type. Evidence for this reasoning is the location of the point in the side of the footwall of a normal fault trace. Additionally, the uplift at the end of the time series may relate to the effect of the footwall after the fading of the lithology's influence.

5.2.2.3.2.6. Platykampos

Candidate point number 29080 was selected as representative of the maximum deformation rate. A plot of this point was depicted in Figure 181.

The deformation behavior of the point through its time series begins with subsidence then changes to uplift.

Subsidence may be attributed to the impact of the alluvial deposit lithology type. Evidence for this reasoning is the location of the point in the side of the footwall of a normal fault trace. Additionally, the uplift at the end of the time series may relate to the beginning of the footwall's effect after the fading of the lithology's influence.

5.2.2.3.2.7. Glafki

Candidate point number 26720 was selected as representative of the maximum deformation rate. A plot of the point was depicted in Figure 182.
The deformation behavior of this point during its time series begins with subsidence then changes to uplift.

Subsidence may be attributed to the impact of the alluvial deposit lithology type. In addition, the stability of subsidence during April 2004 – September 2004 after the beginning of uplift may be attributed to the respective influences of the footwall of a normal fault trace and the type of lithology.

5.2.2.3.2.8. Tyrnavos

Candidate point number 106597 was selected as representative of the maximum deformation rate. A plot of this point was depicted in Figure 183.

The deformation behavior of this point through its time series begins with uplift then changes to subsidence.

Subsidence may be attributed to the impact of the fluvio-lacustrine deposits lithology. However, this type of lithology may be more resistant to subsidence. Furthermore, the location of the point southwest of the footwall of a normal fault trace should not be ignored.

Consequently, subsidence at the end of the time series may be attributed to the fading impact of the footwall, and then the influence of the lithology.

5.2.2.3.2.9. Rodia

Candidate point number 144160 was selected as representative of the maximum deformation rate. A plot of the point was depicted in Figure 184.

The deformation behavior of the point through its time series begins with uplift then changes to subsidence.

Subsidence may be attributed to the fluvio-lacustrine deposits lithology. However, this type of lithology may be more resistant to subsidence. In consequence, this may be the first reason for the uplift deformation behavior at the beginning of time series. Secondly, this uplift may be attributed to a local impact factor, given the location of the point south and west of the hanging walls of two normal fault traces.

5.2.2.3.2.10. Mandra

Candidate point number 41360 was selected as representative of the maximum deformation rate. A plot of this point was depicted in Figure 185.

The deformation behavior of this point through its time series begins with subsidence then changes to uplift.

Subsidence may be attributed to the impact of the terrestrial fluvio-torrential deposits lithology. However, the appearance of uplift at the end of the time series may be attributed to the decreasing or fading impact of the lithology and the consequent impact of footwall activity.

5.2.2.3.2.11. Eleftherai

Candidate point number 27935 was selected as representative of the maximum deformation rate. A plot of this point was depicted in Figure 186.

The deformation behavior of this point through its time series begins with subsidence then changes to uplift.
Subsidence may be attributed to the impact of the terrestrial fluvio-torrential deposits lithology.

5.2.2.3.2.12. Terpsithea

Candidate point number 38866 was selected as representative of the maximum deformation rate. A plot of this point was depicted in Figure 187.

The deformation behavior of the point through its time series begins with subsidence then changes to uplift.

Subsidence may be attributed to the lithology of terrestrial fluvio-torrential deposits. Evidence for this reasoning is the location of the point in the side of the footwall of a normal fault trace.

5.2.2.3.2.13. Nikaia

Candidate point number 20809 was selected as representative of the maximum deformation rate. A plot of this point was depicted in Figure 188.

The deformation behavior of this point through its time series begins with subsidence then changes to uplift. Subsidence may be attributed to the impact of the alluvial lithology type.

5.2.3. Descending track 279

5.2.3.1. Interferometric Stacking

Results of the interferometric stacking technique of the descending track were depicted previously in Figure 22 within the processing chapter. The type of lithology, minimum and maximum rate of ground deformation - subsidence and uplift - of each settlement are depicted in Table 48.

Table 48. Type of lithology and minimum and maximum deformation rates in LOS of interferometric stacking, 1992- 2010

I.d	Settlement	Type of lithology	Minimum subsidence mm	Maximum subsidence mm	Mean	Minimum uplift mm	Maximum uplift mm	Mean
1	Larissa	al	-0.385	-3.048	-1.716	0.276	3.442	1.859
2	Giannouli	al	-0.432	–4.580	-5.012	0.06	0.612	0.336
3	Chalki	al	-0.518	-1.342	-0.927	0.50	0.524	0.512
4	Eleftheron	al	-0.086	-0.862	-0.474	0.044	0.365	0.204
5	Falanna	al	-0.09	-2.524	-1.307	0.191	0.957	0.574
6	Melissochorion	al	-0.02	-1.286	-0.653	0.065	0.86	0.462
7	Galini	al	-0.321	-0.969	-0.645	0.087	0.319	0.203
8	Platykampos	al	0	-1.859	-0.929	0.52	0.53	0.525
9	Glafki	al	-0.23	-1.336	-0.391	Null	Null	Null
10	Itea	al	-0.7	-3.744	-2.222	0.671	1.338	1.00
11	Fyllon	al	-0.219	-1.009	-1.228	Null	Null	Null
12	Palamas	al	-0.11	-2.205	-1.157	0.58	0.6	0.59
13	Marathea	al	-0.058	-1.054	-0.556	Null	Null	Null
14	Nikaia	al	-0.018	-2.142	-1.08	0.445	0.784	0.614
15	Terpsithea	pl-pt	-0.088	-0.849	-0.468	0.046	0.358	0.202
16	Tyrnavos	Pt2	-0.195	-2.157	-1.167	0.36	0.37	0.365
17	Rodia	Pt2	-0.003	-1.425	-0.714	0.348	1.28	0.814
18	Mandra	pl-pt	-0.58	-1.731	-1.155	Null	Null	Null
19	Eleftherai	pl-pt	-0.273	-1.207	-0.74	0.028	0.303	0.165

al= alluvial Pt2= fluvio-lacustrine deposits pl-pt= terrestrial fluvio-torrential deposits

Figure 225 shows the correlation between lithology type and minimum and maximum deformation rate in LOS. The plot indicates that no significant differences are observed between the uplift of settlements which overlie the same type of lithology (alluvial). However, a significant difference is observed between the uplift at Larissa and uplift of other settlements of the same and different types of lithology. It is worth mentioning that this result is similar to the result for the ascending track.

Furthermore, significant differences between the subsidence at settlements which have the same and different type of lithology are observed. The greatest subsidence is observed at Itea, Larissa, and Falanna and it is noticeable that this result is similar to the result for the ascending track.

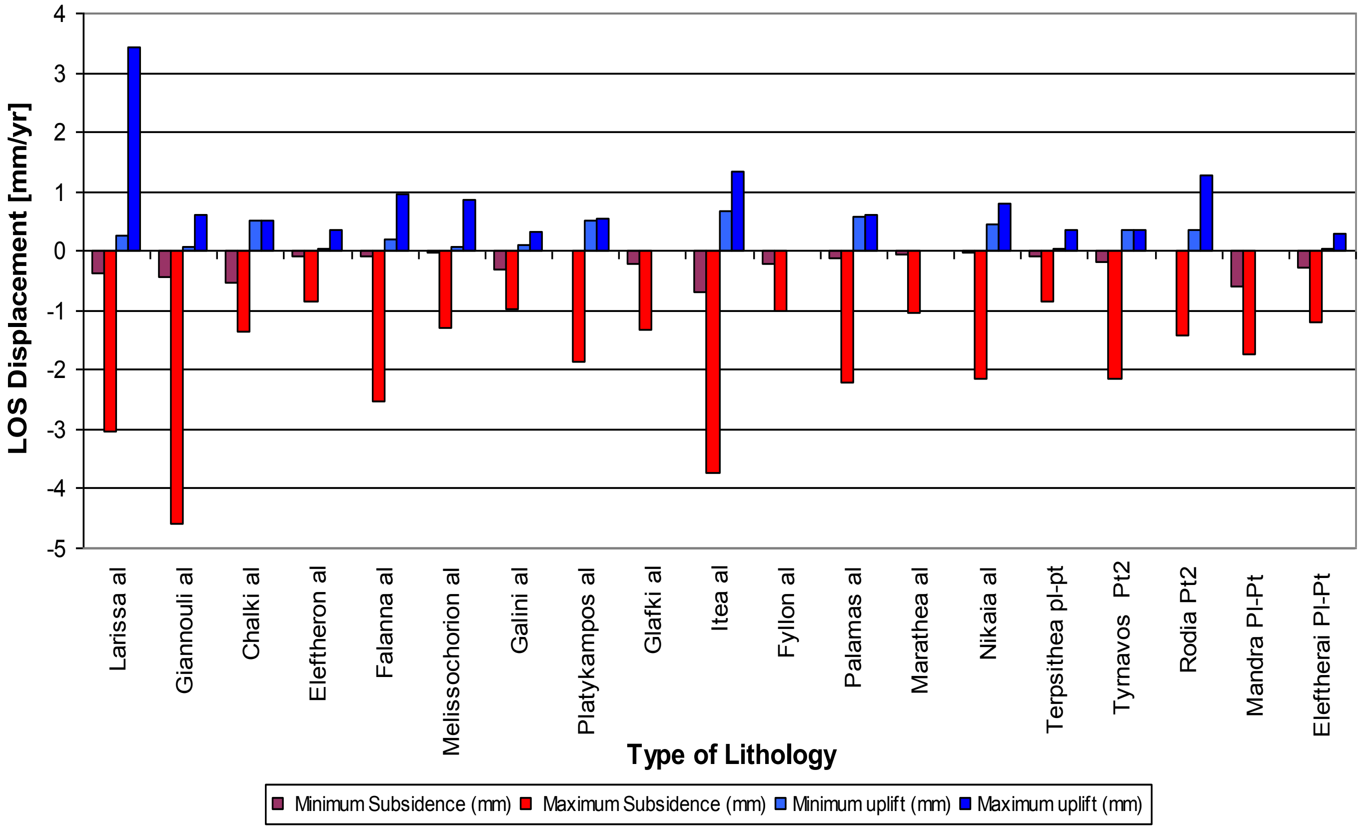

Figure225. Minimum and maximum deformation rates in LOS of interferometric stacking 1992-2010 of nineteen settlements corresponding to type of lithology.

The impact of lithology type on ground deformation will be discussed separately for each settlement.

5.2.3.1.1. <u>Larissa</u>

Results of interferometric stacking patterns and total deformation rate estimation during the period November 1992 – October 2010 for Larissa were shown in Figure 189.

Ground deformation results within the settlement of Larissa indicate that subsidence varies in the range -0.385 – -3.048 mm/year. Uplift varies in the range 0.276 – 3.442 mm/year.

Subsidence within Larissa settlement may be attributed to the alluvial lithology, since it consists mostly of loose fluvial material which is less coherent than other types of material and consequently shows more vulnerability.
Furthermore, the impact of the hanging walls of normal fault traces, as mentioned before, should not be ignored.

5.2.3.1.2. Giannouli

Results of interferometric stacking patterns and total deformation rate estimation during the period November 1992 – October 2010 for Giannouli were shown in Figure 190.

Ground deformation results within Giannouli settlement indicate that the subsidence varies in the range -0.432 – -4.580 mm/year, while uplift varies in the range 0.06 – 0.612 mm/year.

Subsidence may be attributed to the impact of the alluvial lithology. Evidence for this reasoning is the location of the settlement southwest of a normal fault trace in the side of the footwall.

5.2.3.1.3. Chalki

Results of interferometric stacking patterns and total deformation rate estimation during the period November 1992 – October 2010 for Chalki were shown in Figure 191.

Ground deformation results within the settlement of Chalki indicate that the subsidence varies in the range -0.518 – -1.342 mm/year, while uplift varies in the range 0.50 – 0.524 mm/year.

Subsidence may be attributed to the impact of the alluvial lithology. Evidence for this reasoning is the location of subsidence patterns which have been observed in the side of the footwall of a normal fault trace.

5.2.3.1.4. Eleftheron

Results of interferometric stacking patterns and total deformation rate estimation during the period November 1992 – October 2010 for Eleftheron were shown in Figure 192.

Ground deformation results within Eleftheron settlement indicate that the subsidence varies in the range -0.086 – -0.862 mm/year while uplift varies in the range 0.044 – 0.365 mm/year. Subsidence may be attributed to the alluvial lithology. However, the location of the settlement north of the hanging wall of a normal fault trace should not be ignored.

5.2.3.1.5. Falanna

Results of interferometric stacking patterns and total deformation rate estimation during the period November 1992 – October 2010 for Falanna were shown in Figure 193.

Ground deformation results within Falanna settlement indicate that the subsidence varies in the range -0.09 – -2.524 mm/year, while uplift varies in the range 0.191 – 0.957 mm/year.

Subsidence may be attributed to the alluvial lithology. However, the location of the settlement east of the hanging wall of a normal fault trace should not be ignored.

5.2.3.1.6. Melissochorion

Results of interferometric stacking patterns and total deformation rate estimation during the period November 1992 – October 2010 for Melissochorion were shown in Figure 194.

Ground deformation results within Melissochorion settlement indicate that the subsidence varies in the range -0.02 – -1.286 mm/year, while uplift varies in the range 0.065 – 0.86 mm/year.

Subsidence may be attributed to the alluvial lithology. However, the location of the settlement east of the hanging wall of a normal fault trace should not be ignored.

5.2.3.1.7. Galini

Results of interferometric stacking patterns and total deformation rate estimation during the period November 1992 – October 2010 for Galini were shown in Figure 195.

Ground deformation results within Galini settlement indicate that the subsidence varies in the range -0.321 – -0.969 mm/year, while uplift varies in the range 0.087 – 0.319 mm/year.

Subsidence may be attributed to the alluvial lithology. However, the location of the area affected by this type of deformation in the side of the hanging wall of a normal fault trace should not be ignored.

5.2.3.1.8. Platykampos

Results of interferometric stacking patterns and total deformation rate estimation during the period November 1992 – October 2010 for Platykampos were shown in Figure 196.

Ground deformation results within Platykampos settlement indicate that the subsidence varies in the range 0 – -1.859 mm/year, while uplift varies in the range 0.52 – 0.53 mm/year.

Subsidence may be attributed to the alluvial lithology. However, the location of the area affected by this type of deformation in the side of the hanging wall of a normal fault trace should not be ignored.
Additionally, slight subsidence is observed in the southwestern part of the settlement in the side of the footwall of a normal fault trace. This may confirm the influence of the alluvial lithology on the ground deformation.

5.2.3.1.9. Glafki

Results of interferometric stacking patterns and total deformation rate estimation during the period November 1992 – October 2010 for Glafki_were shown in Figure 197.

Ground deformation results within Glafki settlement indicate that the subsidence varies in the range -0.23 – -1.336 mm/year, while uplift was null, although it is observed as pattern phenomena.
Subsidence may be attributed to the alluvial deposits lithology.

5.2.3.1.10. Itea

Results of interferometric stacking patterns and total deformation rate estimation during the period November 1992 – October 2010 for Itea were shown in Figure 198.

Ground deformation results within Itea settlement indicate that the subsidence varies in the range -0.7 – -3.744 mm/year, while uplift varies in the range0.671 – 1.338 mm/year.

Subsidence may be attributed to the alluvial lithology. However, the location of the settlement southwest of the hanging wall of a normal fault trace should not be ignored.

5.2.3.1.11. Fyllon

Results of interferometric stacking patterns and total deformation rate estimation during the period November 1992 – October 2010 for Fyllon were shown in Figure 199.

Ground deformation results within Fyllon settlement indicate that the subsidence varies in the range -0.219 – -1.009 mm/year, while uplift was null. Subsidence may be attributed to the impact of the alluvial deposit lithology.

5.2.3.1.12. Palamas

Results of interferometric stacking patterns and total deformation rate estimation during the period November 1992 – October 2010 for Palamas were shown in Figure 200.

Ground deformation results within Palamas settlement indicate that the subsidence varies in the range -0.11 – -2.205 mm/year, while uplift varies in the range 0.58 – 0.6 mm/year. Subsidence may be attributed to the impact of the alluvial deposit lithology.

5.2.3.1.13. Marathea

Results of interferometric stacking patterns and total deformation rate estimation during the period November 1992 – October 2010 for Marathea were shown in Figure 201.

Ground deformation results within Marathea settlement indicate that the subsidence varies in the range -0.058 – -1.054 mm/year, while uplift is null. Subsidence may be attributed to the impact of the alluvial deposits lithology. Evidence for this reasoning is the location of the settlement west of the footwall of a normal fault trace,

5.2.3.1.14. Nikaia

Results of interferometric stacking patterns and total deformation rate estimation during the period November 1992 – October 2010 for Nikaia were shown in Figure 202.

Ground deformation results within Nikaia settlement indicate that the subsidence varies in the range -0.018 – -2.142 mm/year, while uplift varies in the range 0.445 – 0.784 mm/year.

Subsidence may be attributed to the impact of the alluvial deposits lithology. However, the location of the settlement northeast of the hanging wall of a normal fault trace should not be ignored.

5.2.3.1.15. Terpsithea

Results of interferometric stacking patterns and total deformation rate estimation during the period November 1992 – October 2010 for Terpsithea were shown in Figure 203.

Ground deformation results within Terpsithea settlement indicate that the subsidence varies in the range -0.088 – - 0.849 mm/year, while the uplift varies in the range 0.046 – 0.358 mm/year.

The low rate of subsidence deformation may be attributed to the type of lithology since it is terrestrial fluvio-torrential deposits. Consequently, this type of material may be more resistant to subsidence. Furthermore, the low subsidence may be attributed more to the effect of the footwall of a normal fault trace north of the settlement than the effect of the lithology type or the hanging wall of another normal fault trace to the northeast.

5.2.3.1.16. Tyrnavos

Results of interferometric stacking patterns and total deformation rate estimation during the period November 1992 – October 2010 for Tyrnavos were shown in Figure 204.

Ground deformation results within Tyrnavos settlement indicate that the subsidence varies in the range -0.195 – -2.157 mm/year, while uplift varies in the range 0.36 – 0.37 mm/year.

Subsidence may be attributed to the impact of the fluvio-lacustrine deposits lithology. However, the location of the settlement north of the hanging wall of a normal fault trace should not be ignored.

5.2.3.1.17. Rodia

Results of interferometric stacking patterns and total deformation rate estimation during the period November 1992 – October 2010 for Rodia were shown in Figure 205.

Ground deformation results within Rodia settlement indicate that the subsidence varies in the range -0.003 – -1.425 mm/year, while the uplift varies in the range 0.348 – 1.28 mm/year.

Subsidence may be attributed to the fluvio-lacustrine deposits lithology. However, the location of the settlement south and west of the hanging walls of two normal fault traces should not be ignored.

5.2.3.1.18. Mandra

Results of interferometric stacking patterns and total deformation rate estimation during the period November 1992 – October 2010 for Mandra were shown in Figure 206.

Ground deformation results within Mandra settlement indicate that the subsidence varies in the range -0.58 – -1.731 mm/year, while uplift is null.

Subsidence may be attributed to the impact of terrestrial fluvio-torrential deposits lithology. Evidence for this reasoning is the location of the settlement south and west of the footwalls of two normal fault traces. It is noticeable that these normal fault traces may have a low impact during this period.

5.2.3.1.19. Eleftherai

Results of interferometric stacking patterns and total deformation rate estimation during the period November 1992 – October 2010 for Eleftherai were shown in Figure 207.

Ground deformation results within Eleftherai settlement indicate that the subsidence varies in the range -0.273 – -1.207 mm/year, while uplift varies in the range 0.028 – 0.303 mm/year.

Subsidence may be attributed to the impact of the terrestrial fluvio-torrential deposits lithology. Evidence of this reasoning is the location of the settlement southwest of the footwall of a normal fault trace.

5.2.3.2. Conventional SAR Interferometry

The results of the conventional technique of SAR interferometry which were discussed previously to reveal the impact of fault movements has been used once again to reveal the impact of lithology type on ground deformation. A single interferogram with a short temporal period (19980802_19980906) was chosen within this track, as depicted previously in Figure 21.

However, in this case we will not discuss the deformation rate along the cross-section but will discuss the distribution of subsidence deformation patterns across the settlement of Larissa corresponding to the impact of alluvial deposits lithology type, as was done previously with the ascending track.

Subsidence patterns have been observed distributed over the middle, northern, eastern, south-eastern, and south-western parts of the settlement. Noticeably more explicit subsidence patterns were observed compared with the winter interferogram of the ascending track.

The subsidence deformation rate is -163 mm/LOS during this period. Subsidence could not be attributed to the sole impact of the type of lithology during the short temporal period, as mentioned before with the ascending track. Figure 226 shows the precipitation during 1998 and indicates the amount of precipitation during the period of the interferogram, which varies in the range 0.7 – 37.1 mm.

As mentioned before, the amount of precipitation plays an important role through its impact on the swelling process of clay minerals. Conversely, it plays an important role also by activating shrinkage of clay minerals during periods of drought or low precipitation. Consequently, not only the impact of the alluvial lithology type on ground deformation, but also the amount of precipitation plays an important affective factor. Thus, because of the low amount of precipitation, shrinkage of clay minerals was activated. Subsidence is then the natural result of the shrinkage process. Therefore, several factors have influenced the ground deformation. However, the alluvial lithology may well constitute an essential co-factor to activate the other factors.

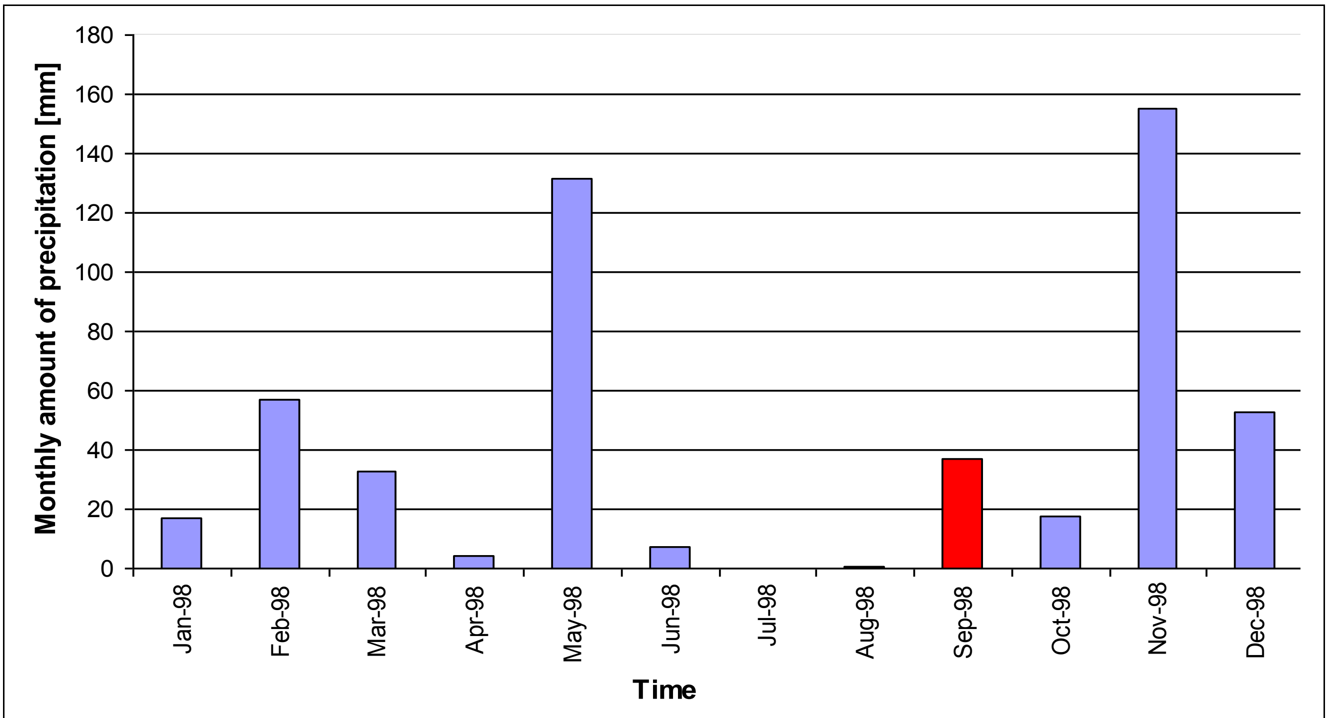

Figure.226 Monthly amount of precipitation during 1998, indicating precipitation during the period of the interferogram.

5.2.3.3. Persistent Scatterers Interferometry

5.2.3.3.1. Minimum deformation rate

5.2.3.3.1.1. Larissa

Candidate point number 171091 was selected as representative of the minimum deformation rate. A plot of this point was depicted in Figure 210.

The ground deformation behavior of this point through its time series begins with uplift then changes to subsidence.

Subsidence may be attributed to the impact of the alluvial deposit lithology. However, the location of the point in the side of the hanging wall of a normal fault trace should not be ignored. Evidence of the lithology's impact is the location of the point southwest of another normal fault trace in the side of the footwall. However, the uplift at the beginning of the time series may be attributed to the impact of this footwall. Furthermore, the impact of the lithology may have begun after the fading of the footwall's effect.

5.2.3.3.1.2. Giannouli

Candidate point number 166001 was selected as representative of the minimum deformation rate. A plot of this point was depicted in Figure 212.

The ground deformation behavior of the point through its time series begins with uplift then changes to subsidence.

Subsidence may be attributed to the impact of the alluvial deposit lithology. A reason for this interpretation is the location of the point in the side of the footwall of a normal fault trace. Additionally, the appearance of subsidence after uplift behavior may be attributed to the fading effect of the footwall of the normal fault trace.

5.2.3.3.1.3. Nikaia

Candidate point number 225264 was selected as representative of the minimum deformation rate. A plot of this point was depicted in Figure 214.

The ground deformation behavior of this point through its time series begins with uplift then changes to subsidence.

Subsidence may be attributed to the impact of the alluvial lithology. Evidence for this reasoning is the location of the point south of a normal fault in the side of the footwall. Additionally, the appearance of subsidence after uplift behavior may be attributed to the fading effect of the footwall of the normal fault trace. However, the impact of the hanging wall of another normal fault trace southwest of the point should not be ignored.

5.2.3.3.1.4. Terpsithea

Candidate point number 202683 was selected as representative of the minimum deformation rate. A plot of this point was depicted in Figure 216.

The ground deformation behavior of the point through its time series begins with uplift then changes to subsidence.

Subsidence may be attributed to the lithology of terrestrial fluvio-torrential deposits. However, the impact of the hanging wall of a normal fault trace southwest of the point should not be ignored.

5.2.3.3.2. Maximum deformation rate

5.2.3.3.2.1. Larissa

Candidate point number 185001 was selected as representative of the maximum deformation rate. A plot of this point was depicted in Figure 218.

The ground deformation behavior of this point through its time series begins with subsidence then changes to uplift.

Subsidence may be attributed to the impact of the alluvial deposit lithology. However, the location of the point north of a normal fault trace in the side of the hanging wall should not be ignored.

5.2.3.3.2.2. Giannouli

Candidate point number 163240 was selected as representative of the maximum deformation rate. A plot of this point was depicted in Figure 219.

The ground deformation behavior of the point through its time series begins with subsidence then changes to uplift.
Subsidence may be attributed to the impact of the alluvial deposit lithology.

5.2.3.3.2.3. Nikaia

Candidate point number 221761 was selected as representative of the maximum deformation rate. A plot of this point was depicted in Figure 220.

The ground deformation behavior of this point through its time series begins with subsidence then changes to uplift.

Subsidence may be attributed to the impact of the alluvial deposit lithology. However, the location of the point northeast of a normal fault trace in the side of the hanging wall should not be ignored.

5.2.3.3.2.4. Terpsithea

Candidate point number 204403 was selected as representative of the maximum deformation rate. A plot of this point was depicted in Figure 221.

The ground deformation behavior of this point through its time series begins with subsidence then changes to uplift.
Subsidence may be attributed to the lithology of terrestrial fluvio-torrential deposits. However, the impact of the hanging wall of a normal fault trace southwest of the point should not be ignored.

Chapter Six: Impact of soil on ground deformation

6.1. Introduction to Soil

Soil is an important element that has many uses, notably agricultural production and many others such as engineering constructions. Thus any adverse influence, either internal or external, on the body of the soil will have a negative impact on plant growth or production and on engineering structures. This chapter will focus on the study of the varieties of soil deformation, whether subsidence or uplift, by using SAR interferometry, and will illustrate the behavior of the soil deformation using statistical analysis, before discussing the parameters which have a major influence on this deformation.

(Soil Survey Staff, 1998) defines soil, like many common words, with several meanings. In its traditional meaning, soil is the natural medium for the growth of land plants, whether or not it has discernible soil horizons. This meaning is still the most common understanding of the word, and the greatest interest in soil is centered on this meaning. People consider soil important because it supports the plants that supply food, fibres, drugs, and other human needs, and because it filters water and recycles wastes. Soil covers the earth's surface as a continuum, except on bare rock, in areas of perpetual frost or deep water, or on the bare ice of glaciers. In this sense, soil has a thickness that is determined by the rooting depth of plants. Soil for the purposes of this text is a natural body comprised of solids (minerals and organic matter), liquid and gases, that occurs on the land surface, occupies space, and is characterized by one or both of the following: horizons, or layers, that are distinguishable from the initial material as a result of additions, losses, transfers, and transformations of energy and matter, or the ability to support rooted plants in a natural environment.

The upper limit of soil is the boundary between soil and air, shallow water, live lands, or plant materials that have not begun to decompose. Areas are not considered to have soil if the surface is permanently covered by water that is too deep (typically more than 2.5 m) for the growth of rooted plants. The horizontal boundaries of soil are areas where the soil grades to deep water, barren areas, rock, or ice. In some places the separation between soil and non-soil is so gradual that clear distinctions cannot be made.

The lower boundary that separates soil from the non-soil underneath is most difficult to define. Soil consists of the horizons near the earth's surface that, in contrast to the underlying parent material, have been altered by the interactions of climate, relief, and living organisms over time. Commonly, soil grades at its lower boundary to hard rock or to earthy materials that are virtually devoid of animals, roots, or other marks of biological activity. The lowest depth of biological activity, however, is difficult to discern and is often gradual. For the purposes of classification, the lower boundary of soil is arbitrarily set at 200 cm. In soils where either biological activity or current pedogenic processes extend to depths greater than 200 cm, the lower limit of the soil for classification purposes is still 200 cm.

6.2. Description of soil orders

It is worth mentioning the general characteristics or properties of each soil order that has been found within the study area. (Soil Survey Staff, 1998) and (Soil Survey Staff, 1999) describes in detail the properties of each order depending on field and laboratory analysis, as will be mentioned below. What will be referred to are the general and standard characteristics of each soil order.

6.2.1. Entisols

The unique properties common to Entisols are dominance of mineral soil materials and absence of distinct pedogenic horizons. The absence of features of any major set of soil-forming processes is itself an important distinction. There can be no accessory characteristics. Entisols are soils in the sense that they support plants, but they may be in any climate and under any vegetation. The absence of pedogenic horizons may be the result of: an inert parent material, such as quartz sand, in which horizons do not readily form; slowly soluble hard rock, such as limestone, which leaves little residue; insufficient time for horizons to form, as in recent deposits of ash or alluvium; occurrence on slopes where the rate of erosion exceeds the rate of formation of pedogenic horizons; recent mixing of horizons by animals or by ploughing to a depth of 1 or 2 m; or the spoils from deep excavations.

6.2.2. Inceptisols

Inceptisols have a wide range of characteristics and occur in a wide variety of climates. They can form in almost any environment, except for an arid environment, and the related differences in vegetation are great. Inceptisols can grade toward any other soil order and occur on a variety of landforms. The unique properties of Inceptisols are a combination of water available to plants for more than half the year, or more than 3 consecutive months during a warm season, and one or more pedogenic horizons of alteration or concentration with little accumulation of translocated materials other than carbonates or amorphous silica. In addition, Inceptisols do not have one or more of the unique properties of Mollisols, which are a thick, dark surface horizon and a high calcium supply, or the unique property of Andisols, which is the dominance of short-range-order minerals or Al-humus complexes.

6.2.3. Mollisols

The unique properties of Mollisols are a combination of a very dark brown to black surface horizon (mollic epipedon) that makes up more than one-third of the combined thickness of the categories of Soil Taxonomy 121 of the A and B horizons, or that is more than 25 cm thick and that has a structure that is not hard or very hard when dry; a dominance of calcium among the extractable cations in the A and B horizons; a dominance of crystalline clay minerals of moderate or high cation-exchange capacity; and less than 30 percent clay in some horizon above 50 cm if the soils have deep, wide cracks (1 cm or more wide) above this depth at some season. Mollisols characteristically form under grass in climates that have a moderate to pronounced seasonal moisture deficit. Some Mollisols, however, have formed under a forest ecosystem, and a few have formed in marshes or in marls in humid climates. Mollisols are extensive soils on the steppes of Europe, Asia, North America, and South America.

6.2.4. Vertisols

These soils have markers of processes related to the failure of soil materials along shear planes (slickensides). Because the soil material moves, the diagnostic properties have many accessory properties. Among them are a high bulk density when the soils are dry, low or very low hydraulic conductivity when the soils are moist, an appreciable rise and fall of the soil surface as the soils become moist and then dry, and rapid drying as a result of open cracks. The unique properties common to Vertisols are a high content of clay, pronounced changes in volume with changes in moisture, cracks that open and close periodically, and evidence of soil movement in the form of slickensides and of wedge-shaped structural aggregates that are tilted at an angle from the horizontal. The development of eluvial/illuvial horizons in some Vertisols suggests that pedoturbation is not rapid enough to preclude long-term translocation processes.

6.2.5. Alfisols

The soils in this order have markers of processes that translocate silicate clays without excessive depletion of bases and without dominance of the processes that lead to the formation of a mollic epipedon. The unique properties of Alfisols are a combination of an ochric or umbric epipedon, an argillic or natric horizon, a medium to high supply of bases in the soils, and water available to mesophytic plants for more than half the year or more than 3 consecutive months during a warm season. Because these soils have water and bases, they are, as a whole, intensively used.

According to the Exploratory Soil Survey and soil classification system (Soil Survey Staff, 1998) and (Soil Survey Staff, 1999), the classification of soil units of the study area (north part of Larissa) has been completed and 5 different orders were recognized (Alfisols, Entisols, Inceptisols, Mollisols, Vertisols (Figure 227). The soil properties of each order have been examined, such as texture, drainage, erosion and slope. Soil data has been manipulated using Arc GIS 9.3 software, and several maps, such as soil texture (depth 0 – 25 cm), soil drainage, slope, and erosion have been created (Figures 228 - 231).The soil data has been obtained from the (Institute of Soil Mapping and Classification of Larissa).

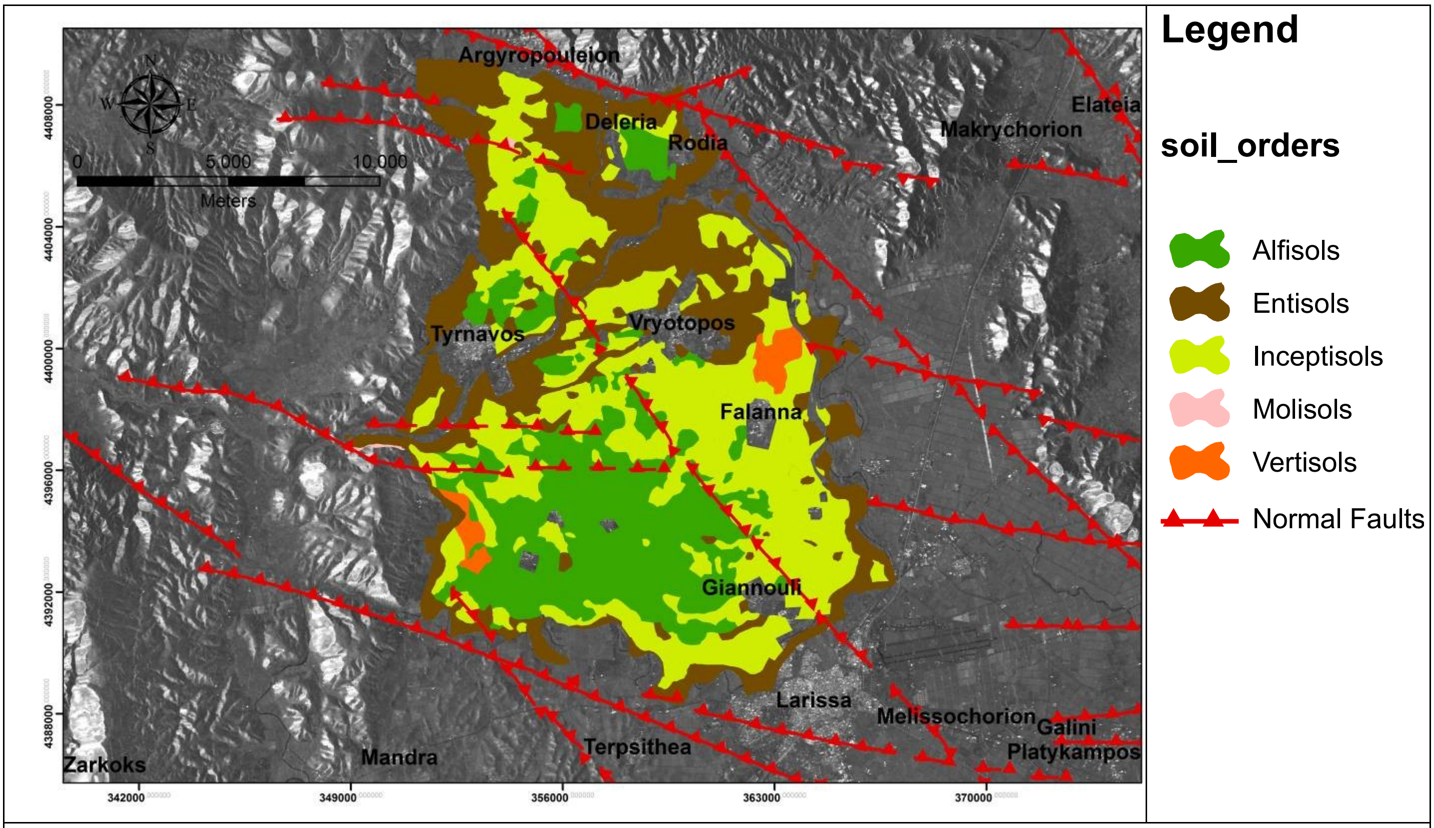

Figure227. Map of exploratory soil survey depicts the distribution of soil orders within the study area in the northern part of Larissa. Based on SLC of SAR image.

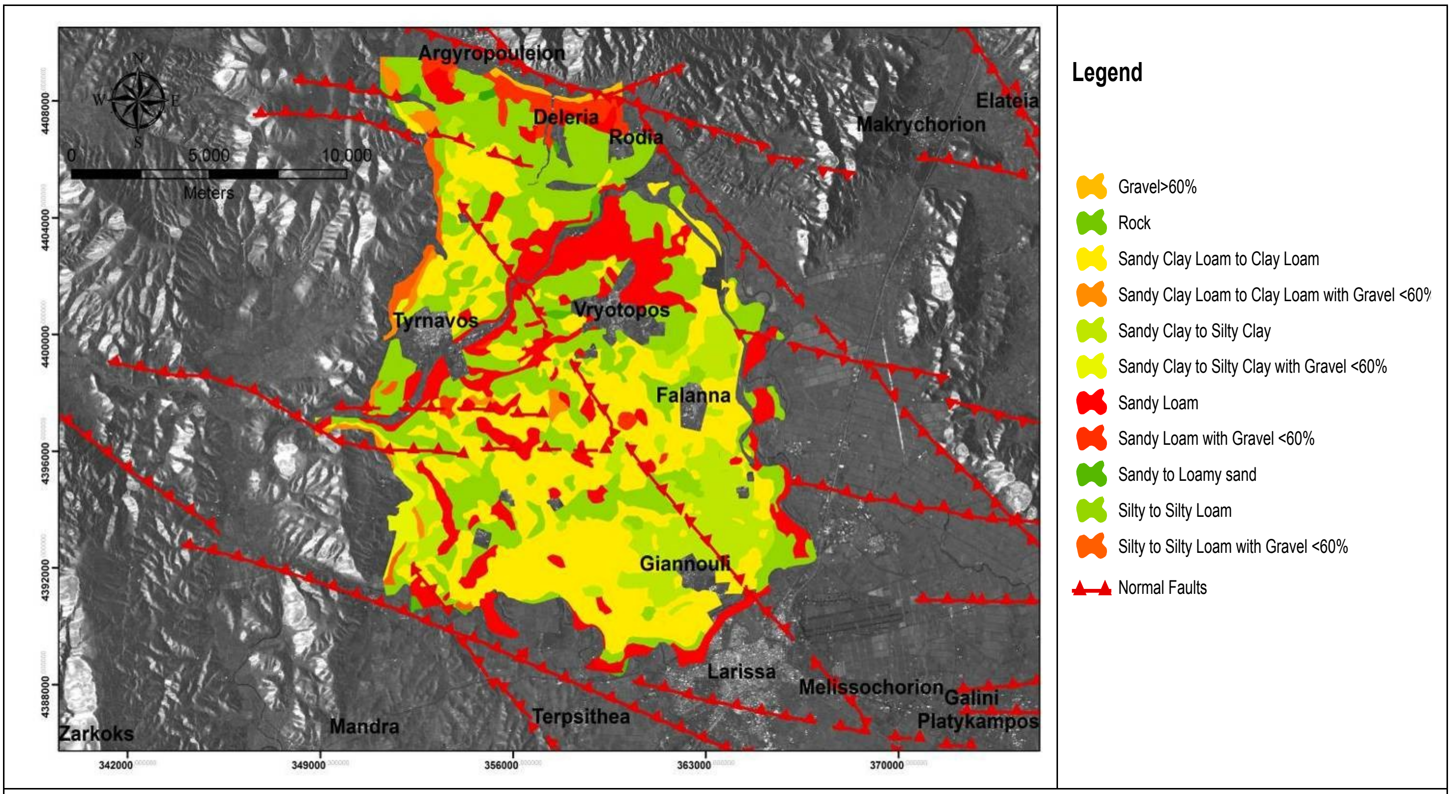

Figure228. Map of soil texture within 0-25 cm, within the study area in the northern part of Larissa. Based on SLC of SAR image.

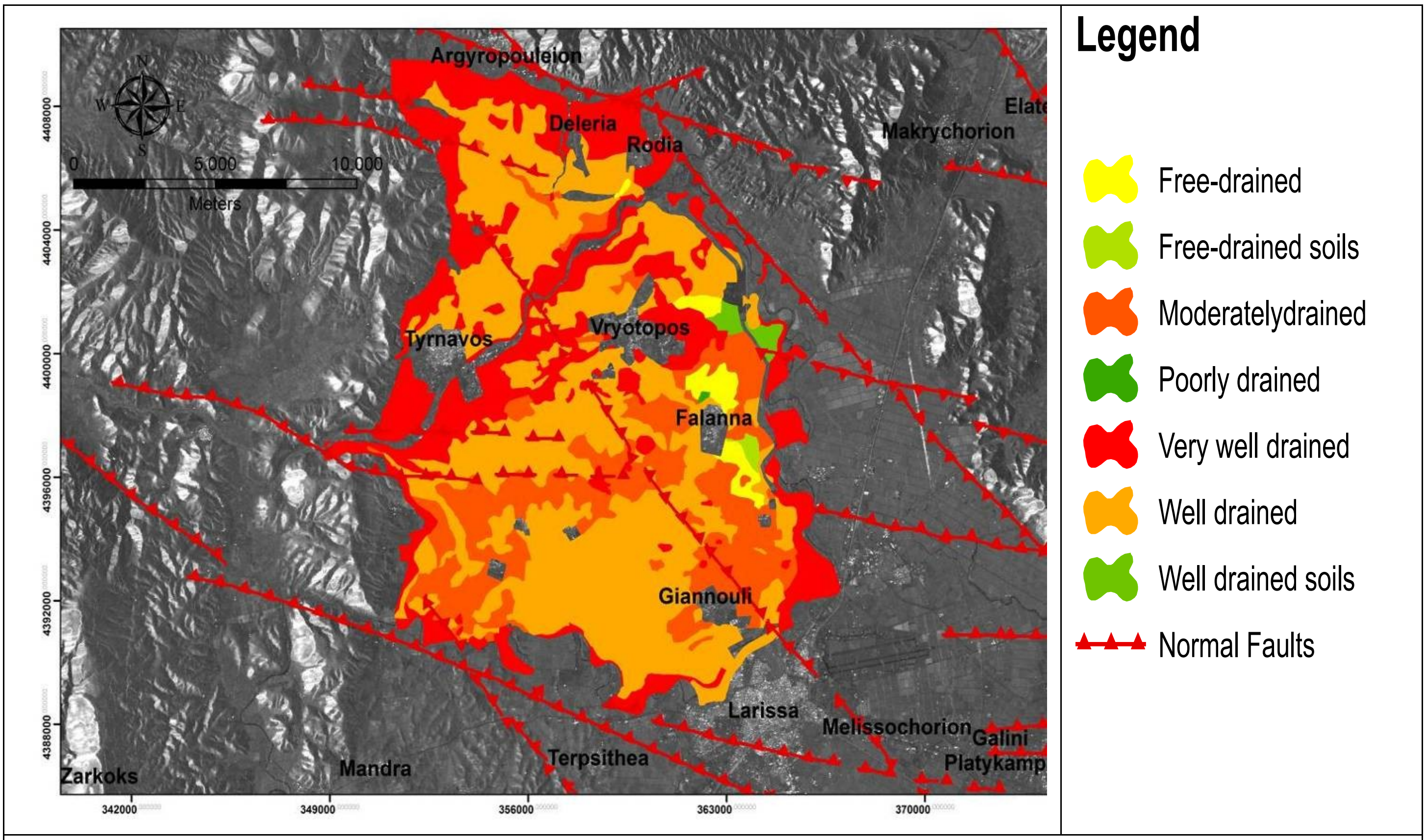

Figure.229 Map of soil drainage within the study area in the northern part of Larissa. Based on SLC of SAR image.

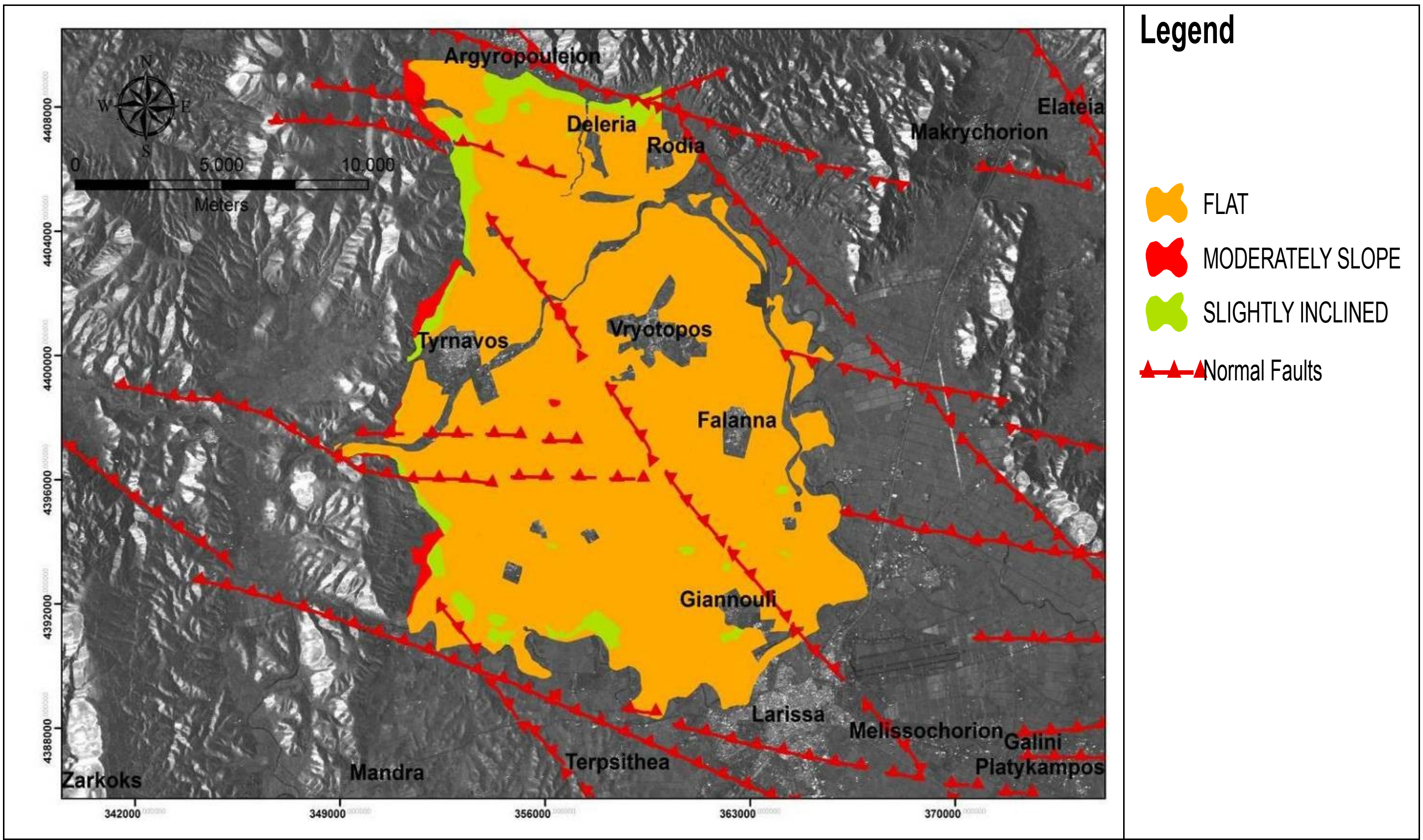

Figure230. Map of soil slope within the study area in the northern part of Larissa. Based on SLC of SAR image.

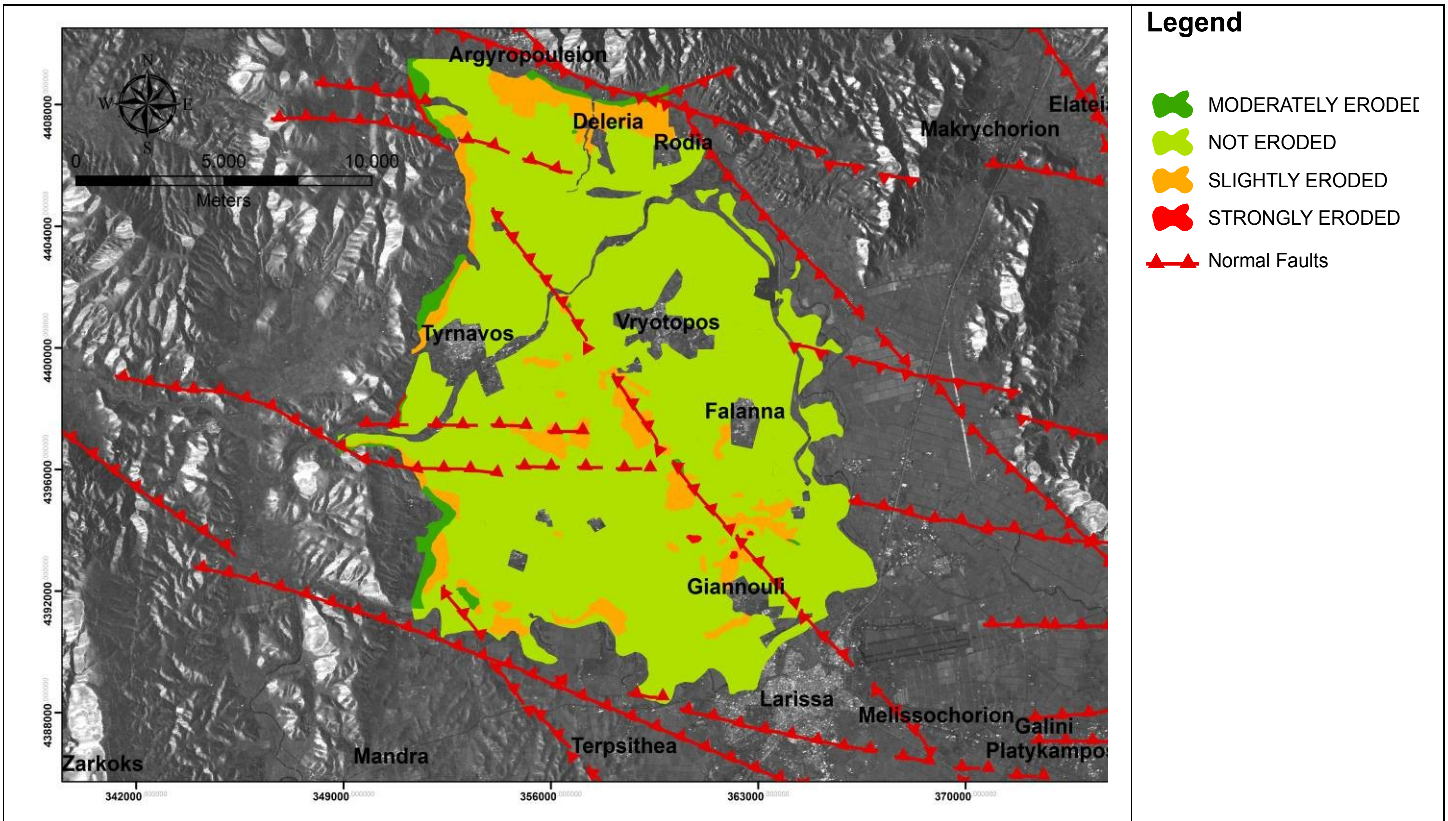

Figure231. Map of soil erosion within the study area in the northern part of Larissa. Based on SLC of SAR image.

6.3. Soil deformation

Soil deformation implies any change in the shape or the volume of the soil body, produced by any external or internal impact, that has negative effects on plant growth and water movement inside the pores as a result of deformations in the size of the soil pores. This will also have an impact on the shape and stability of buildings in the engineering context.

(Fakhri et al., 2012) mentioned that the identification of soil deformation is rather difficult because it is a complicated open system that changes rapidly with time. It is true that all kinds of agricultural operations and characteristics such as tillage irrigation, different cultivation methods and plant growth affect the soil properties and thereafter may as a result have an effect on the structure of the soil body both vertically and horizontally. Nevertheless, the technique of Persistent Scatterers Interferometry (PSI) needs some prerequisites in order to be fulfilled. Firstly, stable "targets" that are not affected by acquisition geometry must be found, and not affected by temporal decorrelation. To find stable points, the decision was to choose stable points inside the field to display reliable phase information. These points should be inside every soil mapping unit so as to express the properties of the soil or soil deformation.

The goal of this chapter is to examine the potential of using the PSI technique to identify the deformation of soil vertically (i.e., line of sight, LOS), and to study the statistical behavior of deformation for each candidate point through the statistical time series schemes of the data set, as well as the effect of soil type on its deformation.

After identifying the soil order classes in the northern part of Larissa, only points which were within the soil map of the study area were finally chosen. Specifically, one point for each soil class has been selected to identify the behaviour of soil deformation for all the area of each mapping unit, for the reason that the characteristics and properties of each soil class as a mapping unit are almost similar, so one point is enough to express the behaviour of the whole soil mapping unit for each soil class.

6.4. Results and discussion

6.4.1. Ascending track 143

The total number of candidate points within the non-urban area was 96, with a deformation rate varying in the range -15 – 30 mm/year. The distribution of the points within the non-urban area is depicted in Figure 232. However, a few of the points have been identified within the soil classification map. The frequency of the candidate points in relation with the deformation rates is depicted in Figure 233. The information of all following selected points' candidates is depicted in appendix C.

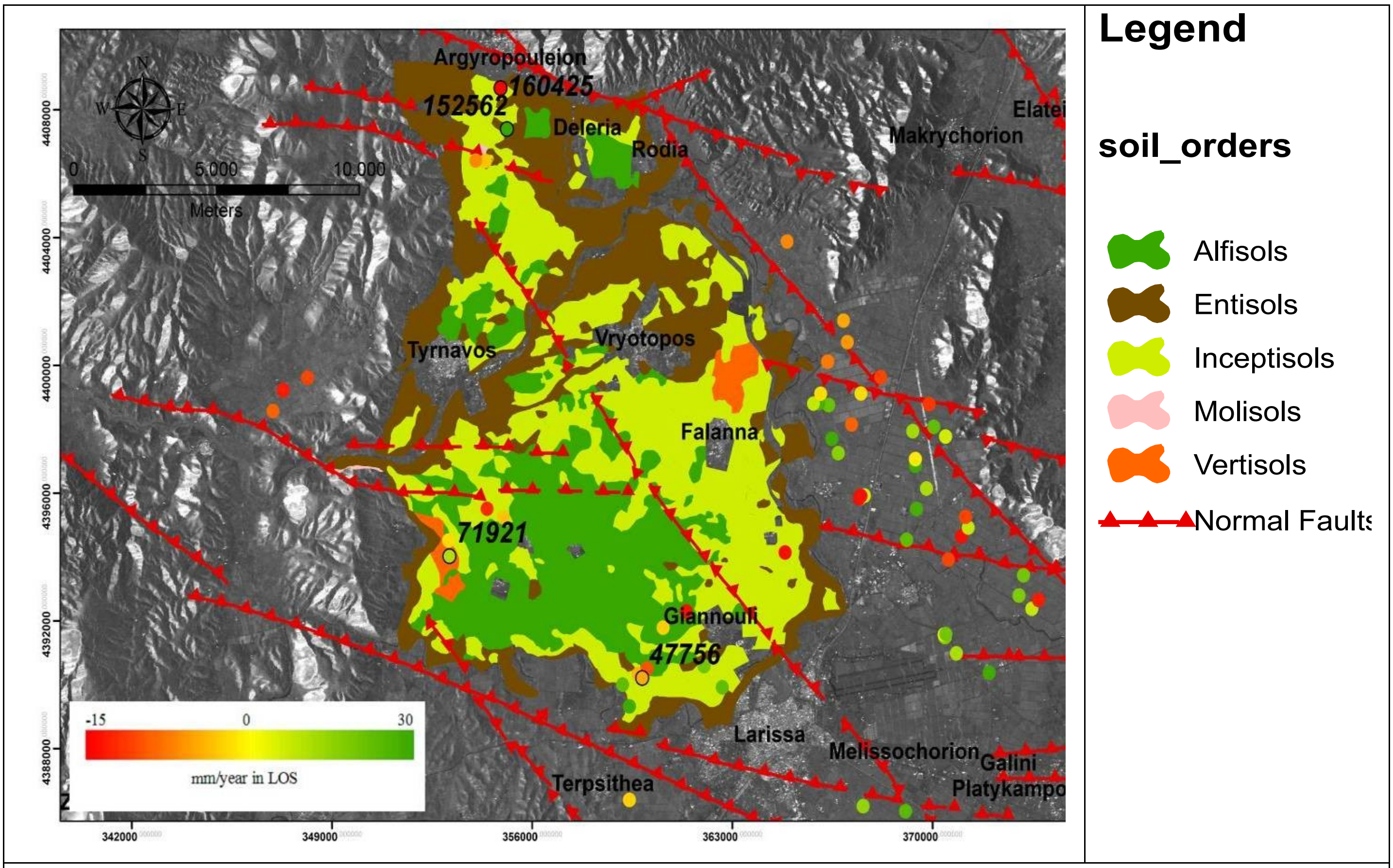

Figure232. PSI candidate points within the non-urban area, mean displacement rates 1995-2006, ascending track 143. Movements are in the satellite line-of-sight direction. Based on SLC of SAR image.

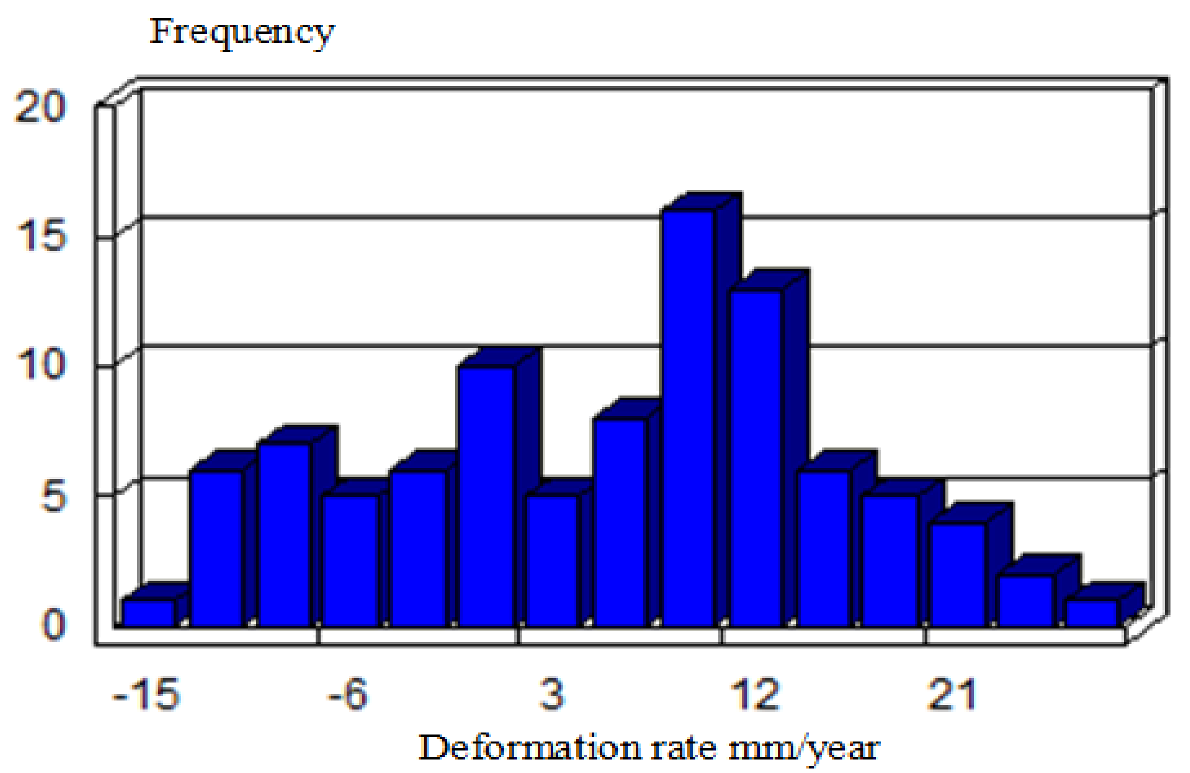

Count: 96, Minimum: - 15, Maximum: 30, Sum: 622, Mean: 6.479167, Standard Deviation: 10.029103

Figure.233 Frequency of deformation rate of points candidates after expansion within agriculture fields

6.4.1.1. Entisols

The properties of this soil type are a silty to silty loam texture, well drained, flat, with no signs of erosion. The candidate point selected within an Entisol soil order was number 152562. The plot of this point (Figure 234) shows that the time series begins with subsidence and then changes to uplift. The minimum subsidence was -0.982 mm (April 2004) and the maximum subsidence was -59.378 mm (December 1995). The minimum uplift was 2.067 mm (May 2005) and the maximum uplift was 14.362 mm (August 2005). The subsidence may be attributed to the location of the point which is between two normal faults in the side of the hanging wall, at a distance of 2.190 km from the first one, which is located in the northern part, and a distance of 1.174 km from the second one, which is located to the south. Probably the lithology of the area, which is fluvio-lacustrine deposits of the Larissa basin, is affecting the subsidence. Conversely, the uplift of this point is probably attributed to the type of soil minerals. No other interpretation of the reason for this uplift can be extracted. The location of this point is depicted in Figure 235.

6.4.1.2. Inceptisols

The properties of this soil type are a silty to silty loam texture, well drained, with slightly inclined slopes and a slight degree of erosion. The candidate point selected within the Inceptisol soil order was number 160425. The plot of this point (Figure 236) shows that it is almost stable through the time series. In particular, it shows subsidence at the beginning of the time series, with a minimum of -1.89 mm (April 2003) and a maximum of -12.34 mm (April 1996). The minimum uplift was 0.53 (August 2003) and the maximum uplift was 7.2 mm (February 2004). The subsidence may be attributed to the erosion process of the area. In particular, the area is characterized by slight erosion, especially to the south of the area, close to the normal fault in the side of the hanging wall, at a distance of 0.97 km. Moreover, the subsidence and uplift are probably affected by the lithology of the area, which is a fluvio-lacustrine deposit of the Larissa basin. The location of this candidate point is depicted in Figure 237.

6.4.1.3. Vertisols

The properties of this soil type are sandy clay to silty clay texture, moderately drained soils, flat, with no signs of erosion. The candidate point selected within a Vertisols soil order is number 71921. The plot of this point (Figure 238) shows that the time series begins with uplift and then changes to subsidence. The minimum uplift was 1.463 mm (August 2004) and the maximum uplift was 113.524 mm (June 1995). The minimum subsidence was -2.903 mm (September 2004) and the maximum was -26.115 mm (December 2006). The uplift may be attributed to the location of the point south of a normal fault in the side of the footwall, at a distance of 2.016 km. In addition, this uplift may be attributed to the type of soil minerals, especially as the maximum uplift was in June, when there is a swelling of soil minerals through the period of irrigation, period, and moreover to precipitation in that month, which amounts to 34.4 mm. The minimum uplift was in August, possibly due to the shrinkage of the soil minerals. In this case, in spite of the probable use of irrigation water, there is not enough precipitation to activate the swelling of the soil minerals. The minimum subsidence was in September and the maximum was in December, which may be attributed to the influence of other parameters. The location of this candidate point is depicted in Figure 239.

6.4.1.4. Alfisols

The properties of this soil type are a sandy clay loam to clay loam, well drained, flat, with no signs of erosion. The candidate point selected within this order is number 47756. The plot of this point is shown in (Figure 240). The time series begins with subsidence and then changes to uplift. The minimum subsidence was -1.426 mm (September 2004) and the maximum subsidence was -286.935 mm (June 1995). The minimum uplift was 23.010 mm (May 2005) and the maximum was 77.001 mm (December 2006). Subsidence may be attributed to the properties of the soil and more exactly to the possibility of including a horizon of organic materials within the soil pedon, which is too thin to meet the requirements for a histic or folistic epipedon (Soil Survey Staff, 1998). Also, oxidation may occur, and moreover there is the possibility of losing material from the eluvial horizons to the illuvial horizons, or for this material to leave with the drainage water. The other reason for the subsidence may be the location of the point 2.050 km north of a normal fault in the side of the hanging wall, although the uplift of this point may equally be attributed to the eluvial horizons and the deposits of the Penios River, especially as the distance between the river and the point is 2.239 km. The location of this point is depicted in Figure 241.

No candidate points were found in the Mollisols soil order.

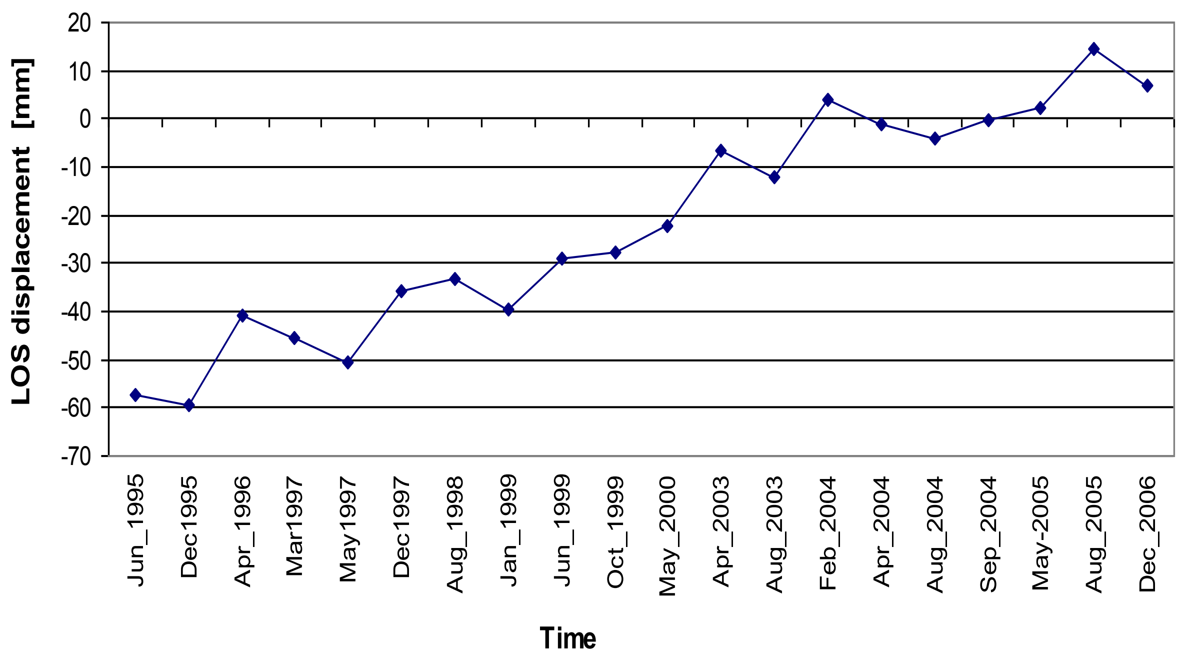

Figure.234 LOS displacement time series (1995-2006) of PSI. Point number 152562-Entisol. Time series are rescaled to the first acquisition (28 June 1995).

Figure235. Location of candidate point 152562 within Entisols soil order.

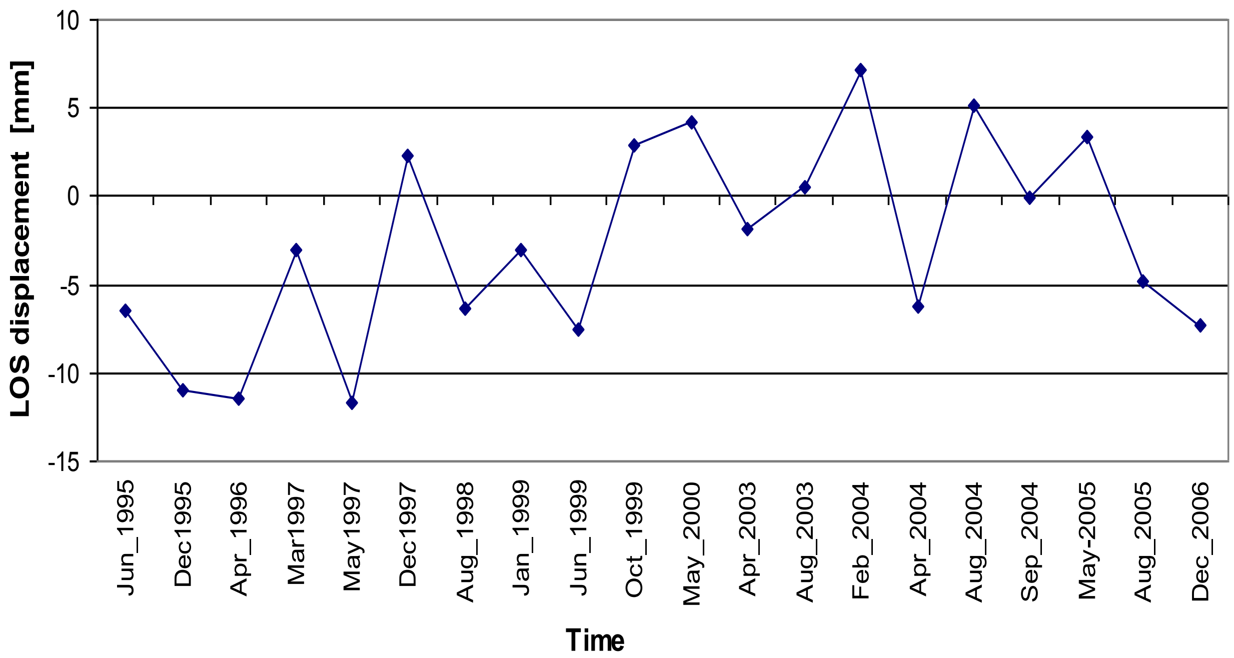

Figure236. LOS displacement time series (1995-2006) of PSI. Point number 160425-Inceptisol. Time series are rescaled to the first acquisition (28 June 1995)

Figure237. Location of candidate point 160425 within Inceptisols soil order.

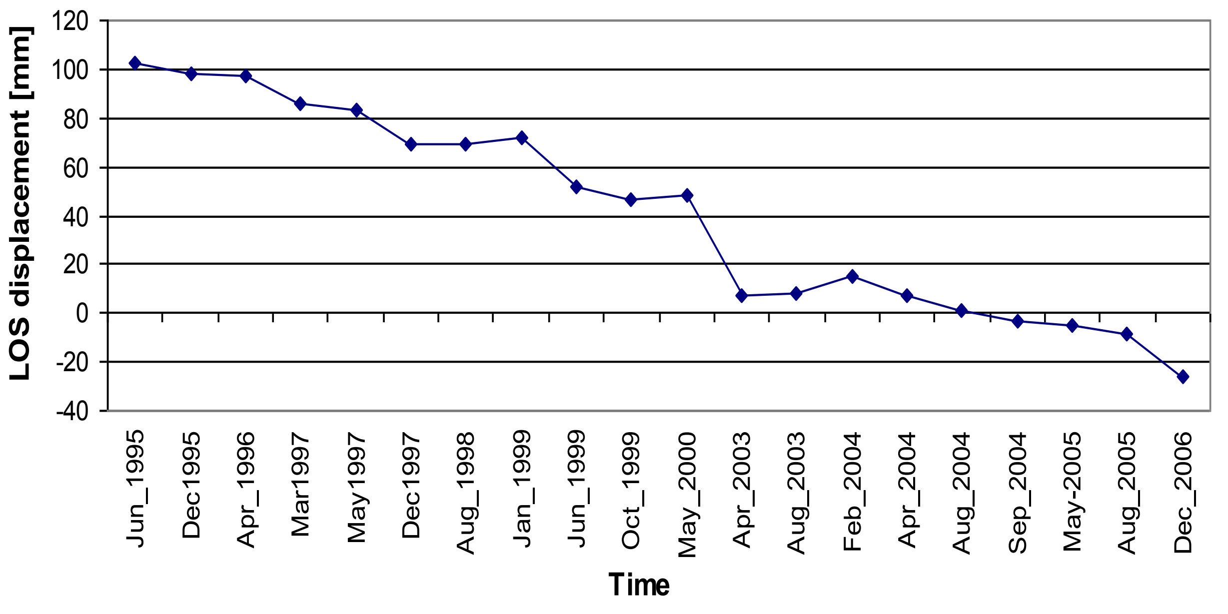

Figure238. LOS displacement time series (1995-2006) of PSI. Point number 71921-Vertisol. Time series are rescaled to the first acquisition (28 June 1995)

Figure239. Location of candidate point 71921 within Vertisols soil order.

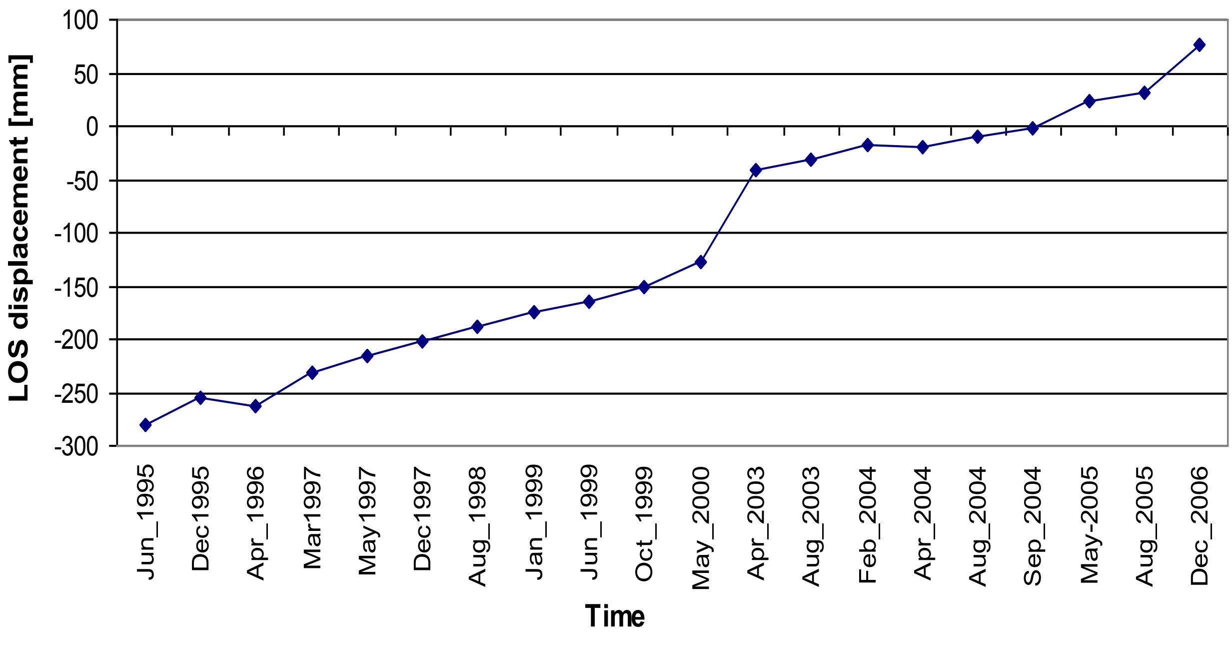

Figure240. LOS displacement time series (1995-2006) of PSI. Point number 47756-Alfisols. Time series are rescaled to the first acquisition (28 June 1995)

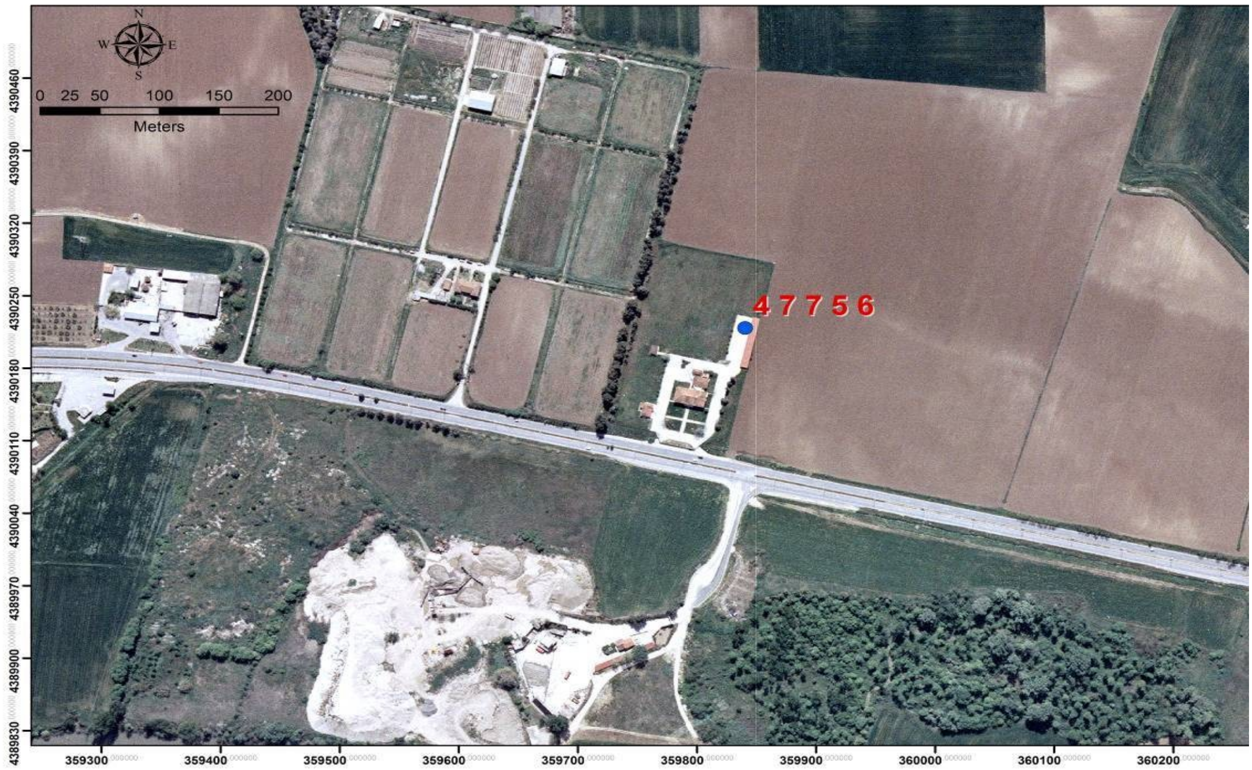

Figure241. Location of candidate point 47756 within Alfisols soil order.

6.4.2. Descending track 279

The total number of candidate points within the non-urban area was 382, with deformation rates varying in the range -7 – 10 mm/year. The distribution of the points within the non-urban area is depicted in Figure 242. Only one point has been selected within each soil mapping unit for the reasons mentioned before. The frequency of candidate points in relation to the deformation rates is depicted in Figure 243. The information of all following selected points' candidates is depicted in appendix C.

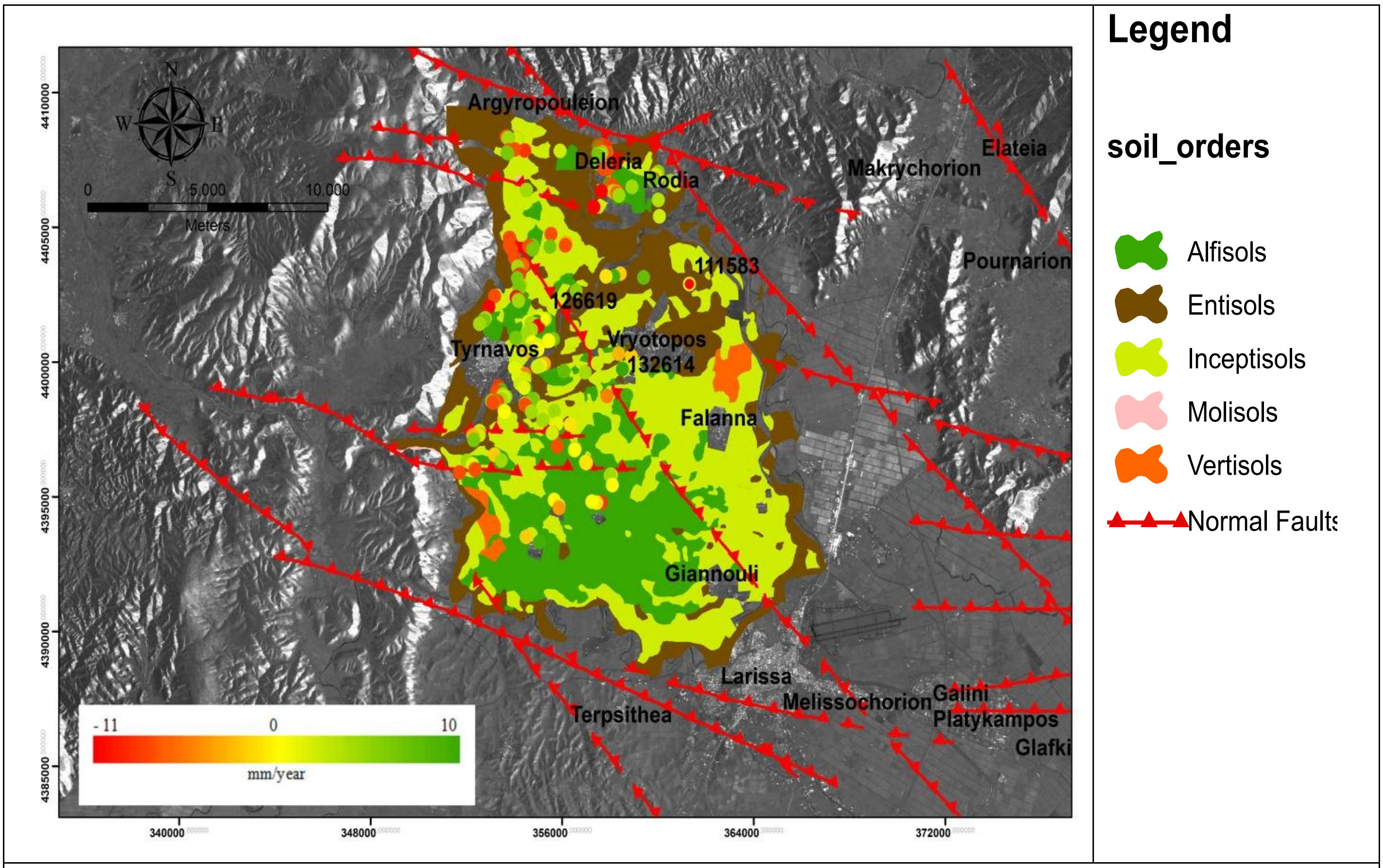

Figure242. PSI candidate points within the non-urban area, mean displacement rates 1992-2010, descending, track 279. Movements are in the satellite line-of-sight direction. Based on SLC of SAR image

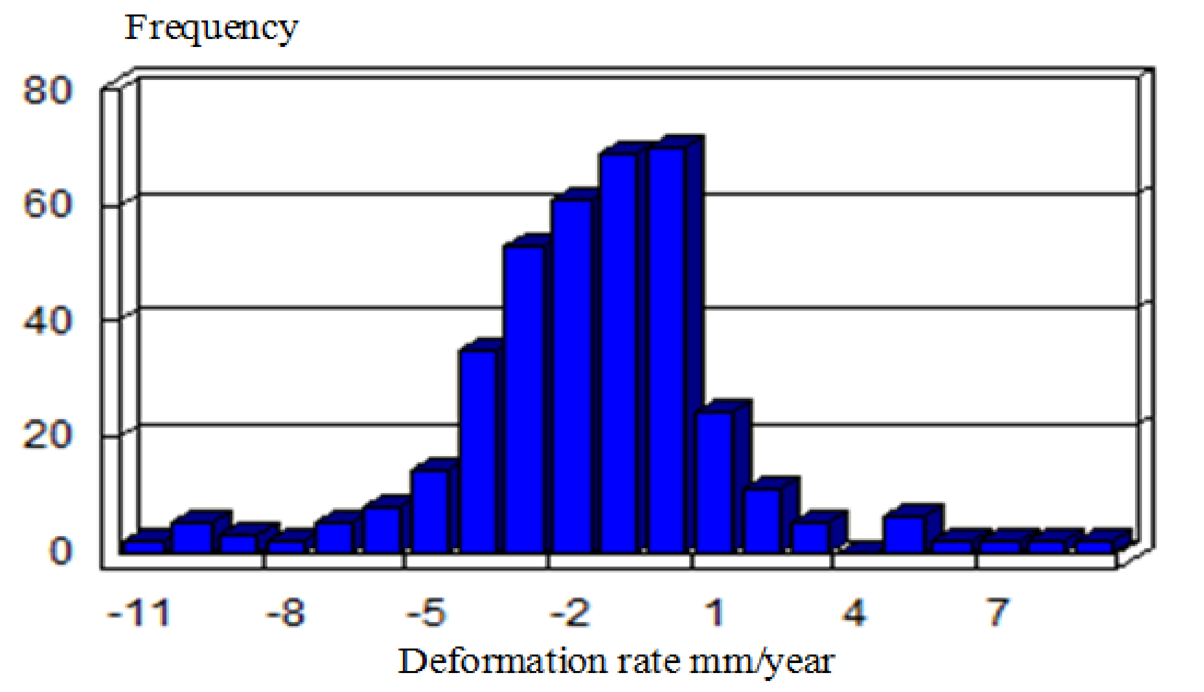

Count: 382, Minimum: - 11, Maximum: 10, Sum: -597, Mean: -1.562827, Standard Deviation: 2.91053
Figure.243 Frequency of deformation rate of points candidates after expansion within agriculture fields

6.4.2.1. Entisols

The properties of this soil type are a sandy loam texture, well drained, flat, with no signs of erosion. The candidate point selected within an Entisol order is number 111583. The plot of this point (Figure 244) shows that the time series begins with uplift and then changes to subsidence. The minimum uplift was 1.21 mm (October 2006) and the maximum uplift was 60.71 mm (August 1993). The minimum subsidence was -2.14 mm (August. 2007) and the maximum was -7.54 mm (April 2009). The uplift is probably attributed to the accumulation of river deposits from the Pinions River which is located 2.38 km to the east of the point. The subsidence is possibly attributed to the proximity of the point to a normal fault 2.39 km to the east in the side of the hanging wall. It is possible that at the beginning of the time series there was no impact or activity of the normal fault. The location of this point is depicted in Figure 245.

6.4.2.2. Inceptisols

The properties of this soil type are a silty to silty loam texture, well drained, flat, with no signs of erosion. The candidate point selected within an Inceptisol order is number

132614. The plot of this point (Figure 246) shows that the time series begins with subsidence and then changes to uplift at the end. The plot shows the subsidence at the beginning of the time series with a minimum of -0.29 mm (April 2008) and a maximum of -53.63 mm (June 1993). The minimum and maximum uplift were 1.05 mm (February 2009) and 12.0 mm (October 2010) respectively. The subsidence is most likely attributed to the type of soil minerals (especially during the swelling and shrinkage during the summer), or to the location of the point close to the eastern part of a normal fault, in the side of the hanging wall, at a distance of 0.78 km. The type of soil minerals appears to be the main reason for the maximum uplift in October and the minimum uplift in February, given their swelling during the rainy period. The location of this point is depicted in Figure 247.

6.4.2.3. Alfisols

The properties of this soil type are a sandy clay loam to clay loam texture, well drained, flat, with no signs of erosion. The candidate point selected within this order is number 126619. The plot of this point is depicted in Figure 248. The time series of this point begins with uplift then changes to subsidence at the end. The minimum uplift was 0.924 mm (July 2006) and the maximum was 56.790 mm (June 1993). The minimum subsidence was -1.484 mm (November 2009) and the maximum was -8.487 mm (October 2010). The subsidence may be attributed to the soil properties and more exactly to the possibility of including a horizon of organic materials within the soil pedon, which is too thin to meet the requirements for a histic or folistic epipedon (Soil Survey Staff, 1998), and oxidation may be occurring, together with a loss of soil material from the eluvial horizons to the illuvial horizons, or this material may instead leave with the drainage water. However, the uplift of this point may be attributed either to the eluvial horizons or to the location of the point in the side of the footwall of a normal fault at a distance 0.830 km. The location of this point is depicted in Figure 249.

No candidate points were found within the Vertisols and Mollisols soil orders.

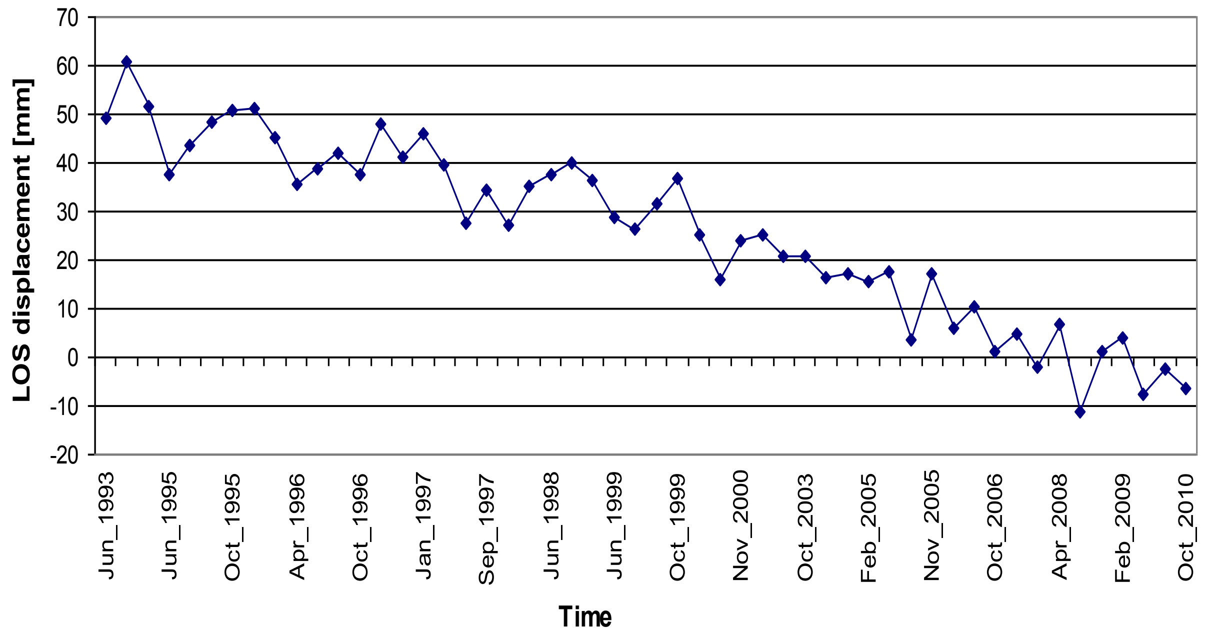

Figure244. LOS displacement time series (1992-2010) of PSI. Point number 111583-Entisols. Time series are rescaled to the first acquisition (i.e 12 Nov 1992).

Figure245. Location of candidate point 111583 within Alfisols soil order.

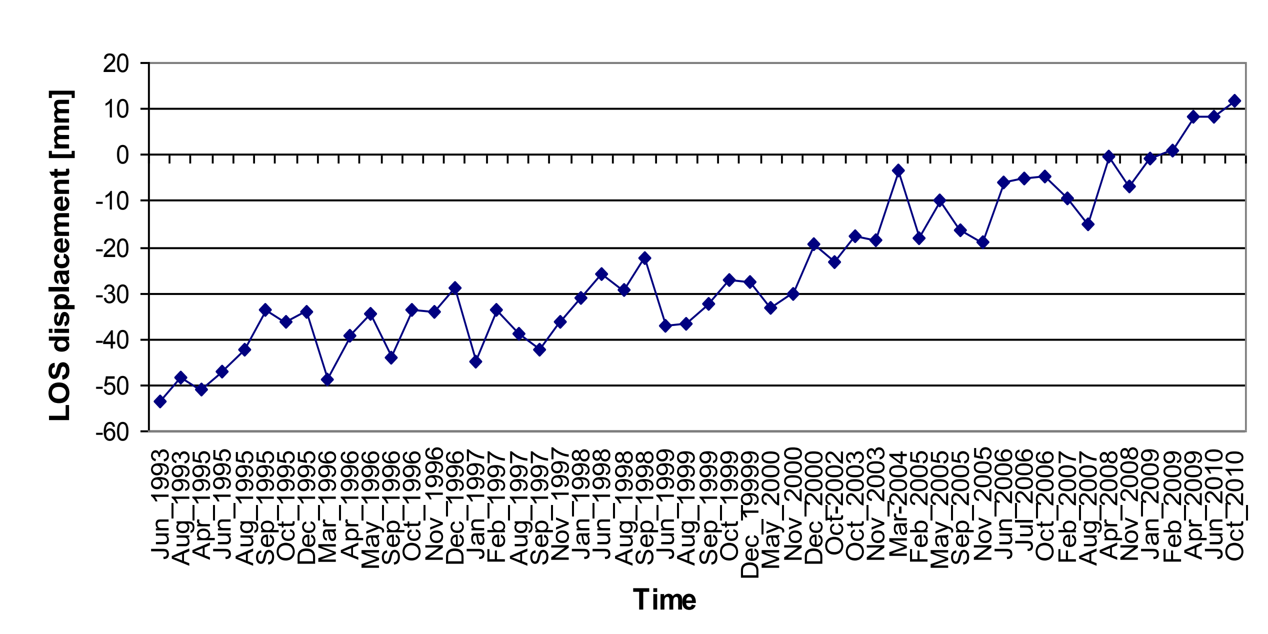

Figure246. LOS displacement time series (1992-2010) of PSI. Point number 132614-Inceptisols.Time series are rescaled to the first acquisition (12 Nov 1992).

Figure247. Location of candidate point 132614 within Inceptisols soil order.

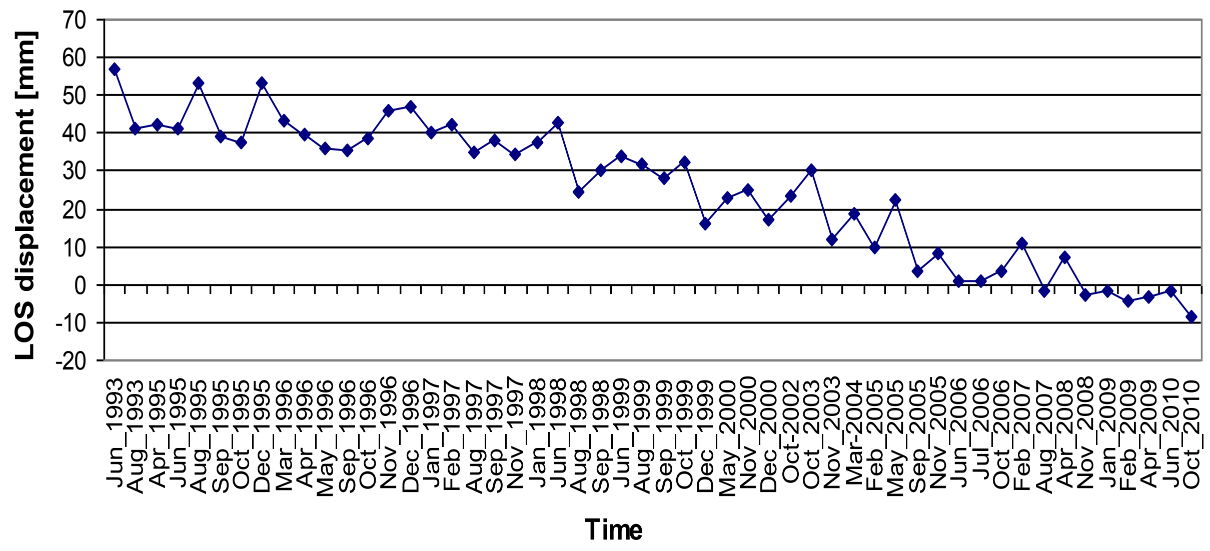

Figure.248 LOS displacement time series (1992-2010) of PSI. Point number 126619-Alfisols. Time series are rescaled to the first acquisition (12 Nov 1992).

Figure249. Location of candidate point 126619 within Alfisols soil order.

6.5. Interference between soil deformation and precipitation (Seasonal deformation)

It is difficult to discuss in practical or theoretical terms the impact of any single parameter on soil or land deformation without mentioning the interference of others. Thus within each parameter such as soil, this chapter will also mention the additional influence of other factors. To clarify the main impact of any parameter on the behaviour of soil deformation and its interference with others, a statistical correlation needs to be created. Note in this chapter that there are other influences on soil deformation, whether uplift or subsidence, through the respective interference of the effects of precipitation and the water table on soil deformation. For this reason, it is possible to regard this impact as a seasonal factor and as geospatial interference.

6.5.1. Ascending track_143

6.5.1.1. Entisols

Interference between soil deformation and the monthly amount of precipitation is shown in Figure 250, the two diagrams of which indicate that there is no continuous significant correlation between either subsidence or uplift and precipitation. The reason for this is that this candidate point is located in a well-drained mapping unit, and consequently there is not enough opportunity for water to remain for long enough to cause swelling and shrinkage or to physically change the volume of the soil. For example, the large subsidence of -59.378 in June 1995 cannot be attributed to the impact of the precipitation, but implies that there may be other factors or parameters influencing the soil deformation.

However, there is an individual influence of the lack of precipitation on soil subsidence through activation of the shrinkage of the soil minerals. Thus the value of subsidence increases with decreasing precipitation through the time series of April 1996, March 1997 and May 1997 respectively.

A similar thing occurs with decreasing subsidence during the increasing precipitation in May 2000 and April 2003 respectively.

The same behavior showing the influence of precipitation on soil deformation occurs once again with increasing subsidence during the decreasing precipitation in August 2004 and May 2005 respectively.

Again, it is noticeable that the uplift behavior decreases with decreasing precipitation in August 2005 and December 2006 respectively.
Interruption or non-continuation of the influence of precipitation on soil deformation behavior during the time series may be attributed to the non-sequence of the data set.

6.5.1.2. Inceptisols

Interference between soil deformation and the monthly amount of precipitation is shown in Figure 251, which indicates that there is no continuous significant correlation between soil deformations, whether uplift, or subsidence, and the monthly amount of precipitation. For instance, the value of subsidence in December 1995 is -16.441 mm while the amount of precipitation in this month is 34.4 mm. With this amount of precipitation, uplift or a small value of soil subsidence could be expected through the impact of the volume of water on the volume of the soil body, affecting the soil particle size by activating swelling. This implies that this subsidence cannot be attributed to the impact of precipitation. However, there are many individual influences of precipitation on soil uplift and subsidence as well. For instance, the impact of precipitation on uplift and subsidence may be observed through decreasing subsidence associated with increasing precipitation in March 1997, and then increasing subsidence associated with decreasing precipitation in May 1997. Thereafter, a transition in the soil deformation from subsidence to uplift occurs as a result of increasing monthly amounts of precipitation from May 1997 to December 1997. Once again a reverse transition occurs from uplift to subsidence due to a decrease in the monthly amount of precipitation from December 1997 to August 1998. Subsequent to a decrease in subsidence as a result of increasing precipitation in January 1999, then an increase in subsidence due to decreasing precipitation in June 1999, another transition in the soil deformation occurs once again, changing from subsidence to uplift with increasing precipitation from June to October 1999. Figure 25 depicts also another individual case of a correlation between soil deformation uplift and subsidence with the monthly amount of precipitation, with a transition from uplift to subsidence, followed by increasing subsidence during a decrease in precipitation from May to August 2005 and December 2006 respectively.

6.5.1.3. Vertisols

The correlation between soil uplift and subsidence with the monthly amount of precipitation is shown in Figure 252, which indicates that there is no continuous significant correlation between soil deformation and precipitation. Perhaps that can be attributed to the interruption of the data set, as mentioned before.

However, there are many individual cases of the influence of precipitation on soil deformation, whether uplift or subsidence. The general behavior of the soil deformation begins with uplift then changes to subsidence. A large uplift value in December 1995 can very probably be attributed to the large amount of precipitation. Thereafter, the decreasing uplift may be attributed to the decreasing precipitation in April 1996, March 1997, and May 1997 respectively.

There is further probable influence of precipitation on soil deformation during the decreasing uplift associated with decreasing precipitation in October 1999, May 2000 and April 2003 respectively. Another example is the increasing subsidence during the decreasing precipitation in May 2005, August 2005 and December 2006. In addition to the direct effect of precipitation on soil deformation, in this case, there is another probable influence through the activation the swelling and shrinkage of clay minerals. Because the continuation of the diagram of the soil deformation begins with uplift then changes to subsidence without any fluctuation reflecting the impact of precipitation, this uplift and subsidence deformation may be attributed to the impact of other parameters; in other words, all or many parameters may be associated together in having effects on soil deformation. On the other hand, the cracks which occur after the shrinkage of soil minerals give an opportunity for soil materials to leave or to migrate physically or with the irrigation water from the upper horizons and then leave with the drainage water. Over time, the volume of the soil body in general will decrease, and this may be the reason for which the behavior of the soil deformation curve continues without any fluctuation.

6.5.1.4. Alfisols

The correlation between soil deformation uplift and subsidence with the monthly amount of precipitation is shown in Figure 2253, which indicates that there is no significant continuous correlation between soil deformation and precipitation, similar to the case of the Vertisols. Although the behavior of the soil diagram begins with subsidence and then changes to uplift, the fluctuation of this diagram is not directly affected by the precipitation. The large value of subsidence in December 1995, which is -254.3 mm, is not attributed to the impact of the monthly amount of precipitation, which is 92.7 mm, which implies that this subsidence has been influenced by other factors or parameters.

In many of the cases mentioned previously for numerous soil orders, there are many individual cases of correlation. For instance, the decreasing subsidence in May 1997 and December 1997 may be attributed to the increasing precipitation. Similar associations occur in June and October 1999, August 2003 and February 2004. A transition occurs from subsidence to uplift during an increase of precipitation from August to September 2004 and in May 2005. There are not many cases of correlation in this type of soil, especially in this mapping unit, which may be attributed to the well-drained soil type, meaning that there is no opportunity for water to remain in the soil body for a long time and to change the volume of the soil by activating various operations.

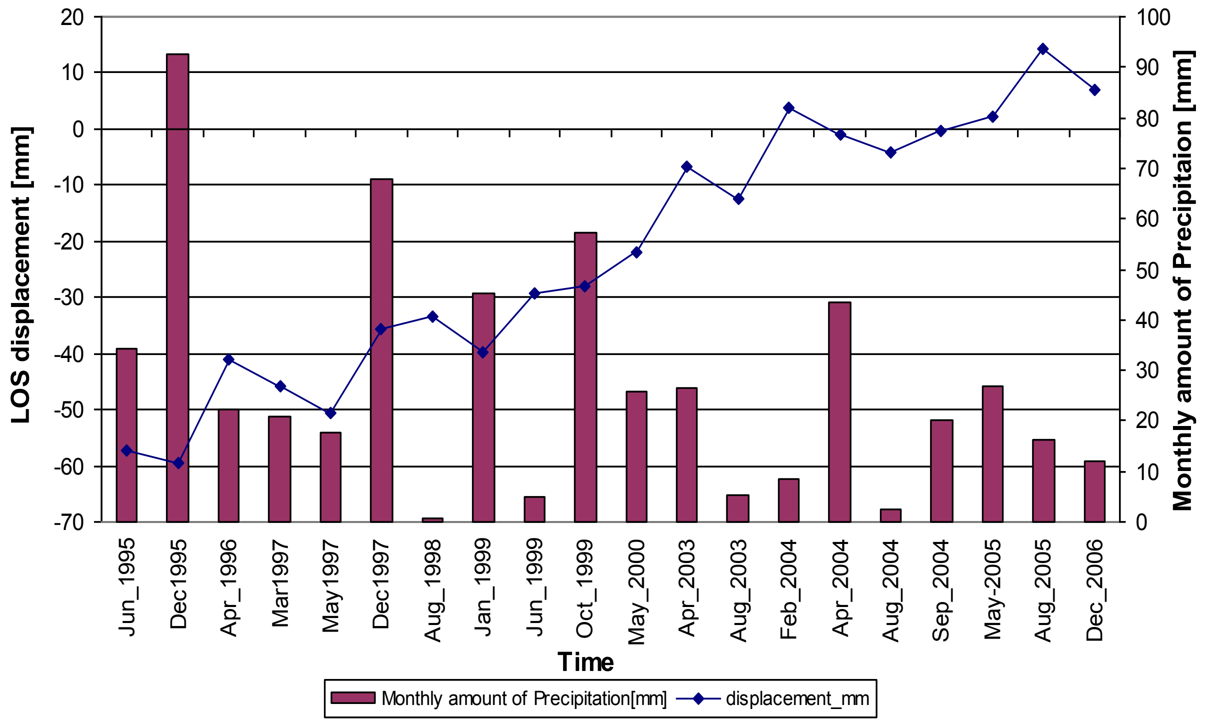

Figure.250 Interference correlation between soil deformation and monthly amount of precipitation for candidate point 152562 within Entisols soil order.

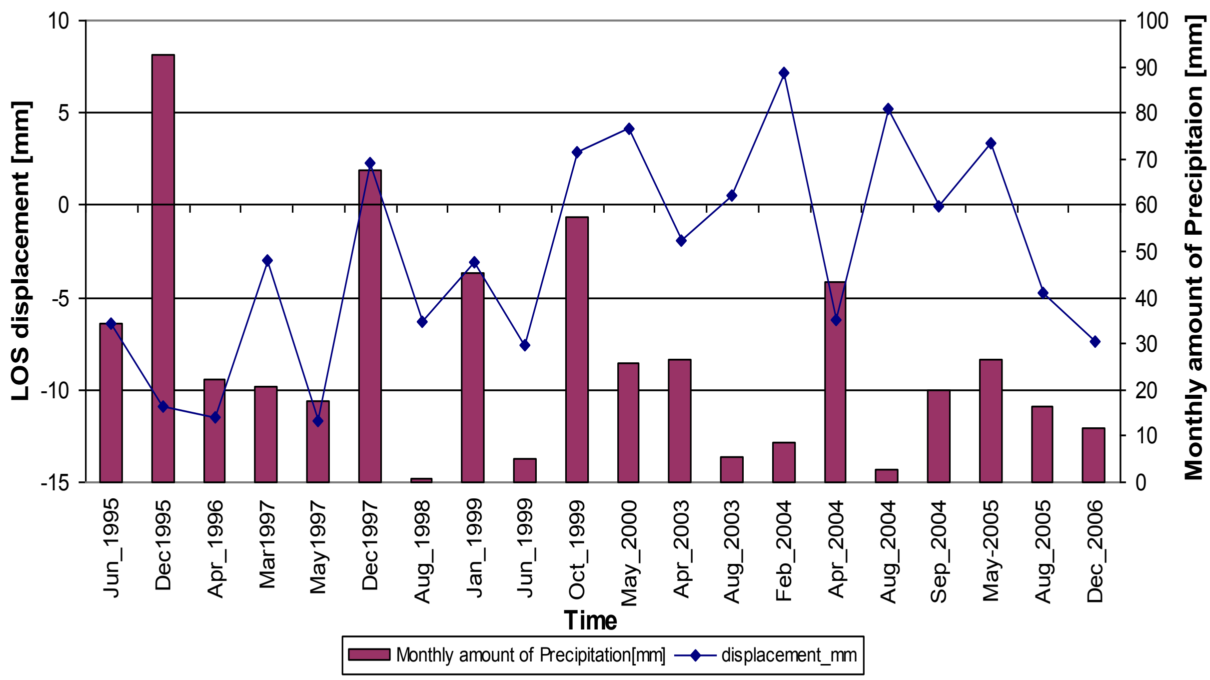

Figure251. Interference correlation between soil deformation and monthly amount of precipitation for candidate point 160425 within Inceptisols soil order.

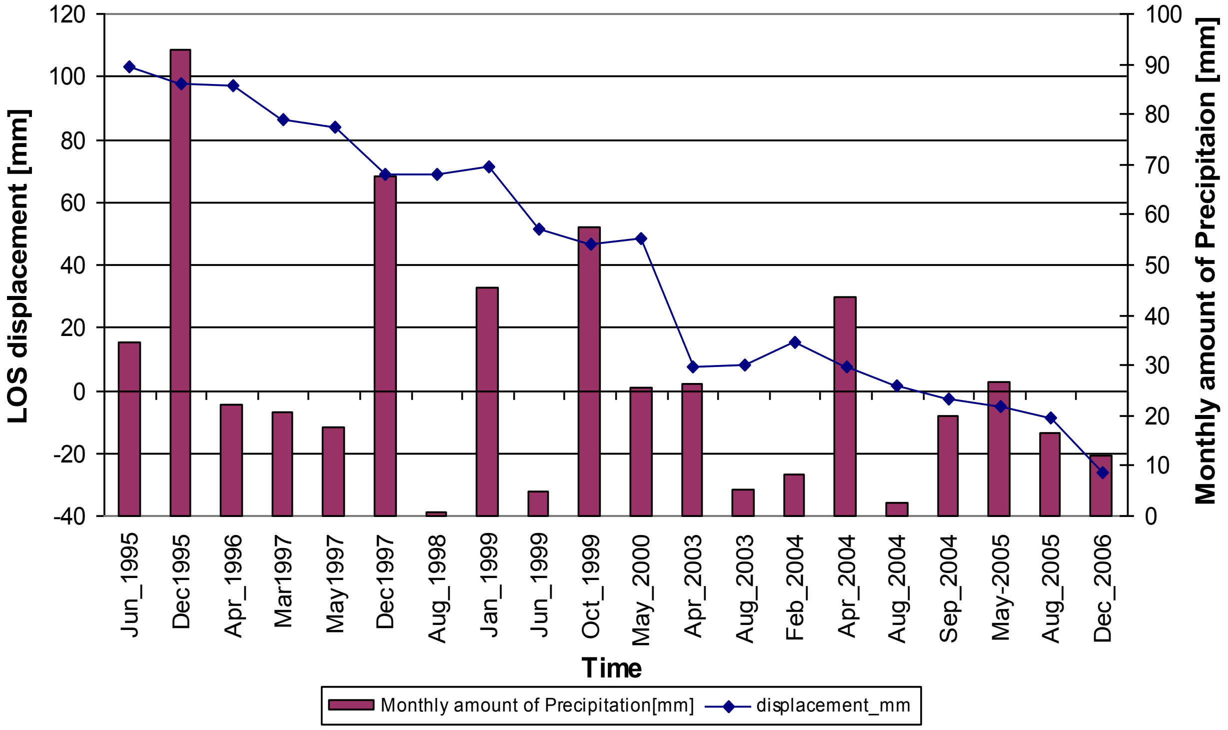

Figure252. Interference correlation between soil deformation and monthly amount of precipitation for candidate point 71921within Vertisols soil order.

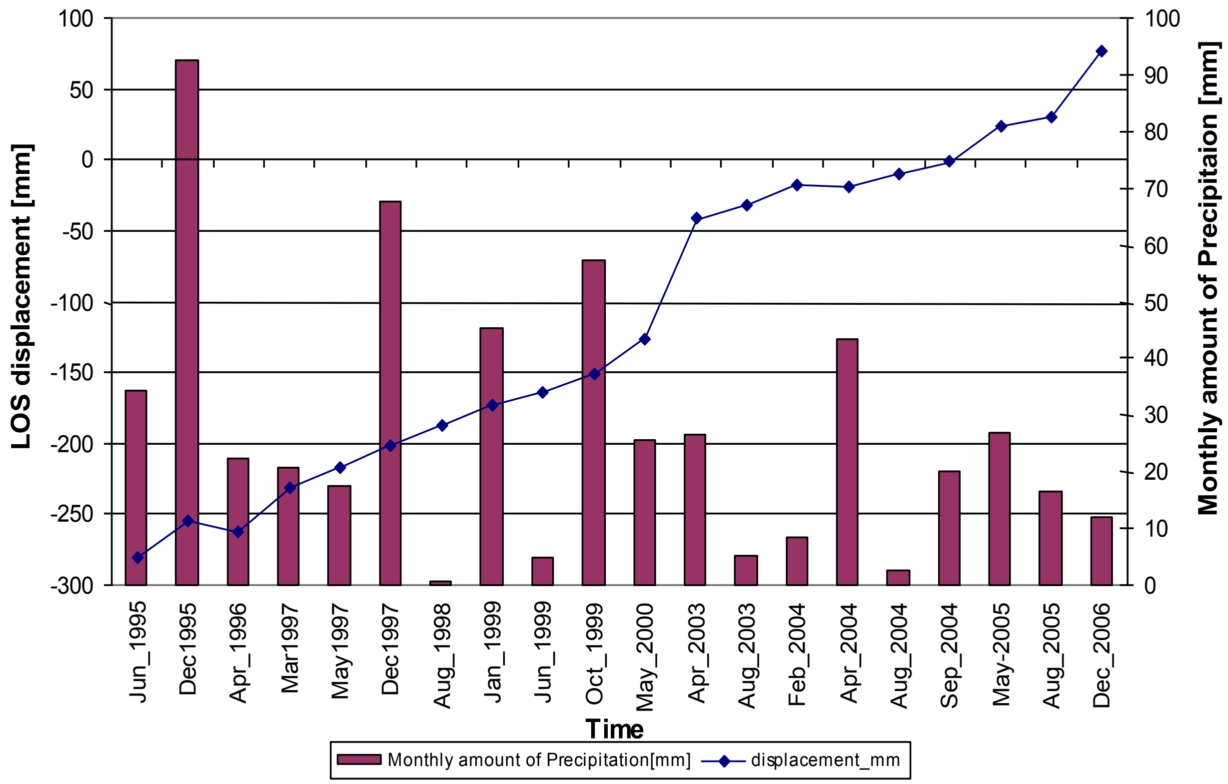

Figure.253 Interference correlation between soil deformation and monthly amount of precipitation for candidate point 47756 within Alfisols soil order.

6.5.2. Descending track 279

6.5.2.1. Entisols

Interference correlation is depicted in Figure 254. As mentioned in the many previous cases of interference correlation between soil deformation and the monthly amount of precipitation, there is no continuous significant correlation between the two parameters, despite the large volume of the data set with the descending track 279. This may imply that there are other accompanying factors or parameters that have an impact on soil deformation. One such case is the declining uplift through the increasing precipitation from April to June 1995. A similar case occurred also with the decreasing uplift during the increasing precipitation from July to October 2006 and the increasing subsidence during the increasing precipitation from June to October 2010. Moreover, the interference correlation is evident during the increase of uplift with the increasing precipitation from August to September 1995. There are many more similar cases, such as the decreasing uplift through the decreasing precipitation from December 1995 to March 1996, April 1996 and May 1996. Thereafter, the decreasing uplift during the increasing precipitation in October 1996 may be attributed to the speedy run-off of the precipitation, going directly into the channels of drainage, meaning that there is not enough time for the water to remain, or to filter through the soil body and reach the water table reservoir. Then the increase in uplift despite decreasing precipitation in November 1996 is either attributed to the water table recharging in the reservoir from the previous accumulation of precipitation, or there is a high probability of an association with water irrigation.

Once more, decreasing uplift occurred from January to February 1997 during a decrease in precipitation, and then increasing uplift occurred with the increase of precipitation in August 1997. The increasing uplift from November 1997 to January 1998, June 1998 and August 1998 is not attributed to precipitation, which decreased during this period. Consequently, the increasing uplift may be for two reasons. The first is an indirect influence of the precipitation on soil deformation by its impact on the water table, increasing its volume through recharging the water table reservoir, as well as the possibility of an association of the irrigation water with recharging the water table reservoir, which may have increased the uplift. The second reason may be the association of other parameters or factors influencing the soil uplift. The continuously decreasing uplift in September 1998, despite increasing precipitation, strengthens the theory of the indirect influence of the water table. Thus in this case the declining level of the water table level may have been an influencing factor on the decline in uplift. Thereafter, the increasing uplift in August, September, and October 1999 was associated with increasing precipitation. The declining uplift in October to December 1999 is perhaps not attributed to the precipitation, given that this decrease in uplift is associated with an increase in precipitation, probably implying that other parameters or factors have an influence on this reduced uplift.

Subsequently, the decreasing uplift from May to September 2005 despite increasing precipitation may consequently be attributed to the decline in the level of the water table. The reason is that this amount of precipitation may be filtered quickly, such that there is not enough time to remain in the soil body; also it does not sufficiently compensate the loss of water through water extraction for irrigation in the summer months between May and September. Afterwards, the increasing uplift due to increasing precipitation from September to November 2005 was followed by declining uplift which was associated with the decrease in precipitation in June 2006. Subsequently, an increase in of uplift occurred once again during an increase in precipitation in July 2006.

6.5.2.2. **Inceptisols**

The interference behavior between soil deformation and the monthly amount of precipitation is depicted in Figure 255. The influence of precipitation on soil deformation is evident from the fluctuation in the soil deformation curve with varying monthly amounts of precipitation. From this point of view, the non-linearity of the soil deformation of this candidate point may be attributed to this fluctuation in precipitation through two routes. The first is the direct impact of precipitation on soil deformation by activating swelling and shrinkage of soil minerals. The second is an indirect influence of the impact of precipitation on the fluctuation of the water table level, which subsequently affects the soil deformation as either uplift or subsidence. In spite of the continuity of the data set, there is no continuity in the impact of precipitation on the soil deformation, which may imply or explain the association with the influence of other parameters on soil deformation. Also, Figure 29 depicts the increasing subsidence as the precipitation increases in April 1995. The reverse case occurs, with subsidence decreasing with the declining precipitation, in August 1995. Thereafter, increasing subsidence occurs once again with decreasing precipitation from December 1995 to March 1996. However, the decreasing subsidence in April and May 1996 is not attributed to the impact of precipitation, because the decrease in subsidence occurred in parallel to the decrease in precipitation; in addition, the increasing subsidence from May to September 1996 is not attributed to the impact of increasing precipitation, which implies that there are other factors or parameters influencing the soil deformation.

An indirect impact of precipitation on soil deformation is evident in November 1997 and January 1998; despite decreasing precipitation, nevertheless the subsidence continued to decrease, which may be attributed to the indirect impact of precipitation on the water table level, in other words, the recharging of the water table reservoir from the precipitation or from the irrigation water from the previous months.

The indirect impact of precipitation on soil deformation either through its impact on the level of the water table, or because of the capacity of the soil to retain water, consequently affects the volume of soil vertically and horizontally.

A transition case from subsidence to uplift occurred despite the declining precipitation from January 2009 to February and April 2009, after which the uplift continued to increase, which may imply that the amount of precipitation which was filtered before had recharged the water table reservoir, or may be attributed to the association with other factors. In the last part of the Figure, the increasing uplift with increasing precipitation is obvious from June to October 2010.

6.5.2.3. Alfisols

The interference correlation between soil deformation and monthly amounts of precipitation is shown in Figure 256. The behavior of the interference does not show a significant continuous correlation, the reason for which may be similar to the cases mentioned before with the other soil orders in descending track 279.

Nonetheless the interference correlation between soil deformation and precipitation is obvious from the fluctuation of the soil deformation curve at many points of the plot. Many other measurements within the graph demonstrate that there is an interruption of this interference; examples include the high uplift values of 56.79 and 41.05 mm in June and August 1993 which cannot be attributed to the influence of precipitation. Another case is the increase in uplift in May 2005 during decreasing precipitation, compared with the previous and next cases in February 2005 and September 2005 respectively. Another case is the decrease in subsidence during the decrease in precipitation in February 2009, April 2009 and June 2010, and thereafter the increase in subsidence during the increase in precipitation in October 2010. In all these cases, as mentioned before, the interruption of the interference correlation may be attributed either to the impact of other factors or parameters on soil deformation or to the indirect influence of precipitation on soil deformation through its impact on other features or characteristics, whether internal or external. Although there are many cases of interference correlation interruption, nevertheless interference correlation does appear within this graph. For example, the decrease in uplift is associated with decreasing precipitation in September and October 1995, then afterwards the increase in uplift during the increasing precipitation in December 1995, and thereafter the gradually decreasing uplift through the decreasing precipitation in March, April, and May 1996.

After that, the increase in uplift was accompanied by increasing precipitation in September and October 1996. However, the uplift continued despite decreasing precipitation in November 1996, which may be attributed to the indirect influence of precipitation on soil deformation through the accumulation of water either from precipitation or from irrigation water in the water table reservoir.

Another instance is the decrease in uplift from December 1996 to February 1997 during a decrease in precipitation, then once more an increase in uplift during an increase in precipitation in August 1997, followed by a reverse case with decreasing uplift occurring during a decrease in precipitation in September 1997.

Subsequently, an increase in uplift in November 1997 and January 1998 is accompanied by decreasing precipitation, which may be attributed to the accumulation of recharging water in the water table reservoir; this is an indication of the indirect impact of the precipitation on soil deformation.

Afterwards, a steep decline in the uplift curve is accompanied by decreasing precipitation in August 1998, proceeding with the precipitation as an influencing factor on soil deformation, through the increase in uplift during increasing precipitation in September 1998, and thereafter a decrease in uplift can be noticed in June and August 1999 during a decrease in precipitation. However, an increase in precipitation is noticed in September 1999, despite a continued decrease in uplift, which may be attributed to the indirect effect of precipitation on soil deformation through its influence on the level of the water table. Consequently, in this case there is not enough time for the precipitation to remain in the soil body and it leaves quickly to the water table reservoir, especially after two dry months (June and August 1999). For this reason there is no direct correlation of increasing precipitation and increasing soil uplift in this case. The evidence for this is the increase in uplift during the increase in precipitation in October 1999. However, there is a steep decline in uplift despite the increase in precipitation in December 1999, which may be attributed to the influence of other parameters or factors.

Thereafter the increase in uplift in May and November 2000, despite the decrease in precipitation, may be either an indicator of other accompanying parameters or factors having an effect on soil uplift or an indirect impact of the precipitation on soil deformation by recharging of the water table reservoir.
Once again, an increase in uplift occurred during increasing precipitation in December 2002, October 2002 and October 2003 respectively.

Then a steep decline in uplift occurred once more during a decrease in precipitation in November 2003. Following on from this impact was an increase and decrease of uplift as a result of increasing and decreasing precipitation in March 2004 and February 2005 respectively.

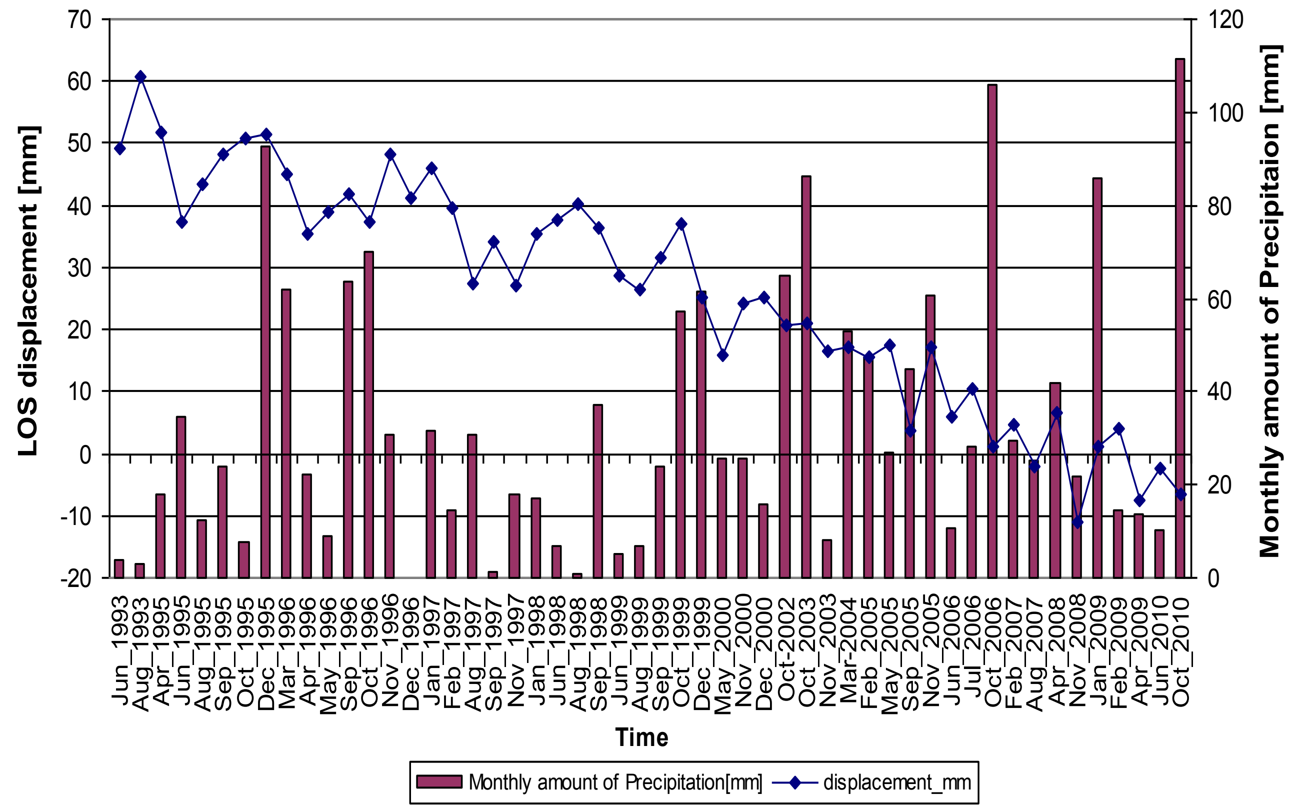

Figure254. Interference correlation between soil deformation and monthly amount of precipitation for candidate point 111583 within Entisols soil order.

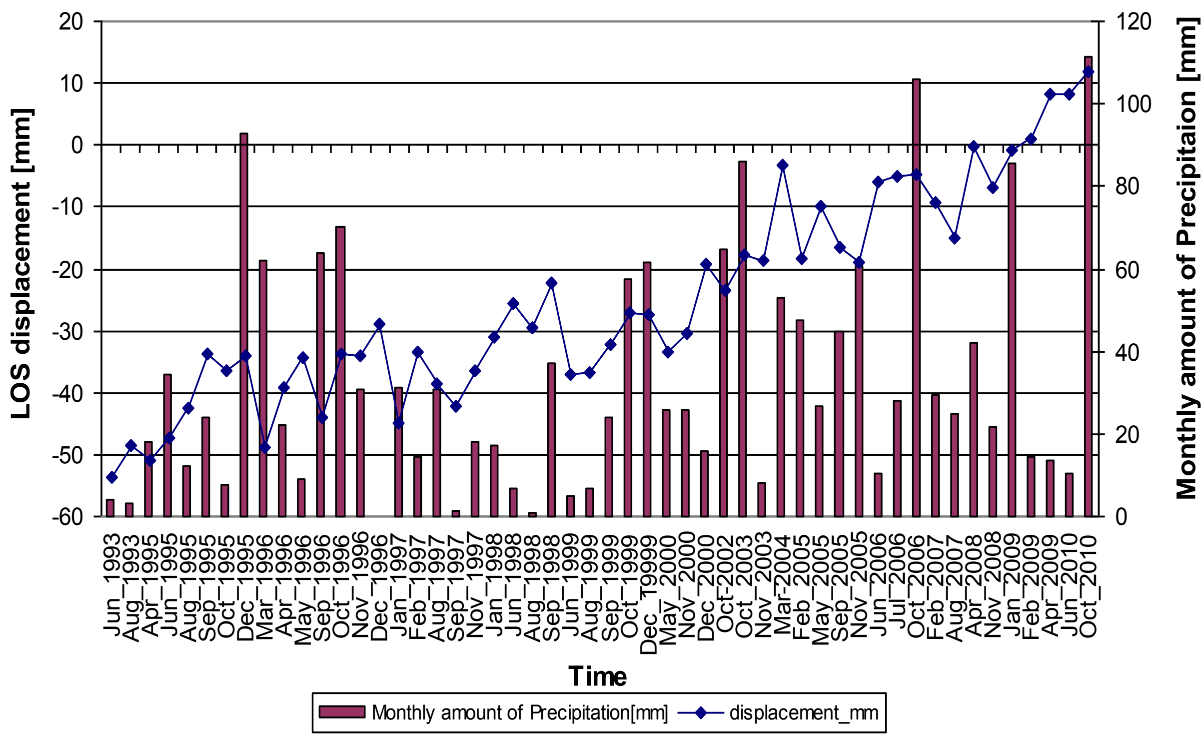

Figure255. Interference correlation between soil deformation and monthly amount of precipitation for candidate point 132614 within Inceptisols soil order.

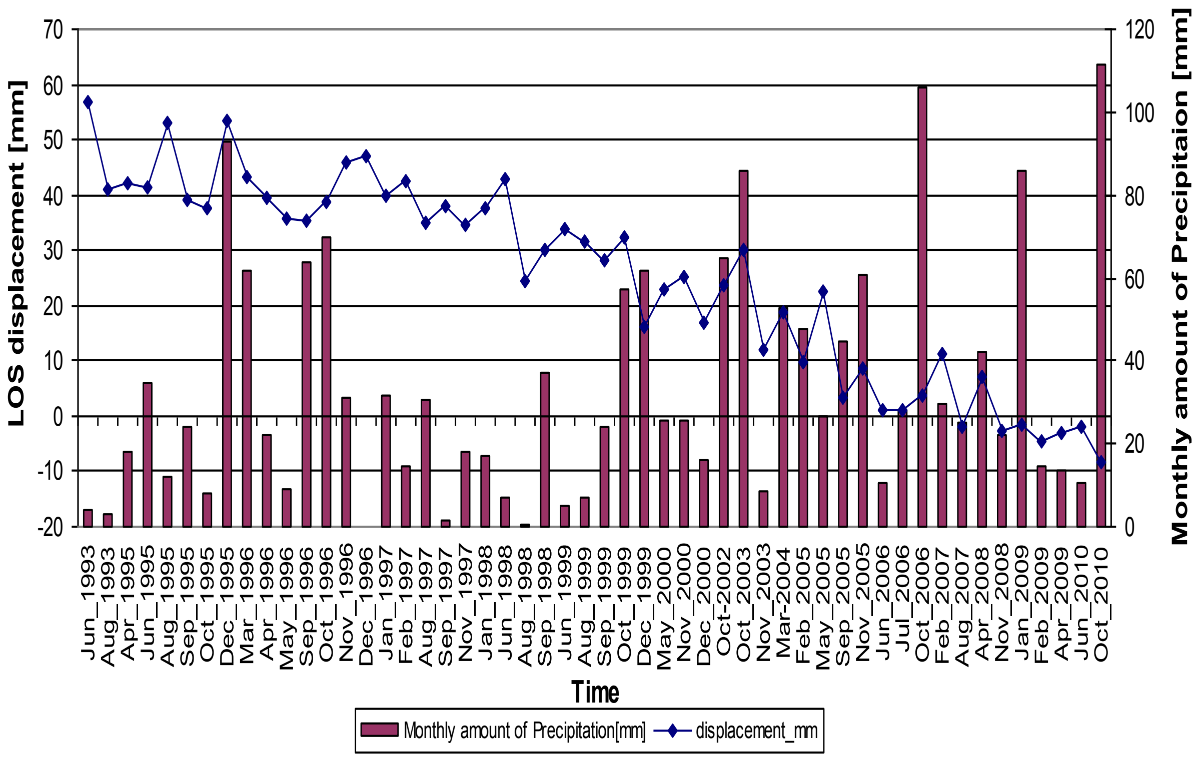

Figure.256 Interference correlation between soil deformation and monthly amount of precipitation for candidate point 126619 within Alfisols soil order.

Chapter Seven: The conclusions derived from this research study and recommendations for future researches

7.1. Conclusions

- The data of SAR images ERS1/2 and ASAR ENVISAT which have been used in this research study are shown the possibility for investigating and identifying the temporal and spatial ground vertical movement within study areas of Larisa basin. However, the cons of these types of data were the spatial resolution which is 20 meters, consequently this spatial resolution does not was large enough to detect the ground deformation for objects which are located within large scale. However, the temporal resolution was applicable good enough to the objectives of this study.

- Data of Groundwater level, monthly amount of precipitation, lithology of geological formation, faults traces and earthquakes, and soil have been taken into account for this research study to identify the causes of ground deformation. However, the important data related to the amount of groundwater withdrawal has not been found.

- - Concerning to the GAMMA (S/W) including IPTA algorithm. This has been used in this research study. Has very high-quality advantages related to the time and results of processing to identify the short and long-term of ground deformation within study area, through the implementing the three techniques. However the con of this software is the user has to transfer the data into other software such as ArcGIS, ERDAS and Excel to implement some processes.

- SAR interferometeric techniques have been applied in this research study, have been identified and investigated the ground deformation of study area appropriately. Additionally the applying spatial and statistical correlations methods provide the possibility to monitor ground deformation. Furthermore identify the influence of each single parameter and factor on ground deformation. Also are revealed the spatial and temporal behavior of ground deformation representative by area or single object.

- The SAR interferometric conventional technique, has pros to investigate the ground deformation during short-term within urban and non-urban area. However, the cons of this technique are the deformation is limited by the atmospheric path delay term.

- The SAR interferometric stacking technique has the advantages to bypass the cons of the atmospheric path delay, however no time series could be obtained for each single object by this technique.

- The persistent scatterers technique has the advantages to obtain the ground deformation for each single object for long-term time series; however the disadvantage of this technique is the hard conditions ought to apply to get the candidates points specially within agricultural fields.

- The implementing of the expansion algorithm aftermath applying the persistent scatterers technique in this research study had an advantage of increase the numbers of candidate point.

- Short-term deformation has been observed within study area during time interval 19960228 – 19960403. Two phase's patterns for subsidence and uplift are distributed through the entire Larissa basin within urban and non-urban area. However, deformation for two phase's patterns subsidence and uplift are confined to the urban-area, and a few phase's patterns of subsidence and uplift has been observed within non-urban area during the time interval 19980802–19980906.

- Results of interferometric phases of individual differential interferograms cover approximately the entire scene, except for the south-eastern part of the scene for an ascending track and except for the northern, eastern and south-eastern parts of the Larissa settlement and south-western part of the scene for the descending track.

- Results of implementing conventional technique point to seasonal deformation. This is attributed to the fluctuation of groundwater level, which plays an important role through its impact on ground deformation during short time periods of up to one month.

- It is noticeable that the fluctuation of groundwater level has a significant correlation with monthly precipitation amount within practically all monitoring data for all boreholes. In addition, the impact of precipitation amount on groundwater level is evident from the behaviour of groundwater level during May and October, which represent the wet and dry periods.

- Water withdrawal is the main cause of groundwater decline within almost all of the boreholes within the study area.

- Approximately all correlation cases between fluctuation of groundwater level and land deformation point to non-continuous significant correlation through the short and long distances between boreholes and point candidates of PSI within ascending and descending tracks. This may be a reflection of the spatial complexity of aquifer systems, the variety of subsidence and uplift deformation, and the large number of illegal wells with different depths.

- Significant correlation has been found between fluctuation of groundwater level and land deformation within ascending and descending tracks, despite of the short time series data of ascending track (1995–2006) and the long distance between boreholes and many point candidates of PSI relevant to descending track. This may be attributable to the short distances between boreholes and many point candidates regarding the ascending track or to the large expansion time series data (1992–2010) of descending track.

- The other main reason for deformation is the compaction of materials deduced by water pumping and this is related with local deformation. This compression of materials may produce a micro-seismic (3 - 4) magnitude.

- It is noticeable that the rate of subsidence during the dry period, represented by August, is more than the rate of subsidence during the wet period, represented by March. This is evidence of the seasonal fluctuation impact of groundwater level on land deformation.

- Significant interferometric fringes are observed within approximately all of the boreholes in two differential interferograms of two tracks, ascending and descending, through the fluctuation of groundwater level.

- Long-term deformation has been observed within study area during two periods 1995 – 2008 and 1992 – 2010, respectively. Two phase's patterns for subsidence and uplift are distributed through all the settlements of Larissa basin.

- Results of patterns phases of interferometric stacking are confined to urban and mountainous areas. However, no results have been observed within agricultural fields within the Larissa basin for ascending and descending tracks.

- Results of interferometric stacking of the descending track indicate a low distribution of patterns density compared with the ascending track.

- Differences in the ground deformation rate of the same settlements resulting from the interferometric stacking technique of two tracks, ascending and descending, may be attributed to the difference between the numbers of interferograms within each interferometric stacking result, since there were 29 items within the ascending track and 70 items within the descending track. Furthermore, there were differences between the time periods of the radar images within each track in addition the place of reference point within each track.

- The number of candidate points within the descending track is fewer than the number of candidate points within the ascending track. An interpretation of this case is that pairs between different seasons typically encounter stronger atmospheric effects (in particular stronger height dependent atmospheric effects). The results have been found that the descending track phases are more difficult to unwrap and that this might reduce the spatial coverage achieved.

- Direct correlation has been found between the number of interferograms and the average coherence with ascending and descending tracks within urban areas. However, an inverse correlation has been found between the number of interferograms and average coherence within agricultural fields.

- Direct correlation has been found between a long perpendicular baseline and the number of interferograms. In addition, direct correlation has been found between the wrapped phases and a long perpendicular baseline.

- The theoretical correlation between locations and distances of ground deformation represented by point candidates of PSI and normal faults indicates a probability of impact of normal fault movement on ground deformation. This result is attributable to the statistics time series behaviour of each point candidate and the location of these points in the side of the footwall or hanging wall.

- The Persistent Scatterers Technique, through the application of spatial correlation between the locations of candidate points and fault traces, reveals or/and indicates the possibility of the influence of fault movements on ground deformation.

- In spite of the controversy regarding the gap of the last large magnitude earthquake in Larissa (1941), which remains a major issue, nevertheless, fault movements, which are the main reason of earthquakes creation, may be attributed to the impact of mutual processes between the swelling and shrinkage of clay minerals. The types of these minerals consists of two layers of aluminium to one layer of silicon, or two to two layers of aluminium to one layer of silicon. These processes are activated through the successive operations of water withdrawal and compensation. In consequence, this reason may explain the low earthquake magnitudes. However, there remains a need to implement a tectonic study within this study area in the eastern part of northern Thessaly.

- The most important ground deformation within the study area can be considered to be the northeastern border of the area, for the reason that this area is near the major fault of the Olympos Ossa zone. Due to the uplift of the Olympos Ossa region in parallel with the throw-down of the basin through the decline of groundwater level, subsidence occurred generally within Larissa basin.

- Subsidence in the northern part of Larissa, identified by implementing three SAR interferometry techniques, may be for two reasons. The first is the influence of the hanging wall of the normal fault trace, and the second is the impact of liquefaction-induced ground disruption.

- SAR interferometry techniques successfully revealed the impact of lithology type on ground deformation through the ascending and descending tracks.

- Subsidence could not be attributed to the sole impact of the type of lithology. This was because there are several nested and interconnected factors such as lithology, fault movements, type of clay minerals and amount of precipitation.

- There is no continuous significant correlation between uplift and subsidence soil deformations and the monthly amount of precipitation at many points within the time series of the data set. This can perhaps be attributed to the interruption of the data set, especially in the ascending track 143.

- There are many cases of interference correlation of the influence of precipitation on soil deformation, as either uplift or subsidence, and these are distributed separately or connected within each time series of each candidate point.

- It is difficult to isolate the behavior of the impact of any parameter on soil deformation separately as an ideal condition or in practical terms, despite using statistical analysis, for the reason that all parameters or factors are associated together to influence soil deformation.

- The non-continuous impact of precipitation on soil deformation is evident at all candidate points within all soil orders through the diagrams and curves produced. This may be attributed to the indirect effect of the monthly amount of precipitation on soil deformation, due to its impact on the fluctuation of the level of the water table. However, there are no bore holes near to the candidate points or within these soil mapping units to emphasize this interference correlation.

- Interference correlation between soil deformation and the monthly amount of precipitation is more obvious in descending track 279 than ascending track 143. This may be because the size of the data set for descending track 279 is larger than for ascending track 143.

- The impact of the fluctuating level of the water table on uplift or subsidence is due to two effects. The first is a direct impact through its horizontal or vertical movement within the soil body, and the second is the accumulation of water either from precipitation or from irrigation water in the water table reservoir.

- Theoretically and without creating any statistical correlations, it is not possible to identify the source of the impacts on soil deformation, or which parameters or factors have the most important influence on the soil or land deformation.

- Despite creating correlation statistics, it remains difficult to separate completely the impact association of factors.

7.2. Recommendations

- Use other sources of radar images with a high resolution to obtain a much greater number of candidate points, especially within the non-urban area.

- Try to build a statistical model to predict the values of deformation within a time series, for the data from radar images which are omitted during the implementation of data processing, for technical or any other reasons, in order to fill the gaps in the data set within the time series for each point.

- An attempt should be made to build a statistical model of ground characteristics and deformation rate resulting from the SAR interferometric techniques, especially the result of the PSI technique, to make it easier to forecast future deformation and furthermore to reveal the size of the impact of each single ground feature on ground deformation.

References

B

Bamler, R. & Hartl, P. (1998) Synthetic Aperture Radar Interferometry. *Inverse Problems* 14**,** R1– R54.

Beibei, C., Huili, G., Xiaojuan, L., Kunchao, L., Youquan, Z., Jiwei, L., Zhaoqin, G. & Yanan, D. (2011) Spatial-Temporal Characteristics Of Land Subsidence Corresponding To Dynamic Groundwater Funnel In Beijing Municipality, China. . *Chinese Geographical Science,* 21(6)**,** 753–764.

Berens, P. (2006) Introduction to Synthetic Aperture Radar (SAR). *In Advanced Radar Signal and Data Processing* 3 -1**,** 3-14

C

Canaslan, F. & Ustun, A. (2012) Impact of Perpendicular and Temporal Baseline Characteristics On Insar Coherence Maps *Remote Sensing Ts05h* I, 5767**,** 1-11.

Caputo, R. (1993) The Rodia Fault System; An Active Complex Share Zone (Larissa Plain, Central Greece). *Bull. Geol. Soc. Greece. ,* Vol. Xxviii/1, **,** 447 – 456.

Caputo, R. (1995) Inference Of A Seismic Gap From Geological Data: Thessaly (Central Greece) As A Case Study *Annali Di Geofisica* Xxxviii, N. 1.

Caputo, R., Bravard, J.-P. & Helly, B. (1994) The Pliocene-Quaternary Tecto-Sedimentary Evolution Of The Larissa Plain (Eastern Thessaly Greece). *Geodinamica Acta* 7**,** 57– 85.

Caputo, R. & Helly, B. (2005) The Holocene Activity Of The Rodi`A Fault Central Greece, . *Geodynamics* 40 153 –169.

Caputo, R., Helly, B., Pavlides, S. & Papadopoulos, G. (2004) Palaeoseismological Investigation Of The Tyrnavos Fault (Thessaly, Central Greece) *Tectonophysics* 394 1 – 20

Caputo, R., Helly, B., Pavlides, S. & Papadopoulos, G. (2006) Archaeo- And Palaeoseismological Investigations In Northern Thessaly (Greece): Insights For The Seismic Potential Of The Region *Nat Hazards* 39**,** 195 – 212

Caputo, R., Hinzen, K.-G., Liberatore, D., Schreiber, S., Helly, B. & Tziafalias, A. (2011) Quantitative Archaeoseismological Investigation Of The Great Theatre Of Larissa, Greece. *Bull. Earthquake Eng, Springer Science Business Media* 9**,** 347-366.

Caputo, R. & Pavlides, S. (1993) Late Cainozoic Geodynamic Evolution Of Thessaly And Surroundings (Central-Northern Greece) *Tectonophysics, Amsterdam,* 223 339-362.

Chang, C. P., Chang, T. Y., Wang, C. T., Kuo, C. H. & Chen, K. S. (2004) Land-Surface Deformation Corresponding To Seasonal Ground-Water Fluctuation, Determining By Sar Interferometry In The Sw Taiwan *Mathematics And Computers In Simulation* 67(4–5) 351–359.

Cigna, F., Osmanoğlu, B., Cabral-Cano, E., Dixon, T. H., Alejandro, J., Ávila-Olivera, J. A., Garduño-Monroy, V. H. G., Demets, C. & Wdowinski, S. (2011) Monitoring Land Subsidence And Its Induced Geological Hazard With Synthetic Aperture Radar Interferometry: A Case Study In Morelia, Mexico *Remote Sensing Of Environment* 117 146–161.

Crosetto, M., Monserrat, O., Iglesias, R. & Crippa, B. (2010) Persistent Scatterer Interferometry: Potential, Limits And Initial Cand X-Band Comparison *Photogrammetric Engineering And Remote Sensing* 76, N. 9**,** 1061-1069.

D

Decentralized Administration Of Thessaly Sterea Elada Direction Of Water Management Of Thessaly. Department Of Water Resource Monitoring And Protection For The Region Of Thessaly, Larissa. . Http://Www.Larissa.Gr/Main.Aspx?Catid=98&Dnsi=21&Tm=47.

Doukas, D. I., Ifadis, M. I. & Savvaidis, P. (2004) Monitoring And Analysis Of Ground Subsidence Due To Water Pumping In The Area Of Thessaloniki, Hellas *Fig Working Week.* Athens, Greece.

E

Eak (2000) Greek Seismic Code, Earthquake Planning & Protection Organization, Athens, Greece, P. 72 And 7 Appendices (In Greek), Consists Of 5 Chapters And 7 Annexes Of 109 Pages., Http://Iisee.Kenken.Go.Jp/Worldlist/21_Greece/21_Greece_Overall.Pdf.

F

Fakhri, F., Psomiadis, E. & Parcharidis, I. (2012) Monitoring Soil Deformation Using Persistent Scatters Interferometry (Psi) Technique: The Case Study Of Thessaly Prefecture (Central Greece). *Igarss* Munch, Germany, Ieee 3903.

Ferretti, A., Prati, C. & Rocca, F. (1999) Permanent Scatterers In Sar Interferometry. *Int. Geosci. Remote Sensing Symp.* Hamburg, Germany.

Ferretti, A., Prati, C. & Rocca, F. (2000) Non-Linear Subsidence Rate Estimation Using Permanent Scatterers In Differential Sar Interferometry *Ieee Trans. Geosci. Remote Sensing,* 38**,** 2202–2212.

Ferretti, A., Prati, C. & Rocca, F. (2001) Permanent Scatterers In Sar Interferometry. *Ieee Transactions On Geoscience And Remote Sensing,* 39(1)**,** 8-20.

Fletcher, K. (2007) *Insar Principles: Guidelines For Sar Interferometry Processing And Interpretation.* , Insar Principles: Guidelines For Sar Interferometry Processing And Interpretation.

Free Encyclopedia (2012) Thessaly Prefecture. *Http://En.Wikipedia.Org/Wiki/Thessaly/References, Www.Google.Gr*

Fruneau, B., Deffontaines, B., Rudant, J. P., Parmentier, A. M. L., Colesanti, C., Mouelic, S. L., Carnec, C. & Ferretti, A. (2003) Conventional And Ps Differential Sar Interferometry For Monitoring Vertical Deformation Due To Water Pumping The Haussmann-St-Lazare Case Example *Fringe Workshop* Frascati, Italy

G

Gamma Remote Sensing (2008) Documentation – User's Guide , Differential Inteferometry And Geocoding Software – Diff&Geo. 1.2 Ed. Worbstrasse 255, Ch -3073 Gumligen, Switzerland, Gamma Remote Sensing Ag

Gens, R. (2006) Phase Unwrapping Insar And Its Applications Geos 639 University Of Alaska.

H

Hanssen, R. F. (2001) *Radar Interferometry: Data Interpretation And Error Analysis*, Kluwer Academic Press, Dordrecht, The Netherlands

Hellenic National Meteorological Service Hnms, Http://Www.Hnms.Gr

Herrera, G., Fernández, J. A., Tomás, R., Cooksley, G. & Mulas, J. (2009) Advanced Interpretation Of Subsidence In Murcia (Se Spain) Using A-Dinsar Data —Modelling And Validation *Natural Hazards And Earth System Sciences* 9(3) 647–661.

I

Institute Of Geodynamics National Observatory Of Athens. Http://Www.Gein.Noa.Gr/En/Seismicity/Earthquake-Catalogs.

Institute Of Soil Mapping And Classification Of Larissa National Agricultural Research **Foundation (Nagref). Http://Www.Ismc.Gr.**

J

Jones, L. D. & Jefferson, I. (2011) Expansive Soils. In: Institution Of Civil Engineers Manuals Series. . Http://Nora.Nerc.Ac.Uk/17002/1/C5_Expansive_Soils_Oct.Pdf.

K

Kontogianni, V., Pytharouli, S. & Stiros, S. (2007) Ground Subsidence, Quaternary Faults And Vulnerability Of Utilities And Transportation Networks In Thessaly, Greece. *Environmental Geology,* 52(6) 1085–1095.

L

Lagios, E. (2007) Long Term and Seasonal Ground Deformation Monitoring Of Larissa Plain (Central Greece) By Ps Insar. *Initial Interpretation Report Prepared For Esa Gmes: Terrafirma* National And Kapodistrian University Of Athens, School Of Science, Faculty Of Geology And Geoenviroment, Department Of Geophysics And Geothermic. .

Li, Z. & Bethel, J. (2008) Image Coregistration In Sar Interferometry The International Archives Of The Photogrammetry. *Remote Sensing And Spatial Information Sciences* Xxxvii. Part B1. Beijing

Loukas, A., Mylopoulos, N. & Vasiliades, L. (2007) A Modeling System For The Evaluation Of Water Resources Management Strategies In Thessaly, Greece. . *Water Resources Manage,* 21 1673 –1702.

Loukas, A. & Vasiliades, L. (2004) Probabilistic Analysis Of Drought Spatiotemporal Characteristics In Thessaly Region, Greece *Natural Hazards And Earth System Sciences,* 4(5–6) 719–731.

M

Mahleras, A., Kontogianni, A. & Skourtos, M. (2007) Pinios River Basin – Greece (Deliverable D34) *Subtitle Report Status Report.* Aqua Money.

Manunta, M. (2009) New Advances In Multi-Temporal Differential Sar Interferometry For Full Resolution Data Analysis. *Electrical and Electronic Engineering.* University Of Cagliari

Massonnet, D. & Feigl, K. (1998) Radar Interferometry And Its Application To Changes In The Earth's Surface. *Geophysical Radar Interferometry Reviews Of Geophysics* 36**,** 441–500.

Matsuoka, M. & Yamazaki, F. (2000) Use Of Interferometric Satellite Sar For Earthquake Damage Detection *Proc. Of 6th International Conference On Seismic Zonation, Eeri.*

Mokhtari, M. & Dehghani, M. (2012) Swell-Shrink Behaviour Of Expansive Soils Damage And Control *Electronic Journal Of Geotechnical Engineering (Ejge)* 17 2673-2682.

Mulas, J., Aragón, R., Martínez, M., Lambán, J., García-Arostegui, J. L., Fernández-Grillo, A. I., Hornero, J., Rodríguez, J. & Rodríguez, J. M. (2003) Geotechnical And Hydrological Analysis Of Land Subsidence In Murcia (Spain) *Rmz – Materials And Geoenvironment* 50(1) 249–252.

P

Papathanassiou, G. & Christaras, B. (2008) Geo-Engineering Assessment Of Liquefaction Hazard Of The Town Of Larissa, Central Greece. *Ii European Conference Of Iaeg, Cities And Their Underground Environment.* Madrid, Spain.

Parcharidis, I., Foumelis, M. & Katsafados, P. (2011) Seasonal Ground Deformation Monitoring Over Southern Larissa Plain (Central Greece) By Sar Interferometry *Environmental Earth Sciences* 2 497– 504.

Petralas, C., Pisinaras, V., Koltsida, K. & Tsihrintzis, V. A. (2005) The Hydrological Regime Of The East Basin Of Thessaly, Greece *9th International Conference On Environmental Science And Technology* Rhodes Island Greece.

R

Rosen, P. A., Hensley, S., Joughin, I. R., Fuk, K. L., Søren, N., Rodríguez, E. & Goldstein, R. (2000) Synthetic Aperture Radar Interferometry. *Proceedings Of The Ieee,* 88.

Rozos, D., Sideri, D., Loupasakis, C. & Apostolidis, E. (2010) Land Subsidence Due To Excessive Groundwater Withdrawal. A Case Study From Stavros - Farsala Site, West Thessaly. *12th International Congress* Patras Greece, Bulletin Of The Geological Society Of Greece.

S

Scharoo, R. & Visser, P. (1998) Precise Orbit Determination And Gravity Field Improvement For The Ers Satellites *Journal Of Geophysical Research* 103**,** 8113–8127.

Seymour, M. S. & Cumming, I. G. (1996) An Iterative Algorithm For Ers Baseline Estimation Ers Sar Interferometry *Fringe 96 Workshop* Zurich, Switzerland.

Sgouras, I. (1994) Relationship Of Calcareous Geological Substrate With The Properties Of Overburden Soil. *Department Of Land Improvement And Agricultural Engineering.* Agricultural University Of Athens,.

Sheng, Y., Wang, Y. G. L. & Rizos, C. (2009) Differential Radar Interferometry And Its Application In Monitoring Underground Coal Mining-Induced Subsidence In Gsem (Ed).

Soil Survey Staff (1998) *Keys To Soil Taxonomy* United States Department Of Agriculture Natural Resources Conservation Service, Eighth Edition.

Soil Survey Staff (1999) *Soil Taxonomy A Basic System Of Soil Classification For Making And Interpreting Soil Surveys* United States Department Of Agriculture Handbook Natural Resources Conservation Service. Number 436. 2nd Edition.

T

Tocher, D. (1958) Movement On Faults,. *http://Www.Iitk.Ac.In/Nicee/Wcee/Article/Vol.1_Session5_551.Pdf,* 11(5)**,** 551–564.

W

Wegmuller , U. & Werner, C. (1997) Gamma Sar Processor And Interferometry Software *3rd Ers Symposium- Abstracts And Papers.* Florence European Space Agency. All Rights Reserved.

Wegmuller, U., Werner, C., Strozzi, T. & Wiesmann, A. (2006) Application Of Sar Interferometric Techniques For Surface Deformation Monitoring. *3rd Iag / 12th Fig Symposium.* Baden

Wegmóller, U. (2005) Gamma Ipta Processing Example Luxemburg Gamma Technical Report 9-Nov.

Wegmóller, U., Werner, C., Strozzi, T. & Wiesmann, A. (2006) Application Of Sar Interferometric Techniques For Surface Deformation Monitoring *3rd Iag / 12th Fig Symposium, Baden.*

Werner, C., Wegmóller, U., Wiesmann, A. & Strozzi, T. (2003a) Interferometric Point Target Analysis With Jers-1 L-Band Sar Data. *Igarss'03.* Toulouse, France.

Werner, C. L., Wegmóller, U., Strozzi, T. & Wiesmann, A. (2003b) Interferometric Point Target Analysis For Deformation Mapping. *Igarss'03 Proceedings.* Toulouse, France.

Y

Yanjie, Z. & Veronique, V. (2004) Insar Coherence Estimation *Ieee Transactions On Geoscience And Remote Sensing,* 5**,** 3353 - 3355

Z

Zhang, Y. & Cheng, X. (2005) Application Of Srtm-Dem Based Two-Pass Sar Interferometry For Detecting Seismic Deformation On High-Altitude Rugged Terrain - A Case Study In Kokoxili Ms8.1 Earthquake, 2001. *Igarss.*

Zou, W., Li, Y., Li, Z. & Ding, X. (2009) Improvement Of The Accuracy Of Insar Image Co-Registration Based On Tie Points *A Review Sensors,* 9**,** 1259 -1281.

Appendixes

Appendix A

The properties of selected points' candidates

I.d	Candidate point number	Easting coordinate	Northing coordinate	Height (m)
1	68587	620213	4395095	67
2	168496	614596	4410160	245
3	69756	619944	4395242	67
4	67381	608562	4392235	120
5	166220	615985	4410060	392
6	166379	618507	4410660	303
7	95360	607965	4397079	104
8	95042	607993	4397024	101
9	96573	607932	4397251	115
10	29192	626988	4385096	75
11	29406	627094	4385251	73
12	29622	627114	4385362	75
13	41577	630404	4391007	61
14	140781	603959	4403255	450
15	41078	630246	4390808	62
16	41694	627727	4390444	67
17	41858	627396	4390438	67
18	41185	627112	4390120	65
19	35265	625901	4387423	75
20	34800	626225	4387269	73
21	33920	625692	4386767	73
22	165801	626871	4389797	69
23	168393	625824	4389544	72
24	170545	624743	4389380	72
25	185134	626075	4387330	72
26	184117	626051	4387455	75
27	189118	625755	4386791	73

Appendix B

The properties of selected points' candidates

I.d	Candidate point number	Easting coordinate	Northing coordinate	Height (m)
1	46536	623422	4391057	69
2	55991	618963	4392385	72
3	80781	619438	4397147	67
4	35637	628347	4388166	69
5	31580	630164	4386871	69
6	32889	631829	4387745	63
7	126115	600834	4400358	412
8	116381	610060	4400709	90
9	142796	616639	4406426	75
10	41227	607969	4385767	94
11	28093	614536	4381695	44
12	36831	615716	4385937	115
13	19557	626275	4380484	91
14	31912	622874	4385336	79
15	50363	619891	4391434	74
16	80751	619378	4397129	67
17	35184	628420	4387954	-11
18	32014	629831	4386966	69
19	29080	631686	4386109	68
20	26720	635084	4385747	61
21	106597	609904	4399122	89
22	144160	616696	4406672	78
23	41360	608132	4385849	95
24	127935	617310	4404408	62
25	38866	616005	4386835	99
26	220809	605551	4417730	608
27	171091	621295	4389956	72
28	166001	619198	4391268	73
29	225264	625955	4380840	91
30	202683	615637	4386248	122
31	185001	622154	4388118	80
32	163240	619279	4391693	75
33	221761	625817	4381391	89
34	204403	615852	4385922	115

Appendix C

The properties of selected points' candidates

I.d	Candidate point number	Easting coordinate	Northing coordinate	Height (m)
1	152562	611921	4406840	69
2	160425	611663	4408116	85
3	71921	610364	4393414	91
4	47756	617390	4390128	72
5	111583	618273	4402552	65
6	132614	615587	4399302	75
7	126619	612292	4401054	81